H.J. VERMEULEN

SAUPEC '98

PROCEEDINGS OF THE SEVENTH SOUTHERN AFRICAN UNIVERSITIES POWER ENGINEERING CONFERENCE 1998

Hosted by

DEPARTMENT OF ELECTRICAL AND ELECTRONIC ENGINEERING UNIVERSITY OF STELLENBOSCH

UNIVERSITEIT VAN STELLENBOSCH
UNIVERSITY OF STELLENBOSCH

20 - 21 JANUARY 1998

SAUPEC '98

SEVENTH SOUTHERN AFRICAN UNIVERSITIES POWER ENGINEERING CONFERENCE

20-21 JANUARY 1998

VENUE:

DEPARTMENT OF ELECTRICAL ENGINEERING BUILDING

UNIVERSITY OF STELLENBOSCH

SAUPEC NATIONAL COUNCIL

Prof A. Petroianu	University of Cape Town
Prof R.G. Harley	University of Natal (Durban)
Prof J.H.R. Enslin	University of Stellenbosch
Prof J.A. Ferreira	Rand Afrikaans University
Prof I.R. Jandrell	University of the Witwatersrand
Mr. J. Gosling	Eskom
Dr. R. Herman	University of Stellenbosch

SAUPEC '98 LOCAL ORGANISING COMMITEE

Dr. R. Herman	University of Stellenbosch - Convenor
Dr. J.P. Holtzhausen	University of Stellenbosch
Mrs. E. Enslin	University of Stellenbosch Short Course Administrator - Organisation

The valuable critique and hard work of the following members of the Papers Review Panel, who evaluated the completed papers presented in these proceedings, are gratefully acknowledged:

Prof. J.H.R Enslin
Dr. H.J. Vermeulen
Mr. C.C. Brozio
Dr. J.P. Holtzhausen
Dr. DuT. Mouton
Dr. M.J. Kamper
Prof. C.T. Gaunt
Mr J. du Preez
Dr. R. Herman

The organising committee wish to record their appreciation to the University of Stellenbosch and The Department of Electrical Engineering for the use of their facilities

---oooOOooo---

TUESDAY 20 JANUARY 1998

08:15 - 09:15 Tea/Coffee and Registration **E & E Engineering Bldg, Level 2**

09:15 - 09:30 Opening address **Auditorium**

09:30 - 10:15 Invited lecture: Dr. H. Einhorn **Auditorium**

Environment, Energy efficiency and Economics

10:15 - 10:45 Tea/Coffee

10:45 - 12:30 Session 1: POWER SYSTEMS **Auditorium**

Failure of power transformers with a view to the tap-changer problems
M.S.A. Minhas, J.P. Reynders, P.J. de Klerk 1

Survey and evaluation of harmonic current sources in terms of IEC 1000-3-2 (1995)
B. Fourie, G. Atkinson-Hope 5

Initial simulation and measurement of monopolar DC harmonic currents on the Cohora Bassa HVDC line
H.N. Holtzhausen, J.H.R. Enslin, A.C. Britten, H. Petersen, F. Venter 9

Evaluation of modelling techniques used to study the transient performance of an earth electrode
K.J. Nixon, I.R. Jandrell, J.M. van Coller 13

Conducted electromagnetic noise measurements and predictions for the Muldersvlei SVC
M. Botha, A.A. Burger, A.C. Britten 17

12:30 - 13:30 Lunch

13:30 - 15:00 Parallel Sessions 2 & 3:

2: MACHINES **Auditorium**

Model of a single-sided linear induction motor for propulsion of railway vehicles
F. Spencer, J.F. Gieras, J.T.J Mokoena 21

Performance calculations for a PM hybrid linear stepping motor by the finite element and reluctance network approach
R. Wang, J.F. Gieras 25

Performance calculation for a shaded-pole single-sided linear induction motor using symmetrical components
I.E Davidson, J.F. Gieras 29

Position sensorless control of a medium power traction reluctance synchronous machine
S.K. Jackson, M.J. Kamper 33

Development and testing of a linear synchronous motor with surface mounted permanent magnets
C.G. Jeans, A. Hansa, R.J. Cruise, C.F. Landy 37

3: POWER SYSTEMS **Lecture Room**

Usage of neural network techniques in condition monitoring applications in power generation environments
E.M.P. van Wyk 41
Resonant characteristics of a transmission line containing an inverter-based series compensator
B.S. Rigby, R.G. Harley 45
Remote metering via cellular telephone network, a viable option
D. McLeary, S. Schoombie 49
Steps toward automating the design of electrification schemes
T. Rajakanthan, A.S. Meyer, B. Dwolatzky 53
Transmission line options for application to the USE concept
R. Herman, B.J. Kundy 57

15:00 - 15:30 Tea/Coffee

15:30 - 17:00 Parallel Sessions 4 & 5 **4: MACHINES** **Lecture Room**

A visually interactive paradigm for the simulation of drives as a pre- and post-processor to CASED
A.G. Levin, C.F. Landy, A.R. Clark 61
Design considerations of linear motor hoists for underground mining operations
R.J. Cruise, C.F. Landy 65
Modelling and simulation of a two-pole "written pole" synchronous motor using CASED
H.G. Acar, C.F. Landy 69
Small scale maglev system with permanent magnets and linear induction motor
Y.W. Tung, J.F. Gieras 73
Small scale maglev system with a V-shaped transverse flux linear induction motor
Y. Chin, J.F. Gieras, J.T.J. Mokoena 77

5: POWER SYSTEMS **Auditorium**

Frequency response of capacitive voltage transformers and insulated current transformers
H.J. Vermeulen, A.C. Britten, M.W. Roberts, J.M. Strauss 81
Impulse response of high voltage capacitive voltage transformers and insulated current transformers
H.J. Vermeulen, A.C. Britten, M.W. Roberts, J.M. Strauss 85
Comparison of excitation methods for power transformer frequency response measurement
C.C. Brozio, J.J. Germishuisen, H.J. Vermeulen, K.J. Cornelissen 89
Computer-aided formulation of network equations in symbolic format, Part I: network functions
C.C. Brozio, H.J. Vermeulen 93
Computer-aided formulation of network equations in symbolic format, Part II: State-space representation
H.J. Vermeulen, C.C. Brozio 97

TUESDAY 21 JANUARY 1998

08:00 - 08:30 Tea/Coffee

08:30 - 10:15 Parallel Sessions 6 & 7:

6: ENERGY USAGE & APPLICATION — Auditorium

Water heater population behaviour under behaviour under centralised control
C.J. Jooste, G.J. Delport, G.L. van Harmelen 101

An analytical model for the statistical description of system level demand characteristics in aid of DSM inspired load control schemes
G.L. van Harmelen, G.J. Delport 105

Preliminary practical results and basic interpretations of modulation notch testing
R. Lourens, G.J. Delport 109

Peak demand control in commercial buildings with direct temperature feedback
A.J. Hoffman 113

Load data preparation for losses estimation
R.L. Sellick, C.T. Gaunt 117

7: POWER SYSTEMS — Lecture Room

A computer model predicting induced voltages on conductors lying in non-ferromagnetic conduit carrying partial lightning impulse current
G.J. Walliser, I.R. Jandrell, J.M. van Coller 121

Investigating the usefulness of Czarnecki's and Slonim's distortion power definitions in identifying sources of distortion.
A.P.J. Rens, M. J. Case 125

Compaction technology: High phase order transmission in the South African context
J. Bortnik, J. P. Reynders 131

Testing of demodulation based frequency estimation algorithm for emergency control in power systems.
A. Pistalovic, R. Zivanovic 135

The importance of structural stability in power systems.
R. Fetea, A. Petroianu 139

10:15 - 10:45 Tea/Coffee

10:45 - 12:30 Parallel Sessions 8 & 9

8: HIGH VOLTAGE — Auditorium

Mechanisms associated with transient earth faults on a 275 kV transmission line: Field data and initial experimental data.
P. V. Taylor. D.A. Hoch 143

The impact of corona ageing on the surface and subsurface layers of silicone rubber insulation.
S.M. Reynders, J. P. Reynders, I. R. Jandrell 147

Corona and sustained arcing on conventional and novel non-ceramic insulator designs.
K. J. Nixon, J. P. Reynders, R. J. Hill 151
Environmental profile for Koeberg insulator pollution test station (KIPTS).
L. van Wyk, W.L. Vosloo, J.P. Holtzhausen 155
A unified approach to AC insulator flashover models. Part I: DC models adapted for AC.
J.P. Holtzhausen, D.A. Swift, F.S. van der Merwe 159
A unified approach to AC insulator flashover models. Part II: AC reignition models, compared to DC models.
J.P. Holtzhausen, D.A. Swift, F.S. van der Merwe 163

9: ENERGY USAGE & APPLICATION Lecture Room

A process control system for a tyre curing press.
A. Retief, T. van Niekerk 167
An investigation of flicker emission prediction techniques for crushers in power systems.
M.Y. Martin, H.S. Mostert, G. Atkinson-Hope 171
Solar pumped water storage system for electricity generation in rural areas.
O.D. Dintchev, A.S. Meyer 175
A microcontroller-based data acquisition and monitoring system for factory applications.
F. Adlam, T.I. van Niekerk, H. Vermeulen 179
Scheduling of cogeneration systems in response to real time pricing.
H.M. Pretorius, G.J. Delport 183
The feasibility of variable speed drives for air-coold heat exchangers with respect to energy consumption and performance.
F. Endrejat, G.J. Delport, H.R. van Niekerk 187

12:30 - 13:30 Lunch

13:30 - 15:00 Parallel Sessions 10 & 11

10: HIGH VOLTAGE Lecture Room

AC and negative lightning impulse voltage breakdown characteristics of gas mixtures in a coaxial cylinder gap.
M. Zhou, J.P. Reynders 191
Corona noise as a measure of corona power loss on single conductors.
J.P. Reynders, M.S. Engelbrecht 195
Neural network recognition of partial discharge signals.
A.J. Hoffman, C.J.A. Tollig 199
Interpretation of PD data for rotating machines.
P.P. Marx 203
Fire-induced corona on power lines.
A.C. Britten, C.R. Evert, D.A. Swift 207
Partial discharge results from a point in air obtained under impulse voltage conditions using an improved experimental set up.
S. D. Nielsen, J.P. Reynders 211

11: MACHINES **Auditorium**

A continuously online trained artificial neural network controller for a micro-turbogenerator.
G.K. Venayagamoorthy, R.G. Harley 215
A low cost, high performance PC based integrated real-time motion Control development system.
A.W. Stylo 219
Test bed system to evaluate the efficiency of variable speed drives under varying load conditions.
M.L. Walker, G. Diana 223
A method of increasing eccentricity harmonic accuracy as applied to sensorless speed detection of an induction motor.
P.S. Somaroo, B. Burton, R.G Harley 227
Practical implementation of a paper rewinder.
B.D. van Blerk, G. Diana 231

15:15 - 15:30 Tea/Coffee

15:30 - 16:45 **Session 12: POWER ELECTRONICS** **Auditorium**

An improved controller for an IGBT inverter forming part of a voltage dip test bed.
A.K. Keus, J.M. van Coller, R.G. Koch 235
An active turn-off snubber for IGBT converters.
H. du T. Mouton, J.H.R. Enslin 239
Control of a simulated single-phase to three phase converter.
E.N. Tshivhilinge, M. Malengret 243
Neural network controlled boost rectifier.
C.A. Worthmann, G. Diana 247

16:45 - 17:00 Closing session **Auditorium**

FAILURE OF POWER TRANSFORMERS WITH A VIEW TO THE TAP-CHANGER PROBLEMS

M S A Minhas J P Reynders
Department of Electrical Engineering
University of the Witwatersrand
Private Bag 3, WITS, 2050, South Africa

P J De Klerk
Eskom - Technology Group (Electrical Technology)
Private Bag 40175
Cleveland 2022, South Africa

Abstract: The results of a study to investigate the most frequent failure causes in large power transformers have been presented in this paper. It has been observed that 25% of the total failures of power transformers are initiated by failures of the tap-changers and regulating windings. In smaller transformers (<100MVA), the failures due to tap-changer problems are more frequent in the later life while in the bigger transformers (>100MVA) the failure rate is relatively higher in early service life.

Keywords: transformer, tap-changer, regulating winding, internal oscillations, power system transients

1 INTRODUCTION

A failure or unscheduled shut down of a power transformer is an extremely damaging event for a power system. The cost involved is not only the replacement/repair cost of the transformer and related switchgear but also the cost of the undelivered electricity.

Tap-changer problems play a very significant role in the failure of the large power transformers. This can produce unbalanced currents and may result in tripping and isolation of the transformer, disturbing the system stability, causing further damage to the tap-changer itself or complete damage to the regulating winding of the transformer. In some cases, the damage is so severe that it can destroy the whole transformer.

The function of a tap-changer is to alter the transformer ratio to control the voltage at the different nodes in the network. To achieve this function, a tap-changer can be situated on any winding of a transformer but generally they are on the high voltage side.

The tap-changer consists of moving and fixed contacts and diverter switches. The function of the diverter switch is to switch the load current in the event of tap selection. The selector switch contacts do not switch the current but operate to change the tapping under no load or in some cases, move while carrying the current.

In practice, tap-changers quite often appear to be the source of failure of the transformer [1]. The usual causes are mostly ageing and increase in the contact resistance [1].

The failure of tap-changers can be classified as:

1. Mechanical system initiated failures
2. Electrically initiated failures.

In some cases, the mechanical contact driving system leads to the failure. During a tap-changing operation, transition of contacts from one tap position to another may not be achieved if the mechanical system is faulty. The operation may lead either to a loose or hardly any connection. Loose connections result in overheating, sparking and erosion of the tap-changer contacts. Bad bearings in a tap-changer mechanism overload the driving motors and tripping of motor during operation can result in a failure of the tap-changer and transformer.

The electrical failure of the tap-changers initiated by the increase in contact resistance. This gives raise to overheating, sparking and sticking of the contacts. The contacts get welded and breaking of components occurs. Figure 2 shows the failure of the tap-changer when the contact was loose. The overheating initiated a sparking and production of severe heat. The contact plate was plated with the vaporised metal of the contacts and connecting leads.

In some utilities, a regular (periodic) inspection and maintenance program is followed to keep the tap-changers in working condition. Some utilities advise the operation of the tap changer to its full tap limits at least once a year [4].

When a transient strikes a transformer, it can trigger internal oscillations or resonance. These oscillations can grow after being reflected from the discontinuities (tap-changer or earth connection). These high electric

stresses can cause failure to the tap-changer or winding [2,3].

A study has been conducted to determine the most dominant modes of transformer failures. More than 1200 maintenance records were studied and investigated and 150 failures were recorded. The rest of them were routine maintenance reports.

2 INVESTIGATION PROCEDURE

In this study, the data was in the form of repair records at the repair facility of Eskom. The records consisted of damage reports, repair plans/diagrams and photographs of the parts needed to be repaired. Background information, where available, was also collected and analysed. The main objective of the study is to determine the most frequent type of failure in the early years of transformer life and the most common faults that may occur in the later years of transformer life. This information will enable utilities to refine maintenance plans for large transformers, which are the most critical and expensive components in their networks [4].

2.1 Definition of failure

A failure has been defined to be an unplanned shut down which requires extensive repair in the field or in a repair facility. Planned preventive or predictive maintenance has not been considered as failure.

Under this definition four different classes of failure has been defined [1,2]. These classes are:

1. Lightning switching surge failures (Lt/Sw)
2. Failures due to ageing of the oil and paper insulation (Ageing)
3. Core problems leading to the failure of the transformer (Core)
4. Tap-changer initiated failures (TC)
5. Others include bushing failures, tank problems, through fault failures, design and handling problems etc (Other)

A total of 150 failures recorded. Figure 1 shows the number of failures on a yearly basis. Only the tap-changer failures are discussed in this paper.

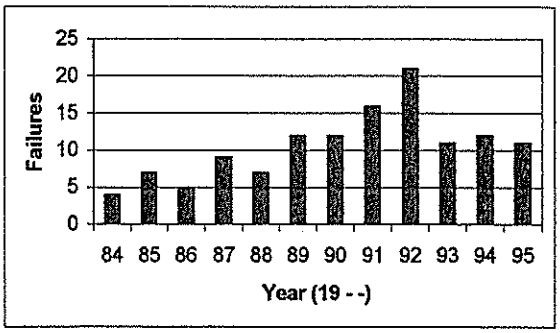

Fig 1: Failures of large power transformers on a yearly basis.

3 RESULTS

The results of the study are shown in Table 1 and the graphical representation in percentage of total failure given in Fig 3.

Failure mode	>100 MVA	<100 MVA	Total
Ageing	24	12	36
Core	15	11	26
Lt/Sw	13	14	27
TC	25	12	37
Other	13	11	24
		Total	150

Table 1. Failure modes of transformers

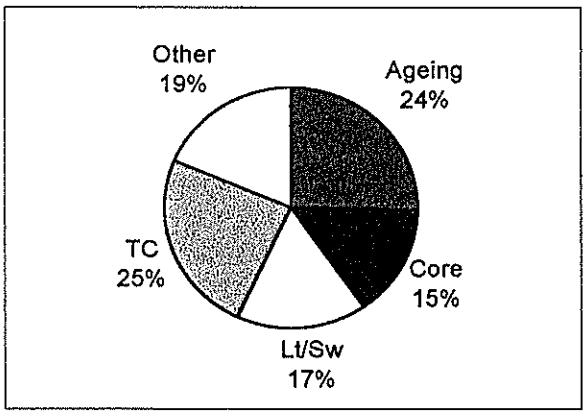

Fig 3: Distribution of different failure modes

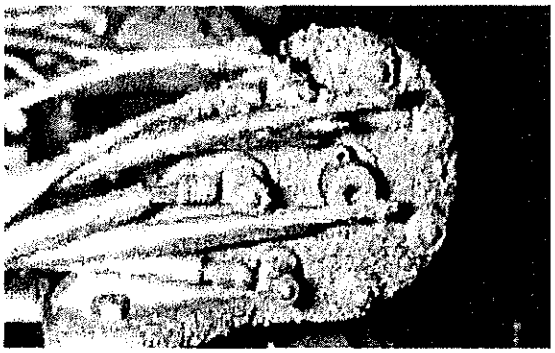

Fig 2: A typical example of tap-changer failure. Due to overheating the contact plate has been plated by the vaporised metal

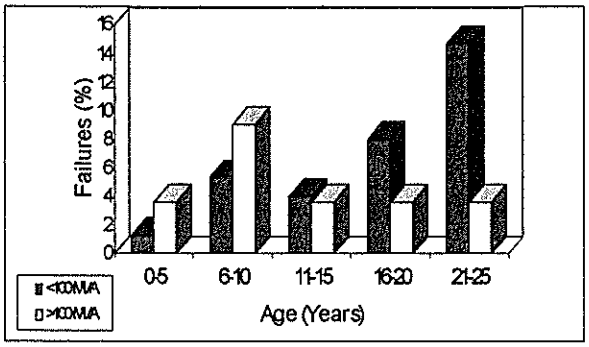

Fig 4: Tap-changer failures vs. the age of transformers

The data has been divided into two classes of >100MVA and <100MVA. Figure 3 shows the contribution of the tap-changers to the failure is highest among all the failure modes and the maximum number of failures have been recorded in small size transformers of <100MVA.

The failures in smaller transformers are more frequent in the later part of their service life. In class >100MVA the trend is opposite (Fig 4) and failure are more frequent in relatively early life.

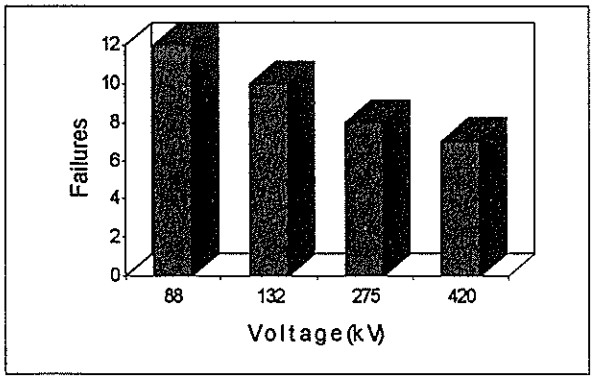

Fig 5. Tap-changer failure vs. the voltage rating of the power transformers

No obvious relationship of tap-changer initiated failures have been found with the voltage rating of the power transformers. Fig 5 shows that maximum number of failures have been recorded for 88kV voltage rating of the transformers which are in fact, the older transformers and the failure rate can be attributed to the age of the transformers.

4 DISCUSSION

A lot of failures of high voltage power transformers are caused by the maloperation of the tap-changers [1,2,3]. The cause of the failure is usually ageing of the contacts of the selector and diverter switch [1]. The ageing usually manifests itself in the form of carbon deposits (Fig 6) on the selector and diverter switch from decomposition of the oil. The carbon deposit increases the contact resistance and causes an increase in temperature of the contacts and accelerates the further decomposition of oil and build up of carbon. A growing increase in contact resistance leads to pitting of contacts and results in sparking and breaking of metallic contacts [1]. The arcs from rough contacts lead to further erosion of contacts and consequently a failure.

The failures due to tap-changers in the <100MVA class is due to age of the transformers which have been in service for a longer period compared to the larger transformers.

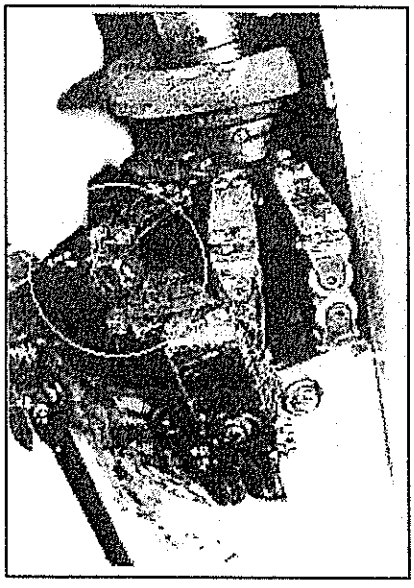

Fig 6: Deposit of carbon and overheating of the contacts of an on-load tap-changer

Transformer oil contains some sulphur. The sulphur reacts with the silver plated contacts and makes a high resistance compound AgS which increases the contact resistance. During a laboratory experiment, a

remarkable increase in contact resistance in a few hours was observed when silver plated contacts were subjected to the 70°C of oil temperature and rated current [4]

5 SUGGESTED MONITORING TECHINIQUES

To ensure the health of the tap-changer, periodic measurement of contact resistance of the contacts is the obvious solution. This is extremely difficult and time consuming.

At KEMA a technique to measure the contact resistance of all the contacts in a period of a few minutes has been developed. This technique is simple but can provide a valuable information about the health of tap-changer contacts [1].

Another very simple yet effective technique is on-line monitoring of differential temperature of the tap-changer compartment and main transformer tank which can give a reasonable idea of the overheating of contacts and can give an early warning when maintenance is necessary.

6 CONCLUSION

Tap-changer problems are more frequent in the later life of the power transformers and are not strongly related to the voltage rating. In larger transformers, the trend is opposite and more failures are recorded in the early service life.

Most of the failures occur due to the increase of contact resistance and overheating of the contacts which further increase the building-up carbon on the contacts.

A visual inspection to ensure the condition of the contacts is very expensive and time consuming.

Differential temperature measurements offer an on-line monitoring technique for tap-changer condition.

References

[1] H F A Verhaart "A diagnostic to determine the condition of the contacts of the tap-changer in a power transformer" 13th International Conference on Electricity Distribution, CIRED, Brussels (1995), paper 1.13

[2] MSA Minhas, PJ de Klerk and JP Reynders "A study of Failure Modes of Large Power System Transformers" 10th International Symposium on High Voltage Engineering, Montreal, Canada August 1997, paper 3517

[3] MSA Minhas, PJ de Klerk and JP Reynders "Failure Modes of Large Power Transformers" Cigrè International Conference on Large Electrical Systems, Cairo, Egypt 27-30 September 1997 paper III-207

[4] C Kroon " Large generator transformers" Cigrè 26 August-1st September 1990, paper 12-208

Contact:

MSA Minhas
Department of Electrical Engineering
University of the Witwatersrand
Private Bag: X3, WITS 2050,
Johannesburg
South Africa
email: minhas@odie.ee.wits.ac.za

SURVEY AND EVALUATION OF HARMONIC CURRENT SOURCES IN TERMS OF IEC 1 000 - 3 -2 (1995)

B. Fourie & G. Atkinson-Hope,
School of Electrical Engineering, Cape Technikon

ABSTRACT

In this paper harmonic measurements were conducted on equipment having an input line current 16 A or less per phase. The measurements have been evaluated in terms of the IEC 1000-3-2 standard which prescribes limits for individual harmonic current components . It further provides that for the purpose of harmonic current limitation equipment is differentiated into a particular class with specific limits which may not be exceeded. A survey was conducted enabling classification of equipment into the four prescribed classes so that the full standard could be applied. The purpose of the survey and the application of the standard was to determine whether equipment being used in South Africa or exported from South Africa to Europe complies with the IEC Standard which is internationally recognised.

1. INTRODUCTION

Harmonics are sinusoidal voltages or currents having frequencies that are multiples of the frequency at which the power supply system operates.

Harmonics are created by non linear loads termed harmonic sources. These sources generate harmonic currents even if the applied voltage to a source is sinusoidal. These currents flow back into the system and if severe enough cause voltages to be distorted.

The presence of harmonics in low voltage electrical power supply systems has been recognised for many years. It is only recently that AC Electrical distribution systems are being used to supply such increasing amounts of non linear loads, that the problem of harmonics has escalated to such an extent and is reaching an uncontrollable situation.

It is therefore for this reason that the standardisation committees are now striving towards the reduction of current harmonics injected into low voltage distribution networks by connected consumer equipment by means of prescribed limits as laid out in the IEC 1000-3-2 Standard [1].

In South Africa (SA) the new NRS 048 standard controls quality of supply [2]. It controls voltage distortion only. No provision is made for current harmonics. The European IEC-1000 series controls both voltage and current distortion [3].

Should SA manufacturers be developing equipment for the European market then they need to be aware of these standards. Equipment imported from Europe into SA and which meets the IEC current standards will insure that the local NRS 048 voltage standard should not be exceeded.

In this paper only the IEC 1000-3-2 standard will be used to evaluate the compliance of equipment with a line input of 16 A or less.

2. IEC 1000-3-2 STANDARD

The standard provides for the classification of equipment into specific classes. Each class prescribes limits which are used to evaluate distortion compliance. Equipment is classified as follows :

(a) Class A : Balanced 3 phase equipment and all other equipment, except that stated in one of the other classes.

(b) Class B : Portable Tools - e.g. Electronic drilling machine, welding machine etc.

(c) Class C : Lighting equipment including dimming devices.

(d) Class D : Equipment having an input current with a "special wave shape" as defined in Fig. 1 and an active input power, $P \leq 600$ W. Equipment shall be deemed to be Class D if under test conditions the shape of each half - period is within the envelope given in Fig. 1 for at least 95% of the duration of each half - period.

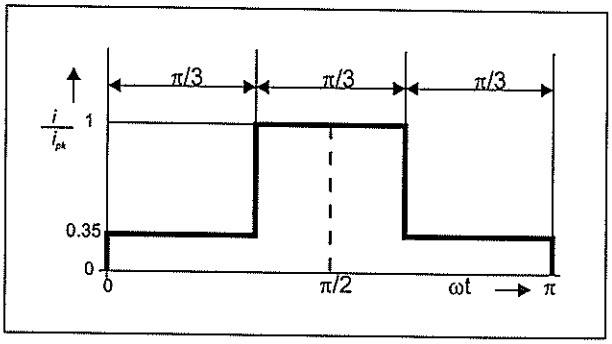

Figure 1 - Envelope defining "special wave shape"

(a) Limits for Class A Equipment :
For Class A equipment the harmonics of the input current shall not exceed the maximum permissible current values given in Table 1. Separate limits are provided for odd (up to 39th) and even (up to 40th) harmonics.

(b) Limits for Class B Equipment :
For Class B equipment, the harmonics of the input current shall not exceed the maximum permissible current values given in Table 1. These values are the product of the Class A limits multiplied by a factor of 1.5 .

(c) Limits for Class C Equipment
The harmonic current limits of lighting equipment shall not exceed the relative limits given in Table 1. These differ from Class A in that the harmonic current is expressed as a percentage of the input current at the fundamental frequency. The harmonic currents of independant dimming devices shall also not exceed the percentage values shown in Table 1. Limits are prescribed mainly for odd harmonics (up to 39th) although a limit is given for the second harmonic.

(d) Limits for Class D Equipment
The limits of harmonic current for Class D equipment shall not exceed the values shown in Table 1. Two limits are specified, milliAmperes/Watt (mA/W) and Amperes (A).

3. ANALYSIS

(a) CLASS A EQUIPMENT

In this class of equipment numerous Variable Speed Drives (VSD's) were tested. For the purpose of this paper only the results of testing done on a 7.5 kW 6-pulse diode input VSD are illustrated. From the survey on VSD's this 7.5 kW VSD was found to exceed the prescribed limits for harmonic currents more than the smaller VSD's tested.

As can be seen by the Harmonic Spectrum in Fig. 2, this Class A equipment does not comply with the prescribed limits as laid down by the IEC 1000-3-2. When compared with the limits shown in Table 1, it is evident that the 5th, 7th, 11th, 13th harmonic currents are higher than the maximum values permitted. The above harmonics are characteristic of a 6-pulse VSD.

It must be mentioned that the 7.5 kW VSD appears lightly loaded due to the fact that it is only supplying a 5 kW motor. The motor is driving the load through a large reduction gearbox hence the low line current. The above test was conducted in the actual work situation in the manner prescribed by the standard. The test requirements were that the equipment be tested at its rated voltage under normal operating conditions.

The other VSD's evaluated displayed a similar tendency although due to their lower line current they complied with the maximum permissible harmonic current limits.

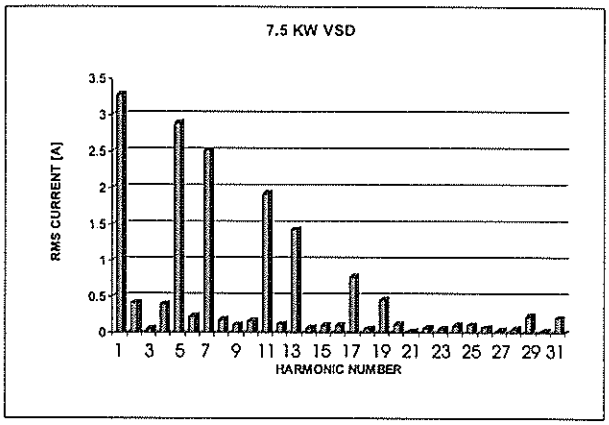

Figure 2 - Harmonic spectrum of a 7.5 kW VSD

(b) CLASS B EQUIPMENT

Numerous types of Class B equipment were tested. These included an electronic drilling machine, portable DC welding machine and an angle grinder amongst others. All equipment tested in this class complied with the standard with regard to the magnitude of their individual harmonic currents. As can be seen from the harmonic spectra shown below in Fig. 3 (750 W Electronic drill) and Fig. 4 (880 W Rotary Hammer drill) this equipment type generated proportionally high third and fifth harmonic components. The portable equipment with electronic speed control caused more individual harmonic components to be generated. It appears that Class B equipment will more than likely comply with the limits of the standard.

TABLE 1 - PRESCRIBED LIMITS AS LAID DOWN BY THE IEC 1000-3-2

LARGEST ALLOWABLE HARMONIC CURRENT FOR THE FOUR CLASSES OF ELECTRICAL EQUIPMENT				
Class	A	B	C	D
Harmonic Order, n	All equipment except B,C & D amperes	Portable tools, amperes	Lights & dimmers ≥ 25W active input, % fundamental input current	Equipment with special wave shape and with ≥75W fundamental active input, mA/W (max. amperes)
Odd				
3	2.30	3.45	30λ*	3.4(2.30)
5	1.14	1.71	10	1.9(1.14)
7	0.77	1.155	7	1.0(0.77)
9	0.40	0.60	5	0.5(0.4)
11	0.33	0.495	3	0.35(0.33)
13	0.21	0.315	3	0.296(0.21)
15≤n≤39	2.25/n	3.375/n	3	3.85/n(2.25/n)
Even				
2	1.08	1.62	2	-
4	0.43	0.645	-	-
6	0.30	0.45	-	-
8≤n≤40	1.84/n	2.76/n	-	-

*λ is the circuit power factor

TABLE 2 - MEASURED VS MAXIMUM PERMISSIBLE CURRENT VALUES

HARMONIC ORDER n	CLASS A 7.5 kW VSD		CLASS B 750 W Electronic drill		CLASS C 600 W Light dimmer		CLASS D Personal computer	
	Measured Value [A]	Maximum Harmonic current [A]	Measured Value [A]	Maximum Harmonic current [A]	Measured Value %	Maximum % Harmonic current	Measured Value [A]	Maximum Harmonic current [A]
2	0.41	1.08	0.09	1.62	0.2	2	0.01	-
3	0.04	2.30	0.38	3.45	43.9	30xλ*	0.09	2.30
4	0.39	0.43	0.04	0.65	0.2	-	0.01	-
5	2.89	1.14	0.20	1.71	14.5	10	0.07	1.14
6	0.22	0.30	0.02	0.45	0.00	-	0.00	-
7	2.51	0.77	0.05	1.155	13.8	7	0.05	0.77
8	0.17	0.23	0.02	0.345	0.1	-	0.00	-
9	0.10	0.40	0.04	0.6	9.1	5	0.02	0.40
10	0.16	0.184	0.01	0.276	0.1	-	0.00	-
11	1.92	0.33	0.03	0.495	8.5	3	0.01	0.33
12	0.12	0.153	0.01	0.23	0.1	-	0.00	-
13	1.43	0.21	0.01	0.315	6.2	3	0.01	0.21

*λ is the circuit power factor

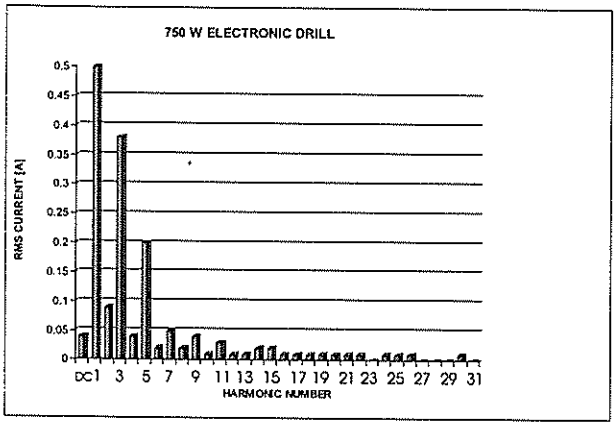

Figure 3 - Harmonic spectrum of an electronic drill

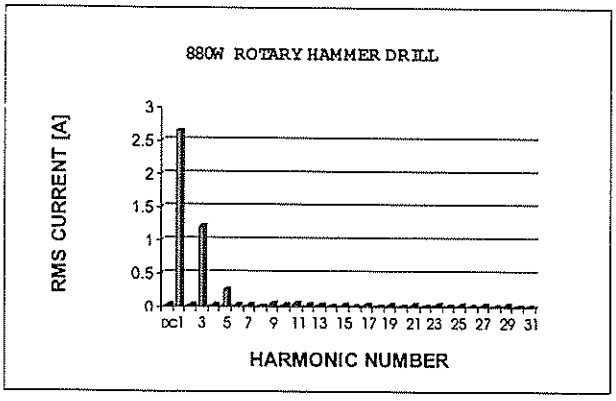

Figure 4 - Harmonic spectrum of a rotary hammer drill

(c) CLASS C EQUIPMENT

In this class, various types of lighting equipment were tested. This included testing a light dimming circuit under the specific test conditions laid down by the IEC 1000 - 3 - 2 standard. For the purpose of this paper the results of testing done on a 5ft fluorescent light fitting as well the results of testing done on a light dimmer circuit are shown below in Fig. 5 and Fig. 6. Both types failed to comply with the standard. In the case of the light fitting, the measured percentage harmonic current exceeded the prescribed limits for the 5th and 11th harmonics while complying with the rest. The light dimming circuit failed to comply with the standard as the measured percentage harmonic current exceeded the prescribed limits for all odd harmonic components. When assessing the results of the above tests one can therefore predict the impact an entire building's lighting load will have on the local low voltage distribution network

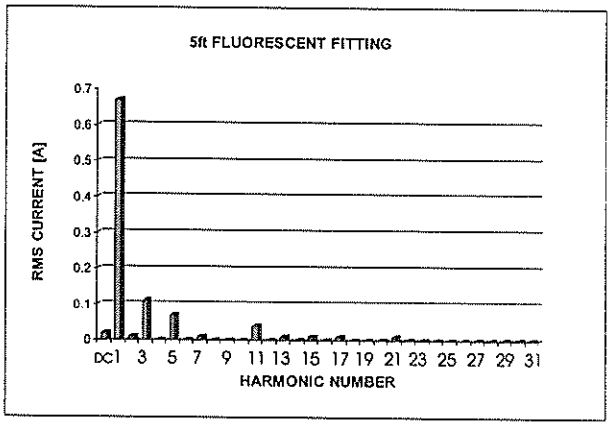

Figure 5 - Harmonic spectrum of a fluorescent fitting

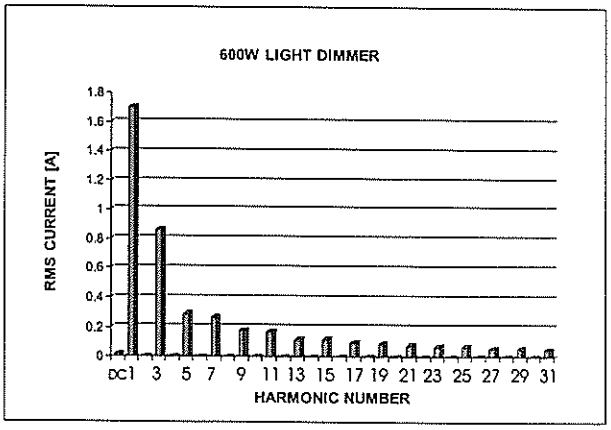

Figure 6 - Harmonic spectrum of a light dimmer

(d) CLASS D EQUIPMENT

Requirements for equipment to fall within this class is that it must have a wave shape typically similar to Figure 1 and have an active input power of less than 600 W. Personal computers (PC'S) use Switch Mode power supplies and generally take less than 600 W and have a wave shape similar to Figure 1. The wave shape of the PC in Figure 7 is clearly similar to that in Figure 1. As can be seen by the harmonic spectrum of the PC in Figure 8 , this equipment complies with the maximum permissible harmonic current limits for this class as shown in Table 2.

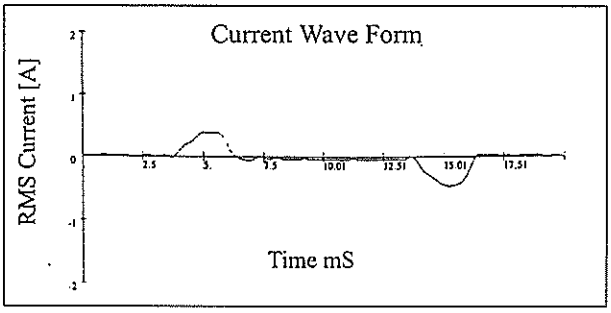

Figure 7 - Current wave form of a personal computer

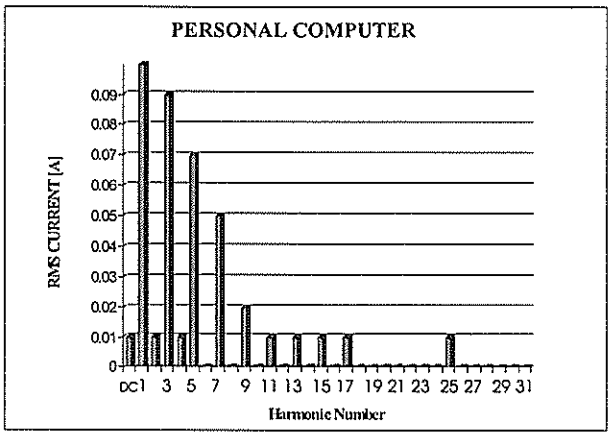

Figure 8 - Harmonic spectrum of a personal computer

4. CONCLUSION

It is evident from testing done on Class A equipment that it is the VSD's that have a tendency to exceed the prescribed limits. This is particular of the larger VSD's tested although small VSD's have high percentage values for the same harmonic components as the larger VSD's as well as many more higher order harmonic components. The small VSD's comply only by virtue of the fact that they have lower line currents, and hence the magnitudes of individual harmonic components are low enough to comply.

It is interesting to note that if the prescribed limits for Class A equipment were to be expressed in percentage values similar to Class C equipment, then many of the small VSD's would also fail to comply with the standard.

In testing done on Class B (portable tools) and Class D (personal computers), the equipment tested complied with the standard on an individual basis, but the impact of an entire building's lighting load or computer network will cause the individual harmonic components to increase dramatically.

The Class C (lighting , dimming equipment) also failed to comply with the prescribed limits of the standard. The light dimmer in particular did not comply with the standard for any of the odd percentage harmonic current values obtained. The cumulative effect of relatively common equipment such as lighting will certainly cause the problems normally associated with harmonics to occur.

As illustrated by the test results, only Class A and Class C equipment failed to comply with the IEC 1000-3-2 standard. It may therefore only be necessary in SA to implement a standard applicable to Class A and Class C equipment. The emphasis on limits expressed in percentage current values similar to Class C equipment as opposed to absolute current values thus ensuring that small VSD's are also forced to comply with the standard.

5. REFERENCES

[1] Electromagnetic Compatibility (EMC) - IEC 1000 Part 3 Limits - Section 2 Limits for Harmonic Current Emissions, 1995

[2] Electricity Supply - Quality of Supply Standards Part 2 : Minimum standards, NRS 048 - 2, 1996

[3] Atkinson-Hope G & Petroianu A - "Power System Harmonic Field Measurements and the Application of Standards Including Simulation", 7th IEEE International Conference on Power Quality and Harmonics, 1996

6. AUTHOR'S ADDRESSES

B. Fourie
17 Klein Welgemoed
Welgemoed
7530

G. Atkinson - Hope
School of Electrical Engineering
Cape Technikon
PO Box 652
Cape Town 8000

INITIAL SIMULATION AND MEASUREMENT OF MONOPOLAR DC HARMONIC CURRENTS ON THE CAHORA BASSA HVDC LINE.

H.N. Holtzhausen, J.H.R. Enslin, A.C. Britten, H. Petersen and F. Venter

FACTS Group, University of Stellenbosch TRI, Eskom Transmission, Eskom

Abstract: The Cahora Bassa line is presently being re-commissioned. In parallel with this process, the magnitude of the dc side current harmonics and the possible interference on adjacent telephone lines are also assessed. This paper considers some of the issues surrounding these harmonics, i.e. the source of the harmonics, their common and differential mode currents and the quantification of the disturbance. Preliminary monopolar line measurements and simulations are then presented. To end off, some discussions and reflections are made on the results and future work.

Keywords: psophometrically weighted current, equivalent disturbing current, dc harmonics, common and differential mode, EMTDC, interference, HVDC

1 INTRODUCTION

The Cahora Bassa HVDC line is currently being re-commissioned. Since the line was taken out of operation in 1985, rapid development in the telephone network has taken place near Apollo substation and Pretoria along the first section of the line. There is consequently some concern about the possible effect of the HVDC line's electromagnetic and electrostatic interference on existing and planned telephone networks. The presence of dc harmonic currents in the HVDC system may be a source of interference.

Figure 1 shows a representation of the Cahora Bassa line in monopolar operation. In this figure, "NBC" represents the in-station neutral bus capacitor. The electrode lines are each about 20 km in length and lead to the ground electrodes. The component blocks that fall within the dashed closed curves are physically located at the converter stations

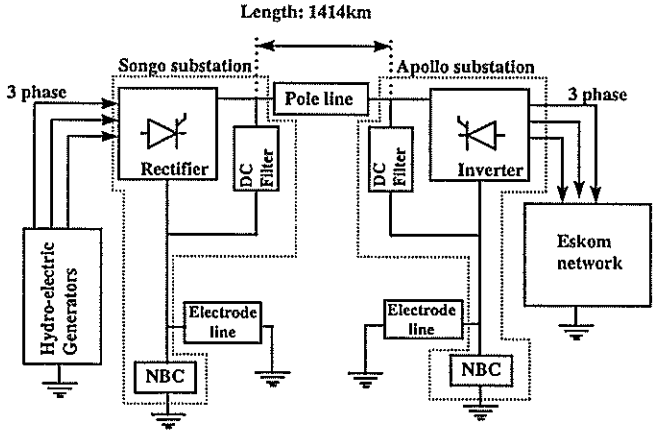

Figure 1: A diagrammatic half station representation of the Cahora Bassa HVDC scheme [6].

2 BACKGROUND

Harmonic Sources

The characteristic dc harmonic voltage generated by a six-pulse converter is of order 6.n (where n = 1,2,3....). The per pole converter at Apollo consists of four six-pulse bridges in series (see Figure 4). These four bridges may be divided into two pairs, where the two bridges of each pair have identical phase angles. There exists a phase difference of 30^{O} between the two pairs. With an equal number of the two differently "phased" bridges in series, complete cancellation of the odd numbered six-pulse harmonics (6n with n=1,3,5,...) will theoretically take place. In this way a twelve-pulse converter is formed.

Common and Differential mode

The above mentioned dc harmonic voltages lead to dc harmonic currents of the same order. Smaller non-characteristic current harmonics are also generated in the conversion from ac to dc. It is expected that their influence on interference will be negligible in the monopolar case, where all the current harmonics are common (ground) mode [2]. This will not be the case in the bipolar case, where common and differential (line) mode currents exist. The *interference* generated by the common mode currents (which consists of predominantly non-characteristic odd triplen frequencies) is usually much higher than those generated by differential mode currents. This is true to such an extent that the differential mode current is usually neglected in bipolar interference calculations[2].

Figure 2 shows a simplified representation of the bipolar and monopolar configurations with the differential and common mode current paths indicated. In-station ground return paths are ignored in this figure.

Quantification of Disturbance

This paper addresses the interference from the HVDC line harmonic side of the problem and the effect of these harmonics on the quality of telephone reception should therefore be determined. A weighting factor, the psophometric weighting, p_f, is consequently used to represent this effect as an function of frequency. The characteristics of the human ear and the response of the

telephone receiver play important roles in determining this index.

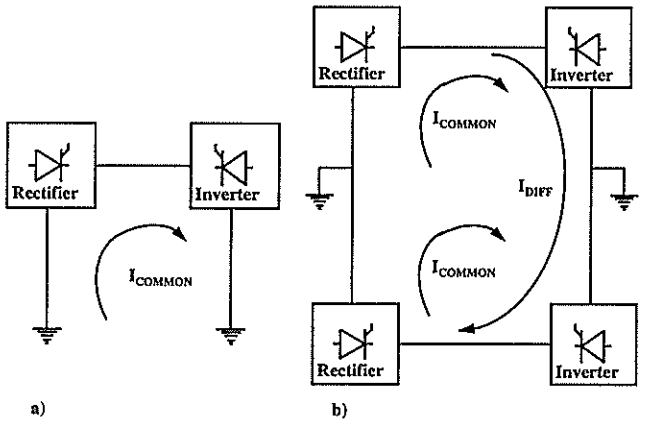

Figure 2: a) A simplified monopolar and b) bipolar HVDC operational mode shown with their common and differential mode currents[2].

Figure 3 shows the different psophometric weightings for the corresponding frequencies. The figure shows that the weighting of frequencies outside the range from 300 Hz to 3 kHz quickly become insignificant.

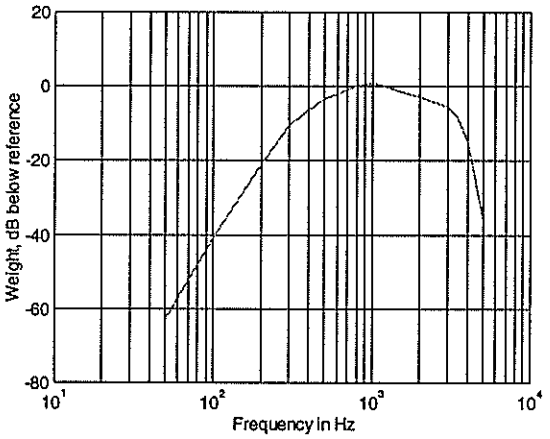

Figure 3: The C.C.I.T.T. psophometric weighting [1].

Two quantities, that use this weighting factor, p_f, are used in this paper. The first one is the equivalent disturbing current (I_{eq})[1].

$$I_{eq} = \sqrt{\sum_{f=0}^{\infty}\left(H_f p_f I_f\right)^2} \quad where \quad H_f = \frac{f}{800}, \qquad (1)$$

In this equation I_f is the rms current (A_{RMS}) and H_f the frequency dependant factor, all at frequency f. H_f represents the coupling with the telephone lines, with the assumption that this coupling is only dependent on the frequency of the harmonics. The other quantity is the psophometric current (I_{PS}):

$$I_{PS} = \sqrt{\sum_{f=0}^{\infty}\left(p_f I_f\right)^2}, \qquad (2)$$

In both equations p_f is the psophometric weighting divided by 1000.

The Passive dc Filters (DCF)

The per pole passive dc filter system (without the neutral bus capacitor) consists of a four frequency filter at 300, 600, 900 and 1200 Hz and a high pass filter, as is shown in Figure 4. In a recent investigation [3], it was found that the measured component values deviate less than 5% from the expected values shown in the Appendix. Passive filters only filter a limited range of frequencies and detuning or a deviation in the ac system's fundamental frequency, may consequently have an adverse effect on their performance (especially when the filters are narrowly tuned). Extensive tests with the complete system in operation are therefore necessary to determine whether additional filtering on the dc side will be necessary.

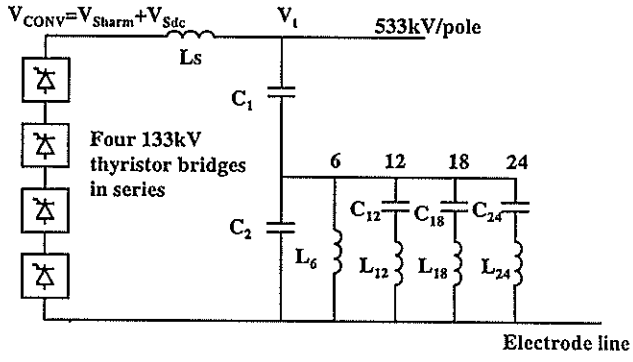

Figure 4: The per pole passive dc filters (DCF) [3].

3 MEASUREMENT SETUP

Figure 5 shows the measurement circuit that is presently being implemented at Apollo converter station. The voltage across a resistor (in series with the pole line) is measured using probes. This voltage signal, which is proportional to the line current, is then converted in the remote unit to an optical signal and is transmitted via the optical cable (about 100 m in length) to the processing area. The Nicolet ISOBE 3000 converts the optical signal back to an electrical signal, which then forms the input to the psophometer, selective voltmeter and oscilloscope. The *psophometer* is an analog instrument that performs a weighting operation similar to that in equation 1 or 2, on the measured current harmonics. When the termination of the instrument's output is inductive an output voltage proportional to I_{eq} is obtained, while a resistive termination results in a output equal to I_{PS}. The latter setting is used for the measurement results of section 5. The *selective voltmeter* is an analog device used to measure the voltage of a specific frequency.

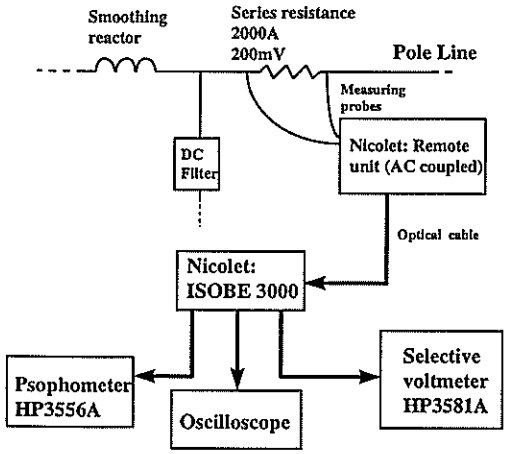

Figure 5: The Measurement circuit at Apollo converter station.

4 EMTDC SIMULATION

EMTDC is a simulation program most suitable for the simulation of high power applications[5].

The Three-pulse model

This model is used to represent the converter output of HVDC converter stations. It was developed to solve the discrepancy that was observed between measured and simulated HVDC dc side harmonics. The main reason for this discrepancy was found to be the coupling between the valve windings and ground in the converter transformers, due to stray capacitance [2].

For the purpose of this paper, a basic knowledge of this model will suffice. Figure 6 shows a six pulse converter using the Three-pulse model, as is used in later simulations. In this figure $U_{3p}(t)$ is the sum of the voltage across three thyristors, V_{6pulse} the six-pulse output voltage of the model, L_{AS} the inductance of the converter transformer, and C_{STRAY} the stray capacitance.

Simulation Implementation

Figure 7 shows the implementation of the monopolar HVDC system with only one of the six pulse bridges in operation. The parameters are given in the Appendix .

5 RESULTS

Figure 8, Table 1 and Table 2 summarise the results. In Table 1 the harmonic components were obtained from the selective voltmeter. The measured I_{PS} is the output of the psophometer, while the calculated value of I_{PS} is that obtained by substituting the harmonic components (shown in table 1) and the weighting factors of Figure 3 into equation 2. I_{eq} is calculated using equation 1 and indicates the prominence of the higher relative to the lower frequency components.

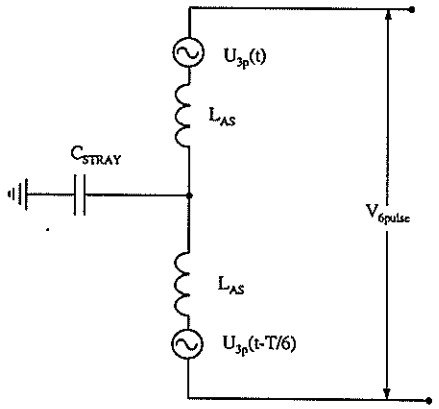

Figure 6: A six pulse bridge modelled, using the Three-pulse model[2]

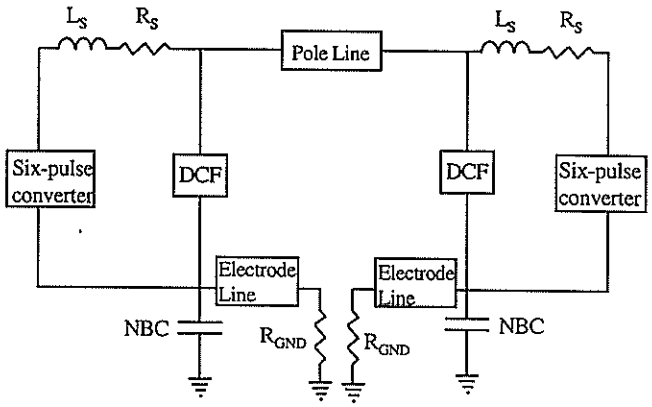

Figure 7: A Simulation representation of the Cahora Bassa line in monopolar operation.

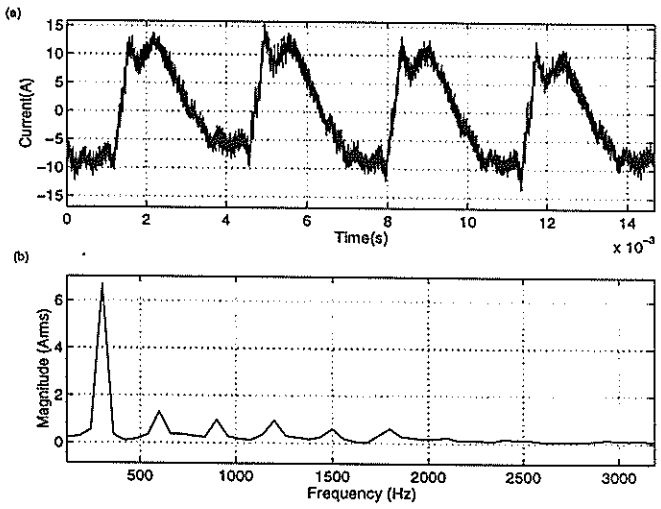

Figure 8: The measured harmonic line current of Trial M1 in a) the time and b) the frequency domain.

Table 1: The measured and simulated dc line harmonics.

	Measurement			Simulation	
	Trial M1	Trial M2	Trial M3	Trial S1	Trial S2
Passive filters in?	Yes	Yes	Yes	No	Yes
V_{dc} (kV)	121	109	123	145	145
I_{dc} (A)	370	430	380	285	285
Measured I_{PS}	2.80	1.75	1.50	1.60	1.09
I_{PS} (Calc)	2.62	1.60	1.49	-----	------
I_{eq}	2.70	2.26	1.28	0.90	0.69
Freq (Hz)	Amplitude (A_{RMS})				
300	6.00	4.00	4.00	5.00	3.41
600	1.50	0.70	0.90	0.54	0.22
900	0.80	0.15	0.35	0.22	0.18
1200	0.95	0.26	0.3	0.25	0.23
1500	0.70	0.48	0.11	0.19	0.16
1800	0.70	0.82	0.11	0.12	0.10
2100	0.30	0.50	0.20	0.06	0.07
2400	0.06	0.18	0.16	0.05	0.06
2700	0.15	0.12	0.35	0.06	0.07
3000	0.11	0.5	0.12	0.06	0.07

Table 2 shows the effect of the passive filter on the measured I_{PS} at three different power levels. One, two and three six-pulse bridges operation was used for the 500, 1000 and 1500 A current level respectively.

Table 2: Measured psophometric current (A) at three different power levels

dc current (A)	Passive filter in	Passive filter out	Attenuation (dB)
500	2.65	7.50	9.04
1000	2.50	4.50	5.10
1500	2.50	5.00	6.02

6 DISCUSSIONS

- ***Inconsistency in the measurements:*** There is a deviation in Table 1 between the I_{PS} of the similar trials M1 and M3. This may be explained through either the standing wave or beat frequency phenomena.
- ***Accuracy of the simulation model:*** The correlation between the measured and simulated results will be improved with more accurate line and converter model parameters.
- ***Effect of the passive filters:*** According to the results (in Table 1 and 2), the passive filters cause an attenuation of between 5 and 10 dB in I_{PS}. This attenuation is dependant on the magnitude of the two ac systems' frequencies. It was found that, without the passive filters, the harmonic inrush currents from the Songo station, and thus also of beat frequencies, disappeared.

7 CONCLUSION

More measurements are necessary to establish confidence in the results. Some measure of the passive filters' effectiveness was, however, obtained. Furthermore, more accurate line and converter model parameter estimation could improve simulation results. A possible limit for I_{eq}, may only be determined once a relation is found (through measurements) between the power line disturbance and the telephone line interference.

8 ACKNOWLEDGEMENTS

The authors thank Eskom for approval to present this work and Miles Roberts and Hein Pienaar of Eskom TRI for their assistance in the measurements conducted at Apollo substation.

9 APPENDIX: Parameters used in the simulation

Passive dc filter(DCF)

$C_1 = 0.15\ \mu F$ $R_{12} = 6\ \Omega$
$C_2 = 0.29\ \mu F$ $L_{18} = 1.0\ H$
$L_6 = 0.236\ H$ $C_{18} = 0.035\ \mu F$
$R_6 = 3\ \Omega$ $R_{18} = 12\ \Omega$
$L_{12} = 0.5314\ H$ $L_{24} = 1.0\ H$
$C_{12} = 0.3\ \mu F$ $C_{24} = 0.018\ \mu F$
$R_{24} = 12\ \Omega$

Other parameters:

$L_S = 0.83\ H$ $R_S = 0.1874\ \Omega$
$NBC = 3.25\ \mu F$ $R_{GND} = 0.0055\ \Omega$

Electrode and Pole line model [6]

Three-pulse model[2]:

$\alpha_{Apollo} = 16°$ $\mu_{Apollo} = \mu_{Songo} = 8°$
$\alpha_{Songo} = 18°$ $C_{STRAY} = 15nF$
$L_{AS} = 24mH$ $f_{Apollo} = f_{Songo} = 50\ Hz$
$U_{dio} = 80kV$

10 REFERENCES

[1] E.W. Kimbark, *Direct Current Transmission*, New York: Wiley-Interscience, 1971.

[2] Cigre Task Force 14.03.02, "DC Side Harmonics and Filtering in HVDC Transmission Systems." *Technical Brochure Ref. 92* , April 1995.

[3] H. Petersen, "DC filter tests at Apollo," Proceedings of the First Southern African Power Quality Conference, May 1997.

[4] A.C. Britten et al, "The Generation, Measurement and Suppression of Telephone Interference on the Cahora Bassa HVDC Transmission System," *Cigre Colloquium on HVDC*, Boston, 1985.

[5] "EMTDC version 3 Users' Manual," Manitoba HVDC Research centre, Winnepeg, Canada, 1988.

[6] K.L. Kent, "DC-side Harmonic Study of the Cahora Bassa HVDC scheme for Eskom," Manitoba Hydro, April 1996.

EVALUATION OF MODELLING TECHNIQUES USED TO STUDY THE TRANSIENT PERFORMANCE OF AN EARTH ELECTRODE

K J Nixon I R Jandrell J M Van Coller

Electric Power Research Group
Department of Electrical Engineering
University of the Witwatersrand
Private Bag 3, 2050 Johannesburg, South Africa

Correct earthing practices are essential, especially in South Africa where a large proportion of industry exists in areas of high lightning ground flash density. Current national standards go a long way to aid engineers and consultants designing and implementing lighting protection systems (LPS). However, some subtle but important implications are frequently misinterpreted or misunderstood. This paper investigates and evaluates different modelling techniques that can be used to study the transient performance of an earth electrode and demonstrate why certain practices are acceptable and others are not. Due to the high average soil resistivity in South Africa, it is essential that the modelling includes the non-linear effects caused by soil ionisation under transient conditions. The advantages and disadvantages of both theoretical and experimental modelling techniques are discussed. It is concluded that both techniques must be used, and careful attention must be paid to the inherent limitations of each.

Keywords: lightning transient, earth electrode, soil ionisation, equipotential platform, modelling.

1 BACKGROUND

The goal of lightning protection is to achieve site-wide immunity of equipment to lightning events. South African national standards for lighting protection are based on IEC standards and are comprehensive [[1],[2],[3],[4]]. The standards introduce the important concept of a lightning protection zone and of equipotentialisation. Key factors are the earth-termination system (earth electrode) and the practice of bonding and screening. In this regard, certain practices have been shown to be successful whereas others are known to cause problems. There is a need for a model that can be used to explain and verify this practical experience. The model can then be used to address bad practice caused by lack of understanding and promote equipotentialisation and bonding.

An earth electrode forms an important part of a lightning protection system and is the subject of this paper. In a companion paper, Walliser et. al. discuss the modelling and importance of screening [[5]].

2 INTRODUCTION

High soil resistivities and significant lightning activity in industrial areas make a thorough understanding of earth-termination systems essential in South Africa. This paper investigates the development of a model of an earth electrode. The principal processes determining the transient response of an earth electrode are studied as well as the modelling techniques normally used to describe the response. Particular emphasis is placed on achieving a model that predicts the overall behaviour of the entire (site-wide) earth-termination system, especially with interconnected buildings. Ways in which the validity and accuracy of the model could be tested are discussed.

3 EQUIPOTENTIAL PLATFORM

Due to the typically high soil resistivities (500-2000 Ωm [[6]]) found throughout the country focus has been placed on achieving a nett low value of earthing electrode resistance without due cognisance of the geometry or extent of the earth electrode The extreme case is the concept of a low resistance (< 1 Ω) "clean earth electrode" that is isolated from any other earth electrode. Just as important as achieving a low resistance to earth is the protection of equipment against damage caused by differential voltages. This is achieved by creating an equipotential platform for the equipment to operate on as described in NRS 042 [[4]].

If any signal or power cables run between two structures, it is essential to ensure that the earth termination systems of both structures are interconnected [[1],[4]]. This is an extension of the concept of an equipotential platform. The behaviour of two such interconnected building earths was investigated by Van Coller and Jandrell [[7]].

These concepts have been applied most successfully in a two year project on a 34 km^2 industrial site [[8]]. The site included HV, MV, LV and various signal systems. Overall emphasis was placed on bonding and the interconnection of earth-termination systems and not

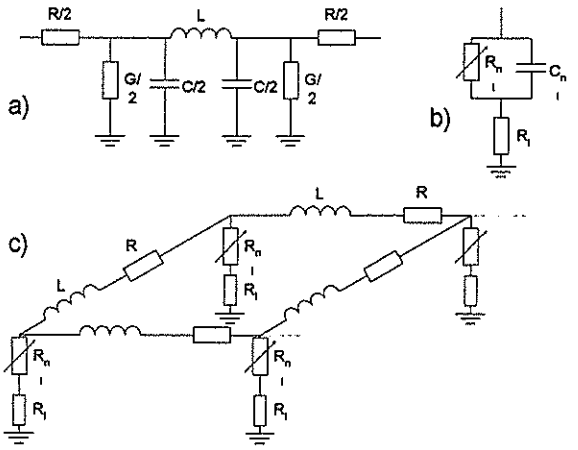

Figure 1. Various circuit models applied to earthing systems.
a) Lossless transmission line element.
b) Concentrated electrode (Kosztaluk)
c) Earthing grid electrode (Kosztaluk)

The advantage of lumped parameter modelling is that the current distribution within the earth electrode system can easily be obtained. However, the disadvantage is that if too few lumped elements are used, ringing effects result at high frequencies.

In order to include the effects of all the phenomena described in the previous section, the most versatile and accessible modelling technique for South African conditions appears to be the lumped parameter approach. However, the merits of other methods must not be forgotten, and for simple electrode geometries, transmission line theory combined with a soil ionisation model appears to supply valuable results.

A lumped parameter model therefore must be developed. This model will be implemented under EMTP and compared against a similar implementation within Matlab™ to identify any possible mathematical modelling errors. The results obtained will also be compared to results previously obtained in the references included in this paper.

6 EXPERIMENT

It is important that the results obtained using the theoretical model chosen can be verified using experimental procedures. The isolated phenomena that make up the surge response of an earth electrode are relatively easy to study experimentally, but perhaps the only way to study the overall response is by using a full scale model [[19],[22]].

Transmission line effects can be tested by building scale models of the electrodes and injecting a suitably scaled current using an impulse generator into a scale model earth electrode in a test vessel. It must be noted that the finite size of the test vessel can influence the results at higher current densities and that the soil used for testing is fully characterised. The resistivity, moisture content, grain size and packing will all affect the results. The effect of soil ionisation has been experimentally studied by Oettle [[23]] to obtain better understanding into the processes involved.

The envisaged experimental arrangement to test the theoretical model will make use of a scale model of the electrode system as shown in *Figure 2*. Rogowski coils will be used at various points in the earthing electrode system to determine the current waveform and distribution. It is anticipated that by using soil with sufficiently high resistivity, the effects of soil ionisation might be studied as well. Comparative tests between wet and dry soil can be used in this regard. Experience gained through the experimental results can then be used to enhance the theoretical model.

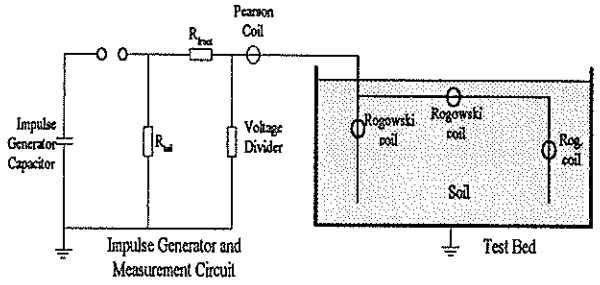

Figure 2. Proposed experimental arrangement.

7 DISCUSSION

Several different methods of modelling can be used to study earth electrode system performance. Due to the complexity of the phenomena that must be modelled, it is obvious that a theoretical and experimental approach is vital to ensure the models are correct. The use of the EMTP is attractive since the behaviour of a much larger system could be modelled (for example, including down conductors or surge protective devices). Matlab™ will be used to verify that the results are not affected by anomalies due to numerical instabilities.

The nature of the waveform to be used for testing is unclear. Realistically, a direct 8/20 μs current impulse will not be directly injected into one corner or point of the earth electrode. Interaction with down conductors in the LPS is inevitable. However, due to lack of further information, both 8/20 μs and 10/350 μs current waveforms will be used where possible for theoretical and experimental modelling.

The main limitation of lumped parameter modelling is the inaccuracies that result at high frequencies. The possibility of modifying existing models used to describe the effects of corona on transmission lines must be considered since an obvious parallel can be drawn to the effects of soil ionisation on a distributed earth electrode.

8 CONCLUSIONS

Various modelling techniques used to study the transient performance of an earth electrode have been

necessarily on achieving low resistance to earth. Models that can be used to quantify and explain the success of the project are desired.

4 TRANSIENT BEHAVIOUR

It is well established that an earth electrode behaves differently under a transient event such as lightning than under a power frequency fault. The low frequency characteristics of different earth electrode configurations have been summarised by Tagg [[9]].

The principal factors affecting the transient behaviour of an earth electrode are [[10]]:

- Geometry.
- Dielectric nature of soil.
- Non-linear, time varying affects of soil ionisation.
- Electromagnetic interaction with adjacent conductors.

An invaluable contribution to the understanding of the transient performance of earth electrodes was made by Sunde [[11]] to the extent that recent work is based on his contribution [[12]]. The dielectric nature of soil results in an earth electrode responding like a transmission line especially for long lengths of buried electrode (relative to the surge propagation time). One of the significant responses of an earth electrode under a transient event is the surge impedance of the electrode which can either be higher or lower than the low frequency impedance.

Resistivity of the soil also has a profound effect on whether or not soil ionisation occurs. This is a non-linear time-varying effect that tends to lower the effective impulse impedance of an earth electrode if the current density at the surface of the electrode is high enough to cause breakdown of the surrounding soil [[13],[14],[15]]. This effect cannot be ignored for South African conditions, where high soil resistivities prevail [[7],[16]].

Three major types of earth electrode can be identified, each with distinguishing characteristics.

- *Concentrated Electrode*. The dimensions of the electrode are small in comparison with the wavelength of the highest frequency components of the lightning current and mainly take the form of vertically driven electrodes. The effects of soil ionisation are known to play an important role.
- *Distributed Electrode*. Typically horizontal buried conductors. The surge impedance of the electrode dominates the response, and can result in large over-voltages.
- *Grid Electrode*. Usually found in substation yards where touch and step potentials under a steady state earth fault must be limited. The behaviour of this type of electrode is more complicated and mutual electromagnetic interaction between conductors is prominent.

The behaviour of different styles of isolated earth electrode is generally understood and form the basis for the standards [[10]]. However, practical and accessible models that allow analysis of interconnected earth electrodes are not readily available. This is due to the complex interactions that make up the transient response.

5 MODELLING TECHNIQUES

In order to understand the combined affect of the phenomenon described in the previous section, as well as to understand the performance of several interconnected earth electrodes a comprehensive model needs to be created. The modelling methods commonly used are summarised by Menter [[17]] and Dawalibi [[18]] as follows:

Electromagnetic field theory. The approach of applying electromagnetic field theory is favoured by Dawalibi since it allows rigorous and detailed analysis from first principles [[18]]. However, the practical engineering value of the results of such detailed analysis becomes difficult to extract. Moreover, the effects of soil ionisation are difficult to include in this modelling method and are typically assumed to be negligible. This method of analysis is not discussed further in this paper.

Transmission line model. Transmission line theory as used by Sunde [[11]] is also popular. This is a relatively simple model to apply and can readily be studied using the Alternative Transients Program (ATP) version of the Electromagnetic Transients Program (EMTP) [[12],[17]]. The use of the EMTP also allows the effects of soil ionisation to be included.

Lumped parameter model. A lumped parameter model was commonly used before significant computing power became available and hence more emphasis was placed on the determination of the dominating factors [[14]]. *Figure 1a* shows the lumped parameter model of a lossless transmission line which was used in conjunction with finite element analysis to study earth electrode performance [[19],[20]]. Typically soil ionisation or mutual electromagnetic interaction effects were ignored to simplify the models.

Kosztaluk et. al. proposed a simple equivalent circuit that included the effects of soil ionisation [[14]]. *Figure 1b* shows the model used for a concentrated earth electrode. A resistance (R_I) is used to describe the electrolytic conduction zone and R_{nl} and C_{nl} are used to describe the ionisation (or channel) zone. *Figure 1c* shows the model Kosztaluk used to model a grid system which included concentrated and distributed electrodes.

evaluated in this paper to determine the model best suited for South African conditions. A favourable modelling technique combines a theoretical lumped parameter model with circuit elements to account for the effect of soil ionisation. Additionally, an experimental scale model should be used to verify the results produced using the theoretical model. The models will be implemented to demonstrate the importance of an equipotential platform especially where interconnected electrical and electronic systems exist.

Acknowledgements

The authors would like to acknowledge Eskom for their support through TESP and the Foundation for Research Development for DTI funding received through THRIP.

9 REFERENCES

[1] "SABS 03:1985 : Code of practice for the protection of structures against lightning," SA Bureau of Standards, 1989, ISBN 0-626-07964-0.

[2] "SABS - IEC 1024-1 : Protection of structures against lightning: Part 1: General principles," IEC, Geneva, (SABS, Pretoria), 1990.

[3] "SABS - IEC 1312-1 : Protection against lightning electromagnetic impulse," IEC, Geneva, (SABS, Pretoria), 1995.

[4] "NRS 042-1996 : Guide for the protection of electronic equipment against damaging transients," NRS Project, SA Bureau of Standards, Pretoria, 1996, ISBN 0-626-11130-7.

[5] G. J. Walliser, I. R. Jandrell and J. M. Van Coller, "Computer model of induced voltages on cables lying in conduit carrying partial lightning impulse current : preliminary results," Paper submitted Nov. 1997 for SAUPEC 1988.

[6] F. Spilkin and N. Goldberg, *South African Earthing Principles*, Steam and Mining Equipment (Pty.) Ltd, 1965.

[7] J. M. Van Coller and I. R. Jandrell, "Behaviour of interconnected building earths under surge conditions [3.06]," in *21st ICLP*, Berlin, Germany, Sept. 1992.

[8] "Private Communication, I. S. McKechnie," McKechnie Wright Associates, Specialist Consulting and Project Management Engineers, Centurion.

[9] G. F. Tagg, *Earth Resistances*, George Newnes Ltd., London, 1964.

[10] "SABS 0199:1985 : Code of Practice for the design and installation of an earth electrode," SA Bureau of Standards, 1985, ISBN 0-626-07488-6.

[11] E. D. Sunde, *Earth Conduction Effects in Transmission Systems*, Dover Publication Inc., New York, 1968.

[12] M. Heimbach and L. D. Grcev, "Simulation of grounding structures within EMTP," in 10th ISH, Montreal, Quebec, Canada, Aug. 1997, vol. 5, pp. 131-135.

[13] A. C. Liew and M. Darveniza, "Dynamic model of impulse characteristics of concentrated earths," *Proceedings of the IEE*, vol. 121, no.2 pp. 123-135, Feb. 1974.

[14] R. Kosztaluk, M. Lovoda and D. Mukhedkar, "Experimental study of transient ground impedances," *IEEE Trans. On Power Apparatus and Systems*, vol. PAS-100, no. 11, pp. 4652-4660, Nov. 1981.

[15] A. M. Mousa, "The soil ionization gradient associated with discharge of high currents into concentrated electrodes," *IEEE Trans. On Power Delivery*, vol. 9, no. 3, pp. 1669-1677, July 1994.

[16] E. E. Oettle, "A new general estimation curve for predicting the impulse impedances of concentrated earth electrodes," *IEEE Trans. On Power Delivery*, vol. 3, pp. 2020-2029, 1988.

[17] F. E. Menter and L. Grcev, "EMTP-based model for grounding system analysis," *IEEE Trans. On Power Delivery*, vol. 9, no. 4, pp. 1838-1849, Oct. 1994.

[18] F. P. Dawalibi, W. Xiong and J. Ma, "Transient performance of substation structures and associated grounding systems," *IEEE Trans. On Industry Applications*, vol. 31, no.3, pp. 520-527, May/June 1995.

[19] A. D. Papalexopoulos and A. P. Meliopoulos, "Frequency dependent characteristics of grounding systems," *IEEE Tans. On Power Delivery*, vol. 2, no. 4, pp. 1073-1081, Oct. 1987.

[20] A. P. Meliopoulos and M. G. Moharam, "Transient analysis of grounding systems," *IEEE Trans. On Power Apparatus and Systems*, vol. PAS-102, no. 2, pp. 389-399, 1983.

[21] R. Velazquez and D. Mukhedkar, "Analytical modelling of grounding electrodes transient behaviour," *IEEE Trans. On Power Apparatus and Systems*, vol. 103, pp. 1314-1322, 1984.

[22] P. L. Bellaschi, R. E. Armington and A. E. Snowden, "Impulse and 60-cycle characteristics of Driven Grounds - II," *AIEE Trans.*, vol. 61, pp. 349-362, 1942.

[23] E. E. Oettle, "The characteristics of electrical breakdown and ionisation processes in soil," *SAIEE Trans.*, vol. 79, no. 2, pp. 63-70, Dec. 1988.

Conducted Electromagnetic Noise Measurements and Predictions for the Muldersvlei SVC

M Botha
Department of Electrical and Electronic Engineering, University of Stellenbosch 7600
Tel. +27-21-808-4354, Fax. +27-21-808-4981
e-mail: mbotha@firga.sun.ac.za

AA Burger, AC Britten
Eskom TRI, Private Bag 40175, Cleveland 2022
Tel. +27-11-629-5033, Fax. +27-11-629-5644
e-mail: A00045@rvtnfs01.eskom.co.za (AC Britten),
arthur@tri.eskom.co.za (AA Burger)

Abstract: This paper describes measurements done in the power line carrier frequency range at the Muldersvlei SVC as well as a scale model which was built at the University of Stellenbosch. Some mathematical modeling of the signal path was undertaken to explain differences in the measured results. These simulations are briefly discussed and some recommendations for future work are also mentioned. It seems as if good agreement may be reached, even with the crude models used for these simulations.

Keywords: SVC, Conducted EMI, Power Line Carrier (PLC), Noise.

1 INTRODUCTION

In 1985 conducted electromagnetic interference measurements were done at the Perseus distribution SVC [1]. Up to 30 dB of noise increase above background levels was detected when this SVC was operating. As the noise and Power Line Carrier (PLC) center frequencies differed, the interference did not disturb the operation of the PLC equipment. Similar measurements were done at the Impala SVC in 1995 [2]. The SVC noise was confined to frequencies below 100 kHz at this SVC, but the possibility of interference still exists.

An investigation into the generic noise characteristics of SVCs was launched to explain the differences in detected noise levels. The project entailed the construction of a scale model SVC [3] and more measurements at the newly installed SVC at Muldersvlei substation. The scale model SVC was developed as a per unit scaled version of the Impala SVC as it was expected that the Muldersvlei SVC would be very similar to the Natal SVCs.

After doing the measurements on the scale model as well as at the Muldersvlei SVC, the results were compared. These comparisons are discussed in the paper. The usefulness of such a scale model in the prediction of noise generated by full-scale SVCs is also investigated.

2 SVC SCALE MODEL MEASUREMENTS

Doing measurements at a full-scale substation is expensive and time-consuming. Many people are involved and special permission must be obtained to switch the SVC into different states. Iterative measurements on a scale model are therefore much easier.

A line matching unit (LMU) was obtained from Eskom for carrier frequency noise measurements on the scale model. The PLC signals are coupled onto and extracted from the high voltage lines by using this filtering unit.

Figure 1 shows a diagram of the scale model SVC measuring set-up. The LMU consists of a high pass filter and impedance matching transformer. The DC block was included as extra protection for the spectrum analyser. The spectrum analyser set-up was as follows:

- 3 kHz Video bandwidth,
- 3 kHz Resolution BW,
- Frequency span 50 kHz to 500 kHz,
- Attenuation 0 dB,
- Sweeptime 200 ms,
- Input impedance = 50 Ω.

Measurements were done at both point A and B.

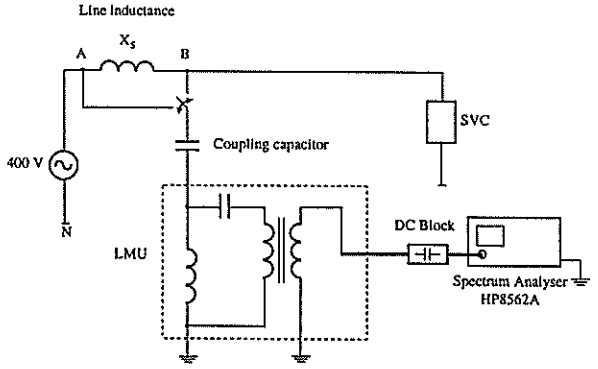

Figure 1 Diagram showing measuring set-up for SVC Scale Model. (Single phase)

For the model the influence of various components on transmitted noise could be determined. These included the effect of amongst other the firing angle and source or line inductance (X_S).

3 MULDERSVLEI SVC MEASUREMENTS

The measurements at the Muldersvlei SVC were done at the PLC communication port inside the control room of the substation. The SVC's transformer and the PLC line trap are not present in the scale model. They also have an influence on the transfer of signals to the PLC port.

The set-up of the spectrum analyser used for the Muldersvlei SVC measurements is similar to the set-up for the scale model measurements.

- 3 kHz Video BW,
- 3 kHz Resolution BW,
- Frequency span 50 kHz to 560 kHz,
- External attenuation 60 dB,
- Sweeptime 200 ms,
- Input impedance = 50 Ω.

4 RESULTS AND DISCUSSION

Some of the scale model's results are shown in Figures 2-4. Two features which need to be mentioned from the model measurements are the effect of the firing angle and the line inductance. More noise was generated by the scale model SVC at higher firing angles than at lower firing angles. This is evident when comparing Figures 2 and 3. The line inductance also seems to act as a filter for the high frequency noise signals. This can be seen from Figure 4 where the two traces are nearly identical. The spectral peaks are attributed to noise already present on the network. The origin of this noise is unknown, but may be due to phenomena such as corona and switching transients.

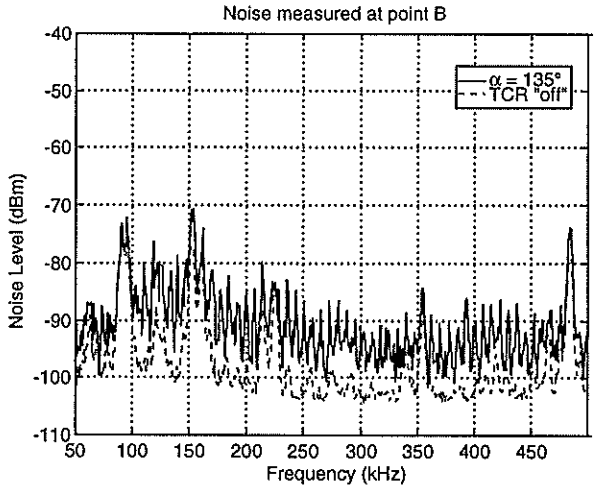

Figure 2 Scale model noise at a firing angle of 135°. (Measured at point B in Figure 1)

The high frequency noise is generated by the collapse of voltage across the thyristors [4]. This is underlined by the fact that the detected noise levels are higher at the higher firing angles (154°) than at the lower firing angles (135°). At 154° the thyristor current is lower than the holding current and therefore the thyristor voltage oscillates between "on" and "off" at the gate pulse frequency which leads to more noise.

Results from the Muldersvlei SVC are shown in Figure 5. It can be seen that almost no extra noise is measured when the SVC is "on". This agrees well with Figure 4, when the model's noise was measured at point A. This leads one to a conclusion that the line inductance and the PLC line trap are electrically equivalent as seen by the PLC signals and noise.

As the transformer and some other components of the full-scale SVC was not included in the scale model, the physical signal "path" for the two systems differs. It was attempted to model this path using circuit theory and correlate the results shown in Figures 2 and 3 to the results in Figure 5. The approach was similar to the one used by Jaekel [5] for noise prediction.

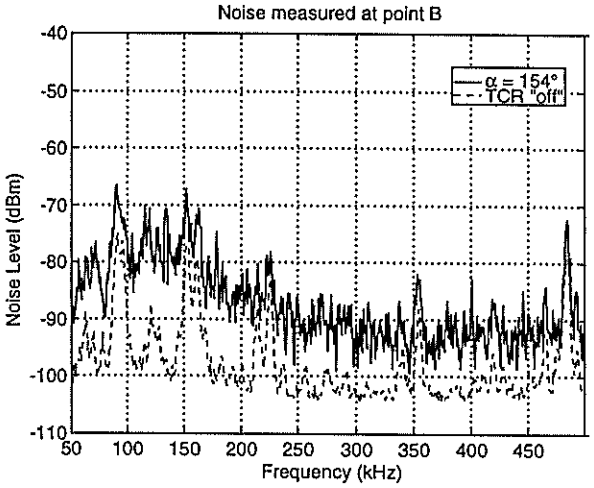

Figure 3 Scale model noise at a firing angle of 154°. (Measured at point B in Figure 1)

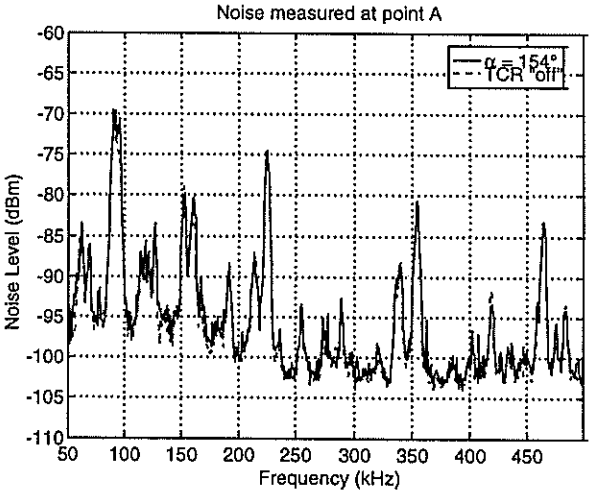

Figure 4 Scale model noise at a firing angle of 154°. Note that the two traces are nearly identical. (Measured at point A in Figure 1)

Symbolic transfer functions for the two systems (scale model and Muldersvlei SVC) were derived. The noise generated by the thyristor controlled reactor (TCR) is modeled as a noise current source. The circuit diagrams are shown in Figure 6.

These circuit diagrams are used to determine the "effective" noise added by the SVC. Some software simulations were implemented in *Matlab* for this purpose. First the voltage across R_T (V_0) is determined from the spectrum analyser power measurements. By dividing this voltage by the transfer function, the "effective" noise current is found. In order to correlate the model and full-scale data for prediction purposes, the total noise added by the SVC must be determined.

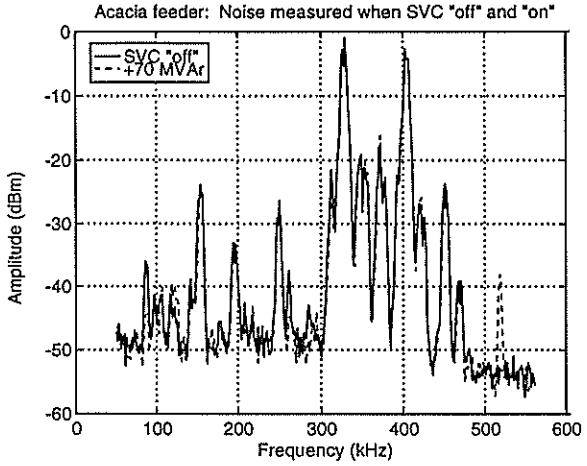

Figure 5 Conducted noise at Muldersvlei SVC on Acacia feeder for the SVC "off" and at 154° (+70 MVAr).

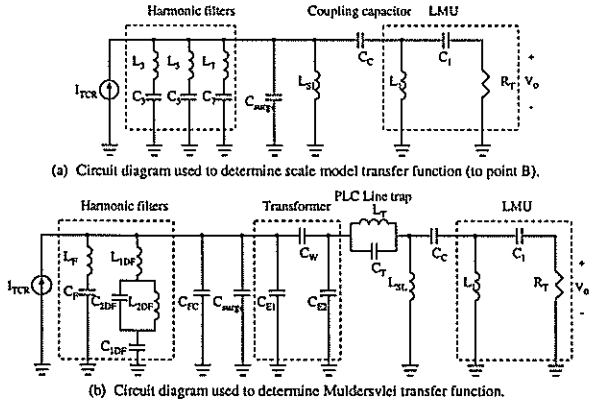

Figure 6 Circuit diagrams used to determine transfer of noise from SVC to LMU.

The added noise generated by the scale model was determined by linearly subtracting the "effective" noise current for the SVC "off" from the "effective" noise current for the SVC "on". This noise current was then rescaled (multiplied by current and impedance ratios) and added to the "effective" noise current for the Muldersvlei SVC "off". The new noise was multiplied by the transfer function of the Muldersvlei SVC to determine the expected noise levels for the Muldersvlei SVC "on".

Figure 7(a) shows the noise levels of the scale model while Figure 7(b) shows the total noise predicted for the Muldersvlei SVC. The bottom two traces look identical. The expected amplitude of the added noise is negligible with respect to the noise already present on the PLC circuits at Muldersvlei substation.

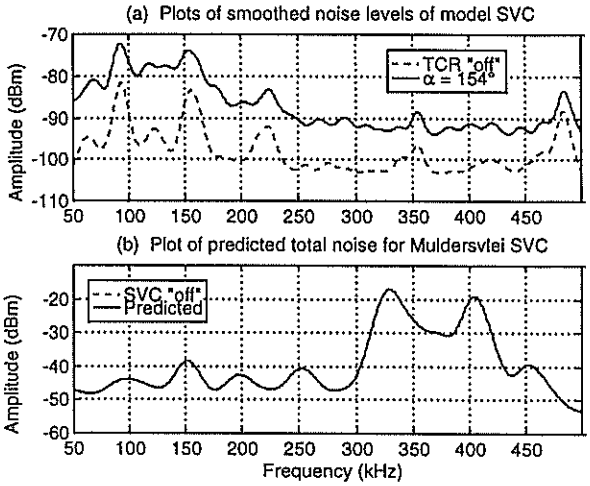

Figure 7 Noise levels of model SVC and predicted noise for the Muldersvlei SVC. Note that the two traces in (b) are identical as the added noise is negligible.

5 CONCLUSIONS

No added noise was detected at the Muldersvlei SVC. This seems to be in contrast with the results from the scale model when measuring on the SVC side of the line inductance (point B). From the results of the software simulations (Figure 7) it is deduced that the signal path has a significant influence on the measured noise.

From Figures 4 and 5 it is deduced that the line inductance (X_S) and the PLC line trap have a similar effect on the transmission of noise in the PLC frequency band. The most basic PLC line trap consists of an inductor. Usually more components are added to achieve a resistive characteristic in the PLC frequency band.

Some limitations to the circuit diagram modeling may be mentioned: The actual transfer function of the scale model should still be measured to determine the accuracy of the circuit diagram model. The real noise currents must also be measured to support the theoretically determined data.

From the results of Figures 4 and 5 and the Matlab simulations it can be deduced that a scale model may

be used to predict noise expected from full-scale SVCs. More work on the theoretical modeling of the signal path still needs to be done.

6 ACKNOWLEDGMENT

The authors wish to thank Eskom TRI for the financial support of this project and the permission to publish this paper. Profs. JH Cloete and JHR Enslin were the study leaders and provided valuable guidance.

7 REFERENCES

[1] Britten AC and Smith DC, "400 kV Static Var Compensator Noise Measurement in a Power Line Carrier Circuit at Perseus", Tech. Rep. TEE/L/85/063, April 1985.

[2] Britten AC, "Investigation into electromagnetic interference and power frequency magnetic field generated by the Impala SVC: Summary report," Tech. Rep. TRR/E/95/EL018, Eskom T-R-I, Aug 1995.

[3] Botha M, Burger AA, Enslin JHR, Cloete JH, "Modeling and Prediction of EMI generated by SVCs", First Southern African Power Quality Conference, Session 5, 12-14 May 1997.

[4] Annestrand SA, "Radio interference from HVDC converter stations," IEEE Transactions on Power Apparatus and Systems, vol. PAS-91, pp. 874-882, May/June 1972.

[5] Jaekel BW, "Investigations on radio interference and power line carrier interference of a back-to-back converter," AC and DC Transmission, Conference Publication, IEE, vol. 423, pp. 58-63, April/May 1996.

Model of a single-sided linear induction motor for propulsion of railway vehicles

F. Spencer, J.F. Gieras and J.T.J. Mokoena
Department of Electrical Engineering, University of Cape Town
http://emf1.ee.uct.ac.za, E-mail: jgieras@eleceng.uct.ac.za

Abstract

Linear induction motors (LIMs) can be successfully used in the propulsion of railway vehicles. Electrical Machines Research Group at UCT had begun research into this area with a project to design and build a smalll-scale linear induction motor for traction use. Tests conducted have indicated that there are discrepancies between the present design software and reality, and that using a finite element method (FEM) for design gives a more accurate design.

1 Introduction

Some of the advantages of using LIMs in railway vehicles are as follows [1, 2]:

- propulsion and braking is independent of adhesion,
- it is easy–to–implement self-steering bogie mechanism,
- in subways, the diameter of the tunnel can be reduced by lowering the floor level of railcars
- the train equipment enables one man operation
- the latest railay technologies for mass reduction, improved maintainability, maintenance manpower saving and improved passenger service can be implemented.

Disadvantages of LIMs when compared to rotary induction motors are that they have:

- a low power factor and efficiency,
- a high current density in primary windings.
- increased energy consumption.

2 Requirements

The aim of the project was to design, build and test a small-scale linear induction motor for use as a traction motor, with the following characteristics:

- flat, single-sided, with moving short primary and longitudinal flux,
- three phase winding, 380 V line to line, 50 Hz,
- low power rating;
- double layer secondary, i.e. aluminium plate over a solid back iron,
- starting thrust of approximately 100 N or more,
- operating speed of 5 m/s;
- primary core built from stacks of standard size single-phase transformer laminations.

The primary was to be supported by a *wheel-on-rail* system (like a practical EMU) with the ability to adjust the size of the air-gap, so that it could be minimized to maximize the thrust.

The electrical design was to be done by a computer software package [1].

3 Design and construction

The electrical design consisted of selecting the following:

- conductive and ferromagnetic materials,
- dimensions of the primary and the secondary,
- number of pole pairs and slots,
- number of turns per phase and diameter of conductor,
- size of the airgap,

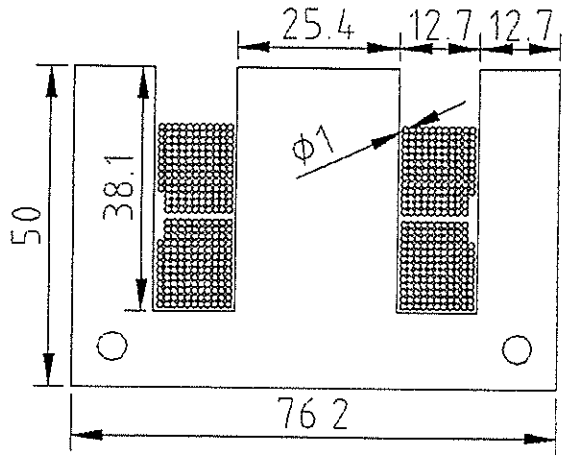

Figure 1: Longitudinal section of the primary stack with two open slots.

- electromagnetic loadings (current density and magnetic flux density)

The computer programme has calculated the predicted characteristics of the LIM such as current, thrust, power, power factor, efficiency, etc. for different values of slip (velocity).

The primary unit has been designed to have $p = 2$ pole pairs. This gives 4 slots per phase and 12 slots totally filled with conductors (two coil sides per slot). The primary winding is a double-layer, 3-phase, star configuration. There are 560 turns per phase, with 4 coils per phase, using ϕ 1,0 mm copper wire.

The primary units consists of 8 stacks of single-phase transformer laminations, as each stack has 2 slots (Fig. 1) This gives a total of 16 slots, of which one has not been used, as only 15 slots have been required for the winding. Each stack has two holes for support, and they are bolted to a $25 \times 25 \times 5$ mm angle iron piece on each side. The dimensions of the primary are then: 610 mm length, 80 mm width and 114 mm pole pitch.

A double layer secondary with aluminium cap wider than the back iron has been designed to reduce the secondary impedance. The dimensions of the iron core are 80 mm width and 10 mm thickness. The dimensions of the aluminium cap are 190 mm width and 3 mm thickness. The aluminium cap behind the back iron forms end bars 13 mm thick. The construction of the secondary fixed to the track is shown in Fig. 2.

The smallest airgap that it has been thought possible to manufacture was 2 mm.

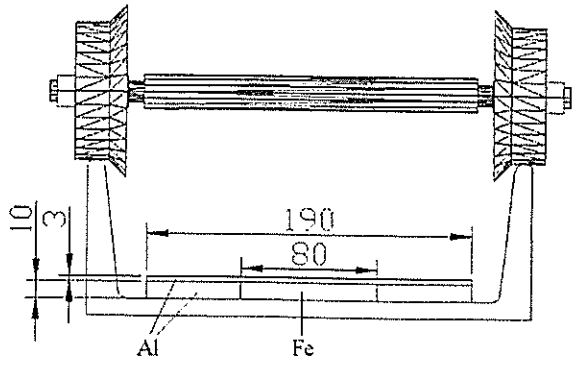

Figure 2: The secondary (reaction rail) fixed to the track and wheel–rail contact.

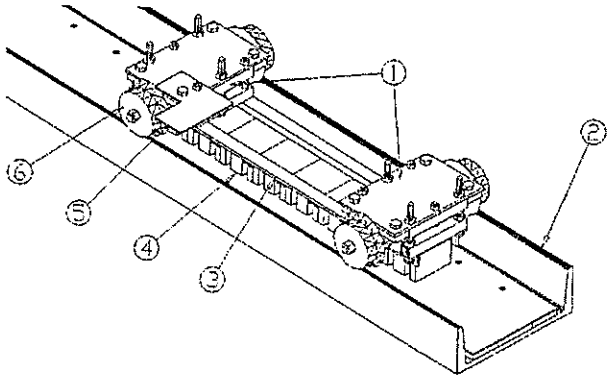

Figure 3: The complete assembly of the model of a LIM driven railcar bogie: 1 — suspension system, 2 — track with the secondary, 3 — LIM stack support, 4 — LIM laminated stack, 5 — 3-phase terminal board, 6 — wheel.

The mechanical design consisted of designing the supports for the lamination stacks that make up the primary, the suspension system for the primary to form the motorised bogie, and the design of the track to support the secondary and for the bogie to run on.

The suspension system consists of a two plates, each with two self-aligning Y-bearings in plummer-block housings bolted to them. Each plate is then in turn attached to the angle iron supports of the primary via square tubing and 3 bolts. These three bolts give the system the ability to adjust the size of the air-gap.

The two axles have been designed such that the ends were threaded. This allows the wheels to be positioned accurately on the shaft by nuts placed on either side of each wheel. The wheels and axles are self-aligning thet the bogie does not run off the track designed for it.

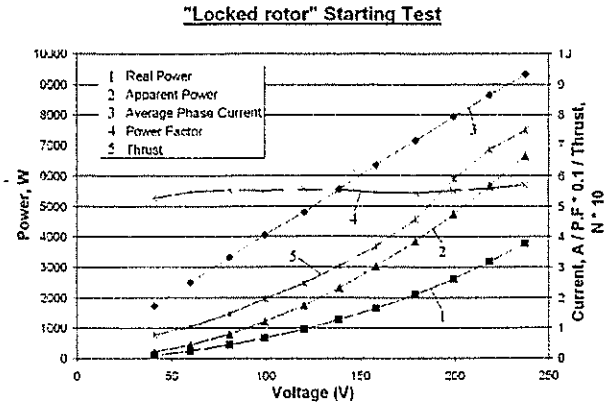

Figure 4: Thrust, phase current, active input power, apparent input power and power factor versus phase voltage at speed $v = 0$.

The track selected consisted of a large channel iron section, with a width of 260 mm, height of 90 mm, and thickness of 10mm. Owing to weight considerations, it has been decided to construct three, 2-m long sections of track. The iron and aluminium that made up the secondary was bolted and riveted to the inside of the channel bars. The wheels of the primary then run on the tops of the sides of the channel iron, which therefore are the rails. The complete assembly is shown in Fig. 3,

4 Experimental tests

For the locked bogie (primary) the following characteristics have been measured:

- thrust versus input voltage
- phase current versus input voltage
- input power versus input voltage

On the basis of the above measurements the power factor versus input voltage and apparent power versus input voltage curves have been calculated. All characteristics for the speed $v = 0$ are shown in Fig. 3. The measured resistance per phase is 5.5 Ω. The measured average force to overcome friction is 13.5 N.

5 Finite element analysis

An analysis of the magnetic flux in the longitudinal section using the FEM has indicated high leakage fluxes. The thrust versus phase current obtained from the FEM and measurements are compared in Fig. 5. The LIM operate satisfactory up to the current of 10

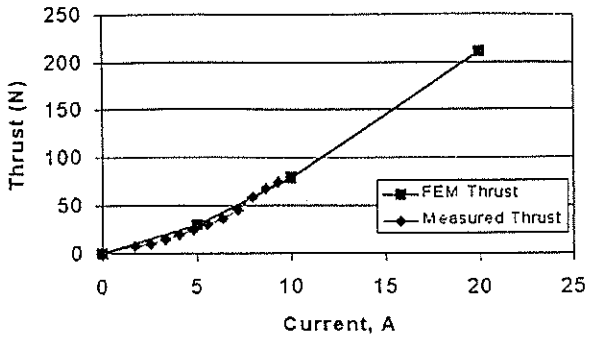

Figure 5: Thrust versus phase current: 1 — FEM, 2 — measurements.

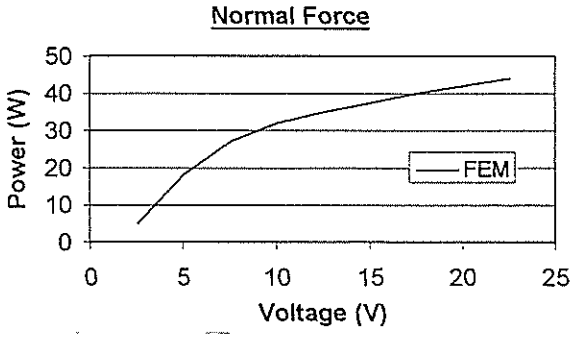

Figure 6: Normal force versus phase current as calculated by the FEM.

A. Above 10 A the LIM becomes hot. The normal force, i.e. attractive force between the primary and secondary predicted by the FEM is plotted in Fig. 6.

6 Conclusions

The model of a LIM-driven railcar bogie has been successfully completed and is now under extensive testing. Some charactersitics have been shown in Figs 4 and 5.

The experimental tests can provide a lot of data for improving the computer software for the design of LIMs. Two problems have been found: (1) varying airgap with the displacement and (2) aluminium and steel components of the secondary do not make a continuous good electric contact. These effects are beleived to be the major contributors to the discrepency beteen calculations and measurements.

The project is still under development. The construction of a second two-axle bogie is in progress. A model of two-bogie (four-axle) railcar with on-board inverter will be controlled using DSP technique. After completing an extensive test programme, a larger model will be designed and manufactured.

Acknowledgement

This work was supported by the FRD, Eskom and University of Cape Town. Windings were made by *Metro Rail* in Cape Town. All mechanical components were manufactured by the first author.

References

[1] Gieras, J.F. *Linear induction drives*, Clarendon Press, Oxford, 1994.

[2] Gieras, J.F., Sone, S., Mizuma, T. and Takagi, R.: *Linear motor driven railcars: subway lines No. 12 in Tokyo and No. 7 in Osaka*, **Int. Conf. on Modern Electric Traction MET'97**, Warsaw, 1997, pp. 169–174.

Performance Calculations for a PM Hybrid Linear Stepping Motor by the Finite Element and Reluctance Network Approach

Rongjie Wang and J.F. Gieras
Department of Electrical Engineering
University of Cape Town
http://emf1.ee.uct.ac.za
Email: jgieras@eleceng.uct.ac.za

Abstract— **In this paper, a hybrid linear stepping motor (HLSM) has been analysed by using both the finite element method (FEM) and reluctance network approach (RNA). The results have been compared with measurements. It has been found that both the FEM and RNA give results very close to measurements.**

Keywords— **Hybrid linear stepping motor. Finite element method. Reluctance network approach.**

I. Introduction

Hybrid linear stepping motors (HLSMs) are regarded as an excellent solution to positioning systems that require a high accuracy and rapid acceleration. The advantages such as high efficiency, high throughput, mechanical simplicity, high reliability, precise open-loop operation, low inertia of the system, etc. have made this kind of motor more and more attractive in such applications as factory automation, high speed positioning, computer peripherals, numerically controlled machine tools and welding apparatus. This motor drive is especially suitable for machine tools in which a high positioning accuracy and repeatability are the key problems.

In this paper, both the finite element method (FEM) and the reluctance network approach (RNA) have been employed for calculating the performance of the HLSM. Both methods have shown a good agreement with experimental results.

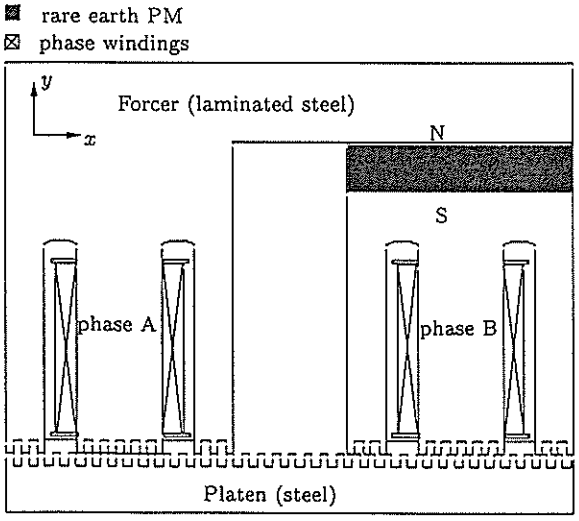

Fig. 1. Longitudinal section of a stack of HLSM

II. Construction and Geometry

The Compumotor's L20 HLSM (Fig. 1) consists of two parts: the forcer and the platen[8]. Both of them are evenly toothed and made of high permeability laminated steel. The forcer is the moving part with two rare earth permanent magnets (PMs) and four monofilar windings built in. There is a very small airgap between the two parts which is maintained by strong air flow produced by a compressor. Table 1 gives some of the design data.

TABLE I
Design data of the tested HLSM

Specification data	Value
Tooth width	0.4572 mm
Slot width	0.5588 mm
Forcer length	117.475 mm
Platen width	49.53 mm
Winding turns	57
Magnet face area	273.79 mm^2
Airgap dimension	0.0127 mm
Peak phase current	2.7 A
Magnet type	NdFeB
Forcer material	laminated steel

III. Finite element approach

The magnetic circuits of stepping motors are usually highly saturated. Therefore, it is often difficult to calculate and analyse motor performance by using classical circuital approach. Using the FEM or other numerical methods more accurate results can be obtained.

Since the HLSM consists of two independent stacks, it is acceptable to model each stack separately. There is one potential difficulty in the modelling of the HLSM. This arises as a result of the tiny airgap (see Table 1). For a better accuracy of the calculation the airgap requires three or four layers of elements which in turn leads to high aspect ratios[3]. Thus, the tangential subdivisions have to be increased as to maintain a reasonable aspect ratio (near unity), which of course leads to higher number of elements. In this paper, single layer elements have been used in the airgap region in order to reduce their number.

Both the virtual work method and Maxwell stress tensor have been used for the thrust (tangential force) force calculation. The classical virtual work method needs two solutions and the choice of suitable displacement has a direct influence on the calculation accuracy. The following one solution approach based on Coulomb's approach [2] has been used and implemented for calculating the tangential force:

$$F_x = -\sum_e \left(\frac{\vec{B}^T}{\mu_0}\frac{\partial \vec{B}}{\partial x} + \frac{\vec{B}^T\vec{B}}{2\mu_0}[G]^{-1}\frac{\partial [G]}{\partial x}\right)\cdot V_e \qquad (1)$$

where $\vec{B}$ is the vector of magnetic flux density in the airgap region, $\vec{B}^T$ is the inverse matrix of $\vec{B}$, $[G]$ is Jacobian matrix and

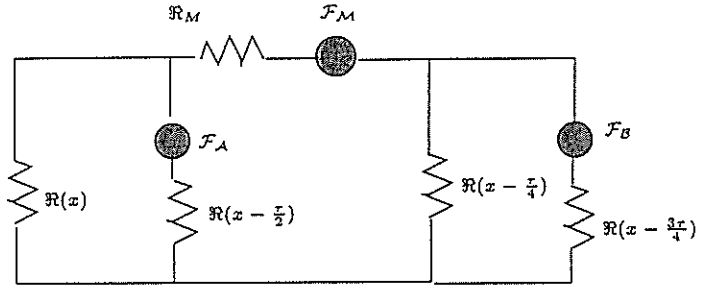

Fig. 2. Equivalent magnetic circuit of a two-phase HLSM.

V_e is the volume of an element. For linear triangular elements, the above equation can further be simplified to the following form:

$$F_x = \sum_{e,i} \frac{1}{4\mu_0}[(y_2-y_3)\Delta_1^2+2(x_3-x_2)\Delta_1\Delta_2-(y_2-y_3)\Delta_2^2] \quad (2)$$

Similarly, the dual formulation for calculating the normal force is obtained as

$$F_y = \sum_{e,i} \frac{1}{4\mu_0}[(x_3-x_2)\Delta_1^2+2(y_3-y_2)\Delta_1\Delta_2-(x_3-x_2)\Delta_2^2] \quad (3)$$

In both eqns (4) and (5), x, y are rectangular coordinates of the $2D$ model, e and i are the numbers of virtually distorted elements and virtually moved nodes within an element, respectively, and subscripts 1,2 and 3 correspond to the nodes of a triangular element. The parameters Δ_1 and Δ_2 are defined as

$$\Delta_1 = \frac{A_1(x_3-x_2)+A_2(x_1-x_3)+A_3(x_2-x_1)}{[G]} \quad (4)$$

$$\Delta_2 = \frac{A_1(y_3-y_2)+A_2(y_1-y_3)+A_3(y_2-y_1)}{[G]} \quad (5)$$

where A_1 to A_3 are magnitudes of the magnetic vector potential corresponding to each node of a triangular element.

IV. Reluctance network approach

In the recent years, a lot of research has been done on modelling electrical devices with the aid of the RNA. Stepping motors have been discussed in papers[5][6][7][9]. The RNA is simpler than the FEM and reduces the computation time.

In this section the equivalent magnetic circuit of the HLSM is described, then the RNA combined with co-energy principle is used for calculating the motor performance.

As shown in Fig. 1, the fluxes of individual poles are dependent on the PM MMF, winding current and reluctances. Beside the main fluxes a leakage flux exists which takes path entirely or partially through the air or non-ferromagnetic parts of the forcer. The amount of such a flux is small as compared with the main flux and can, therefore, be neglected.

After some simplification, the equivalent magnetic circuit can be brought to that in Fig. 2, in which the $\mathcal{F}_M$, $\mathcal{F}_A$ and $\mathcal{F}_B$ are MMFs of the PM and phase windings A and B, respectively, $\Re(x)$, $\Re(x-\frac{1}{2}\tau)$, $\Re(x-\frac{1}{4}\tau)$ and $\Re(x-\frac{3}{4}\tau)$ are the reluctances of a single pole which varies with tooth alignments. The tooth pitch is τ.

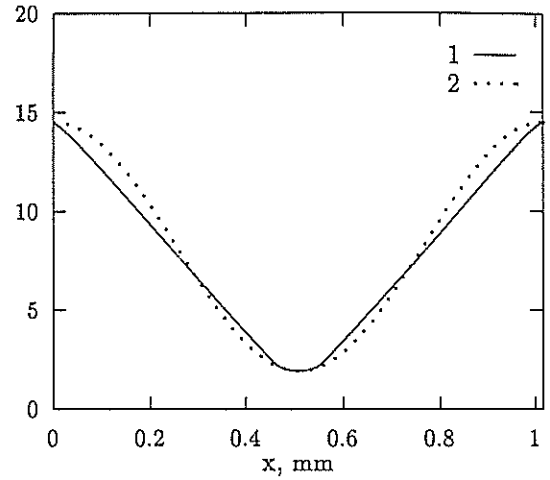

Fig. 3. Comparison of calculated permeance per pole: (1) according to Fig. 2, (2) according to eqn. 8.

A. Permeance model

For calculation of tooth layer reluctance of the HLSM, a set of formulae developed by Chai [1] have been used. For a pole consisting of n teeth, the reluctance of one pole is $\Re_p = \frac{1}{n}\Re_t$ where $\Re_t$ stands for the reluctance of a pair of teeth.

For a non-saturated magnetic circuit ($\mu \to \infty$) all flux lines are perpendicular to the laminated stack surfaces. As the teeth begin to saturate, which does happen in a practical motor, the effective length of the flux path in the air decreases. This results in a higher permeance for the flux emanating from the sides of teeth.

Toothed surface of the forcer and platen involves the permeance variation with respect to the linear displacement according to a periodical function. Similar as in [1], the permeance fluctuation can be approximated with the aid of the following equation:

$$P = \frac{1}{2}[(P_{max}+P_{min})+(P_{max}-P_{min})\cos\frac{2\pi}{\tau}x] \quad (6)$$

where τ is the tooth pitch and P_{max} and P_{min} are defined as

$$P_{max} = \mu_0 L[\frac{W_t}{l_g}+\frac{2}{\pi}\ln(1+\frac{\pi W_v}{2l_g})] \quad (7)$$

$$P_{min} = \mu_0 L[\frac{W_v-W_t}{C}+\frac{8}{\pi}\ln\frac{l_g+0.25\pi W_v}{C}] \quad (8)$$

where $C = l_g + 0.25\pi(W_v - W_t)$, where W_t and W_v are tooth and slot width, respectively. The approximation can furtherly help finding the derivative of reluctance with respect to the displacement, i.e.

$$\frac{\partial P}{\partial x} = -\frac{\pi}{\tau}(P_{max}-P_{min})\sin\frac{2\pi}{\tau}x \quad (9)$$

The calculated permeances over one tooth pitch by using Chai's permeance formulae and its periodical approximation are plotted in Fig. 3.

B. Modelling the permanent magnet

In the magnetic circuit approach the PM can be modelled as an MMF source $\mathcal{F}_M$ in series with an internal reluctance $\Re_M$ [4] and described by the following equations:

$$\mathcal{F}_M = \frac{B_r h}{\mu_0\mu_r}, \quad \Re_M = \frac{h}{\mu_0\mu_r S} \quad (10)$$

where B_r is the remanent magnetic flux density, h is the full length of the PM in the direction of polarisation, μ_r is the relative permeability of the PM and S is the cross-section area of the PM.

C. Phase current waveform and excitation MMF

For microstepping mode the phase current waveform of the HLSM is of sinusoidal shape. A third harmonic of amplitude I_3 has been added or subtracted to suppress the detent effects as given in [4].

$$\mathcal{F}_A = N_c i_A, \quad \mathcal{F}_B = N_c i_B \tag{11}$$

where N_c is the number of turns per phase winding. The windings are assumed to be identical.

D. Tangential force calculation

Having obtained the reluctance model, next step is to evaluate the reluctance forces of the HLSM. On the basis of eqn (8) the tangential force per pole is then

$$F_{px} = \frac{1}{2}\Phi^2 \frac{\partial \Re}{\partial x} = -\frac{1}{2n}\Phi^2 [\frac{1}{P^2}\frac{\partial P}{\partial x}] \tag{12}$$

where Φ is the flux through the pole. Thus for an m pole HLSM, the overall available tangential force is simply

$$F_{tx} = -\sum_{i=1}^{m} \frac{1}{2n}\Phi^2 [\frac{1}{P^2}\frac{\partial P}{\partial x}] \tag{13}$$

E. Normal force calculation

The normal force can be written in the form of the derivative of co-energy W with regard to the airgap length l_g i.e.

$$F_n = \frac{\partial W}{\partial l_g} = -\sum_{i=1}^{m} \frac{1}{2n}\Phi^2 [\frac{1}{P^2}\frac{\partial P}{\partial l_g}] \tag{14}$$

The following approximation can be made to simplify the normal force calculation [4]

$$\frac{\partial \Re}{\partial l_g} = -\frac{1}{P^2}\frac{\partial P}{\partial l_g} = \frac{\Re_{max} - \Re_{min}}{l_{gmax} - l_{gmin}} \tag{15}$$

To calculate either tangential or normal forces, it is always necessary to find the flux of each pole. However, there is no shortcut for the flux calculation. This is because the flux of each pole have to be determined by winding MMFs, PM flux and all the reluctances.

V. Comparison of Results

A. Static characteristics

The following static characteristics have been compared:(1) static force versus forcer position and (2) holding force versus peak phase current value when only one phase is fed. The results obtained from FEM, RNA and measurements are shown in Figs 4 and 5.

It can be seen that the maximum holding force from FEM, measurements and RNA are 70 N, 85 N and 120 N, respectively. FEM results correlate well with the experimental results in the case of static characteristics. The RNA tends to overestimate the force since a lot of assumptions have been made to simplify the calculations.

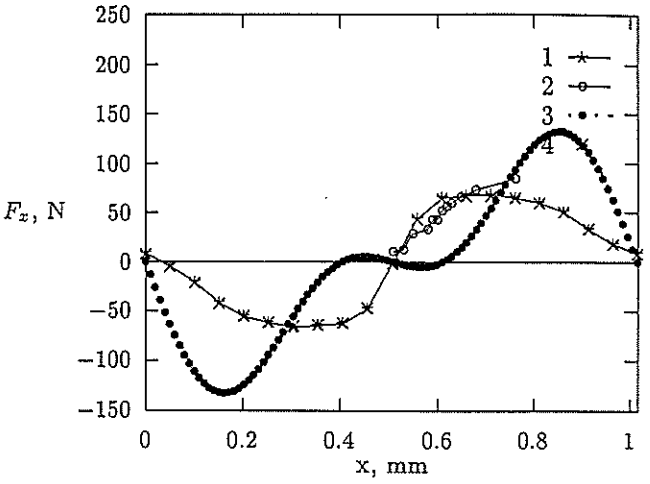

Fig. 4. Tangential force versus displacement (when one phase of the motor is fed with 2.7 A current): 1– Coulomb's approach, 2– measurements, 3– reluctance network approach, 4– Maxwell stress tensor.

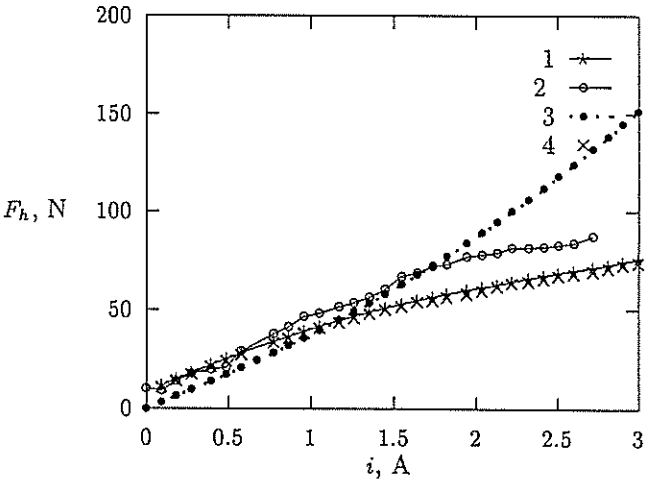

Fig. 5. Holding force versus current: 1– Coulomb's approach, 2– measurements, 3– reluctance network approach, 4– Maxwell stress tensor.

B. Instantaneous characteristics

The instantaneous characteristics of the HLSM refer to the output tangential force versus motor position when the HLSM has been powered up and reaching its steady state. Different excitation current waveforms have been used in testing and simulations. These are pure-sine wave excitation and quasi-sinusoidal (with 10% of 3rd harmonics added), respectively.

The simulated results from both the FEM and RNA are then plotted and compared with measurements as shown in Figs 6 to 8. Since the HLSM has moved with constant speed of 0.0508 m/s, the force–time curves can be easily transferred to force–displacement curves. It can be seen (Figs 6 and 7) that the tangential force ripple can be improved by including $3rd$ harmonic in the phase current. The amplitude of tangential force ripple is defined as the difference between maximum and minimum force values within one period. Fig. 8 gives the relations between the amplitude of tangential force ripple and peak current values, which has been done by calculating the maximum

force ripple for each peak value of the excitation current.

In general, the RNA tends to overestimate the force when compared with the measured values, while virtual work gives more accurate (although lower than measurements) results. However, the RNA is a very efficient approach considering the computation time.

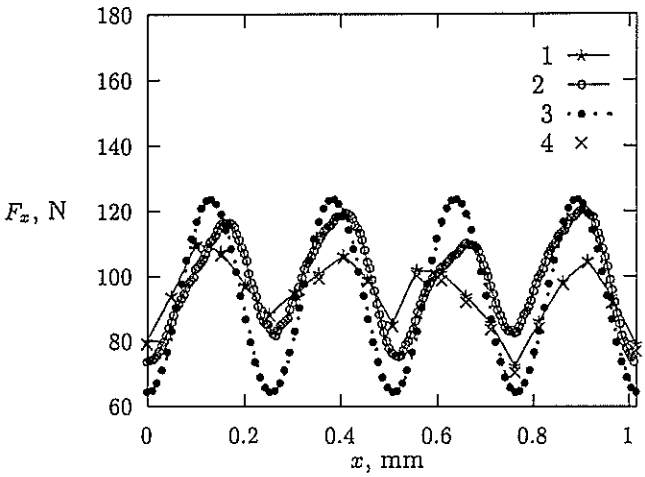

Fig. 6. Instantaneous tangential forces versus displacement (when the phase A of the HLSM is driven with pure sine wave and phase B with pure cosine wave): 1– Coulomb's approach, 2– measurements, 3– reluctance network approach, 4– Maxwell stress tensor.

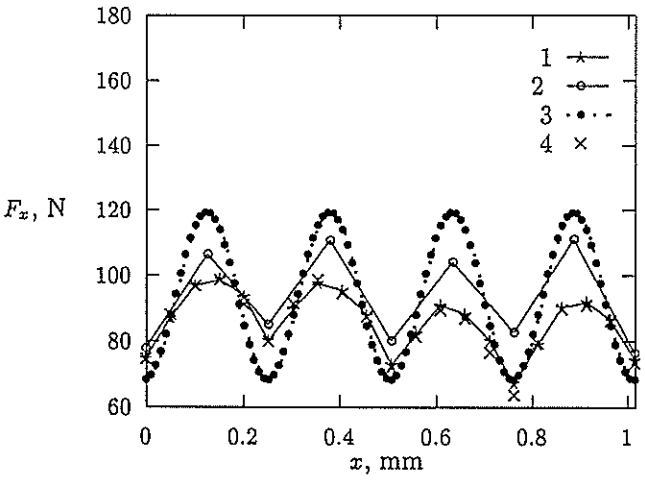

Fig. 7. Instantaneous tangential force versus displacement (when 10% 3rd harmonic has been injected into phase current): 1– Coulomb's approach, 2– measurements, 3– reluctance network approach, 4– Maxwell stress tensor.

VI. Conclusion

In this paper the static forces and instantaneous force have been calculated and compared with measurements. Both the FEM and RNA give results very close to the test results. The accuracy of the FEM much depends on the discretization of the airgap region while the accuracy of the RNA depends on the evaluation of reluctances.

The existence of PMs and toothed structure is the main factor for generating the ripple force. The reduction of ripple forces is

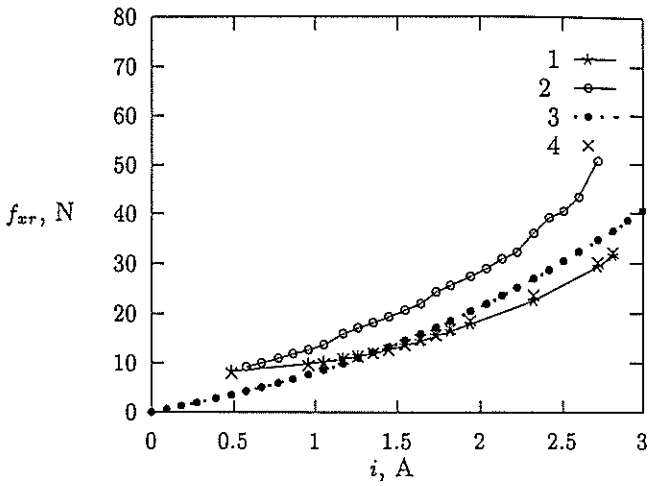

Fig. 8. Tangential force ripple amplitude as a function of peak current, 1– Coulomb's approach, 2– measurements, 3– reluctance network approach, 4– Maxwell stress tensor.

necessary to obtain a smooth operation of the motor and minimise the audible noise. The force pulsations can be suppressed by modifying the input current waveforms.

HLSMs with adjustable current profiles offer new options of motion control. An accurate prediction of forces is necessary not only for motor design purposes but also for predicting the performance of a HLSM drive system.

VII. Acknowledgements

This work was supported by the FRD, Eskom TESP and University of Cape Town. The authors also highly appreciate the co-operation with Parker Hannifin Corporation.

References

[1] H.D. Chai, "Permeance Model and Reluctance Force between Toothed Structures". In the book, *Theory and Applications of Step Motors*,B.C. Kuo ed., West Publishing, 1974, pp. 141–153.

[2] J.L. Coulomb and G. Meunier, "Finite Element Implementation of Virtual Work Principle for Magnetic or Electric Force and Torque Computation", *IEEE Trans. Magnetics*, MAG-20(5), 1984, pp. 1894–1896.

[3] J.D. Edwards and E.M. Freeman, "MagNet 5.1 User Guide – Using the MagNet Version 5.1 Package from Infolytica", published by Infolytica, London and Montreal, 1995.

[4] S. Ellerthorpe and J. Blaney, "Force Estimation for Linear Step Motor with Variable Airgap", *25th Annual Symposium on Incremental Motion Control System and Devices*, San Jose, CA, 1996, pp. 327–335.

[5] S.H. Khan, A.A. Ivanov, "Methods of Calculation of Magnetic Fields and Static Characteristics of Linear Step Motor For Control Rod Drives of Nuclear Reactors", *IEEE Trans. Magnetics*, MAG-28(5), 1992, pp. 2277–2279.

[6] S.H. Khan, A.A. Ivanov, "An Analytical Method for the Calculation of Static Characteristics of Linear Step Motor For Control Rod Drives in Nuclear Reactors", *IEEE Trans. Magnetics*, MAG-31(3), 1995, pp. 2324–2330.

[7] N. Matsui, M. Nakamura and T. Kosaka, "Instantaneous Torque Analysis of Hybrid Stepping Motor", *IEEE Trans. Industry Application*, vol.32, no.5, 1996, pp. 1176–1182".

[8] Parker Hannifin Corporation, "Compumotor Digiplan: Positioning Control Systems and Drives", Rohnert Park, CA, USA, 1995.

[9] K. Rajagopal, M. Krishnaswamy, B. Singh and B.P. Singh, "High thrust density linear motor and its applications", *LDIA'95* Nagasaki, Japan, 1995, pp. 183–186.

Performance Calculation for a Shaded-pole Single-sided Linear Induction Motor Using Symmetrical Components

DAVIDSON, Innocent E, GIERAS, Jacek F,
Department of Electrical and Electronic Engineering,
University of CapeTown
E-Mail: jgieras@eleceng.uct.ac.za

Abstract

The paper presents the circuital approach and performance calculation for a shaded-pole single-sided linear induction motor using symmetrical components for a 2-phase system. The physical model has been built. Results obtained from the circuital approach and experimental tests are compared and discussed.
Key words: linear induction motor, shaded-pole motors, symmetrical components.

1 Shaded-pole Motor

Shaded-pole motors are recognized to be among one of the most robust and simple-to-design machines but difficult to analyze when compared to other induction motors[1],[2]. The single-phase single-sided shaded-pole linear induction motor with a rotating disc[3],[4] and a stationary primary stack has salient poles with a main multi-turn winding with concentrated parameters and slots accommodating auxiliary single-turn shorted coils (auxiliary winding).

Since the currents in the main and auxiliary windings are shifted by an angle less than 90° and the space angle between the two windings is also less than 90°, an elliptical travelling magnetic field is produced in the airgap. The normal component of the magnetic flux density distribution in the airgap can be described by the following equation:

$$b(x,t) = \sum_{\nu=1}^{\infty} [B^{+}_{m\nu} e^{j(\omega^{+}_{s\nu} t - \beta_\nu x)} + B^{-}_{m\nu} e^{j(\omega^{-}_{s\nu} t + \beta_\nu x)}] \tag{1}$$

where $B^{+}_{m\nu}$ and $B^{-}_{m\nu}$ are the peak values of the ν^{th} space harmonic waves travelling in the x-direction (along the pole pitch), $\nu = 1, 3, 5...$ are the higher space harmonics, $\omega^{+}_{s\nu}$ is the angular frequency for the forward travelling field, $\omega^{-}_{s\nu}$ is the angular frequency for the backward travelling field, $\beta_\nu = \nu\pi/\tau$, and τ is the pole pitch. The peak values of magnetic flux densities are:

$$B^{+}_{m\nu} = 0.5[B_a b_{\nu a} + B_b b_{\nu b} e^{-j(\beta - \nu\alpha)}]$$

$$B^{-}_{m\nu} = 0.5[B_a b_{\nu a} + B_b b_{\nu b} e^{-j(\beta + \nu\alpha)}]$$

where B_a, B_b are the normal components of the magnetic flux density (rectangular distribution) in the symmetry axis of the phase a and b, respectively, $b_{\nu a}$, $b_{\nu b}$ are Fourier's coefficients, $\beta < 90°$ is the phase angle between the currents in phase a and b, and α is the angle between symmetry axes of phase a and b.

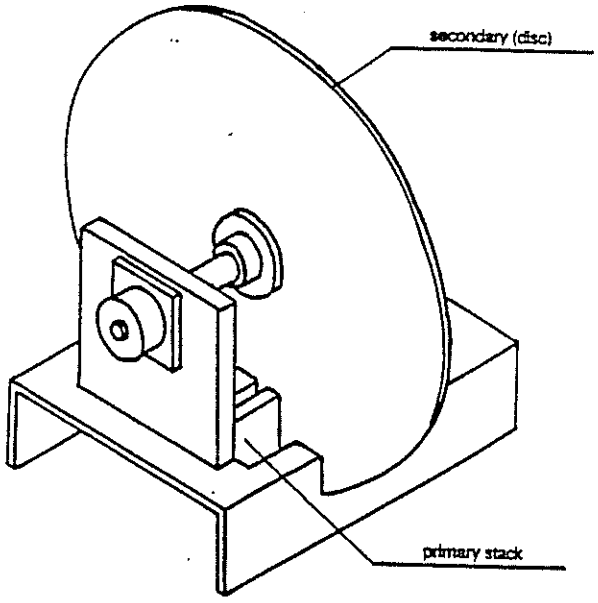

Fig.1 General Asembly of Shaded-pole LIM.

For $\nu = 1$ the angular frequencies are: $\omega^{+}_{s\nu=1} = 2\pi fs$, $\omega^{-}_{s\nu=1} = 2\pi f(2-s)$, where s is the slip. The slip relative to the $+ve$ and $-ve$ sequence field is;

$$s^{+} = \frac{\omega_1 - \omega_2}{\omega_1}, \qquad s^{-} = 2 - s^{+} \tag{2}$$

where ω_1 - synchronous speed (stator supply frequency) for fundamental harmonic, ω_2 - rotor speed.

The tested shaded-pole LIM has a rotor (secondary) which is a double-layer disc made of aluminium and back-iron plates. The motor is shown in Fig.1 and the design data is presented in Table 1. The construction has been described in paper [4].

In the circuital approach to single-phase or two-phase motors, symmetrical components for a 2-phase system are usually used.

Table 1. LIM Design Data

Quantity	Value	Unit
Length of primary stack	$L_\tau = 0.192$	m
Width of primary stack	$L_i = 0.09$	m
Number of pole pairs	$p = 2$	
Number of turns per main phase	$N_a = 520$	
Resistance of main winding for dc current	$R_{dc} = 12.813$	Ω
Primary winding factor	$k_{wa} = 1$	
Pole pitch	$\tau = 0.048$	m
Air gap	$g = 0.0015$	m
Height of pole	$h_P = 0.048$	m
Width of pole	$w_p = 0.016$	m
Diameter of wire with insulation	$d_w = 0.00125$	m
C.S.A of copper wire	1.227×10^{-6}	m^2
Height of shading ring slot	$h_s = 0.005$	m
Width of shading pole slot	$w_s = 0.005$	m
Conductivity of aluminium disc at $20°C$	36×10^6	S/m
Conductivity of back iron at $20°C$	5×10^6	S/m

2 Equations for Phase Currents

For an angle α between phases a and b, where $\alpha \neq 90°$, the positive and negative sequence components are defined as;

$$I_a^+ = \frac{I_a}{2} + \frac{I_b e^{-j\alpha}}{2}, \qquad I_a^- = \frac{I_a}{2} + \frac{I_b e^{j\alpha}}{2}$$

where $I_b^+ = I_a^+ e^{j\alpha}, \qquad I_b^- = I_a^- e^{-j\alpha}$

The current in phase a,

$$I_a = -j\left(\frac{I_a^+}{sin\alpha} e^{j\alpha} - \frac{I_a^-}{sin\alpha} e^{-j\alpha}\right) \tag{3}$$

For the phase b,

$$I_b = j\left(\frac{I_a^+}{sin\alpha} - \frac{I_a^-}{sin\alpha}\right) \tag{4}$$

3 Voltage Equations

The input voltage across the main phase terminals is

$$V_a = I_a Z_{1a} + I_a^+ Z^+ + I_a^- Z^- + (I_a + I_b) Z_{ab} \tag{5}$$

Similar equations can be written for the auxiliary phase

$$V_b = 0 = I_b Z_{1b} + I_b^+ Z^+ + I_b^- Z^- + (I_a + I_b) Z_{ab} \tag{6}$$

The impedances Z_{1a}, Z_{1b}, Z^+ and Z^- are explained in Sections 4 and 8.

4 Stator Winding Impedances

The winding impedances for the main and auxiliary phases are

$$Z_{1a} = R_{1a} + jX_{1a}, \qquad Z_{1b} = R_{1b} + jX_{1b} \tag{7}$$

where R_{1a}, X_{1a} – resistance and leakage reactance of main stator winding, and R_{1b}, X_{1b} – resistance and leakage reactance of auxiliary winding.

The transformation factor, k_{tr}, i.e. .turns ratio between the primary and secondary system for the resistance and leakage reactances, is

$$k_{tr} = \frac{4(N_a k_{w1a})^2}{p} \tag{8}$$

where N_a is the number of turns of the main phase, k_{w1a} is the winding factor of the main phase a for fundamental space harmonic and p is the number of pole pairs.

The primary winding resistance of the main phase is

$$R_{1a} = \frac{N_a l_{av}}{\sigma_{cu} A_{cu}} \tag{9}$$

where the electric conductivity of copper σ_{cu} should be calculated for $75°C$. The average length of turn l_{av} can be found as in the case of any other winding with concentrated parameters.

5 Stator Leakage Reactance

For main stator phase a the leakage reactance is [6],

$$X_{1a} \approx \gamma(\sigma_1 - 1) X_m \tag{10}$$

where linkage factor, γ =0.6 ... 0.9, and σ_1 =1.1 ... 1.16, is leakage factor of main winding. For auxiliary phase b,

$$X_{1b} = 0.5\mu_0 f \lambda_{1b} L_i \tag{11}$$

where λ_{1b} is the specific leakage permeance.

The impedance of the auxiliary phase referred to the main phase is

$$X'_{1b} = \left(\frac{k_{w1a}}{k_{w1b}} N_{1a}\right)^2 \cdot X_{1b} \tag{12}$$

where $k_{w1a} = 1, \qquad k_{w1b} = sin\left(\frac{b_{sh}}{b_p}\frac{\pi}{2}\right)$

and b_{sh} is width of shading ring edge and b_p is the width of pole.

MMFs of both two phases balance each other, i.e. $I_b N_b k_{w1b} = I_a N_a k_{w1a}$, where N is number of turns of the respective winding and k_w is winding factor.

Refer shading ring winding to main stator winding side by similar transformation; $I_b' = I_b/k_{ab}$, where $k_{ab} = N_a k_{w1a}/k_{w1b}$.

6 Impedance of Vertical Branch

The mutual reactance referred to the main phase a is [5]

$$X_m = \frac{8}{\pi} f \frac{\mu_0 (N_a k_{wa})^2}{p(g + d_{Al}) k_{sat}} \tau L_i \qquad (13)$$

where g is the airgap (mechanical clearance) d_{Al} is the thickness of the aluminium layer, k_{sat} is the saturation factor of magnetic circuit and L_i is the effective width of the primary stack. It is convenient to replace the parallel connection of R_{Fe} and X_m by series connection

$$Z_o = R_o + jX_o = \frac{R_{Fe} X_m}{R_{Fe} + jX_m} \qquad (14)$$

where R_{Fe} is the resistance representing core losses.

7 Mutual Reactance Between Main and Auxiliary Phases

The mutual reactance is

$$Z_{ab} = jX_{ab} = j\omega M_{ab} \qquad (15)$$

where X_{ab} is mutual reactance between main phase a and auxiliary phase b[7]. In practical calculations,

$$X_{ab} \approx \frac{\alpha_b}{\alpha_a} \frac{X_o}{2p} \qquad (16)$$

where α_b is the angle representing the width of shading ring and α_a is the angle representing the width of the main pole, and X_o is according to equation (14).

8 Rotor (Secondary) Impedance

The impedances of aluminium cap $Z'_{Al}(s)$ and solid back iron $Z'_{Fe}(s)$ for the fundamental space harmonic $\nu = 1$ have been found on the basis of [5],

The secondary circuit impedances referred to the primary system for the fundamental harmonic is,

$$Z_2'^{+} = Z_2'(s) = \frac{Z'_{Al}(s) Z'_{Fe}(s)}{Z'_{Al}(s) + Z'_{Fe}(s)} \frac{1}{s} \qquad (17)$$

$$Z_2'^{-} = Z_2'(2-s) = \frac{Z'_{Al}(2-s) Z'_{Fe}(2-s)}{Z'_{Al}(2-s) + Z'_{Fe}(2-s)} \frac{1}{2-s} \qquad (18)$$

9 Total Impedance of LIM

Total impedance as seen from the input terminals of the equivalent circuit,

$$Z_t^{+} = -j\frac{Z_{1a} \cdot e^{j\alpha}}{sin\alpha} + j\frac{Z_{ab}(1 - e^{j\alpha})}{sin\alpha} + Z^{+} \qquad (19)$$

$$Z_t^{-} = j\frac{Z_{1a} \cdot e^{-j\alpha}}{sin\alpha} - j\frac{Z_{ab}(1 - e^{-j\alpha})}{sin\alpha} + Z^{-} \qquad (20)$$

The impedances of the vertical and secondary branch are

$$Z^{+} = \frac{Z_0 \cdot Z_2'^{+}}{Z_0 + Z_2'^{+}}, \qquad Z^{-} = \frac{Z_0 \cdot Z_2'^{-}}{Z_0 + Z_2'^{-}} \qquad (21)$$

10 Electromagnetic Torque

The phase currents I_a^{+}, I_a^{-} can be found on the basis of equations (5) and (6).

The symmetrical components of the secondary currents referred to the main winding as obtained from the equivalent circuits are;

$$I_2'^{+} = I_a^{+} \frac{|Z_o|}{|Z_o + Z_2'^{+}|}, \quad I_2'^{-} = I_a^{-} \frac{|Z_o|}{|Z_o + Z_2'^{-}|} \qquad (22)$$

where, $Z_2'^{+}$ and $Z_2'^{-}$ are forward and backward impedances of the secondary referred to the main stator winding turns.

The electromagnetic torque components for the forward and backward sequence are,

$$T^{+} = \frac{2(I_2'^{+})^2 R_2'(s)}{\omega_1 s}, \quad T^{-} = \frac{2(I_2'^{-})^2 R_2'(2-s)}{\omega_1 (2-s)} \qquad (23)$$

where $I_2'^{+}$, $I_2'^{-}$ are the secondary currents referred to the stator main winding, and $R_2'^{+}$, $R_2'^{-}$ are the referred rotor resistances. These components are referred to the secondary side by the transformation factor between the stator and rotor, $k = 2m(N_a k_{w,a})^2/p$.

The difference between the positive and negative sequence torques is the resultant torque $T = T^{+} - T^{-}$.

11 Comparison of Results

Figs 2 and 3 show the shaft torque $T = F_x r$ against velocity at constant frequency. The agreement between computation and measurements is satisfactory. The measured efficiency curves are shown in Fig.4.

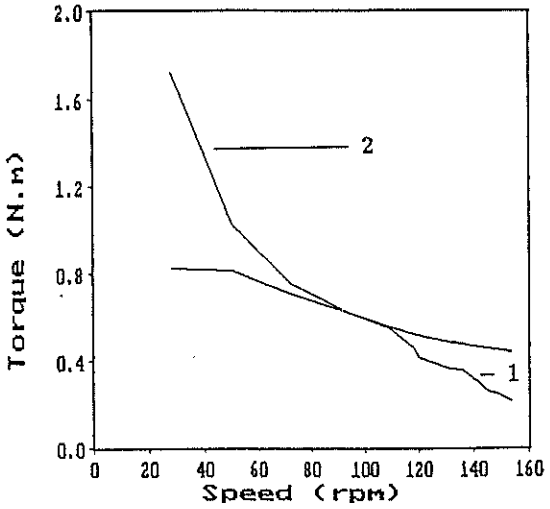

Fig.2 Torque against linear velocity at $f = 75Hz$:, 1 - measurements, 2 - symmetrical components.

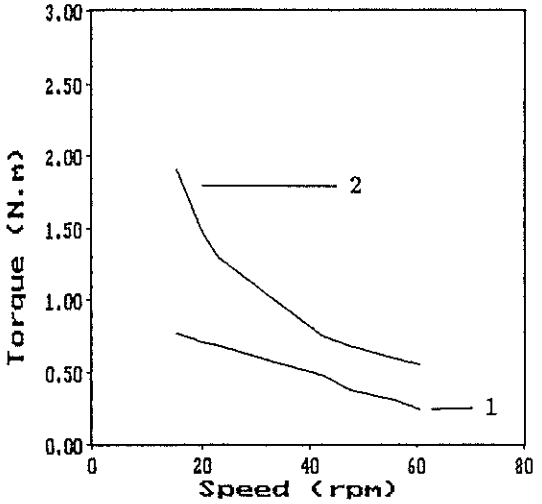

Fig.3 Torque against linear velocity at $f = 40Hz$: 1 - measurements, 2 - symmetrical components.

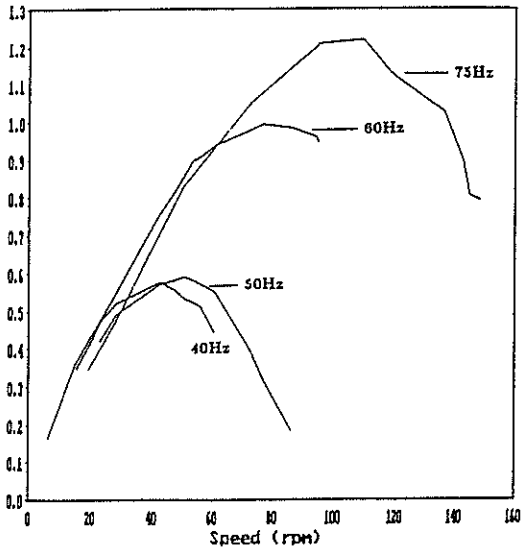

Fig.4 Efficiency vs Speed (f = 40 to 75Hz)

12 Conclusion

The performance calculation of the single-phase single-sided shaded-pole LIM using the method of symmetrical components of two phase systems has been presented. The results compared with experimental tests are satisfactory. With a large air gap of 1.5 mm, the magnetizing current in the LIM increases significantly and consequently the power loss I^2R in the shading coil (auxiliary winding), thereby reducing the efficiency and power factor $\cos\varphi$. The efficiency of the shaded-pole LIM is very low at power frequency. However, it has been found that the efficiency increases with the input frequency as shown in Fig.4.

The shaded-pole LIM is a robust and simple-to-design machine, though difficult to analyze when compared to other induction motors. It can find applications in turntables used in industry. It also finds ready use in small mechanisms where a three-phase power supply is not available or the price and simplicity of drive is important. In countries like India, South Africa and Australia, these motors can be used in rural areas with simple single-phase recticulation systems.

References

[1] M. Akbaba and S. Q. Fakhro, *Field Distribution and Iron Loss Computation in Reluctance Augmented Shaded-Pole Motors Using Finite Element Method*, IEEE Transactions on Energy Conversion, Vol.7, No.2, 1992, pp 302-307.

[2] S. S. L. Chang, *Equivalent circuits and their application in designing shaded pole motors*, AIEE Transactions, Vol.70, 1951, pp 690-699.

[3] I. E. Davidson and J. F. Gieras, *Performance Calculation for a Single-phase Single-sided Shaded-pole Linear Induction Motor Using Finite Element Method*, In Proc. of 1st Int. Conf. on Linear Drives for Industry Applications, Nagasaki, Japan, volume LDIA '95, pages 377-380, 1995.

[4] J. F. Gieras and P. Kleinhans and M. L. Manchen and E. Voss, *Experimental Investigations of a Shaded-Pole Flat Linear Induction Motor*, Africon '92, Swaziland, 1992, pp 404-408.

[5] J. F. Gieras, *Linear Induction Drives*, Clarendon Press, Oxford, 1993.

[6] N. R. Ermolin, *Small Power Electrical Machines (in Russian)*, Energia, Moscow, 1962.

[7] J. Pustola and T. Sliwinski, *Construction and operation of single-phase motors (in Polish)*, WNT, Warsaw, 1964.

POSITION SENSORLESS CONTROL OF A MEDIUM POWER TRACTION RELUCTANCE SYNCHRONOUS MACHINE

S.K. Jackson, M.J. Kamper
Department of Electrical and Electronic Engineering
University Of Stellenbosch, Banhoek Road
7600 Stellenbosch, South Africa

Abstract-The purpose of the paper is to discuss a proposed control system and power electronics drive for position sensorless control of a 42 kW, normal laminated flux barrier rotor, traction reluctance synchronous machine. Different position sensorless control techniques are briefly discussed. Special attention is given to the direct torque control technique. The use of the TMS320 F240 DSP controller for the implementation of direct torque control is described.

Keywords: reluctance synchronous machine, position sensorless control, direct torque control, DSP controller.

1 INTRODUCTION

Previous work by authors on Reluctance Synchronous Machines (RSMs) and position sensorless control of these machines was generally done on small machines that were not necessarily optimally designed as RSMs. Some of the authors on this subject are Bolognani [1], Lagerquist, Boldea and Miller [2], Arefeen, Ehsani and Lipo [3], Kreindler, Testa and Lipo [4], Matsuo and Lipo [5] and Schroedel and Weinmeier [6]. Usually an axially laminated reluctance rotor is used with a standard induction machine stator frame.

A need was thus recognized to investigate developing an industry-ready control system for position sensorless control of medium power flux barrier rotor RSMs. A 42 kW (265 Nm @1500 r/min), 6000 r/min maximum, flux barrier rotor, traction RSM for a diesel-electric drive has been designed and built. A 200 kVA IGBT Inverter was also built for powering the motor. It was decided to use the 20 MIPS fixed point Texas Instruments TMS320F240 DSP controller for the core of the control system. This device is specifically designed for motor control applications and so it is very suitable for the purpose of this project, making it possible to implement the major part of the control system on this single device. This would be very favourable in terms of compactness and cost saving for industry applications.

The position sensorless control technique implemented in this project is Direct Torque Control (DTC). In [2] (Kreindler et al) this technique is called Torque Vector Control (TVC). It was decided to use DTC as it gives the best combination of computational intensity, parameter dependence and performance level of the position sensorless techniques investigated.

With direct torque control an excellent torque response can be achieved. Very good performance is achieved at high, as well as low speed operation, unlike some other sensorless schemes where good performance is limited either to high or low speeds. Field weakening operation is also easily implemented with DTC. Also, only the stator phase resistances are required as opposed to other techniques where the direct and quadrature inductances of the machine are required for operation.

2 POSITION SENSORLESS CONTROL TECHNIQUES

A variety of position sensorless control techniques for RSMs were investigated in search of one to implement on the available machine. The following sections give an overview of the techniques recently published. The DTC technique is described in section 3.

A. Sensorless Control Based on Modification of the Switching.

This method was investigated by Arefeen et al in [3]. The switching pattern of the inverter devices are modified at the zero crossing of the current in a phase. The rotor position is then obtained at this zero crossing. In the proposed method, six rotor positions are obtained within one electrical cycle of the machine. The position detection scheme works well at all speeds, but its low resolution per rotation makes high control performance very difficult to obtain, particularly at low speeds.

B. Sensorless Control Scheme Based on Stator Phase Third Harmonic Voltage

In [4], Kreindler et al propose a technique where the position of the fundamental component of the air-gap flux with respect to the stator fixed reference can be

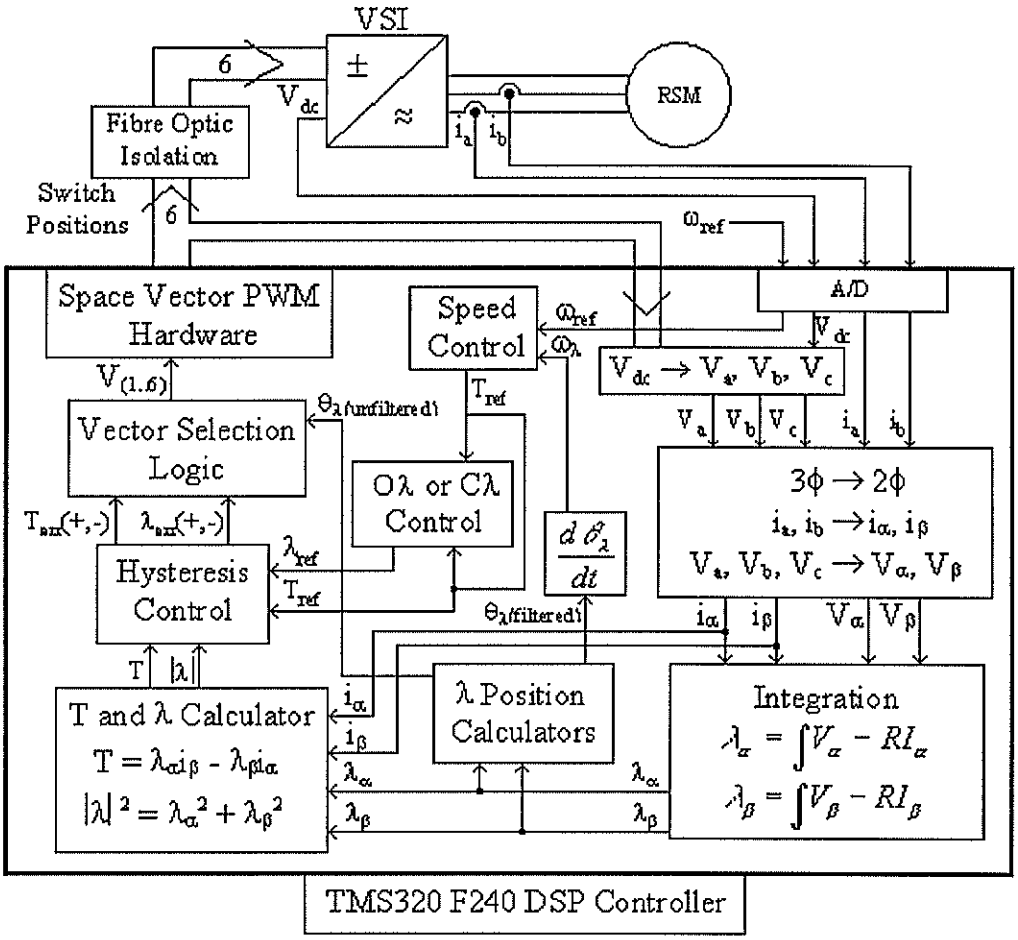

Figure 2. Block Diagram of position sensorless control with DTC implemented on the TMS320 F240

The position of the flux vector can be determined by a look-up table to an arctan function. The speed is estimated from the derivative of the flux vector position, and is filtered.

4 IMPLEMENTATION OF DIRECT TORQUE CONTROL WITH THE TMS320 F240 DSP CONTROLLER

In this section the implementation of DTC on the mentioned DSP controller is briefly described.

The basic block diagram describing the operation of DTC using the TMS320 F240 is shown in figure 2. The operation of the block diagram will now be described. Four analogue measurements are done and converted by the analogue-to-digital converters. One of these, the DC link voltage (V_{dc}) is transformed to three phase voltages (V_a, V_b and V_c) with the help of the state of the inverter switches. The three phase values of current and voltage are now transformed to a static two phase reference frame with the α axis on the phase A winding and the β axis displaced 90° from the α axis. The α and β flux-linkage values λ_α and λ_β are then determined by integration of the two phase voltages and RI voltage drops. From these λ values and the two phase currents, the produced electrical torque (T) and magnitude of the resultant flux-linkage in the machine is determined. These magnitudes are now compared with the torque and flux-linkage reference values (T_{ref} and λ_{ref}) from the speed control and flux-linkage control block. The flux-linkage control block provides the reference flux-linkage value either through optimum flux-linkage control (Oλ) or constant flux-linkage control (Cλ). With hysteresis control, a positive or negative error level for the torque and the flux-linkage (T_{err}(+,-) and λ_{err}(+,-)) is produced. With the position of the flux-linkage vector determined from the values of λ_α and λ_β, the vector selection logic block now determines which voltage vector to apply to the machine. This selection is done according to table 1. The desired states of the inverter switches are then transferred with fibre optic cable to the inverter (VSI). The output of the λ position calculator is differentiated and filtered to

located by detecting the third harmonic zero sequence voltage induced in the stator phases. The third harmonic voltage component is obtained by summing the three-phase voltages. A minimum electrical stator frequency of 0.5Hz, for the best method proposed in this paper, is required for stable operation. Also, the machine must always be operated under saturation.

C. Position Detection Scheme Based on Current Measurements.

The rotor position detection scheme proposed by Matsuo and Lipo in [5] is based on motor current measurements. The machine currents are controlled by a hysteresis current-controlled inverter. The inverter switching creates ripple in the stator phase current. The rate of change of current in the ripple is then detected and converted to a rotor position signal. The scheme is well suited for low and even zero speeds and is dependent on the d-axis and q-axis inductances of the machine. The accuracy of the position detection decreases as the rotor speed increases.

D. Position Detection with Separate Methods for Low and High Speeds

Schroedel and Weinmeier [6] used a different method for position detection at high speeds from that used at low speeds. In the low-speed range, the method used is called indirect flux detection by on-line reactance measurement (INFORM). The different reactances in the d- and q-axis are used for detection. At high speeds, an emf-based algorithm which uses much less processing time is used for position detection. The detected rotor angular position is used as input to a Kalman filter to obtain optimal information of actual speed, position and load torque. This technique is very computationally intensive. Operation is also dependent on machine parameters, i.e. direct and quadrature inductances.

3 OPERATION OF DIRECT TORQUE CONTROL

The basic operation principles of DTC will now be discussed. The basis of operation is that, from current and DC-link voltage measurements, the immediate torque and flux-linkage levels of the machine are calculated. These values are then compared with the command values from the speed controller.

The torque error signal is not translated into a current signal and then used in a current controller as is the case in a general speed control system. With DTC both the required torque and flux commands are converted to a binary increase or decrease in torque or flux. This increase or decrease is then used to select one of the six available voltage vectors produced by the inverter. In this way, if an increase in torque and a decrease in flux is required, one voltage vector is applied. If a decrease in torque and an increase in flux is required, another voltage vector is applied.

There is a unique set of voltage vectors, as described above, to be applied for each of the six electrical sectors in which the resultant flux-linkage vector can be. Figure 1 shows these six electrical flux sectors as well as the six non-zero voltage vectors that can be applied by the inverter. In the description of the voltage vectors, $V_1(1,0,0)$ means that in the first phase arm the top power switch is on and in the second and third phase arms, the bottom power switches are on. Voltage vectors $V_0(0,0,0)$ and $V_7(1,1,1)$ are the zero voltage vectors where no voltage is applied to the machine.

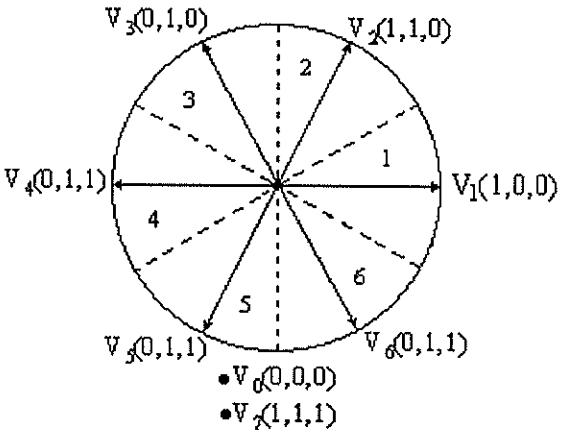

Figure 1 Flux sectors and voltage vectors on a three phase machine and inverter

Table 1 shows for each electrical sector which voltage vector is applied to achieve which results. The table is set up for a counterclockwise rotating rotor and flux-linkage vector.

Table 1 Direct torque control Voltage vectors.

Flux Sector		1	2	3	4	5	6
λ^+	T^+	V_2	V_3	V_4	V_5	V_6	V_1
λ^+	T^-	V_6	V_1	V_2	V_3	V_4	V_5
λ^-	T^+	V_3	V_4	V_5	V_6	V_1	V_2
λ^-	T^-	V_5	V_6	V_1	V_2	V_3	V_4

Note that T^+ and T^- represent an increase or decrease in torque and λ^+ and λ^- represent an increase or decrease in flux-linkage.

produce the speed. This speed value is then used as input to the speed control block.

The TMS320 F240 DSP controller has 16k Flash RAM, 2 x 8 channel A/D converters (< 10 μs), 28 IO pins including PWM/Compare outputs. With all these features it would be possible to implement the major part of the control system on this single device. This is thought to be possible, as an experiment was done by Texas Instruments [8] where the entire control system for position sensorless control of a permanent magnet synchronous machine was implemented on the TMS320 F240.

The TMS320 F240 is thus equipped with hardware to generate PWM outputs for inverter control. One of the PWM modes available, is called space vector PWM as shown in figure 2. In this mode, the desired time length for the application of any two adjacent voltage vectors within one PWM period can be specified. The space vector PWM mode on the F240 is intended to approximate a desired voltage to be applied to the machine. The desired voltage vector is then decomposed into two adjacent vectors, each with their applied application time within a period. The relation between the resultant output voltage vector and the applied vectors is then given in [7] by

$$V_{out} = \frac{t_1}{t_p} V_x + \frac{t_2}{t_p} V_{x+60^\circ} + \frac{t_0}{t_p} (V_0(0,0,0) \text{ or } V_7(1,1,1)) \quad ..(1).$$

Here V_{out} is the desired resultant voltage to be applied to the machine by the inverter, t_p is the PWM period time, V_x is one of the voltage vectors to be applied and V_{x+60° is the adjacent voltage vector. The vectors $V_0(0,0,0)$ and $V_7(1,1,1)$ are the zero voltage vectors. Time lengths t_1, t_2, and t_0 are the time lengths that V_x, V_{x+60° and the zero voltage vector will be applied within one PWM period.

For the implementation of DTC with the space vector PWM mode of the TMS320 F240, only one voltage vector would be applied to the machine within each PWM cycle. This would be done by setting $t_1 = t_p$ and $t_2 = t_0 = 0$ s in (1). A useful feature of the TMS320 F240 is that the PWM outputs have programmable deadbands incorporated in the hardware.

5 CONCLUSION

In this paper a system is proposed to implement sensorless control on a medium power, flux barrier, traction reluctance synchronous machine with the TMS320 F240 DSP controller. A selection of position sensorless control techniques are investigated and briefly evaluated. Direct torque control is selected as the most favourable to implement. It was shown that direct torque control could effectively be implemented on the TMS320 F240, with most of the control system being implemented on this device. In this way a cost effective solution for industrial variable speed drives with medium power reluctance synchronous machines can be developed.

6 REFERENCES

[1] S. Bolognani, "Torque Angle Calculator for Sensorless Reluctance Motor drives," EPE Firenze, pp 4-013 - 4-017, 1991.

[2] R. Lagerquist, I. Boldea and T.J.E. Miller, "Sensorless Control of the Synchronous Reluctance Motor," IEEE Transactions on Industry Applications, Vol. 30, pp 673 - 682, May/June 1994.

[3] M. S. Arefeen, M. Ehsani, and T.A. Lipo, "Sensorless Position Measurement in Synchronous Reluctance Motor," IEEE transactions on Power Electronics, Vol. 9, pp. 624-630, November 1994.

[4] L. Kreindler, A. Testa and T.A. Lipo "Position Sensorless Synchronous Reluctance Motor Drive Using the Stator Phase Voltage Third Harmonic," Conference Record of IEEE IAS Annual Meeting, pp. 679-686, 1993.

[5] T. Matsuo and T.A. Lipo, "Rotor Position Detection Scheme for Synchronous Reluctance Machine Based on Current measurements," IEEE Transactions on Industry Applications, Vol. 31, no. 4, pp. 860-868, July/August 1995.

[6] M. Schroedel and P. Weinmeier, "Sensorless Control of Reluctance Machines at Arbitrary Operating Conditions Including Standstill," IEEE Transactions on Power Electronics, Vol. 9, pp. 225-231, March 1994.

[7] Texas Instruments, "TMS320C24X DSP Controllers Peripheral Library and Specific Devices, Reference Set, Volume 2", March 1997.

[8] Texas Instruments, "DSP Solution for Permanent Magnet Synchronous Motor", Application Report, pp. 25-27, 1996

DEVELOPMENT AND TESTING OF A LINEAR SYNCHRONOUS MOTOR WITH SURFACE MOUNTED PERMANENT MAGNETS

C.G. Jeans A. Hansa R.J. Cruise C.F. Landy
Department of Electrical Engineering, University of the Witwatersrand, Johannesburg.

The purpose of this paper was to make a comparison between buried and surface mounted permanent magnets of linear synchronous motors. Initial studies were undertaken using the finite element method (FEM) of analysis. These studies allowed for an optimal theoretical system to be designed. This system was then built and tested. Results from the testing show that the percentage error between FEM and practical results was less than 7%. The surface mounted system proved the better configuration with a measured maximum static thrust force of 883N [Nd-Fe-B35]. The buried system yielded a maximum static thrust force of 392N [Nd-Fe-B30]. The surface mounted system was able to achieve its results with 80% of the active material than that of the buried system. Reduction of Detent Force by magnet length optimisation is more easily done for the surface mounted system, however it is deemed not to be a viable solution.

Keywords : Linear Synchronous Motors, Permanent Magnets, Buried, Surface Mounted, Nd-Fe-B

1 INTRODUCTION

At present a linear synchronous motor is operational in the Laboratories of the Department of Electrical Engineering at the University of the Witwatersrand as the result of a previous fourth year project. This project has spearheaded a great deal of interest in the use of this system for ropeless hoisting in ultra-deep level mining. The benefits of such a system are numerous and will thus change the methods of how mining is to be conducted in the future.

Feasibility studies have shown [1] that in terms of hoisting requirements a smaller rated linear machine can achieve the same results as its rotary counterpart. The ramifications of such a system are that a smaller diameter shaft needs to be sunk, hence reducing capital costs and shaft-sinking time dramatically. Although the initial costs of a linear system are high, the reduced operating costs coupled with the inherent safety features make the linear system a viable system.

At present the depth of a single shaft is limited owing to safety considerations. A safety factor of ten is incorporated in the diameter of the hoisting rope. This significantly increases the size of the rope and hence its mass. A point is reached whereby the rope becomes too heavy to support itself [2] and thus the depth is limited. Hence under the conventional mining system, there is a need for sub-vertical shafts that not only increase capital costs significantly, but also the amount of time taken travelling to the work area, thereby decreasing productivity further.

2 BACKGROUND

This particular system was of the long primary, short secondary design. The primary was energised as would the stator of its rotary counterpart and the secondary had a constant magnetomotive force (MMF) provided by permanent magnets (PM). The main advantage of a linear motor is that it develops a tremendous thrust force without any mechanical contact between the stationary and moving parts of the system [3].

Two methods of mounting the magnets of the secondary are possible, namely : buried or surface mounted. The buried design uses PM's interspersed by mild steel pole shoes as shown in Fig. 2.1 below.

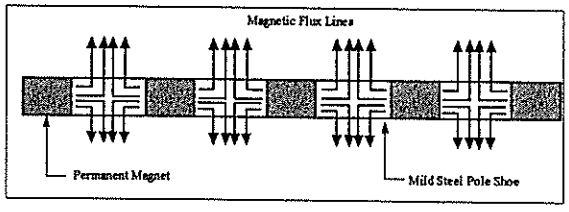

Figure 2.1 Buried Arrangement

The above diagram is that of a four pole secondary as used in the present design. The PM's are orientated in such a manner as to produce the field lines as shown thus making the mild steel act as a pole shoe.

The second design option is to have surface mounted magnets that are mounted on a substantial backiron to allow for the path of flux lines.

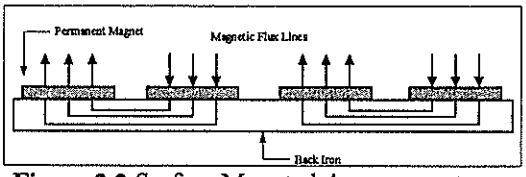

Figure 2.2 Surface Mounted Arrangement

One can observe that the flux exists almost totally on one side, the side facing the primary teeth. This is unlike the buried system whereby the flux lines exit on both faces of the mild steel pole shoe.

3 CHOICE OF PMS

The choice of using Nd-Fe-B as the PMs can be summarised as follows [4] :

- A high saturation (hence high remnance and useful flux density)
- High intrinsic coercivity - they strongly resist demagnetisation
- A very 'square' **B** versus **H** loop shape , often without a knee in the second quadrant. (High $\mathbf{H_k}$, straight-line **B** versus **H**, $\mu_r \cong 1$)
- A spatially very rigid magnetisation vector. (Due to the large anisotropy field.)

The above gives numerous advantages for designs incorporating permanent magnets :

- The magnets can be considered as "magnetic batteries" with a high fixed MMF, providing the combined applied and self-demagnetising fields do not exceed the knee field, H_k.
- The MMF is almost field independent.
- They can generally be placed right at or near the airgap where the flux is needed, thus minimising stray flux.
- Several rare earth PMs and current-carrying coils may be put in close proximity, with their fields simply summing vectorially without significantly affecting other members of the array.

4 SECONDARY DESIGN

The design of the secondaries were carried out for rated current conditions (I=12A).

4.1 Buried PM Design

This was initially designed by Le Roux and El-Hage [5]. The secondary consisted of five PM's interspersed by four mild steel pole shoes. The primary had a pole pitch of 114.5mm, hence this gave a starting point from which to asses the PM and pole shoe sizes. Professor Gieras [6] suggested that the length of a pole shoe should be between 55% and 75% of the pole pitch. The design used, made a compromise and settled for 66% of a pole pitch. The necessary drawings were set up in Maxwell™, a finite element method (FEM) package, for which the static forces were solved.

In order to try and reduce the Detent Force of the buried system, various lengths of PM's were chosen and examined using FEM. From this exercise it can be proved that for the buried case, an optimisation of magnet length does not give better results as fringing from the mild steel pole shoe will always be present.

Table 4.1 Dimensions of the Buried Secondary

PM Dimensions	76.2 x 25.4 x 38.1 mm
Pole Shoe Dimensions	76.2 x 25.0 x 75.9 mm
Secondary Height	191 mm
Secondary Length	494 mm
Secondary Mass	19.2 kg

The flux line plot for the buried system, Fig. 4.1, clearly shows the presence of leakage flux. This flux is more pronounced on the side of the magnets facing away from the primary.

4.2 Surface Mounted Design

In order to obtain a meaningful comparison a PM of the same or comparative volume to those already used in the buried system was required. The same volume is used so as to keep the energy density of the two systems of similar values. However, for the buried system five PM's were used as the mild steel acted as the poles whereas for the surface mounted system only four PM's will be used as the PM's themselves act as the poles owing to their orientation.

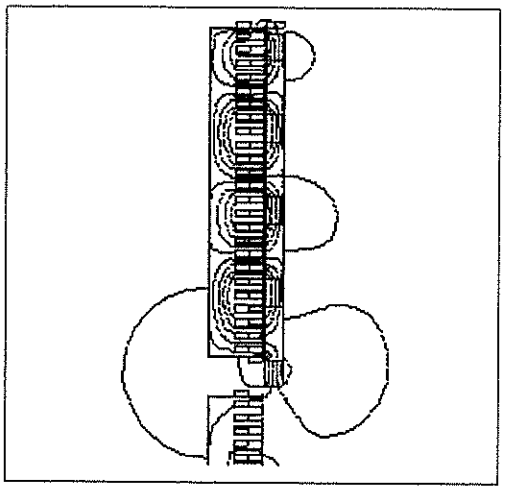

Figure 4.1 Flux Plot of Buried System Reduced Current

The magnet dimensions were optimised in order to reduce Detent Force. Yoshimura et al [7] proposed methods of optimising magnet sizes. Their studies are easily extended to that of a four-pole system From this it is possible to conclude that the magnet length should be :

$$(5+{}^{1}/_{4})\cdot\tau_S \qquad (4.1)$$

where τ_S is the slot pitch.

Thus final magnet and backiron dimensions were obtained.

The flux line plot for the surface mounted system is shown in Fig. 4.2. The improvement is clear when compared with the buried system, as no leakage flux is evident.

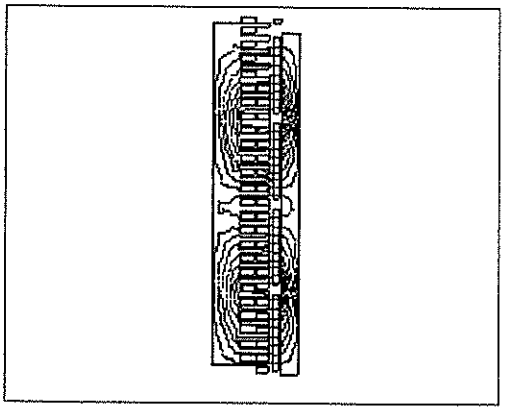

Figure 4.2 Flux Plot of Surface Mounted System at Reduced Current

5 DISCUSSION OF FEM RESULTS

The simulations were only performed for one side as symmetry could be employed and it also reduced processing time considerably. Incidentally, it was found that the simulation time was as much as four times longer for the buried system than for the surface mounted system.

5.1 Buried System

The maximum force under reduced current (I=4A) conditions was 547N using Nd-Fe-B35. Under rated conditions (I=12A) the maximum force was calculated to be 1473N. However, using Nd-Fe-B30 a maximum static thrust force of 418N under reduced current conditions was obtained.

5.2 Surface Mounted System

The surface mounted system was designed to run at rated current and hence magnet length optimisation was carried out at this rated current. However testing was only carried out under reduced conditions and Detent Forces became evident. Thus magnet length optimisation does not seem to be a viable solution to Detent Force reduction. The maximum force under reduced current conditions was 840N. The maximum force under rated current conditions was 1681N.

6 PHYSICAL TEST RESULTS

6.1 Results of the Buried System

The maximum weight that the mover could lift before becoming unstable was 204N in addition to the weight of the secondary itself which was 188N. The total force that the buried secondary was able to generate was 392N. This value is slightly less than the FEM result of 418N achieved by Le Roux and El-Hage [5] and the recalculated value of 547N, even though the air gap on either side was decreased by 0.5 mm. This recalculated FEM value is inflated as Nd-Fe-B35 was used in the simulation and not the actual Nd-Fe-B30 that was used in the physical system. However as FEM ties in so well with practical measurements it is possible for one to make a theoretical comparison with acceptable accuracy.

6.2 Results of the Surface Mounted System

The mover was able to lift 525N in addition to its own weight of 216N and frictional force of 142N. Hence the maximum static thrust force generated was 883N.

7 CONCLUSIONS

The accuracy of FEM was tested once again and faired well with physical measurements proving how invaluable a FEM package such as Maxwell™ is. Although there are inherent errors in finite element analysis the results nonetheless tie in well with practical systems.

More specifically the buried PM design gave a maximum static thrust force through FEM, at reduced current, of 418N [Nd-Fe-B30]. Physical measurements gave the result of 382N. The percentage error between these two measurements is 6.25%. FEM predicted a maximum static thrust force of 840N for the surface mounted case and measurements concluded with a result of 883N giving a percentage error of 5%. Both systems have percentage errors within the predicted ±10% range. Hence there is good correlation between FEM and practical systems.

From FEM the surface mounted system provided more force even though it only had 80% of the active material. This will become significant on a large scale prototype as the costs will be reduced accordingly as well. Furthermore, the back-iron gives incredible strength to the surface mounted system which gives it a design advantage for future use in the harsh environment of the mining industry.

Thus in conclusion the surface mounted system is the more advantageous system, for the following reasons :

- Greater lifting force
- Mechanically stronger and robust
- Reduced magnetic fields within the cage
- Stronger regenerative breaking possibilities

8 REFERENCES

[1] Gore, V.C., Cruise, R.J., Landy, C.F., Economic Considerations of Linear Synchronous Motors in the South African Mining Industry, The University of the Witwatersrand, 1997.

[2] Cruise, R.J. and Landy, C.F., Linear Synchronous Motor Propelled Hoists, *Symposium on Power Electronics Electric Drives and Advanced Electric Motors, Capri, June 1996.*

[3] Cruise, R.J. and Landy, C.F., Linear Motors and their Suitability to an Integrated Transport System, *SAIMechE Conference on Design and Operation of Underground Locomotives and Associated Equipment, Johannesburg, October 1996.*

[4] Strnat, Karl J., Modern Permanent Magnets for Applications in Electro-Technology, *Proc. of the IEEE, vol. 78, no. 6, June 1990, p937.*

[5] Le Roux, B., El-Hage, N., Investigation into the Position Control of a Linear Synchronous Motor, University of the Witwatersrand, Johannesburg, 1995.

[6] Gieras, J.F. MSc(EI Eng.), PhD, DSc, DEEE, University of Cape Town, Private Bag, Rondebosch, 7700, Republic of South Africa.

[7] Yoshimura, T., Watada, M., Torrii , S., Ebihara, D., Study on the Reduction of Detent Force of Permanent Magnet Linear Synchronous Motor, *The 1st International Symposium on Linear Drives for Industry Applications, 31 May - 2 June, 1995, Ioujima, Nagasaki, Japan.*

Usage of Neural Network techniques in Condition monitoring applications in Power Generation environments

ERNST M.P. VAN WYK

This paper investigates a practical neural network implementation of the Karhunen-Loeve transform to reduce the number of input variables used for modelling. The reduced number of variables can be used in standard signal processing techniques or in neural networks to model the state of a device. This particular paper deals with the modelling of turbo generator information to ascertain the condition of this machine and forms part of a larger study on condition monitoring in power generation. The paper also deals with the reasons for using modelling on large machine variables. Some practical examples are used to explain usage of models.

I. INTRODUCTION

Condition monitoring is essentially predictive maintenance. In other words, the state of operation of a machine or system is predicted through a statistical or digital signal processing technique. The system is maintained according to the predicted future state. The main system this paper will focus on is on of the GEC-Alsthom 650 MW 50Hz turbo-driven generators at Lethabo power station located in Viljoensdrif, South Africa.

Certain variables are used to describe the operating state of the generator, that is: power output, running speed etc. Other variables are used to describe the condition of the machine – variables like Stator end-winding (SEW) vibrations. The operating variables are the controllable, or semi-controllable ones – the independent ones, whereas the condition variables cannot be controlled. In this particular case the SEW vibrations shows long-term trends. Since the higher these vibrations get, the more serious the condition of the generator, it is desirable to know in which direction this trend is going – and how fast is it going there.

A. Operating state variables

Since these variables are normally operated and controlled or semi-controlled (that is: they will change in close relationship with a controlled variable), it seems reasonable that these variables will remain between set limits. Where the SEW vibrations tends to show upward or downward trends over time, these variables display cyclic behaviour, usually associated with time of day, day of week or season. By applying simple regression modelling it is clear that the trends cannot be modelled with consistency (that is: over large train and test sets of data). This statement is not entirely correct although it holds water especially for linear systems. For non-linear activation functions for the neural nodes (usually Sigmoid functions), a certain percentage of the trend can be modelled – this raises the question of what is causing this trend, and can it be eliminated. If the set of variables were independent of each other, it would be easy to check which input neuron has the most activation – the set however is not independent. Sets of these variables are shown in figure 1.

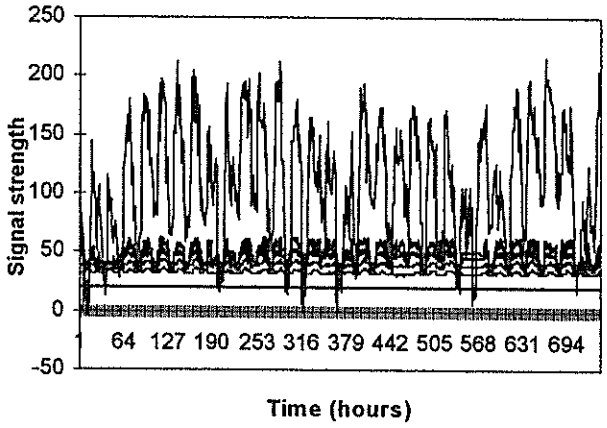

Fig. 1. Operating state variables

B. Condition Variables

Which condition variables used or investigated is up to the investigator, and these may be some of the so-called semi-controlled variables. For this investigation, a particular problem that ESKOM experiences with these generators was addressed. This problem is namely the drifting of SEW vibrations; when these vibrations reach a certain maximum limit the machine is no longer under the manufacturers guarantee and the machine has to be rewound – a process which costs millions. The first objective is to have an early warning system that alerts operators of impending

catastrophe. The second is to find out what is causing this drifting, and eliminate this effect or avoid overexposing the unit to this effect. These variables do however contain some of the information (or variance) that is contained in the operating state variables – especially the cyclic higher frequency information. Sets of these variables are shown in figure 2.

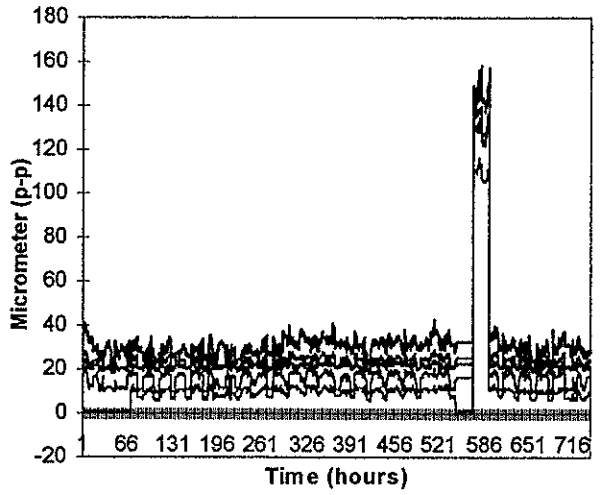

Fig. 2. Condition variables (SEW vibrations)

If the two sets (condition variables and state variables) are compared it is clear that restarting a generator has a large effect on the vibrations. Due to the high cyclic, erratic changes and of course a hefty dose of noise, it is quite difficult to extract a long-term trend. A feasible way to do this is to find a moving average of the set and plot it [1]. There is however, a problem with this, namely that averaging requires populations with size – the greater the size, the better the average. This presents a degree of freedom problem – the more points used in the averaging, the more difficult it becomes in determining the time position.

II. TRENDFINDING

A. General methods

A number of methods exist of finding such a low frequency movement or trend. The methods mentioned here will deal with neural network techniques only.

Kohonen

The Kohonen [4] map is a two-dimensional (or for the more adventurous: a multi-dimensional) distribution of neurons. The training procedure is unsupervised and has a natural tendency to group similar inputs together. To identify a condition the inputs are fed into the network and one of the neurons will be activated. According to the position of the activated neuron, the condition may be classified. Trends may also be identified in this way, since in a transitional phase the activated neurons will follow a path to the new state. This method however may give false alarms or not warn the observer at all, since it groups by relationships. Normally, however, it will deviate when a vibration starts to drift; though, this may only happen when the drift is already visible by naked eye.

Ramptraining

If it is suspected that a signal (vibration) has a continuous approximately linear trend, an additional input can be used to train the network. This input would be a continuous ramp function (or a function that the investigator suspects the data to follow). After training, the weight of this node will give a fair indication of what is to follow. This method, however, needs an educated guess of the form of the trend, and will not allow for sudden changes.

Predicted Error Evaluation

Another method is that of evaluating the error that a prediction makes. For want of a better name, we'll call it ***Predicted Error Evaluation.*** If we predict the condition with the help of the state variables (that do not contain information about the trend) and plot the difference we should end up with a trend. This is the method explored further.

B. Using Predicted Error Evaluation

The idea is simple but works extremely well. For testing, the following set-up was tested. A signal was generated by a linear combination of ten different random signals. A low frequency sinusoidal wave was then generated with 15% noise. The signal was then modulated on this distorted sinusoidal wave.

A Neural network was used in a feedforward form to predict the signal with the ten independent signals. The difference was plot. This is shown in figure 3. Note that in the original signal the sinusoid is not detectable by naked eye (since the sine wave is only about 1% the strength of the created signal).

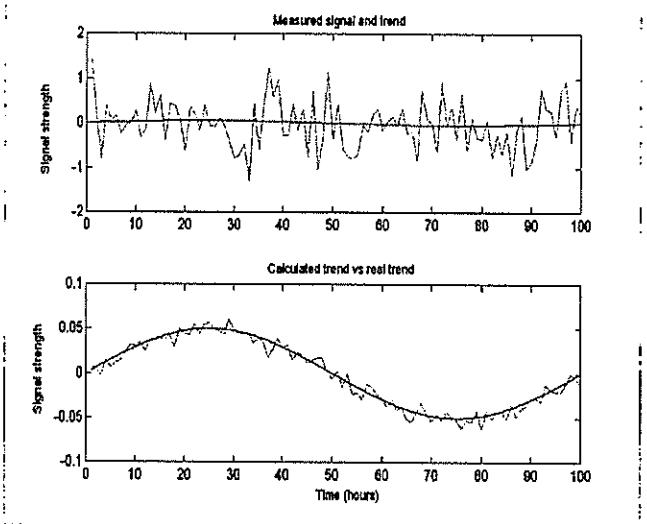

Fig. 3. Predicted Error Evaluation test

A major problem with the using of models in this type of environment, is the fact that there are so many state variables. On a generator, the number may be as high as 500 different variables. A Visual Automation (VA) system on Lethabo station records about 300 variables – a further problem is that these variables recorded are not all connected to the operation of the generator. This issue is ad-

dressed later – for now the above-mentioned method will be tested with 10 selected inputs. The training set consisted of one month of data, collected every 3 minutes. The test set was collected six months later and consisted of 3 weeks of data. The difference plot is shown in figure 4. Note that the signal being modelled has a span of 15 to 50 □m p-p and that the difference is plot runs from –5 to 5.

Although the plot has a lot of noise and variance, the downward trend can be seen. The major problem here is

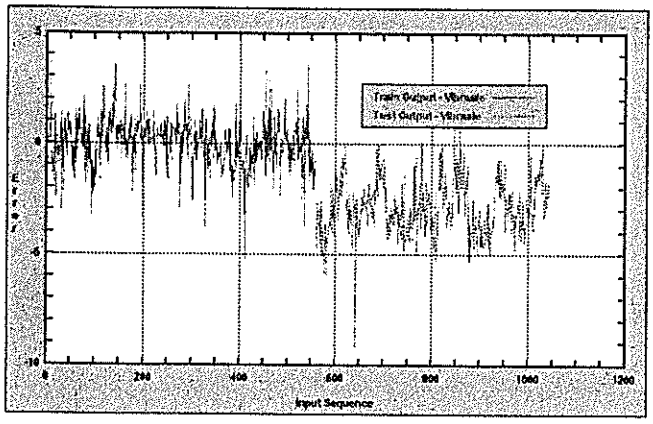

Fig. 4. Predicted error of real data

the fact that only 10 of the 500 operating state variables was used.

III. Reduction of Data

As already demonstrated there are two major reasons for removing redundant information from the set of state variables. The first would be that it is difficult for to manipulate large sets of variables – and when training neural networks, it is also time consuming. The second reason is the fact that if redundant information is removed the activation of different neurons could be used to ascertain which input has what effect on the output.

Two methods for removing redundant information are mentioned.

A. Principle Component Analysis (PCA)

A principle component analysis of a set of m variables generates a new set of m variables so that the new set contains all the variance of the original set. The new set is however ordered in order of the amount of variance it contains. Depending on the investigator, several of the variables can be selected so that the set still contains the most variance possible. This is a lengthy process, and will only do a linear component analysis [2].

B. Neural network realisation of Karhunen-Loeve transform

The alternative method is to use a neural net set-up to reduce the number of signals. The net looks like figure 5[3].

It works by forcing the inputs through a lesser number of nodes – the outputs of these nodes are used to model the original input set. The outputs of the hidden layer in figure 5 should be signals that contain all the information about the input signals, since they can recreate the input signals by multiplying them with the appropriate weights. This method works well if the interdependencies are linear – even if the activation functions are non-linear, it will still produce a linear PCA-like set. This method can however also be used to obtain a set of vectors that have non-linear

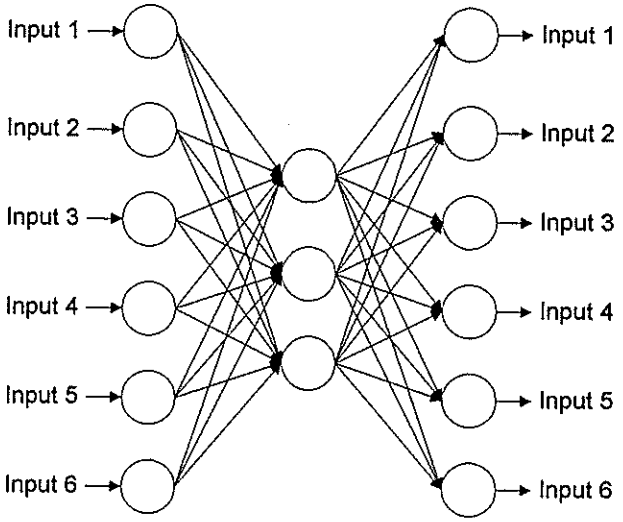

Fig. 5. Reduction network

dependencies on the input set. To obtain a non-linear set, there need only be two extra hidden layers in the network. Since these networks are easier to use and provide more flexibility – they are the preferred method for reducing data.

The trick with these networks is to find the right number if hidden nodes. The best method would be to plot the training correlation for each of a number of nodes. Such a run is shown in figure 6 for the 10 input network used in the Predicted Error Evaluation example earlier.

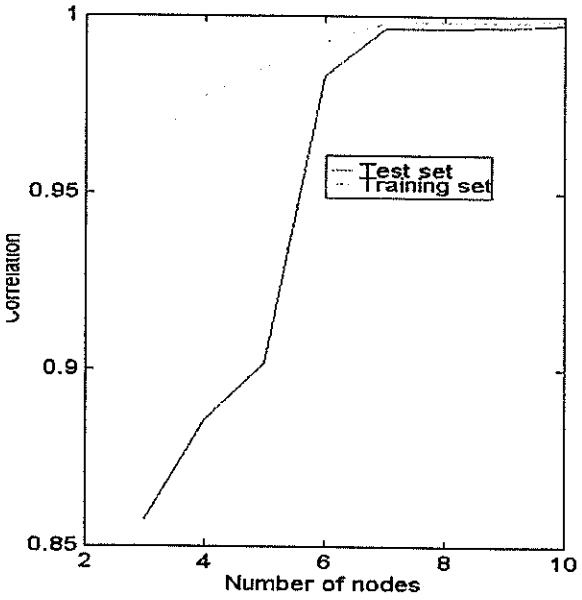

Fig. 6. Reduction versus correlation

For this example, a seven-node reduction seems to be the best, although a six-node would probably work well enough. We will use the seven nodes – a reduction of 30% is still sufficient to reduce the number of 300 signals to 210. The neural network package this author uses is Vesta services' Qnet version 97. This package can input a maximum of 256 signals – thus this reduction is already significant.

For interest sake, the signal set that produced the lowest correlation between input and output (0.98871 – the state variable ***Hydrogen out Temperature***) is plotted in figure 7.

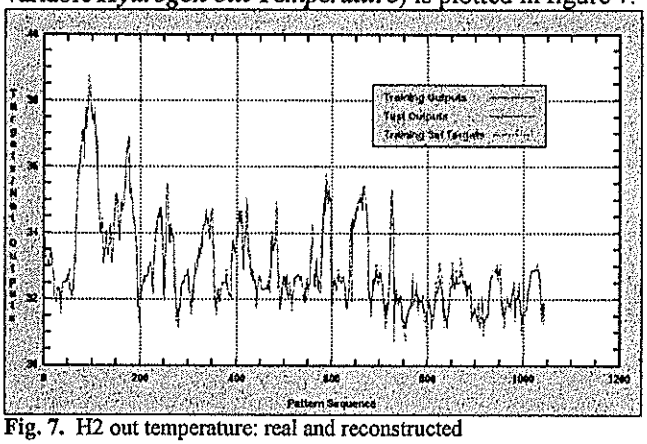

Fig. 7. H2 out temperature: real and reconstructed

The test made was quite interesting – modelling with the reduced number of inputs seems to work even better than modelling with all 10. The network trained with a correlation of 0.999057 for the training set and 0.998752 for the test set – whereas the corresponding numbers for the 10 input test were 0.952338 and 0.930658. In addition, the network trained more than twice as fast. The output of the reduced input network is shown in figure 8.

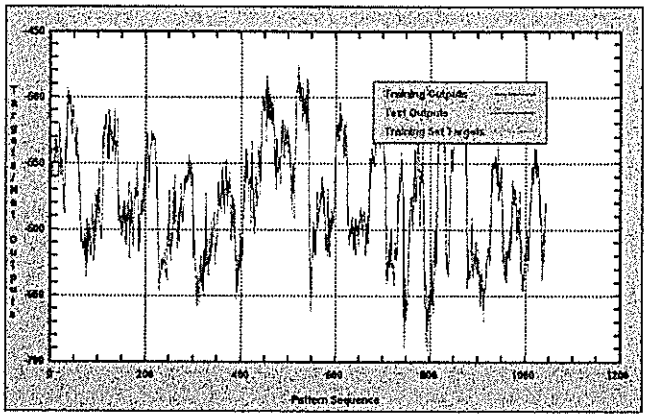

Fig. 8. Output of reduced network

IV. Summary

Although this seems to be a very good result, there is however something less gratifying about it. The network trains too well – it even starts to notice the trend – it is therefore not of such great use in the predicted error evaluation application mentioned above.

It should also be mentioned that the reduction configuration could be used for calibration of instruments. Since all the input signals have redundancy, it follows that, should one input signal suddenly start to drift, the other input signals will still aid in the reconstruction of the output signals. The moment that the in- and output signal of a certain variable starts to differ noticeably, then that sensor is running out of calibration. Of course, the outputs also provide information that is more accurate in this case. An example is given in figure 9. The example is 10 random signals with some linear redundancy that is run through a six-node network. When a slight drift is introduced into one signal – the network will correct that signal. The difference between inputs and outputs is shown in the bottom graph.

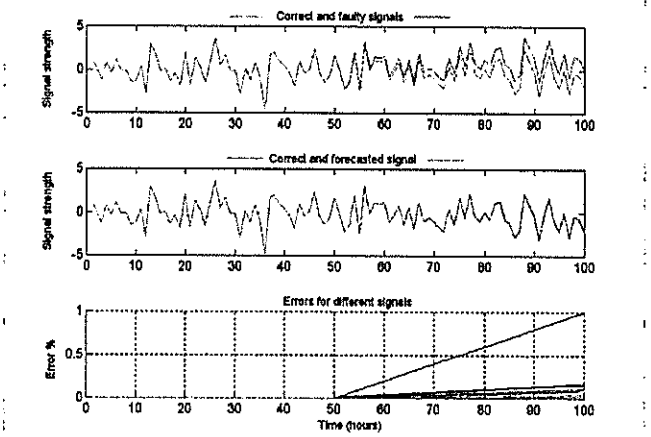

Fig. 9. Calibration of sensors

Although calibration is an important application, the major use for these types of networks will probably be the reduction of the number of state variables.

References

[1] Richard J. Harris, *A Primer on Multivariate Statistics,* United Kingdom, Academic Press, 1975.

[2] A.A. Afifi and V. Clark, *Computer aided Multivariate analysis,* Third edition, Chapman & Hall, 1996.

[3] Robert E. Uhrig et al, *Instrument Surveillance and Calibration Verification Through Plant Wide Monitoring Using Neural Networks,* University of Tennessee.

[4] Teuvo Kohonen, "The Self-Organising Map", *Proceedings of the IEEE,* vol.78, no. 9, pp.1464-1477, Sept. 1990.

RESONANT CHARACTERISTICS OF A TRANSMISSION LINE CONTAINING AN INVERTER-BASED SERIES COMPENSATOR

B. S. Rigby and R. G. Harley
Department of Electrical Engineering, University of Natal
Private Bag X10, Dalbridge, 4014, South Africa
email: brigby@eng.und.ac.za

ABSTRACT

This paper presents a brief, frequency-response analysis of the impedance of a transmission line which contains an inverter-based series compensator. The results demonstrate that the inverter-based series compensator produces a similar resonant-impedance effect in the compensated line to that found in transmission lines compensated with conventional series capacitors.

INTRODUCTION

Internationally, the growth of environmental awareness has made it increasingly difficult to commission new power generation plant and to secure right of way for additional transmission lines. This, coupled with the increased pressure on utilities for more reliable operation of the power system has been behind the major research initiative to develop Flexible AC Transmission Systems (FACTS) technologies [1]. The challenges facing Southern Africa, both to provide rural electrification and to interconnect the various countries of the subcontinent via a sub-Saharan grid, have similarly led to growing interest in the benefits offered by FACTS technologies. In particular the long distances over which power is transmitted in Southern Africa, and the attendant stability problems, make FACTS technologies particularly attractive.

To date several FACTS technologies have begun to emerge which will enable faster, power-electronic control of many of the factors which influence power flow in a transmission line; one FACTS initiative receiving much attention is the proposed use of two back-to-back, high-power, voltage-source inverters in a transmission line to achieve rapid control of several of the factors influencing power flow, the so called Unified Power Flow Controller (UPFC) concept [2]. Studies have shown the UPFC to be capable of providing dynamically controllable series compensation, phase shifting and static Var compensation [2].

The series capacitor compensation capability of the UPFC is of particular interest in the Southern African context because of the unique problems which are associated with the transmission of power over long distances. Static capacitor banks have traditionally been employed in series with long transmission lines in order to compensate for their large inductive reactance, which would otherwise limit the amount of power which can be transferred down the line. However the extent to which a transmission line can be compensated with conventional series capacitance is often severely restricted by concerns for the destructive effects which can occur as a result of series resonance between these capacitors and the transmission line inductance. A rapidly controllable series compensator however has the *potential* to avoid or damp out such harmful resonances, thereby enabling the full steady-state benefit of series compensation to be realised. Furthermore, a controllable series capacitor would also enable fast control of the power transmitted by the line during transient power swings, thus allowing the transmission system to be safely operated much closer to its theoretical stability limit [1].

One of the key advantages of the UPFC concept is its modularity: with only a single inverter, certain of the power flow control functions of the UPFC can be realised individually where desirable. Thus for example, a continuously-controllable, series reactance compensator can in principle be implemented by means of a single voltage-source inverter connected in series with a transmission line. This paper describes a particular scheme for implementing an inverter-based series compensator, based on a stand-alone inverter, which has been developed at the University of Natal. The principles of operation of this inverter-based series compensator are discussed only briefly, since the development of the scheme has been described in several other local publications during the progress of this project. The purpose of this paper is to examine whether the series compensating reactance provided by this new inverter-based scheme can cause series resonances similar to those which characterise transmission lines compensated with conventional dielectric capacitors.

OPERATING PRINCIPLES OF THE INVERTER-BASED SERIES COMPENSATOR

Fig. 1 shows a block diagram of the inverter-based series compensator and its control scheme. The compensator is based on a six-switch, voltage-source, sinusoidal PWM inverter fed from a dc storage capacitor C charged to a voltage V_{dc}; the inverter's ac voltages v_{ca}, v_{cb} and v_{cc} are connected in series with a three phase transmission line via three series-injection transformers. The purpose of the voltage-source inverter is to emulate the behaviour of a series capacitive reactance in the transmission line. Hence the inverter is used to insert in series with the line, 50 Hz voltages which lag the 50 Hz line currents by 90 degrees; the amplitude of these injected voltages is controlled in order to be proportional to the amplitude of the line currents. Mathematically these two relationships can be represented by the phasor equation

$$V_c = k\, I\, e^{-j\pi/2} = X_C\, I\, e^{-j\pi/2} \qquad (1)$$

Equation (1) shows that by choosing the constant of proportionality to be $k = X_C$, the ac voltage injected by the inverter appears, to the transmission line, to be the volt drop across a capacitive reactance of magnitude X_C ohms. In addition to the two control requirements at the ac terminals of the inverter (ie. magnitude and angle of V_c), there is a third

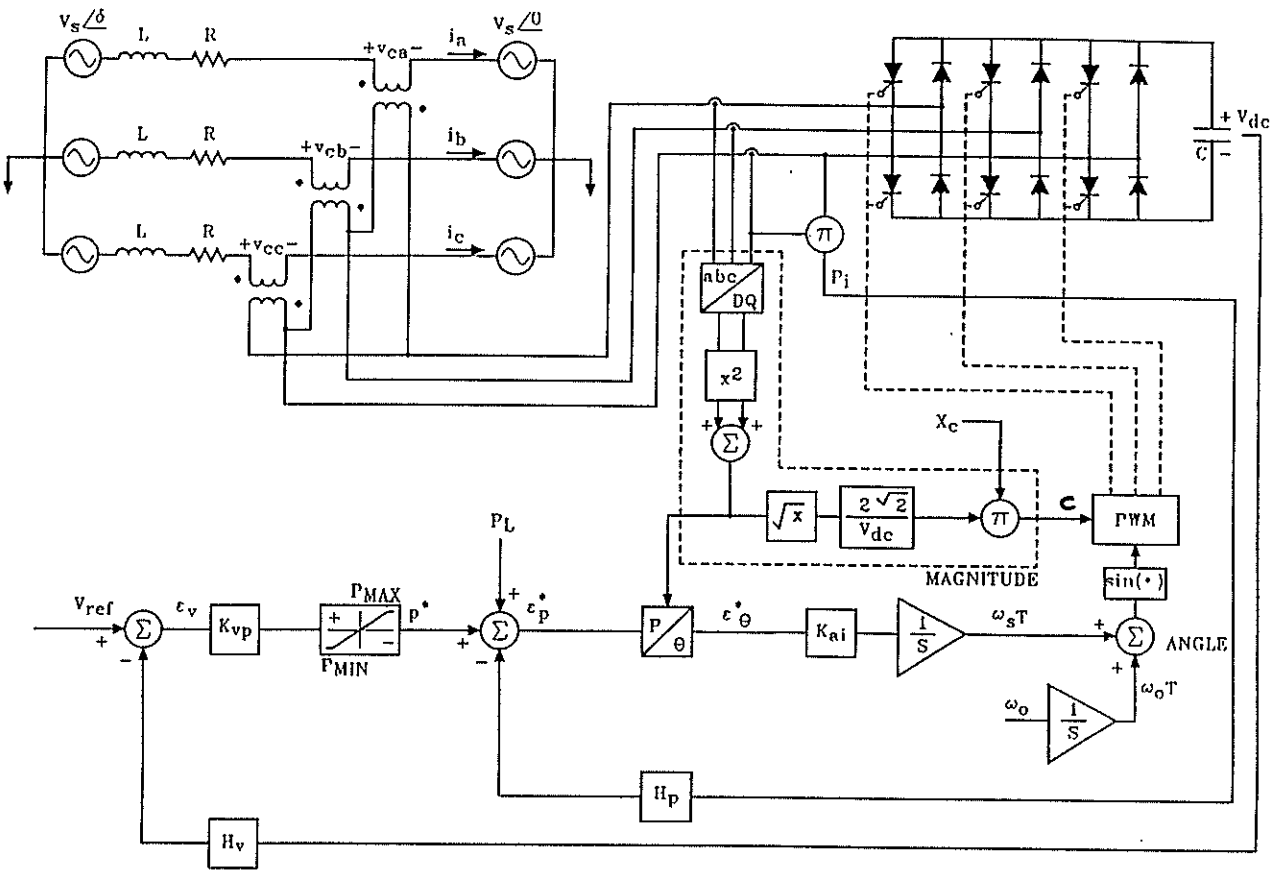

Fig. 1. The inverter-based series compensator and its control scheme.

control requirement: the inverter-based compensator's control scheme must regulate the inverter's dc voltage, since the inverter has no auxiliary dc supply. The manner in which the control scheme in Fig. 1 meets these three requirements can be outlined as follows.

The principal feature of the control scheme in Fig. 1 is the inverter's voltage regulator, the purpose of which is twofold: on the dc side it ensures that the required magnitude of V_{dc} (the inverter's "voltage source") is maintained; on the ac side it ensures that the ac compensating voltage vector V_c has the correct phase relative to the line current vector I to appear as a capacitive reactive volt drop to the transmission line. The voltage regulator comprises two distinct loops, an outer voltage control loop and an inner power control loop. The voltage V_{dc} is fed back and subtracted from the reference value V_{ref} to form the voltage error ε_v in the outer loop; the voltage controller acts on this error ε_v to form the commanded power P^*. The instantaneous real power P_i at the ac terminals of the inverter is fed back and subtracted from the commanded power P^* to form the error ε_p^* in the commanded power in the inner loop. This error signal ε_p^* is then used to steer the phase angle ω_{sT} of the sinusoidal template waveform in the inverter's PWM scheme.

Thus indirectly, the error in the inverter's dc voltage is used to steer the phase of its ac voltages. For example, if vector V_c is not in quadrature with vector I, real power exists at the ac terminals of the inverter which then either charges or discharges capacitor C resulting in a deviation in the voltage V_{dc} from its set point. The resulting error signals ε_V and ε_p^* in the outer and inner loops of the voltage regulator then advance or retard the phase of vector V_c relative to the vector I in order to adjust the power at the ac terminals and return V_{dc} to its set point. At steady state when the voltage V_{dc} remains constant, no real power is exchanged at the inverter's ac terminals. Convergence of the voltage regulator therefore ensures that the injected voltages remain phase locked in quadrature with the line currents at steady state. The injected voltages therefore appear to the transmission line currents to be reactive volt drops; the positive polarity of the signal at point **c** ensures that these reactive voltages lag the line current so as to appear capacitive [3,4].

The magnitude of the injected voltages on the ac side of the inverter is determined by the magnitude of the signal applied at point **c**. In order for the inverter to reproduce a desired ohmic value of series compensating reactance X_c in the line, the signal arriving at point **c** must then be calculated to ensure that the required ratio between the magnitudes of the vectors V_c and I is maintained in the line. The signal processing blocks in the initial scheme of Fig. 1 [5] are included to ensure a desired ohmic value of compensating reactance as follows. The instantaneous abc line currents are sampled and used to calculate the peak magnitude $|I_{pk}|$ of the three phase current space vector. The required peak magnitude $|V_{c\,pk}|$ of the compensating voltage vector is then determined by multiplying the value of $|I_{pk}|$ by the desired ohmic value of reactance which is specified at the input X_c. The correct signal at **c** is then determined by scaling $|V_{c\,pk}|$ by the factor $2\sqrt{2}/V_{dc}$ to account for the gain across the inverter and its PWM scheme.

The gain values in the inner and outer loops of the voltage

regulator in Fig. 1 are chosen to ensure suitable performance of the phase lock between the injected voltages and the line currents under dynamic conditions in the transmission line. The design and dynamic performance characteristics of the scheme in Fig. 1 are discussed in reference [7].

FREQUENCY RESPONSE TESTS ON THE TRANSMISSION LINE IMPEDANCE

A previous publication by the authors [6] has verified that the inverter-based series compensator in Fig. 1 behaves as a series capacitive reactance of the desired magnitude X_C at the steady state operating frequency of the transmission system (50 Hz). However, the series reactance presented by this inverter-based compensator at frequencies other than 50 Hz has not yet been examined in the literature. The magnitude-versus-frequency characteristics of any form of series compensating reactance are of critical importance because they determine whether any frequencies exist at which the impedance of the compensated line exhibits a resonant minimum. This point can be explained using the example of a transmission line compensated with conventional series capacitors.

The diagram in Fig. 2 illustrates the phenomenon of resonance in a transmission line compensated with conventional series capacitors. Fig. 2 shows that the inductive reactance X_L of the line itself, and the capacitive reactance X_C of the conventional dielectric series capacitors used to compensated the line, are both functions of frequency. The series compensating reactance is typically chosen such that its value $X_C(f_o)$ at the fundamental operating frequency f_o of the line is less than the inductive reactance $X_L(f_o)$ of the line itself; the effect is that the net reactance of the line is reduced to a value $X_L(f_o) - X_C(f_o)$. However, Fig. 2 also shows that a subsynchronous frequency f_{er} exists at which the reactance of the compensating capacitors is *equal in magnitude* to the inductive reactance of the line; at this frequency the net reactance of the line is zero and the flow of transmission line currents is thus limited only by the small resistance of the line. This resonant impedance characteristic of conventionally compensated transmission lines is responsible for the phenomenon of subsynchronous resonance (SSR) [9], a form of dynamic instability which can lead to serious damage in turbine-generators connected to the system.

In order to evaluate whether the series compensating reactance provided by the inverter-based scheme could cause SSR, the impedance of the transmission line in Fig. 1 as a function of frequency has been determined by performing frequency-response tests on a mathematical model of the system. Fig. 3(a) shows the results of these tests, whilst Fig. 3(b) shows the impedance versus frequency of the same line compensated with conventional capacitors. In both Fig. 3(a) and (b) the inductive reactance of the line at 50 Hz is $X_L = 23.45\ \Omega$, its resistance is $R_L = 1.48\ \Omega$ and the capacitive reactance of the compensator at 50 Hz is $X_C = 3.25\ \Omega$. However, in Fig. 3(a) the 50 Hz value of compensating reactance $X_C = 3.25\ \Omega$ is provided by the inverter-based series compensator whilst in Fig. 3(b) the 50 Hz value of compensating reactance $X_C = 3.25\ \Omega$ is provided by conventional series capacitors.

Figs. 3(a) and (b) show that in the case of both forms of series

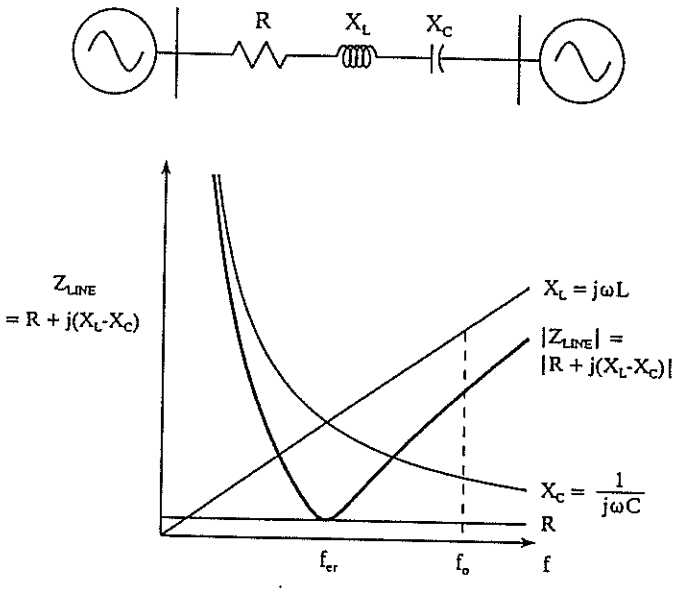

Fig. 2. Impedance characteristics in a conventionally compensated transmission line.

compensation, a subsynchronous frequency f_{er} exists at which the impedance of the line exhibits a resonant minimum, and that its impedance is purely resistive at this frequency. However, Figs. 3(a) and (b) show that the frequency at which this resonant minimum in the line impedance occurs is distinct for the two forms of compensation. Furthermore, comparison of Figs. 3(a) and (b) shows that in the transmission line compensated with the inverter-based series compensator, the impedance at resonance is larger than is the case in the conventionally compensated line.

The results in Fig. 3(a) indicate that, as is the case with conventional capacitive reactance, the compensating reactance provided by the inverter-based scheme completely cancels the inductive reactance of the line at a subsynchronous frequency. However, since the series resistance at resonance in Fig. 3(a) (2.73 Ω) is larger than the resistance of the line alone ($R_L = 1.48\ \Omega$), the results also indicate that the inverter-based series compensator inserts an additional component of resistance in series with the line at this resonant frequency. The presence of a resonant minimum in the line impedance in Fig. 3(a) indicates that the inverter-based series compensator does have the potential to cause SSR in neighbouring turbine-generators. However the additional series resistance which the inverter-based compensator introduces into to the line at resonance suggests that the system is an improvement over conventional series capacitor compensation. (Increasing the series resistance of a transmission line is known to improve SSR stability [10])

CONCLUSION

This paper has presented a brief, frequency-response analysis of the impedance of a transmission line which contains an inverter-based series compensator. The results indicate that this particular inverter-based series compensator causes a resonant impedance characteristic in the transmission line which is similar to that caused by conventional series capacitor compensation, and that the inverter-based compensator therefore has the *potential* to cause SSR in

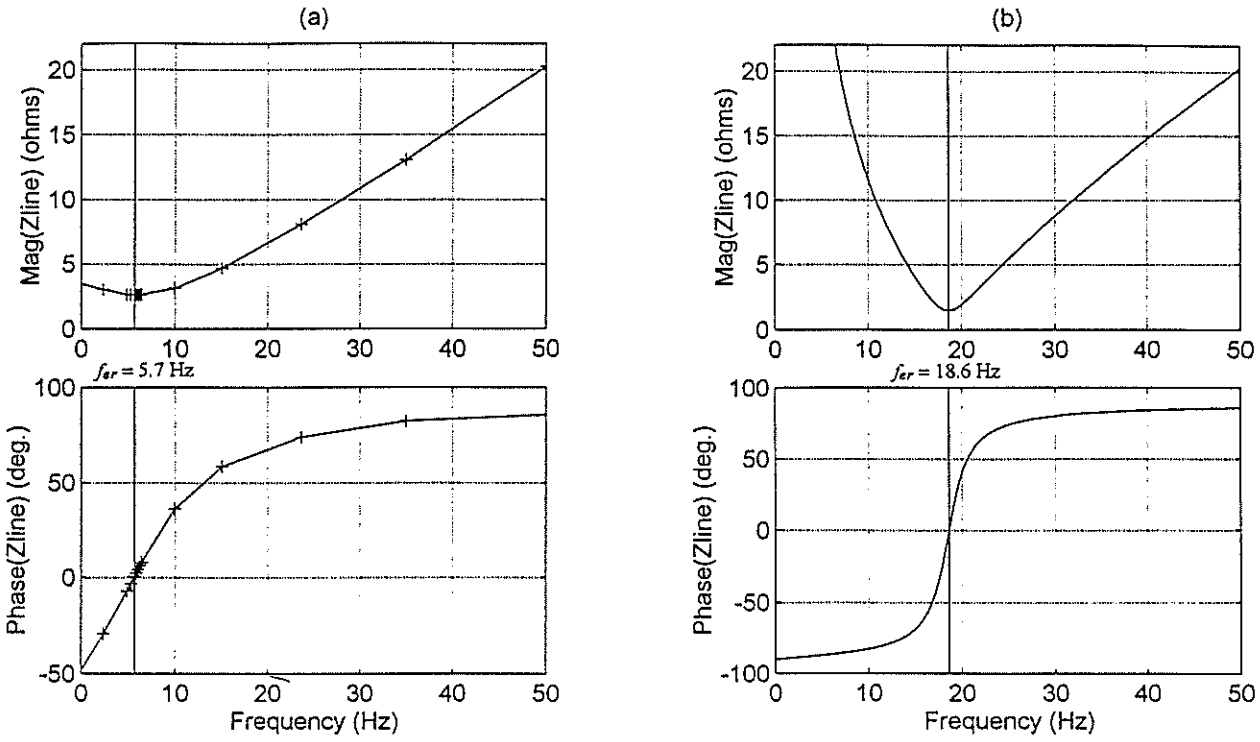

Fig. 3. Transmission line impedance as a function of frequency when the line is compensated with (a) the inverter-based compensator, and (b) conventional series capacitors.

neighbouring turbine-generators. The phenomenon of SSR in a series compensated transmission system is complex, and requires careful analysis using detailed system models before definitive conclusions can be made. However, the preliminary results presented here indicate that in the case of inverter-based series compensation the issue of SSR certainly should not be ignored, and that further detailed SSR analysis is essential before this form of compensation can be implemented in practice.

APPENDIX

Transmission system parameters in all studies are as follows:

$V_s = V_r = 220$ Vrms, $\delta = 65°$, $R_L = 1.48\Omega$, $X_L = \omega_o L = 23.45\Omega$

$C = 1000\ \mu F$, $V_{dco} = V_{ref}/H_v = 300$ V, $\omega_o = 314.159$ rad s^{-1}

Controller gains:

V_{ref}=30, $H_v = 0.1$, $K_{vp} = 80$, $H_P = 0.3$, $K_{ai} = 3.9*\omega_o$

ACKNOWLEDGEMENTS

The authors gratefully acknowledge the financial support of the Foundation for Research Development and the University of Natal.

REFERENCES

[1] "Flexible AC Transmission Systems (FACTS): Scoping Study, Vol. 2, Part 1: Analytical Studies", EPRI Report EL-6943, Sept. 1991.

[2] Gyugyi L, Schauder C D, Williams S L, Rietman T R, Torgerson D R and Edris A, "The Unified Power Flow Controller: A New Approach To Power Transmission Control", IEEE Transactions on Power Delivery, Vol. 10, No. 2, April 1995, pp. 1085-1093.

[3] Wang X, Dai S-Z and Ooi B T, "A Series Capacitive Reactance Compensator Based on Voltage Source PWM Converter", IEEE IAS Conf. Rec., 1991, pp. 918-924

[4] Ooi B T, Dai S-Z and Wang X, "Solid-State Series Capacitive Reactance Compensators" IEEE Transactions on Power Delivery, Vol. 7, No. 2, April 1990, pp. 914-919.

[5] Harley R G, Rigby B S and Jennings G D, "Design of a Controlled Converter which Emulates a Series Capacitive Compensator for Long Power Lines", Proceedings of the International Conference on Power Electronics and Motion Control PEMC'94, Warsaw, Poland, September 1994, pp. 213-218.

[6] Rigby B S, Harley R G, "An Improved Control Scheme for Solid State Series Reactance Compensation", Proceedings of the Sixth Southern African Universities Power Engineering Conference SAUPEC-96, Johannesburg, South Africa, January 1996, pp 117-120.

[7] Rigby B S, Harley R G, "The Development of an Advanced Series Compensator Based on a Single Voltage Source Inverter", IEEE Africon Conference Record, Stellenbosch, South Africa, September 1996, pp 215-220.

[8] Rigby B S, Harley R G, "An Improved Control Scheme for a Series Capacitive Reactance Compensator Based on a Voltage Source Inverter", Conference Record of the IEEE IAS Annual Meeting, San Diego, USA, October 1996, pp 870-877.

[9] IEEE Subsynchronous Resonance Working Group: "Reader's Guide to Subsynchronous Resonance", *IEEE Transactions on Power Systems*, Vol. 7, No. 1, Feb. 1992, pp 150-157.

[10] Kilgore L A, Ramey D G and Hall M C: "Simplified Transmission and Generation System Analysis Procedures for Subsynchronous Resonance Problems", *IEEE Transactions on Power Apparatus and Systems*, PAS-96, No. 6, Nov/Dec. 1977, pp 1840-1846.

REMOTE METERING VIA THE CELLULAR TELEPHONE NETWORK. A VIABLE OPTION.

David McLeavy Sarel Schoombie

ESKOM PTM&C UITENHAGE PORT ELIZABETH TECHNIKON

ABSTRACT

This document describes how cellular telephones could be used to communicate with electrical energy meters that are situated in remote areas. These energy meters are used typically to measure the energy consumption of large power user customers. They are normally situated in difficult to reach areas and ESKOM staff spend a great deal of time traveling to these meters to record the month end readings in order for the customers bill to be calculated. Instead of physically traveling to the meters the cellular network could be utilized thus bringing about a saving to ESKOM in future costs.

1. INTRODUCTION

ESKOM has 268 large power users and 183 statistical metering points that are the responsibility of the metering section situated in Uitenhage. These metering points are spread over a large area and include areas such as Graaf-Reinet, Cradock, Uniondale, Grahamstown and Storms River.

At the end of each month or billing period electricians from the various depots travel to the meters and physically take the readings and then reset the meters for the next month. This task takes a few days to complete. The meter reading sheets are then verified by the depot supervisors and sent to the finance department in East London. The finance department then calculates how much the customers owes and sends out a bill.

Technology now allows for these readings to be retrieved each month by simply phoning into the meter using the cellular network.

2. DEFINITION OF CONCEPTS

PCMCIA - Personal Computer Memory Card International Association. A standard used to define the physical operational characteristics of a credit card sized memory device for portable computers[2].

SIM - Subscriber Identity Module. A SIM card is a credit card type smart card which stores information e.g. telephone numbers [2].

LPU - Large Power User. An electricity consumer with a notifiable maximum demand greater than 100 KVA. Typical customers include municipalities and farmers.

RS 232 - Recommended standard no. 232. A communications standard[1].

AT Commands – A group of commands, issued from a computer terminal, that allows control of the data card while in command mode[2].

S registers – Registers that contain information affecting the data card parameters[2].

Profile data – half-hourly data e.g. kWh and kVarh.

Wheeling customers – e.g. Aberdeen Municipality. ESKOM supplies to the municipality and then purchases electricity again from the municipality in order to supply a township which falls within Aberdeen's municipal boundaries.

3. HOW THE SYSTEM WORKS

The complete remote system consists of:

- Desktop computer with modem attached (base station).
- Nokia 2110 cellphone.
- Nokia datacard.
- Vdot Cardhost Pro (PCMCIA / RS 232 adapter) [6].

A simple explanation of the working of the system is as follows.

Most electronic meters now have the option of an RS 232 output, which can be used for remote communication[3]. The RS 232 output from the meter is connected to an RS 232/PCMCIA adapter. The PCMCIA data card is connected directly to the cellphone and is also inserted into this RS 232/PCMCIA adapter.

Using the remote communication software PMAX you would dial into the cellphone from a computer with a modem attached. Either a Telkom line could be used or you could phone from cellphone to cellphone[4].

The remote software uses AT Commands to initialize the desktop modem. The actual initialization string would be ATDT and the cellphone number that is preceded by a zero to access a telephone line. Each Enermax meter has its own unique serial number and this is linked to the cellphone number when the meter is first setup. The Nokia datacard is used to control the cellphone and various S registers have to be set-up before communication is able to take place between the remote software and the Nokia cellphone. The two main registers are :

1. ATS0=2 This enables the autoanswer function on the phone to answer after two incoming rings[2].
2. ATS35=7 Autobaud setting for the cellphone.

The remote cellphone answers the incoming call after a predetermined number of rings and a communication link is established between the computer and the meter. The meter software then works as it normally would and communication takes place between the meter software and the meter.

4. PROBLEMS ENCOUNTERED

Obtaining the RS 232/PCMCIA adapter.
Programming the PCMCIA data card. Using AT commands various S registers must be set up to allow communication to take place. These settings then have to be saved and used as the boot up option.

5. BENEFITS OF THE REMOTE SYSTEM

5.1 Savings

A huge saving can be made on future labour and transport costs. In order to retrieve the month end meter readings 7596 kilometers are traveled and 168 man-hours are used. The total monthly cost is approximately R19300 [refer to table 1].

TABLE 1. TRANSPORT AND LABOUR COSTS

Depot	Man-hours	Distance	Cost
Adelaide	3 hrs	200 km	R 439
Albany	20 hrs	630 km	R 1804
Alexandria	16 hrs	400 km	R 1277
Cradock	24 hrs	1761 km	R 3773
Graaf-Reinet	10 hrs	800 km	R 1678
Joubertina	28 hrs	1196 km	R 3028
Kareedouw	24 hrs	400 km	R 1915
Kirkwood	24 hrs	861 km	R 2333
Patensie	11 hrs	504 km	R 1642
Transmission	5 hrs	390 km	R 823
Uitenhage	3 hrs	254 km	R 515

Labour costs – Artisan R 27/hr Assistant R 12.83/hr
Transport costs – R 1.60/ kilometer

5.2 Late meter readings

Depot staff sometimes experience difficulty in obtaining readings on time. This is because attending to a system fault obviously has a greater priority than meter readings. This can lead to the customer's bill being sent out late by the finance department and a loss of revenue occurs. The new system would eliminate this problem completely and at the same time improve customer satisfaction.

In the case of wheeling customers where the data must be retrieved with the aid of a laptop computer the readings are always late. The readings are downloaded onto hard disk and then sent to Measurements support in East London via courier or over the computer network. They then have to calculate the simultaneous demands before the bill can be calculated. Using the new PMAX software finance could obtain the readings immediately and the software calculates the KVA demand. This effectively cuts down the number of people needed from four to one.

5.3. Time of use customers

In the case of time of use customers it is imperative that the time on the meter is correct. Meter times tend to drift and this can lead to the customer consuming electricity in the wrong period e.g. the customer uses his pumps in peak times when he in fact thinks he is in off peak times.

The only way off rectifying this problem at the moment is for the depot to report it to the metering section. They then have to travel out to the meter and reprogram the correct time. The new system would eliminate this because each time the billing data is retrieved the time is checked and reset if necessary.

5.4 Other benefits

Metering technicians can access profile data at any time without having to travel long distances. The data could now be accessed in minutes thus improving overall productivity.

Meter schemes can be amended at any time. e.g. on the miniflex tariff public holidays have to be reprogrammed each year.

A new ESKOM requirement for statistical metering is voltage profiles. Meter manufacturers will in the future allow for this facility [3] and the profile would then be retrieved remotely instead of traveling to the meter. At present power factor profiles can be obtained.

In the future there would be no use for recording equipment to be used to monitor quality of supply issues. The meter would double as a recorder and if a customer query is received the meter could be interrogated immediately and the problem rectified. This would also lead to improved customer satisfaction.

6. SECURITY OF THE SYSTEM

The remote system has exactly the same security as the present system. In order to gain access the remote software is needed as well as the telephone number of the particular meter. Each meter also has a unique serial number that is linked to the telephone number of the meter. This link is established in the meter set-up when the meter is

first programmed. A password is also needed before the meter can be reprogrammed.

7. CONCLUSION

The cost of a complete remote unit is R 4400 and this must be compared to the savings that would be made in transport and labour costs. The monthly subscription cost would be R 34 for a 2400-baud rate data line and this new tariff will be launched by MTN in November [5].

I think that using the cellular network is a viable option especially where the electronic meter is situated in a remote area far from the depot. Meters that are situated close to the depot should still be read manually as the cost of the remote equipment cannot be justified.

The system will save ESKOM considerably in future costs and at the same time it will take us a step closer in terms of legendary customer service

8. REFERENCES

Manuals

[1] Instrument Data Communication Pty Ltd. 1997. Manual. Boston Technical Books.

[2] Nokia Cellular Data Users Guide. 1997. Users guide. Hansaprint.

Telephone conversations

[3] Muller, F. 1997 Conversation with F.Muller from Strike Technologies on the 19 February 1997 regards capability of Enermax meter and possibility of remote option.

[4] Newham, P. 1997 Conversation with P.Newham from PJ Technologies on 24 February 1997 about the remote meter reading software Pmax. He kindly agreed to provide a copy of the software on loan for the duration of the project.

[5] Jooste, J 1997 Conversation with J.Jooste from MTN on the 13 March 1997 regards cellphone applications and data transfer. MTN provided a demonstration SIM card for the duration of the project

[6] Bodkin, K 1997 Conversation with K.Bodkin from Cellular Solution Providers on the 31 March 1997 about data transfer and adapters.

STEPS TOWARDS AUTOMATING THE DESIGN OF ELECTRIFICATION SCHEMES

T Rajakanthan AS Meyer B Dwolatzky

Department of Electrical Engineering
University of the Witwatersrand, Pvt Bag 3, PO Wits 2050, Johannesburg, SA

Abstract - As part of the work being done by the Software for Electrical Distribution (SED) Group, at the University of the Witwatersrand to automate the design of rural distribution schemes, this paper focuses on certain aspects of the project. Any software tool aimed at automating facilities design requires an "intelligent" map that will allow it to perceive pertinent features in the same way as a human is able to comprehend information from maps. A software module was developed to create such an intelligent map. Using the "intelligent" map, suitable transformer zones can be determined by the computer. The complexity inherent in the latter problem is discussed and a solution is proposed. Various optimisation modules have been previously developed with the intention of eventually integrating them into a complete package that will relieve the designer of much routine tasks, thus being freed to make more creative decisions.

Keywords: automation of rural distribution design, "intelligent" map, transformer zone

1. INTRODUCTION

As is well known, major strides are underway in South Africa to supply electricity to the majority of the people. Designing electrification schemes manually is time consuming and little or no optimisation can be done due to time constraints. Furthermore, skilled manpower is required to design low cost effective electrical distribution schemes and the time available for optimising layouts is often insufficient.

To aid the electrification projects, the SED Group has for a number of years been involved in the development of several software modules that optimise various aspects of the rural distribution design process. The end goal is to integrate these modules into a single package called ASED (Automation Software for Electrical Distribution) which will enable a design of an electrification scheme to be automatically generated, with adequate accuracy. The cost benefit is that such a design could be created within a matter of hours as opposed to days or weeks.

CART (Computer Aided Reticulation of Townships) was developed initially as a tool to increase the speed of reticulation design [1]. The current version of CART (CART3) under development has powerful features that make this possible. Even though this tool is valuable, it requires considerable designer interaction. Developing an integrated package that automates the entire design process would save even more time and would facilitate a thorough search for an optimised solution. This package will incorporate the optimisation modules previously developed which include the following:

- Determination of non-domestic loads [2].
- Determination of cable routes [3].
- Calculation of voltage drops and selection of cable sizes accounting for the statistical consumer load distribution [4].
- Determination of optimum junction positions [5].
- Determination of optimum transformer junction cable connectivity [6].

Previously, these modules were incorporated within a "testbed" environment to demonstrate its functionality and interoperability [7]. Maps required by the testbed had to be manually processed so that a database can be created enabling the testbed to "visualise" the map. In order to develop a completely independent package, that can be readily used within a drafting office environment, a module had to be developed for rapidly creating such a database from real township maps. This paper discusses such a module which creates this database or more popularly referred to as an "intelligent" map. The concept was developed [8] and implemented as part of a fourth year research project.

Furthermore, a vital but time consuming part of the design process is the determination of transformer zones. This paper discusses a software module developed for the determination of these zones, which is feasible using the "intelligent" map.

2. INTELLIGENT MAPS

For manual computer based distribution design a township map in the form of a CAD file, must be available at the start of the project. However, any tool aimed at automated facilities design requires an "intelligent" map which implies a non-graphic database linked to the CAD file. The database provides appropriate information about the entities represented on the map. Thus an intelligent map enables the

optimisation software to perceive features on a map in the same the way as a human.

A specific form of an intelligent map is required by ASED. The relevant features, after defining, are filed in a text file (*.map) and are as follows:

1. The co-ordinates of the vertices that make up road or stand boundaries must all be listed. Text labels for all stands must be defined since their location is assumed to coincide with the termination point for the consumer service cable.
2. Cost regions must be defined in order for the cable router to function [3]. The townplan must contain non-overlapping cost regions and have a cost multiplier assigned that specifies the degree of difficulty in erecting a line over that region. Therefore, an additional list, similar to the one for stands and roads, is required for representing cost regions. In this case the label will be a number representing the cost multiplier.

The process of intelligent map creation is shown in the following flowchart

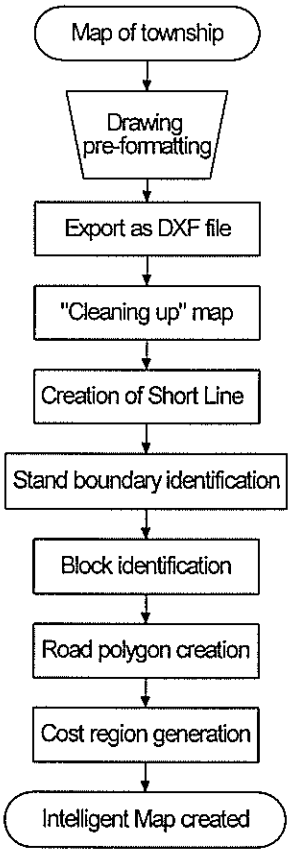

Figure 1 - Flowchart of Intelligent Map creation

The following sections will describe each of the steps shown in Figure 1.

Drawing Pre-formatting. In ASED any form of CAD package or Geographic Information System (GIS) can be used provided that they can export drawing files in AutoCAD™ DXF format. Aerial photographs and harcopy maps are usually digitised into either CAD or GIS files and then dealt with in the same way. The method used here is to segregate only those groups of features necessary for creating an intelligent map. A layer will contain all the stand boundaries while another layer will contain the text labels. A boundary is drawn around the township defining the workspace or optimisation area.

Exporting a DXF file. On completion of these steps, the map of the township is exported from its native format to an AutoCAD™ DXF format. DXF is an internationally accepted standard for exchanging drawing information. The intelligent map creation module now extracts the relevant information from the DXF file.

"Cleaning up" Maps. Digitised maps as drawn vary in quality which may imply one or both of the following defects:

- Lines drawn may not terminate exactly on other lines as intended but fall short or overshoot them. Either of these conditions will not allow computer software to correctly determine the connectivity between the various lines.
- Several vertices may be located within close range of each other near the same intended location. Therefore, there may be more than one line representing the same feature.

The following cleaning up operations are performed.

- Any two endpoints apart by less than a distance r (which has a default value of 1m but can be altered by the user) are assumed to be identical.
- Any line that falls short or overshoots a line by a distance less than r is adjusted to terminate on that line.
- All duplicate lines are eliminated.

Creation of Short lines. Execution of the short line algorithm will break up all the long lines into short ones so that each of those define a section of the boundary for not more than two adjacent stands.

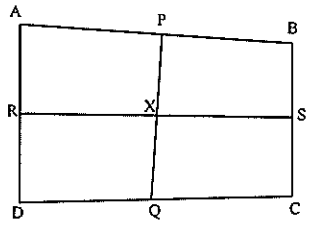

Figure 2

As an example, in drawing the block of stands (Figure 2) *ABCD* was first drawn as a polygon and *PQ* and *RS* as long lines. These long lines and the polygon need to be segmented as necessary for the stand boundary recognition algorithm. Therefore intercept points *P*, *Q*, *R*, *S* and *X* must be inserted and all the long lines segmented accordingly.

Stand Boundary Identification. This routine will identify stand boundaries given the consumer cable termination point which is the location of the stand labelling text node. This routine initially identifies the nearest boundary line and traces the remaining lines by identifying coincident endpoints. All the boundary lines for that stand are thus identified and this information is then written to the MAP file.

Street Block Identification. Before roads can be identified the street blocks must be defined. A block is defined as a boundary encompassing a group of contingent stands.

Road Polygon Creation. While roads are often drawn on maps as separate polylines a short distance from the blocks, in this work all the regions between blocks are considered to be the road reserve. There will be no separate space for the kerb. This procedure is to simplify the complexity of the problem and is an acceptable assumption particularly if the areas being electrified are informal settlements.

The areas between all the identified blocks and the township boundary is now defined as road polygons. Consider the following simple township consisting of a boundary and two blocks as shown in Figure 3a.

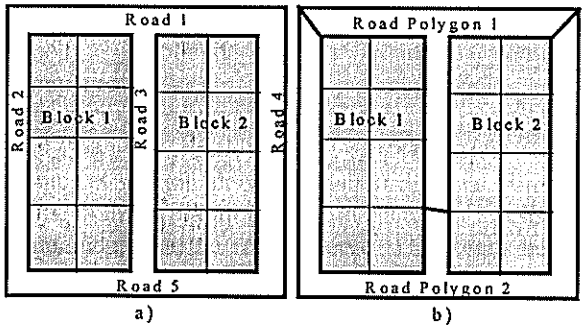

Figure 3

It can be clearly seen that valid road polygons cannot be created merely by tracing vertices on either the township or block boundaries. Interconnecting lines are required, as shown in Figure 3b, in order for road polygons to be defined. These interconnecting lines are used when tracing out road polygons which are then added to the map file.

Cost Region Generation Algorithm. It is a special requirement for the operation of the cable router, that the entire area within the township boundary consist of cost regions. When a draftsman designs the cable layout, the routes are determined by associating certain regions with a cost multiplier measuring the degree of difficulty in erecting a cable through that region. Since computer software is not able to perceive this information it has to be explicitly supplied in the form of convex polygons assigned with a suitable cost multiplier [3]. This information is appended to the MAP file.

Thus an intelligent map has been created consisting of lists of stands, roads and cost regions. The designer is provided with the opportunity to change the cost multiplier if the area encompassed by any of the cost regions warrant it.

3. DETERMINING TRANSFORMER ZONES

At present, transformer zones are determined manually. The designer starts by delineating regions that are to be supplied by a single transformer using visual inspection. The entire area of the township is thus broken up into transformer zones. The designer now counts the stands within each zone and if any have more than the transformer's capacity then they are assigned to adjacent zones as deemed appropriate and vice versa. This is a tedious and time consuming task. Once the zones have been finalised the transformers are located at a suitable position near the load centre of gravity of each zone (again determined by visual inspection).

This methodology is adequate for small areas but the degree of complexity increase substantially when considering areas that require five or more transformers. Therefore locations identified manually not only would have taken a great deal of time but may also be far from optimum.

It is for these reasons that techniques are being investigated for efficiently determining transformer zones. In order to do this an "intelligent" map is required. Existing algorithms, which address this problem, assume that the consumer density is constant and select the best transformer location from a few potential sites. One algorithm (Grimsdale et al [9]) is capable of locating the specified number of transformers on given map of a township. The zones determined using this method were all approximately uniform in area. In a township, with varying load densities, this results in a vast difference in consumers allocated per transformer.

Since this method only produced a partially acceptable solution, further processing is done to resolve this issue whereby zones that have more consumers than the maximum are transferred to the nearest adjacent transformer. Then that transformer will in turn transfer its consumers to other transformers if required and so on. Optimisation will stop when the total straight line distances from the transformer to every consumer within every allocation is approximately the same. This would result in some zones covering larger areas but encompassing fewer consumers and vice versa. Logically, this is the desired result since longer cable runs imply higher voltage drops and thus fewer consumers can be connected to those lines. On the other hand in densely populated areas more consumers can be connected to shorter lines. The transference algorithm is not discussed as its complex and beyond the scope of this paper.

This technique in its present state has a limitation in that it does not allow the locations of the transformers to be influenced by the MV line route. Furthermore, it is accepted that the zones determined will not be completely accurate and a designer may still have to modify the zones as required to facilitate special features on the map.

4. CONCLUSIONS

In the quest for complete automation of distribution design, it is clear that a further step has now been achieved to relieve the user of more routine tasks and only requiring him or her to make creative decisions. With the means for rapidly creating "intelligent" maps, ASED optimisation routines is intended to greatly accelerate the design process as compared to the use of conventional GIS which are widely used in conjunction with non-graphical distribution design calculating software packages.

Furthermore, the availability of an "intelligent" map made it feasible to develop software for determining transformer zones. Even though this routine may not calculate completely correct zones, it will provide a good starting point for the designer from which the best zones can be quickly identified.

It is accepted that while computer software will never be able to completely automate the design process, such a tool will prove valuable if it is convenient to use and ensures that the degree of user intervention required is low.

5. REFERENCES

[1] Meyer AS, Dwolatzky B, Design Tools for Mass Electrification, *International World Energy System Conference, Canada, June 1996.*

[2] Patricios MP, Dwolatzky B, Meyer AS, Utilisation of a rule based expert system to aid in Power Reticulation Design, *South African Universities Power Engineering Conference '96*, pp 227-230.

[3] West NA, Dwolatzky B, Meyer AS, Terrain-Based Routing of Distribution Cables, *IEEE Computer Applications in Power, vol 10, no 1, January 1997*, pp 42-46.

[4] Nicolson JM, Object oriented design of cable selection software for low voltage networks, *M.Sc. (Thesis) Engineering - University of the Witwatersrand, 1993.*

[5] Apostolellis J, Dwolatzky B, Meyer AS, The evolution of CAD-Based Optimisation Tools for Distribution Network Design, *IEEE Africon, Volume 1, September '96*, Pg 496-499.

[6] Tumazos SCJ, An expert/algorithm hybrid software system for automatically configuring feeder cables in low voltage distribution networks, *M.Sc. (Thesis) Engineering, University of the Witwatersrand, 1997.*

[7] Dwolatzky B, Meyer AS, A Software based Design Methodology for the Design of Low-Cost Electrical Reticulation Networks, *International Conference on Electricity Distribution (CIRED), 1997.*

[8] Rajakanthan T, Meyer AS, Dwolatzky B, Smart Maps Streamline Distribution Design, *IEEE Computer Applications in Power, January 1998.*

[9] Grimsdale RL, Sinclare PH, The Design of Housing Estate Distribution System Using a Digital Computer, *Proceedings of the IEE 1960,* 107A, pp 295-305.

Transmission line options for application to the USE concept

R. Herman and B. J. Kundy

University of Stellenbosch, Dept. of Electrical and Electronic Engineering, MATIELAND 7602, Stellenbosch, South Africa

Abstract: The paper examines available transmission line options for application to the USE (Universal Semiconductor Electrification) concept. The central point lies in so called deep rural areas where current methods of connecting to the grid are considered unfeasible due to high costs.

Keywords: Rural Electrification, USE, Voltage Regulation

1. INTRODUCTION

Power distribution in developing countries comprising, as they generally do, of rural and semi-urban areas are associated with high capital, operating and maintenance costs[1]. The electricity demand for these areas is characterized by a low annual utilization of the connected load. The combination of long distribution lines and scattered consumers is the major reason for the high cost of supplying electricity to rural areas [2].

It is well known that electricity is one of the main parameters on which the development of rural and suburban areas of developing countries depends. In South Africa, the number of people without access to electricity in rural areas is estimated to be not more than 15% [3]. In Kenya, less than 2% of total electricity revenue is from rural areas where the majority of the population lives [4].

Availability of good quality power supply at the electrical consumer terminals is the main objective of a utility. The supply voltage to electrical consumers, particularly in rural areas, is affected by high voltage drops along the MV distribution network and interruption of supply due to lightning surges. In finding a solution to the voltage regulation problem and reduction of cost in rural area networks, especially those called deep rural, the FACTS group at the University of Stellenbosch developed a μFACTS device that can compensate for voltage drops of up to 40% along the MV distribution network.

2. EXISTING METHODS OF RURAL ELECTRIFICATION

Single wire return (SWER) distribution lines are extensively applied in CAPELEC due to its relative low cost for distributing power in sparsely spread rural communities [5]. In the USA, three phase four wire systems are employed as backbone feeders throughout the rural areas. Two phase and phase to neutral lines are tapped directly from the backbone. In Ireland, a typical 10kV feeder in a rural area consists of a three phase backbone line and of single phase spurs [6]. In South Africa, the majority of its rural distribution networks are three phase systems. At present ESKOM, the power utility company in South Africa, uses some SWER distribution lines in rural areas [7].

In general, adoption of a three phase system as a backbone seems to be the trend in most rural networks in different parts of the world. The use of single phase, two phase and single-wire earth return systems are facilitated by tapping from the backbone feeder. In these systems, poor voltage regulation is common [6,8]. Voltage control measures suggested and recommended are the use of voltage regulators and fixed and switched shunt capacitors [9]. The choice of an appropriate system for the USE concept should be economically evaluated, reflecting the type of load to be served and the actual distance from the backbone line. Direct current distribution is currently being evaluated in Sweden, supplying 3MW power at a distance of 10km at ± 10kV [10].

In the so called deep rural areas, the grid connection system is not feasible due to the high installation cost and renewable energy sources are currently recommended [4].

3. CHARACTERISTICS OF THE USE DEVICES

The μFACTS device, which is an AC/DC/AC converter, employs an active rectifier, inverter, output filter and controller. At present, the system is intended to be a temporary solution in rural electrification schemes especially to areas termed as deep rural [11]. The poor voltage regulation attributed to long MV distribution lines is the main concern of any rural electrification project. The

main objective of USE devices is to compensate for the voltage drop along the MV distribution network of up to 40% and hence enabling the reduction of costs by:

- adoption of cheap conductor material such as steel wires
- utilization of longer length of standard conductors which is not possible in current practices due to voltage constraint.

To examine the capability of the developed USE devices, a laboratory set up shown in fig. 1 was used and experimental parameter values are shown in table 1 [11].

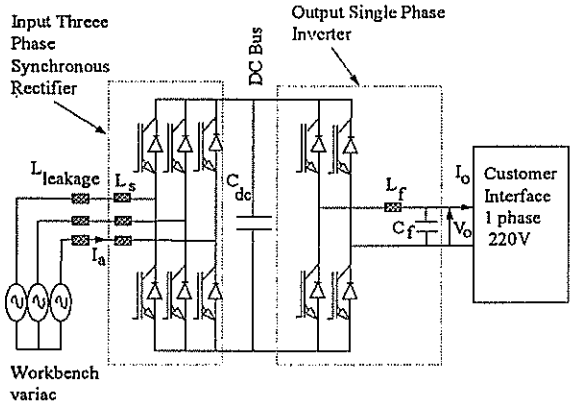

Fig. 1: Experimental setup

The device was tested against input voltage variations, load step response, induction motor start-up transient and application of non-linear diode-capacitor load. The results obtained are very encouraging. In the mean time, preparation for testing the device using an electrical full-scale model is being prepared and the results will be published in due course.

In general, at this stage, it can be concluded that, within its capability, the USE devices have the following features:

- can maintain a stable dc bus voltage irrespective of the voltage drop along the MV distribution line
- can achieve a system of unity power factor by controlling the input current phase angle
- can draw sinusoidal input line currents but only confined to mainly switching noise that can be controlled to within TDH specifications
- can maintain the input power by increasing the input line current for any voltage drop along the MV distribution line
- capable of regulating its a.c output voltage to a set value during normal conditions
- induction motor start up transients have no effect to the performance
- the a.c output voltage remains sinusoidal under application of non-linear loads [11,12].

4. POSSIBLE LINE TOPOLOGIES FOR APPLICATION IN THE USE CONCEPT

Electrical power delivery in a.c distribution network systems and in particularly in rural electrification schemes, can be facilitated by the use of four different line topologies namely: SWER, single phase, two phase and three phase systems as shown in fig. 2.

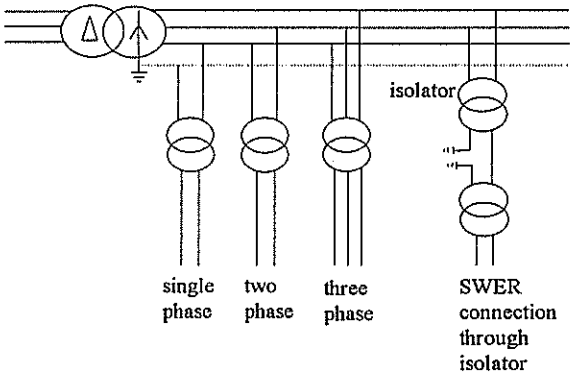

Fig. 2: Four types of line topologies suitable for power delivery to rural distribution systems

According to fig. 2, the USE devices can handle the presented line topologies [12]. In general, for any system, criteria for the choice of the appropriate line topology to be applied are based on the following:

- the length of the MV distribution line
- type of the load to be supplied i.e. low or high load density
- the magnitude of the load i.e. low load or high load
- prospects for load growth i.e. growth of population, increase in commercial activities, development of industries and etc.

4.1. USE CONCEPT SYSTEM

At present, the USE devices are limited to a current of 200A [12]. In order to be able to select an appropriate line topology for the USE system, the line topologies have to be evaluated in regard to the voltage drop and the power loss along the MV distribution line. This will be based on assumed conditions of equal load power transfer and equal length of the line. Two types of line conductor

under consideration are Bloudraad- steel and Mole-ACSR. These conductors are selected to give a relative low initial capital cost distribution network. The power losses and the voltage drops for various load powers are as shown in fig. (3),(4),(5) and (6) while the maximum possible line length with and without the USE concept at a load power of 45kW is shown in table (1),(2),(3) and (4).

5. PRELIMINARY ASSESSMENT

Normally, the rural distribution networks are designed on the basis of voltage drop. The USE concept is superior to current practice in regard to voltage drop limitation. It's capability to absorb up to 40% voltage drop along the MV distribution line at the rated power, suggests that the solution for deep rural areas is at least now manageable, taking into consideration the expected initial low consumer load demand. From these results, and in reference to table 1 and table 3, the preliminary choice of line topologies fit for the USE concept are three phase and SWER for Bloudraad-steel conductor while three phase, two phase, single phase and SWER are fit for Mole-ACSR conductor.

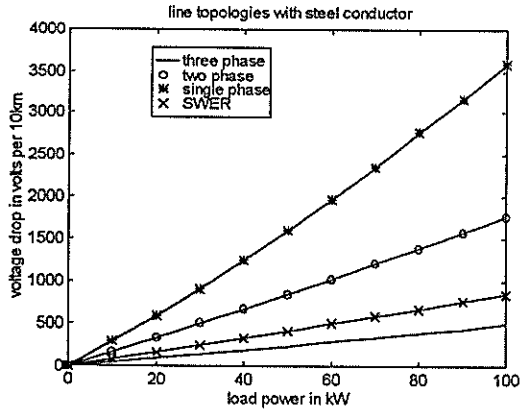

Fig. 3: Voltage drop per 10km at 22kV using Bloudraad-steel conductor

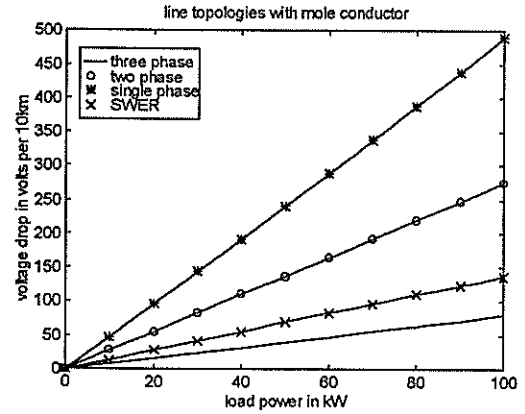

Fig. 4: Voltage drop per 10km at 22kV using Mole-ACSR conductor

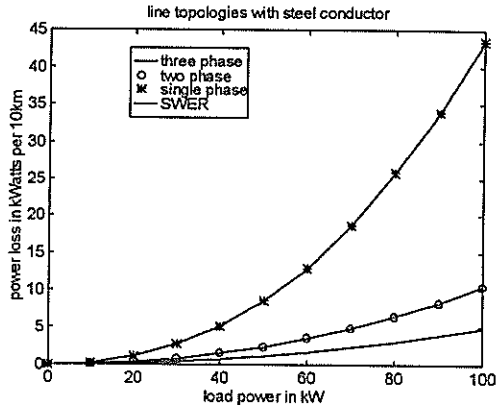

Fig. 5: Power losses per 10km at 22kV using Bloudraad-steel conductor

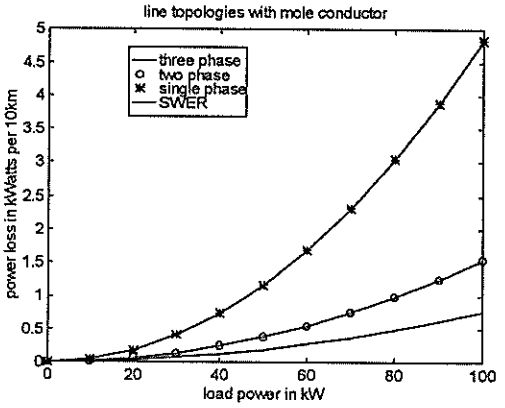

Fig. 6: Power losses per 10km at 22kV using Mole-ACSR conductor

Table 1: Maximum possible line length at 22kV for the USE concept using Bloudraad-steel conductor at a load power of 45kW

line topology	maximum possible length in km
SWER	164
single phase	27
two phase	82
three phase	164

Table 2: Maximum possible line length at 22kV without the USE concept using Bloadraad-steel conductor at a load power of 45kW

line topology	maximum possible length in km
SWER	54
single phase	9
two phase	27
three phase	54

Table 3: Maximum possible line length at 22kV for the USE concept using Mole-ACSR conductor at a load power of 45kW

line topology	maximum possible length in km
SWER	954
single phase	155
two phase	479
three phase	978

Table 4: Maximum possible line length at 22kV without the USE concept using Mole-ACSR conductor at a load power of 45kW

line topology	maximum possible length in km
SWER	325
single phase	54
two phase	162
three phase	325

6. FUTURE WORK

Future work will look into the system's capability to sustain the dc bus at higher voltages under more realistic power ratings in the order of 45kW [12]. Transient system behavior, cost of losses, system protection and reliability assessment are the topics to be investigated. The one line diagram for the electrical full-scale testing model is shown in fig.7. In order to have an accurate assessment of the line topologies, analytical work is a prerequisite. For this purpose, analytical work will be presented in the future.

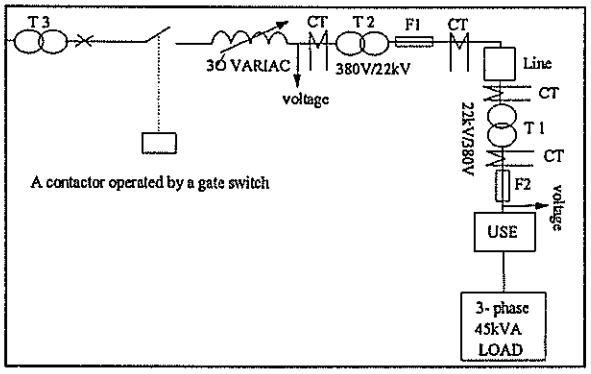

FIG. 7: ONE LINE DIAGRAM

7. CONCLUSION

The USE concept has the potential to be the solution to making rural electrification schemes possible especially in those areas termed as deep rural that are considered unfeasible by the current practices. It has been shown that the USE devices are applicable to any of the mentioned line topologies. The success of a rural electrification undertaking in developing countries lies in the implementation of low cost power distribution supply network schemes which are reliable.

8. REFERENCES

[1] Menon, S.G., Rao, B.B.V.R., "Planning of distribution systems in developing countries" IEE Proceedings, Vol. 133, No. 7, November 1986, pp. 384-388.

[2] Sabharwal, S., "Rural electrification cost including transmission and distribution losses and investment", IEEE Trans. on Energy Conversion, Vol. 5, No.3, September 1990, pp. 493-501.

[3] Dutkiewicz, R.K., 'The ANC National Meeting on Electrification', Journal of Energy R&D in South Africa, Vol.3, No.1, 1992, pp. 19-22.

[4] Ijumba, N.M., Wekesah, C.W., "Potential of renewable energy sources in rural electrification", South African University Power Engineering Conference'96, 1996, pp. 133-136.

[5] Effeney, T., "Options and evaluation for the refurbishment of the Capriconia electricity rural distribution network", Conference on Electric Energy, 1992, pp. 35-39.

[6] Shiel, P., "Evaluation of rural distribution network performance", UPEC, 1994, PP. 530-533.

[7] ESKOM Electrification Tool Box, "SWER Single wire earth return systems", January 1997.

[8] Douglas, J.A.K., "Ranking of design criteria to improve rural network performance", Reliability of Transmission and Distribution Equipment, Conference Publication No. 406, March 1995, pp. 145-150.

[9] Macey, R.E., (1989), "The influence of regulators, capacitors and reclosers on rural electrification system design" Electron, July 1989, pp.27-31.

[10] Hjort, T., Elnat AB, V., "Direct current distribution line installed in Sweden", Transmission & Distribution World, September 1997, pp.80-83.

[11] Mostert, C, Thiel, S., Enslin, J.H.R., Herman, R., Stephen, R., "Investigating the different combinations of μFacts devices in low cost rural electrification", CIGRE, September 1997.

[12] Thiel, S., Mostert, C., Enslin, J.H.R., "Universal power electronic solution to low-cost rural electrification", Electron, Nov/Dec 1996, pp. 9-12.

A VISUALLY INTERACTIVE PARADIGM FOR THE SIMULATION OF DRIVES AS A PRE- AND POST-PROCESSOR TO CASED

A.G. Levin C.F. Landy A.R. Clark
Department of Electrical Engineering, University of the Witwatersrand, Johannesburg

CASED—Computer Analysis and Simulation of Electrical Drives—provides a simulation environment tailored specifically to the analysis of complete drive systems. The technical competence of CASED as a simulation package for drives has been well established, however, the utility and usability of CASED is lacking in that the current computer interface is not very accessible to non-experienced users. This paper therefore includes a description of CASED Ver. 3.1 and an explanation of the limitations of its interface. A visually interactive simulation environment for CASED is then proposed and its improved usability over the old interface is demonstrated through a practical modelling and simulation example.

Keywords: CASED, visual interactive simulation, simulation of electrical drives.

1. INTRODUCTION

As the complexity and diversity of the application of DC and AC drives has increased, so too has the occurrence of problems, which are often caused by the interaction of various drive components. The Computer Analysis and Simulation of Electrical Drives (CASED) provides a simulation environment which is suitable for investigating the response of a wide variety of complete drive systems [1].

CASED provides a useful tool for analysing drive systems during the design phase as well as in the investigation of machinery that has malfunctioned. During design a simulation of the system is carried out using CASED. If any problems are encountered, suitable modifications to the design can be made before the drive system is implemented. Additionally, situations often arise where a drive or any machine system has failed in some way and damage has been caused to other machinery. Here, it is necessary to investigate the origin of the fault and CASED can be used to model the fault situation and enable the dynamics of the occurrence to be analysed [2].

Through situations described in the previous paragraph and cited in other papers [2], the accuracy, validity and therefore usefulness of CASED as a drive simulation tool has been confirmed. However, the utility and usability of CASED is lacking in that the current computer interface is not very accessible to non-experienced users. In this paper the limitations of CASED Ver. 3.1 are discussed. From this it is clear that an interface which combines the functionality of the CASED suite of programs into an integrated simulation environment is required. Visual Interactive Simulation is proposed as a paradigm for a pre- and post-processor for CASED and its improved usability over the old interface is demonstrated through a practical modelling and simulation example.

2. CASED VERSION 3.1

CASED is a suite of programs which are designed to interact with each other to produce a simulation environment for electrical drive systems. It is a menu driven interface and the user is required to run through a series of programs in order to analyse a drive system. A typical program sequence that one may use is: NETGEN, CREATE, SIM and GRAPH. Users may specify their own converter topology, may choose from standard library models of various drive components and define their own component modules containing a model for any physical system—including analogue and digital controllers.

In order to develop a model of a complete drive system, the user must define each drive module separately. In some cases this will mean that the modules are defined in different programs—the topology of a converter is specified using NETGEN, a user defined module must be written in C code, compiled and linked into the CASED simulation engine and then defined again in the CASED component model linker, CREATE. All the simulation modules, including any standard CASED library models, are specified and linked to one another in CREATE. SIM, the ordinary differential equation solver, can then be called to perform the simulation and GRAPH is used to view the results.

The greatest limitation with this procedure is that the user is required to follow a pre-set order of inputs and is therefore unable to backtrack and make modifications. In addition, due to the type of system that is modelled, CASED requires a large amount of information from the user which is then not very accessible for alteration. Each time the user wishes to make a modification to the converter topology or a user defined model, NETGEN must be invoked or the user defined module must be re-compiled. If any module parameters or the ODE solver require

alteration etc., this must be done from CREATE.

In addition, an overview of the simulation model is only available to the user in a text format and therefore in large projects the linking of the separate modules can be very confusing and may arise in user error. All these factors result in a user interface which is extremely time consuming to learn and use. The CASED Manual [1] contains the following paragraphs on the topic:

"It is often useful to make one small change in the information, and it is tedious to use the standard interface routines. One may therefore change the information by editing the necessary files directly using a normal text editor.

NOTE:
When editing CASED generated files CARE must be taken to ensure that the correct information is entered in the correct format. Failure to do so will cause run time errors and program termination. Edit at your own peril!"

From the above illustration it is clear that there is a need for an interface which combines the CASED Ver. 3.1 suite of programs into a single graphical simulation environment which provides an efficient direct manipulation interface of the model under investigation.

3. VISUAL INTERACTIVE SIMULATION

Visual Interactive Simulation (VIS) is a term that has been coined to describe a simulation environment where the simulation model is developed graphically, the simulation output is displayed dynamically and the user has an interactive capacity while the simulation is running. The user interaction can be such that the simulation halts and requests further information from the user at a certain point, or the user stops the program at will and interacts with the simulation by making some alteration to the model after which the simulation is continued.

With a graphical programming facility, the user is able to build models in an easier and more natural way. During the model specification phase, a graphical programming interface guides the user in a structured and interactive way, thus minimising modelling errors. At any point the user will have the ability to have the graphical model of the problem interpreted and the simulation begun. In such a model development environment, the user can explore different facets of the problem modularly and increase the complexity of the model incrementally [3].

4. THE MODULAR NATURE OF CASED AND VISUAL INTERACTIVE SIMULATION

There are two possible schemes for obtaining a model of a complete drive system. The first is to derive a model of the system as a whole, thereby obtaining only one model. The second approach is to model each of the components separately and then to link these individual models to form a complete model of the required system. CASED implements the latter approach.

This method of using modular models has a number of advantages over using a lumped model. Firstly each of the individual component models need to be developed only once, i.e. it can be re-used in another system if required. Secondly this method allows one to change the complexity of one component without having to redefine the models of the other system constituents. Any drive system model can be quickly developed from predefined standard building blocks which are easily generated [4]. And lastly, the modular nature of the drive model, and indeed the physical system itself, lends itself to being developed and displayed in a schematic format that resembles the physical layout of the drive system.

The use of individual component models requires a method by which models can interchange data amongst one another. The quantities used as interface values between the component models are voltage and current between electrical models, and torque and speed between mechanical models [4]. CASED Version 3.1 uses a text prompt to link the various input and output parameters and it is here that the greatest confusion can arise. A much more efficient method would be to graphically draw the connections between the individual component modules.

5. VISUAL CASED

An implementation of Visual Interactive Simulation—Visual CASED—has been proposed as a pre-processor and post-processor to the CASED simulation backbone. A flow-chart overview of Visual CASED is given in Figure 1.

The Graphical Model Developer forms the basis of the model development interface. The layout and connection of the various modules in a simulation project is arranged by the user and displayed graphically on the screen. A button bar menu allows the user to select the required drive component and drag it onto the Graphical Model Developer window. This will then invoke the model data editor associated with that type of model—the Model Data Editor for standard library modules, the Generalised Converter Model Generator or the User Model Developer. The model data editors will provide the user with GUI interfaces to capture the model parameters or other details as required. The Model Connection Manager provides a visually interactive method of connecting the individual drive components to form a complete model of the required system.

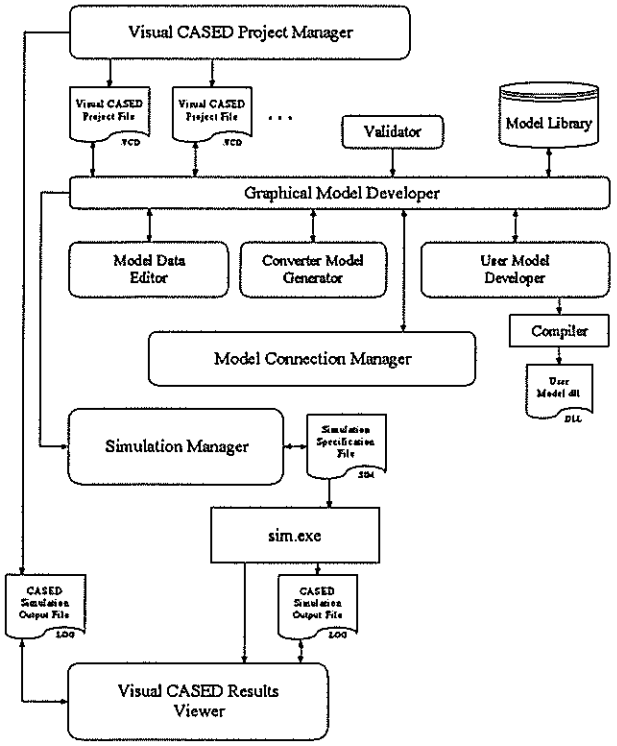

Figure 1: Overview of Visual CASED

The Simulation Manager allows the user to define the simulation parameters such as which ODE to use, the accuracy criteria and the simulation duration etc. However, its principal power lies in providing the user with interactive functionality while the simulation is running. The user may specify a number of machine parameters to be graphed concurrent to the simulation calculations. This allows trends to be viewed while the simulation is running and to thus enable the user to determine when a model parameter should be changed. For instance, once a synchronous motor has run-up as an induction motor, the field winding must be energised, and once the motor has synchronised, the full load must be applied. By pausing the simulation at the correct time, the user can make modifications to the system model or state values and then continue the simulation. In this way, three simulation iterations can be carried out in one simulation pass. Similarly, machine parameters can be altered during the simulation to model fault conditions etc. and interactively view the response.

6. A PRACTICAL EXAMPLE

An example is given which demonstrates the improved usability of Visual CASED over the CASED Ver. 3.1 interface in terms of the ease of building a simulation model. The development of a simulation model for the rotor-flux-oriented vector control of an induction motor is given.

As for DC machines, torque control in AC machines is achieved by controlling the motor currents. However, in contrast to a DC machine both the phase angle and the modulus of the current vector has to be controlled. In DC machines the orientation of the field flux and armature *mmf* is fixed by the commutator and the brushes, while in AC machines the field flux and the spatial angle of the armature *mmf* require external control. In the absence of this control, the spatial angle between the various fields vary with the load and yield unwanted oscillating dynamic responses.

With vector control of AC machines, the torque and flux producing current components are decoupled and the transient response characteristics are similar to those of a separately excited DC machine. As a result, the system will be able to adapt to any load disturbances and/or reference value variations as fast as a DC machine [5].

In modelling the above system the following drive components were identified: an induction motor and square law load, a three phase AC supply, a voltage source inverter, a rotor-flux-oriented vector controller and a pulse-width modulation timing generator for the inverter. Three phase currents from the induction motor are fed into the vector controller. The vector controller then computes the supply voltages that result in the required machine performance and passes them to the PWM timing generator. The timing generator supplies the voltage source inverter with the switch timing information required to generate the motor supply voltage waveforms.

In CASED Ver. 3.1 the above drive components must be developed separately. This results in the process of developing a model for a complete drive system being very disjointed. The induction motor, square law load and sinusoidal supply models are standard CASED library models and are therefore specified in CREATE. However, the voltage source inverter must be developed separately in NETGEN and PWM timing generator and the vector controller must be developed as separate user defined models written in C and then compiled and linked to the CASED simulation engine. All the component modules must be defined and linked to one another in CREATE.

The most user-friendly interface in CASED Ver. 3.1 is NETGEN. At the heart of NETGEN is the graphical editor into which the converter is entered in schematic form on the screen. Once the converter has been set up in the editor window using the standard converter building block symbols, NETGEN automatically generates the piecewise linear state space model of the converter schematic [1]. The voltage source inverter as developed in the NETGEN editor is given in Figure 2.

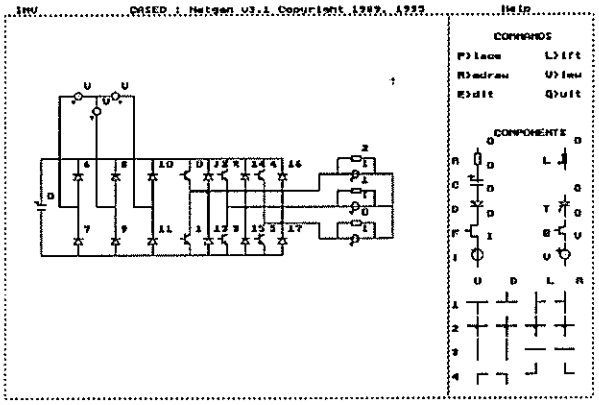

Figure 2: NETGEN model of the Voltage Source Inverter

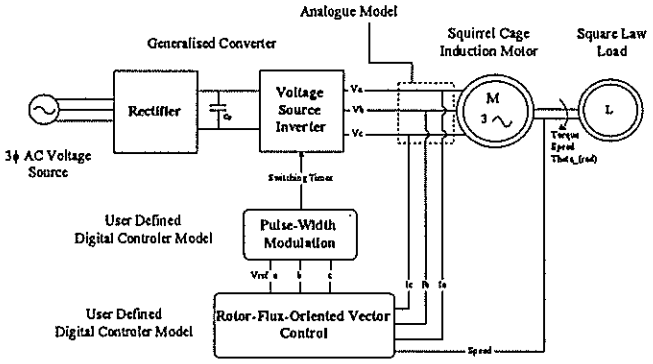

Figure 3: Visual CASED simulation model of a Vector Controller

Next, the vector controller and the PWM timing user defined modules must be written. This means that the user is required to be familiar with the C programming language. Since these are discrete time processes the digital controller model template must be used.

Once the controller and the PWM timing modules have been written and compiled, all the sub-models must be defined and linked to one another in CREATE. The user is asked to define which inputs and outputs of the modules connect to each other in order to generate the complete simulation model.

However, the motor currents and speed need to be fed back to the inverter and the load respectively, as well as being passed to the vector controller. CASED will not allow this since each interface parameter may only be linked to one other interface parameter. A further user defined model which in effect 'double adapts' these parameters must therefore be written and compiled. To do this the user must exit CREATE, write the analogue model, and start CREATE from the beginning. Similarly, each time a modification needs to be made to any of the user defined models or the converter model, they must be edited from their relevant interface program. Any of the constant parameters defined in CREATE can only be edited by re-running through the entire CREATE program.

Visual CASED, on the other hand, will provide an integrated model development environment. Figure 3 shows a schematic of the model as it will appear in the Visual CASED Model Developer. The model is developed schematically by dragging the required drive components onto the screen. The sub-model details are then edited by invoking that module's data editor—this includes an interface which steps the user through developing user defined models. Connecting the modules is achieved graphically, which eliminates confusion, and the analogue 'double adapter' model is generated automatically.

7. CONCLUSION

The technical competence of CASED as a simulation package for drives has been well established, however, various limitations of CASED Ver. 3.1 have been identified. It is for this reason that a visually interactive simulation environment as a pre-processor and post-processor to CASED has been proposed.

The suitability of this paradigm to CASED has been demonstrated through a practical example. The graphical representation formalism achieved in Visual CASED enhances conceptualisation of simulation models and acts as a communication medium among people who are involved in the project. It also enhances effective navigation throughout the model definition despite the vastness of the information structure. User interaction during simulation simplifies the modelling of systems where certain conditions change with time and allow problems and implications of different drive strategies to be easily analysed.

8. REFERENCES

[1] McCulloch, M.D. and Kleinhans, C.E., *CASED (Ver 3.1) User Reference Manual*, Department of Electrical Engineering, University of the Witwatersrand, 1995.

[2] Keinhans, C.E., Harley, R.G., Diana, G., McCulloch, M.D. and Landy, C.F., The application of CASED as a research, design and educational toolbox for drives, *Proceedings SAUPEC'96*, January 1996, pp. 153-155.

[3] Ozden, M.H., Graphical programming of simulation models in an object-oriented environment, *Technical article, Simulation 56:2*, Feb. 1991, pp. 104-116.

[4] McCulloch, M.D., Landy, C.F., Levy, W. and MacLeod I., CASED: A simulation package designed for variable speed drives, *Technical article, Simulation 57:4*, Oct. 1991, pp 216-226.

[5] Vas, P., *Vector Control of AC Machines*, Oxford University Press, New York, 1990.

DESIGN CONSIDERATIONS OF LINEAR MOTOR HOISTS FOR UNDERGROUND MINING OPERATIONS

R.J. Cruise C.F. Landy

Department of Electrical Engineering, University of the Witwatersrand, Johannesburg.

Linear motor hoists have been proposed as one alternative to conventional hoisting methods. The main advantage of the linear motor system is the lack of a requirement of a hoisting rope. Without the rope, the efficiency of the hoist is independent of depth and therefore the depth of operation is not limited by the weight of the rope. The successful design and implementation of a linear motor hoist is dependent on two main factors; namely the force to weight ratio that the motor can produce and the size and hence cost of the motor. Both analytical and finite element methods are used to show that a linear motor hoist is both a safe and feasible option for underground mining operations.

Keywords: linear synchronous motors, permanent magnets, Detent force

1. INTRODUCTION

Linear motor propelled hoists are being considered as one alternative to alleviate the transportation problem associated with ultra deep-level mines [1]. Due to the wide variety of linear motor configurations and sizes available, it is often difficult for the design engineer to select the best configuration for a particular application. This is partly due to the specialised nature of linear motor applications. Consequently, the design considerations for each application vary so widely that it is almost impossible to come up with a generalised analytical design procedure for linear motor systems. This paper presents a design procedure specifically for linear motor propelled hoists. Analytical equations as well as *Finite Element Methods* (FEM) will be used to verify the validity of certain design decisions.

2. CONVENTIONAL VS. ROPELESS HOISTS

One criteria for assessing the performance of a hoist is the efficiency of the overall system [2].

$$\eta = \frac{P_{payload}}{P_{total}} \qquad (1)$$

where

η	Efficiency of the system
$P_{payload}$	Mechanical power required to lift the payload (kW)
P_{total}	Total mechanical power required to operate the system (kW)

2.1 Conventional Hoist

Neglecting friction and assuming a constant speed of operation, the efficiency of a conventional hoist can be re-defined as follows:-

$$\eta = \frac{m_{payload}}{m_{payload} + m_{skip} + m_{rope}} \qquad (2)$$

where

$m_{payload}$	Mass of the payload (kg)
$m_{payload}$	Mass of the skip (kg)
$m_{payload}$	Mass of the rope (kg)

If it is assumed that the mass of the skip and the mass of the payload are both kept constant, then the efficiency of the system becomes entirely dependent on the mass of the rope.

$$m_{rope} = \frac{\pi D^2}{4} d\rho \qquad (3)$$

where

D	Diameter of the hoisting rope (m)
d	Depth of the shaft (m)
ρ	Density of steel (kg.m^{-3})

The mass of the rope is dependent on the depth of operation d. The deeper the shaft, the longer and therefore the heavier the hoisting rope becomes. The heavier the hoisting rope, the larger the cross-sectional area of the rope has to be in order to be able to withstand the increased tensile stresses. The increase in diameter contributes further to the weight of the rope which has a marked effect on the overall efficiency of the system (Figure 1).

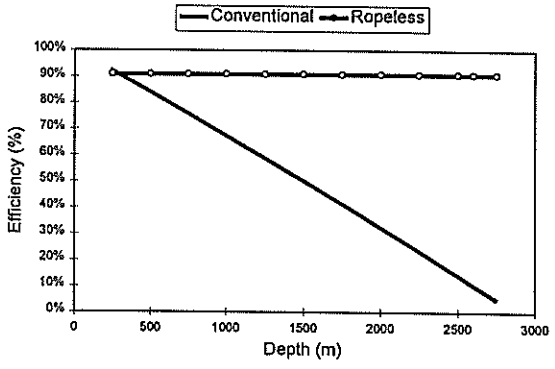

Figure 1: Efficiency of hoisting systems.

The conventional hoist's efficiency tends to zero as the system approaches its maximum operating depth. Consequently, a conventional hoist cannot operate below depths of 2800m.

2.2 Ropeless Hoists

If the hoisting rope is removed, then the efficiency of the system depends only on the mass of the skip and the mass of the payload.

$$\eta = \frac{m_{payload}}{m_{payload} + m_{skip}} \quad (4)$$

The mass of the skip and the mass of the payload are kept constant and therefore the efficiency of the system is independent of depth. The efficiency of the hoist is then determined by the maximum thrust force that can be produced per unit weight of the lift cage. The *Force to Weight Ratio* (FWR) of a ropeless hoist is therefore a critical parameter as it has a marked influence on the performance of the system. If it were assumed that a ropeless hoist could produce a FWR of 10 (i.e. the skip would weigh one tenth of the weight of the payload), then the efficiency of the ropeless system would be 91% irrespective of depth (Figure 1).

2.3 Operating Costs

The following operating costs have been calculated from results obtained from an in-depth analysis of the power requirements of each system [3]. Table 1 clearly shows that the elimination of the hoisting rope results in a significant saving in operating costs. This saving, extended over the life of the mine (i.e. 50 years), amounts to a value in excess of R1.5 billion.

Table 1: The operating costs of hoisting systems.

Description	*Conventional*	*Ropeless*
P_{total}	20MW	2.2MW
Energy cost	0.2R/kWh	0.2R/kWh
Annual operating cost	R35 million	R3.8 million

3. LINEAR MOTOR HOISTS

As with conventional electric machines there are two main parts to linear motors, that is, the primary (stator) and the secondary (rotor). There are also various forms of linear machines, long-primary, short-secondary machines or short-primary, long-secondary machines. In both cases either the primary or secondary part can be stationary, with the other member being the one that moves. The two types of linear motors investigated for use in hoisting applications are the *linear induction motor (LIM)* and the *linear synchronous motor (LSM)*.

3.1 Linear induction motors

Short-primary, long-secondary LIM's have been considered for hoisting applications [3]. One of the main reasons for this is that the track (a sheet of aluminium mounted on an iron backing) has a low cost per distance ratio. However, LIM's require a small air-gap (<1mm) in order to ensure an adequate FWR. This, together with the low efficiency and poor power factor of the motor, rendered the short-primary, long-secondary LIM impractical for mining applications.

3.2 Linear synchronous motors

A long-primary, short-secondary LSM is another alternative for hoisting applications [4,5]. The main advantage is that in the event of a power failure, the dynamic braking characteristics [6] of the system can control the falling mover to ensure a safe descent. LSM's have both a better efficiency and power factor and are easier to control than LIM's. Even with a relatively large air-gap (≈5mm), high FWR's are achievable. The major disadvantage is the high capital cost of the system. Apart from the high cost, the LSM hoisting system appears to be well suited for the vertical transportation of men and ore in ultra-deep mines.

4. FEASIBILITY OF LSM HOISTS

4.1 Design Equations

The size of the linear motor is an important criteria for assessing the feasibility of using ropeless hoists in ultra deep-level mines [7]. The force per unit area of the air-gap can be related to the specific electrical and magnetic loading of the machine by the following equation:-

$$F = \overline{B}Q \quad (5)$$

where

F tangential force per unit area of the air-gap (N/m^2)
$\overline{B}$ specific magnetic loading (T)
Q specific electrical loading (A/m)

The vertical thrust force F_{thrust} depends on the area of the air-gap between the primary and secondary members of the motor. For a double sided or a twin single-sided linear motor the following equation holds:-

$$F_{thrust} = 2\overline{B}Qlw \quad (6)$$

where

l total length of the pole faces (m)
w width of the pole faces (m)

The above equation relates the size of the linear motor to the thrust force that can be produced. Typical values for the specific magnetic and electrical loading are given below [8].

$$\overline{B} = 0.5 - 1.0\ \mathrm{T}$$
$$Q = 30 - 80\ \mathrm{kA.m^{-1}} \quad (7)$$

4.2 Full-scale Prototype

Since the linear motor propelled hoist is of a long primary construction, the width of the primary stack is an important criteria for assessing the feasibility of the final design. By way of example, a lift cage of height 2.2 m propelled by a LSM with a secondary of width 0.2 m should be able to produce a thrust force F_{thrust} between 13kN and 70kN (depending on the specific electrical loading and average air-gap flux density of the machine). A LSM of the above dimensions is quite capable of transporting a load of 1 tonne.

4.3 Cost of Material

Costing of the device shows that the high capital cost will be offset against the reduced operating costs within two years.

5. DESIGN CONSIDERATIONS

5.1 Speed of Travel

The speed of travel v is directly related to the pole-pitch and frequency of the supply.

$$v = 2\tau f \quad (8)$$

where

- v speed ($m.s^{-1}$)
- τ pole-pitch (m)
- f supply frequency (Hz)

The speed has a direct effect on the power required by the motor.

$$P_{total} = F_{thrust} v \quad (9)$$

In order to reduce the power requirements, a relatively slow speed (2 $m.s^{-1}$) is necessary. If the system is to be run directly off the main supply, the pole-pitch will be relatively short (20 mm) resulting in small and mechanically weak teeth. The design essentially reduces to a trade-off between keeping the power requirements to a minimum or using a fixed frequency supply.

5.2 Secondary Configuration

Two types of secondary configurations are available, namely; surface mounted permanent magnets [9] and buried permanent magnets [10]. An investigation of the two systems has shown that the surface mounted system produces a higher FWR than the buried system. An analysis of the flux density waveform shows that the surface mounted system has a significantly better form factor than the buried configuration (even though both have the same amount of active material).

5.3 Detent/Cogging Forces

The Detent or Cogging force is due to the interaction between the edge of the permanent magnets and the stator teeth [11]. Numerous methods for reducing Detent forces have been investigated, namely; the skewing of the stator slots; the inclusion of semi-closed slots and the optimisation of the magnet dimensions. The results of an FEM investigation of the different methods to reduce the Detent force are shown in Figure 2 to Figure 5.

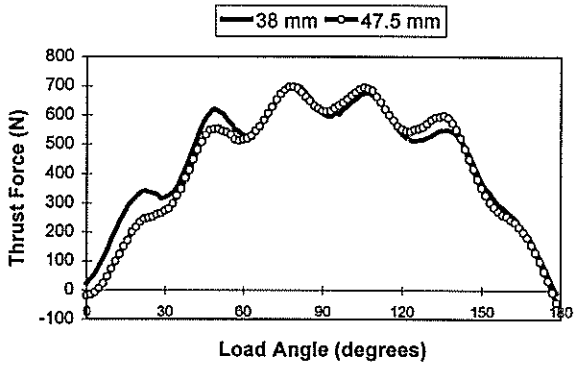

Figure 2: Optimisation of magnet length for buried permanent magnets

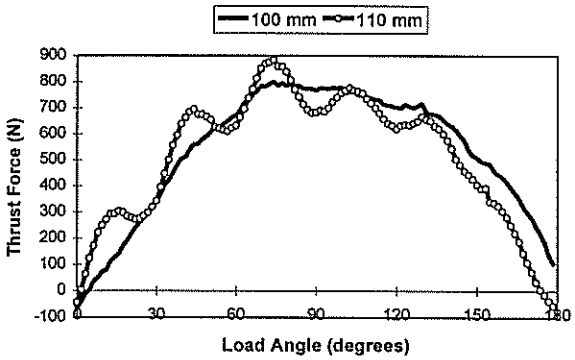

Figure 3: Optimisation of magnet length for surface mounted permanent magnets

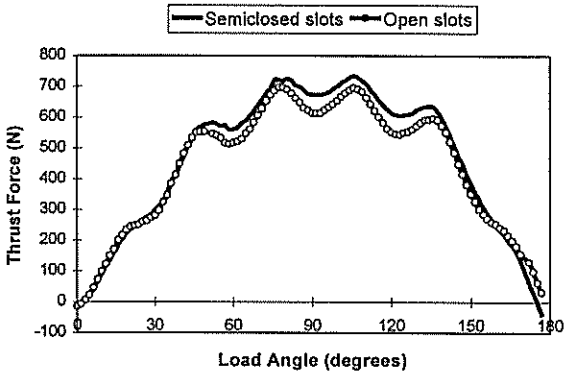

Figure 4: Comparison between semi-closed slots and open-slots

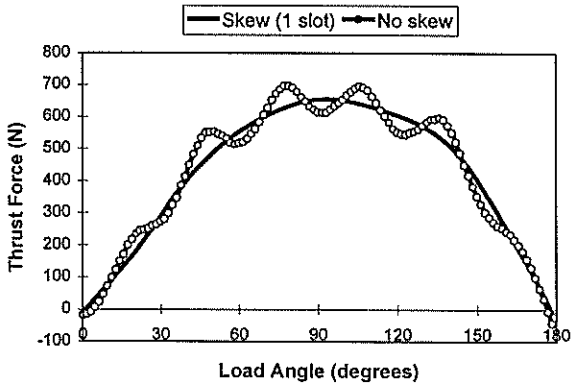

Figure 5: The effect of a skew of one slot pitch

From the above results it is clear that skewing is the most effective method of reducing the Detent force for both buried and surface mounted systems.

5.4 Mechanical Considerations

The most important mechanical consideration for a linear motor hoist is maintaining the air-gap between the primary and secondary. Over a distance of 5000m, it becomes almost impossible to ensure that small tolerances are achieved across the entire length of track. Therefore, an air-gap of at least 5 mm has to be accounted for when designing the LSM.

5.5 Thermal Considerations

Unlike rotary machines where a fan can be easily installed, a linear motor has to rely on natural cooling. Although there is a greater exposed surface area from which heat is dissipated, it may be necessary to have some form of forced cooling. This aspect of the design needs further investigation.

6. PROTOTYPE IMPLEMENTATION

Two LSM prototypes have been designed and constructed. A comparison between the predicted and measured thrust force is given in Figure 6.

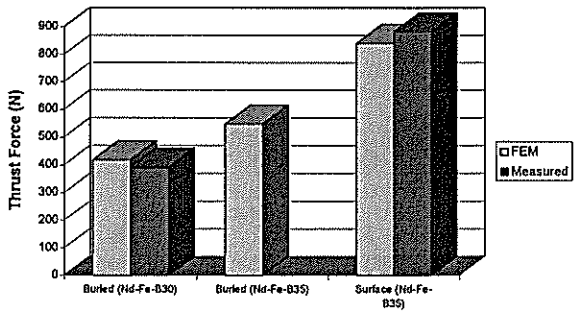

Figure 6: Predicted and measured thrust force

Since there was good correlation between predicted and measured results, the thrust force of the full-scale model could be.

7. CONCLUSION

Both the predicted and measured results indicate that the linear synchronous motor hoist is both a safe and economically viable option for ultra deep-level mines. Work is currently underway on the design and construction of a full-scale linear synchronous motor propelled hoist capable of lifting a load of one tonne through a height of 30 metres.

8. REFERENCES

[1] R.J. Cruise, N. El-Hage, B.T. le Roux, and C.F. Landy, Linear synchronous motor propelled hoist, *Symposium on Power Electronics, Electric Drives and Advanced Electric Motors*, Capri, June 1996.

[2] R.J. Cruise, and C.F. Landy, Linear synchronous motor propelled hoists for mining applications, *The 31st IEEE Industry Applications Conference*, San Diego, October 1996.

[3] H. Yamada, Y. Nakamura, T. Nakada, T. Meguro, T. Shinya and J.F. Gieras, Vertical motion analysis of a linear induction motor elevator, *Linear Drives for Industry Applications*, Nagasaki, June 1995.

[4] M. Miyatake, N. Ishikawa, T. Koseki and S. Sone, Experimental and operational study on vertical transportation system driven by a linear synchronous motor using permanent magnets, *Linear Drives for Industry Applications*, Nagasaki, June 1995.

[5] H.J. Kim, I. Muraoka, S. Torri, M. Watada and D. Ebihara, The study of the control system for ropeless elevator with vertical linear synchronous motor, *Linear Drives for Industry Applications*, Nagasaki, June 1995.

[6] H. Yamaguchi and T. Watanabe, Dynamic braking characteristic of linear synchronous motor with permanent magnet secondary and long stators for elevator, *Linear Drives for Industry Applications*, Nagasaki, June 1995.

[7] R.J. Cruise and C.F. Landy, Linear synchronous motor hoists, *The 8th International Conference on Electrical Machines and Drives*, Cambridge, September 1997.

[8] M.G. Say, 1983, *Alternating Current Machines*, Longman Scientific and Technical, 1983.

[9] M. Sanada, S. Morimoto and Y. Takeda, Design and analysis of permanent magnet linear synchronous motor for wide speed operation, *Linear Drives for Industry Applications*, Nagasaki, June 1995.

[10] J.F. Gieras, A. Spannenberg, M. Wing and H. Yamada, Analysis of a linear synchronous motors with buried permanent magnets, *Linear Drives for Industry Applications*, Nagasaki, June 1995.

[11] T. Yoshimura, M. Watada, S. Torii and D. Ebihara, Study on the reduction of Detent force of permanent magnet linear synchronous motor, *Linear Drives for Industry Applications*, Nagasaki, June 1995.

MODELLING AND SIMULATION OF A TWO POLE "WRITTEN-POLE" SYNCHRONOUS MOTOR BY USING " CASED"

H.G. ACAR & C.F. LANDY

UNIVERSITY OF THE WITWATERSRAND, JOHANNESBURG, SOUTH AFRICA

E-MAIL : LANDY@ODIE.EE.WITS.AC.ZA TEL: 27-11-716-5357 FAX:27-11-403-1929

Abstract: A new type of AC machine has been developed which can open new possibilities for rural electric co-operatives. This paper will summarize the technology and the two-axes theory developed for the Written-pole operation and the simulation aspects of the "Written-Pole"machine by using a research toolbox: **CASED**

Keywords: Synchronous motor, Written-Pole motor, Generalized machine theory, CASED, field flux vector, divided rotor winding, simulation.

List of symbols:

R,L,X = resistance, inductance,reactance
V= voltage
I = current
M = mutual inductance
ω_r = rotor speed
ω_s = synchronous speed
θ = load angle

suffixes:

d,q = direct, quadrature axis
s, t = damper windings
F_D, F_Q = field windings
Lad, Laq = d and q axis armature wdgs
m = maximum value
lr = rotor leakage
ls = stator leakage

1. INTRODUCTION

Written-Pole technology has been around for over a decade.[1] The recent development of the Written-Pole motor (W-P) promises a solution to serving large horsepower loads on rural single phase lines. The motor employs a new technique; once the unit attains 80% of synchronous speed, an exciter coil in the stator turns on and writes or flashes temporary poles onto a layer of semi-permeable magnets in the rotor. The temporary written-poles permit the motor to develop the high torque of a synchronous machine when it approaches its synchronous speed. The number of poles decreases as the motor speeds up thus allowing the motor to lock on to its synchronous speed. Many conventional synchronous machines employ a wound rotor with external d.c. applied to the rotor (field) winding.The Written-Pole motor has a high resistance squirrel cage rotor without field windings. The field system of the conventional machine is substituted by the pole writing mechanism.[2] The technique applied here provides an effective way for controlling the position of the field flux vector. Previous field and laboratory tests proved that the Written-Pole motor develops starting torque due to the hysteresis of the magnetic layer and the high resistance squirrel cage.The rotor is designed for 20% slip or more and the inherent hysteresis torque brings the rotor close to synchronous speed before the motor exciter coil is energized. The exciter coil is energized such that it writes a pole pattern on the rotor magnetic surface. The position and the number of poles of the magnetic field can be changed as the machine rotates. This effectively allows the machine to operate in such a way that the speed and the frequency are independent of each other because the number of poles is a controlled variable.[3]

Fig 1: Construction of "Written-Pole" motor

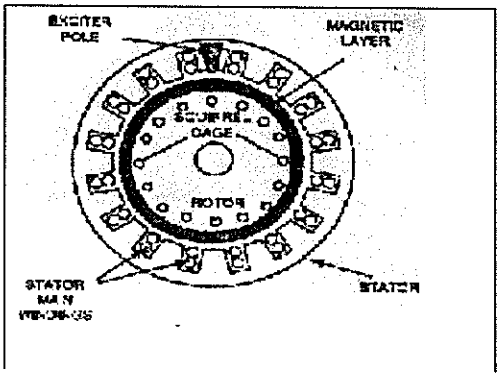

2. WRITTEN-POLE MOTOR MODEL

In order to obtain a Written-Pole motor model, the conventional synchronous machine (SM) model has been used. The SM model comprises a stator winding that is provided with two orthogonal axes of symmetry; a d-axis coincident with the pole axis and a q-axis situated midway between the poles. The three phase stator windings of both machines can be transformed into d-q axes armature (d and q) windings. The rotor of the SM is equipped with one or more damper windings which act as the cage of an induction motor. The squirrel cage rotor of the W-P motor is represented as two damper windings (s and t). In most cases it is sufficient to include two damper windings in order to represent the transient characteristics [5].

The ability to electrically place the magnetic poles in any position allows for the control of the position of the rotor field with respect to the stator field. This concept may be modelled as dividing the rotor field winding into d and q axis windings respectively (F_D and F_Q). The resultant field flux vector and stator flux vector can be made to interact and accelerate the machine to synchronous speed with maximum torque. Figure 2 shows the W-P motor model with the stator and rotor windings interchanged for the convenience of analysis.

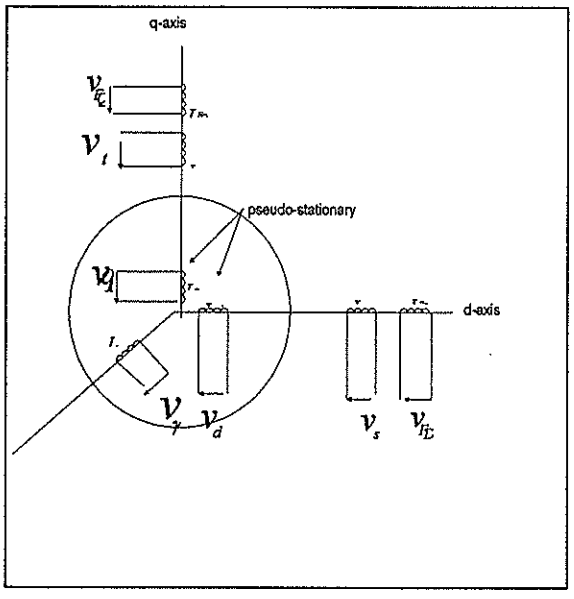

Fig 2: Three phase winding representation of a Written-Pole synchronous machine

3. "WRITTEN-POLE" MOTOR VARIABLES IN MATRIX FORM

Using the notation of figure 2 , the electrical equations of the Written-Pole machine in the rotor reference frame and with two stator field and two damper windings, can be written as follows [6]:

$$\left[V_{dq\gamma F_D stF_Q}\right]=\left\{\left[R_{dq\gamma F_D stF_Q}\right]+\left[L_{dq\gamma F_D stF_Q}\right]p+\omega_r\left[G_{dq\gamma F_D stF_Q}\right]\right\}\left[I_{dq\gamma F_D stF_Q}\right]$$

$$\begin{bmatrix} V_d \\ V_q \\ V_\gamma \\ V_{F_D} \\ V_S=0 \\ V_t=0 \\ V_{F_Q} \end{bmatrix} = \begin{bmatrix} (R+pL_d) & -\omega_r L_q & 0 & M_{dF_D}p & M_{ds}p & -\omega_r M_{qt} & -\omega_r M_{qF_Q} \\ \omega_r L_d & (R+pL_q) & 0 & \omega_r M_{dF_D} & \omega_r M_{ds} & M_{qt}p & M_{qF_Q}p \\ 0 & 0 & (R+pL_l) & 0 & 0 & 0 & 0 \\ M_{dF_D} & 0 & 0 & (R_{F_D}+pL_{F_D}) & M_{F_D s}p & 0 & 0 \\ M_{ds}p & 0 & 0 & M_{sF_D}p & (R_s+pL_s) & 0 & 0 \\ 0 & M_{qt}p & 0 & 0 & 0 & (R_t+pL_t) & M_{tF_Q} \\ 0 & M_{qF_Q}p & 0 & 0 & 0 & M_{F_Q t}p & (R_{F_Q}+pL_{F_Q}) \end{bmatrix} \begin{bmatrix} i_d \\ i_q \\ i_\gamma \\ i_{F_D} \\ i_s \\ i_t \\ i_{F_Q} \end{bmatrix}$$

expanding this equation

$$V_d = Ri_d + p(L_d i_d + M_{dF_D} i_{F_D} + M_{ds} i_s) - \omega_r\left(L_q i_q + M_{qt} i_t + M_{qF_Q} i_{F_Q}\right)$$

$$V_q = Ri_q + p(L_q i_q + M_{qt} i_t + M_{qF_Q} i_{F_Q}) + \omega_r(L_d i_d + M_{dF_D} i_{F_D} + M_{ds} i_s)$$

$$V_\gamma = Ri_\gamma + p(L_l i_\gamma)$$

$$V_{F_D} = R_{F_D} i_{F_D} + p(M_{dF_D} i_{F_D} + L_{F_D} i_{F_D} + M_{F_D s} i_s)$$

$$V_S = 0 = R_s i_s + p(M_{ds} i_d + M_{sF_D} i_{F_D} + L_s i_s)$$

$$V_t = 0 = R_t i_t + p(M_{qt} i_q + L_t i_t + M_{tF_Q} i_{F_Q})$$

$$V_{F_Q} = i_{F_Q} R_{F_Q} + p(M_{qF_Q} i_q + M_{F_Q t} i_t + L_{F_Q} i_{F_Q})$$

where $p=\frac{d}{dt}$ M is the mutual inductance, V is a vector of voltages, R is a diagonal matrix of resistances, L is a matrix of inductances, and G is a matrix of speed voltages.

Under steady-state operation, the damper windings are short circuited. Since there is no voltage applied to the squirrel cage windings ; they are taken as equal to 0.

4. EVALUATION OF PARAMETERS USED IN CASED

In order to obtain computed results , a procedure has been followed in the simulation which covers the three operational modes of the experimental motor.

Initially the machine is simulated as an induction motor starting and during run-up. At some subsynchronous speed the machine is switched to a

synchronous machine where the final conditions pertaining to the induction motor operation are used as initial conditions for this mode of operation. Finally the W-P operation is simulated by adjusting the field currents appropriately.

Initially the field system of the experimental motor was disabled temporarily by disconnecting the exciter winding connections. This allowed the standard Induction motor tests to be done on the motor, giving the results indicated below:

1) Stator resistance: $R_S = 0.3$ ohm.

2) Light running test : No load impedance

$X_{NL}=X_M+X_{ls}=X_M+X'_{lr} = 7.18$ ohm.

3) Locked rotor test:

Magnetising reactance: $X_M=5.15$ ohm.

Rotor resistance: $R'_2=0.4$ ohm.

The parameters used in the general model of the W-P motor are determined from the actual test results of the induction mode. The reason for this can be explained as:

- In a multi-winding machine, if the single turn equivalent coil is considered, then the mutual inductances between coils located on the same axis can be taken as equal to each other [7].

The d-axis mutual inductances L_{ad} then equal the three mutual inductances between the d-axis field damper and rotor windings ie,

$$M_{F_D s} = M_{ds} = M_{F_D d} = L_{ad}$$

Similarly the q-axis mutual inductance L_{aq} equals the three mutual inductances on the q-axis.

$$M_{F_Q t} = M_{qt} = M_{F_Q q} = L_{aq}$$

Another useful simplification for the W-P motor model is the non-salient structure of the motor. The saliency effect of the exciter winding in the stator structure can be ignored and the machine can be regarded as an uniform airgap machine. This provides the equality of the d and q axes mutual fluxes and inductances.

$$L_{ad} = L_{aq} = M$$

5. COMPLETE MOTOR MODEL IN CASED

CASED is a C based software toolbox which provides a simulation environment suited to the design and analysis of a wide variety of complete drive systems. To date most simulations of VSD applications have been specific to one particular type of topology, or have been simplified to model either the converter or the motor. CASED overcomes this limitations by providing a simulation environment which is suitable for checking the response of a wide variety of complete drive systems including supply, the converter, the motor and the mechanical load [8].

The complete W-P motor model has been obtained by linking separately the d-q axis motor model, user defined field and speed models and supply and load models. When the rotor approaches synchronous speed the rotor field pattern is fixed and the rotor runs at synchronous speed. This speed dependent excitation system has been created in CASED as a user defined model. The motor model and user defined models have been linked together to give an exact motor model.

Simulation results:

In order to start the motor in induction motor mode, the field winding resistances are set at high values (1.5Mohm). In the synchronous motor or W-P mode the field winding resistances were re-set to their actual values. This results in the speed and torque traces are shown in figures 3 and 4. In the first 9.5 seconds the machine is starting and running as an induction motor. At some speed it is switched to W-P operation and at the maximum speed of this mode the machine is switched to synchronous machine operation. The associated torque transients are clearly visible.

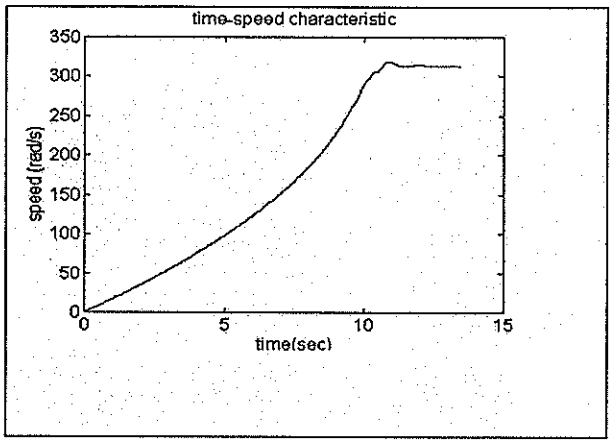

Fig: 3 Free acceleration curve of motor

In order to simulate the W-P mode the voltages applied to the two field windings (in the simulation) are given by

$$V_{FD} = V_m Sin(|\omega_s - \omega_r|t + \theta)$$

$$V_{FQ} = V_m Cos(|\omega_s - \omega_r|t + \theta)$$

It can be seen that these rotor speed dependant voltages develop time varying excitation voltages. When the rotor synchronises the excitation becomes only a function of the load angle.

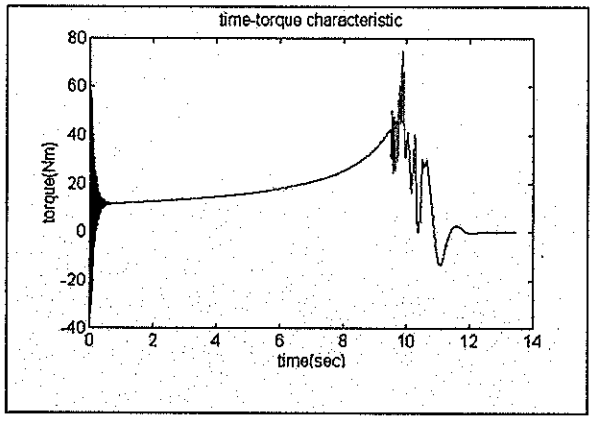

Fig: 4 Torque curve of motor

6. FURTHER WORK

In order to verify the modelled results, speed and acceleration tests will be done on the W-P motor using the double disk system. The measurement technique used in this set-up relies on differentiating the speed to give the acceleration, which yields the torque under no load conditions. [9] Subsequently the effects of other switching modes and delays can be assessed.

7. CONCLUSION

A new design for synchronous motors has been developed that offers performance advantages not available with machines of conventional construction. By controlling the rotor magnetic field the motor can be designed for very soft start. This feature allows the machine to be built up to 100-hp for single-phase application.

REFERENCES

1. Introduction and Overview of W-P technology.
John.F. Roesel Jr.
Proceedings of the 1995 IEE Technical Applications Conference and Workshops NORTHCON'95

2. Electrical Field Measurements on an Epri Two-Pole 20 Hp. W-P Motor. Alan Hannah
IEE Transactions On Industry Applications Vol:33 No.2 March/April 97

3. Operating and Electrical Characteristics of "W-P" Machines Ronnie Barber & Richard T. Morash
Proceedings of the 1995 IEE Technical Applications Conference and Workshops NORTHCON'95

4. CASED: A Simulation Package Designed For Variable Speed Drives.
M.D.Mcculloch,C.F.Landy,W.Levy,I.MacLeod
Technical Article Simulation 57:4 October 1991. simulation councils. Inc.ISSN 0037-5497/91 USA pp. 216-226

5. Analysis of Electric Machinery
Paul C. Krause, Oleg Wasynczuk, Scott D.Sudhoff
IEEE Press 1994 NJ

6. Introduction to Generalized Electrical Machine Theory
O'Kelly D, Simmons S. 1968. London, McGraw -Hill

7. Alternating Current Machines
M.G. Say Edinburgh 1976

8. The Application of CASED As A Research, Design and Educational Toolbox For Drives
C.E. Kleinhans, R.G. Harley, G. Diana, M.D.Mcculloch
South African Universities Power Engineering Conference'96

9. Modelling and Simulation of Induction Motors for Variable Speed Drives With Special Reference To Deep Bar and Saturation Effects.
Warren Levy Ph.D Thesis 1990.
University Of Witwatersrand

Small scale maglev system with permanent magnets and a linear induction motor.

Y. W. Tung and J. F. Gieras
Department of Electrical Engineering
University of Cape Town.
http://emf1.ee.uct.ac.za,
Email: jgieras@eleceng.uct.ac.za

Abstract

This paper describes the use of permanent magnets and a linear induction motor for a maglev vehicle. Tests were performed to investigate the optimum thickness of the undercarriage of the vehicle and the effect of varying the air-gap. The performance can be substantially improved by decreasing the air-gap.

Keyword Maglev. Permanent magnets. Linear induction motors. Magnetic levitation.

1. Introduction

Maglev systems are said to be the transport of the future and the main reason is that such a system is energy efficient. The advantages are numerous for example, low level of noise, low level of vibration, no air pollution and fast transport. It therefore demands a thorough understanding of maglev systems.

The main aim of this project is to demonstrate the repulsive forces between permanent magnets [1, 2, 3, 4, 8] and propulsion forces produced by a linear induction motor (LIM) [5, 6, 7,]. Throughout this experiment, the stabilisation problem is being solved by providing lateral constraints. Tests were being performed to find the optimum levitation and thickness of the undercarriage and also the effect of the air-gap on the thrust exerted by the vehicle.

One of the difficult problems in maglev systems is control. It requires a very precise positioning. Normally, sensors are being used.

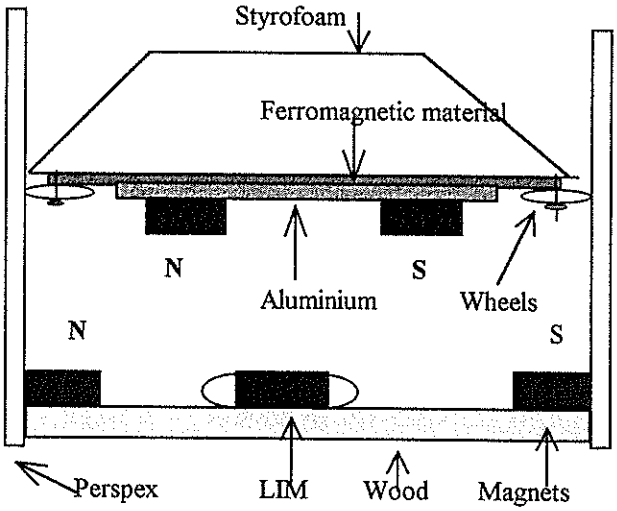

Fig. 1 Outline of suspension system.

2. Construction and dimensions

In this system, the levitation has been achieved using (NdFeB) permanent magnets (PMs). The magnets have been aligned on a track of 1m length and also placed on the vehicle. To protect the magnets from rough treatments such as the impact of attractive forces or the clamping down of the magnets on the vehicle, a C-shaped aluminium cover has been used. Then, the whole structure has then been glued to an L-shaped wood as shown in Fig 2.

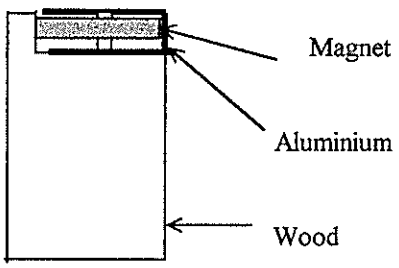

Fig. 2: Front view of the C-shaped cover.

Based on Earnshaw's theorem [8], a levitating vehicle cannot be stabilised using PM alone. Owing to time constraints, the control section has been left out. So, *Perspex* walls have been used, fixed to the wooden structure by means of brass screws, to stabilise the whole system. This keeps the vehicle inside the track.

The only mechanical way to reduce the friction to a minimum is to use ball bearings. A wheel has been made using a new product called *Tufcot*. This synthetic material is chosen as it has a lower coefficient of friction compared to the other materials and also it does not store static charges. Therefore, no distortion of magnetic field is expected inside the track when using *Tufcot*.

The number of turns of wires that can fit in a slot had to be made and numerous tests have been performed with different thicknesses of the wires.

To make the windings, calculations have been made to find the diameter of the wires. The calculated current from a computer programme is 2.8 A and based on the standards, the round 0.95 mm wire has been found to be the most appropriate.

Winding coils in the slots of the transformer laminations make a LIM. The laminations are stacked with width of 25 mm and clamped by an L-shaped aluminium bar. The windings are star connected. The whole LIM has then been dipped in a resin which has basically three purposes: firstly to "glue" the laminations together and secondly to strengthen the insulation system and thirdly to improve the heat transfer.

After numerous experiments the optimum suspension height was found to be 24 mm. The size of the vehicle is 150 by 200 mm. The whole size of the system is 200 mm by 1000 mm.

3.Experimental tests.

A pulley system and brass weights have been used to measure the thrust. This thrust is very small as the air-gap is large.

Different thicknesses of the undercarriage have been tested and graphs in Fig 3, 4 have been plotted. The graphs of current and power factor (P.F) against thrust have been plotted. From these graphs, the 3 mm plate seems to be the best as the LIM draws less current.

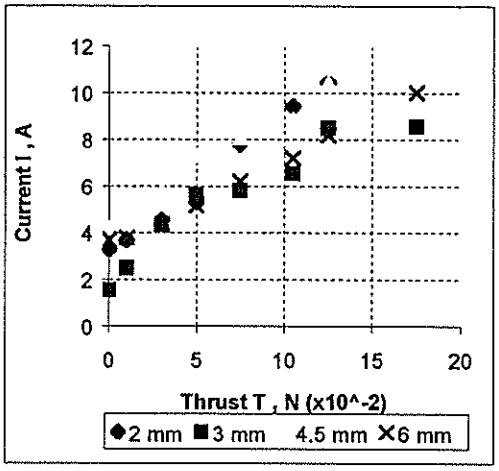

Fig. 3: Phase current against thrust at different thicknesses of the undercarriage (air-gap 24 mm).

The 3 mm plate is the more energy efficient compared to the other plates.

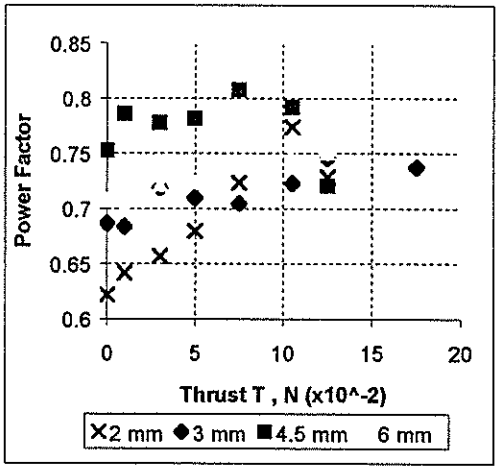

Fig. 4 : Power factor against thrust at different thicknesses of the undercarriage (air-gap 24 mm).

The P.F for the 3 mm bottom is also lower than that for the other plates (Fig 4). Since this is a

small-scale system, the P.F is expected to be low.

Also, the air-gap between the vehicle and the LIM has been reduced. As can be seen from the graphs, the current drawn is smaller (compared to the previous tests shown in Fig. 3, 4). The air-gap was reduced from 24 mm to 20 mm. The problem in this case is the stronger attractive force between the ball bearings and the magnets on the track when the air-gap is reduced further. However, if the air-gap is reduced further, the thrust measured is inaccurate.

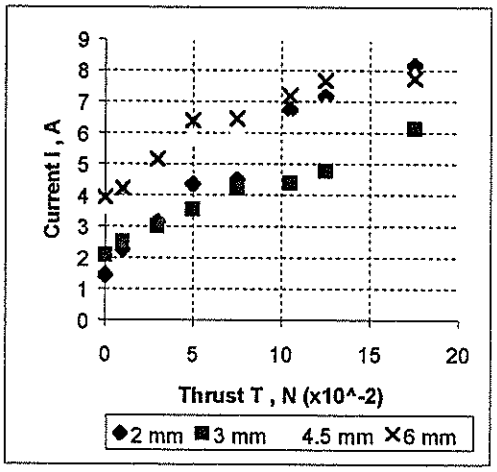

Fig. 5: Phase current against thrust at different thickness of the undercarriage (air-gap 20 mm).

As it can be seen, the current drawn by the LIM in the case of a 3 mm plate is lower compared to the other plates (Fig 5) and also compared to the previous test (Fig. 3).

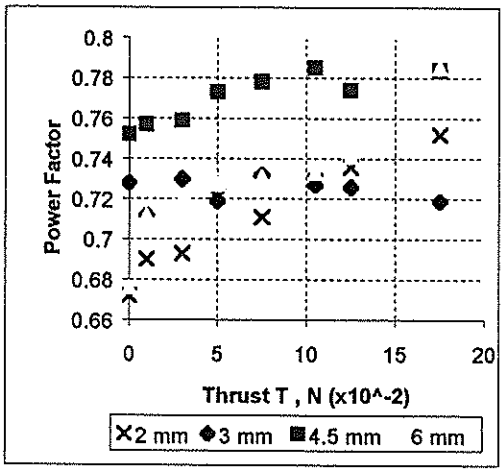

Fig. 6: Power factor against thrust at different thickness of the undercarriage (air-gap 20 mm).

The P.F is slightly lower than that in the previous test (Fig 6).

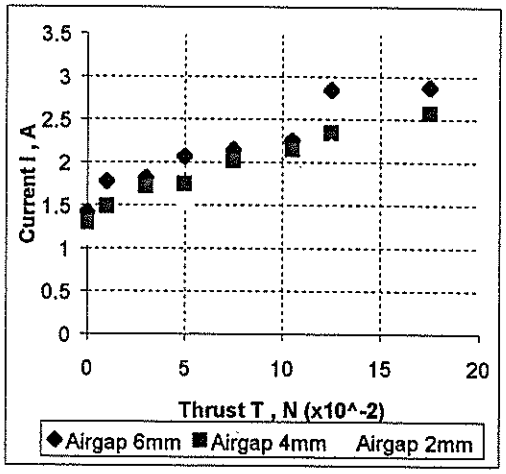

Fig. 7: Current against thrust at 3 mm bottom of the undercarriage and different air-gaps.

As the air-gaps have been varied, it was observed that in the case of the 2 mm air-gap, less amount of current can do the same amount of work (Fig 7).

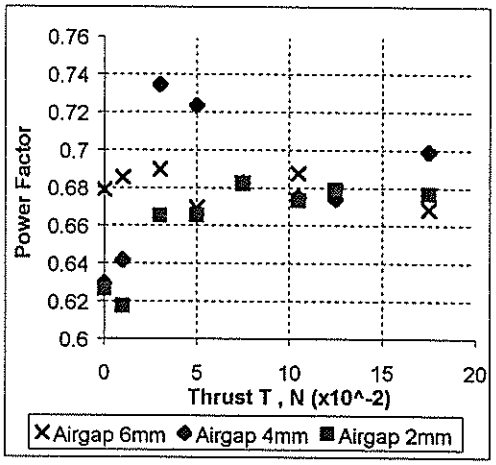

Fig. 8: Power factor against thrust at 3 m bottom and different air-gaps.

The P.F is found in the region of 0.68. (lower than in Fig. 6 and Fig.8).

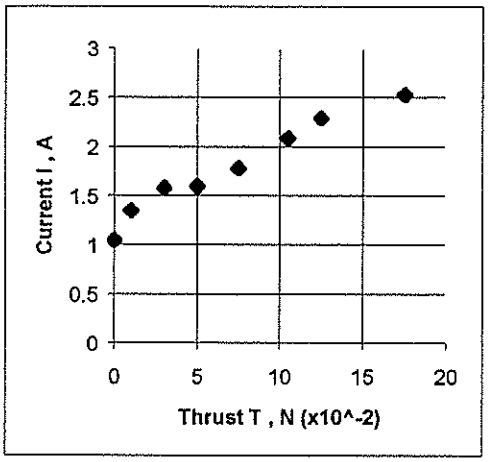

Fig. 9: Current against thrust at 5 mm back iron fixed to the top of the undercarriage.

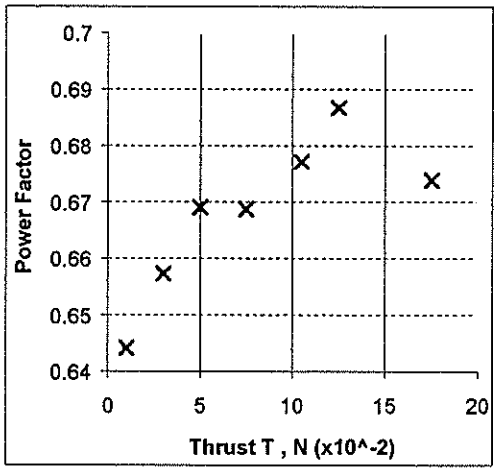

Fig. 10: Power factor against thrust at 5 mm back iron fixed to the top of the undercarriage.

The thickness of the ferromagnetic material (back iron) of the undercarriage has also been increased in order to reduce the magnetic saturation (Fig 1). The effect of the increased thickness of the ferromagnetic material on the overall performance of the system can be seen in Fig. 9, 10.

4. Conclusion

Test results show that the thickness of the undercarriage (both aluminium plate and back iron) of the vehicle and the air-gap affects the performance of the system. From the graphs shown in section 3, the reason why the 3 mm plate was chosen is obvious. The LIM draws less current compared to other designs. There is also quite a big difference in the amount of power consumed by the LIM with the vehicle of different thickness of its bottom.
The air-gap is also very important in this experiment. The smaller the air-gap, the smaller the current drawn. To improve the efficiency, the air-gap must be reduced to the minimum. On the other hand, the mechanical clearance could be smaller than 6 to 8 mm.

5. Acknowledgement

This work was supported by the FRD, Eskom and University of Cape Town.
Mr Mike Paterson of Metro Rail in Cape Town made the windings for the LIM.

REFERENCES

1. E.Okamato, S. Torii, M. Watada, D. Ebihara, S. Komura, T. Ohhara. Characteristics of Electrodynamic suspension system with the combination of levitation and propulsion, LIDA' 95 Nagasaki, 1995, pp. 89-92

2. E. G. Knolle, Bright future for languishing maglev technology, pp. 340- 345, International Conference on speedup technology Stech' 93, Yokohama, 1993 Vol. 1, pp 340-345

3. T. Mizuno, K. Araki, T. Ouchi Repulsive magnetic levitation system with movable PMs. LIDA' 95 Nagasaki,1995 , pp. 143-146

4. H. Tsunashima ; Permanent magnets suspension for maglev transport vehicle, Report of the Research Institute of Industries, Nihon University, No. 50, 1997.

5. J. F. Gieras , Linear Induction Drives. Clarendon Press, Oxford 1994.

6. E. R. Laithwaite, Induction machines for special purposes, G. Newnes Ltd, London, 1966.

7. E. R. Laithwaite, Propulsion without wheels, English University Press, 1966

8. V. Jayawant, Electromagnetic Levitation and Suspension Techniques, Electromagnetic Levitation and Suspension Techniques, Edward Arnold, 1981.

Small-scale maglev system with a V-shaped transverse flux linear induction motor

Y. Chin, J.F. Gieras and J.T.J. Mokoena
Department of Electrical Engineering, University of Cape Town
http://emf1.ee.uct.ac.za, E-mail: jgieras@eleceng.uct.ac.za

Abstract

A special experimental small-scale linear induction motor (LIM) with transverse flux, salient poles and V-shaped magnetic circuit has been discussed. The V-shaped secondary made of high conductivity nonferomagnetic material has been suspended, propelled and stabilized electrodynamically. The small-scale transportation system has been tested experimentally. The following problems have been investigated: (1) the influence of the thickness of the secondary on the system performance, (2) effect of the input voltage on the hover-height and thrust and (3) the stability of the V-shaped secondary.

1 Introduction

The linear induction motor (LIM) with transverse magnetic flux can find many applications in factory transportation systems. It is possible to construct the primary and the secondary in such a way that the thrust, the lift force and the lateral stabilization force are produced simultaneously by the same excitation system. Eddy currents are induced in the secondary by the primary magnetic field and, in addition to the thrust, a lift force is produced [1, 7, 6].

The paper refers to a special V-shaped magnetic circuit of a LIM with transverse flux, salient poles and V-shaped nonferromagnetic secondary made of aluminium. The secondary (or maglev vehicle) is suspended electrodynamically and propelled by travelling magnetic field excited by the primary unit (Fig. 1). The optimisation of the shape and structure of the secondary are essential for the improvement of the system performance.

2 Construction

The long primary consists of 54 electromagnets with the E-type laminated cores distributed in two parallel rows (each row consists of 27 electromagnets). Three electromagnets are assembled together to form a *three-a-group* unit, and each unit is bolted onto the 1700-mm long and 150-mm wide steel plate. There are 60 laminations of standard thickenss 0.5 mm per each core. The number of turns per one core is 217. The pedestal of the model consists of three 1800 × 76 × 38 mm C-channels which are welded together by using 10 ϕ 12.7-mm steel pipes placed between three channels. The angle adjusting mechanism is designed to vary the superelevation angle of each of the electromagnet row. The model is also furnished with a level-adjusting mechanism under the pedestal (Fig. 2). The pole pitch is $\tau = 0.18$ m, the number of pole pairs is $p = 3$, and the number of phases is $m = 3$. The three-phase primary winding is star-connected and fed with a 50 Hz three-phase power supply. The sequence of connection of the electromagnets in each row is A, -B, C, -A, B, -C, ... etc. where A, B and

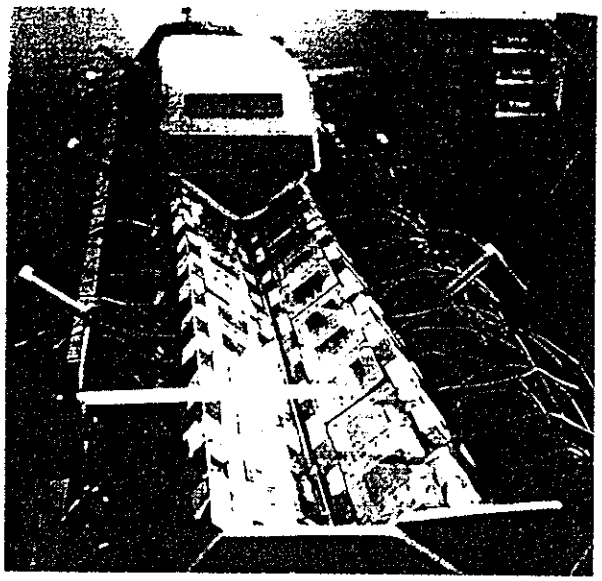

Figure 1: LIM with transverse flux magnetic flux and the V-Shape secondary suspended electrodynamically.

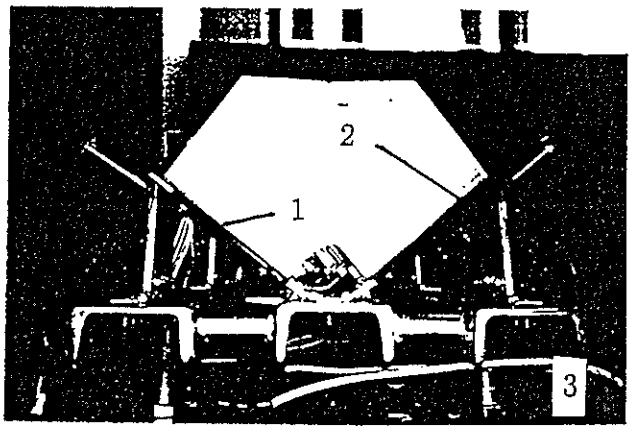

Figure 2: Construction of the small-scale model: 1 — V-shaped track, 2 — angle adjusting mechanism, 3 — level adjusting mechanism.

C are the phase windings [2, 3, 4, 5]. The secondary (vehicle) is made of a V-shaped aluminum plate with its thickness of 4.5 mm or 6 mm. The length of the plate is 300 mm and the width is 150 mm.

3 Power supply and 'shuttle operation'

The transverse flux LIM is fed from a 50 Hz, three-phase power supply via a three-phase autotransformer. The maximum line current is 20A. The voltage and current waveforms are practically sinusoidal with a low percentage of total harmonic distortion THD (less than 3.2%). Owing to the limitation of the length of the track, the model is designed for a *shuttle operation*. This has been obtained by employing two limit switches at both ends of the track and two contactors. Contactors reverse the sequence of the phase currents and the direction of the travelling magnetic field when the limit switch is triggered on by the secondary (vehicle).

4 Steady–state characteristics

The hover-height of the secondary is measured as a function of the input voltage at constant mass (Fig. 3). Fig. 4 shows the comparison of the hover-height for two plates of different thicknesses (4.5 mm and 6 mm). The measured thrust (tangential force on the secondary) as a function of the input voltage at constant mass is plotted in Fig. 5. The thrust–voltage

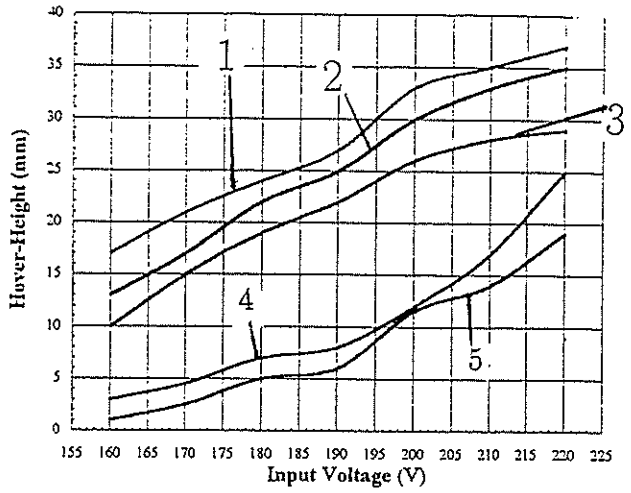

Figure 3: Hover–height plotted against the input voltage at constant mass and 50 Hz: 1 — $m = 342$ g, 2 — $m = 485.3$ g, 3 — $m = 543$ g, 4 — $m = 653$ g, 5 — $m = 784.3$ g. The thickness of the plate is 6 mm and the speed of the secondary is zero.

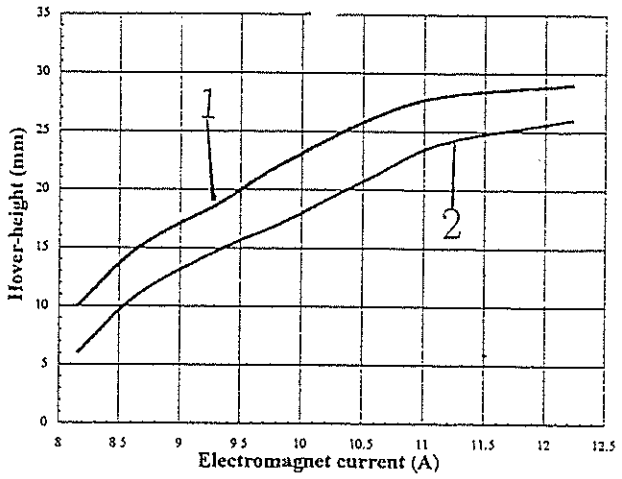

Figure 4: Hover-height plotted against the input current at 50 Hz and two different thickness of the secondary: 1 — $d = 6$ mm, 2 — $d = 4.5$ mm. The mass of the secondary is 491.2 g and its velocity is zero.

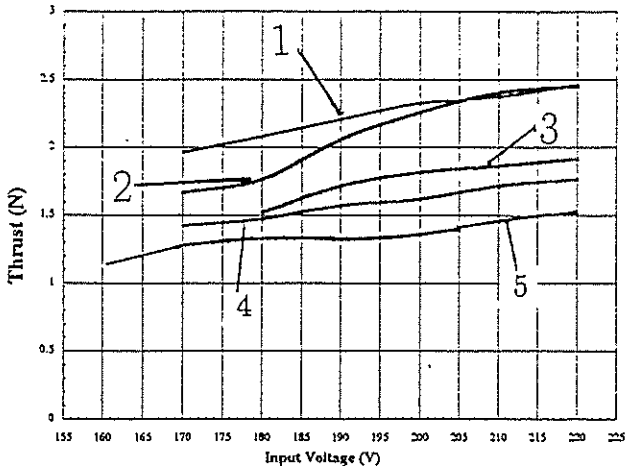

Figure 5: Thrust plotted against the input voltage for constant mass of the secondary: 1 — $m = 409.1$ g, 2 — $m = 485.3$ g, 3 — $m = 491.2$ g, 4 — $m = 543$ g, 5 — $m = 563$ g. The input frequency is 50 Hz and the velocity is zero.

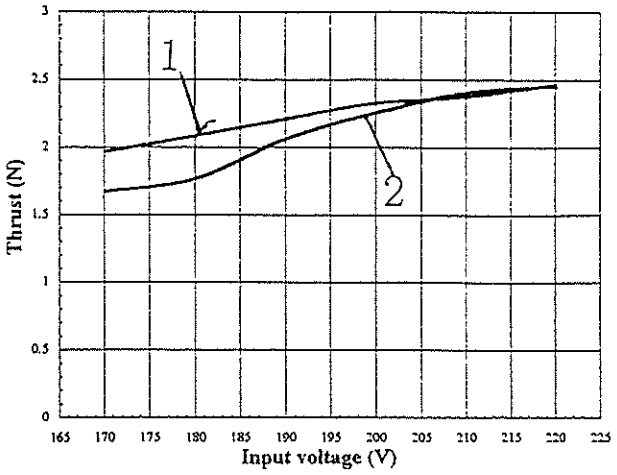

Figure 6: Thrust plotted against the input voltage at 50 Hz for different thicknesses of the plate: 1 — $d = 4.5$ mm; 2 — $d = 6$ mm. The mass of the secondary is 784.3 g and its velocity is zero.

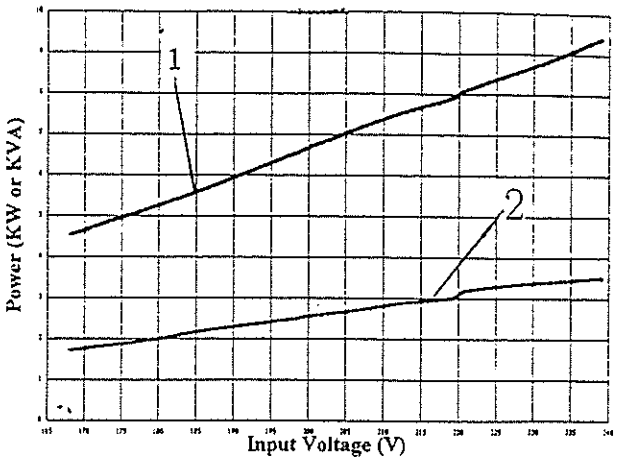

Figure 7: Apparent and active power plotted against the input voltage at 50 Hz, 6-mm thick aluminium secondary ($m = 784.2$ g) and zero speed: 1 — apparent power, 2 — active power.

characteristics for two plates of different thicknesses and the same mass are shown in Fig. 6.

The input power absorbed by the track as a function of the input voltage when the 6-mm, 784.2-g aluminum secondary is at standstill is plotted in Fig. 7.

5 Finite element analysis

The electromagnetic field distribution and forces have been calculated by using the finite element method (FEM). The normal and tangential forces produced by a single electromagnet are shown in Fig. 8.

6 Conclusions

The V-shaped construction improves the stability of the vehicle. The angle and level adjusting mechanisms are essential for smooth operation. The width of the aluminum plate is limited. There is no lateral stability of the vehicle if the width is less than 150 mm.

It has been found on the basis of experimental tests that:

- the secondary with V-shaped bottom and 40 degrees superelevation angle is the best construction from the lateral stabilization point of view;
- the most suitable length for the smooth shuttle operation is 300 mm;
- both 4.5-mm and 6-mm plates are suitable for the shuttle operation, however, the 6-mm plate

(a)

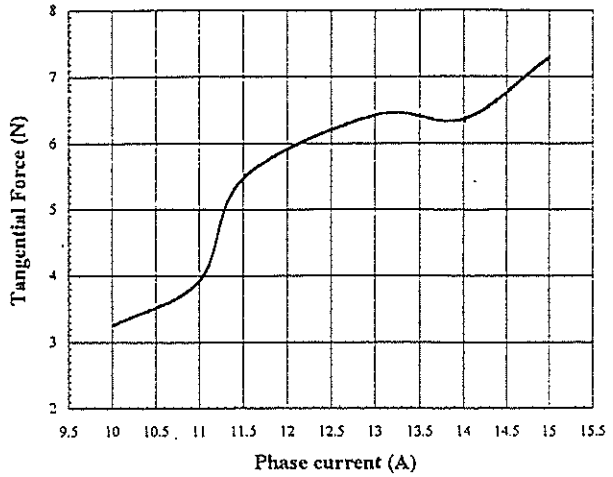

(b)

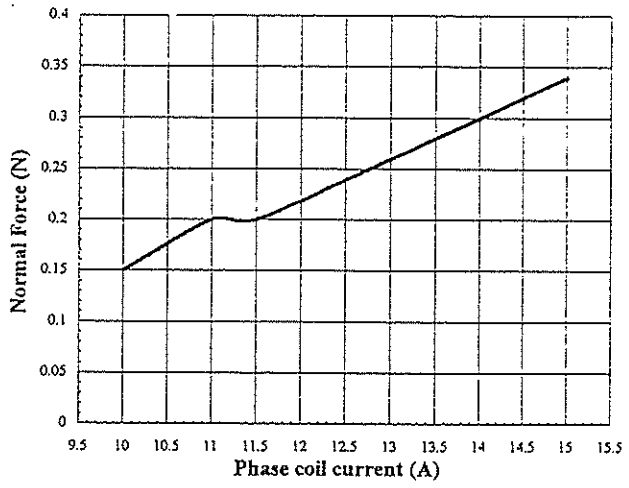

Figure 8: Normal and tangential forces produced by a single electromagnet as functions of the current: (a) tangential force (thrust),(b) normal force.

can produce higher thrust and lift forces at the same input voltage;

- both the thrust and lift forces increase as the input voltage increases when the mass of the secondary is kept constant.
- vehicles can not reach the steady state speed due to the short track length since the theoretical synchronous speed at 50 Hz is approximately 20 m/s.

These conclusions can be slightly different for a copper secondary because both the electric conductivity and specific mass density of copper are higher than those for aluminum.

Acknowledgements

This work was supported by the FRD, Eskom and the University of Cape Town.

References

[1] Eastham, J.F. and Laithwaite, E.R.: *Linear induction motors as 'electromagnetic rivers'*. **Proc. IEE, 121** No. 10, 1974, pp. 1099–1108.

[2] Gieras, J.F.: *Electrodynamic levitation forces — theory and small-scale test result*, **Acta Technica ČSAV, 26**, No. 4, 1981, pp. 389–414.

[3] Gieras, J.F.: *Linear induction motors with transverse flux in electrodynamic levitation system*. **Int. Conf. on Electr. Machines ICEM'82, 3**, Budapest, 1982, pp. 980–983.

[4] Gieras, J.F.: *Influence of structure and material of secondary suspended electrodynamically on steady performance characteristics of linear induction motor with transverse flux*. **etzArchiv, 6**, 1984, pp. 255–260.

[5] Gieras, J.F. *Transverse flux electrodynamic levitation systems*. **Int. Conf. on Maglev Transport**, Tokyo, Japan, 1985, pp. 207–215.

[6] Gieras J.F.: **Linear induction drives**, Clarendon Press, Oxford, 1994.

[7] Laithwaite, E.R., Eastham J.F., Bolton H.R. and Fellows T.G.:*Linear motors with transverse flux*, **Proc. IEE, 118**, No. 2, 1971, pp. 1761–1767.

FREQUENCY RESPONSE OF CAPACITIVE VOLTAGE TRANSFORMERS AND INSULATED CURRENT TRANSFORMERS

H.J. Vermeulen, A.C. Britten*, M.W. Roberts* and J.M. Strauss

Department of Electrical and Electronic Engineering, University of Stellenbosch

* Technology Group, ESKOM

Abstract – This paper presents the results of an investigation to determine the steady-state frequency responses of the capacitances measured between the high voltage terminals and grounding points of a 400 kV capacitive voltage transformer and an insulated 132 kV current transformer respectively. The test arrangements are described, particularly with reference to the excitation methods, and frequency response results are given and interpreted for the frequency range from 100 Hz to 500 kHz. The results show that the terminal capacitances of both test devices exhibit excellent wideband responses up to 100 kHz.

Keywords: capacitive voltage transformer, current transformer, frequency response

1 INTRODUCTION

The measurement of wideband high voltage (HV) signals is becoming increasingly important for power system monitoring activities such as harmonic penetration studies, quantifying transient phenomena and studying the causes and effects of high frequency noise. The accuracy of standard high voltage transducers such as capacitive and magnetic voltage transformers (CVTs and VTs) is, however, specified for the rated frequency only and it has been showed that these devices have limited bandwidth [1,2]. Wideband voltage measurements on HV systems are therefore expensive, disruptive and time-consuming due to the need to install special wideband transducers. This motivates the need to determine whether standard substation equipment such as VTs, CVTs and current transformers (CTs) can be used, possibly in non-standard topologies, for wideband HV measurements.

The proposed strategy for using CVTs and insulated CTs for HV measurements relies on the fact that the terminal impedance of the devices, as observed between the HV terminals and ground points, represents a capacitor at the frequencies of interest. The devices can therefore be used in a capacitive divider topology, i.e. where the device is earthed through an additional measuring capacitor and the output voltage is obtained from the resultant capacitive divider midpoint. Alternatively, the device can be used in a transconductance topology, i.e. where the input voltage is derived from the ground return current by integration.

This paper presents the results of an investigation to experimentally determine the frequency responses of the terminal capacitances of a CVT and an insulated CT respectively for the frequency band from 100 Hz to 500 kHz.

2 EXPERIMENTAL DETERMINATION OF THE FREQUENCY RESPONSES

The experimental work for the CVT was conducted for the base unit, i.e. without the complemental capacitors, as this reduces the required excitation voltage by a factor of three. The required excitation currents were simulated for excitation voltages of 0.1%, 0.5% and 1% of the rated voltages of the test devices, i.e. $400/(3\sqrt{3})$ kV for the CVT base unit and $132/\sqrt{3}$ kV for the insulated CT, for the frequency range from 100 Hz to 500 kHz. Both devices reflected capacitive input impedances for frequencies higher than the rated frequency. The excitation currents therefore increased linearly with frequency and excitation voltage. The terminal capacitance of the CVT base unit was obtained from the nameplate of the unit, yielding a value of 9 nF. A capacitance of 1.082 nF was measured for the insulated CT, using a 50 Hz sinusoidal excitation signal. The excitation current predicted for the CVT base unit ranged from 0.44 mA (0.1% excitation at 100Hz) to 22 A (1% excitation at 500 kHz). The excitation current predicted for the insulated CT ranged from 52 μA (0.1% excitation at 100Hz) to 2.6 A (1% excitation at 500 kHz).

The above results impose relatively severe specifications on the excitation equipment in terms of bandwidth and excitation voltage. Different excitation methods were therefore adopted for the various frequency bands in order to obtain reasonable excitation levels, i.e. of the order of 0.5% of rated value, with total harmonic distortion figures below 1%. These can be summarised as follows:

(i) **100Hz to 1 kHz:** Fig. 1 shows the measuring arrangement used for the frequency range from 100 Hz to 1 kHz. It features the standard excitation topology for medium frequency

high voltage applications, i.e. a wideband amplifier cascaded with a step-up transformer. This configuration yields excellent results up to 1 kHz, but the available output voltage and harmonic distortion deteriorate rapidly above this frequency due to the resonant nature and limited bandwidth of the step-up transformer.

(ii) **1 kHz to 100 kHz:** Fig. 2 shows the measuring arrangement used for the frequency range from 1 kHz to 100 kHz. It features a wideband amplifier which drives a series-resonant circuit consisting of an adjustable, low-loss inductor and the capacitive input impedance of the CVT base unit or CT. Voltage amplification factors of the order of 15 to 20 were obtained. The total harmonic distortion was low (below 0.5%) due to the resonant nature of the circuit.

(iii) **100 kHz to 500 kHz:** Due to the limited bandwidth of the voltage amplifier, the series resonant excitation method was found unsuitable for frequencies above 100 kHz. Increased losses also reduced the Q-factor of the arrangement, thereby limiting the achievable voltage amplification. The measurements in this frequency band were therefore obtained at a reduced excitation level, i.e. 0.005% of rated value, using direct excitation with a low voltage signal generator.

Tables I and II summarise the excitation methods and excitation voltages magnitudes used for the CVT base unit and insulated CT respectively.

Table I: Excitation details for the CVT.

Frequency Range	Excitation	
	Method	Magnitude (% of rating)
100 Hz – 1 kHz	Step-up transformer	0.5, 0.25 and 0.1
1 kHz – 100 kHz	Series resonance	0.5, 0.25 and 0.1
100 kHz – 500 kHz	Signal generator	0.005

Table II: Excitation details for the CT.

Frequency Range	Excitation	
	Method	Magnitude (% of rating)
100 Hz – 1 kHz	Step-up transformer	0.3, 0.15 and 0.05
1 kHz – 100 kHz	Series resonance	0.3, 0.15 and 0.05
100 kHz – 500 kHz	Signal generator	0.005

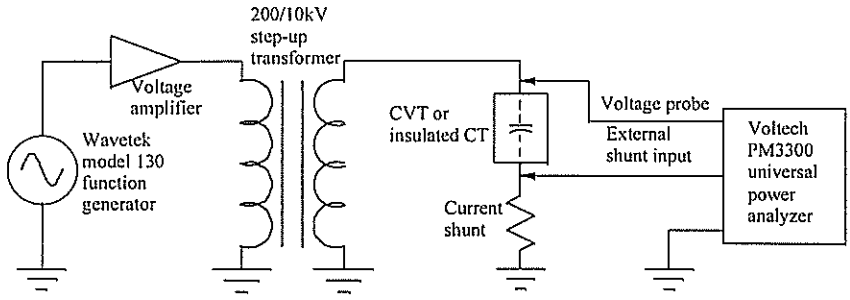

Fig.1: Test arrangement for the frequency range from 100 Hz to 1 kHz

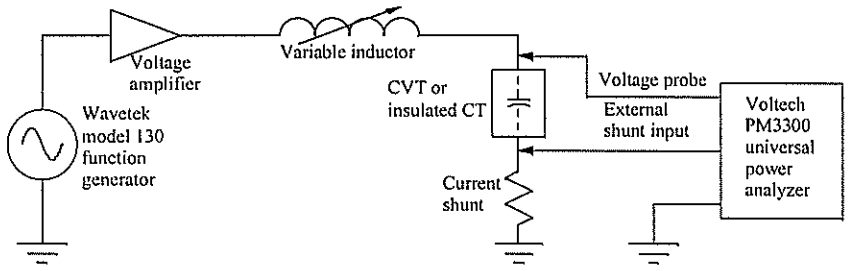

Fig.2: Test arrangement for the frequency range from 1 kHz to 100.

3 FREQUENCY RESPONSE RESULTS

The frequency response properties of the two measuring topologies are best expressed in terms of the frequency responses of the capacitances measured between the HV terminals and relevant grounding points of the test devices. The results give the normalised values of the measured capacitances, with the normalising carried out as follows for the respective test devices:

(i) CVT base unit: Normalised with respect to the capacitance given for the divider stack on the nameplate of the device, i.e. 9 nF.

(ii) Insulated CT: Normalised with respect to the equivalent capacitance measured at 50 Hz, i.e. 1.082 nF.

Figures 3 and 4 show the frequency responses of the normalised terminal capacitance of the CVT base unit for the frequency ranges from 100 Hz to 100 kHz and from 100 kHz to 500 kHz respectively. The tests were conducted with the ferroresonant damping circuit disconnected and with one set of $110/\sqrt{3}$ V secondary windings grounded.

The results given in figure 3 show a variation of less than 3.5% in the measured capacitance for the frequency range from 100 Hz to 100 kHz, and the capacitance exhibits a decreasing trend with increased frequency. This can be attributed to increased dielectric losses at the higher frequencies. The maximum deviation between the curves for the various excitation voltages, at any particular excitation frequency, is less than 0.5%. This indicates that the capacitance exhibits a good degree of linearity with excitation voltage magnitude for excitation magnitudes of the order of 1% of rated value.

The result in figure 4 shows that the measured capacitance increases dramatically with increased excitation frequency in the frequency range from 100 kHz to 500 kHz. The phase angle was observed to decrease from 90°. This is attributed to the fact that the excitation frequency approaches the selfresonant frequency of the capacitive divider section of the CVT base unit, which has been determined to be in the vicinity of 1 MHz.

The frequency response tests for the CVT base unit were repeated for a test topology with the ferroresonant circuit connected. This affects the results in the low frequency region, i.e. around 100 Hz, in the sense that the responses exhibit increased dependence on excitation level. This confirms the results reported in literature [3]. From approximately 200 Hz, however, the responses are similar to those given in figures 3 and 4. It follows that the terminal capacitance of the CVT base unit is not affected significantly by the damping arrangement in the frequency range from 200 Hz to 100 kHz.

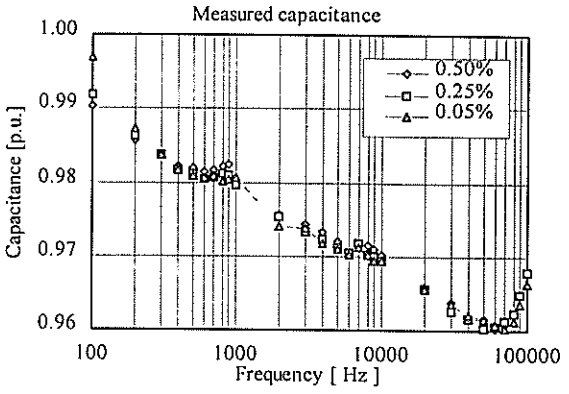

Fig. 3: Frequency responses of the terminal capacitance for the CVT base unit for the frequency range from 100 Hz to 100 kHz. Excitation magnitudes: 0.5%, 0.25% and 0.05% of rated value.

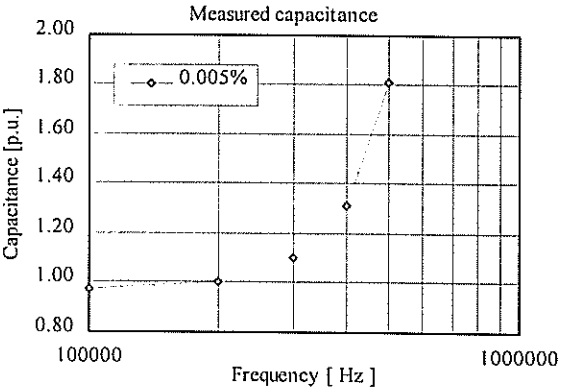

Fig. 4: Frequency response of the terminal capacitance of the CVT base unit for the frequency range from 100 kHz to 500 kHz. Excitation magnitude: 0.005% of rated value.

Figures 5 and 6 show the frequency responses of the normalised terminal capacitance of the insulated CT for the frequency ranges from 100 Hz to 100 kHz and from 100 kHz to 500 kHz respectively. The tests were conducted for a test topology with one set of the secondary windings shorted but not grounded.

The results given in figure 5 show a variation of less than 3.5% in the measured capacitance over the frequency range from 100 Hz to 100 kHz, and the capacitance exhibits a decreasing trend with increased frequency. As in the case for the CVT base unit, this can be attributed to increased dielectric losses at the higher frequencies. The maximum deviation between the curves for the various excitation voltages, at any particular excitation frequency, is less than 0.5%. This indicates that the capacitance of the device exhibits a

good degree of linearity with excitation voltage magnitude for excitation magnitudes of the order of 1% of rated value.

The result in figure 6 shows that the measured capacitance increases dramatically with increased excitation frequency in the frequency range from 100 kHz to 500 kHz. As in the case of the CVT, this is attributed to the fact that the excitation frequency approaches the selfresonant frequency of the insulated CT, which has been determined to be in the vicinity of 3 MHz.

The frequency response tests for the insulated CT were repeated for a test topology with one set of the secondary windings shorted and grounded. The responses are similar to those given in figures 5 and 6. It follows that the terminal capacitance of the insulated CT is not affected significantly by the grounding arrangement of the secondary windings.

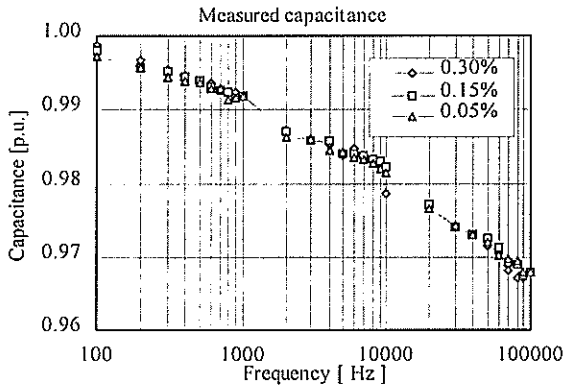

Fig. 5: Frequency response of the terminal capacitance of the insulated CT for the frequency range from 100 Hz to 100 kHz. Excitation magnitudes: 0.30%, 0.15% and 0.05% of rated value.

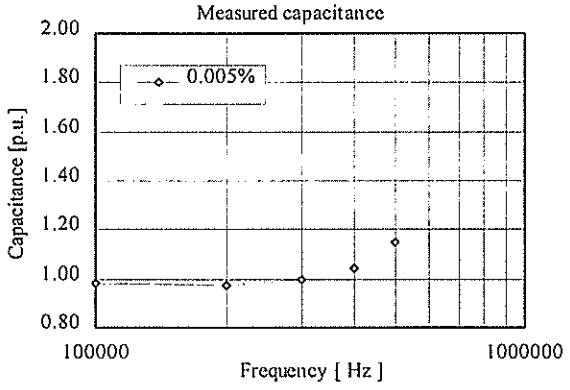

Fig. 6: Frequency response of the terminal capacitance of the insulated CT for the frequency range from 100 kHz to 500 kHz. Excitation magnitude: 0.005% of rated value.

4 CONCLUSION

Measured results have been given for the steady-state frequency responses of the terminal capacitances between the HV terminals and grounding points of a 400 kV CVT base unit and an insulated 132 kV CT. The results show that stable capacitances are obtained for both test devices up to 100 kHz.

The transfer functions associated with the two potential voltage measuring topologies, i.e. the capacitive divider topology and the transconductance topology, are closely related. Any factors (e.g. nonlinearities and resonant behaviour) which affect either one will also affect the other similarly. The two topologies have, however, the following different practical implications:

(i) Capacitive divider topology:

Measuring the output voltage across the sensing capacitor is relatively easy. This topology, however, has the important disadvantage that the normal grounding arrangement of the CVT or CT has to be replaced with a potentially less secure connection in the form of a sensing capacitor.

(ii) Transconductance topology:

If a non-intrusive current measuring technique is used, this topology has the advantage that a secure grounding arrangement can be maintained. Wideband sensing of relatively small currents can however be difficult and expensive. It is also not trivial to construct an accurate wideband integrator given the wide dynamic range of the input signals.

ACKNOWLEDGEMENT

The authors gratefully acknowledge the financial and material support of ESKOM in sponsoring this research.

REFERENCES

[1] Bradley D A, Bodger P S and Hyland R P, "Harmonic Response Tests on Voltage Transducers for the New Zealand Power System", IEEE Trans. on Power Apparatus and Systems, Vol. PAS-104, No 7, July 1985.

[2] Douglass D A, "Potential Transformer Accuracy at 60 Hz Voltages Above and Below Rating and at Frequencies Above 60 Hz", IEEE Trans. on Power Apparatus and Systems, Vol. PAS-100, pp. 1370-1375, March 1981.

[3] Vermeulen H J and Davel P: "Voltage Harmonic Distortion Measurements Using Capacitive Voltage Transformers", 4th Africon Conference in Africa (Africon'96), September 1996, Stellenbosch, South Africa, pp. 1012 – 1017.

IMPULSE RESPONSE OF HIGH VOLTAGE CAPACITIVE VOLTAGE TRANSFORMERS AND INSULATED CURRENT TRANSFORMERS

H.J. Vermeulen, A.C. Britten*, M.W Roberts* and J.M. Strauss

Department of Electrical and Electronic Engineering, University of Stellenbosch

* Technology Group, ESKOM

Abstract – This paper presents the results of an investigation to assess the feasibility of using capacitive voltage transformers and insulated current transformers for impulse voltage measurements on high voltage systems. Time-domain impulse responses were obtained for a 400 kV CVTcapacitive voltage transformer and an insulated 132kV current transformer under laboratory conditions. Two measuring topologies are considered, namely a capacitive divider topology and a transconductance topology. The measured impulse responses, obtained for risetimes of the order of 4μs and 2μs for the capacitive voltage transformer and insulated current transformer respectively and for a range of peak values, indicate that impulse voltage peak values can be measured with accuracies of the order of 3 % for the capacitive divider topology and 10 % for the transconductance topology.

Keywords: capacitive voltage transformer, insulated current transformer, impulse response

1 INTRODUCTION

Qualitative and quantitative assessment of lightning and switching impulses in high voltage (HV) transmission systems are essential for determining the short-term and long-term effects of these phenomena on the condition of power system apparatus. In practice, however, the monitoring of impulses is hampered by the unavailability of suitable wideband transducers.

Instrument transformers such as capacitive voltage transformers (CVTs) and magnetic voltage transformers (VTs), when used in the normal configuration, exhibit bandlimited responses which disqualify these devices for impulse measurements [1,2]. Special wideband transducers such as compensated capacitive dividers have therefore to be installed. This is too expensive, disruptive and time-consuming for widespread routine application. Ideally, such an activity would only be practically feasible if standard substation equipment can be used for the impulse voltage measurements.

This paper present the results of an investigation to determine the impulse response properties of the following alternative measuring topologies of a CVT and an insulated current transformer (CT):

(i) Capacitive divider topology, i.e. where the grounding point of the device is earthed through an additional measuring capacitor, and the output voltage signal is obtained from the midpoint of the resultant divider.

(ii) Transconductance topology, i.e. where the input voltage signal is derived from the ground return current of the device by integration.

2 EXPERIMENTAL DETERMINATION OF THE IMPULSE RESPONSES

The experimental work for the CVT was conducted for the base unit, i.e. without the complemental capacitors, as this reduces the required excitation voltage by a factor of three. The CVT and CT reflected capacitive input impedances between the HV terminals and grounding points for frequencies higher than the rated frequency. A terminal capacitance of 9 nF was obtained for the CVT base unit from the nameplate of the device. A terminal capacitance of 1.082 nF was measured for the CT, using a 50 Hz sinusoidal excitation signal. The impulse response tests were conducted for a range of impulse voltage magnitudes and pulse shapes.

Figures 1 and 2 show the measuring arrangements used for the capacitive divider and transconductance topologies respectively. The impulse voltage was recorded using a precision capacitive divider comprised of C_o and C_u, with C_o = 120 pF and C_u = 1.2 nF, yielding a transformation ratio of 100.

In the case of the capacitive divider topology, the CVT base unit or insulated CT was terminated to ground through a precision measuring capacitor C_T, with C_T = 241.25 nF. The output voltages of the resultant capacitive dividers were interfaced to the recording instrumentation by means of 75 Ω coaxial cable with 75 Ω series resistive compensation.

In the case of the transconductance topology, the ground return current was sensed using a Tektronix P6303 current probe and AM503 current amplifier with a bandwidth of 5 MHz. All waveforms were recorded at a sampling rate of 5 MHz using a Yokogawa model 3656 analysing recorder and downloaded to the host computer for processing.

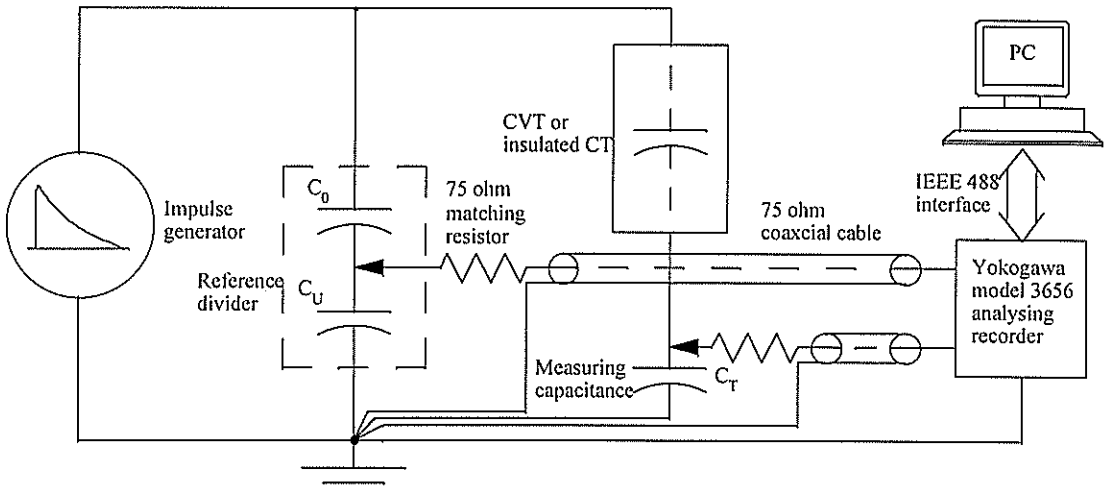

Fig. 1: Test arrangement for the capacitive divider topology.

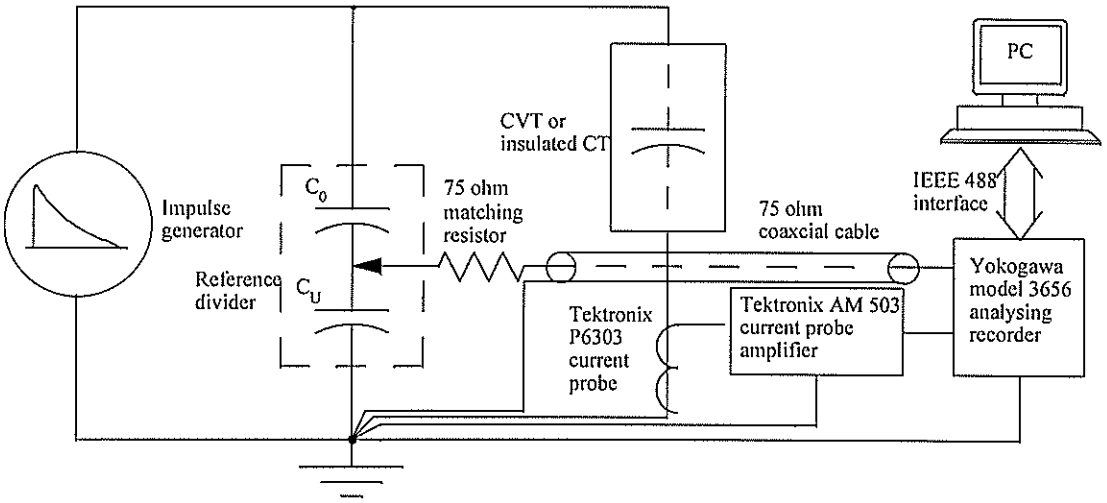

Fig. 2: Test arrangement for the transconductance topology.

3 IMPULSE RESPONSE RESULTS

The impulse responses were obtained for a range of impulse voltages, up to a peak value determined by the capabilities of the impulse generator, the load represented by the test device and the dynamic range of the data acquisition equipment. The input capacitances of the two devices differ by a factor of approximately 10, i.e. 9 nF for the CVT base unit and 1.082 nF for the insulated CT. Higher peak voltages were therefore obtained for the insulated CT compared to CVT base unit. This factor also affected the maximum risetimes that could be obtained, in the sense that a lower maximum risetime was obtained for the CVT base unit compared to the insulated CT. The impulse responses for the CVT base unit were obtained for the following test conditions:

Risetime of the input waveform: 4μs

Peak voltages of the input waveform: 3, 5, 14 and 28 kV approximately

Ferroresonant damping circuit: Disconnected

Tables I and II summarise the results obtained for the CVT base unit for the capacitive divider and transconductance topologies respectively.

Table I: Impulse response results for the capacitive divider topology of the CVT base unit.

Peak impulse voltage [kV]		Deviation
Reference divider	CVT base unit	[%]
2.856	2.791	-2.25
5.304	5.127	-3.33
14.12	13.68	-3.11
28.32	27.47	-2.99

Table II: Impulse response results for transconductance topology of the CVT base unit.

Peak impulse voltage [kV]		Deviation [%]
Reference divider	CVT base unit	
2.928	2.593	-11.4
5.364	4.640	-13.5
14.28	12.55	-12.1
28.32	24.84	-12.28

The results given in table I for the capacitive divider topology show that a maximum deviation of 3.33 % was recorded between the peak values obtained with the reference divider and the CVT base unit respectively. The relatively narrow band of deviations obtained for the various excitation voltages, i.e. 2.25 % to 3.33 %, indicates that the impulse response of this measuring topology is independent of the excitation voltage magnitude.

The results given in table II for transconductance topology show that a maximum deviation of 13.5 % was recorded between the peak values obtained with the reference divider and the CVT base unit respectively. This relatively large error, compared to the capacitive divider topology, is attributed to the inadequate accuracy of the current sensing equipment, rather than CVT response. Due to the differentiating action of the CVT, the ground return current exhibits a very fast rise time and wide dynamic range. Bandwidths and sampling speeds in excess of 5 MHz are required to sample these waveforms adequately for accurate digital integration. Offsets in the measuring instrumentation also contributed a significant error during the integration process. As with the capacitive divider topology, the narrow deviation for the various excitation voltages, i.e. 11.4 % to 13.5 %, indicates that the impulse response of this measuring topology is independent of the excitation voltage magnitude.

The performance of the CVT base unit was also evaluated with the ferroresonant damping circuit connected. For an impulse test with a peak value of 28.44 kV for the capacitive divider topology, a deviation of 7.71 % was recorded between the impulse peak values obtained with the reference divider and the CVT base unit respectively. This indicates that the connection status of the ferroresonant damping arrangement has an effect of approximately 4 % on the peak measuring accuracy of this topology.

For an impulse test with a peak value of 28.68 kV for the transconductance topology, a deviation of 37.61 % was recorded between the impulse peak values obtained with the reference divider and the CVT base unit respectively. The deviation with the damping circuit connected is more than twice that of the largest deviation with the damping circuit disconnected, this indicates that the connection status of the ferroresonant damping circuit has an effect on the accuracy of this measuring topology. Although the arguments given above for the current measurement apply, this large deviation cannot currently be satisfactorily explained.

The impulse responses for the insulated CT were obtained for the following test conditions:

Risetime of the input waveform: 2μs

Peak voltage of the input waveform: 5, 9, 22, 45 and 60 kV approximately

Excitation: Applied to one of the primary bars

Secondary windings: One secondary winding shorted and floating

Tables III and IV summarise the results obtained for the impulse response tests on the insulated CT for the capacitive divider and transconductance topologies respectively.

Table III: Impulse response results for the capacitive divider topology of the insulated CT.

Peak impulse voltage [kV]		Deviation [%]
Reference divider	Insulated CT	
4.812	4.730	-1.70
9.040	9.272	2.57
22.56	22.31	-1.12
45.12	44.61	-1.12
59.76	60.20	0.74

Table IV: Impulse response results for the transconductance topology of the insulated CT.

Peak impulse voltage [kV]		Deviation [%]
Reference divider	Insulated CT	
4.8884	4.363	-10.7
8.960	8.337	-6.95
22.44	22.19	-1.10
44.64	42.16	-5.55
60.12	56.59	-5.87

The results given in table III for the capacitive divider topology show that a maximum deviation of 2.57% was recorded between the impulse peak values

obtained with the reference divider and the insulated CT respectively. In order to assess the effects of the risetime specification, similar tests were conducted using a risetime of 10 μs, in which case a maximum deviation of 4.48% was recorded. The test results showed no trend to indicate that the risetime of the impulse waveforms affects the accuracy of this measuring topology in any particular way, provided that a high enough sampling speed can be used. A relatively narrow band of deviations were obtained for the various excitation voltages, i.e. -1.12 % to 2.57% for the results in table III and –2.09% to 4.48% for impulses with a risetime of 10μs. This, together with the fact that the recorded deviations show no definite trend, indicates that the impulse response of this measuring topology is independent on the excitation voltage magnitude.

The results given in table IV for the transconductance topology show that a maximum deviation of –10.7% was recorded between the impulse peak values obtained with the reference divider and the insulated CT respectively. This result was obtained for the lowest excitation voltage, and the results for the other excitation voltages are of the order of 6%. The deviations show a decreasing trend increased peak value, with a minimum of 5.32% recorded for the highest excitation voltage. As in the case for the CVT, the relatively poor accuracy of this measuring topology, particularly for the lower excitation voltages, is attributed to the limitations of the current measuring and data acquisition equipment, rather than the response of the CT. Similar tests were conducted for rise times of 10 μs, and a maximum deviation of 37.2% was recorded.

In order to assess the effects of the grounding arrangement of the secondary windings, impulse tests were conducted for the capacitive divider topology with one set of secondary windings shorted and grounded to the external enclosure and with the excitation applied to one end of the primary bar. This yielded deviations of –1.19% and –1.52% between the impulse peak values obtained with the reference divider and CT for impulses with risetimes of 2 μs and 10 μs and peak values of 44.88 kV and 15.68 kV respectively. This indicates that the impulse response of this measuring topology is not affected significantly by the grounding arrangement of the secondary windings.

In order to determine whether the point of application of the impulse affects the response, impulse tests were also conducted for the capacitive divider topology with one set of secondary windings shorted and floating from ground and with the excitation applied to both ends of the primary bar. This yielded deviations of -1.53% and -1.39% between the impulse peak values obtained with the reference divider and CT divider for impulses with risetimes of 2 μs and 10 μs and peak values of 44.76 kV and 15.84 kV respectively. This indicate that the impulse response of this measuring topology is not affected significantly by the primary bar end used for excitation.

4 CONCLUSION

The capacitive divider topology yielded good accuracy, i.e. of the order of 3%, for the impulse peak measurements for both devices. The transconductance topology yielded less accurate results, i.e. of the order of 12% for CVT base unit and 6% for the CT. This is attributed to the fact that the specifications, i.e. sampling speed, dynamic range and offset in particular, of the current measuring instrumentation was inadequate for accurate integration of the recorded ground return current waveforms. This problem can be addressed by using a precision analog integrator.

Both topologies are promising for practical use, provided that suitable instrumentation is used for the current measurement in the case of the transconductance topology. Although the measuring technology required by the transconductance topology is more sophisticated compared to the capacitive divider topology, it is offset by the advantage that a secure grounding arrangement can be maintained.

ACKNOWLEDGEMENT

The authors gratefully acknowledge the financial and material support of ESKOM in sponsoring this research.

REFERENCES

[1] Bradley D A, Bodger P S and Hyland R P, "Harmonic Response Tests on Voltage Transducers for the New Zealand Power System", IEEE Trans. on Power Apparatus and Systems, Vol. PAS-104, No 7, July 1985.

[2] Douglass D A, "Potential Transformer Accuracy at 60 Hz Voltages Above and Below Rating and at Frequencies Above 60 Hz", IEEE Trans. on Power Apparatus and Systems, Vol. PAS-100, pp. 1370-1375, March 1981.

[3] Furioli G, "Measurement of Switching Overvoltages in HV Power Systems by Pure Capacitive Dividers", Energia Elettrica, V. 63, N 11, Nov. 1986, pp 427-433.

COMPARISON OF EXCITATION METHODS FOR POWER TRANSFORMER FREQUENCY RESPONSE MEASUREMENT

C.C. Brozio, J.J. Germishuizen, H.J. Vermeulen and K.J. Cornelissen

Department of Electrical and Electronic Engineering, University of Stellenbosch

Abstract - A variety of methods exist by which the frequency response characteristics of power transformers can be determined. In essence these methods differ only in the type of excitation signal that is applied to the transformer under test during frequency response measurements. As transformers are inherently non-linear devices, the choice of excitation signal will have an effect on the frequency responses estimated from time-domain measurements. This paper presents the use of variable-frequency, impulse and pseudo-random binary sequence excitation signals for transformer frequency response measurements and discusses their relative merits and disadvantages. It was found that all excitation sources can be applied successfully at high frequencies. However, impulse excitation was found to yield poor or invalid results at low frequencies.

Keywords: transformers, frequency response, frequency response estimation

1 INTRODUCTION

Accurate determination of the frequency response characteristics of power transformers is of great importance in a variety of power engineering fields, including the following:

i) Transformer model validation.

ii) Studies to determine the propagation of power system harmonics and carrier signals.

iii) Transformer condition monitoring by the so-called Frequency Response Analysis (FRA) technique.

Due to the inherent non-linearities of iron-cored transformers, the excitation level at which a frequency response measurement is performed has a significant effect on the results [1]. This is especially true of the open-circuit input impedance characteristics at lower frequencies (typically below 1 kHz). Here the frequency response is dominated by the magnetising inductance, which in turn is a function of the slope of the magnetisation curve of the core material. The 'effective' slope of the magnetisation curve will depend on the magnitude of the excitation current or voltage. For this reason, it is in the low-frequency range where transformer frequency response measurements are most problematic.

To motivate the need for accurate transformer frequency response measurements in the low-frequency range, consider e.g. power system harmonic penetration simulations, which are generally carried out in the frequency domain. Clearly a reasonable estimate of transformer frequency response characteristics in the harmonic frequency range is required. Condition monitoring applications also require low-frequency response estimates. Bak-Jensen, et al [2] found the most significant changes in transformer frequency response, due to internal faults and ageing, to be in the low-frequency region.

This paper discusses variable-frequency, impulse and pseudo-random binary sequence excitation signals and their application to power transformer frequency response measurements, emphasising the low-frequency range. The properties of each excitation method are discussed, followed by practical results to illustrate the advantages and disadvantages of each method.

2 VARIABLE FREQUENCY EXCITATION

Variable-frequency response measurements are carried out by using a sine-wave generator and linear power amplifier to drive the transformer. This method is well established and generally yields good results [2, 3]. However, this excitation method is limited by the bandwidth of the power amplifier and excitation levels above 2% to 3% of the transformer rating are difficult to achieve across a reasonable frequency range. A higher excitation voltage can be obtained by using a separate step-up transformer and/or by series resonating the transformer impedance with an external, adjustable inductance or capacitance, X_r, as shown in figure 1.

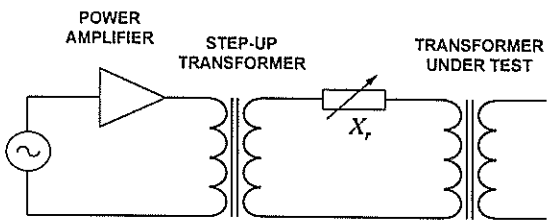

Figure 1. *Excitation system for variable-frequency measurements.*

Manual sweeping of the input frequency is required as a careful eye has to be kept on the input current and voltage to the transformer, in order to

i) maintain a constant excitation level and

ii) ensure that the voltage and current waveforms are not distorted too severely at frequencies where the amplifier is unable to cope with the transformer input impedance.

It is clear that a frequency response measurement using this excitation method is tedious and very time-consuming, particularly when adjusting an external resonating capacitance or inductance. The method also suffers from the disadvantage that practical power amplifiers and step-up transformers are band-limited, thereby limiting the attainable test frequency range. However, the use of variable-frequency excitation signal has the advantage that the non-linear properties of the transformer under test can be observed and analysed.

3 WIDEBAND EXCITATION SIGNALS

3.1 Impulse excitation

Low-voltage impulse excitation has become the standard excitation method for transformer frequency response measurements, especially for condition monitoring applications using the FRA method. The FRA method is based on the premise that a physical change, or fault in the transformer, will cause a change in its electrical parameters. Such a change can then be detected by comparing a measured transformer frequency response to a 'fingerprint' response measurement obtained with the transformer in a healthy condition [4].

Low voltage impulses are typically generated by a circuit such as the one shown in figure 2.

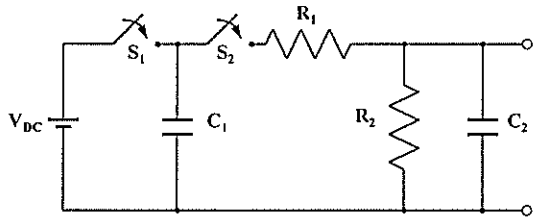

Figure 2. *Impulse generator for transformer frequency response measurements.*

The supply voltage, V_{DC}, is in the order of 100 V. An impulse is formed by discharging C_1 via a pulse shaping circuit by closing S_2, after charging C_1 via S_1. The excitation level can be adjusted by changing the peak voltage of the impulse and the frequency domain characteristics of the impulse can be modified to some degree by adjusting component values in the impulse generation circuitry. The impulse source used for this investigation features plug-in modules, containing a variety of impulse-shaping circuits [5]. This makes it possible to easily adjust the impulse shape to the application at hand. The disadvantage of this approach is that changes to the frequency response of the impulse signal require physical changes to the excitation circuit. The power spectral density of the low-voltage impulse signal is also relatively low. Additionally, the signal is uni-polar, resulting in uni-directional magnetisation of the transformer core.

3.2 Pseudo-random binary sequence excitation

Pseudo-Random Binary Sequences (PRBS), also referred to as a Binary Maximum Length Sequences (BMLS), or M-sequences, have a number of characteristics which make them suitable for frequency response measurements.

As its name implies, a PRBS has only two states, i.e. the amplitude of the PRBS is either $+a$ or $-a$ (as a function of time), where a is the chosen amplitude of the sequence (see figure 3). The frequency domain characteristics of a PRBS are determined by the length of the sequence (N) and the clock frequency (f_c) at which it is generated [6]. The power spectral density remains almost constant in amplitude over a wide range, with -3 dB points determined by N and f_c. As N and f_c increase, the range of the -3 dB power spectral density, increases. By adjusting N and f_c, the user is able to obtain a wide range of PRBS signals and has the ability to 'zoom in' on a frequency range of particular interest.

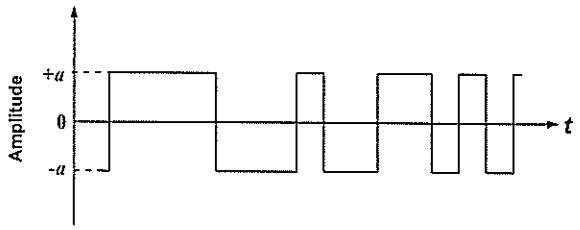

Figure 3. *PRBS signal* ($N = 2^4$-1).

By using a PRBS signal, with levels 0 and 1, to control the state of semiconductor switches, an excitation source with high output levels can be realised [7]. The measurement results described in this paper were obtained by connecting the test transformer to a DC current source, I_a, via a MOSFET bridge, thus causing a PRBS current, with levels $\pm I_a$, to be forced through the transformer windings as shown in figure 4 [1].

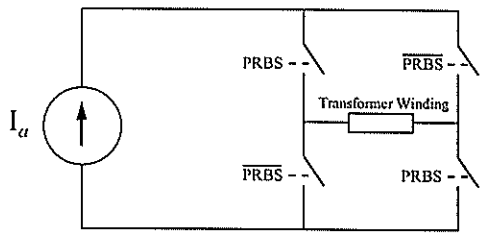

Figure 4. *PRBS excitation source.*

Practically, the system is limited by the maximum switching frequency of the MOSFET switches and the dynamic control properties of the current source. With the system used in this investigation, switching

frequencies of more than 100 kHz could be obtained [7]. The current source is realised by a fast current controller, to supply a constant current from a voltage source of up to 800 V. A maximum current of 5 A is possible, subject to the 150 W power dissipation capability of the current controller. The current reference of the controller can be adjusted to alter the PRBS current level, I_a.

3.3 Frequency response estimation

When using wideband excitation signals, some signal processing is required to obtain frequency response estimates from sampled time-domain waveforms. E.g. to determine the transformer voltage transfer function, $H(j\omega)$, the transformer is excited with an impulse or PRBS signal. The input voltage signal, $x(t)$, is sampled together with the response to that signal, $y(t)$. From these two time-domain signals, the transfer function can be estimated. The most straight-forward method is to find the spectra of $x(t)$ and $y(t)$, i.e. $X(j\omega)$ and $Y(j\omega)$ respectively, by performing a Discrete Fourier Transform (DFT), from which the transfer function can be estimated by the relationship [8]

$$\hat{H}(j\omega) = \frac{Y(j\omega)}{X(j\omega)}. \qquad (1)$$

By taking the input voltage as $y(t)$ and the input current as $x(t)$, a similar result follows for an estimate of the driving point impedance, $\hat{Z}(j\omega)$, for a particular transformer configuration. In practice, the variance of the transfer function estimate is quite high as it is equal to the signal-to-noise ratio at each frequency. This results in a 'noisy' transfer function. By averaging the results of a number of measurements in the frequency domain, the problem can be remedied to some extent, and good results can be obtained in this manner. It is also important to use good quality anti-aliasing filters at the inputs of the digitising instrument and to use a suitable time-domain windowing function to improve the quality of the transfer function estimate.

To reduce the number of measurements that have to be taken (i.e. to avoid averaging a large number of individual measurements) and to allow estimation of the frequency response at frequencies other than multiples of f_s/n (where f_s is the sampling rate and n is the number of samples), a more sophisticated spectral estimation algorithm is employed. The procedure, described by Ljung [8], is based on the assumption that the values of the transfer function at different frequencies are related. To estimate the transfer function at a frequency ω_n, a frequency window is used to form a weighted average of the components of $\hat{H}(j\omega)$, over a certain frequency interval centred about ω_n, with the highest weighting applying to the components in the close vicinity of ω_n. At the same time, the components in the interval are weighted according to their inverse variance. The procedure is computationally more intensive, but yields much better results than the estimate described by (1) above.

4 PRACTICAL RESULTS

Frequency response measurements, using the three excitation methods discussed above, were carried out on a 16kVA, 22kV/242V single-phase distribution transformer.

Figure 5 shows the measured frequency response of the secondary (low-voltage), open-circuit input impedance of the transformer, up to 100 kHz. The amplitude scale for these results is referred to the power system frequency (50 Hz) input impedance of the transformer. All three measurements show excellent agreement at frequencies above 1 kHz. This is the expected result, as the non-linear behaviour of the core does not significantly influence the frequency response characteristics in this frequency range [1, 3]. At frequencies below 1 kHz, the effect of excitation level is noticeable. A higher excitation level could be obtained from the PRBS excitation source than was possible with variable-frequency excitation. This explains the slightly lower first resonance frequency measured with PRBS excitation. Meaningful results could not be obtained with the impulse excitation source at frequencies below 1 kHz. It is believed that the interaction of the impulse signal with the transformer non-linearities is responsible for the invalid results obtained in this region. However, further investigation is required to determine the exact mechanism responsible for this.

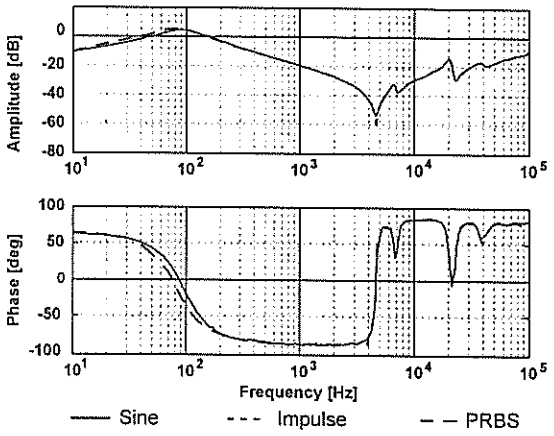

Figure 5. *Secondary (LV) open-circuit input impedance using swept-frequency, impulse and PRBS excitation. Impulse excitation results are only shown for frequencies above 1 kHz.*

To further illustrate the effect of excitation level, the open-circuit input impedance from the high-voltage side was measured. One set of results was obtained using variable-frequency sinusoidal excitation, at an excitation voltage of 220 V. Two sets of results were obtained with PRBS excitation, which was applied via a step-up transformer to obtain excitation magnitudes

of 1 kV and 2.5 kV respectively. Due to the high input impedance of the transformer under test, a PRBS current signal could not be applied. The system shown in figure 4 yields a voltage excitation signal, as the non-ideal current source effectively becomes a voltage source for a high load impedance. Again, it was not possible to obtain a meaningful result using the impulse excitation source. The results of these measurements are shown in figure 6. It can be seen how the first resonant frequency of the input impedance reduces as a function of excitation amplitude.

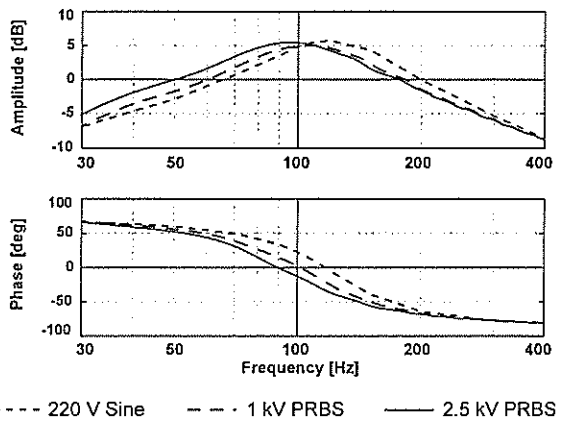

Figure 6. *Primary (HV) open-circuit input impedance at various excitation levels.*

5 CONCLUSION

The characteristics of variable-frequency, impulse and PRBS excitation signals, and their application to power transformer frequency response measurement were discussed.

Good frequency response measurement results can be obtained using variable-frequency excitation. Due to the limitations of the excitation equipment, high excitation levels can not be obtained. Further, manual frequency sweeping and adjustment of the excitation equipment is required, resulting in a time-consuming procedure.

Rapid measurements can be made with impulse excitation. However, adjustment of the frequency domain properties of the excitation signal is a problem. It was also found that impulse excitation is not suitable for estimation of transformer frequency response characteristics in the low-frequency range, where non-linearities play a significant role.

Most of the above problems can be eliminated, or reduced, by the use of PRBS excitation. Relatively high excitation levels can be obtained across a wide frequency range and it is possible to easily adjust the frequency domain properties of the PRBS signal.

The results of the investigation confirmed that it is important to choose an excitation method and excitation magnitude that is suitable for time- and frequency domain properties of the device under test in the frequency range of interest.

6 REFERENCES

[1] C.C. Brozio, H.J. Vermeulen, K.J. Cornelissen, 'Power Transformer Frequency Response Measurement using Pseudo-Random Binary Sequence Excitation', *32nd Universities Power Engineering Conference (UPEC '97)*, Manchester, pp. 121 - 124, September 1997.

[2] J. Bak-Jensen, B. Bak-Jensen and S.D. Mikkelsen, 'Detection of Faults and Ageing Phenomena in Transformers by Transfer Functions', *IEEE Trans. on Power Delivery*, Vol. 10, No. 1, January 1995.

[3] S.P. Ladewig, C.C. Brozio, H.J. Vermeulen, K.J. Cornelissen, 'An Alternative Broadband Lumped Parameter Equivalent Circuit Model for Two-Winding Transformers' *31st Universities Power Engineering Conference (UPEC '96)*, Greece, pp. 493-496, September 1996.

[4] P.T.M. Vaessen and E. Hanique, 'A New Frequency Response Analysis Method for Power Transformers', *IEEE Trans. on Power Delivery*, Vol. 7, No. 1, pp. 384-391, January 1992.

[5] J.J. Germishuizen, *Transformer Frequency Response Measurement Using Impulse Excitation*, University of Stellenbosch, November 1997.

[6] W.D.T. Davies, *System Identification for Self-Adaptive Control*, Wiley-Interscience, pp. 44-88, 1970.

[7] K.J. Cornelissen, C.C. Brozio, H.J. Vermeulen, 'A Programmable Pseudo-Random Binary Sequence Generator for System Identification Applications', *32nd Universities Power Engineering Conference (UPEC '97)*, Manchester, pp. 742 - 745, September 1997.

[8] Ljung, L, *System Identification: Theory for the User*, Prentice-Hall Inc., pp. 141-167, 1987.

COMPUTER-AIDED FORMULATION OF NETWORK EQUATIONS IN SYMBOLIC FORMAT
PART I: NETWORK FUNCTIONS

C.C. Brozio and H.J. Vermeulen

Department of Electrical and Electronic Engineering, University of Stellenbosch

Abstract - Models of power system apparatus often take the form of lumped parameter equivalent circuits. For all but the most basic models, direct measurement of the model parameters requires complicated measurement procedures or is simply not possible. It is then necessary to use more complex parameter estimation methods to obtain the parameter values. In such cases it is desirable to have a mathematical description of the model available in symbolic form. Manual derivation of such a symbolic description, in terms of the lumped parameter circuit elements, is a time-consuming and error-prone task. This paper describes a software tool for the computer-generation of symbolic network functions, which was implemented using MATLAB. A further paper discusses the computer-aided determination of the symbolic state-equations of lumped parameter networks, implemented in *Mathematica*.

Keywords: symbolic network functions, state-space, system identification

1 INTRODUCTION

Mathematical models for a wide variety of power system apparatus often take the form of a lumped parameter equivalent circuit. This allows physical insight into the behaviour of the equipment and simplifies use of the model in network analysis software such as the EMTP or SPICE. A problematic aspect of using equivalent circuit models is the determination of the various model parameters, i.e. the values of the individual circuit elements. For very simple models the parameters can normally be determined by direct measurement, but more sophisticated models require the use of parameter estimation techniques. In this case, it is necessary to have a mathematical representation of the model available in symbolic form. Typically, this would be a symbolic state-space representation or one or more symbolic network functions associated with the equivalent circuit. This paper will focus on the derivation of symbolic network functions. In addition to the parameter estimation application, there are a number of other reasons for the derivation of symbolic network functions [1]:

a) Better physical insight into the operation of the equipment, or system that is being modelled, can be gained.

b) For many applications, computational efficiency is improved when substituting numerical values directly into a symbolic network function, rather than evaluating the complete network for each condition of interest (e.g. frequency response calculations).

c) In some cases the numerical accuracy of results can be improved. Roundoff and loss of significance can introduce errors during numerical manipulation and solution of network equations.

d) Parameter sensitivity analysis.

Manual derivation of symbolic network functions of an equivalent circuit model is a time-consuming and error-prone task, even when considering models of modest complexity. Over the years a variety of methods for computer generation of partially or fully symbolic network functions have been developed [2, 3]. Most of these algorithms are based on some form of topological analysis of the network [2], i.e. the network functions are derived from some graph associated with the network. Rather than employing such a topological method, a conceptually much simpler approach is followed here [3]. First, the (symbolic) nodal admittance matrix, Y_n, is constructed directly from a topological description of the network. The required network functions can then be written in terms of the determinant and cofactors of Y_n. The availability of symbolic mathematics software such as the MATLAB Symbolic Math Toolbox [4] or *Mathematica* [5] makes the difficulty of programming the method comparable to programming its numerical equivalent.

2 NODAL ADMITTANCE MATRIX

This section discusses the construction of the symbolic nodal admittance matrix, Y_n, from which the required network functions can be obtained directly. In general, nodal analysis involves the solution of node voltages, i.e. the elements of the nodal voltage vector V_n, using the relationship

$$J_n = Y_n V_n , \qquad (1)$$

where J_n is the equivalent nodal current source vector. Consider an electrical network, consisting of b

branches and n+1 nodes. The nodes are numbered from 0 to n and the branches are numbered from 1 to b. Node 0 is defined as the reference node. For the general case considered here, a branch can be either of the composite branches shown in figure 1. Only branches containing RLC elements, independent voltage- or current sources, or voltage-controlled current sources can be specified. In practice this is not a serious limitation but it does simplify programming of the procedure [3].

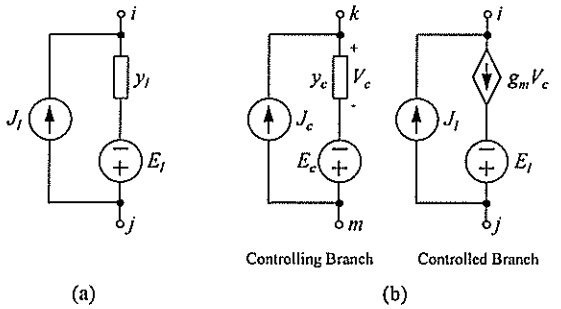

Figure 1. *(a) Composite admittance branch and (b) controlled-source branch with controlling branch.*

As a starting point, zero-matrices are defined for $\boldsymbol{Y}_n$ and $\boldsymbol{J}_n$. Thus, initially $\boldsymbol{Y}_n$ is a $(n \times n)$ matrix of which all elements are 0; similarly $\boldsymbol{J}_n$ is an n vector, with all elements set to 0. Entries can now be made in $\boldsymbol{Y}_n$ and $\boldsymbol{Jn}$ for each branch in turn, given the two nodes at which a branch is incident and the (symbolic) element values. The two branch types shown in figure 1, i.e. admittance branches and controlled-source branches, are each treated in a separate manner.

Admittance branches. Consider the lth composite admittance branch directed from node i to node j, with element values y_l, J_l and E_l. Letting y' denote the existing value of an element of $\boldsymbol{Y}_n$, the elements of $\boldsymbol{Y}_n$ are updated for the lth branch as follows [3]:

$$\begin{aligned} y_{ii} &= y_{ii}'+y_l \\ y_{ij} &= y_{ij}'-y_l \\ y_{ji} &= y_{ji}'-y_l \\ y_{jj} &= y_{jj}'+y_l \end{aligned} \tag{2}$$

In general, each y_l appears in four places in $\boldsymbol{Y}_n$. However, if $i = 0$ or $j = 0$, requiring entries in the non-existent row 0 or column 0 of $\boldsymbol{Y}_n$, the entry is not made. If row 0 and column 0 were present, the resulting matrix, called the indefinite admittance matrix, has a determinant equal to zero and equal cofactors, and can thus not be used to solve (1). Entries into $\boldsymbol{J}_n$ are made as follows:

$$\begin{aligned} j_i &= j_i'+(J_l - y_l E_l) \\ j_j &= j_j'-(J_l - y_l E_l) \end{aligned} \tag{3}$$

where j' denotes an element value of $\boldsymbol{J}_n$ before the entry for the lth branch was made.

Controlled-source branches. Only controlled-source branches of the voltage-controlled current source type are considered here. As can be seen from figure 1, the controlled-source branch differs from the admittance branch only in that y_l is replaced by a controlled current source with current value $g_m V_c$. V_c is the controlling voltage, measured across the admittance element of the controlling composite branch. Consider the lth composite controlled branch, directed from node i to node j, with the controlling branch directed from node k to node m. The rules for entering the branch details into $\boldsymbol{Y}_n$ and $\boldsymbol{J}_n$ are as follows:

$$\begin{aligned} y_{ik} &= y_{ik}'+g_m \\ y_{im} &= y_{im}'-g_m \\ y_{jk} &= y_{jk}'-g_m \\ y_{jm} &= y_{jm}'+g_m \end{aligned} \tag{4}$$

and

$$\begin{aligned} j_i &= j_i'+(J_l - g_m E_l) \\ j_j &= j_j'-(J_l - g_m E_l). \end{aligned} \tag{5}$$

Using the MATLAB Symbolic Math Toolbox [5], programming of the above procedure is only slightly more complex than programming an equivalent numerical procedure, mainly due to the more complicated syntax required for symbolic matrix manipulation.

3 MUTUALLY COUPLED BRANCHES

More often than not, lumped parameter models of power system apparatus include a number of mutually coupled branches. Including a system of mutually coupled branches in the nodal admittance matrix presents some complications and will thus be discussed here briefly. A system of k mutually coupled branches is usually represented as follows:

$$\begin{bmatrix} V_1 \\ V_2 \\ \vdots \\ V_k \end{bmatrix} = s \begin{bmatrix} L_{11} & M_{12} & \cdots & M_{1k} \\ M_{21} & L_{22} & \cdots & M_{2k} \\ \vdots & \vdots & \cdots & \vdots \\ M_{k1} & M_{k2} & \cdots & L_{kk} \end{bmatrix} \begin{bmatrix} I_1 \\ I_2 \\ \vdots \\ I_k \end{bmatrix}, \tag{6}$$

or

$$\boldsymbol{V}_L = s\boldsymbol{L}\boldsymbol{I}_L. \tag{7}$$

It is clear that (6) can not be included in $\boldsymbol{Y}_n$ directly as this would require the use of current-controlled voltage sources, as shown in figure 2 (a). By rewriting (7) as

$$\boldsymbol{I}_L = \tfrac{1}{s}\Gamma \boldsymbol{V}_L, \tag{8}$$

where

$$\Gamma = \boldsymbol{L}^{-1}, \tag{9}$$

the system of mutually coupled branches can be written in terms of voltage-controlled current sources as illustrated by figure 2 (b). Once Γ has been found, k entries have to be made in Y_n for each mutually coupled branch in the coupled system. The reciprocal self-inductance of the lth branch, $\frac{1}{s}\Gamma_{ll}$, directed from node i to j, is entered as an admittance branch from node i to node j. Also connected between nodes i and j are k-1 controlled current sources, controlled by the voltages across the reciprocal self-inductances of all the coupled branches except, of course, the lth branch. Thus, the current source resulting from the coupling of the mth branch to the lth branch is entered into Y_n as a controlled-source branch with $g_m = \frac{1}{s}\Gamma_{lm}$.

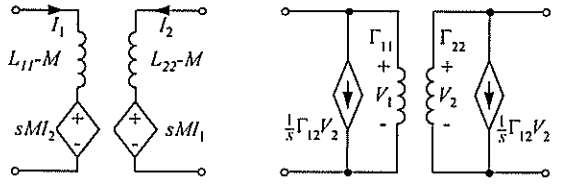

Figure 2. *Mutually coupled branches using (a) current-controlled voltage sources and (b) voltage-controlled current sources.*

The symbolic inversion of L is problematic, even for small numbers of coupled branches. Although the inversion is easily handled by MATLAB or *Mathematica*, the result is an unwieldy set of symbolic expressions which complicates the result eventually obtained for Y_n. In most cases it is easier and more efficient to directly use a symbolic Γ in the construction of Y_n, rather than using a Γ derived from L by inversion. At the point where numerical values are substituted for the various symbolic variables, it is a simple matter to derive L from Γ by numerical matrix inversion.

4 OBTAINING NETWORK FUNCTIONS

Consider a network with RLC and voltage-controlled current source elements with nodes numbered as shown in figure 3. The network has n+1 nodes, with node 0 chosen as the reference node. The nodal equations take the form

$$\begin{bmatrix} I_1 \\ 0 \\ \vdots \\ 0 \end{bmatrix} = Y_n \begin{bmatrix} V_1 \\ V_2 \\ \vdots \\ V_n \end{bmatrix}. \qquad (10)$$

Solving for V_1 and V_2 produces the following result:

$$V_1 = \frac{\Delta_{11}}{\Delta} I_1 \qquad (11)$$

and

$$V_2 = \frac{\Delta_{12}}{\Delta} I_1 \qquad (12)$$

where Δ is the determinant and Δ_{ij} is the ijth cofactor of Y_n. From (11) and (12), the following network transfer functions can be written directly:

$$\frac{V_o}{V_{in}} = \frac{V_2}{V_1} = \frac{\Delta_{12}}{\Delta_{11}} \qquad (13)$$

$$\frac{V_o}{I_{in}} = \frac{V_2}{I_1} = \frac{\Delta_{12}}{\Delta} \qquad (14)$$

The input impedance, Z_{in}, is given by

$$Z_{in} = \frac{V_{in}}{I_{in}} = \frac{V_1}{I_1} = \frac{\Delta_{11}}{\Delta}. \qquad (15)$$

Both MATLAB [4] and *Mathematica* [5] are able to symbolically evaluate determinants, making it a relatively simple matter to implement the above results in the symbolic network function program.

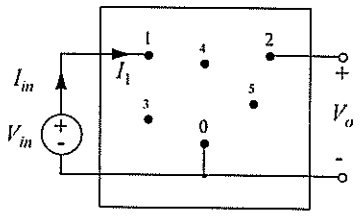

Figure 3. *Network node numbering for determination of network functions.*

5 PRACTICAL EXAMPLE AND RESULTS

To illustrate the generation of symbolic network functions, consider the circuit shown in figure 4. This circuit has been proposed by Douglass [6] to model voltage transformers in the power system harmonic frequency range.

Firstly, using the node numbers shown in figure 4, the symbolic admittance matrix for the equivalent circuit is constructed. After the details of each branch have been entered, the nodal admittance matrix becomes

$$Y_n = \begin{bmatrix} sC_P + sC_{PS} + \frac{1}{R_{PS}} & -sC_{PS} & -\frac{1}{R_{PS}} & 0 \\ -sC_{PS} & sC_P + sC_{PS} + \frac{1}{R_e} + \frac{1}{sL_{PS}} & -\frac{1}{sL_{PS}} & -\frac{1}{R_e} \\ -\frac{1}{R_{PS}} & -\frac{1}{sL_{PS}} & \frac{1}{R_{PS}} + \frac{1}{sL_{PS}} & 0 \\ 0 & -\frac{1}{R_e} & 0 & \frac{1}{R_e} + \frac{1}{sL_e} \end{bmatrix}. \quad (16)$$

The voltage transfer function can now be determined, using (13). For this example, this yields:

$$\frac{V_o}{V_{in}} = \frac{a_3 s^3 + a_2 s^2 + a_1 s + a_0}{b_3 s^3 + b_2 s^2 + b_1 s + b_0}, \quad (17)$$

where the coefficients are defined as follows:

$$\begin{aligned} a_0 &= R_e \\ a_1 &= L_e + C_{PS} R_e R_{PS} \\ a_2 &= C_{PS} L_{PS} R_e + C_{PS} R_{PS} L_e \\ a_3 &= C_{PS} L_{PS} L_e \\ b_0 &= R_e + R_{PS} \\ b_1 &= L_e + L_{PS} + C_{PS} R_e R_{PS} + C_s R_e R_{PS} \\ b_2 &= C_{PS} L_{PS} R_e + C_{PS} R_{PS} L_e + C_s L_{PS} R_e + C_s R_{PS} L_e \\ b_3 &= C_{PS} L_{PS} L_e + C_s L_{PS} L_e . \end{aligned} \quad (18)$$

The above results were obtained from a MATLAB Symbolic Math Toolbox implementation of the network function determination method, using only the incident nodes and element values of each branch as inputs.

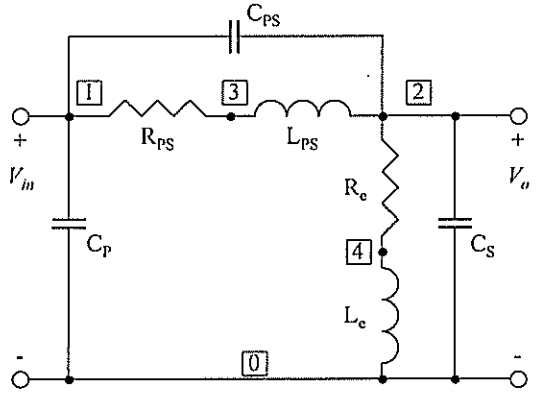

Figure 4. *Voltage transformer equivalent circuit proposed by Douglass [6].*

6 CONCLUSION

A software tool has been presented with which symbolic or partially symbolic network equations of an RLC-g_m network can be determined. The tool takes the form of a program for symbolic mathematics software such as the MATLAB Symbolic Math Toolbox [4] or *Mathematica* [5]. A MATLAB version was implemented by the authors and it was found to be an invaluable aid during the development, validation and parameter estimation of power system equipment models.

As the complexity of networks increases, the coefficients of the network transfer functions rapidly become unwieldy. For parameter estimation applications this is problematic, as a solution of the network element values in terms of the estimated network function coefficients is generally required. In many cases it is better to use a state-space representation of the network for parameter estimation as the coefficients of the state-equations are generally less complex than those of a network transfer function. Part II of this paper discusses the derivation of symbolic state-equations for application in such cases.

7 REFERENCES

[1] P.M. Lin, 'A Survey of Applications of Symbolic Network Functions', *IEEE Transactions on Circuit Theory*, Vol. CT-20, No. 6, November 1973.

[2] G.E. Alderson and P.M. Lin, 'Computer Generation of Symbolic Network Functions - A New Theory and Implementation', *IEEE Transactions on Circuit Theory*, Vol. CT-20, No. 1, pp. 48-56, January 1973.

[3] L.O. Chua and P.M. Lin, *Computer-aided Analysis of Electronic Circuits: Algorithms and Computational Techniques*, Prentice-Hall, Inc., New Jersey, 1975.

[4] The Mathworks, Inc., *Symbolic Math Toolbox*, 24 Prime Park Way, Natick, Mass. 01760, 1994.

[5] S. Wolfram, *Mathematica - A System for Doing Mathematics by Computer*, Addison-Wesley Publishing Company, 1988.

[6] D.A. Douglass, 'Potential Transformer Accuracy at 60 Hz Voltages Above and Below Rating and at Frequencies Above 60 Hz', *IEEE Transactions on Power Apparatus and Systems*, Vol. PAS-100, No. 3, March 1981.

COMPUTER-AIDED FORMULATION OF NETWORK EQUATIONS IN SYMBOLIC FORMAT
PART II: STATE-SPACE REPRESENTATION

H.J. Vermeulen and C.C. Brozio

Department of Electrical and Electronic Engineering, University of Stellenbosch

Abstract - This paper presents a software tool with which the state-equations of RLCM networks, i.e. networks consisting of resistors, inductors, capacitors and mutually coupled branches, can be obtained in symbolic form. This is a valuable tool to assist during the development, validation and parameter estimation of lumped parameter equivalent circuit models. The method has been implemented using the *Mathematica* software package and can be used to determine the state-equations of a network from a topological description of that network. The method is illustrated by deriving the symbolic state-equations of a broadband voltage transformer equivalent circuit model.

Keywords: symbolic network functions, state-space, system identification

1 INTRODUCTION

Lumped parameter equivalent circuits are commonly employed to model a variety of power system apparatus. Parameter estimation techniques have to be employed to determine the equivalent circuit element values, as these can often not be obtained by direct measurement. Normally, an estimation algorithm is employed to determine an estimate of the coefficients of a network function or the network state-equations. To determine the values of the individual network elements, an expression for each coefficient, in terms of the network element values, has to be known. As discussed in part I of this paper, the coefficients of a network function are lengthy expressions of the equivalent circuit parameters, even for relatively simple networks. The coefficients of the state equations are generally simpler expressions. This, together with the ability to easily handle multi-input, multi-output systems, makes the use of state-space representations for system identification applications a good one. The state-space representation is also favoured by parameter estimation software, such as the MATLAB System Identification Toolbox [1, 2].

Manual derivation of the symbolic state-equation coefficients, in terms of the various equivalent circuit parameters, is an arduous task during which errors are difficult to avoid. This, together with the fact that the development and validation of a model topology often requires repeated formulation of a state-space representation, motivates the need for computer-aided formulation of symbolic state-equations.

This paper describes a software tool, implemented in *Mathematica* [3], for the computer-aided determination of state-equations of RLCM networks in symbolic form. The generalised algorithm for writing the state equations [4] is discussed and the method is illustrated by presenting results obtained for an equivalent circuit broadband transformer model.

2 GENERALISED ALGORITHM

2.1 Overview

Consistent and unique expressions for the state-equations can be obtained, provided that the network under consideration meets the following requirements:

a) The network does not contain loops consisting of independent voltage sources.

b) The network does not contain cutsets consisting of independent current sources.

The algorithm comprises the following main procedures [4]:

a) The circuit topology is represented by a node-branch incidence matrix A, and branch element matrices are constructed for each of the element types, i.e. independent sources, capacitors, resistors and inductors.

b) The incidence matrix is partitioned into tree and link components, denoted by A_T and A_L respectively, based on the definition of a normal tree, i.e. a tree which contains all the independent voltage sources, no independent current sources, as many of the capacitors as possible and as few of the inductors as possible.

c) The partitioned incidence matrix is transformed to yield a fundamental cutset matrix, $\boldsymbol{D}$.

d) A state-space expression of the form

$$\dot{x}_1 = Ax_1 + B_1 u + B_2 \dot{u} \qquad (1)$$

is derived, where x_1 and u denote the state-variable and input vectors respectively. A denotes the state dynamics matrix and B_1 and B_2 denote the transformation matrices for the input variables and their derivatives.

e) The derivative of the input vector can be removed from (1) by a change of variables to

yield the standard state-space expression

$$\dot{x} = Ax + Bu. \tag{2}$$

2.2 Incidence Matrix

Kirchhoff's current law (KCL) can be expressed in the form [4]

$$Ai = 0, \tag{3}$$

where A and i denote the node-branch incidence matrix and the branch current vector respectively, for the network under consideration. A network with n nodes and b branches gives rise to a $(n \times b)$ node-branch incidence matrix of the form

$$A = [a_{ij}], \tag{4}$$

where

$a_{ij} = 1$ if branch j is incident at node i and the positive current is defined away from node i,

$a_{ij} = -1$ if branch j is incident at node i and the positive current is defined towards node i, and

$a_{ij} = 0$ if branch j is not incident at node i.

The elements of the current vector are ordered according to the following criteria [4]:

a) The branch currents are first ordered with respect to the type of network element involved, i.e. sequentially in the order of independent voltage sources, capacitors, resistors, inductors and independent current sources.

b) The capacitive and inductive branch currents are subsequently ordered, still maintaining the broader sequence defined by (a) above, to reflect the preferred allocation of state variables.

The system of equations represented by (3) is over-determined. A set of independent KCL equations is obtained by deleting one of the rows. This yields a reduced incidence matrix. The resultant matrix equation is now transformed to row-echelon form by a series of elementary row operations. Rearranging the set of equations so that the first non-zero entries lie on the diagonal then yields a reduced incidence matrix in the form

$$A = \left[A_T \middle| A_L\right], \tag{5}$$

where A_T and A_L denote tree and link partitions for the network.

2.3 Cutset Matrix

In order to obtain the fundamental cutset matrix D for the network, the reduced incidence matrix of (5) is transformed using the relationship

$$D = A_T^{-1} A, \tag{6}$$

which yields

$$Di = [0], \tag{7}$$

where

$$D = \left[\begin{array}{cccc|cccc} 1_{ET} & 0 & 0 & 0 & F_{11} & F_{12} & F_{13} & F_{14} \\ 0 & 1_{CT} & 0 & 0 & F_{21} & F_{22} & F_{23} & F_{24} \\ 0 & 0 & 1_{RT} & 0 & F_{31} & F_{32} & F_{33} & F_{34} \\ 0 & 0 & 0 & 1_{LT} & F_{41} & F_{42} & F_{43} & F_{44} \end{array}\right] \tag{8}$$

and

$$i = \left[i_{ET} \;\; i_{CT} \;\; i_{RT} \;\; i_{LT} \;\; i_{JL} \;\; i_{LL} \;\; i_{RL} \;\; i_{CL}\right]^T. \tag{9}$$

The entries in the cutset matrix are all submatrices comprised of ones and zeros. Submatrices designated by 1 denote diagonal unity matrices. Subscripts T and L denote tree and link entries respectively, while subscripts E, C, R, L and J denote the type of branch element, i.e. independent voltage source, capacitor, resistor, inductor or independent current source.

2.4 Matrix Expressions for the State Equation

Matrices A, B_1 and B_2 in (1) are obtained from the relationships [4]

$$A = [M^{(0)}]^{-1} A^{(0)}, \tag{10}$$

$$B_1 = [M^{(0)}]^{-1} B_1^{(0)} \tag{11}$$

and

$$B_2 = [M^{(0)}]^{-1} B_2^{(0)} \tag{12}$$

where

$$M^{(0)} = \begin{bmatrix} C_T + F_{24} C_L F_{24}^T & 0 \\ 0 & L_{LL} - F_{24}^T L_{TL} - L_{LT} F_{42} + F_{42}^T L_{TT} F_{42} \end{bmatrix} \tag{13}$$

$$A^{(0)} = \begin{bmatrix} -F_{23} R^{-1} F_{23}^T & -F_{22} + F_{23} R^{-1} F_{33}^{-1} R_T F_{32} \\ F_{22}^T - F_{32}^T G^{-1} F_{33} G_L F_{23}^T & -F_{32}^T G^{-1} F_{32} \end{bmatrix} \tag{14}$$

$$B_1^{(0)} = \begin{bmatrix} -F_{23} R^{-1} F_{13}^T & -F_{21} + F_{23} R^{-1} F_{33}^T R_T F_{31} \\ F_{12}^T - F_{32}^T G^{-1} F_{33} G_L F_{13}^T & -F_{23}^T G^{-1} F_{31} \end{bmatrix} \tag{15}$$

$$B_2^{(0)} = \begin{bmatrix} -F_{24} C_L F_{14}^T & 0 \\ 0 & -F_{42}^T L_{TT} F_{41} + L_{LT} F_{41} \end{bmatrix} \tag{16}$$

Submatrices C_T and C_L are square diagonal matrices which contain the values of the capacitances associated with the tree and link networks respectively. Submatrices R_T and R_L are defined similarly for the resistive elements. Submatrices R and G are diagonal square matrices, containing all resistances and conductances respectively, i.e. tree values followed by the link values. Submatrices L_{TT} and L_{LL} are square matrices containing the self and mutual inductances of

the tree and link networks respectively, while L_{TL} and L_{LT} are square matrices containing the mutual inductances between the tree and link elements. The order of the elements in the above element submatrices adheres to the order defined for current vector i in (9).

2.5 Eliminating derivatives of the input vector

The derivatives of the input vector, i.e. the term containing $\dot{u}$ in (1), can be eliminated by linear transformation of the state-variables, using the relationship

$$x = x_1 - B_2 u \,. \tag{17}$$

This yields the standard form of the state-space equation as defined in (2), where

$$B = B_1 + AB_2 \,. \tag{18}$$

2.6 Formulation of the output equations

For the majority of applications for which the symbolic state-equation generation method was developed, the output variables are in fact one of the state variables. This makes it simple to formulate the output equations manually. Although algorithms exist for the computer formulation of the output equations [4], such an algorithm has not yet been implemented in the current version of the symbolic state-space representation program and will thus not be discussed here.

3 APPLICATION

Practical implementation of the procedure detailed above is best illustrated by means of an example. Figure 1 shows a lumped parameter equivalent circuit for voltage transformers, proposed by Douglass [5] for use in the power system harmonic frequency range. Current source i_1 represents a broadband current perturbation source, which would typically be used as excitation source in parameter estimation experiments.

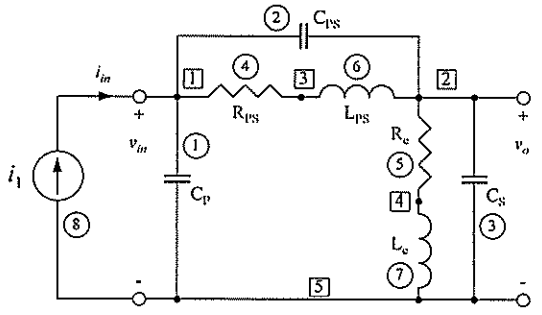

Figure 1. *Voltage transformer equivalent circuit proposed by Douglass [5].*

The node- and branch numbers used to construct the incidence matrix are boxed and circled respectively in figure 1. The current vector and the associated incidence matrix for the circuit are given by

$$i = [i_{Cp} \quad i_{Cps} \quad i_{Cs} \quad i_{Rps} \quad i_{Re} \quad i_{Lps} \quad i_{Le} \quad i_1]^T \tag{19}$$

and

$$A = \begin{bmatrix} 1 & 1 & 0 & 1 & 0 & 0 & 0 & -1 \\ 0 & -1 & 1 & 0 & 1 & -1 & 0 & 0 \\ 0 & 0 & 0 & -1 & 0 & 1 & 0 & 0 \\ 0 & 0 & 0 & 0 & -1 & 0 & 1 & 0 \\ -1 & 0 & -1 & 0 & 0 & 0 & -1 & 1 \end{bmatrix}. \tag{20}$$

The element matrices, before tree and link partitioning are given by

$$E = [\,], \tag{21}$$

$$C = \begin{bmatrix} C_P & 0 & 0 \\ 0 & C_{PS} & 0 \\ 0 & 0 & C_S \end{bmatrix}, \tag{22}$$

$$R = \begin{bmatrix} R_{PS} & 0 \\ 0 & R_e \end{bmatrix}, \tag{23}$$

$$G = \begin{bmatrix} \frac{1}{R_{PS}} & 0 \\ 0 & \frac{1}{R_e} \end{bmatrix}, \tag{24}$$

$$L = \begin{bmatrix} L_{PS} & 0 \\ 0 & L_e \end{bmatrix} \tag{25}$$

and

$$J = [i_1] \,. \tag{26}$$

The incidence matrix defined by (20) gives rise to a cutset matrix, $\boldsymbol{D}$, of the form

$$D = \left[\begin{array}{cccc|cccc} 1 & 0 & 0 & 0 & 1 & 0 & 1 & -1 \\ 0 & 1 & 0 & 0 & -1 & 1 & -1 & 0 \\ 0 & 0 & 1 & 0 & 0 & -1 & 0 & 0 \\ 0 & 0 & 0 & 1 & 0 & 0 & -1 & 0 \end{array}\right]. \tag{27}$$

The current vector and the tree- and link submatrices are given by

$$i = \left[\begin{array}{cccc|cccc} i_{C_P} & i_{C_{PS}} & i_{R_{PS}} & i_{R_e} & i_1 & i_{L_{PS}} & i_{L_e} & i_{C_S} \end{array}\right]^T \tag{28}$$

$$E_T = [0], \qquad J_l = [i_1],$$

$$C_T = \begin{bmatrix} C_P & 0 \\ 0 & C_{PS} \end{bmatrix}, \qquad C_L = [0],$$

$$R_T = \begin{bmatrix} R_{PS} & 0 \\ 0 & R_e \end{bmatrix}, \qquad R_L = [0],$$

$$L_T = [0] \quad \text{and} \quad L_L = \begin{bmatrix} L_{PS} & 0 \\ 0 & L_e \end{bmatrix}. \tag{29}$$

Using (10) to (16), the following results are obtained

for x_1, A, B_1 and B_2 of expression (1):

$$x_1 = \begin{bmatrix} v_{C_P} & v_{C_{PS}} & i_{L_{PS}} & i_{L_e} \end{bmatrix}^T \tag{30}$$

$$A = \begin{bmatrix} 0 & 0 & \frac{-C_S}{C_PC_{PS}+C_PC_S+C_{PS}C_S} & \frac{-C_{PS}}{C_PC_{PS}+C_PC_S+C_{PS}C_S} \\ 0 & 0 & \frac{-(C_P+C_S)}{C_PC_{PS}+C_PC_S+C_{PS}C_S} & \frac{C_P}{C_PC_{PS}+C_PC_S+C_{PS}C_S} \\ 0 & \frac{1}{L_{PS}} & -\frac{R_{PS}}{L_{PS}} & 0 \\ \frac{1}{L_e} & -\frac{1}{L_e} & 0 & -\frac{R_e}{L_e} \end{bmatrix} \tag{31}$$

$$B_1 = \begin{bmatrix} \frac{-C_S}{C_PC_{PS}+C_PC_S+C_{PS}C_S} \\ \frac{-C_S}{C_PC_{PS}+C_PC_S+C_{PS}C_S} \\ 0 \\ 0 \end{bmatrix} \quad \text{and} \quad B_2 = \begin{bmatrix} 0 \\ 0 \\ 0 \\ 0 \end{bmatrix} \tag{32}$$

The result for B_2 indicates that the derivative of the input vector does not appear in the state-equations as defined by (1). This makes it possible to directly write the state-equations in the desired form of (2) by simply setting $B = B_1$. Typically, the input voltage response, v_{in}, of the circuit would be of interest as output variable. This output quantity is equal to the voltage across C_P, which is a state variable, so that the coefficient matrices of the output equation can be written as

$$C = \begin{bmatrix} 1 \\ 0 \\ 0 \\ 0 \end{bmatrix} \quad \text{and} \quad D = [0]. \tag{33}$$

Network functions of the same equivalent circuit model shown in figure 1 were derived in part I of this paper. Note that the state-equation coefficients are generally less complex functions of the individual network element values than the coefficients of a network function. This makes the use of a state-space network representation preferable to network functions for parameter estimation applications. To illustrate this, consider (31) and (32), assuming that the elements of A and B have been determined (numerically) by an estimation algorithm. Note that the system is overdetermined in this case, with

$$a_{23} = a_{13} - a_{24}, \qquad a_{41} = -a_{42},$$
$$b_1 = a_{24} - a_{13} \quad \text{and} \quad b_2 = -a_{13}. \tag{34}$$

The availability of A and B in symbolic form makes it possible to determine these relationships between the state-equation coefficients and to include them in the system description that is used as input to the estimation procedure. Once the elements of A and B have been estimated, the equivalent circuit element parameters can be found by:

$$L_{PS} = \frac{1}{a_{32}}, \qquad R_{PS} = \frac{a_{33}}{-a_{32}},$$

$$R_e = \frac{a_{44}}{-a_{41}}, \qquad L_e = \frac{1}{a_{41}},$$

$$C_P = \frac{-a_{24}}{a_{13}a_{14}-a_{14}a_{24}-a_{13}a_{24}},$$

$$C_{PS} = \frac{a_{14}}{a_{13}a_{14}-a_{14}a_{24}-a_{13}a_{24}} \quad \text{and}$$

$$C_S = \frac{-a_{13}}{a_{13}a_{14}-a_{14}a_{24}-a_{13}a_{24}}. \tag{35}$$

4 CONCLUSION

A software tool has been presented by which the state-equations of an RLCM network can be determined, in symbolic form. The method has been implemented as a *Mathematica* program, but other symbolic mathematics packages, such as the MATLAB Symbolic Math Toolbox are also suitable [6]. The *Mathematica* program has been used extensively by the authors during the development, validation and identification of models for a variety of power system apparatus. The program made it possible to generate accurate symbolic state-space representations of relatively complex networks within minutes.

5 REFERENCES

[1] L. Ljung, *System Identification: Theory for the User*, Prentice-Hall, Inc., Englewood Cliffs, New Jersey 07632, 1987.

[2] L. Ljung, *System Identification Toolbox*, The Mathworks, Inc., 24 Prime Park Way, Natick, Mass 01760, 1993.

[3] S. Wolfram, *Mathematica - A System for Doing Mathematics by Computer*, Addison-Wesley Publishing Company, Inc., 1988.

[4] L.O. Chua and P.M. Lin, *Computer-Aided Analysis of Electronic Circuits*, Prentice-Hall, Inc., Englewood Cliffs, New Jersey, 1975.

[5] D.A. Douglass, 'Potential Transformer Accuracy at 60 Hz Voltages Above and Below Rating and at Frequencies Above 60 Hz', *IEEE Transactions on Power Apparatus and Systems*, Vol. PAS-100, No. 3, March 1981.

[6] The Mathworks, Inc., *Symbolic Math Toolbox*, 24 Prime Park Way, Natick, Mass 01760, 1994.

WATER HEATER POPULATION BEHAVIOUR UNDER CENTRALISED CONTROL

C.J. Jooste, G.J. Delport &
Centre for New Electricity Studies
Department of Electric and Electronic Engineering
University of Pretoria
Pretoria, 0002

G.L. van Harmelen
Electricity Demand Department
Eskom, Megawatt Park
P.O. Box 1091
Johannesburg, 2000

Abstract – A model is developed to study the behaviour of water temperatures in Electric Storage Water Heater (ESWH) populations en enabling the user to determine the probability of experiencing cold water. The is used to quantify consumer discomfort caused by ESWH control. Four operating states is defined and probability density functions is derived for each. State information provides the expected number of devices in the on state from which the load profile can be determined. First the equations governing the cumulative distribution functions of temperature is derived and from it the partial differential equations governing the behaviour of the probability density functions. Analytical solutions exists only for simple so that numerical methods have to be employed.

Keywords: electrical load modelling, residential hot water load control, residential demand-side management.

1. INTRODUCTION

Electric storage water heaters (ESWHs) are estimated to make up between 30 and 50% of South African domestic energy consumption [1]. The domestic sector accounts for about 15% of national electricity consumption [2] and for some 35% of total municipal energy purchases [3]. In addition to the substantial energy consumption, the ESWH load is estimated to contribute up to 30% of the national daily maximum demand in winter [1].

According to Surtees[3] it is possible that the system peak demand contribution of this sector might reach 15 GW, by the year 2015. He concludes that demand-side interventions within the domestic sector will be required. Growth of this sector will lower the national load factor even more and DSM options may solve the problems of shrinking generation margins.

Impacts of residential demand-side management (RDSM) measures have been studied, and it has been found cost-effective [4]. The magnitude of the ESWH load as well as the coincidence with system peak demand makes it a prime candidate for RDSM measures. Availability of hardware, coupled with the relatively low impact on consumers, have led numerous redistributors of electricity to install water heater control systems. These centralised load control systems are mainly utilised to limit the maximum demand components of the individual redistributor's energy bill.

Centralised load control systems are valuable assets that are, currently, not optimally utilised by the individual parties nor is the collective use of these systems properly orchestrated on a national level. Co-ordination of control efforts will render greater benefit than is currently obtained by the sum of the individual efforts. It has been found to be a very promising RDSM alternative and savings of up to 2GW on national maximum demand have been estimated [2].

The sub-optimal utilisation of the ESWH control resource is partly due to the fact that if a certain maximum is set within a billing period, little or no incentive exists to keep demand below this level for the rest of the billing period under current tariffs.

Supply-side measures like adding generating capacity to a power system is 100% sure of alleviating shrinking generation margins while DSM planning is less straight-forward, it is not as easy as doing load flow studies after adding some generating capacity to the power system.

This paper concerns itself with the load and consumer impacts of a hypothetical centralised water heater control RDSM program. It deals with more engineering related issues of planning ESWH control measures and ignores marketing, customer relations and business related issues that also play an integral role in the DSM planning process.

The next section proposes the structure for the load model. Section 3 introduces the theory upon which the model is based and the theory is employed to develop the mathematical model. Section 4 touches on some issues related to implementation of the mathematical model in order to extract useful data from the model. Some results are presented to show demonstrate the model The authors conclude with some remarks on the model.

2. LOAD MODEL STRUCTURE

The load and consumer impact information is the outputs that we require from the model. These impacts are the effects that a proposed ESWH control strategy will have on the load profile and on the consumer comfort (i.e. water temperature).

Assuming that discomfort is solely water temperature dependent, one way to define consumer discomfort (impact) is to equate it to the probability that the consumer will experience water temperatures below a certain temperature, Tcomf. The figure shows how a "discomfort index" can be determined in terms of an integral on the PDF[1] of water temperature.

[1] The cumulative distribution function (CDF) of a random variable, $\mathbf{x}$, represents the probability that a trial will result in $\{\mathbf{x}<x\}$ and is dependent on x. The derivative of the CDF is called the probability density function (PDF) of $\mathbf{x}$.

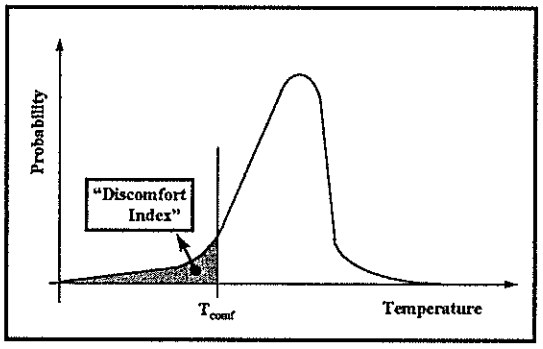

Figure 1 - Definition of consumer discomfort from temperature PDF

While arbitrary, this definition of consumer discomfort is simple and logical, particularly in view of the fact that the arcane details of what consumers perceive as comfortable may never be understood.

The load profile of a sample of devices can also be determined from statistical data. The probability of finding a device in the on state, the number of devices and the device rating will be enough to determine the expected load.

To obtain the statistical data needed to derive the required outputs it is necessary to investigate the available inputs. Parties involved in the hot water and energy demand process are:

- ***Hot water consumers***: The water usage profile is solely determined by the water user. Hot water demand is dependent on the way people schedule domestic activities requiring hot water.
- ***Electricity supplier***: Redistributors control electricity supply and can influence load profiles simply by shedding load. Obligations to deliver acceptable service necessitates the installation of systems to allow flexible control of the hot water load. These control systems are used to manage energy demand in order to save on energy purchases.
- ***ESWH device***: The thermal characteristics of the water heater determines how the environment, hot water use and electricity supply will influence the water temperature and this, in turn determines whether the thermostat will be on or off. ESWH behaviour relates water consumption , load control and environmental conditions to water temperature and energy consumption. The device parameters like tank volume, element rating and insulation level will also influence this relation.

Figure 2 shows the structure that is proposed for the load model considering the previous discussion.

The modelling part has been split up into a primary model that will produce the statistical data and a secondary model that will interpret the statistical model render the required impact data outputs.

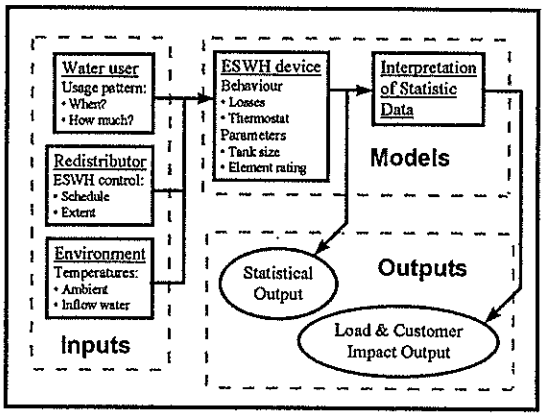

Figure 3 - ESWH load model structure

3. MODEL DEVELOPMENT

The thermal model used for the ESWH device is based on an energy conservation equation:

$$\frac{dx}{dt} = -a\left(x(t) - x_a(t)\right) - A \cdot q(t) + R \cdot m(t) \quad \ldots\ldots 1$$

The rate of water temperature change is,

- inversely proportional to the difference of water and ambient temperatures, (standing/pipe losses),
- inversely proportional to the rate of water extraction, $Aq(t)$, and
- proportional to the rating of the heating element, R, when the heating element is switched on.

The hot water demand is modelled as a Markov-type[2] process as proposed by Malhame [5].The term, $Aq(t)$, in eq.1 represents the water extraction. $q(t)$ can take on two values: $q(t)=0$ when no water is drawn and $q(t)=1$ when there is. A is a constant depending on the tank volume and the heating element rating. The state transition probabilities shown in figure 3 is defined as:

$$\Pr\left[q(t+\Delta t)=1 \middle| q(t)=0\right] = \alpha_1 \Delta t$$
$$\Pr\left[q(t+\Delta t)=0 \middle| q(t)=1\right] = \alpha_0 \Delta t \quad \ldots\ldots 2$$

Pr[ ] is the probability operator.

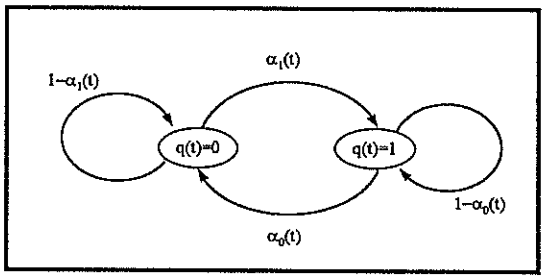

Figure 2 - Markov-type behaviour of water demand process

[2] True Markov processes have constant state transition probabilities. The Markov approach used in this work approach allows us to describe the hot water demand in terms of time-varying state transition probabilities and as two discrete states: Either water is being extracted or no water is being extracted.

Another state determine the condition of a device: The thermostat state. It can be off ($m(t)=0$) or on ($m(t)=1$). $m(t)$ is determined by the temperature of the water inside the device. The thermostat switches on below a temperature, x_-, and turns off above, x_+.

Combining water demand and thermostat states, results in four operating states:

States	$q(t)=0$	$q(t)=1$
$m(t)=0$	$i=0'$	$i=0$
$m(t)=1$	$i=1'$	$i=1$

For each of these states we assume that there exists a PDF for the water temperature at a specific time, $x(t)$[3]:

$$f_i(\lambda,t)d\lambda = \Pr[\lambda \le x(t) \le \lambda + d\lambda] \quad \text{for each state}, i = 0, 0', 1, 1' \quad \ldots\ldots 3$$

Take the CDF, in state i of water temperature at a specific time, $F_i(x,t)$, and consider F_i after a small time interval, $F_i(x,t+\Delta t)$. Assume the net addition of energy to the water is negative, i.e. water temperature dropped during the interval and the probability of experiencing colder water increased. The probability of colder water at the end of the interval is related to the probability of slightly warmer water at the start of the interval:

$$\therefore F_i(x,t+\Delta t) \propto F_i(x+\Delta x,t) \quad with\ x+\Delta x \ge x \ldots\ldots 4$$

In fact, the probability that the temperature is at or below x at time $t+\Delta t$ is equal to the probability that the water was at a temperature $x+\Delta x$ at time, t, with Δx being the exact amount of cooling experienced during Δt.

$$\therefore F_i(x,t+\Delta t) = F_i(x+\Delta x,t) \quad \ldots\ldots 5$$

We define the rate of temperature drop in state i:

$$r_i = \lim_{\Delta t \to 0} \frac{\Delta x}{\Delta t} \quad \ldots\ldots 6$$

Note that r_i may be dependent on time and temperature. Substituting this into eq. 5:

$$\Delta x = r_i(x,t)\Delta t$$

$$\therefore F_i(x,t+\Delta t) = F_i\left(\left(x + r_i(x,t)\Delta t\right),t\right) \quad \ldots\ldots 7$$

Eq.7 ignores state transitions ($\alpha_1=\alpha_0=0$). Recall that the state $q(t)$, may change at any moment. Denote state i' as a state where $q(t)=0$ and i where $q(t)=1$. Consider the possibility that a transition may occur from state i to state i'. F_i is dependent on the fact that the temperature dropped from $x+\Delta x$ (in the same state) and that the state did not change to i' during the interval, that is $\{q(t+\Delta t)=1 | q(t)=1\}$. From eq.2:

$$\Pr[q(t+\Delta t)=1 | q(t)=1] = 1 - a_0\Delta t \quad \ldots\ldots 8$$

if these two probabilities are statistically independent

$$F_i(x,t+\Delta t) = F_i\left(x + r_i(x,t)\Delta t,t\right)\left(1-\alpha_0\Delta t\right) \quad \ldots\ldots 9$$

Consider next transitions from i' to state i during Δt. This state change influences $F_i(x,t+\Delta t$ only when it actually occurs and when it occurred below temperature x. The probability for the state transition is $\alpha_1\Delta t$ and the probability that the temperature is below x at $t+\Delta t$ in state i' is $F_{i'}(x,t+\Delta t)$.

By substituting the corresponding r-value and using eq. 7 we can write:

$$F_{i'}(x,t+\Delta t) = F_{i'}\left(x + r_{i'}(x,t)\Delta t,t\right) \quad \ldots\ldots 10$$

Assuming statistical independence, the probability of both occurring is:

$$a_1\Delta t F_{i'}\left(x + r_{i'}(x,t)\Delta t,t\right) \quad \ldots\ldots 11$$

Considering temperature and state changes:

$$F_i(x,t+\Delta t) = F_i\left(x + r_i(x,t)\Delta t,t\right)(1-\alpha_0\Delta t) + \alpha_1\Delta t F_{i'}\left(x + r_{i'}(x,t)\Delta t,t\right) \quad \ldots\ldots 12$$

The derivation of eq. 12 using the CDF approach was intuitive and produced a difference equation describing the evolution of the CDF's of temperature with advancing time.

The next step is to obtain differential equations so that a solution can be attempted. This procedure involves nothing more advanced than Taylor series expansions and basic calculus, but only the result will be given:

$$\frac{\partial}{\partial t}\begin{bmatrix} f_i(\lambda,t) \\ f_{i'}(\lambda,t)\end{bmatrix} = \frac{\partial}{\partial\lambda}\left(\begin{bmatrix} r_i(\lambda,t) & 0 \\ 0 & r_{i'}(\lambda,t)\end{bmatrix}\begin{bmatrix} f_i(\lambda,t) \\ f_{i'}(\lambda,t)\end{bmatrix}\right) + \left(\begin{bmatrix} -\alpha_0 & \alpha_1 \\ \alpha_0 & -\alpha_1\end{bmatrix}\begin{bmatrix} f_i(\lambda,t) \\ f_{i'}(\lambda,t)\end{bmatrix}\right)$$

$$for\ i = 0, 1 \quad \ldots\ldots 13$$

This set of four coupled partial differential equations forms a hyperbolic system of conservation laws that describe the statistical behaviour of the system. The physical model of the ESWH , is incorporated into the differential equations through the $r(\lambda,t)$-terms. Eq.6 defines r as the rate of temperature change and eq.1 describes how to calculate it.

There is additional coupling between the individual equations of the system at the thermostat switching temperatures, x_+ and x_-, because transitions between *1* and *0* states and *1'* and *0'* states occur only at the ends of the thermostat range. These state changes can be incorporated into the system of equations as boundary conditions at x_+ and x_-.

4. SOLUTION AND RESULTS

Numerical solution of the system represented in eq.13 presents unique challenges. It is a set of conservation laws that states that the total probability represented by the integral of the various PDF's must always add up to

[3] Both x and λ and denote temperature: $F_i(x,t)$ is the CDF that corresponds to $f_i(\lambda,t)$. The CDF, $F_i=F_i(x,t)=Pr[x(t)<\lambda]$.

one. Ordinary finite difference methods violate conservation principles and special finite difference methods, known as Lax-Wendroff methods need to be applied towards the solution of the system.

Numerical solution of the equations was attempted with a computer code written in C. It was used to simulate 150 litre devices with element ratings of 3000W. The thermal loss parameter was 5W/K and the simulation was run with ambient temperatures of a typical winter day in Pretoria (0°C to 20°C). The thermostat endpoints were taken as 55°C and 60°C.

Water usage data was obtained from a instant water heater measuring experiment and the average household water use amounted to 300 litre per day. Figure 4 shows the cumulative water and energy use of one device in the absence of any load control. (Energy use is the straighter of the two curves.)

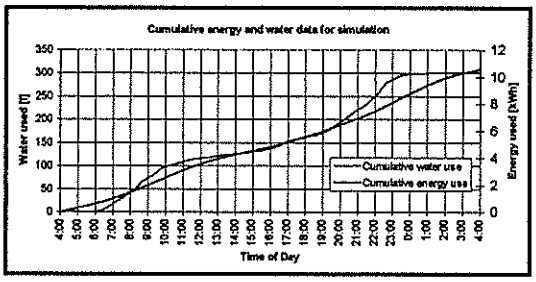

Figure 4 - Cumulative water and energy usage under no control

Figure 5 shows the kind of load impact data produced by the load model. The uncontrolled case is presented for reference. In this particular instance the ESWH load was split into ten groups and these groups were individually disconnected individually so as to limit the after diversity demand to 600W per device.

The blocks were subsequently reconnected but also on the condition that the 600W limit was not exceeded. It can clearly be seen how the controlled load approaches the uncontrolled profile as the controlled devices recover the energy that could not be supplied during the control interval.

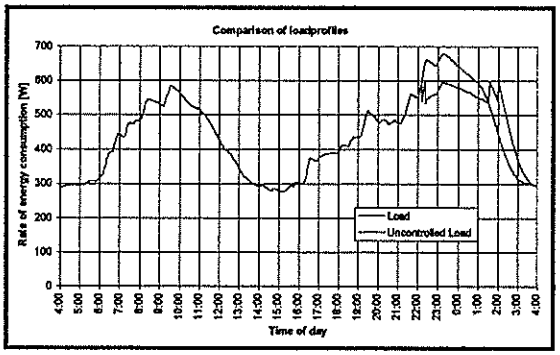

Figure 5 - Controlled vs. uncontrolled load

(From the number of discontinuities in the controlled profile it can be seen that the 600W target was reached by using only two of the blocks.)

5. CONCLUSION

The model displayed conceptually correct behaviour. The model lends itself to the application of problems involving populations of devices because of the statistical nature of the model outputs.

The model is complex enough to model the effects of most parameters affecting the hot water and energy demand process while at the same time remaining solvable with modest computer hardware.

One can also argue that the complexity is a drawback especially in applications where the detailed statistical output is not needed. The model is also input data intensive and the hot water usage data may not be available in all cases. In such cases the model may prove useful in deriving the hot water usage profiles if most of the other data is available to the load modeller.

6. REFERENCES

[1] Beute N., "Domestic Utilisation of Electrical Grid Energy in South Africa", Ph.D. Thesis, Potchestroomste Universiteit vir CHO, Potchefrstroom, 1993

[2] Beute N., "Financial Considerations for Electrical Supply Authorities in Controlling the Residential Water Heating Load", Proceedings of the Second Conference on Domestic Use of Electrical Energy (DUEE-95), pp. 33-38, Cape Town, 3-4 April 1995

[3] Surtees R.M., "The Impacts of Electrification on the South African Electricity Demand Profile", Proceedings of the First Conference on Domestic Use of Electrical Energy (DUEE-93), pp. 3-8, Cape Town, 18-19 October 1993

[4] Russouw P.A., "A Review of Demand-Side Management Measures in the Developed Domestic Sector of South Africa", Proceedings of the Second Conference on Domestic Use of Electrical Energy (DUEE-95), pp. 14-21, Cape Town, 3-4 April 1995

[5] Malhame R., "A Jump-Driven Markovian Electric Load Model", Advances in Applied Probability, No. 22, pp. 564-586, 1990

AN ANALYTIC MODEL FOR THE STATISTICAL DESCRIPTION OF SYSTEM LEVEL DEMAND CHARACTERISTICS IN AID OF DSM INSPIRED LOAD CONTROL SCHEMES

G.L. van Harmelen
Electricity Demand Department
Eskom Megawatt Park
P.O. Box 1091
Johannesburg, 2000

&

G.J. Delport
Centre for New Electricity Studies
Department of Electrical and Electronic Engineering
University of Pretoria
Pretoria, 0002

Abstract – An analytic model for the statistical description of demand during a specified fixed interval of time is proposed in this paper. This has traditional been required for the hour of system peak, for network design purposes, but the introduction of DSM inspired load control schemes have necessitated that such characteristics be able for all periods of the day, as well as shorter or longer intervals of time. The formulation presented here is based on the generation process that characterizes residential consumption type behavior such as electrical energy or water consumption. The formulation delivers a two-dimensional probability distribution variable, whose marginal distribution with relation to demand itself, delivers a probability distribution function that has been observed in previous practical work performed by other authors.

Keywords : DSM, ADMD, statistical distributions, residential load control, Poisson, Erlang

1. INTRODUCTION

Electricity utility companies are constantly being faced with the problem of predicting the future in order to be better prepared to meet the power needs of their customers. Utilities can match the supply and demand for electrical power essentially through two approaches: (1) supply-side management, and (2) demand-side management. Demand-side management strives to affect the customer demand for electrical power so that it produces the desired changes in the utility's load shape, benefiting both the utility as well as the customers [1,2].

The increasing volatility of future demand [3], the recent inflation of fuel costs, higher risks and costs associated with the building new power plants, the increasing move towards competitive markets, environmental preservation pressures and regulatory changes are forcing utilities to seriously consider DSM type options to achieve the balance between the supply and demand for electricity [4].

DSM programs offer the utility management many alternatives towards improving customer satisfaction while maintaining good customer relations in the increasingly competitive area of electric supply. This is besides also being able to improve the utility's financial health.

Unprecedented growth in electrical demand has been reported from all the major continents where the greatest part of the growth (± 40% in most cases) is being ascribed to the residential sector. The residential component compromises about 25% of total demand during a typical day [5]. The residential sector is regarded as being amenable to load management [5], and due to its relative importance, is a key area in assisting the increase of power system efficiency.

1.1 Background

Diversity factor and after diversity maximum demand (ADMD) are well known electrical network parameters which are used for the statistical description and the effective design of residential distribution networks [6]. In DSM, they may be used for calculating the effective maximum demand savings that can be achieved from DSM inspired peak clipping schemes.

The stochastic nature of residential loads gives rise to uncertainties concerning the distribution characterizing the ADMD at the time of system peak (or at the time of a control intervention), so that it cannot be described by simple average values. Several issues need to be addressed in this regard. These include the impact of the number of consumers, types of appliances being targeted and climatic conditions [7].

1.2 Previous work

Traditionally, natural diversity distribution parameters have been estimated with a Gaussian distribution so that the probability of different maximum demands can be obtained at different confidence levels [8]. This distribution is normally employed to describe the distribution of loads at the time of maximum demand (only for the natural or uncontrolled diversity) and may be Gaussian in the case for the limit of a large number of customers, (by the central limit theorem). However, for smaller number of customers, and for the case of interference with the natural process (e.g. load

control, or special type of circuit breaker) the Gaussian assumption can no longer be made.

Chan et al [9] presented a joint probability distribution approach which in conjunction with an estimate of the peak connected load, can calculate the temporal average value of the diversified load, for uncontrolled, and centrally controlled cases. Yu et al [10] have presented work on modeling the effects of load control on the diversity distribution at time of system peak. An analytic method for calculating the natural diversity of air-conditioning load is shown by these authors, for homogenous and non-homogenous groups of consumers. In this work the effects of diversity for a centrally controlled case is presented, being calculated using a Monte-Carlo approach.

1.3 Contents of this paper

It is desirable to quantify the description of the electrical load frequency distribution at various times, especially in customer tailored load control algorithm cases [8]. In its determination, the natural generation process that leads to the generation of the system peak can give valuable insight into the development of the model. A model is required which is able to determine the ADMD distribution function parameters, for small to large numbers of customers, for different appliances, and for different usage rates.

Work shown in this paper proposes the first stages of such a model that has the potential of addressing the issues as raised in this section. Section 2 describes the theory of the model, resulting in a two dimensional probability density function. Section 3 shows results as obtained with this model, while section 4 concludes and presents some future work.

2 GENERATING PROCESS MODEL

It is proposed that three primary quantities influence demand distribution statistics in the residential sector. These are the frequency of use within a single home, the magnitude of that use (e.g. appliance load current), and the number of homes that together aggregate in order to produce the system level profile.

An intuitive way to describe appliance usage would be to determine its frequency of use per defined time period. In it's reciprocal form this would relate the average time between discrete events.

If we let λ stand for the average number of events per unit time in a single home, for an arbitrary appliance, then generally, depending on the time of day, this value could change and therefore $\lambda = \lambda(t)$ (i.e. for non-homogenous cases). Suppose further that such events occurring in a household conform to the following postulates:

1) The duration of non-overlapping intervals between events is independent and obeys the events per unit time criterion.

2) For a small interval Δt, the chance of an event occurring in that interval, is approximately proportional to the duration of that interval.

$$\frac{P(\text{exactly 1 event in}(t, t+\Delta t))}{\Delta t} \rightarrow \lambda(t) \quad as \quad \Delta t \rightarrow 0 \quad (1)$$

This means that for small time intervals, doubling the length of the interval will double the probability that an event occurs in that interval.

3) The chance of more that 1 event in an interval of length Δt is negligible for $\Delta t \cong 0$

Under these postulates, the process is called a non-homogeneous Poisson process, or a Poisson process in a varying environment. We know that if λ were constant and these postulates were satisfied, then N_t, the number of events in the period [0,t], is Poisson distributed with parameter λt.

In order to determine N_t if λ is a function of time, split the interval [0,t] into several smaller intervals so that $\lambda(t) \cong \lambda(t_i)$ is approximately constant on the i'th subinterval. The total number of events in [0,t] is then $N_t = N + \ldots N_n$ which is the sum of n independent Poisson random variables. Consequently, N_t is also a Poisson variable, distributed with parameter equal to the sum of the parameters :

$$\lambda(t_1)\Delta t + \lambda(t_2)\Delta t + \ldots + \lambda(t_n)\Delta t = \sum_{j=1}^{n} \lambda(t_j)\Delta t \quad (2)$$

When this sum is taken in the limit, it becomes an integral such that

$$\Lambda(t) = \int_0^t \lambda(u)du \quad (3)$$

This means that for $j \geq 0$

$$P(N_t = j) = \frac{\Lambda(t)^j}{j!} e^{-\Lambda(t)} \quad (4)$$

with $\Lambda(t)$ called the intensity function. From this, the probability may be found that the number of events are equal to some specific value j. This is however not very useful for determining when those events occurred and consequently the formulation for inter-event times is required instead.

2.1 Modeling inter-event times

If we let T_1 be the time until the first event occurs, then following on from eq. 4

$$\begin{aligned} P(T_1 > t) &= P(\textit{no arrivals in } [0,t]) \\ &= P(N_t) = 0 \\ &= \frac{\Lambda(t)^0}{0!} e^{-\Lambda(t)} \\ &= e^{-\Lambda(t)} \end{aligned} \tag{5}$$

which implies that T_1 is exponentially distributed with parameter $\Lambda(t)$. Because non-overlapping intervals are independent, the same holds for T_2, because the process could be considered to have started at T_1 (independence) and therefore the same argument can be used for the time between T_2 and T_1.

From the definition of the probability distribution function

$$F(t) = P(T_1 \le t) \tag{6}$$

so that

$$1 - F(t) = P(T_1 > t) = e^{-\Lambda(t)} \tag{7}$$

and

$$F(t) = \begin{cases} 0 & t \le 0 \\ 1 - e^{-\Lambda(t)} & t \ge 0 \end{cases} \tag{8}$$

Since the probability density function is the derivative of the probability distribution function

$$f(t) = \begin{cases} 0 & t < 0 \\ e^{-\Lambda(t)} \dfrac{d\Lambda(t)}{dt} & t > 0 \end{cases} \tag{9}$$

We have thus found a way to determine the inter-event times for a non-homogeneous Poisson process if we know the intensity function. Although the previous formulation is applied to time between events (progress of time), time may be equated with load current in amps or water consumption in liters (consumption or progress of) for homogenous and non-homogenous cases. In this analogy, the variable t in equations 1 to 9 could then be replaced by I (amps), or L (liters).

If one takes a fixed time interval then, for example a single hour, during which the average consumption rates are assumed constant, and wishes to summate the total consumption during that hour in a single home), then

$$I_t = I + I_2 + \cdots + I_n \tag{10}$$

Where I_t is the total consumption for the hour, and where I_1-I_n are the individual consumptions (analogous to duration in equations 1 to 9) of each of the occurrences. The sum of n iid exponential random variables (the total consumption for the hour) however has an Erlang Distribution [11],

$$f_X(x) = \frac{(\lambda x)^{m-1} \lambda e^{-\lambda x}}{(m-1)!} \tag{11}$$

where m is a positive integer (the number of cases), and where $1/\lambda =$ E[X], is the average expected consumption of a single occurrence. During a specified period therefore, e.q. 11 allow one to calculate the distribution of the summation of the consumption.

We are thus left with determining how many occurrences indeed occur during that fixed time interval. This may be obtained from the Poisson process formulation as previously shown in equations 1 to 9, for homogenous and non-homogenous cases.

Combining these two formulations, it is thus possible to determine a two dimensional probability distribution, with consumption in general on the x-axis (e.g. load current, water consumption), and the number of occurrences of use on the y-axis as in e.q. 12.

$$f_{XY}(x,y) = \frac{\alpha^x}{x!} e^{-\alpha} \frac{\lambda e^{-\lambda y} (\lambda y)^{x-1}}{(x-1)!} \tag{12}$$

In eq. 12, $E[X] = \alpha$ for the Poisson component, and $\lambda = 1/E[Z]$ where Z represents one of the iid exponential distributions which are being summated to form the Erlang distribution of eq. 11.

For the group considered therefore, λ represents the average or expected consumption per occurrence, where α represents the average number of occurrences expected.

3. RESULTS

The two dimensional distribution shown in eq. 11 is plotted in Fig. 1 for arbitrary chosen parameters, as follows (on a time interval of 30 minutes) :

Table 1. Parameters and explanations for test case.

PARAMETER	EXPLANATION
$m = 1..30$	30 appliances chosen, if one assumes 1 appliance per home, this is 30 homes
$\alpha = 8$	during the chosen period, on average, 8 appliance usage events occur
$1/\lambda = 1\,kW$	the average consumption observed per chosen time period equates to 1kW

Of greater interest however is the marginal distribution for load only, so that event occurrence probabilities are removed, which can be obtained from

$$f_Y(y) = \int_{-\infty}^{+\infty} f_{X,Y}(x', y)\, dx' \tag{13}$$

and by numerical integration resulting in Fig. 2.

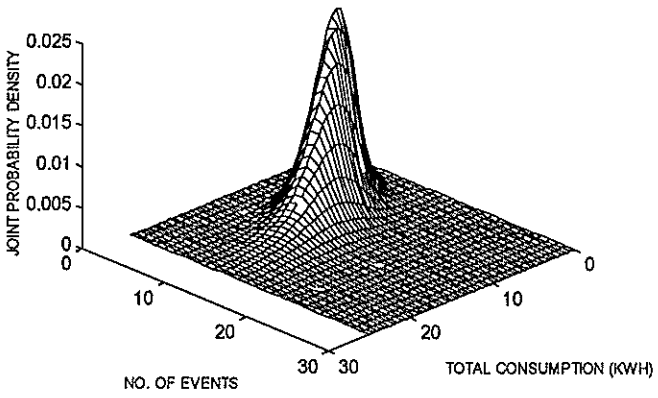

Fig. 1 Joint probability distribution function

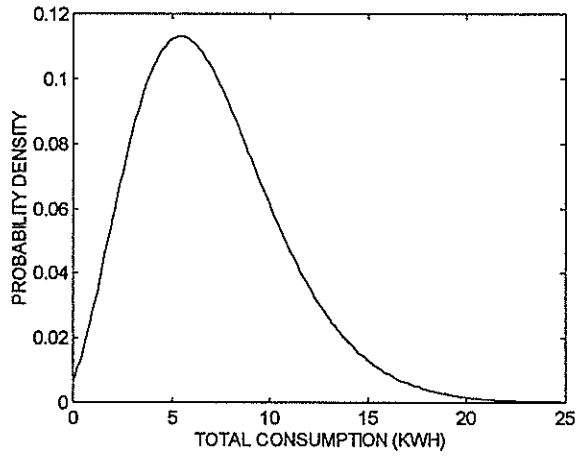

Fig. 2. Marginal distribution resulting in ADMD distribution characteristic.

The result in Fig. 2 is well known from previously practically measured results for electrical as well as water consumption loads [7,8].

4. CONCLUSIONS AND FUTURE WORK

In this work, an analytical method was shown for determining the statistical description of demand, for an arbitrary period of time (usually one hour). The theory is however not limited to any specific timer period, and allows the number of houses, the average events per time interval, as well as the average consumption per event to be explicitly incorporated. From the two dimensional distribution which describes this probability space, a marginal distribution for demand (e.g. load current) was obtained.

The work shown in this paper is introductory, where future work will entail specific case studies for periods of different lengths (i.e. not only 1 hour) and during and after different types of DSM inspired control actions.

5. LIST OF SYMBOLS

iid : *independent identically distributed*
ADMD : *After Diversity Maximum Demand*
DSM : *Demand Side Management*

6. REFERENCES

[1] Gellings, C.W.: "The concept of demand-side management for electric utilities", Proceedings of the IEEE, Vol. 73, No. 10, October 1985, pp. 1468-1470.

[2] Limaye, D.R.: "Implementation of Demand-Side Management Programs", Proceedings of the IEEE, Vol. 73, No. 10, October 1985, pp. 1503-1511.

[3] Bhattacgaryya, K., Crow, M.L.: "A Fuzzy Logic Based Approach to Direct Load Control", IEEE Transactions on Power Systems, Vol. 11, No. 2, May 1996, pp. 708-713.

[4] Kumar, B.: "Win-Win DSM conservation strategies for utilities and customers", Energy Engineering, Vol. 86, No. 5, 1989, pp. 26-37.

[5] Deering, S., Newborough, M., Probert, S.D.: "Rescheduling Electricity Demands in Domestic Buildings", Applied Energy, Vol. 44, 1993, pp. 1-62.

[6] Dekenah, M., Gaunt, C.T.: "Simulation of Residential Consumer Loads and Voltage Drop on LV Distribution Feeders Based on Data Collected from Load Restricted Consumers", Transactions of the SA Institute of Electrical Engineers (SAIEE), March 1993, pp. 21-31.

[7] Herman, R.: "Domestic Consumer After Diversity Maximum Demand, its Characteristics and Estimation", Municipal Engineer (South Africa), April 1991, pp. 5-13.

[8] Herman, R., Kritzinger, J.J.: "The Statistical Description of Grouped Domestic Electrical Load currents", Electric Power Systems Research, Vol. 27, 1993, pp. 43-48.

[9] Chan, M.L., Ackerman, G.B.: "Simulation based load synthesis methodology for evaluating load management programs", IEEE Transactions on Power Apparatus and Systems, Vol. PAS-100, No. 4, April 1981, pp. 1771-1778.

[10] Yu, Zuwei, Breipohl, A.M., Lee, F.N., Adapa, R.: "An analytical method for comparing natural diversity to DSM controlled diversity", IEEE Transactions on Power Systems, Vol. 11, No. 3, August 1996, pp. 1201-1208.

[11] Leon-Garcia, A.: Probability and Random Processes for Electrical Engineering, University of Toronto, Addison-Wesley Publishing Company, 1989, pp. 194-258.

PRELIMINARY PRACTICAL RESULTS AND BASIC INTERPRETANTIONS OF MODULATION NOTCH TESTING

R. Lourens & **G.J. Delport**
eemsrl@lantic.co.za
Centre for New Electricity Studies
Department of Electrical and Electronic Engineering
University of Pretoria
Pretoria, 0002

Abstract – A brief discussion of some of the results that were obtained as part of Eskom's National Notch Test Series is given. Certain new aspects is brought forward in terms of residential hot water control. The obtained results are derived from the Modulation Notch Testing that was developed and conducted by the authors.

Keywords : MNT, ADMD, Load Normalisation, Cold Load Pick Up, Undisturbed Hot Water Load

1. INTRODUCTION

The need to model domestic hot water load in South-Africa has formed the basis of various studies currently available [1,2,3,4] in literature. It is however an enormously difficult task to verify the models with practical results due to the extent and nature of obtaining usable actual load data [5]. Modulation Notch Testing (MNT) formed the basis of Eskom's initiative to obtain domestic hot water data. The test series involved 12 different municipalities as part of the national notch testing focusing on various areas of domestic hot water usage. The focus areas were load amplitude and load dynamics for different time slots and seasons [1]. This paper will focus on the shape of the undisturbed hot water load profile and the basic governing model that explains the dynamics of the domestic hot water load.

1.1. BACKGROUND

MNT consists of 4 basic tests conducted over a 2 week period at a municipality with an active hot water control system in place, for example ripple control. The two week test period is repeated four times during an one year period in order to obtain the influence of seasonal changes on hot water dynamics. The load data is gathered at 30 second integral periods as opposed to the normal 30 minute integral metering equipment filters out the relevant data needed [7]. During the test periods Eskom ignores the maximum demand charges in the form of a tariff rebate due the increase maximum demand resulting from MNT. The four different tests were developed to address different areas of hot water dynamics [1]. The exact reasoning for each test will not be discussed in this paper.

2. UNDISTURBED HOT WATER LOAD PROFILE

Test 1 forms the basis for determining both the undisturbed hot water load profile and the uncontrollable municipal base load. An example of a test 1 result is given in figure 1.

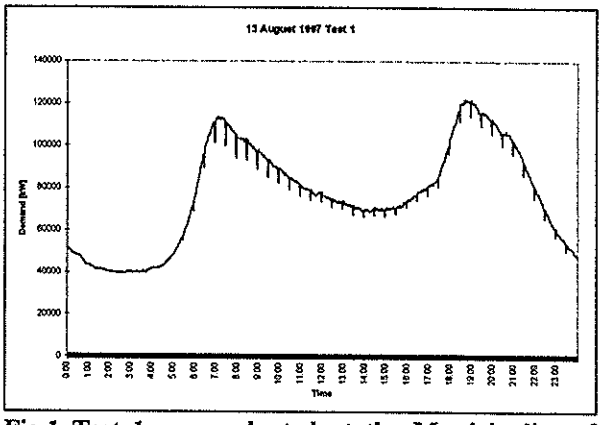

Fig.1 Test 1, as conducted at the Municipality of Greater Benoni.

Test 1 is performed by shedding all the available controllable hot water load for a short duration (normally 2 minutes). This switching scheme is known as a notch, the notch is repeated every 30 minutes, while the demand controller is inactive. The notch amplitude thus represents the undisturbed instantaneous hot water load for the test site under question. The test 1 data is filtered to obtain a total undisturbed hot water load profile for the specific test day, as can be seen in figure 2. By comparing figure 1 and figure 2 it can be seen that the largest municipal peak occurs in the evening whereas the hot water peak occurs in the morning. The morning hot water usage is not as spread out as the evening hot water usage due to the fact that people generally start preparing for a working day in the same time period.

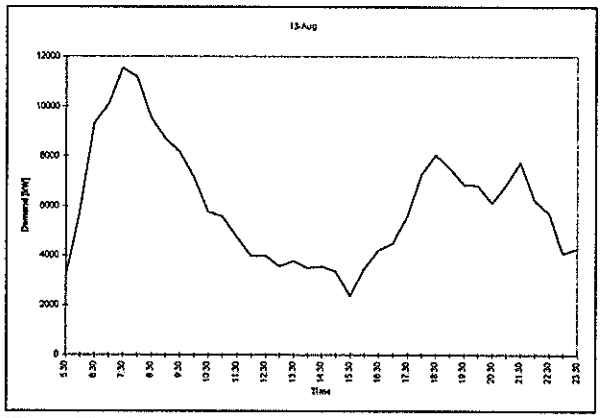

Fig. 2 Undisturbed hot water profile for 13 August

Figure 2 alone leaves certain unanswered questions such as:

- How does the hot water load amplitude change with temperature?
- What influence will a specific season have on the general shape of the hot water load, i.e. do hot water usage patterns change from season to season?
- What is the influence of demographics? For example, can hot water usage in the Cape be compared to that in Gauteng?

The undisturbed hot water load profile for 6 different days are shown in figure 3.

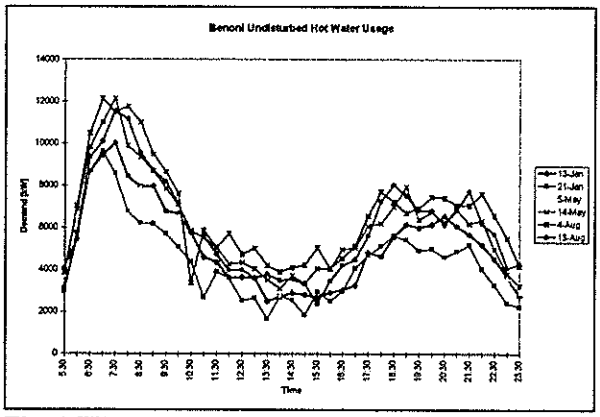

Fig. 3 Filtered outputs for various times of the year at the City Council of Greater Benoni.

The amount of Energy used for hot water generation is considerably higher during winter than that for summer due to the lower inlet water temperature to the hot water cylinder during winter periods. Linked to this, is the possibility that people use more hot water (on average) when it is colder. The shape of the undisturbed hot water load profiles do however essentially remain the same when viewing figure 3. The statement can be further investigated by generating a average undisturbed hot water load profile. This is done by normalizing the individual graphs to have a unity integral area and taking the average instantaneous value for a specific periods. The resultant average undisturbed hot water load profile is shown in figure 4.

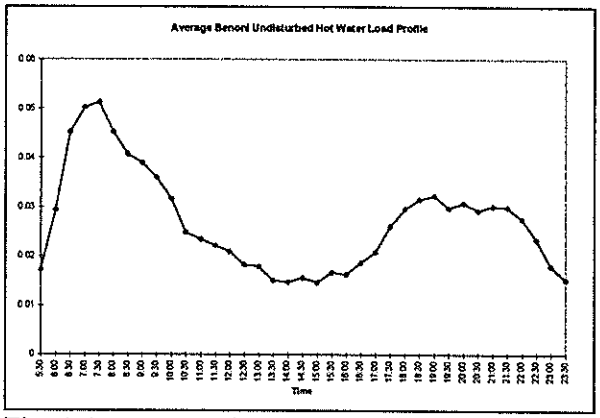

Fig. 4 Average undisturbed hot water load profile for the Municipality of Greater Benoni.

The average undisturbed hot water load profile can be multiplied by a constant to obtain the same integral area as the practical results which is known as the compensated undisturbed hot water load profile. The compensated hot water load profile is compared with the actual undisturbed hot water load profile in figures 5,6, & 7.

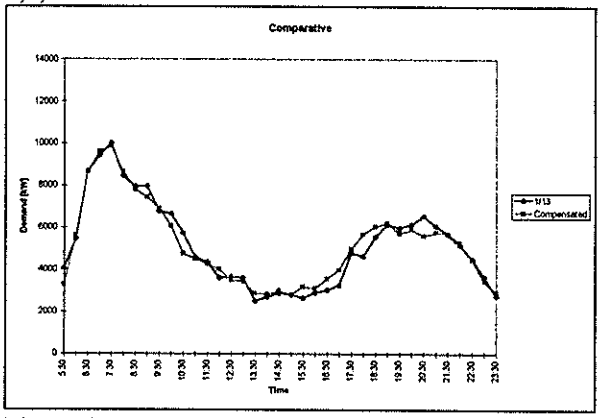

Fig. 5 Compensated versus actual undisturbed hot water load profile - 13 January 1997

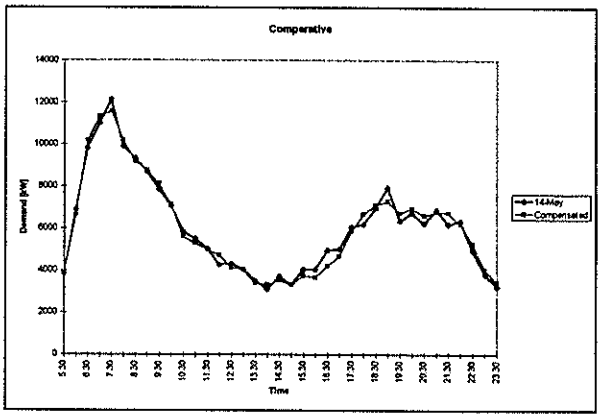

Fig. 6 Compensated versus actual undisturbed hot water load profile - 14 May 1997

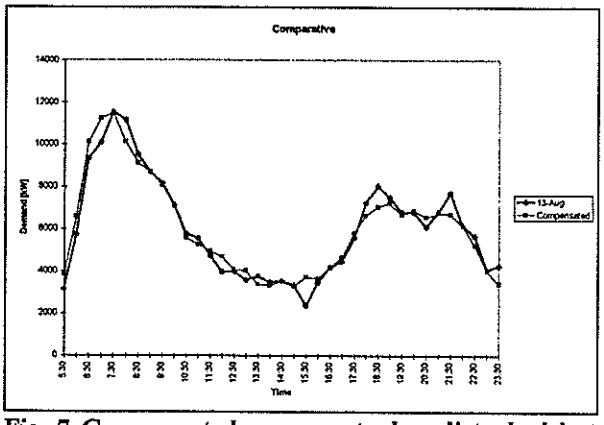

Fig. 7 Compensated versus actual undisturbed hot water load profile - 13 August 1997

The compensated load curve can thus be used, irrespective of the time of the year, as the shape of the undisturbed hot water load profile remains the same. This will make load control motivation a simple task as one only needs one or two data points per day to accurately assess exactly what the load would have been had no load control or energy shifting had been done for a specific day. The compensated load curve will be an essential tool for load management personnel when real time pricing tariffs become available for municipal clients.

Everything up to this point has been based on Benoni. A single data day obtained at Durbanville is compared with the same Benoni compensated load profile with the correct constant multiplier in figure 8.

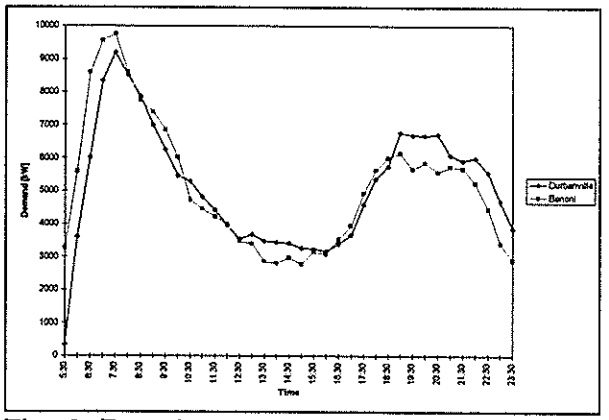

Fig. 8 Benoni compensated versus Durbanville actual undisturbed hot water load profile.

From figure 8, it seems that the morning Cape peak is less prominent than the Gauteng morning peak and that the Cape evening peak lags behind Gauteng evening peak. The Gauteng evening peak is lower than that of the Cape. This can be attributed to the different times.

3. LOAD DYNAMICS

The dynamic behaviour of the municipal load has previously been modeled around Guassian distributions [2 & 3] which could not be fully practically verified. Once MNT data became available it was realized that the model explained the amount of energy exchange correctly when blocks of energy are shifted, but that the response was not accurate. The assumption is made that cold load pick-up and load normalization are governed by the following general equations.

It is expected that cold load pick-up due to load shedding will follow the curve

$$y=a(1-e^{-kt}) \tag{1}$$

where k and a are constants to be determined from the notch test data and both time t and the amplitude y are the independent variables. k and a can best be obtained by means of least square curve fitting [6]. The load normalization curve after load restoration will follow equation 2

$$y=he^{-ct} \tag{2}$$

c and h can be obtained by means of least square curve fitting [6]. The validity of equation 1 & 2 can be proven as follows:

The filtered test data from test 1 and test 4 [1] from the same week are compared in figure 9. The difference between these two filtered outputs are also included. This difference is called the dynamic curve and is an indication of the dynamics of the hot water load in terms of cold load pickup and load normalization.

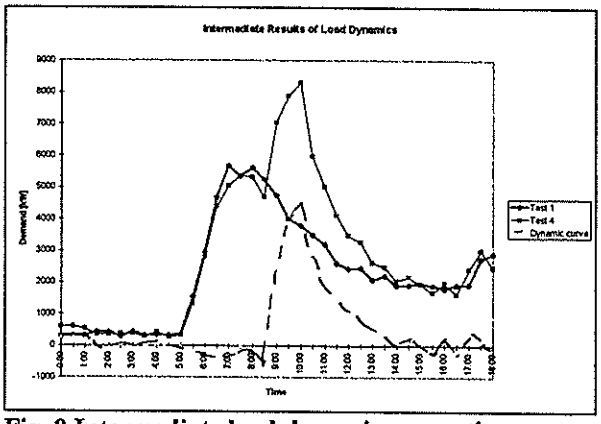

Fig. 9 Intermediate load dynamic generation

The profiles in figures 10 and 11 were normalised in terms of a factor of energy shedding by dividing the amplitude by the amount of energy which is normally shed at T=0 (08:30 in figure 9). This normalisation shows that if the load is shed for 1.5 hours, the amount of energy which is shed must be virtually added back into the system during the restoration period. For

example, if 15 MW is shed for 1.5 hours and then reconnected, a total load of 30 MW will be added to the system.

Figure 11 proves that the dynamics of the hot water load are indeed governed by equation 1 and 2.

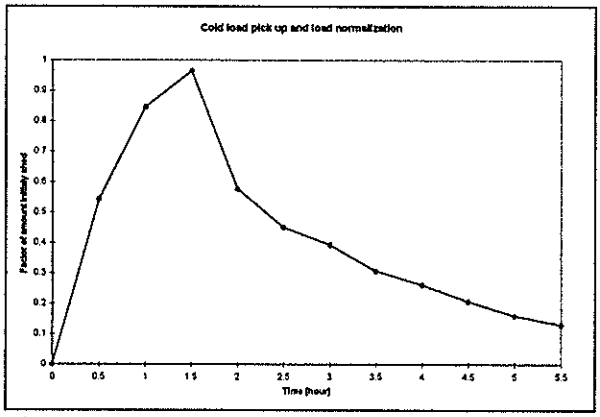

Fig. 10 The dynamic component of hot water loads magnified for the purpose of model verification

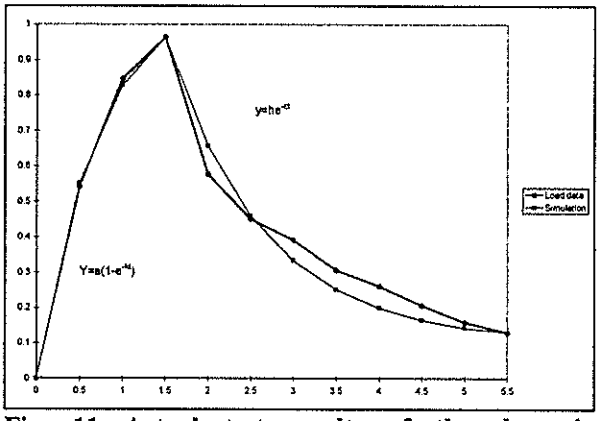

Fig. 11 Actual test results of the dynamic component of hot water loads plotted against the theoretical values of equations 1 and 2.

The constants *c* & *k* of equations1 & 2 are will be different for different times of the day and can be obtained from the practical results of test 2,3 & 4 [1].

4. CONCLUSION AND FUTURE WORK

MNT delivered the necessary data to develop a comprehensive model for the residential hot water load in South Africa. Without such a model the practical implementation of real time pricing tariffs will be impractical to implement and motivate. At this point in time a lot more is known regarding the municipal hot water load as a result of MNT.

5. REFERENCES

[1] Lourens, R, "Determination Of Water Heating Load Characteristics By A Modulation Notch Test Programme" B-Eng Project, Faculty of Engineering, University of Pretoria, October 1997

[2] Van Tonder, J.C., "Disaggregated Domestic Load Models", M.Eng Thesis, Faculty of Engineering, University of Pretoria, August 1995, pp. 80-106.

[3] Beute, N., "Domestic Utilization Of Electrical Grid Energy In South Africa", Philosophiae Doctor (Engineering), Potchefstroom University for Christian Higher Education.

[4] Van Harmelen, G.L., "An Analytic Model For The Statistical Description Of System Level Demand Characteristics In Aid Of DSM Inspired Load Control Schemes", Paper to be presented at the SAUPEC'98 Conference, January 1998.

[5] Ihara, S., Schweppe, F.C., "Physically based Modelling of Cold Load Pickup", IEEE Transactions on Power Apparatus and Systems, vol PAS-100, September 1981.

[6] Mathews, J.H., "Numerical Methods", Second Edition, Prentice-Hall International, 1987, pp. 258-302.

[7] Lourens R, van Harmelen GL, Delport GJ, Forlee C. Determination of National Water Heating Load Characteristics by a National Notch-Test Program. 4th Domestic Use of Electrical Energy Conference, Cape Town, March 1997. page 60 - 65.

Peak demand control in commercial buildings with direct temperature feedback

A. J. Hoffman
Potchefstroom University for CHE

Abstract

Peak demand control in commercial buildings can potentially have a significant impact on the national peak demand for electricity. It is however essential to take an approach which will not compromise the convenience of tenants. Traditionally peak demand control was performed with overall demand as only objective function of the control algorithm. With such a approach either convenience has to be compromised, or overly stringent limits have to be placed upon the control parameters, thus decreasing the potential for peak demand savings. This paper reports on one of the first peak demand control systems with direct temperature feedback that has been installed in South Africa in a commercial building. The system, that was installed at the Parliament complex in Cape Town, performs peak demand control using overall demand, as well as temperatures reflecting the status of equipment being controlled, as objective functions of the control algorithm. In this way peak demand control can be optimised without compromising the primary functions of the sheddable equipment.

1. Introduction

Buildings accounts for 36% to 42% of the total world primary energy consumption. [1,2,3,4,5] In the building sector housing accounts for 65%, commercial and public sector buildings for 29%, and industrial buildings for 6% of the national energy consumption of the United Kingdom.[4] Similar results were obtained for the Cape Town region in South Africa. According to Anderssen, housing accounts for 53%, commercial sector buildings for 20%, and industrial buildings 27% of the total municipal energy consumption.[6]

Most of the energy in commercial buildings are consumed by air-conditioning and lighting equipment. According to Spoormaker, air-conditioning contributes between 30% and 50% of the total energy consumption of a building.[7] Anderssen & Partners have concluded that air-conditioning in the Cape Town region accounts for 80% of the building demand during summer peak hours and 70% of its energy consumption.[8]

Most buildings are not equipped with either building management systems or with electricity demand controllers, since these systems are regarded as being too expensive. The energy profiles and potential for demand side management of these buildings are hence unknown, and the mutual benefits that it holds for the property owner and utility are not exploited.

This situation is however changing. The availability of cost-effective technology for control and communication in buildings has created opportunities to introduce demand side management practises into buildings that will benefit both the property owner and the utility.

The ideal energy management strategy must implement self-adjusting DSM control, which on the one hand creates interruptibility, and on the other hand complies with the constraints of end-use equipment and the limitations of commercially available communications and control technology. This paper describes the design and implementation of a demand control system which is based on the following principles:

- load prediction algorithms which are used to estimate future demand;
- a control algorithm which determines and continually adjusts the shedding schedule, in order to keep actual demand below the target peak demand; and
- continuous monitoring of the internal parameters of plant, and feeding back these parameters to the control algorithm to maintain acceptable operating conditions for such plant.

2. The concept of intelligent distributed control

Traditional control systems are based on centralised intelligence, which rests on the principle that all information is fed to a central point. At this point all required processing is performed on input data, the processed data is fed to a control algorithm, and the control algorithm generates control commands which are communicated to the various points of control, where equipment could be switched on or off.

Centralised command based control systems suffers from the following disadvantages:

- a large amount of raw data must be communicated from the various points of monitoring to the central point;
- if no intelligence is available at points of monitoring, analogue variables need to be communicated over large distances at high costs;
- a powerful central processor is required, since it must process all data in real time, implement prediction models of all equipment being controlled, and execute the control algorithm;
- system operation depends on the continuous availability of both the central processor and of all the communication links, since every control action involves both these elements.

In contrast to this, a distributed control system has the following advantages:

- pre-processing of data can take place at the point of monitoring, reducing the amount of data to be communicated;
- analogue wiring over long distances is replaced by a single digital communications bus;

- a powerful central processor is not required, since the processing is distributed between a number of intelligent nodes, each of which implements prediction models for the equipment that it controls;
- the operation of the system status based rather than command based - in a situation where the master controller or the communication with a specific node is off-line, each node can still operate based on the last status information received from the rest of the system.

3. The peak demand control algorithm

The primary objective of the control algorithm is to minimise the peak demand of the complex over any demand period of 15 minutes, during the specific month. The secondary objectives are to keep each separate piece of sheddable equipment within acceptable control limits.

The principles on which the control algorithm is based, are summarised as follows:

1. The target peak demand for a month is determined as the average historic peak demand of that month for the previous four years, multiplied by a target savings factor based on the predicted potential peak savings.
2. The 15 minute demand period is divided into a number of decision periods (at this stage decision periods of length 30 seconds are used).
3. At the start of each decision period, the following parameters are determined:
   - the sheddability status of each piece of equipment, based on the status of its internal parameters and on the limitations defined to maintain its primary functions;
   - the current kVA level of each piece of equipment, the expected kVAh till the end of the demand period, the kVAh that could be shed by switching off the equipment, and the kVAh that could be added by switching the equipment on;
   - the maximum time duration for which the equipment can be kept in its off state, starting from the current state.
4. The predicted kVAh for the demand period is calculated, based on the kVAh predictions for the various equipment, added to the predicted baseload of the complex. This is subtracted from the target peak demand for the month to obtain the required kVAh to be shed during the remainder of the period (kVAhReq).
5. Equipment which have become unsheddable based on internal status parameters are switched on again.
6. If kVAhReq is positive, the algorithm will identify equipment for shedding, based on a priority level allocated to each type of equipment. For equipment with the same priority level, the algorithm would first select equipment which can be shed for the longest time duration (e.g. if two chillers are available for shedding, the one with the coldest chiller water would be selected first). This process will continue either till a sufficient number of loads have been selected for shedding, or until all sheddable loads have been selected.
7. If kVAhReq is negative, the algorithm will identify loads which have been shed and which could be switched on again. A safety margin is allowed to prevent frequent on-off cycling due to statistical fluctuations in the baseload.
8. Should the target peak demand be exceeded during the course of the month, the target peak would be adjusted upward to the maximum actual demand level attained up to that point in time.

During off-peak periods (when the target peak demand is not threatened by actual demand), the energy storage levels are hence maintained as close as possible to their maximum levels. When the actual demand threatens to exceed the target peak demand, this stored energy is released to keep actual demand below the target level. Table 1 below outlines the equipment that were available for shedding, as well as their respective control limits.

Table 1 Characteristics of sheddable equipment

Type of equipment	kW rating	Parameters monitored
Chillers	660 653 2 X 373 4 X 90	Chiller water kept between 6°C and 10°C Minimum on time 5 minutes
Cooling fans	3 X 15 2 X 20	Air temperature kept between 28°C and 33°C Minimum on time 5 minutes
Calorifiers	2 X 17	Minimum on time 5 minutes
Boiler	850 250	Water kept above 80°C during off-peak times

Figure 1 below displays the behaviour of the accumulated kWh during the 15 minute demand period for the same on-off cycle, as well as the accumulated kWh shed during the demand period. It is shown that the target peak demand level is adjusted upwards when the actual kWh for a 15 minute demand period exceeds the previous target value.

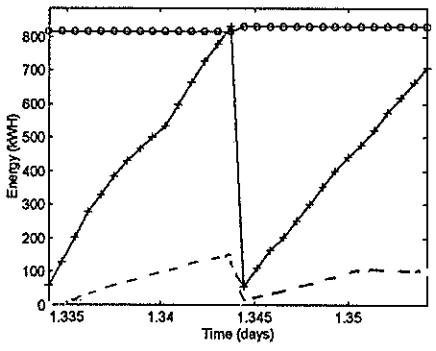

Fig 1 Accumulated kWh during a typical demand period.
+ accumulated total kWh
*** accumulated kWh shed**
o target peak kWh

4. Modelling of equipment behaviour

Estimation of the expected kVAh contribution of each piece of sheddable equipment requires a model describing the expected thermal and electrical behaviour of the equipment based on its current internal temperature, its existing thermal load, and other parameters describing its internal state. Modelling chillers behaviour were the most important, since chillers represented the biggest sheddable loads, and since their internal behaviour are the most complex of the sheddable loads. Since the power usage of the individual equipment are not measured directly on a permanent basis, it is derived from the difference between the in- and outgoing temperature levels of the chiller water.

The model for the behaviour of the chillers are described as follows:

- When a chiller is running in a stable state, it internally adjusts its kVA level according to the current thermal load; this kVA level is assumed to be proportional to the difference between the temperatures of the incoming and the outgoing chiller water.
- When the chiller is shed, the kVA level is assumed to drop to a predetermined value (for some chillers this value is zero, while other chillers are shed to a fixed minimum on state). During such a period, it is assumed that the chiller water temperature will increase exponentially towards the ambient temperature (the chiller water is hence modelled as a first order thermal system). The approximate time constant was determined by measuring the chiller water temperature behaviour during an on-off cycle.
- When the chiller has been off, and is switched on again, its kVA level is assumed to abruptly change to its maximum level, and then to decrease exponentially towards its equilibrium value, corresponding to the current thermal load on the system. It is assumed that the total kVAh "saved" while the chiller was off, would equal the extra kVAh required after switching the chiller on again, to re-establish thermal equilibrium. This determines the exponential rate at which the equilibrium kVA level would be approached. Practical measurements proved these assumptions to be close to reality.

This behaviour is described in figure 2 below. It is important to notice that the chiller behaviour will cause a secondary peak in the kVAh level in the demand period during which it is switched on again, which is caused by the increase in the kVA level at termination of a shedding period.

For the other types of sheddable loads (cooling fans, calorifiers and boilers) the kVA level for each load had only two possible values: kVA equal to maximum rating in the on state, and kVA zero in the off state.

5. Application of the control algorithm on a distributed basis

In the system that was implemented, tasks are divided between the distributed processors. The intelligent node situated at each piece of sheddable equipment, performs the following tasks:

- monitoring of the on/off status;
- monitoring of temperature variables;
- keeping track of on/off time durations;
- determining the sheddability status of that piece of equipment;
- estimating the kVAh contribution of the equipment for the remainder of the control period;
- implementing the on/off control command received from the control node.

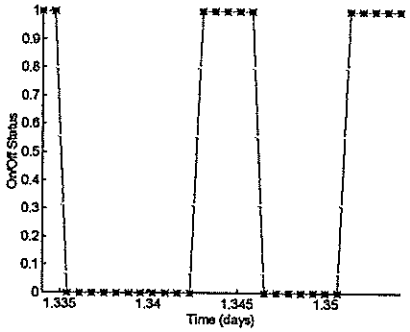

(a) On/Off status of chiller

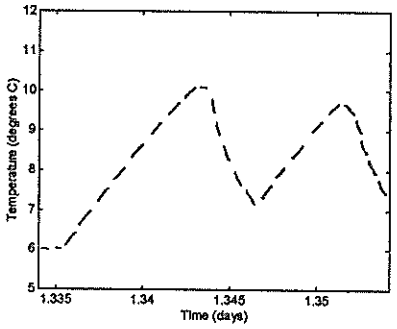

(b) Chiller water temperature

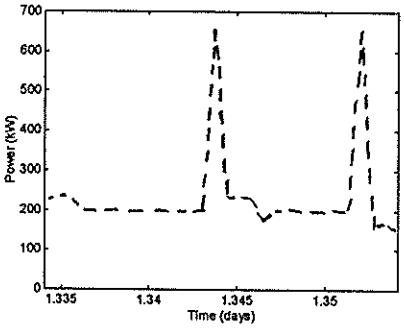

(c) Power usage of chiller

Fig 2 Chiller behaviour during on-off cycling

The control node, situated at the main electricity meter, performs the following functions:

- counting of kVA and kW pulses from the mains meter, and converting that to instantaneous kVA and kW;
- calculating the kVAh for the demand period and the kWh for the month;
- reading the demand period pulse, and starting the control algorithm for that period;

- initiating the events for each decision period;
- calculating the required kVAh to shed for the demand period;
- receiving sheddability status information from the various nodes, an using that to generate on/off control commands for the various equipment.

Should the control node lose communication with any specific node, it would assume that the equipment at that node is not sheddable. In the same way, a node which loses communication with the control node, would switch the sheddability status of its equipment off, and keep its equipment in the on state.

In principle, it is possible to extend the distributed nature of the control algorithm even further, in order to extend the independent operation of each intelligent node. The same control algorithm, as is currently implemented at the control node, could be implemented at each separate node, each node taking note of the status information from the other nodes, and generating control commands for its own equipment. Should communication between nodes be lost temporarily, or should one or more nodes go off-line, the remaining nodes will still behave normally, assuming that equipment at off-line nodes are non-sheddable.

6. Expected and practical results

The peak demand control algorithm is still under evaluation at the installation site, and hence no final results about achieved savings can currently be reported. Measurements of the overall demand of the complex has shown that the peak demand normally lies between the +2 and +3 sigma points of long term statistical behaviour. If sufficient sheddable loads are available to keep demand below the +1 sigma point of the normal statistical behaviour, the peak demand will be reduced by approximately 10%. The total sheddable load exceeds this value, but it must still be proved in practice that these loads can be moved between demand periods on a continuous basis to dynamically limit peak demand. Since the maximum shedding period for loads during times of high thermal loading are close to the length of the demand period, an optimal control algorithm can be expected to make an appreciable difference to peak demand.

The following comments can be made about what has been learnt till the present:

- The majority of sheddable loads are running continuously if not interfered with. The function of the peak demand control system is to use the storage capacity of these systems to level out statistical fluctuations in overall system demand. The stability of the dynamic response of the control system is of critical importance to improve rather than to aggravate the peak demand situation.
- The prediction of the base load for the remainder of each demand period has a significant influence on the stability of the control algorithm. The future kVA base load is currently estimated as a smoothed version of past values, but better performance may be achieved through an autoregressive model.
- The system currently applies only on-off control to equipment, since the hardware does not allow linear control. This limitation increases the risk of oscillations in total system demand.
- Control limits and internal control parameters should be defined to maximise storage capacity. E.g. the internal temperature of chillers should be set to as low a value as possible. The external peak demand control can then force the system temperatures down during periods of low demand to increase storage capacity. Such a strategy may however increase not be optimal in terms of thermal efficiency.
- It appears that the objective of 10% savings on peak demand levels could be achievable during summer months. During winter months the chillers are however normally running at low levels, leaving the system with a smaller effective sheddable load, hence decreasing potential savings.

7. Conclusion

The objective of this project is to prove that it is possible to achieve significant peak demand savings in a commercial building complex, without compromising the convenience of users. The real-time availability of information reflecting both the status of the peak demand situation and the internal status of sheddable equipment, makes it possible to find an optimal trade-off between two potentially conflicting objectives. True optimisation of such a system can only be achieved through accurate simulation of the thermal behaviour of the various systems being controlled, as well as that of the overall complex. Practical results that have been achieved up to date emphasises the importance of establishing optimal control limits for sheddable equipment. The existing installation has proved that a peak demand control system, distributed through several building complexes, can be reliably implemented using existing communication and control technology, achieving a pay-back period of approximately one year.

1 D. Carrol, Energy consumption and conservation in buildings: An international comparison, Proc. 3rd Int. Symp. Energy Conservation in the Built Environment, Vol. 1A, CIB/An Foras Forbartha, Dublin, pp. 190-203 1982.

2 Bevington, R. and Rosenfeld, A.H., Energy for buildings and homes, Scient. Amer., pp. 39-45, September 1990.

3 A. Thumann, Fundamentals of energy engineering, Prentice-Hall, New Jersey (1984).

4 A.B. Birtles, Getting energy efficiency applied in buildings, Building Reasearch Establishment, Watford WD2 7JR, UK, pp. 221-252 (1993).

5 M.A. Piette and R Riley, Energy use and peak power for new commercial buildings from the BEACON Data Calculation: Key findings and issues, Lawrence Berkely Laboratory Report LBL-20896 (1986).

6 J.J. Anderssen, Cape Town Load study: An end-use segmentation, Seminar and main steering committee meeting for DSM and related projects (27 April 1993).

7 H.J. Spoormaker, Conserving energy through the building brief, Enerconomy '93, Pretoria, South Africa, October 1993.

8 J.J. Anderssen, Cape Town Load study: An end-use segmentation, Seminar and main steering committee meeting for DSM and related projects (27 April 1993).

LOAD DATA PREPARATION FOR LOSSES ESTIMATION

RL Sellick and CT Gaunt
Department of Electrical Engineering, University of Cape Town, Private Bag, RONDEBOSCH, 7700

Abstract This paper presents an approach towards the estimation of distribution network losses. The consumer load data from various groups around South Africa is analysed, in order to determine various quantities which describe and characterise the particular consumer group. This is done statistically, as an attempt to characterise generic communities, rather than merely provide information about the communities which have already been electrified. The characteristic values to be considered include maximum load, load factor, maximum losses and loss factor. These need to be determined as average values for small subsets of consumers within a consumer group, for numbers of consumers ranging from 1 up to the maximum available number of consumers.

Keywords: load factor, loss load factor, load data logger

1. INTRODUCTION

The accurate estimation of electrical losses enables the supply authority to determine with greater accuracy the operating costs for maintaining supply to low voltage domestic consumers. This in turn enables a more accurate estimate of the system lifetime costs, over the expected life of the installation.

This paper presents an approach which is currently being used to estimate the electrical losses in low voltage distribution feeders in residential townships throughout South Africa.

2. LOAD DATA

The load data is provided in the form of logger tables, recorded over 5-minute averaging intervals from various townships within South Africa.

This load data consists of a date / time stamp, a channel number and a load current reading. The zero channel is used to monitor the supply voltage at the metering point. The remaining channels, which are presented consecutively in the format obtained from the National Load Research Co-ordinator, contain the electrical load current averaged over the 5-minute interval, with the date / time stamp occurring in the middle of the interval. Each of these channels records the electrical load current monitored at an individual domestic dwelling within the township.

For any one township, several logger tables are available. However, these loggers do not necessarily record data of exactly the same logging interval. Thus, the data sets from various loggers within a township must be synchronised with the date / time stamp, to ensure an accurate representation of the population diversity.

3. DATA MANIPULATION

The logger data files are combined in such a manner that a single master-table for the entire township population recorded is created. This file contains a single date / time column, and columns for each channel which contains valid readings during the duration of the township logging period. This synchronisation process intrinsically creates "holes" (ie. readings for which no value is recorded), as not all the loggers will overlap exactly for the logging period. Further, when down-loading occurs, the channels are disconnected. For any particular logger, there are periods in the master table where no data is recorded.

Typically, a township sample of 80 consumers measured over a year results in a master table occupying roughly 65MB of disk space, using the Delphi Developer Database Table format. For data sets of this size, a spreadsheet-type application is not a suitable tool for analysis. A spreadsheet can be used simply to graph summary statistics, etc.

In the creation of this master table, which resembles a matrix, all invalid channels are ignored and not inserted. When an invalid single load reading is encountered, this value is omitted from the matrix. A zero cannot be inserted to replace these values, as the load current is unknown, and probably non-zero. A blank, referred to as a "hole" is created in the matrix.

The resulting matrix tables obtained for four of the available data sets, taken before October 1996, are summarised in Table 1.

In Table 1, the matrix density quoted is the ratio of the number of actual values (excluding holes) to the number of possible values, ie.

$$\text{Density} = \frac{\text{no. of valid readings} * 100}{(\text{no. of channels}) \times (\text{no. of records})} \quad (1)$$

The values quoted for matrix density must be seen in context, as holes arise partially due to mis-synchronisation of logger recording periods. The value quoted is not necessarily an indicator of the sampling efficiency, and must be viewed simply as an index of the density of the number of channels over the total recording period.

The maximum load current quoted in Table 1 is the maximum load current in the matrix table, excluding those values above the 80A assumed threshold. Invalid data, error thresholds and logger errors are discussed in Sections 4 and 5 below.

4. LOGGER ERRORS

There are several errors associated with the load current readings as recorded in the logger tables, which arise from generic sources [1]. Some of these are described below:

4.1 Data handling and data transfer errors

A corruption of the file format, which is a data handling error, can occur as a result of the file format being changed and saved with the same name and extension.

Electrical noise is classified here as a data transfer error. This error constitutes non-numeric characters (such as alphabetic or graphic characters) being inserted into the logger data file. This can also affect the formatting of a particular field.

Software has been developed to address these problems, which have been ignored for the purposes of this study.

4.2 Data logger handling (software and hardware)

The logger software may be incorrectly set up, which causes a logger handling error. This may affect any of the logger identity, date and time for the on-board real-time clock, logger sample averaging interval, and the number of active channels.

Hardware setup problems, which are typically 'physical' (eg. accidental disconnection of a plug, or a channel number not being used), cause holes (periods where no readings are recorded) in the data set. These holes constitute lost data, and must be accomodated in any analysis which is based on the logger load data sets.

The identification and removal of these errors is discussed in Section 5.

5. ERROR IDENTIFICATION AND REMOVAL

Errors are identified through a software-based application written in Delphi Developer, which runs in a Windows 95 environment.

Certain channels are deemed to be non-valid, in that these channels have not been initialised, or used, but are recorded in the logger output file. These channels are not transported to the resulting matrix, and are ignored in the matrix generation process. A channel is considered to be invalid under the following conditions:

- Low maximum - if the maximum reading within a channel is lower than 100 mA, the channel is considered invalid. The threshold has been determined by consideration of a 40W incandescent lamp. Such a lamp would draw a root-mean-square load current of approximately 174 mA.
- Low mean - if the average value of the reading over the life in which a channel is active, is less than 30 mA, the channel is ignored. The threshold has been determined by consideration of a 40W incandescent lamp, which is used for 5 hours per night. Such a lamp would draw an average load current, per day, of approximately 36 mA.

Population	*Claremont*	*Cloetesville*	*Manyatseng*	*Umlazi*
Total no. of loggers	4	7	22	12
Total no. of channels	19	82	88	36
No. of invalid channels	2	0	4	1
No. of valid channels	17	82	84	35
No. of records	44074	102944	24206	99226
Duration [days]	153.05	373.88	110.25	463.56
Number of holes	32809	459052	760124	190982
Matrix density [%]	95.62	94.56	62.62	94.50
Maximum load current [A]	77.36	55.40	35.74	25

Table 1 : Summary of load population matrices

- High mean - if the average reading over the life of the channel is greater than 80 A, the channel is considered to be invalid. This threshold is conservative, and is assumed to be the maximum possible value of consumer circuit-breaker size. In reality, most circuit-breakers for newly-electrified townships will be between 20A and 60A.

If an individual reading is invalid, this reading is ignored for all purposes of determining channel validity, and generating of the population matrix. When an invalid reading is encountered, the reading is omitted and a blank, or "hole" is inserted into the township matrix. An individual reading is considered invalid under the following conditions:

- negative reading - all loads are positive (ie. non-generative)
- high reading - if the reading is greater than 80A, the reading is omitted. This threshold is similar to the high mean threshold used for channel validity.
- non-numeric reading - if the reading contains non-numeric characters, it is omitted. There are non-numeric characters which are exceptions to this rule, and do form part of floating-point numbers. These are '+', '-', and 'E'. The 'E' symbol is used for exponential scientific notation, and does occur in some of the data sets.

6. DISCUSSION OF RESULTS

Analysis on the data sets from Umlazi and Cloetesville will be useful as each of these logging periods is greater than a year, and the matrix is more than 94% full. By contrast, analysis performed on Manyatseng will be of only academic interest due to the short logging period, and lower efficiency of roughly 63%.

No invalid channels are present in the Cloetesville sample. This represents good logger utilisation by the operator, and is indicative of the understanding by the operator of the importance of accurate load logging.

The high maximum load current in the Claremont sample could be indicative that the threshold for maximum valid current values should be reduced from the 80A setting to, say, 60A. A load reading of 77A could result in a logger failure to 100A for, say, two thirds of the sampling interval, and a load reading of 20A for the remaining third of the sample interval

7. LOAD MATRIX SAMPLING

With the resulting matrix of consumers for each population, it is possible to cut the matrix in several ways. For example, the matrix may be cut horizontally (representing a snapshot at a single time instant), and compared with other such cuts to establish the changing consumer load current distributions as these change over time.

For the project envisaged, these matrices will be used to generate information with regard to the particular population as follows:

- For each possible number of consumers, being subsets of the available sample size, several groups of consumers will be randomly chosen (ie. choose say 10 groups of 1 consumer, 10 different groups of 2 consumers, etc., up to the total number of valid channels available for that population group). These groups are chosen without replacement, to ensure that within each sample group no channel will appear twice.
- For each group, the load factor and loss load factor will be derived. This will be done on a monthly basis (ie. for each group derive the load factor for each calendar month), and on an annual basis where possible.
- The load and loss load factors applicable to any particular time period and group size derived above are averaged to determine a factor, within tolerances, applicable to that group of consumers.

The result is a set of load factor and loss load factor curves, as a function of calendar month, for each population group, for any number of consumers up to the maximum available size.

8. ELECTRICAL LOSS ESTIMATION

The electrical losses are estimated using the loss load factor. The loss load factor is determined from the square of the sum of the individual load currents for the consumers in the sample group, at each sample instant for the period under consideration (be it a month or a year). It is important to note that the individual currents must be summed before any further manipulation takes place, to ensure an adequate treatment of diversity. This constitutes the load-dependent factor of the losses, and using the loss load factor over the month in question.

In order to perform an estimation of the electrical losses, a network is required, which includes cables sizes, and consumers located at various points within the network. This network is used as a reference test case for all the populations load data.

To determine the losses in the phase conductors, the loss load factor for the number of consumers connected to that phase on that section of cable, combined with the maximum expected load current, is used. The period of loss estimation would then be the same period for which the loss load factor was calculated.

To determine the electrical losses in the neutral conductor, an approximation is made. For an equal number of consumers located on each phase, no losses are assumed in the neutral. For unequal numbers of consumers, the loss load factors are added geometrically , to determine an approximation to the resulting losses in the neutral. This approximation, while not being accurate, gives some measure of the neutral losses.

The load factor (LF) is not used directly, but as a test on the loss load factor (LLF) , since the following inequality must always be satisfied:

$$0 < LF^2 < LLF < LF < 1 \qquad (2)$$

If this inequality is not satisfied, there are errors in the calculation process.

9. VALIDATION OF RESULTS

As there is no software known to the authors which performs a similar process, software validation is difficult. Checks have been implemented to ensure that the values calculated and procedures employed are correct, and that there are no systematic errors (due to floating-point arithmetic errors, etc.).

The steps which have been taken to validate the software include:

- Comparison of errors recorded with those recorded by other researchers. When an invalid channel or reading is encountered, the error is removed and the error condition and occurrence recorded in a file for comparison with the results of the efforts of other researchers, to ensure that the same errors are consistently detected and removed.
- Testing the bounds of the loss load factor (see Equation 2 above)
- Visually scanning the data-set to ensure correct transposition of values. This is difficult considering the size of the data sets, and is mostly useful in checking the extremities of a channel (ie. start and end).

10. CONCLUSIONS

A tool has been developed which assists in the determination of the load factors and loss load factors for the various months of the year for any given set of disorganised load data. These factors will allow the determination, within a tolerance, of the system electrical losses in each of the phase conductors and to a lesser degree of the neutral conductor.

The calculation process is repeatable for other data sets which are presented in the same format as that currently used for the national load research.

This software tool is continually being updated and improved as comments / feedback are received from various parties.

11. REFERENCES

[1] Dekenah M, *"The NRS LR Project : Note on Data Handling & Processing"*, Marcus Dekenah Consulting, Pretoria, 1997

[2] Lakervi E, and Holmes EJ, *"Electricity distribution network design"*, Peter Peregrinus on behalf of The Institution of Electrical Engineers, 2nd Edition, London, 1995

AUTHORS

RL Sellick E-mail: rsellick@iafrica.com
Fax: +27 -21 245571

Prof CT Gaunt E-mail: tgaunt@hkslg.lawco.com
Fax: +27 -21 245571

A COMPUTER MODEL PREDICTING INDUCED VOLTAGES ON CONDUCTORS LYING IN NON-FERROMAGNETIC CONDUIT CARRYING PARTIAL LIGHTNING IMPULSE CURRENT

G. J. Walliser, I.R. Jandrell and J.M. Van Coller

Electric Power Research Group
Department of Electrical Engineering
University of the Witwatersrand
Private Bag 3, WITS, 2050, South Africa

Metal conduit and cable-trays are used extensively in industry to run electric and signal cables from place to place on a site. The latest local and international lightning protection standards advocate bonding both conduit and cable trays at least at both ends to form part of an equipotential platform which includes the common earthing network. Doing this encourages large currents to flow along these paths and the shielding effectiveness of conduit and cable trays under these conditions must therefore be quantified. This paper investigates the shielding characteristics of a tubular, non-ferromagnetic conduit with partial lightning currents flowing along its length. Theory governing the coupling of the resulting fields to inner conductors is presented and the concept of transfer impedance is discussed and incorporated into a computer simulation tool.

Keywords: equipotential, shielding, transfer impedance, partial lightning current, EMI, EMC, conduit, cable-tray.

1 BACKGROUND

In South African industry, conduit and cable trays are very often not bonded at both ends and are not galvanically continuous along their length. They are seldom thought of as shields for the reduction of electromagnetic interference (EMI) [1]. The latest lightning and EMC standards, locally (NRS 042 [2]) and internationally (SABS-IEC 1024-1 [3], 1024-1-1 [4], 1312-1 [5] and 1662 [6]) require such bonding to take place in an effort to create equipotential platforms which limit the formation of differential voltages between bonded areas or zones. The standards advocate the bonding together of all conduits, cable trays and shielding cabinets which should then also be bonded into the common earthing system [2,5]. Modelling the behaviour of the earthing system during transient current impulses is the subject of a paper by Nixon et al [7] to be presented at Saupec 1998.

In the event of a lightning strike, partial lightning currents flow along the bonded shields with a minimum voltage build-up thus equipotentialising the site. However, these partial currents flowing on the outer surfaces of shields which house power and signal cables may give rise to significant voltages along the cables, particularly if the shield is long or has thin walls [1,8,9]. A need exists, therefore, to quantify the effectiveness of cable shields under these conditions and then to emphasise their usefulness in reducing differential voltage magnitudes during lightning events.

Lightning induced surges present a particularly significant threat in South Africa as much of the industry involved in the use of sensitive electronic systems is located in and around Johannesburg, an area of high lightning incidence (approximately 7 strikes per square km per year) and high soil resistivity [1]. For this reason, the 8/20μs lightning current impulse waveform was chosen as the basis for all simulations performed on the conduit and the focus of the paper will be on lightning-related surges only.

2 INTRODUCTION

The purpose of cable shields is to reduce the magnitude of induced interference voltages on signal cables caused by incident electromagnetic fields [10]. The shield presents a surface of high conductivity which attenuates the electric field inside. When current is allowed to flow along the shield, the magnetic field is also attenuated.

In addition, certain shields, such as conduit or cable trays, may also form part of the common earthing network and sometimes carry large impulse currents, such as those occurring during a lightning strike. Although the current flows mainly on the outer surface of the conduit and no magnetic fields exist inside the shield, a longitudinal or tangential electric field is generated on the inner surface of the shield. This electric field would then couple directly to any inner cabling and induce interference voltages along its length. This paper considers the tubular shield or conduit under such conditions. A frequency-domain model of the conduit, under impulse conditions, is presented in which the transfer impedance is calculated and used to predict the magnitudes of induced interference voltages for a length of non-ferromagnetic conduit.

3 ELECTROMAGNETIC SHIELDING THEORY

For the purposes of this paper, the conduit with inner signal cables is treated as a coaxial arrangement with the disturbance current flowing on the outer shield only. Due to the skin effect, most of the partial lightning current will be forced to flow along the outer surface of the shield [1,10,9]. It is the magnitude of the current density at the inner surface of the tube, however, which determines the tangential (or axial) electric field inside the shield (E_t) as follows [10] :

$$E_t = \frac{J_t}{\sigma} \qquad (1)$$

Where: E_t = Electric field vector tangential to the surface of the shield
J_t = Current density vector in the axial direction i.e. tangential to the surface of the shield.
σ = Conductivity of the shield.

Figure 1 shows a likely electric field distribution in a conduit wall when a lightning impulse current (I_p) is flowing along it.

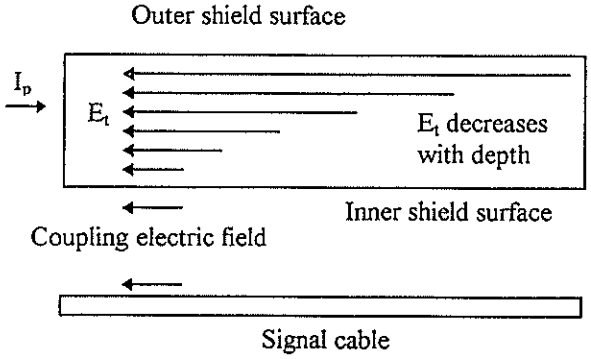

Figure 1: Diagram showing the reduction in tangential electric field with depth into the shield. Note that the electric field remains constant across the conductor-air boundary and exists outside the shield with an almost unchanged magnitude [10].

It is clear from Ampere's law that no magnetic field will exist inside the tube as a result of the current flowing on the shield [10]:

$$\oint H.dl = I = 0 \qquad (2)$$

Where: H = Magnetic field.
dl = infinitesimal element of path length.
I = Enclosed current which is zero in this case.

There is, however, inductive coupling caused by the common flux linkage between the field generated outside of the tube and both the shield and inner conductors. This coupling induces an equivalent, common mode voltage in both the shield and the central conductor and thus has no bearing on the differential mode voltage. This is not the case for braids or tubes with slots or joints. In both of these cases, magnetic field leakage occurs and becomes the dominant effect at high frequency (>1MHz) [9]. Further research into this area will result in computer models able to simulate this effect.

4 TRANSFER IMPEDANCE

The complex relation between the current flowing on the tube and the electric field generated at the inner surface of the tube is dependent on many factors such as the geometry of the shield and inner conductor, the material of the shield and the duration of the pulse. It is practical, especially for measurement purposes, to simplify the relation for a given shield and express it as a transfer impedance [9]:

$$dZt = \frac{Et}{Icm} dl \qquad (4)$$

Where: dZ_t = Infinitesimal element of transfer impedance.
E_t = Tangential electric field (frequency domain)
I_{cm} = Common mode current flowing along the tube to earth (frequency domain).
dl = The axial length of the conduit

The transfer impedance is a useful way of characterising the effectiveness of a shield. Conduit with a low transfer impedance is a better shield than conduit with a higher Z_t for a given frequency. Note that due to the frequency dependent nature of the skin-effect and hence the transfer impedance, the Fourier transform of both the common mode current and differential mode induced voltage must be taken to determine the Z_t spectrum in this case [9]. This is necessary because the lightning impulse is a transient event and the waveform cannot be described by a single frequency or, therefore, a single Z_t.

5 COMPUTER SIMULATION

The aim of simulating a partial lightning current flowing on a conduit is to predict the differential mode voltage waveform, V_{dm}, which will appear between the inner signal cable and the shield. To do this, it is necessary to analytically determine the transfer impedance over the frequency range of interest for a

given conduit. This may be done by first calculating the skin depths at these frequencies using the following equation:

$$\delta = \frac{1}{\sqrt{\pi f \mu_0 \mu_r}} \qquad (4)$$

Where : δ = Skin depth (m).
μ_0 = Permeability of free space.
μ_r = Relative permeability of the tube material.
f = frequency (Hz)

The transfer impedance for a solid walled tube is then given by [9]:

$$Z_t = \frac{R_o(kT)}{\sinh(kT)} \qquad (5)$$

Where : Ro = $1/(2\pi\sigma T)$ = DC resistance of the shield per unit length.
$k = (1+j)/\delta$ = The eddy current constant.
T = Thickness of the tube.

For the purposes of this paper, tubular aluminium conduit is used as an example because it is non-ferromagnetic and has a well documented characteristic.

Figure 2 shows the magnitude of the predicted transfer impedance of a 3m length of aluminium conduit with a 20 mm diameter and 1,6 mm wall thickness, plotted against frequency. The plot compares favourably to published results [9].

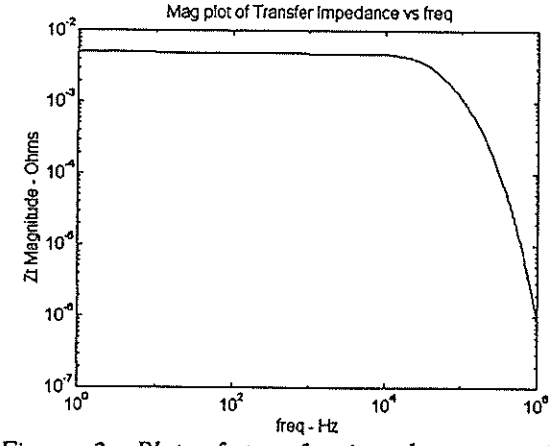

Figure 2: Plot of transfer impedance magnitude against frequency.

Knowing Z_t for the range of frequencies now allows us to find the Fourier transform of the lightning current waveform and multiply the two together to determine the spectrum of the differential mode interference voltage:

$$V_{dm} = Z_t . I_{cm} \qquad (6)$$

Finding the inverse transform of V_{dm} yields the time-domain waveform of the induced voltage surge on the signal cable.

Figure 3 shows the predicted waveform for a 3m length of aluminium conduit with a 1kA, 8/20μs lightning impulse current flowing along its length. The conduit has a thickness of 1.6 mm.

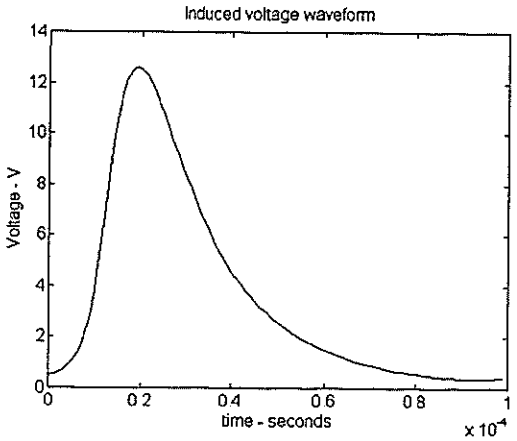

Figure 3: Plot showing the predicted differential voltage waveform in the time domain.

An important assumption when modelling the lightning current on the conduit is that it is uniform along the length of the tube for an instant in time [9]. This assumption may only be made if the tube is short when compared to the spatial distribution of the impulse or the wavelength of its highest frequency component.

A lightning impulse waveform is normally represented as a current magnitude with respect to time. It may also be represented as a current magnitude with respect to displacement if the velocity of the current flow is considered to be a constant. If the spatial distribution of the impulse is much greater than the length of the conduit, it is possible to assume that an approximately uniform current is flowing along the length of the tube. If this assumption is not valid for the length of conduit being considered, it may be necessary to model the conduit with transmission line theory and view the impulse as a travelling wave.

6 EXPERIMENTAL PROCEDURE

As it is the tangential electric field inside the conduit which leads to a differential voltage between the conduit and inner cables, it is necessary to take measurements which isolate the effects of this field. The most commonly used method of measuring the tangential electric field involves short circuiting the shield to the core at the current injection end, earthing

the shield at the far end of the tube and taking a measurement of the core voltage with respect to that earth [11]. Such a test circuit is shown in figure 4 below:

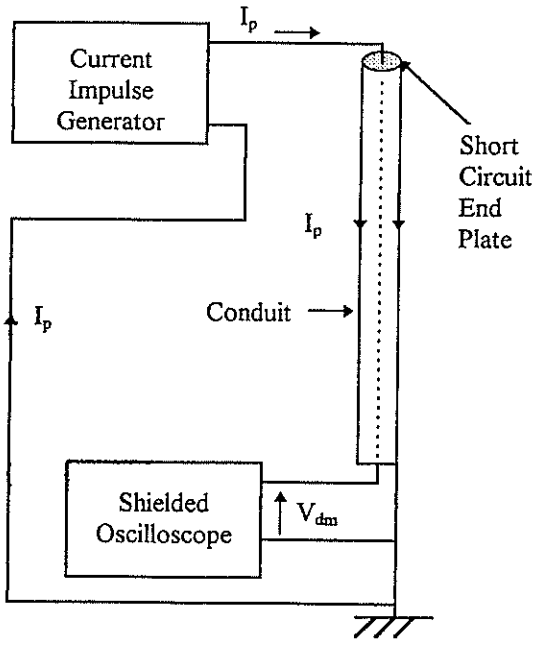

Figure 4 : Diagram showing the test circuit used to measure the tangential electric field inside a conduit.

The distance between the conduit and the current return path of I_p will influence the measurement of V_{dm}. Ideally, flux produced by the return path should not link with the conduit.

7 PRELIMINARY RESULTS AND EXPERIMENTAL PROCEDURE

Using the above recommended circuit, a test fixture was constructed. A combination impulse generator was used to apply the 8/20 μs current impulse to an aluminium conduit and the preliminary observations have highlighted the need to limit interference from all electromagnetic sources other than that under observation.

8 CONCLUSIONS

While the advantages of bonding conduit and cable trays to form equipotentials is clear, the differential mode voltages which arise due to high current flowing on the shield must be considered. It has been established that the tangential electric field produced at the inner surface of the conduit is the main source of this interference voltage. Methods of measuring this voltage have been outlined and predictions from a simulation program using the transfer impedance concept have been presented for tubular non-ferromagnetic conduit. Correctly modelling conduit, cable trays and armouring allows accurate prediction of interference voltages. This knowledge may be used to quantify the risk to electronic equipment and to accurately specify the ratings of surge protective devices on the system.

9 REFERENCES

1. Van Coller JM, Jandrell IR (1992). "Behaviour of interconnected building earths under surge conditions." Paper 3-06, 21st International Conference on Lightning Protection.
2. NRS 042 (1996): "Guide for the protection of electronic equipment against damaging transients." NRS, 1996. ISBN 0-626-11130-7
3. SABS-IEC 1024-1 (1990) "Protection of structures against lightning : Part 1: General principles." IEC, 1990 (SABS, Pretoria).
4. SABS-IEC 1024-1-1 (1993): "Protection of structures against lightning : Part 1: General principles: Guide A - Selection of protection levels for lightning protection systems." IEC, 1993 (SABS, Pretoria).
5. SABS-IEC 1312 (1995): "Protection against lightning electromagnetic pulse (LEMP), Part 1: General principles." IEC, 1995 (SABS, Pretoria).
6. SABS-IEC 1662 (1995): "Assessment of risk damage due to lightning." IEC, 1995 (SABS, Pretoria).
7. Kern A, Weisenger J, Zischank W (1991). "Calculation of the longitudinal voltage along metal tubes caused by lightning currents and protection measures." Paper 83-13, 7th International Symposium on High Voltage Engineering, Dresden, August 1991.
8. Kern A, Lang U, Weisenger J, Zischank W (1989). "The longitudinal voltage of cable tubes with a screening mesh caused by partial lightning currents." Paper 27-10, 6th International Symposium on High Voltage Engineering, New Orleans, August/September 1989.
9. Vance EF. "Coupling to shielded cables", John Wiley & Sons Inc., 1978.
10. Kraus JD. "Electromagnetics." McGraw-Hill,1991.
11. Nixon KJ, Jandrell IR, Van Coller JM "Evaluation of modelling techniques used to study the transient performance of an earth electrode." Paper submitted to Saupec 1998.

10 ACKNOWLEDGEMENTS

The authors would like to acknowledge Eskom for their support through TESP, the Foundation for Research and Development for DTI funding received through THRIP and Lightning & Transient Surge Suppression (Pty) Ltd for their funding of the Electric Power Research Group.

INVESTIGATING THE USEFULNESS OF CZARNECKI's AND SLONIM's DISTORTION POWER DEFINITIONS IN IDENTIFYING SOURCES OF DISTORTION

A.P.J. Rens, M.J. Case
PU for CHE RAU

Abstract: Distortion-generating sources in the power grid are a concern. Techniques to uniquely identify such sources in an interconnected grid do not exist currently. This paper compares the usefulness of two scientist's (Czarnecki and Slonim) power definitions as indicators of distortion to localise such distortion sources. The basis of each is stated very briefly, then applied to a simplified single phase situation. From the calculated results, it is concluded that indeed the Czarnecki's orthogonal selective decomposition of currents renders further investigation as Discriminative Distortion Source indicators.
Keywords: Power system harmonics, distortion source localizing, nonsinusoidal power definitions, distortion power.

1. Introduction

It is well known that power systems experiencing nonsinusoidal conditions complicate the definition of power to be used to describe the performance of such a system. The debate on the applicability and validity of definitions used, is a theme of ongoing debate. The purpose of this paper is neither to join the debate nor to support any theory's validity. None of them are clearly unfounded or not based on acceptable electrical principles. It is rather a matter of interpretation and nature of the problem applied to.

No clear guidelines or well proven techniques exist currently to localize the source of distortion in an interconnected grid unambiguously. This paper will thus investigate the validity when defining a subnetwork as seen from the measuring terminals as the source of distortion by investigating two contributor's views on the power theory of nonsinusoidal systems, namely Czarnecki's and Slonim's definitions. Both contain interesting features that are calculable from either simulated or measured systems.This paper use simulated measurements to demonstrate the principles.

2. The existence of Distortion Power

As the power definitions of academics attempting to describe the power effects in a nonsinusoidal system are based on realizing that traditional power definitions no longer apply, a demonstrating example of this is briefly presented. Budeanu was one of the first scientist's to realize when applying the accepted concept of active and reactive power that something was missing and termed this amount the **Distortion Power** (Czarnecki, 1987:834-837), **D**. Apparent power relates traditionally to Active and Reactive power as $S := P + j \cdot Q$ and because of the orthogonality, the relation $S^2 := P^2 + Q^2$ thus applies.

The Schwartz inequality for a nonsinusoidal system is known as:

$S^2 \geq P^2 + Q^2$ from which Budeanu's D was defined as

$D^2 := S^2 - P^2 - Q^2$. **Equation 1**

Demonstrating the existence of D is done by simulating (using ATP) a full bridge uncontrolled rectifier. These generated measurements are used in a Mathcad program implementing the definitions. The current and voltage feeding this bridge is distorted because the bridge draws nonlinear current and the nonzero source impedance cause the voltage to be distorted.

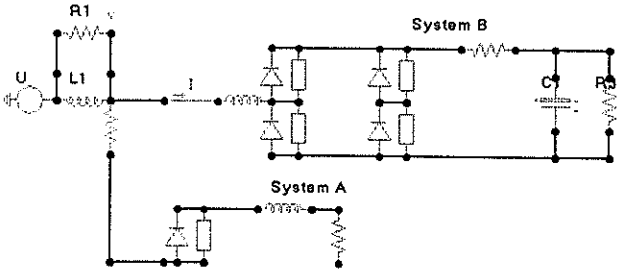

Figure 1: A Single Phase Diode Rectifier

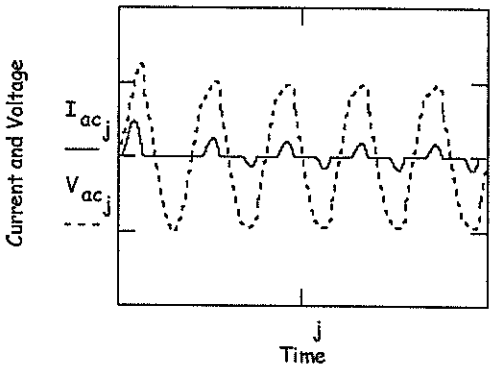

Figure 2: Voltage and Current feeding the Rectifier

The Frequency contents:

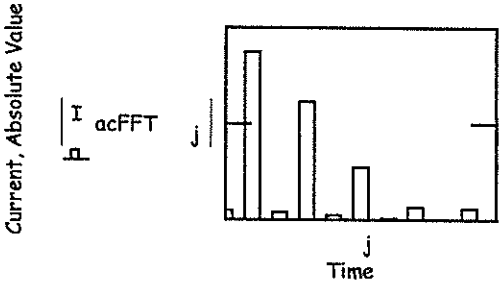

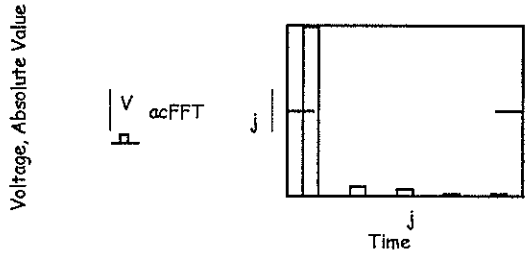

Figure 3: Frequency content of Voltage and Current in Figure 2

The Joint Active and Reactive Power are calculated taking into account the first 50 harmonic numbers including the fundamental; **P=8.473E+4 Watts; Q=1.282E+4 VAR**

The Apparent Power is calculated as **S=8.672E+4 VA**. From the orthogonality between P and Q; **S=8.569E+4 VA**. This two approaches delivers different answers. The missing quantity is called the Budeanu Distortion Power; **D=1.332E+4.** This D is the theme of an ongoing argument of definition between academics (Depenbrock,1993,381-387). In the case of figure 1 it was known that the dominant distortion producing source is on the right hand side of the measuring cross section. Unfortunately the calculation of D only proves the existence of D but in the case of an interconnected grid is quite useless in determining the source of distortion as it is without direction.

Calculating only the Joint Harmonic Active Power is promising for single phase cases and special three phase cases as it does give direction of net active power flow. It proves to be useless (Swart, 1993:109-116) as a Distortion Source Indicator in the three phase case when these sources are distributed over the network and operated independently. In the next sections Slonim's and Czarnecki's definitions will be investigated for usefulness as source indicators as they have suggested ways of directly calculating distortion parameters. It is important to note that the exercise is not an attempt to justify the definitions as such, it will only comment on the applicability as Distortion Source Indicators.

3. Slonim Distortion Power properties

Slonim and van Wyk (1988:76-84) have defined power components for nonsinusoidal systems that appeared promising; Slonim (1990:769-778) attempted to expand some of their original ideas to include the case for the nonlinear load. Although he used 4 examples (Slonim; 1990:769-778) to build his definitions on; it is possible to repeat his results with only 2 examples. It will be discussed very briefly.

3.1.1 A Linear Load containing Reactance and Resistance fed by a Nonsinusoidal Voltage.

As there are no elements in the demonstrating circuit to generate nonsinusoidal currents (generating distortion) the supply voltage is defined to be nonsinusoidal:

$$v(t) := \sqrt{2}\cdot\left(V_1\cdot\sin\theta + V_2\cdot\sin(2\cdot\theta + \Phi_2)\right)$$

Equation 2

with $\theta = 2\pi f_1 t$; f_1 frequency 1; ϕ_2 is the phase difference between V_2 and V_1. The resulting instantaneous current when applying this voltage to an impedance load is:

$$i(t) := \sqrt{2}\cdot\left(I_1\cdot\sin(\theta + \Phi_1) + I_2\cdot\sin(2\cdot\theta + \Phi_2)\right)$$

Equation 3

$$\text{with } \tan(\phi_1) := \frac{x_1}{r_1} \text{ and } \tan(\phi_2 + \Phi_2) := \frac{x_2}{r_2}$$

The resistance's and load impedance's for frequencies ω and 2ω are r_1; r_2; x_1; x_2 respectively.

The apparent power is accepted as S = VI. When the waveforms are containing more than one frequency, the **effective values** for **Voltage** and **Current** have to be used. The Voltage and Current measured are decomposed into frequency components by selecting a stable data window on a fundamental frequency cycle that is known before applying the Fourier transform. In the demonstration, only a fundamental component at frequency ω and a second harmonic at frequency 2ω exist.

Take the square of the apparent power and substitute their effective values:

$$S^2 := \left(V_1^2 + V_2^2\right)\cdot\left(I_1^2 + I_2^2\right)$$ **Equation 4**

Because of the orthogonality between the components of z, z^2 will be $z^2 := r^2 + x^2$. Equation 4 equates to the following after multiplication and substitution:

$$S^2 := r_1^2\cdot I_1^4 + x_1^2\cdot I_1^4 + r_1^2\cdot I_1^2\cdot I_2^2 + x_1^2\cdot I_1^2\cdot I_2^2 + r_2^2\cdot I_2^2\cdot I_1^2 + x_2^2\cdot I_2^2\cdot I_1^2 + r_2^2\cdot I_2^4 + x_2^2\cdot I_2^4$$

Rearranging, manipulation and arranging into $(a+b)^2$ notation:

$$S^2 := \left(r_1\cdot I_1^2 + r_2\cdot I_2^2\right)^2 + \left(r_1 - r_2\right)^2\cdot I_1^2\cdot I_2^2 + \left(x_1\cdot I_1^2 + x_2\cdot I_2^2\right)^2 \ldots + \left(x_1 - x_2\right)^2\cdot I_1^2\cdot I_2^2$$

Equation 5

From this last equation Slonim defined the different terms for the linear load case:

Active Power	$P^2 := \left(r_1\cdot I_1^2 + r_2\cdot I_2^2\right)^2$
Reactive Power	$Q^2 := \left(x_1\cdot I_1^2 + x_2\cdot I_2^2\right)^2$
Distortion Active Power Unit: Watt-Distortion	$D_{al}^2 := \left(r_1 - r_2\right)^2\cdot I_1^2\cdot I_2^2$
Distortion Reactive Power Unit: VAR-Distortion	$D_{rl}^2 := \left(x_1 - x_2\right)^2\cdot I_1^2\cdot I_2^2$
Total Distortion Power	$D^2 := D_{al}^2 + D_{rl}^2$
Relation to S	$S^2 := P^2 + D_{al}^2 + Q^2 + D_{rl}^2$

Table 1: Slonim; The linear load definitions

The subscript a and r indicates active and reactive respectively and the subscript l indicates the linear case.

3.1.2 The Nonlinear load

The nonlinear load experiencing a nonsinusoidal supply is characterized by frequency spectra for voltage and current that differ. Applying the voltage in equation 3 to a nonlinear load would produce a nonlinear current:

$$i(t) := \sqrt{2}\cdot\left(I_1\cdot\sin(\theta + \Phi_1) + I_2\cdot\sin\left(2\cdot\theta + \Phi_2\right) + I_3\cdot\sin\left(3\cdot\theta + \Phi_3\right)\right)$$

Apparent power thus:

$$S^2 := \left(V_1^2 + V_2^2\right)\cdot\left(I_1^2 + I_2^2 + I_3^2\right)$$ **Equation 6**

Applying the same procedure as in the previous section in calculating the apparent power leads to:

$$S^2 := P^2 + Q^2 + D_{al}^2 + D_{rl}^2 + D_{an}^2 + D_{ar}^2$$ **Equation 7**

where the new terms are:

The Active Nonlinear Power	$D_{an}^2 := \left(r_1^2 \cdot I_1^2 + r_2^2 \cdot I_2^2\right) \cdot I_3^2$
The Reactive Nonlinear Power	$D_{rn}^2 := \left(x_1^2 \cdot I_1^2 + x_2^2 \cdot I_2^2\right) \cdot I_3^2$
The Total Distortion Power	$D^2 := D_{al}^2 + D_{rl}^2 + D_{an}^2 + D_{ar}^2$

Table 2: The Nonlinear Case

Generalizing these results for voltage and current spectra that differ is straightforward. Table 1 and 2 implicates that the impedance characteristic of the system under investigating must be known. It is possible to calculate Z from the voltage and current relationship per harmonic number ($Z_h = V_h * I_h$). When one consider the formulas in Table 1 and 2 it indicates that only D_{al} and D_{rl} indicates direction intrinsically when not squared to obtain either Total D or S. Unfortunately D_{an} and D_m can't be calculated without using the squared relationship, thus it is losing directionality. Therefore they are useless as Distortion Source Indicators, but maybe of value as Amount of Distortion Indicators.

3.1.2.1 Slonim's Definitions as Distortion Indicators

As Slonim achieved (questionable or not) to distinguish between the various components of Linear Distortion Power, one can investigate the use of the Active Distortion Power resulting from the linearity (D_{al}) as possible Distortion Source Indicator. For this purpose a system unknown to the left (subsystem A) or right (subsystem B) can be considered as in figure 1.

The reference current is from left to right.

Slonim Powers	Subsystem A	Subsystem B
$D_{al} > 0$	A is a Linear Distortion Active Power source	B is a Linear Distortion Active Power sink
$D_{al} < 0$	A is a Linear Distortion Active Power sink	B is a Linear Distortion Active Power source

Table 3: Interpretation of Slonim's definitions

3.1.2.2 An Example

The Slonim's generalized formula for **Linear Active Distortion Power** is (Slonim;1990:769-778):

$$D_{al} := \sum_{k=0}^{\infty} \sum_{n=0}^{\infty} \left(r_k - r_n\right) \cdot \left|I_{acFFT_k}\right| \cdot \left|I_{acFFT_n}\right|$$

Applying this and the corresponding formula for **Linear Distortion Reactive Power** to the frequency content of figure 1 results in:

D_{al}	-1.205E-11 Watt-Distortion
D_{rl}	-2.821E-12 VAR-Distortion.
$\sum_{h=2}^{\infty} P_h$	-43.076 Watts: Joint Harmonic Active Power flowing from System B

Table 4: Calculated results

It is clear that the size of D_{al} and D_{rl} implies a measurement problem. Although the mathematics and circuit principles used by Slonim to arrive at his orthogonal components of distortion power does not seem totally unvalid, the practical use thereof is questionable.

3.2 Czarnecki's Discriminative Decomposition of Distortion Power

Czarnecki have shared his understanding of Power in Nonsinusoidal systems very enthusiastically (Czarnecki,1987:834-837) during the past two decades. Although a lot of his effort has gone into proving that other scientists in the field are either wrong and leading the power community into a "blind alley" (numerous references to be found), or that they are just stating what he has stated before in other ways, some interesting suggestions were made by Czarnecki over the years. The selective decomposition of currents (Czarnecki; 1990:340-345) contains promising features. If the situation in figure 1 applies again it implicates that the detail of the subnetworks to either side is unknown. It is though valid to represent the subsystems by an equivalent complex admittance's for A and B (Y_{nA} and Y_{nB}) defined as:

$$Y_{nA} := \frac{-S_n}{\left(\left|V_n\right|\right)^2} = G_{na} + jB_{nA}$$

The complex admittance for subsystem B is calculated in a similar way, substituting A with B above.

The assumptions made state that when $P_n < 0$ in figure 1 with the reference current from left to right, then the source of this P_n is on the right; $P_n > 0$ implicates the source is in the left- thus subsystem A have distortion producing elements and subsystem B is receiving this. The harmonic orders for which $P_n \geq 0$ are grouped into a number set Π_A; the harmonic orders where $P_n < 0$ are grouped into Π_B. The complete number set Π contain thus two separable sets, together they are the complete frequency spectrum of the measurements at the cross-section. In a nutshell it means that Harmonic Powers are calculated and grouped according to sign. The terminal quantities can thus be grouped:

$$i := \sum_{n} i_n = \sum_{n=\Pi_A}^{\infty} i_n + \sum_{n=\Pi_B}^{\infty} i_n = i_A + i_B$$

$$v := \sum_{n=\Pi}^{\infty} v_n = \sum_{n=\Pi_A}^{\infty} v_n + \sum_{n=\Pi_B}^{\infty} v_n = v_A - v_B$$

$$P := \sum_{n=\Pi}^{\infty} P_n = \sum_{n=\Pi_A}^{\infty} P_n + \sum_{n=\Pi_B}^{\infty} P_n = P_A - P_B$$

Equation 8

As the two number sets are separable, the currents i_A and i_B and voltages v_A and v_B are mutually orthogonal. The total voltage and current are thus related to them as:

$$\left(\left|i\right|\right)^2 := \left(\left|i_A\right|\right)^2 + \left(\left|i_B\right|\right)^2 \quad \left(\left|v\right|\right)^2 := \left(\left|v_A\right|\right)^2 + \left(\left|v_B\right|\right)^2$$

The **effective values** of i_A and i_B are then calculated.

Both currents i_A and i_B for each subsystem can be decomposed (Czarnecki; 1985:399-403) (Czarnecki; 1988:398-402) into the **active, scattered** and **reactive** currents respectively:

$$i_A := i_{aA} + i_{sA} + i_{rA} \qquad i_B := i_{aB} + i_{sB} + i_{rB}$$

With the equivalent conductance's of these subnetworks defined as;

$$G_{eA} := \frac{P_A}{(|v_A|)^2}$$ the current components are:

$$i_{aA} := G_{eA}\cdot(|v_A|)^2 \qquad |i_{sA}| := \sqrt{\sum_h (G_{hA} - G_{eA})^2 \cdot V_{hA}^2}$$

$$|i_{rA}| := \sqrt{\sum_h B_{hA}^2 \cdot V_{hA}^2}$$

Equation 9

The values for system B are calculated in the same fashion substituting A with B.

Thus the current at the measuring cross-section can be considered as consisting of 6 components:

$$(|i|)^2 := (|i_{aA}|)^2 + (|i_{sA}|)^2 + (|i_{rA}|)^2 + (|i_{aB}|)^2 + (|i_{sB}|)^2 + (|i_{rB}|)^2$$

From this current decomposition the Apparent Power S at the measurement cross-section is decomposed:

$$S^2 := S_{0A}^2 + S_{BA}^2 + S_{0B}^2 + S_{AB}^2 \text{ also;}$$

$$S^2 := (|i_A|)^2\cdot(|v_A|)^2 + (|i_A|)^2\cdot(|v_B|)^2 \ldots + (|i_B|)^2\cdot(|v_B|)^2 + (|i_B|)^2\cdot(|v_A|)^2$$

Equation 10

The terms S_{0A}^2 and S_{0B}^2 may be decomposed further into the **active, scattered** and **reactive** powers:

$$S_{0A}^2 := P_A^2 + D_{sA}^2 + Q_{rA}^2 \qquad S_{0B}^2 := P_B^2 + D_{sB}^2 + Q_{rB}^2$$

Equation 11

The terms S_{AB} and S_{BA} "force" the total Apparent Power higher with:

$$S_F^2 := S_{AB}^2 + S_{BA}^2$$

The respective **scattered** and **reactive** powers are calculated as:

$$D_{sA} := |i_{sA}|\cdot|v_A| \qquad Q_{rA} := |i_{rA}|\cdot|v_A|$$

$$D_{sB} := |i_{sB}|\cdot|v_B| \qquad Q_{rB} := |i_{rB}|\cdot|v_B|$$

Equation 12

3.2.1 Czarnecki's Discriminative Distortion Source Indicators

As the decomposition suggested by Czarnecki is discriminative towards the origins of the respective Harmonic Powers, the definitions of the different powers as described by equations 14,15 and 16 can be interpreted as **Discriminative Distortion Source Indicators**. The next table will describe the interpretation of each:

P_A and P_B:	The Total Active Power consumed by each subsystem. The dominant figure is the one containing the fundamental component which was intended as the main source of useful work to be done. The amount which the dominant one is higher than the Fundamental Active power, is Harmonic Active Power consumed simultaneously.
S_F :	This amount of Apparent Power have it's origin in the mutual interaction of voltages and currents generated by each subsystem that are different in harmonic numbers but have no useful effect; it only "forces" the Apparent Power of the system higher - thus increasing the loading of the Total System.
S :	The Total Apparent Power existing in the system.
S_{0A} and S_{0B}:	The amount of Apparent Power contributed by each subsystem excluding S_F
q_r. and q_r. :	They represent the Total Reactive Power that represents the reciprocating flow of energy for each subsystem existing at the measurement terminals. They are also useless to get work done and should be compensated for.
D_{sB} and D_{sA} :	This Total Scattered Power is generated respectively by each subsystem. Each one quantifies thus the amount of distortion contributed by the respective subsystem towards the Total Distortion present at the measurement terminals. Their existence is rooted in the harmonic conductance change per harmonic order (resulting from the nonlinearity of the system). They may be used thus as an indicator of the amount of distortion contributed by each and is one of the most useful indicators quantifying each subsystem distortion performance.

Table 5: Interpretation of parameters

The system analyzed in figure 1 according to this discriminative procedure results in:

P_{total}	8.718E+4 Watt	S_B	8.954E+4 VA
S_{0A}	5.711E+3 VA	Q_{rA}	5.711E+3 Var
S_{0B}	8.924E+4 VA	Q_{rB}	1.885E+4 Var
S_F	6.945E+4 VA	D_{sA}	42.537 Watt
S_A	6.93E+4 VA	D_{sB}	471.125 Watt

Table 6: Discriminative Decomposition Procedure

The results are self-explanatory. It is interesting though to note as expected that subsystem B is the one who generates most of the distortion. To validate the results one can prove that currents do not disappear:

$$i := \sqrt{i_{aA}^2 + i_{sA}^2 + i_{rA}^2 + i_{aB}^2 + i_{sB}^2 + i_{rB}^2}$$

i = 113.556 A and

$$i_{test} := \sqrt{\sum_{h=1}^{100} \left(|I_{acFFT\ h}|\right)^2}$$

i = 113.558 A

4. Conclusion

The Czarnecki decomposition of the current at the point of measurement allows the discriminative grouping of powers according to their origin. It makes it thus possible to distinguish which subsystem is contributing towards what at this measurement point. The simulated results demonstrated the principle of calculation on simplified system and delivers interpretable results. It is important to realize that calculating the Joint Harmonic Power would have indicated only the net flow of the Harmonic Power at the terminals. Thus we would have only known that subsystem B is generating an amount of Harmonic Power without knowing that some Harmonic Power is actually flowing from subsystem A and consumed by B simultaneously with the Fundamental Active Power delivered by the voltage source.

This technique renders thus further investigation towards a more real world situation. Firstly the calculation procedure will be expanded to include three phase situations taking into account that the three phase case actually decompose into five (Czarnecki,1988:30-34) currents. As measurements at various points in the network made in a synchronous (Swart, 1993:109-116) way seemed promising as aid in the search of reliable Distortion Source Indicators, the combination of that and the Czarnecki's Discriminative procedure will be investigated. The simulation investigation will then be complimented by physical measurements.

5. References

1. L.S. Czarnecki, "Considerations on reactive power in nonsinusoidal systems", *IEEE Trans. Instrumen. Meas.*, vol. IM-34, pp. 399-404, Sept. 1985.
2. M.A. Slonim and J.D. van Wyk, "Power components in a system with sinusoidal and nonsinusoidal voltages and/or currents", *Inst. Elec. Eng. Proc.*, vol. 135, pt B, no. 2, Mar. 1988.
3. M.A. Slonim, "Distortion power in linear and nonlinear systems", *Int. J. Electronics.*, vol. 68, no. 5, 1990, pp 769-778.
4. L.S. Czarnecki, "Power in Nonsinusoidal Networks: Their Interpretation, Analysis, and Measurement", *IEEE Trans. Instrumen. Meas.*, vol. 39, no. 2, April 1990, pp 340-345.
5. L.S. Czarnecki, " Orthogonal Decomposition of the Currents in a 3-Phase Nonlinear Asymmetrical Circuit with a Nonsinusoidal Voltage Source", *IEEE Trans. Instrumen. Meas.*, vol. 37, no. 1, March 1988, pp 30-34.
6. L.S. Czarnecki, "What is wrong with the Budeanu Concept of Reactive Power and Distortion Power and why it should be abondoned", *IEEE Trans. Instrumen. Meas.*, vol. IM-36, no. 3, Sept. 1987, pp 834-837.
7. L.S. Czarnecki, "Active, Reactive and Scattered Current in Circuits with Nonsinusoidal Waveforms and their Compensation", *IEEE Trans. Instrumen. Meas.*, vol. 40, no. 3, June 1989, pp. 563-567.
8. M. Depenbrock, "The FBD Method, A Generally Applicable Tool for Analyzing Power Relations", IEEE Trans. On Power Systems, vol. 8, no. 2, May 1993, pp. 381-387.
9. P.H. Swart, J.D. van Wyk and M.J. Case, "On Techniques for Localisation of Sources Producing Distortion in Three-Phase Networks", *3rd International Workshop on Power Defintion Measurements under Non-sinusoidal Conditions*, Milano, Sept. 1995, pp. 109-116.
10. P.H. Swart, J.D. van Wyk and M.J. Case, "On Techniques for Localisation of Sources Producing Distortion in Electric Power Networks", *2nd International Workshop on Power Definition Measurements under Non-sinusoidal Conditions*, Stresa, Sept. 1993, pp. 187-190.
11. ATP Rule Book, 1995
12. Mathcad User's Book, 1995.

COMPACTION TECHNOLOGY: HIGH PHASE ORDER TRANSMISSION IN THE SOUTH AFRICAN CONTEXT

J Bortnik JP Reynders

Department of Electrical Engineering
University of the Witwatersrand, Pvt Bag 3, PO Wits 2050, Johannesburg, SA

Abstract - High phase order (HPO) power transmission i.e. using more then the conventional 3 phases for transmitting power, is a relatively new way of maximising the power transfer over a given right of way (ROW). This paper initially addresses the need for such power maximisation, and demonstrates the relative inefficiency with which current systems utilise the transmission corridor. The generic advantages of HPO transmission are then listed, and two of the most common questions regarding transformer connections, and line protection, are briefly addressed. The paper concludes with work currently being carried out at the university of the Witwatersrand in this field, which is the economic comparison of a modern 3 phase line with a HPO in the South African context.

Keywords: High phase order (HPO), transmission line compaction,

1. INTRODUCTION

It is common knowledge that electrical loads throughout the world are rapidly increasing, and placing an ever growing strain on existing transmission systems. In the United States, for example, the current transmission system was primarily constructed during the years of rapid expansion following World War II, and is approaching what is typically considered the end of its normal service life of 40 years.

It is clear then, that the electrical infrastructure is heading for a period of extensive upgrading, and in 1991 the addition of 13 000 circuit miles was planned in the US. This addition however, faces several complications: the high, and at times prohibitive cost of land, public opposition focusing on electrical environmental effects - and the subsequent legislation concerning maximum field levels, carcinogenic effects, aesthetic concerns, and so on. This had the effect of delaying and sometimes even preventing the construction of new lines (this is particularly true in north-eastern America, where it can take between 3 and 7 years from the start of licensing of a new transmission facility until it is placed in service), dictating a certain width of right-of-way (ROW), field levels at the edge of the ROW, and hence an upper limit on the capacity of the line. This has raised much concern among power engineers, as well as a serious need to re-evaluate the efficiency with which power was being transmitted.

In their classic 1973 paper[1], H. C. Barnes and L. O. Barthold were faced with the same question and as a possible solution proposed a complete return to fundamentals, and a reconfiguration of the basic philosophy with which power was being transmitted.

Their argument went as follows:

We know that the flow of electromagnetic power at any point in space can be universally described by the Poynting vector as:

$$\mathbf{S} = \mathbf{E} \times \mathbf{H} \qquad \ldots (1)$$

Where:

S = Power density in Watts/m^2

$\mathbf{E}$ = Electric field intensity in V/m

$\mathbf{H}$ = Magnetic field intensity in A/m[1]

and the total power flowing through some plane (say for instance, the plane perpendicular to the transmission line) is:

$$P = \int_X \int_Y S \, dx \, dy \qquad \ldots (2)$$

with X and Y extending to infinity in both negative and positive directions.

Furthermore, $\mathbf{E}$ and $\mathbf{H}$ are related by the impedance of free space (377Ω), and the electric field intensity $\mathbf{E}$ has a natural limit at the electric breakdown strength of air, approximately 3MV/m. This implies that $\mathbf{H}$ is also limited, and thus there is only a finite amount of

[1] Please note that all vectors are written in bold capitals, for convention.

power that can be sustained by the air medium, under standard conditions.

This is:

$$|\mathbf{S}| = |\mathbf{E} \times \mathbf{H}| = E.E/Z = (3\times10^6)^2 / 377$$

$$= 9\times10^{12} / 377$$

$$= 24 \text{ GW/m}^2 \quad \text{peak}$$

$$= 12 \text{ GW/m}^2 \quad \text{RMS}$$

Theoretically then, to make optimal use of transmission corridors, the power density throughout the corridor's cross section should be at, or very near this limit. So, the inevitable question is how do practical lines compare to this?

To quote Barnes and Barthold[1], "Densities of this magnitude are approached only very close to the surface of conductors in traditional transmission line construction. It is estimated that on typical 3 phase lines, over 95% of the energy stored in the field surrounding a conductor is contained within a radius equal to 5% of the phase-phase spacing."

Clearly, the corridor cannot be practically loaded at this energy density, but significant improvements can be made by re-examining the basics: the conductor configuration, and number of phases used.

2. CONCEPTS OF HPO TRANSMISSION

Traditionally, electric power has been transmitted in 3 phase, AC mode. This had several advantages: AC (as opposed to DC) transmission meant cheaper generation, transformation, and ease of switching. Single phase transmission had the disadvantage of pulsating power, whereas 2 phase transmission delivered constant power, but was an inherently unbalanced system requiring a heavy neutral wire for the return current. A 3 phase system delivers DC power, is a naturally balanced system, has superior material utilisation compared to the lower phase order systems, and is the lowest and simplest of the N-phase, N+1 wire systems to achieve the above advantages. It has thus been the transmission system of choice for power engineers world-wide.

High Phase Order (HPO) transmission utilises 6 or 12 phases as opposed to the original 3. Gross[14] shows that material utilisation remains constant for an N-phase system (where N>3), so where do the benefits lie? The answer to this question lies in the phase-phase voltage of the system. Figure 1A 1B and 1C illustrate this point.

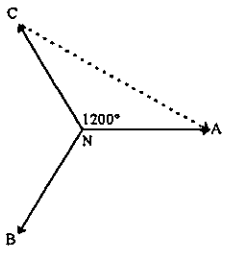

Fig. 1A - Phasor representation of a 3 phase system

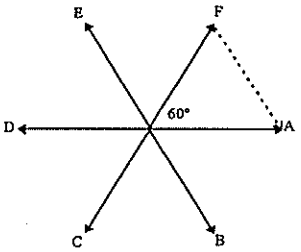

Fig. 1B - Phasor representation of a 6 phase system

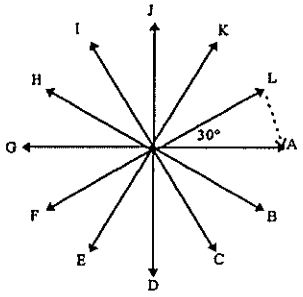

Fig. 1C - Phasor representation of a 12 phase system

If the phase-ground voltage in the above diagrams is defined as 1p.u., then the phase-phase voltages of the 3, 6, and 12 phase systems are $\sqrt{3}$, 1, and 0.5 respectively. The advantage of this is readily apparent: the higher the phase number, the smaller is the phase-phase voltage and hence adjacent phases can be brought closer together. This implies that a far larger amount of power can be squeezed into the same ROW.

3. GENERIC ADVANTAGES OF HPO

HPO transmission has been shown to be the most efficient method of power transmission in the air dielectric at low frequencies[13], but besides that, has several other advantages which are rapidly gaining importance. Some of these are:

- Current unbalance: the circular HPO conductor array is naturally far more balanced, and has been shown to perform far better then equivalent 3 phase lines[2].
- Single pole switching: with 1 phase of the 6 de-energised, the line is still able to carry 83% of the load for hours, with minimal unbalances. This adds a significant element of flexibility in protection, as well as making the line more reliable[2,3,5].
- Field mitigation: studies conducted on HPO lines and standard 3 phase lines of similar capacity have shown that HPO lines have significantly

improved electric[2,3,8,9,11] and magnetic[9,10,11] field profiles.

- Corona related effects: this is perhaps the most dramatic category of improvement - surface electric fields, and consequently corona loss, audible noise, and radio interference are dramatically reduced due to a change of phasing, even with a $\sqrt{3}$ reduction in phase-phase spacing (to account for the lower phase-phase voltage)[2,3]

- Economic benefit: due to the smaller, lighter structures, the cost of the HPO line itself is lower then a similar capacity 3 phase line. However, terminal costs are larger due to the increased number of circuit breakers and transformers, so a "break-even" distance can be developed above which HPO lines are cheaper to install[3,4,6,7,8].

- Other benefits: there are number of other benefits, including complete compatibility and integrability into an existing 3 phase system, aesthetic appeal due to smaller, tighter bundle, more stable, better damped response to transient events on the network, and more closely matched line ampacities to existing equipment which is suited to developing countries which cannot develop EHV systems for bulk transmission.

4. HPO TECHNOLOGY

4.1 Transformers

A key aspect of HPO technology is that it does not require a complete re-architecture of the power grid, but can very easily integrate into an existing 3 phase system. This requires an analysis of various transformer connections and the implications of each.

Conceptually, to achieve the correct phasing, two 3-phase circuits are required. For instance a star-star connected transformer will provide the first 3-phase set. Then, an additional secondary winding must be wound such that each secondary voltage of the first set is exactly 180 electrical degrees out of phase with the first set, for example star-inverted star. Adding the two 3 phase sets together will produce a 6 phase set as illustrated in figure 2 below.

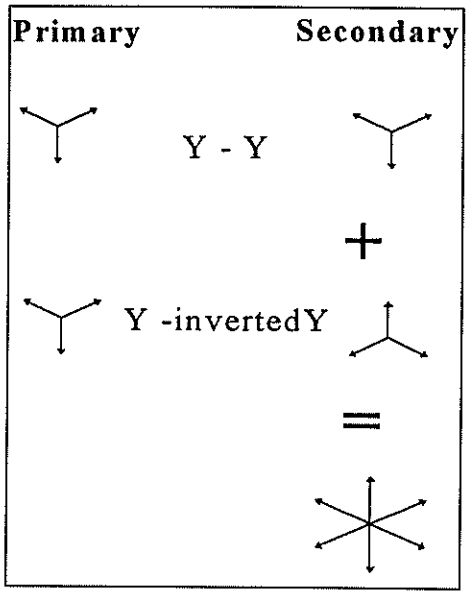

Fig 2 - Transformer connections for 6 phase set

In the uprating of the Goudey-Oakdale line, Stewart[12], examined the use of 3 different transformer topologies to achieve the required 6 phase system. The final configuration and advantages and disadvantages of each are summarised in Table 1 below:

Topology	*Advantages*	*Disadvantages*
6 single phase transformers	allows single phase tripping, ease of analysis, lack of magnetic coupling between phases in the transformer, is a very flexible system allowing for easy interconnection	there is a severe price penalty, as well as taking up more space (which is at a premium in already established 3 phase substations).
3 Leg core form, or shell form units	cheapest of all the choices, space saving advantage, is the preferred design	the 2 secondary windings could have insulation problems, does not allow single phase tripping on the 3 phase side, magnetic coupling to the open phase.
5 leg core form or shell form units	the additional iron in the 5 leg transformer provides a return path for zero sequence flux.	voltage induced on open phase, anticipated problems with ferroresonance of magnetising impedance and line capacitance, increased cost

Table 1 Comparison of various transformer interconnections

The final consideration was whether to use a ΔY or YY connections. Of these, the former ΔY was selected because the delta breaks the zero sequence network and provides a well defined shunt path in the zero sequence network without a tertiary winding.

4.2 Protection

Implementing a 6 phase line, complicates the protection significantly, in that it introduces 120 possible fault combinations. This requires a careful evaluation of the trip logic, but is simplified by the fact that only 1 phase can be tripped at a time leaving the others to carry the load.

In the Goudey-Oakdale line[2,5] 3 different protection schemes will be used:

1. Current differential relay
2. Segregated phase comparison
3. Digital distance protection

The first 2 will use a fibre optic cable for the communication to the substations, and the trip signal will be given when (at least) 2 out of 3 protection schemes have sent a trip signal.

5. CONCLUSION AND FURTHER WORK

High phase order transmission is a relatively new concept for maximising power density in a given ROW. It was proven to be not only technologically feasible, but also to have many other benefits including field mitigation, and lower corona related activity.

To study its effectiveness in the South African context, a HPO (6-phase) line will be designed to the same capacity as a 765kV 3-phase line, and compared primarily on the basis of cost, with other benefits listed where appropriate. To make the comparison even more relevant, the 3 phase line will be suspended from a guyed, cross rope suspension tower, which represents the most modern and economic means of tower design in South Africa to date.

6. REFERENCES:

[1] Barnes H.C., Barhold L.O., "High Phase Order Power Transmission", Cigre SC31 Electra no.24 1973 pp 139-153

[2] Stewart J.R., Wilson D.D., "High Phase Order Transmission - A Feasibility Analysis, Part I - Steady State Considerations" IEEE Trans. PA&S Vol. PAS-97, No. 6, pp 2300-2307

[3] Stewart J.R., Grant I.S., "High Phase Order - Ready for Application", IEEE paper 81 TD 675-8, IEEE PES 1981 Transmission and Distribution Conference, Minneapolis, Sept 20-25, 1981

[4] Kallaur E., Stewart J.R., " Uprating Without Re-conductoring - the Potential of Six Phase" Canadian communications and energy conference, IEEE 82 CH 1825-9, 1982, p120

[5] D.D. Wilson, Stewart J.R., "Switching Surge Characteristics of Six-Phase Transmission Lines", IEEE 1984 Transmission and Distribution Conference and Exposition, Kansas City, Missouri, April 29-May 4, 1984

[6] Stewart J.R., Grant I.S., Kallaur E., "Economics of High Phase Order Transmission" same as [5]

[7] Stewart J.R., Zelingher S., Stilman G.I., "HPO Line Practical for Limited R/W" Transmission and Distribution, October 1985 pp 32-36

[8] Wilson D.D., Stewart J.R., Gnadt P., "12 Phase as a Transmission Alternative" IEEE/CSEE Joint Conference on High Voltage Transmission Systems in China, October 17-22, 1987, Beijing, China

[9] Stewart J.R., "138kV 12 Phase Transmission Line Research" - Summary of PTI Experience in HPO Transmission

[10] Stewart J.R., Dale S.J., Klein K.W., "Magnetic Field Reduction Using High Phase Order Lines", IEEE/PES Transmission and Distribution Winter Meeting, New York NY, January 26-30, 1992

[11] Stewart J.R., Oppel L.J., Thomann G.C., Dorazio T.F., Brown M.T., "Insulation Coordination, Environmental and System Analysis of Existing Double Circuit Line Reconfigured to Six Phase Operation" Proceedings - 1991 IEEE Power Engineering Society, Transmission and Distribution Conference pp 978-982

[12] Stewart J.R., Oppel L.J., Thomann G.C., Dorazio T.F., Rebbaparagada R.V., "Transformer Winding Selection Associated With Reconfiguration of Existing Double Circuit Line to Six-Phase Operation" Proceedings - 1991 IEEE Power Engineering Society, Transmission and Distribution Conference pp 991-997

[13] "Fundamental Optimisation Study for Open Wire Transmission Systems" US Department of Energy Report DOE/CE/29325 - 1, February 1990

[14] Gross, Charles A., 1986, "Power System Analysis - 2nd Edition", John Wiley & Sons, P15-20

TESTING OF DEMODULATION BASED FREQUENCY ESTIMATION ALGORITHM FOR EMERGENCY CONTROL IN POWER SYSTEMS

A.Pistalovic and R.Zivanovic
Technikon Pretoria

Abstract

In this paper a demodulation based frequency estimation algorithm is presented and tested. This algorithm plays a very important role in emergency control of power systems. It has been shown that the algorithm is very accurate in presence of harmonics and unbalance in a system. At the same time the algorithm is simple to implement. It is suitable for real-time application as well as for off-line processing.

1. Introduction

Large disturbances in power systems such as loss of a generating unit or fault on a critical line are manifested by sudden and large frequency change. In this case the system needs to be protected and controlled, so that it can be returned to a normal and secure state as soon as possible. There are several methods developed for control and protection of power system during large disturbances. Most of them involve frequency estimation.

In emergency situation, after large disturbance, the protection/control strategy is based on use of under-frequency load shedding relays [1][2]. The emergency control strategies are developed:

- to prevent (or control in optimal way) system separation,
- to prevent large frequency drop, and
- to prevent voltage instability.

The frequency measurement used in the emergency control [3] is based on the following algorithms [4]:

- Change of angle for phasor measurement.
- Kalman filter.
- Zero crossing detection.
- Demodulation.
- Estimation using identification theory.
- Numerical optimisation.

In the first part of the paper the basic ideas about emergency control of power systems are presented. The role of frequency measurements in emergency control is explained in the same section. The frequency estimation algorithm is presented in the second section. The third section explains testing procedure for the frequency estimation algorithm. Selected results from a simulation testing are presented in this section as well.

2. Emergency control

The power system frequency, as an indicator of relationship between generation and load, is a very important parameter in emergency control of power systems [3]. If generation exceeds the load, the frequency will rise, and if generation is less than load, the frequency will fall. Since the load changes randomly, the frequency will follow the changes and vary. To make an accurate record of frequency, microprocessor devices are used. The power systems are supported by SCADA (Supervisory Control and Data Acquisition) system [1][2] which should include frequency measurement at various points in the network in order to estimate a frequency of the centre of inertia.

Load shedding is the important emergency control action which is based on frequency measurement. The rate of change of frequency (df / dt) is an additional measured value used in load shedding. This is an instantaneous indicator of MW imbalance, and it provides more selective and faster processing. During the examination of df / dt function, as one of the values used in developing the scheme for load shedding , it has been concluded that [1]:

- A smaller system inertia causes a larger peak-to-peak value of the oscillation in df / dt, which slows the calculation of df / dt.
- The relays should calculate the average of df / dt to overcome oscillation problems.
- The average of df / dt should be calculated from the measurements located close to the centre of inertia.

In order to create more advanced emergency load shedding controls, the additional information about the system is needed:

- estimation of bus voltages,
- estimation of spinning reserve,
- estimation of total system inertia, and centre of inertia,
- estimation of load etc.

The values of spinning reserve, system inertia and load characteristics can be periodically estimated by using SCADA system and provided to the relays, so that they can be set to improve load shedding scheme. For an accurate estimation, high-speed communication and sophisticated network analysis techniques are required.

One typical sequence of system events leading to an action of load shedding emergency control is explained here. The overloading of one element in power system can cause an overloading of other elements. If the overloading is not reduced in time, the separation of system will start, producing the islands with imbalance between generation and load. The consequence of that will be a frequency deviation from its nominal value. If the generators can't handle this problem, the load shedding is the only solution for quick recovery of the frequency to its nominal value.

For the load shedding emergency control, the most important part is a fast and accurate frequency estimation algorithm. One such algorithm is presented and tested in this paper.

3. Frequency estimation algorithm

Typical ways of using frequency estimation are classified as follows:

- real time applications (relaying),
- on-line monitoring, and
- off-line analysis of records from transient recorders.

The computation time limit for different applications determinates the type of frequency estimation algorithm and filtering technique that should be used. To find the best method of frequency estimation for the specified application, we need to assess the following characteristics of each algorithm:

- speed of convergence,
- computation speed,
- accuracy, and
- noise rejection.

The method tested in this research is based on demodulation of a complex signal. This complex signal is obtained from three-phase voltages by using Park transformation. The main advantage of this method over the classical demodulation technique is that a double frequency component is not produced in the calculation process [4].

In the classical demodulation algorithm the scalar input is multiplied with a sine and cosine signals with a known frequency. The result signal has two parts. Each part consists of two components of different frequency. The result signal must be low-pass filtered to reduce the double frequency component. The remaining part of the signal is used to estimate the unknown frequency. The classical demodulation introduces a double frequency component, and the filter that reduces that component will often slow down the frequency estimation algorithm.

The first step of the proposed algorithm is the power-invariant Park transform. The transform is used to convert the three phase quantities to one complex quantity, as shown below:

$$\underline{v} = v_d + jv_q, \tag{1}$$

where the real and imaginary parts are calculated from

$$\begin{bmatrix} v_d \\ v_q \end{bmatrix} = \sqrt{\frac{2}{3}} \begin{bmatrix} 1 & \frac{-1}{2} & \frac{-1}{2} \\ 0 & \frac{\sqrt{3}}{2} & \frac{-\sqrt{3}}{2} \end{bmatrix} \begin{bmatrix} v_a \\ v_b \\ v_c \end{bmatrix}. \tag{2}$$

In transformation (2) v_a, v_b, and v_c are the samples of three phase voltages. The real part of the complex quantity (1) is the in-phase component, and the imaginary part is the orthogonal component of the signal. The transform (2) does not include zero sequence. The harmonics that are zero sequence (as third harmonics) are blocked by this transformation.

Demodulation of the complex signal (1) is done with a shifting complex signal $\exp(-j\omega_0 t)$, where ω_0 is the fundamental frequency. This complex signal is in opposite direction compared to the input signal. Difference between actual and fundamental frequency is obtained from the calculated angle difference between two consecutive samples. These phase angles are obtained from the demodulated complex signal. If the frequency is equal to fundamental the phase angle difference between two samples is zero. Only when the frequency is different from fundamental the angle starts changing from one sample to another.

4. Testing of frequency estimation algorithm

The prototype program implementing the frequency estimation algorithm was written in MATLAB and presented in Ref. 4. This program was used in our research. It has been shown that it works well for signal-to noise ratio (SNR) above 80 dB, but for lower signal to noise ratios the frequency estimate needs to be filtered [4].

The test signal used in this paper is a sudden change of frequency from 50Hz to 51Hz simulated by logistic (sigmoid) function. To this signal we added normally distributed noise, as well as certain harmonics and unbalance. In continuation we present the most representative results from this study.

In the first test (**initial case**) the frequency signal was distorted with:

- white noise with SNR 40dB,
- 5% of 3rd harmonic (zero sequence),
- 3% of 5th harmonic (negative sequence).

The filter used was 3rd order low pass Butterworth filter (causal filter) with a cross over frequency of 20 Hz. Figure 1 presents the simulation results. The causal filter introduces a time delay between actual frequency and estimated one, as shown in Figure 1.

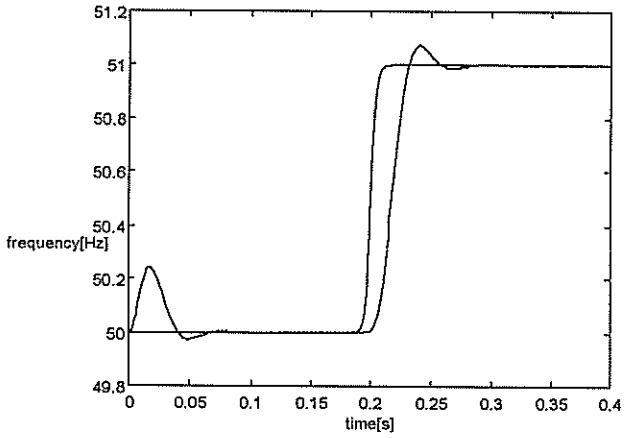

Figure 1: True and estimated frequency with casual filter for initial case distortion specification

In the second simulation test we added the same distortion (**initial case**) to the frequency signal. The frequency estimate is filtered twice, first forward and then backward. Forward-backward filtering is done with the same 3rd order low pass Butterworth filter. The resulting non causal filter has zero-phase distortion but the order of the filter is doubled. The simulation result is presented in Figure 2. At the beginning and end there is error due to filter initial transients. This kind of filter is used mainly for off-line calculation.

We have done further testing of the algorithm, by changing the harmonics content, and by changing phase angles (i.e. making the system of three phase voltages non balanced).

First we changed the 3rd harmonic and the 5th harmonic percentage content to 1%. The three phase voltage angles are the same as for the initial case, i.e. the system was symmetrical.

Then we changed both harmonics to 5%, leaving the system symmetrical.

The next testing was done by changing the phase angle between phases a-b and a-c for -1,67% (new value is 118 degrees) while harmonics are the same as for the initial case. In the last study phase angles between a-b and a-c changed for 2.5% and 4.16% while harmonics stays the same as for the initial case.

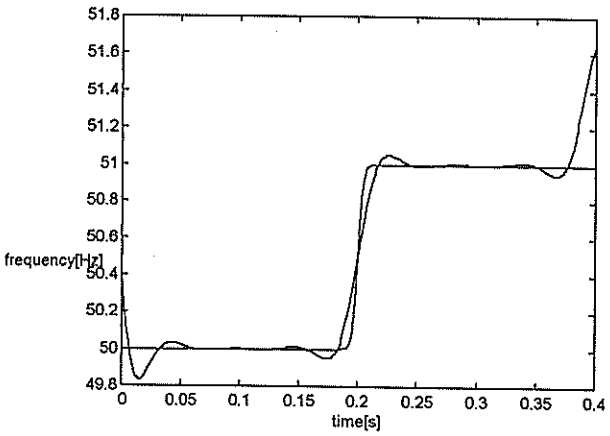

Figure 2: True and estimated frequency with non casual filter for initial case distortion specification

The relative error was calculated for all of the simulated cases by using the following formula:

$$e\% = \frac{|f_{est} - f_0|}{f_0} \times 100 \qquad (3)$$

where f_{est} is the estimated filtered frequency, and f_0 is the nominal frequency. The results are tabulated in Table 1.

Table 1: Simulation results

Harmonics		Phase angles	Relative error %
3rd 5th	5% 3%	symmetrical system	1.86
3rd 5th	1% 1%	symmetrical system	0.67
3rd 5th	5% 5%	symmetrical system	2.91
3rd 5th	5% 3%	1.67% unbalance	1.74
3rd 5th	5% 3%	2.5% unbalance	1.97
3rd 5th	5% 3%	4.16% unbalance	1.98

5. Conclusions

In this paper the results of simulation testing of the advanced frequency estimation algorithm are presented. The algorithm is based on frequency demodulation of complex signal obtained from three phase voltages through Park transformation. The following conclusions can be drawn:

- Harmonics (error introduced by the 5th harmonic is more significant then error produced by the 3rd harmonic) have bigger influence on the frequency estimation than the non symmetry of the three phase voltages.
- For non symmetrical phase voltages, the proposed method will introduce small double frequency component.
- When using the Park transform for symmetrical phase voltages there is no need for filtering a double frequency component coming from demodulation process. The filters are needed only for filtering the white noise and harmonics.
- Non-causal filter has zero phase shift what is the advantage over the causal one, but it can be used only for off-line frequency estimation.

6. References

1. D.Novosel 'SM, Khoi T. Vu 'M, D. Hart 'M, E.Udren 'SM, "Practical protection and control strategies during large power-system disturbances", Conferency paper- IEEE 0-7803-3522-8/96,pp. 560-565, 1996.
2. A.P.J.Malt ,BSc, FIEE;G.D.Clarke, DipEE, CEng, MIEE; P.E.Robinson, MA, CEng, MIEE, "Computer-based supervisory control and energy management system for the city of Cape Town", IEE Proceedings, Vol.135, Pt.C, No. 1, pp. 41-50, January 1988.
3. R.K.Adams, J.M.McIntyre, F.W.Symonds, "Characteristics of the eastern interconnection line frequency", IEEE Transactions on power apparatus and systems, Vol. PAS-101, No.12, pp. 4542-4547, Decenber 1982.
4. Magnus Akke, "Frequency estimation by demodulation of two complex signals", IEEE Transactions on power delivery, Vol.12, No. 1, pp. 157-163, 1997.

THE IMPORTANCE OF STRUCTURAL STABILITY IN POWER SYSTEMS

Remus Fetea and Alexander Petroianu
Department of Physics, Department of Electrical Engineering, University of Cape Town, Private Bag 7701, Cape Town, South Africa, Fax 021-650.3352, E-mail: apetroianu@eleceng.uct.ac.za, rfetea@physci.uct.ac.za

Abstract. The aim of this presentation is to illustrate the applications of Theory of Dynamical Systems (TDS) in Power Systems and to present a few calculations on a simple but representative example; it shows how the stability can be evaluated and how the bifurcation points calculated. The approach might provide a re-assessment of actual stability procedures used by utilities. This theory provides a new concept for the stability of a system: the *structural stability*. This concept accommodates better our requirements for dealing with a non-linear Dynamic System. Structural stability helps to evaluate those locations in state space where the system could change suddenly its properties (e.g. loosing the stability). These locations are called bifurcation points.

1. Introduction

Most real-world systems and almost all-natural phenomena are non-linear and many of them exhibit chaotic behaviour. Because of the lack of understanding and tools, in the past linearization methods were routinely used for prediction and control[4]. This presentation will show that even if the understanding is not complete, TDS is substantial and tools are becoming available.
In the first part we provide introductory notions about non-linear dynamics with emphasis on the concept of structural stability. In the last part of the presentation, a simple system is treated in detail to assess its stability.
Conclusions are drawn concerning the advantages of using TDS in Electrical Power System.

2. Brief Presentation of Structural Stability

The behaviour of a dynamical system may be described by a set of N first order non-linear ordinary differential equations of the following form:

$$\dot{x}_i = f_i(x_1, x_2, \ldots x_n; u_1, u_2, \ldots u_r; t) \qquad i = 1,\ldots,n \qquad (1)$$

where "n" is the order of the system and "r" is the number of inputs. Using vector-matrix notation (1) becomes:

$$\dot{\mathbf{x}} = f(\mathbf{x}, \mathbf{u}, t) \qquad (2)$$

This will be the main equation for our study. We will concentrate our attention on this non-linear equation. The essential difference between this approach and the former linearization approaches used in Power System Analysis is that the TDS considers all the non-linear terms of the system equation. This acknowledgement of non-linearity implies, in principle, a loss of the possibility to calculate exactly some quantities defining the state. However, TDS is able to make more reliable quantitative predictions about points of stability than the linear approximation of the system.

Coming back to our equation (2), from now on, we will move in the state space. In this N-dimensional space, a trajectory or many trajectories describe the evolution of our system. For each point of this space a velocity is defined. All these velocities constitute a vector field. The state space, filled with trajectories, is called the *phase portrait* of the dynamical system. We introduce now few definitions to describe the state space. The first one is for the *critical point*. We say that a point in the phase space is a *critical point* or an *equilibrium point* if:

$$\dot{\mathbf{x}} = f(\mathbf{x}, \mathbf{u}, t) = 0 \qquad (3)$$

There are many cases, which respect the condition of critical points. For example in 2D there are 5 possibilities (2 types of attractors, one saddle and two types of repellors).
If the system reaches these points then all the quantities remain constant as long as no external perturbation intervenes. These are the desired points where we want to keep the system.
It can happen that the system is not sticking to a point but rather to a finite and small region in the phase space. Then the system evolves and the trajectories will wrap around and around the same curve. This curve is called a closed trajectory or a cycle (fig.1).
The closed trajectory can take any shape in the state space (e.g.a torus etc.).

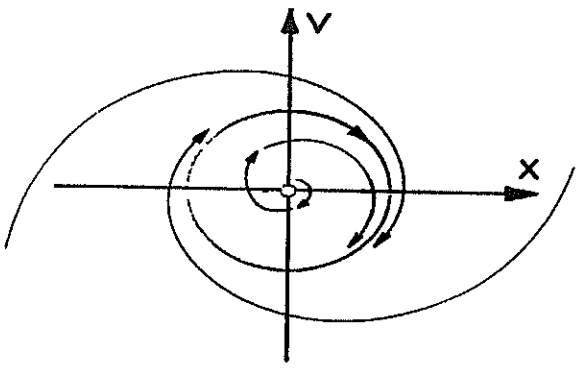

Fig.1

A trajectory should start from a point and should end up in a point. We call *α-limit set* the points from where trajectories are starting and *ω-limit set* the points

where trajectories are ending up. Of all limit sets that represent possible dynamical equilibrium states of the system, the *attractors* are the most prominent from a practical point of view.
All the trajectories that are coming to an equilibrium point are making up an *inset*. Usually an equilibrium point has an inset and an *outset* (all the trajectories which are leaving the point). An attractor is a limit set with an open inset. That is, there is an open neighbourhood of the limit set within its inset or in other words all the trajectories are coming into and no one is leaving the point. This will be a state with a highly equilibrium probability.
Figure 2 shows two attractors, a saddle point and a separatrix (a trajectory which divides regions of different structure and is going to a non-attractor).

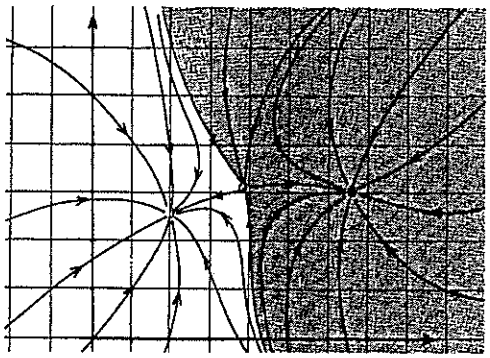

Fig. 2

With all these ingredients we can now tackle the problem of structural stability.
Let us give an intuitive image of the structural stability. Let us consider a vectorfield and a small perturbation. The perturbation is itself a vectorfield as shown in figure 3. The effect of adding this perturbing vectorfield to the original one is to modify it at each point in the state space.

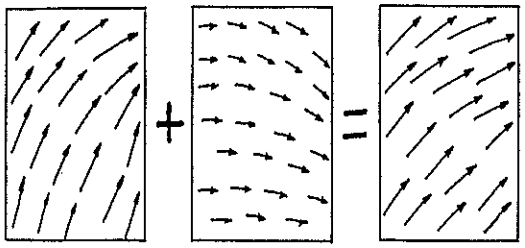

Fig. 3

The final phase portrait is *topological equivalent* with the initial one. The topological equivalence of two phase portraits means that there is a homeomorphism of the state space, or a continuos "rubber sheet" deformation which maps one of the portraits to the other, preserving the arrow of time on each trajectory.
It is possible that under a small perturbation, the system loses the stability and jumps into another state. At this moment a bifurcation is taking place. This means that in the phase space the trajectory has a discontinuity or is splitting at least in other two new trajectories.

With the concepts of structural stability and bifurcation one can treat a large variety of systems, from an organism to a power network.

3. Example and Results

To illustrate the ideas presented above we will use a simple model, Single Machine Infinite Bus (SMIB) fig. 4.

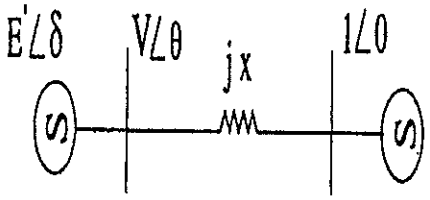

Fig.4

The mathematical equations which describe SMIB are:

$$\begin{aligned} \delta' &= \omega \\ M\omega' &= -D\omega + (P_M - BV\sin\theta) \end{aligned} \qquad (1)$$

where:
δ - machine angle
ω - machine frequency deviation in p.u.
M- moment of inertia
D- damping factor in p.u.
P_M - mechanical power input p.u.
BVsin(θ) – the electric power output.

Rearranging the equations with $\alpha = \frac{D}{M}$ and $\beta = \frac{P_M}{M}$, we get:

$$\begin{aligned} \delta' &= \omega \\ \omega' &= -\alpha\omega + \beta - \frac{BV}{M}\sin\theta) \end{aligned} \qquad (2)$$

In this final form, δ, ω are the state variables and α,β are parameters.
We compare the behaviour of (2) for different values of the parameters α and β. The bifurcation diagram is given in fig. 5.
The parameter space is divided in 3 regions. The system within each region exhibits the same number of solutions independent of the values of α and β. All solutions in each region have the same characteristics. According to our definitions, the system is *structurally stable.*

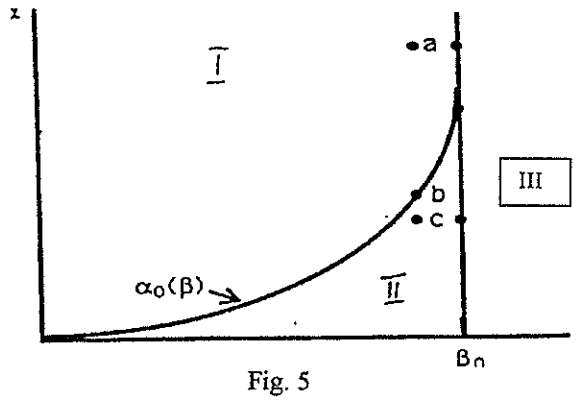

Fig. 5

Suppose (α,β) are in 'a'. The phase portrait is shown in fig. 6.

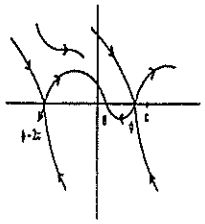

Fig.6

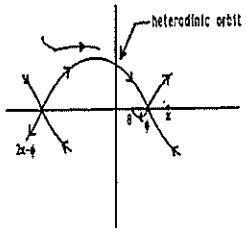

Fig.7

There are two equilibria, namely $(\omega=0,\theta)$ and $(\omega=0,\phi)$. The damping is decreased until $\alpha=\alpha_0(\beta)$ and the parameter is at 'b'. The phase portrait now changes to that of fig. 7.

Since the phase portraits of fig. 6 and fig. 7 are not structurally stable, points on α_0 (fig. 5) are bifurcation points.

Changing further more the parameters α and β, we will get different phase portraits for the regions I, II,III. It can be seen that having a mechanism to visualise the phase space for a system, points of bifurcation could be calculated and therefore the system can be kept in one region. It is desirable to confine the system to a region, because in this way conditions for stability are met. As the system is jumping from one region to the other, solutions or equilibrium points are lost or gained, therefore the stability is affected and difficult to be controlled. In essence, as long as the system is structurally unstable, the stability of the power system is changing.

We continue the study of structural stability, extending the model to include reactive power balance. We use the case of a single generator supplying a PQ load over a lossless transmission line as in fig. 8.

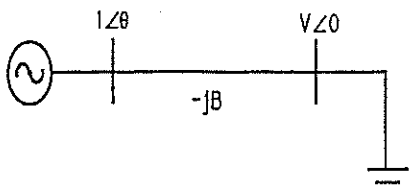

Fig. 8

The equations which model our system are:

$$\begin{aligned} 0 &= P_M - BV\sin\theta \\ 0 &= Q - BV\cos\theta + BV^2 \\ M\ddot{\theta} + D\dot{\theta} &= P_M - BV\sin\theta \end{aligned} \qquad (3)$$

where P+jQ is the load complex power.

For our one generator supplying a PQ load, the load dependence on frequency and voltage is:

$$P = P_0\left(\frac{U}{U_0}\right)^{\alpha} \times \left(\frac{\omega}{\omega_0}\right)^{\gamma} \text{ : active load}$$

$$Q = Q_0\left(\frac{U}{U_0}\right)^{\beta} \times \left(\frac{\omega}{\omega_0}\right)^{\delta} \text{ : reactive load}$$

In the following, we will try to change slightly the structure of P to study the structural stability of the system. The next set of values will be used:

$\alpha=0.9$, $\gamma=1$, $\beta=2$, $\delta=0$

The system is analysed by using the software package EUROSTAG [11].

The power load is increased from P =600 MW to 605 MW and the reactive power is increased from Q=200 MVAR to 202 MVAR. The characteristics of the system are listed in appendix A.

From the graph 9 (a), it can be seen that the system is not in an equilibrium point. The system exhibits a

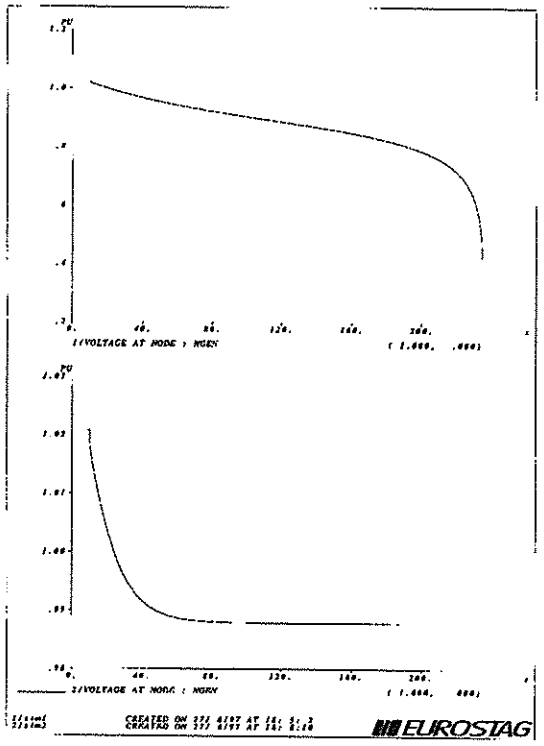

Fig. 9(a) and 9(b)

voltage collapse situation after 230s. At this stage it is not clear if the voltage collapse is a result of the power increases or because of the approximations made by the software. In order to eliminate these ambiguities,

another set of values is chosen but slightly different from the previous one: α=1.0, γ=1, β=2, δ=0.
The system and all the conditions are the same. The only minor difference is the power of the voltage in the real power (α=1). From the graph 9 (b) it can be seen that the voltage has been stabilised after 50s very close to the initial value.
The conclusion is that this dramatic change in behaviour, from voltage collapse to stability, is due only to the change of power dependency on voltage, nothing else being changed in these two situations.
Once again we can see the important role played by the structural stability in a Power System.

4. Conclusion

We summarise a few conclusions which are relevant to Power Systems.

- First the concept of Structural Stability is playing an important role in assessing the stability of a system and sometimes it is wrong associated with the stability of the system. Their definitions are completely different but a relationship between them is established.
- Second, the structural instability implies the apparition of a bifurcation. Hence the system is changing the number of equilibrium points, which affects finally the stability of that system. It is desired in Power System to control the system so that, in the parameter space, the system remains in the same region. Usually, bifurcation points mean loss of stability.
- Third, in the TDS, the bifurcation is associated in some situations with a route to chaos. This is another reason why bifurcation points should be known and avoided in real situations.
- Fourth, a better understanding of phase space and parameter space gives us a deeper insight into the problem of voltage collapse.
- Fifth, unfortunately when the system is complex, N generators, some calculations in TDS are impossible to be done and the phase space becomes N-dimensional, i.e. it offers no information because we are not able to visualise it.
- Sixth, fortunately, new methods are emerging in TDS which allow cutting slices in these N-dimensional phase space and therefore one is able to extract information about the system.

5. References

[1].D. K. Arrowsmith, C. M. Place: An Introduction to Dynamical Systems, Cambridge University Press, 1990.
[2].J. H. Hubbard, B. H. West: Differential Equations: A Dynamical Systems Approach, New York, Springer-Verlag, 1995.
[3].S. Wiggins: Introduction to Applied Non-linear Dynamical Systems and Chaos, New York, Springer-Verlag, 1990.
[4].P. Kundur: Power System Stability and Control, The EPRI Power System Engineering Series, McGraw-Hill, 1994.
[5].R. Abraham, D. Christopher: Dynamics-The Geometry of Behaviour, Santa Cruz, Calif: Aerial press, 1988.
[6].R. Seydel: From Equilibrium to Chaos, Elsevier Applied Science Publishers Ltd., 1988.
[7].L.L. Alexander: Structural Stability Analysis and its Applications to Power Systems, Ph.D. Thesis, Graduate College of Texas A&M University, 1987.
[8].S. Shelli Kay: Application of Normal Forms of Vectors Fields to Stress Power Systems, Ph.D. Thesis, Iowa State University, 1994.
[9].V. Vittal, W. Kliemann, A. Fouad: Application of the Normal Form of Vector Fields to Predict Interarea Separation in Power Systems, Denver, IEEE/PES Summer Meeting, 1996.
[10].A. Fouad, W.Klienmann, V. Vittal: Stability Boundary Approximation of a Power System using the Real Normal Form of Vectors Fields, Denver, IEEE/PES Summer Meeting, 1996.
[11].B. Meyer, M. Stubbe: EUROSTAG, A Single Tool For Power-System Simulation, Transmission &Distribution International March 1992.

Appendix A.

Characteristics for generator, load and line.

Generator:
Active Power: 1150 MVA
Rated Turbine Power: 1000 MW
Base Voltage: 24 kV
Stator Resistor: 0.0004
Direct Reactance: 2.57
Direct Transient Reactance: 0.422
d axis mutual inductance: 2.351
Direct Transient Time Constant: 7.695 s
Direct Sub-Transient Time Constant: 0.061 s
Mechanical Damping Coefficient: 0

Load

Base Voltage: 150 kV
Active Load: 600 MW
Reactive Load: 200 MVAR
Active Losses: 0 kW

Line
Total Line Resistance: 0.00208 p.u.
Total Line Reactance: 0.022285
Line Rated Power: 1000 MVA

MECHANISMS ASSOCIATED WITH TRANSIENT EARTH FAULTS ON A 275 kV TRANSMISSION LINE : FIELD DATA AND INITIAL EXPERIMENTAL DATA

P.V. Taylor
ESKOM TRANSMISSION

D.A. Hoch
UNIVERSITY OF NATAL

ABSTRACT

The high trip rate of a particular 275 kV transmission line in kWa-Zulu Natal has been investigated. A number of measures have been previously under-taken to reduce the trip incidences but have enjoyed limited success. The majority of the transient earth faults could not be correlated with pollution severity, lightning or switching operations. This indicated that an unusual failure mechanism may be responsible and the faults have been attributed to bird streamers that partially bridge out the air gap of the tower window and result in a phase-earth flashover. This paper presents the results of an investigation into the mechanism responsible for the earth faults and includes the results of field investigations, computations of the electric field distributions in the tower top, laboratory experiments and service experience after measures had been taken to move birds away from regions of the tower where bird streamers will result in flashovers.

1. Introduction

The high trip rate of the Georgedale Venus 275 kV lines has been investigated. A number of measures have been previously under taken to reduce the trip incidences but have enjoyed limited success. These measures included re-insulation with silicone composite insulators which would be expected to provide better pollution performance. The majority of the earth faults could not be correlated with pollution severity, lightning, and switching operations. Indications are that an unusual failure mechanism may be responsible.

These lines were constructed using the A1V, 275 kV towers series. The shortest distance from the live end to earth is 2.1 metres.

Numerical calculation of the electric stress distribution within the tower window with and without a bird streamer present indicated that the electrical clearance of these towers may make them sensitive to bird streamers 1.5 to 2 metres in length. The calculations indicated that the impact of bird streamers on the stress distribution will be minimised if the bird streamer is moved laterally away from the centre of the tower window by more than 0.75m.

Bird Guards that move the bird streamer laterally away from the centre of the tower by 1 metre have been installed on the troublesome sections of the line and have reduced the trip incidence to zero for the white phase for a period of 18 months. Operational experience strongly supports that bird streamer is the most probable cause of transient earth faults on these 275 kV lines.

The Georgedale Venus lines originally formed part of the Ingagane Georgedale lines which were commission in early 1960's. Venus Substation was commissioned in June 1990. Operational experience of these lines is summarised in table 1.

Year	Georgedale-Venus 1 140 km # Faults/year	Georgedale-Venus 2 140 km # Faults/year
June-December 1990	10	9
1991	9	14
1992	13	16
1993	12	7

Table 1: Georgedale Venus Performance Summary 1990-1993.

An investigation into these lines' poor performance was initiated in 1993 by Eskom Transmission Line Technology [1]. Their investigation concluded the following :

Electrical clearances sufficient for:

- One minute power frequency withstand of 460 kV
- Switching impulse of 850 kV
- Lightning Impulse withstand of 1050 kV

Insulator creepage distances varied between 14.9 and 15.9 mm/kV respectively.

Average mist days in Pietermaritzburg vary from 1 - 4.9 days per month.

ESDD (equivalent salt deposit density) levels on the insulators were low. (Although moss was found to be growing on insulators).

The first 70 km of line from Georgedale Substation had extensive pin corrosion.
Lightning density of the line between Mooiriver and Colenso is 7-8 strikes per km^2. Tower footing resistance on the towers varied between 4-47 ohms with an average of 15 ohms. LPATTS has confirmed that lightning is not solely responsible for the line faults.
Bird Problems were identified as a probable cause of trips. However their impact was only limited to the identified vulture restaurants - one at the Mooiriver crossing and the other at Griffins hill, 15 km north of Mooiriver.

2. Transmission Operations and Maintenance [TOM] Implementation of Findings.

Georgedale Venus 1 was selectively re-insulated with glass armour disc insulators. The re-insulation projected was completed by the end of 1994.

Georgedale Venus 2, first 100 km from Georgedale Substation, was completely re-insulated with silicone composite insulators (excluding strain towers) by the end of October 1995. The performance of the lines is summarised in Table 2.

Year	Georgedale-Venus 1 140 km #Faults/year	Georgedale-Venus 2 140 km #Faults/year
1994	18	16
1995	7	16
1996	15	29
1997	8	9

Table 2: Georgedale Venus Performance Summary 1994-present

The poor line performance prompted TOM to re-investigate the lines. There was no correlation between the earth faults and :

1. Natal's low network loading period or time of day of faults.
2. Switching surges or other system faults.
3. Lightning strikes (no correlation with LPATTS).

Fault patrols recorded evidence of flash marks appearing to emanate on the corona rings and terminate directly above the yoke plates on the tower lattice. This evidence suggested that the root cause of the majority of earth faults was an air gap breakdown phenomena. Bird streamers were the only source of conducting fluid which could account for the numerous trips on the trip. Florida Light and Power had recorded similar such findings [2].

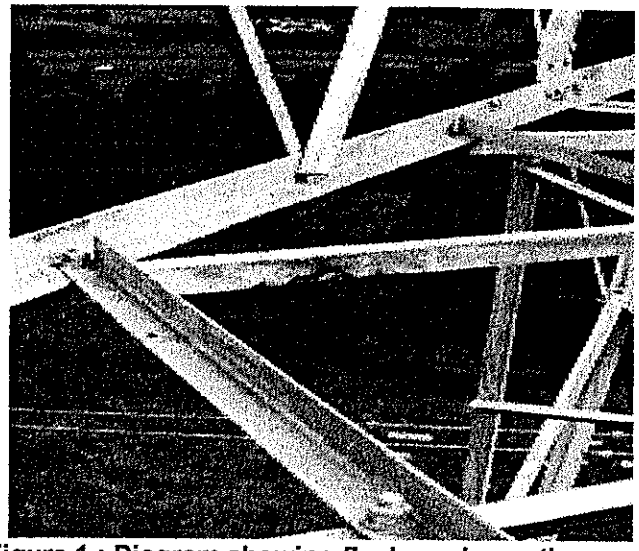

Figure 1 : Diagram showing flash marks on the tower struts.

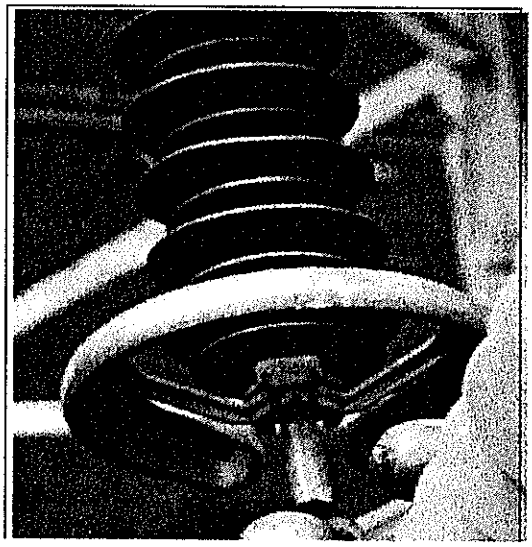

Figure 2: Photos illustrating Flash Marks on the corona ring.

The bird streamer mechanism is defined as:

a. A streamer which bridges the entire air gap between the yoke plate and the tower lattice. This then acts as a fuse as the current through the streamer increases and vaporises the liquid through Joule heating. An arc will then form between the HV conductor and earth.

b. The bird streamer acts as a conducting intrusion into the air gap that drastically alters the electrical stress distribution in the tower window. The resulting field enhancement results in air gap breakdown for the air gap between the nearest HV point and the streamer.

3. Laboratory investigation into breakdown of simple rod-plane air gaps.

A starting point for the experimental investigation related to examining the classical rod-plane geometry at gaps that will flashover for voltages of interest to this work i.e. 275 kV. Rod-plane gaps will flash at this voltage for gap distances greater than 400 mm. In order to investigate the flashover of these air gaps and in particular the effect of the rod electrode (shape of tip and diameter), a wider range of gap distances were investigated. The results are shown in the figures below. The experiments with simple rod-plane geometries are supported by the results of Rizk who reported similar tests but for a limited range of rod geometries [3].

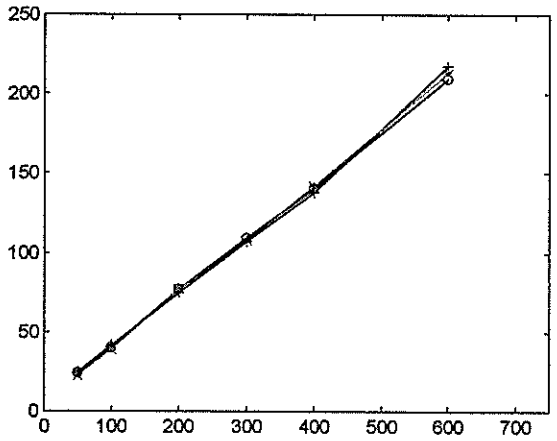

+ - 3 mm diameter pointed rod
o - 6 mm diameter pointed rod
* - 12 mm diameter pointed rod

Figure 3: Breakdown Voltage versus Air Gap Length (rod-plane) for a 3mm diameter rod (pointed tip).

Note that each data point represents the arithmetic mean of between six and ten achieved breakdowns. The standard deviations of the measured data were ~3% in most cases.

The data for a 6 mm and a 12 mm diameter pointed tip rod were within 3 % of the 3 mm diameter electrode. This indicates that the size of the rod electrode does not play a significant role.

In order to ascertain whether the shape of the rod electrode tip has any effect on the flashover voltage, a 3 mm diameter rod was machined in such a way that three different tip shapes resulted; these are referred to as point (as in Figure 3 above), hemispherically capped and flat cut (where the rod is cut square at its tip). The data shown in Figure 4 summarise these results and indicates a minimal effect of the shape of the electrode tip for this geometry.

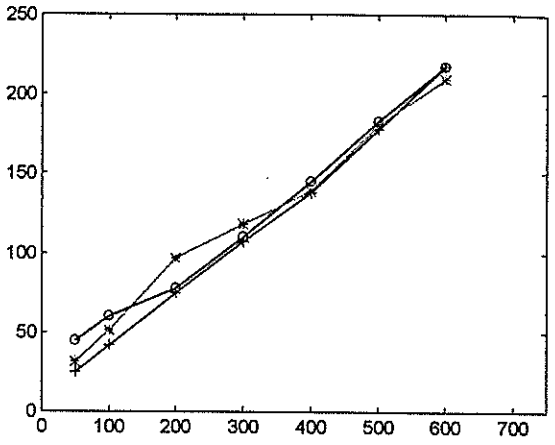

o - Square cut rod
+ - Sharpened point rod
* - Hemispherically tipped rod

Figure 4 : Effect of rod tip on breakdown voltages of rod-plane gaps of varying gap length.

For a 275 kV system voltage the bird streamer would have to decrease the effective air gap clearance to less than 450mm before the streamer encroaches on the measured air gap insulation strength and lead to flashover.

The experiments also show that at nominal operating voltage the AC breakdown voltage is virtually independent of the electrode tip shape.

4. Electric field modelling of tower top

Electric field modelling of a tower window has been performed using a three dimensional finite element package. The distorted equipotential plot for the tower top geometry of the Georgedale Venus line when a bird streamer is present is depicted below.

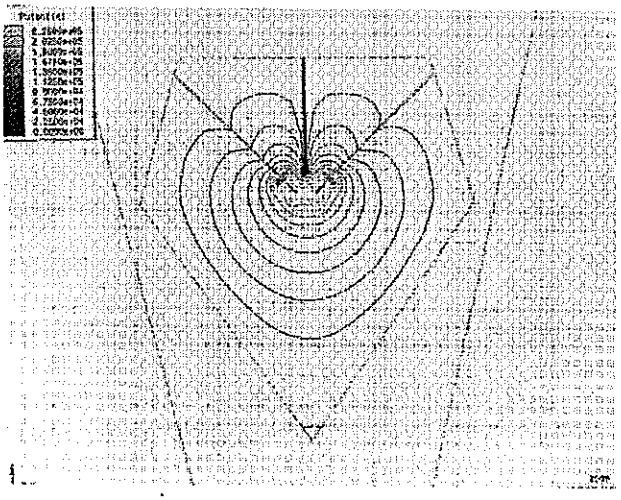

Figure 5: Equipotential plot for the 275 kV Tower: Silicone Composite Insulators; bird streamer present.

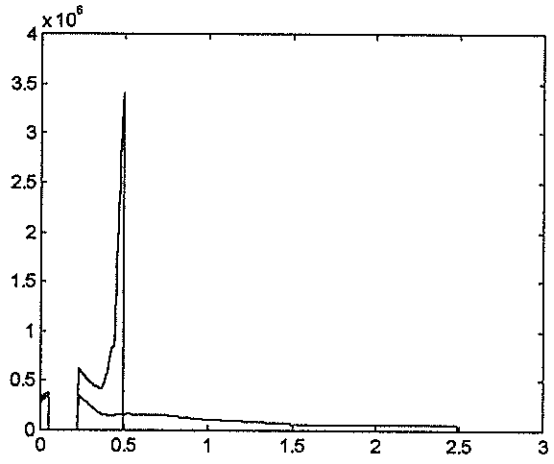

Figure 6 : Comparative electric field plots for Georgedale Venus tower top geometry with (top curve) and without (bottom curve) a bird streamer present.

The electric field along the shortest path from bird streamer to the nearest HV point is also depicted with a 2m bird streamer aimed at the centre of the insulator assembly and where the bird streamer is moved 0.5m away from the nearest HV point.

A literature survey on air gap breakdown leads to the following conclusion:

a. Streamer inception occurs when the electric field in air ~30kV/cm[4].
b. A streamer will propagate within the air gap up to the point where the electric field, in the absence of the streamer, is 4-6 kV/cm[5].

Applying the above criteria, the streamer illustrated in figure 5 is likely to cause flashover. As the streamer is moved away more than 450mm from the nearest live component, the electric field strength drops to a level at which flashover is not likely to occur.

5. Operational experience attained with the application of "Bird Guards".

Bird guards have been installed on the two lines since the end of July 1996. These guards were installed on the centre phase and on all towers. There has been no reported faults on the welded rod bird guard, but there have been three on towers protected by whirly birds. The bird guard types are depicted below.

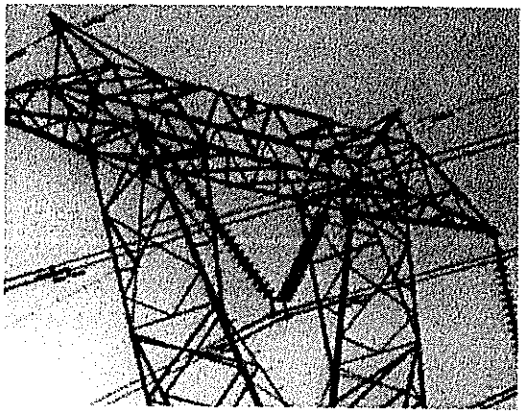

Figure 7: Illustration of Whirly Bird

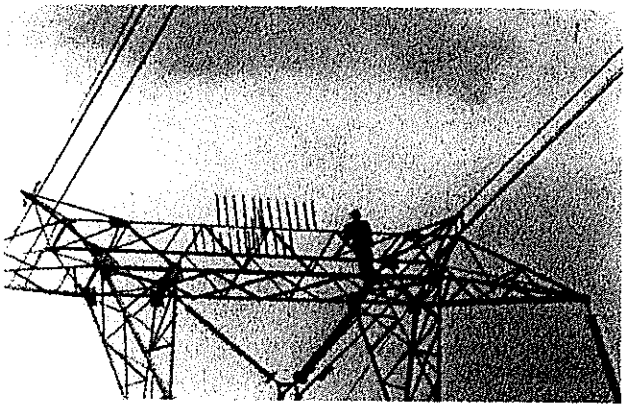

Figure 8: Illustration of Welded Rod Bird Guard

6. Conclusion

The bird streamer mechanism has been identified as a root cause of earth faults on the Georgedale Venus 275 transmission lines. A possible method to prevent these faults has been investigated both theoretically and practically. The field results obtained substantiate the theoretical predictions.

A mathematical model of the bird streamer mechanism that satisfactorily describes both necessary and sufficient conditions for flashover to occur is still under investigation.

6. References

1. Steynberg, B and Gouws, T., "Georgedale Venus 275 kV lines", Eskom Line Technology,1993
2. Burnham, J, "Bird Streamer Flashovers on FPL Transmission Lines", IEEE Transactions on Power Delivery, Vol 10, No 2, April 1995, 970-978.
3. Rizk, F.A.M., Beausejour, Y., Shi Xiong, H., "Sparkover Characteristics of Long Fog-Contaminated Air Gaps.", IEEE Trans. of Power App., Pas100, No11, 1981, 4604-4611
4. Hutzler, B., Hutzler-Barre, D., "Leader Propagation model for predetermination of switching surge flashover voltage of large air gaps.", IEEE Trans. of Power Appar., PAS 97, No 4,1978,1087-1095
5. Gallimberti, I, "A computer model of streamer propagation.", J, Phys. D: Appl. Phys, Vol 5, 1972, 2179-2189.

THE IMPACT OF CORONA AGEING ON THE SURFACE AND SUBSURFACE LAYERS OF SILICONE RUBBER INSULATION

S M Reynders

Greater Johannesburg Metropolitan Electricity
P O Box 699
Johannesburg 2000

J P Reynders I R Jandrell

Department of Electrical Engineering
University of the Witwatersrand,
Pvt Bag 3, PO Wits 2050, Johannesburg, SA

Abstract - This paper presents a brief review of current knowledge and experimental work on accelerated ageing of silicone rubber insulation. Samples were aged for periods ranging from 1 minute to 27 days and recovery was monitored over long periods of up to 3.7 months. The ageing was thermally accelerated at temperatures ranging from 25 °C to 100°C. Ageing and recovery were quantified using contact angle measurements and X-ray Photoelectron Spectroscopy - surface and depth profile chemical analysis. Contact angle observations showed complete recovery, provided a sufficient resting period was allowed. However, chemical analysis reveals how corona breaks up the polymer to allow diffusion to the surface and that permanent ageing is present in terms of a loss of silicone polymer immediately below the surface layers, despite the recovery of the contact angle.

Keywords: silicone rubber, non-ceramic insulators, corona ageing, thermal acceleration

1. INTRODUCTION

Silicone Rubber (SR) insulators have been successfully used in transmission systems for over 30 years [1, 11]. Their hydrophobic properties are very well known and documented, and the ability to transfer the hydophobicity to surface pollution [2, 7, 10]. They have been used in upgrading projects, where voltages are increased but tower dimensions are kept the same, where with previous conventional insulators 60 day washing was required, the SR has been maintenance free [11]. However "uncontrolled leakage current promotes intense dry band arching, which on polymers can ultimately lead to material degradation in the form of tracking and erosion , and /or flashover at the operating voltage," [8] and "...the insulator may suffer mechanically and line dropping cannot be excluded." [13]

The loss and recovery of hydrophobicity of SR is a very complex phenomenon and considerable research has been done to understand the fundamental mechanisms and to select the best design / polymer composition from the ever growing range of non-ceramic insulators(NCI). In virtually all of the very wide range of accelerated ageing tests, it is possible to select conditions such that the NCI will loose hydrophobicity in a very short period of time (as little as 100 seconds of corona exposure [12]) and fail. Most environmental ageing tests, however, show very good performance even in heavy pollution e.g. Germany North sea coast [13] after 16 years, no line drops, or flashovers. Consequently most accelerated tests show little agreement with service experience [14]. When it comes to comparison, all tests agree is that SR ages slower and recovers hydrophobicity faster than any other kind of NCI.

Very interesting research has also been performed with respect to the filler type and quantity used in the SR formulation [10]. Fillers such as ATH or Silica are added to the basic elastomer for tensile strength and electrical properties. "The development of leakage current on coatings is related to the amount of ATH filler. Coatings with increased filler levels develop leakage current earlier then those with lower filler levels. However coatings with increased filler levels suppress leakage currents after the hydrophobic surface converts to a hydrophilic surface" [1].

The destruction of insulators is primarily caused by electrical discharges on the surface of the insulators. Before the surface has lost its hydrophobicity, leakage currents are less than 0.1mA [3] , there is no dry band arching and the only source of discharge is surface water droplets, which intensify the electric field and give rise to corona [15]. Corona has been isolated as a physical process which causes a loss of hydrophobicity in SR insulators [4, 5, 6]. Once the hydrophobicity is lost, larger leakage currents (1-10mA) flow across the surface of insulators [3], causing dry-band arcing and associated erosion. It was decided to conduct further investigations using corona as the only mechanism for ageing. Other factors such as salt-fog, wetting cycles, dust and UV, used extensively in ageing tests, were not included in order to isolate the effect of corona.

The work described in this paper is essentially developed on the view that the ageing mechanism is electro-chemical with the corona providing the energy to cause the silicone polymers to break up into shorter chain molecules. These shorter chains are volatile and

leave the surface as a vapour [5]. This process is chemical and can thus be accelerated by increasing the temperature, without changing the fundamental ageing mechanism. As the insulation recovers silicone polymers from deeper down diffuse up to the surface, replacing those that have been lost [12]. The molecular processes are complex and many statistical variations exist.

2. EXPERIMENTAL SETUP

Ageing of Silicone Rubber (SR) samples was conducted inside a thermally insulated chamber previously described [9]. Flat rectangular samples (47mm X 25mm) were used and corona was generated from a triangular copper protrusion on the sample surface, in contact with the high voltage electrode.

3. OBSERVATIONS

3.1 Hydrophobicity measurements

Hydrophobicity was measured by means of static contact angle, this standard technique has been well documented [4, 6, 9]

In order to determine the effect of temperature on corona ageing of SR, tests were performed at 25°C, 50°C, 70°C and 90°C. The supply voltage and hence the electric field at the tip of the corona generating protrusion were maintained constant. This is assumed to maintain the intensity of the corona constant. Tests were performed on 0.4mm RTV SR coatings (applied on ceramic tiles) and on sections of solid HTV SR, cut from the sheds of insulators, for a duration of 1, 5, 10 and 20 minutes and 23 and 45 hours. Contact angles were measured before ageing and at intervals after the ageing period until hydrophobicity had stabilised. Before the contact angle is measured it is necessary to let the drop stand for about 2 minutes for the forces to gain equilibrium. Measurements taken before the standing time is up can be high by up to 10°. Statistical variations of up to 30° were observed in measuring contact angles of droplets in very close proximity. Owing to these variations, each recorded measurement is a worst case measurement. Approximately 10 drops were placed on the sample and the worst contact angle was recorded.

The key results are summarised below:

- Irrespective of temperature, for ageing times greater than 20 minutes, for both RTV and HTV samples, the contact angle was 0° immediately on completion of ageing.
- For longer periods, 23 and 45 hours, the acceleration of ageing with temperature was found to have an direct relationship. This confirms previous work [9].
- Recovery rates varied considerably. Using the notion that recovery followed a first order exponential [4, 6], time constants ranging from 20 to 200 hours were obtained. In some cases the fit to a first order exponential was very poor.
- Recovery was not uniform on the surface, but differed considerably for locations in close proximity.
- The recovery of the HTV samples was significantly faster than the recovery of the RTV samples in comparative test runs.
- In all tests recovery of hydrophobicity was complete, provided a sufficient resting period was allowed.
- Samples subjected to heat and not corona showed no loss of hydrophobicity.

3.2 Chemical Analysis

3.2.1 Surface analysis

This was accomplished using X-ray Photoelectron Spectroscopy (XPS), analysing only the Si 2p binding energy peak in detail [9]. This peak can be resolved into two separate peaks, Silica (SiO_2), 103,5eV which is the filler and polydimethylsiloxane $((CH_3)SiO)_n$ at 101,6eV the silicone polymer. XPS plots of a virgin sample and the 280 hour aged sample(100°C at a voltage of 25kV), after recovery for three hours are presented in Figures 1 and 2 below. Data on further recovery with has been published previously [9].

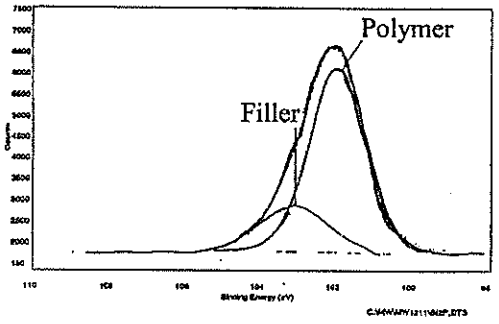

Figure 1: Binding Energy for Si of a virgin HTV sample

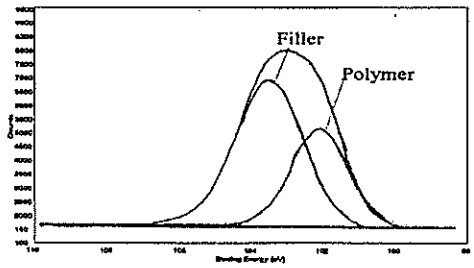

Figure 2: Binding Energy for Si of an aged sample (280hrs) after 3hrs recovery

3.2.2 Depth profiling

Depth profiling is a relatively new technique [9], that uses Argon sputtering to remove the upper layers (about 5nm) and the surface is rescanned at the new depth, the process is repeated , until a depth of 200nm has been reached. The data is fitted with the curves, as for a single surface scan, and the changes in relative quantities of SiO_2 and $((CH_3)SiO)_n$ with depth are plotted. The depth profile of a virgin sample is shown in Figure 3. A solid section of SR insulator (HTV) was aged for 27 days at 100°C with an excitation voltage of 25kV. A sputter depth profile was performed after the sample was allowed to rest for 3.7 months and is shown in Figure 4. For an intermediate result, a sample was aged for 45 hours and allowed to recover for 1 week, the sputter depth profile is shown in Figure 5.

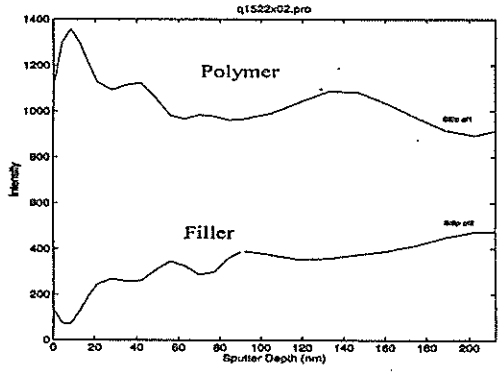

Figure 3: Depth profile of virgin HTV sample

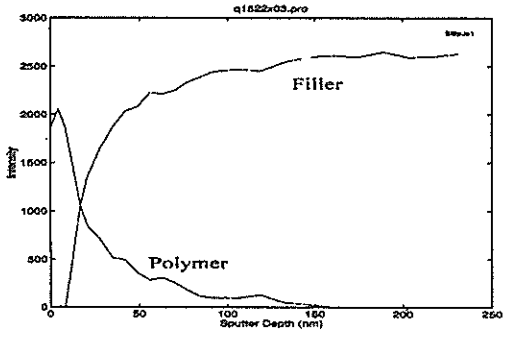

Figure 4: Depth profile of HTV sample aged for 27 days after 3.7 months recovery

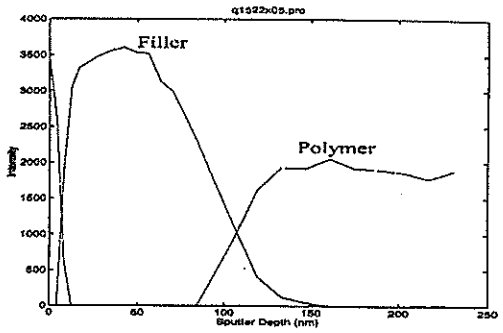

Figure 5: Depth profile of HTV sample aged for 45 hours after 1 week recovery

Before ageing, the polymer component dominated over the filler at the surface and into the bulk to at least 200nm. After ageing, the polymer still dominates on the surface, but further into the sample, it has been depleted and the filler dominates. Figure 5 shows that increased ageing depletes polymer deeper into the bulk, and that all the bulk polymer does not diffuse to the surface. Further evidence of a changing composition was the appearance of surface cracks. Despite these changes in composition, the quantity of polymer at the surface, after the recovery time, was still sufficient to ensure hydrophobicity.

4. DISCUSSION

4.1 Hydrophobicity measurements

From the above observations it is clear that the ageing of the samples was very severe, resulting in total wetting after 20 minutes of exposure to the corona. The non uniformities and variances in hydrophobicity are a result of the statistical variances involved in the recovery process as the polymer diffuses to the surface [8]. The faster recovery of the solid HTV samples compared to the RTV coating can be attributed to the higher quantity of LMW polymer reserve in the thicker HTV sample. The complete recovery of hydrophobicity shows there was still sufficient polymer left in the samples after ageing to replenish the surface and to restore hydrophobicity.

4.2 Chemical analysis

The $((CH_3)SiO)_n$ component is an elastomer, the methyl groups make it strongly hydrophobic. SR contains may different lengths of the polymer, the shorter chains are regarded as a LMW silicone oil [12]. The very high content (80%) of the polymer on the surface of the virgin sample agrees with the hydrophobicity of the new material. Following ageing, the polymer is depleted and the filler material is exposed as shown in Figures 1 and 2. With time, diffusion of the LMW silicones leads to an increase in

the percentage of polymer on the surface [8]. The energy of the corona breaks up the polymer chains of elastomer until they are so small that they become volatile and evaporate [12]. The corona that the samples were subjected to was intense enough to provide energy to remove most of the surface layers of polymer, exposing the filler.

When the sample was subjected to this kind of ageing for a long period of the polymer was depleted not only on the surface but deep into the bulk of the insulator. When the sample was allowed to recover, the small quantity of remaining polymer of low enough molecular weight diffused to the surface allowing the sample to regain hydrophobicity. A comparison between figures 4 and 5 shows that increased ageing breaks up polymer deeper down, but that the polymer reserves (deeper than 100nm figure 5) are of too long chains to be able to diffuse to the surface. It would appear that if the severely aged sample was subjected to corona once more after recovery, when all the remaining polymer molecules had diffused to the surface, they would be removed and hydrophobicity might not be regained.

The cracks on the surface are due to the depletion of the polymer, which gives the SR its elasticity. The filler material is hard and cracks when large quantities of the polymer are removed. If this were to continue for longer periods, the cracks would deepen and possibly penetrate through the SR exposing the core in an insulator.

5. CONCLUSIONS

- Long ageing periods at high temperatures result in very severe ageing.
- Longer time constants for recovery were obtained in comparison to Bhana [6] and Dickson [4]. In some cases recovery did not even fit a 1st order exponential curve.
- There is a direct relationship between temperature and corona initiated loss of hydrophobicity in silicone rubber.
- The corona itself is responsible for the shortening of polymer chains, some of which evaporate, and some diffuse to the surface after corona treatment has ceased, resulting in a recovery of hydrophobicity
- Permanent ageing has been obtained in the form of a depletion of the silicone rubber polymer in the body of the material, despite the recovery of hydrophobicity.

6. REFERENCES

[1] Kim S H, Cherney E A, Hackman R, "The Loss and Recovery of Hydrophobicity of RTV Silicone Rubber Insulator Coatings" IEEE Transactions on Power Delivery, Vol 5, No 3, July 1990.

[2] Vlastos A E, Gubanski S M, "Surface Structural Changes of Naturally Aged Silicone and EPDM Composite Insulators", IEEE Transactions on Power Delivery, Vol. 6, No.2 , pp 888-900, April 1991

[3] Barsch R, Lambrecht J, Winter H J, "On the Valuation of the Early Ageing Period of Polymer Insulator Surfaces During Accelerated Ageing Tests". 9th ISH Graz 1995, 3023.

[4] Dickson A E, Reynders J P, "The effects of Corona on the surface properties and Chemical Composition of Silicon Rubber Insulators." 9th ISH Graz 1995, 3023.

[5] Dickson A E, "The Effects of Corona on the Physical and Chemical surface properties of Silicone Rubber Insulators" MSc(Eng.) dissertation, University of the Witwatersrand, 1996

[6] Bhana D K, Swift D A, "An investigation into the Temporary Loss of Hydrophobicity of Some Polymeric Insulators and Coatings". Proceedings of the 4th International Conference on Properties and Applications of Dielectric Materials, Brisbane, 1994, 5208.

[7] Gorur R S, Johnson L A, Hervig H C, "Contamination performance of Silicone Rubber Cable Terminations", IEEE Transactions on Power Delivery, Vol. 6, No. 4, October 1991.

[8] Chang J W and Gorur R S. "Surface Recovery of Silicone Rubber Used for HV Outdoor Insulation", IEEE Transactions on Dielectrics and Electrical Insulation, Vol 1 No 6, December 1994, pp 1039 - 1045.

[9] Reynders S M, Hendey P, Reynders J P, "Thermally accelerated Corona Ageing of Silicone Rubber Insulation", ISH '97, 3516.

[10] Kahle M, Adolf H, "The Influence of the Structure of Elastomeric Insulator coatings on the Degredation and Recovery Process" 9th ISH Graz 1995, 3031.

[11] Kindersberger J, Schultz A, Kamer H C, v.d. Huir R, "Service Performance, Material Design and Applications of Composite Insulators with Silicone Rubber Housings", CIGRE paper 33-303, session 1996

[12] Toth A, Bertoti I, Blazso M, Banhegyi G, Bognar A, Szaplonczay P, "Oxidative Damage and Recovery of Silicone Rubber Surfaces. I. X-ray Photoelectron Spectroscopic Study", Journal of Applied Polymer Science, Vol 52, 1293 - 1307 (1994) John Wiley and Sons, Inc.

[13] Kindersberger J, Kuhl M, Barsch R, "Evaluation of the condition of non-ceramic insulators after long-term operation under service conditions" 9th ISH Graz 1995, 3193.

[14] Besztercey G, Banhegyi G, Zelenyanszki E, Tamas F, Kimata R, Bognar A, "Comparison of Electrical Erosion Tests on Materials used for Insulators", 9th ISH Graz 1995, 3037.

[15] Phillips A J, Childs D J, Schneider H M, "Ageing of Non-Ceramic insulators due to Corona from Water Drops", Accepted for presentation, 1998 Winter Meeting, 98 WM 236, PES.

CORONA AND SUSTAINED ARCING ON CONVENTIONAL AND NOVEL NON-CERAMIC INSULATOR DESIGNS

K. J. Nixon J. P. Reynders

Department of Electrical Engineering
University of the Witwatersrand
Private Bag 3, 2050, South Africa

R. J. Hill

MacLean Power Systems
Reliable Power Products
11411 Addison, Franklin Park, IL 60131, USA

The effect of corona and sustained arcing on two non-ceramic insulator (NCI) designs is investigated. The one NCI design uses a standard distributed shed arrangement, whereas the other uses a stacked shed arrangement at the high voltage end. Both designs were placed in service and studied for 12 months in an heavily polluted area. Observations made showed continuous arcing that remained stationary for long periods of time (several hours). Preliminary experiments show that continuous arcing appears to have less effect on the hydrophobicity of silicone polymer than corona activity. Finite element method (FEM) software is used to analyse the electric field distribution on both NCI designs under clean and dry conditions.

Keywords: Non-ceramic insulator, water drop corona, dry band arcing, stacked shed, distributed shed, pollution

1 INTRODUCTION

The use of non-ceramic insulators (NCI) is recommended in areas subject to very heavy pollution. The hydrophobic properties of the NCI material limit wetting and excessive leakage currents that would otherwise occur with traditional insulator materials. The performance two NCI designs is discussed in this paper, in particular the behaviour under heavy pollution with sustained localised arcing as well as the effect on hydrophobicity caused by corona from water drops [1,2].

2 NCI DESIGNS

The profile of a typical NCI with distributed sheds is shown in *Figure 1*, as well as a novel design favouring a stacked shed arrangement at the high voltage end. The performance of both NCI designs is discussed in this paper.

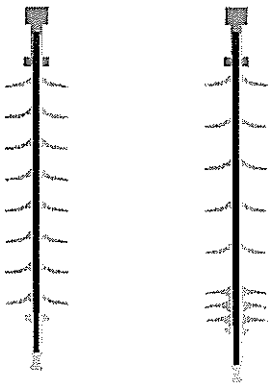

Figure 1. Distributed shed and stacked shed NCI designs.

3 POLLUTION

The physical processes that dominate the performance of a NCI under heavy pollution conditions are not completely understood. It is believed that the build up of pollution on the surface of the insulation results in the formation of a conducting layer once wetted. This means that the normally capacitive behaviour of the NCI becomes dominated by a resistive characteristic. Consequently, the electric field distribution changes radically.

The two NCI designs were installed in an heavily polluted area in South West Cape, South Africa. After a period of some months in service, video of the insulators was taken with an image intensifying camera (Corocam). Digital stills obtained from the video are shown in *Figure 2*, from which several interesting observations arise.

Figure 2a shows two clear sources of sustained arcing on the distributed shed NCI, one arc just below the second shed from the live end, and a less intense arc near the earth end-fitting. These were observed to continue unabated for several hours (5 to 10 hours) without extinguishing. This can only be caused by pollution altering the electric field distribution, since the field modelling discussed in the following section reveals that on a clean insulator the high field stresses occur near the live end.

Similar performance for the stacked shed NCI was observed and is shown in *Figure 2b*. In this case the continuous arcing was occurring under the shed closest to the earth end-fitting as well as a shed near the middle of the NCI.

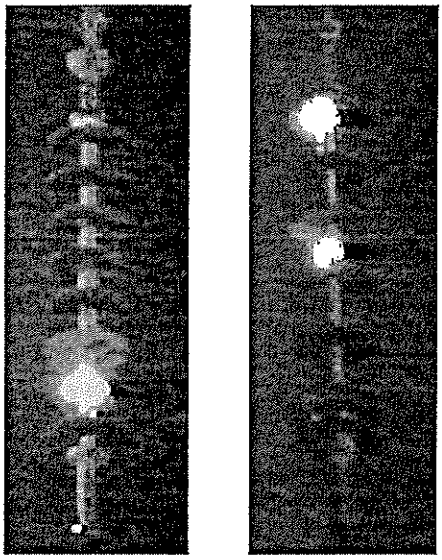

a) Sustained arcing on distributed shed NCI

b) Sustained arcing on stacked shed NCI

Figure 2. Digital still frames captured from an image intensification camera. The live ends are at the bottom of the image.

A physical examination of the insulators after 12 months on test revealed no visible sign of degradation on the stacked shed unit, and only slight traces of sheath erosion on the distributed design in the area of sustained arcing between the first and second shed. It should be noted that these insulators were both under-dimensioned for this environment (19 mm/kV as opposed to 31 mm/kV creepage distance) in order to accelerate any ageing or erosion.

4 FIELD ANALYSIS

Finite element method (FEM) software (Maxwell) was used to study the electric field distribution of each NCI design. Knowledge of E-field magnitude along the surface of an insulator is useful for identifying potential problem areas. Analysis was limited to electrostatic conditions at line voltage. The models used did not account for pollution or wetting, and the results therefore only apply for a clean and dry NCI. The results presented were produced using 2D axi-symmetric models. However, it should be noted that 3D modelling is more accurate, since the shielding effect of the live conductor can be taken into account.

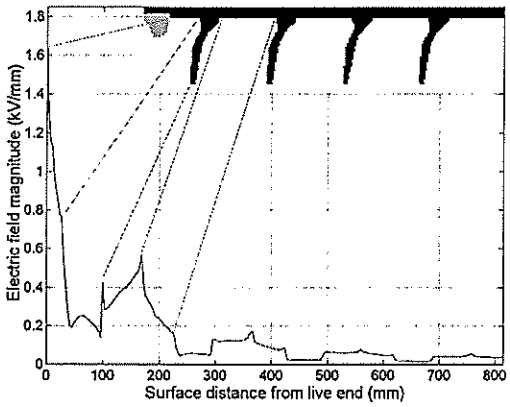

Figure 3. E-field magnitude along distributed shed NCI surface. Points of interest and extent of analysis are also shown.

The results of the analysis are shown in *Figures 2* and *3*. Care must be taken when interpreting these results since only the magnitude, and not the direction of the E-field is indicated (the implication is discussed in Section 5).

The most significant E-field is near the live end, with slight increases in magnitude at the shed extremities and in the joins between the stacked sheds. Points of interest have been indicated clearly on the figures. For both designs, the magnitude of the E-field has fallen by 90% within 500 mm surface distance from the live end.

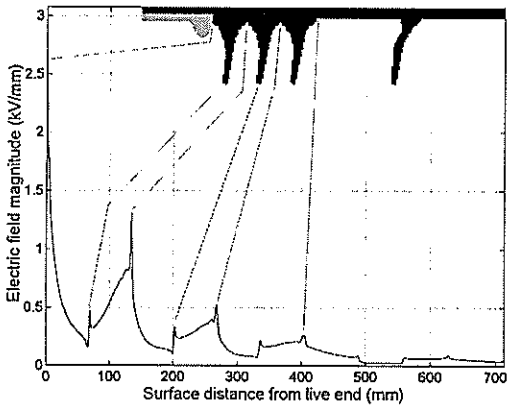

Figure 4. E-field magnitude along stacked shed NCI surface. Points of interest and extent of analysis are also shown.

The E-field on the surface of the sheath of the stacked shed NCI does not exceed 0.3 kV/mm at any point. The first length of sheath on the distributed design is subjected to an E-field between 0.5 kV/mm and 1,5 kV/mm.

5 EFFECTS OF CORONA ON A NCI

Corona on the surface of a silicone dielectric is known to cause chemical changes to the silicone polymer [1, 0, 4] which result in changes to its hydrophobic performance. Phillips et al demonstrated that water droplets on the surface of hydrophobic insulators cause a significant enhancement of the local electric field and give rise to corona at lower field gradients than in the absence of water droplets [2].

An experiment was devised to obtain the magnitude of electric field strength required for the onset of corona activity. The result of the experiment can be used in with the field modelling results discussed in the previous section to identify areas of interest in the NCI designs.

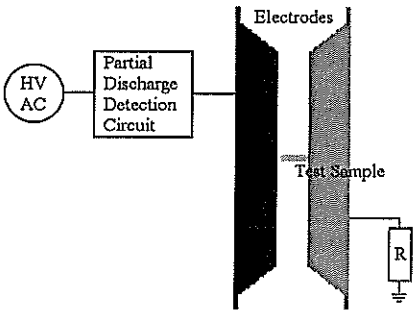

Figure 5. Experimental arrangement used to determine corona onset E-field.

The test arrangement used is shown in *Figure 5*. A partial discharge detection unit was used to determine the voltage at which corona activity began. Care was taken to ensure that the experimental layout was discharge free. In this regard, a conducting paste consisting of petroleum jelly and salt solution was used between the silicone sample and the electrodes to eliminate air voids. A large series resistance was included in the circuit to restrict damage to the silicone sample should flashover occur. A uniform electric field was established by using two flat metal dishes at a constant separation.

A slice of silicone 6mm thick and 23 mm wide was cut from a shed and cleaned with soap. A drop of ordinary tap-water was placed on the silicone, in the middle of the gap. The applied voltage was slowly increased, and the onset of corona was easily detected using the partial discharge detection circuit. FEM and the applied voltage at which corona began were used to calculate the effective electric field required for the onset of corona activity. Two drop volumes were investigated, 10 µl and 25 µl. An accurate micro-dispenser was used to measure these volumes.

For 10 µl drops of water, corona onset typically occurred for an applied E-field of 0.75 kV/mm. The behaviour of a 25 µl drop of water was much more defined. Partial decomposition of the drop occurred at an applied E-field of 0.59 kV/mm followed by discharge activity which commenced at 0.73 kV/mm. These results compare favourably with work done by Phillips who used a different experimental arrangement [2]. Phillips shows that increasing the drop volume decreases the corona onset until around 80 µl after which no significant change occurs. Thus a suitable range to use for analysis is 0.6 kV/mm to 0.75 kV/mm.

The direction of the electric field is important. In the experiment and analysis described above, the E-field is always in the direction parallel to the surface of the polymer. Corona activity directly across the polymer surface has much more effect on the material than discharges away from the drop, normal to the surface.

Returning to the results of the FEM analysis, several conclusions can be made. From *Figure 3* it is clear that water droplet corona will occur for the first part of the sheath of the distributed shed NCI and perhaps even after the first shed. *Figure 4* indicates high stress levels in the gaps between the stacked sheds. However, the area of particular concern is the sheath itself where the amount of insulating material is far less than for the sheds. Therefore the stacked shed design has successfully moved the high surface E-field away from the sheath to the sheds where it is less of a concern.

6 EFFECTS OF CORONA AND ARCING

Given the results of field testing discussed in Section 3 and the effects of water droplet corona discussed in the previous section, an experiment was set up to investigate any differences between the two effects. The experimental arrangement was similar to that shown in *Figure 5*, except that the discharge detection circuit was removed and the value of resistance was selected to achieve the desired arcing current. Two small, pointed electrodes were used to ensure the arc remained in the same place across the silicone surface.

For the corona test, a thin slice of perspex was placed between the silicone slab and the earth electrode. A piece of solder shaped like an elongated 10 µl water drop was placed in the middle to produce consistent corona since water would evaporate after 8 hours [5]. A pointed electrode was found to be necessary to prevent space charge accumulating and quenching the corona activity.

Samples of width 24 mm were tested under a different conditions, see *Table 1*. All samples were taken from an old NCI, and all were cleaned with soapy water, except for one sample which was tested with the pollution intact.

Silicone	Test Details	Contact Angle Before	Contact Angle After	Time Const. (min)
Cleaned	7.3 mA 5 hr	115	65	36
Polluted	4.8 mA 8 hr	105	50	39
Cleaned	4.8 mA 8 hr	115	60	44
Cleaned	Corona 8 hr	100	20	76

Table 1. Results of continuous arcing and corona experiment.

The recovery of the samples was tested at regular intervals after the relevant testing period. A camera and microscope were used to take pictures from which the contact angle could be measured. A photograph of an accurately measured 10 µl drop of water was taken to measure the contact angle. A dry swab was used to carefully remove the drop immediately after taking a photograph. At least two photographs were taken after each time period to ensure accurate contact angle measurements.

The results of the experiment are shown in *Figure 6* and *Table 1* and sample photographs are shown in *Figure 7*. The trend indicates that the silicone recovers its hydrophobicity quicker after arcing than after corona activity. A first-order exponential trend is assumed to calculate the time constants given in *Table 1* [6]. The silicone appears to recover twice as quick after arcing than after corona.

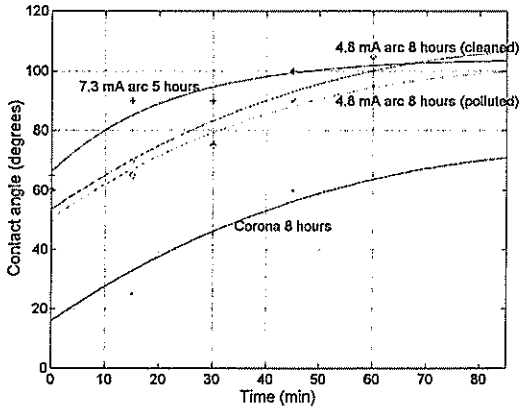

Figure 6. Graph showing recovery curves of hydrophobicity for the various samples tested (See *Table 1*).

These are only preliminary results, but they are consistent with the results obtained by Bhana [6]. A source of concern is that the samples exposed to long periods of arcing were quite hot after being removed (at least hotter than 50°C). It is possible that this increased temperature accelerates the chemical processes that govern the recovery of the silicone polymer. X-Ray Photoelectron Spectroscopy (XPS) needs to be performed on the test samples to obtain the surface and depth profile chemical analysis.

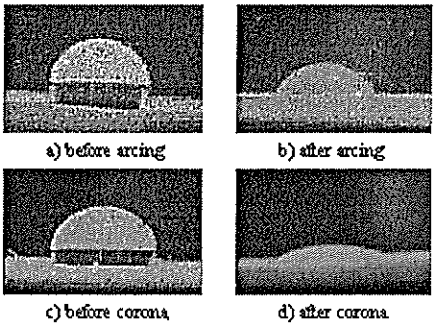

Figure 7. Contact angles for a 10 µl drop of water before and after the 8 hour test period.

7 CONCLUSIONS

1. Under heavy pollution, the field gradient is dominated by the pollution deposit and arcing can occur at any position where dry bands form. This is usually on the sheath, underneath a shed for vertically mounted insulators.
2. Corona onset due to a water drop on a NCI surface can be expected for a field strength of between 0.6 kV/mm to 0.75 kV/mm in the direction parallel to the surface.
3. The stacked shed design modifies the electric field distribution at the high voltage end of the insulator under clean and light pollution conditions. This ensures that water droplets cannot cause sufficient field enhancement to initiate corona on the sheath.
4. Under the test conditions used in this study, corona appeared to have more of an effect on the hydrophobicity of the silicone polymer than did arcing. This may be due to the acceleration of recovery caused by heating from the arcing.

8 REFERENCES

[1] A. E. Dickson and J. P. Reynders, "The effects of corona on the surface properties and chemical composition of silicone rubber insulators" in 9th ISH, Graz, Austria, 1995, 3231-1.

[2] A. J. Phillips, D. J. Childs and H. M. Schneider, "Aging of Non-Ceramic Insulators due to Corona from Water Drops", Accepted for representation, 1998 Winter Meeting, 98 WM 236, PES.

[3] S. M. Reynders, J. P. Reynders and I. R. Jandrell, "Recovery of Corona-Aged Silicone Rubber Insulation", Cigre, Cairo, Egypt, Sept. 1997, V-304.

[4] A. Toth, et.al., "Oxidative Damage and Recovery of Silicone Rubber Surfaces I. X-ray Photoelectron Spectroscopic Study", *Journal of Applied Polymer Science*, Vol. 52, 1293-1307, 1994.

[5] Suggestion made by Dr A. J. Phillips.

[6] D. K. Bhana and D. A. Swift, "An investigation into the temporary loss of hydrophobicity of some polymeric insulators and coatings", in Proceedings of the 4th Intl Conference on Properties and Applications of Dielectric Materials, Brisbane, 1994, 5208.

ENVIRONMENTAL PROFILE FOR KOEBERG INSULATOR POLLUTION TEST STATION (KIPTS)

L. Van Wyk **W.L. Vosloo** **J.P. Holtzhausen**

Department of Electrical Engineering, University of Stellenbosch, , Private Bag X1, Matieland, 7601

Abstract

An environmental profile has been established for Koeberg Insulator Pollution Test Station (KIPTS), situated along the Cape west coast. The profile indicates the factors that have a significant effect on the performance of ceramic and polymeric insulators. The profile includes the trends of yearly weather patterns, pollution sources in a radius of 20 km from KIPTS, and site severity measurements used to determine the influence of pollution fall-out on insulators. From the results, KIPTS can be classified as a site with a heavy pollution index. It has been found that it is crucial to implement the correct insulator profile for site severity measurements to obtain a correct pollution index.

1 INTRODUCTION

The integrity and performance of line insulation is very much dependent on the effects of meteorological and environmental factors. These are quantified by the measurement of weather parameters and pollution deposits, emitted from different sources. Various monitors are available to assess pollution severity. However, the monitor needs to be sensitive to the type of pollutant found at the area under test. This is achieved by evaluating the possible pollution sources and types in the greater area of the site, together with the dominant winds. From this the correct pollution severity monitors are chosen and used to classify the site according to a pollution index. The site can then be insulated for the correct level, in terms of mm/kV as prescribed by the IEC 815 [1].

2 WEATHER PATTERNS

The weather influences wetting cycles, ~~have~~ has temperature and UV radiation effects and the wind is a carrier and depositor of air-borne particles. These affect the surface condition of insulation and needs to be monitored.

Environmental conditions at KIPTS include dry summers, high temperatures, strong southerly (S, SE, SW) winds and occasional mist banks. Pollution levels are usually very high. Winters are characterised by high rainfall, frequent mist banks and moderate north-westerly winds. To quantify the weather conditions encountered at KIPTS, the following weather parameters were monitored:

- *Rainfall (mm)*
  This indicates to what extent natural washing, such as rain or mist, can occur on the insulator surface.
- *Wind speed (m/s) and direction (deg)*
  Wind is the main carrier and depositor of particles on the insulator surface. High winds can, however, lead to the removal of deposited dusts. The dominant wind direction can be obtained by studying the pollution on the underside of insulators. Dust and heavier particles usually accumulate on the lee-side of the glass disk.
- *Relative humidity (%)*
  High moisture levels cause salts in the contamination layer to dissolve, which form an electrolyte that allows leakage current flow.
- *UV solar radiation ($\mu W/cm^2$)*
  UV rays possess sufficient energy to penetrate the polymer of polymeric insulators, interact with the atoms and cause polymeric bonds to break.

3 POLLUTION SOURCES

KIPTS (indicated in the center of the map in figure 1) was constructed next to the Koeberg Nuclear Power Plant due to the unique environmental conditions and extremely high pollution levels in the area.

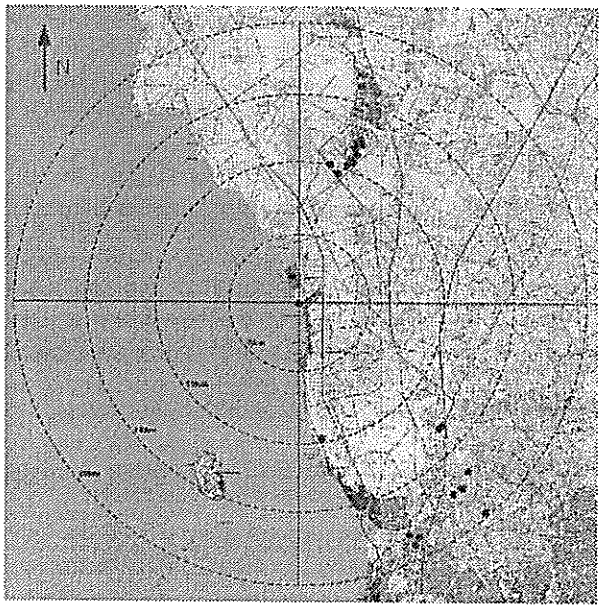

Figure 1 Map of pollution sources within a radius of 20 km from KIPTS

KIPTS is situated in a strategic position with regards to pollution for the following reasons:

The Atlantic Ocean lies to the west of the test station. Wave action, sea breezes/winds and periodic mist banks cause the high influx of moisture and salt particles. The salt causes a high marine pollution build-up on the insulator surfaces. The breakwater wall at the Koeberg Nuclear Plant north of KIPTS causes local mist banks to occur.

To the east a predominantly agricultural area (wheat, vineyards) is found, with occasional veld fires, ploughing, harvesting and crop spraying taking place.

North-east of KIPTS (10 – 13 km) an industrial area (Atlantis) emits burnt diesel, coal and heavy fuel oil (HFO) particles into the atmosphere.

10 km south of the test station a lime plant is stationed.

To the SSE heavy industries such as a fertiliser plant and oil refineries are the main cause of severe particle emissions.

In table 1 the main sources that surround and contribute to KIPTS' pollution are given:

Table 1: Table of pollution sources surrounding KIPTS

Area	Pollution Source	Direction from KIPTS	Distance from KIPTS	Type of pollution
Atlantis	Atlantis Diesel Engines (ADE)	NNE	10 km	Burn diesel and coal
	Aries Packing	NNE	12 km	Burn diesel
	Baja Industries	NNE	12 km	Burn HFO
	Barbican Investments	NNE	10 km	Burn coal
	Biopolymers	NNE	11 km	Burn HFF
	Unita	NNE	12.5 km	Burn scrapwood
	Promeal	NNE	10 km	Burn diesel and coal
	Rotex	NNE	12.5 km	Burn coal and HFF
	SA Fine Worsteds	NNE	13 km	Burn coal and HFO
Duinefontein	Koeberg Nuclear Power Plant	N	2 km	Burn diesel
Bloubergrand	Kilson Lime Works	SSE	10 km	Lime
Milnerton	Caltex Refinery	SSE	18 km	SOx, NOx, burn gas and oil
	Kynoch Fertiliser	SSE	18 km	NOx, CO2, and Particulate
	Fertiliser Producers	SSE	18 km	NOx, CO2, and Particulate
	Alpha Stone and Ready Mix	SE	17 km	Particulate
	FFS Refiners	SE	13 km	SO2,NO2 and burn HFF
	Wastetech	SE	13 km	Burn diesel
	CBS Cioli Brothers	SE	17 km	Particulate
	Tygerberg Quarries and Concrete	SE	20 km	Particulate
	More Asphalt	SE	17 km	Burn HFO

It can therefore be seen that the pollution in the KIPTS area comes from marine, agricultural and industrial sources. The particles become wind-borne and can be carried over extensive distances before fall-out occurs. This dust fall-out is the main contributor to the severe surface pollution layers found on KIPTS insulators.

Elemental analysis, using the EDAX method (energy dispersive analysis of x-rays) was performed on the contaminant collected in the dust gauges from the four wind directions. This indicated high levels of marine pollutant (Na, Cl, Ca), industrial (Mg, S, K, Al) and agricultural pollutant.

4 SITE SEVERITY MEASUREMENTS

The Round Robin Pollution Monitor Study Test Protocol, developed by the Cigré Task Force 33.04.03, was implemented at KIPTS to study the impact of environmental and meteorological factors that can have an effect on insulators in a specific area [2]. The study included the following tests performed on a monthly basis:

(i) ESDD (equivalent salt deposit density)

The ESDD value indicates the amount of soluble, conductive salts in mg/cm^2 on the insulator surface. The ESDD value usually differs for the top and bottom surface due to difference in the insulator profile and therefore aerodynamic catch properties. The ESDD measurements were performed on the U120BS (South African standard) glass cap and pin insulator and on the F160/146 (international standard) glass cap and pin insulator, both strings being unenergised. The F160/146 unit has a larger surface area and a deeper, more protected under-rib profile, compared to that of the more open-profile U120BS. The insulator is exposed to natural washing (rain, mist) of the pollution layer, especially during winter months. This cleaning effect decreases the ESDD value measured at the end of the month. The ESDD value is therefore a function of the environmental interaction with the insulator during the month.

(ii) NSDD (non-soluble deposit density)

The NSDD defines the amount of non-soluble inert deposits in mg/cm^2. These particles have little contribution to the conductance of the pollutant but rather act as binding material for the soluble salt particles. The NSDD measurements were performed on the same U120BS and the F160/146 insulators.

(iii) DDDG (directional dust deposit gauges)

Four directional gauges measure the amount of pollution deposit that an insulator would experience from each main wind direction. The gauge is designed to collect wind deposit rather than gravity deposited pollution, since the former is the main cause of pollution deposition on vertical insulator strings. The dust gauges accumulate pollution through the month and none is lost due to natural washing.

5 RESULTS

In figure 2 the monthly ESDD results for the F160/146, for the period August 1996 to September 1997, are given. Indicated in the figure is the IEC 815 pollution classification for ESDD levels.

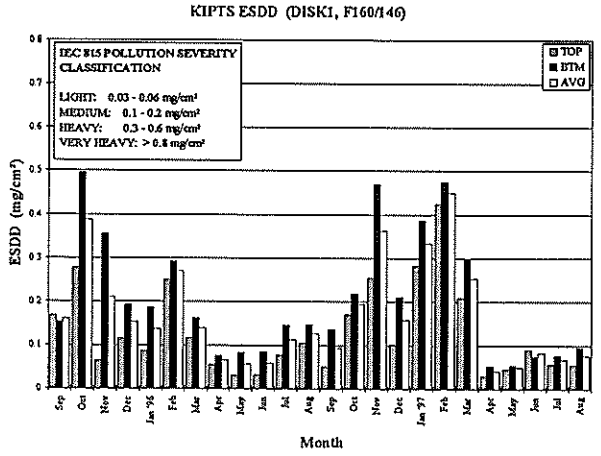

Figure 2 Results of monthly ESDD measurements on the F160/146 for a period of two years

Medium to heavy ESDD levels were measured during summer periods, and light to medium levels during the winter seasons. Similar trends, yet significantly higher ESDD levels, were measured with the U120BS insulator profile which was exposed to the same environment.

Statistically, the U120BS had a 70% and the F160/146 a 40% probability of indicating a medium severity at KIPTS. For heavy pollution indexes the U120BS indicated a 20% and the F160/146 a 5% probability. This supports the fact that the U120BS collects more pollutant per cm^2 due to its open profile.

The monthly NSDD results for the F160/146 for the same period are given in figure 3. A classification for NSDD levels, derived by Riquel, [3], are given in figure 3. No classification for NSDD has yet been published in the IEC 815.

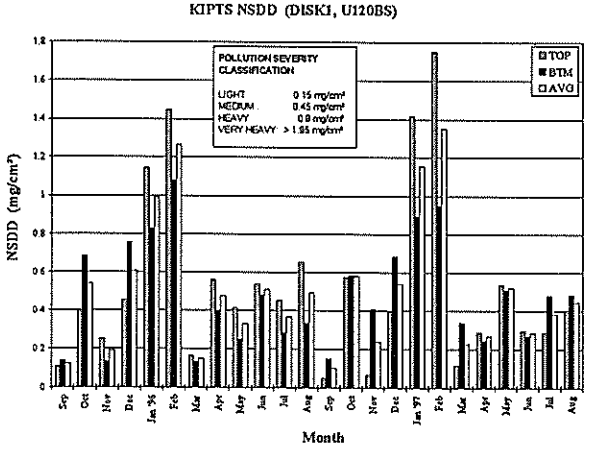

Figure 3 Results of monthly NSDD measurements on the F160/146 for a period of two years

Medium to heavy NSDD levels are measured during summer periods and light to medium levels during the winter seasons. This corresponds to the severity classifications indicated by the ESDD measurements. It is found, however, that the NSDD measurement is less sensitive than that of the ESDD. Statistically, the U120BS has a 55% and the F160/146 a 20% probability of indicating a medium severity.

If the effects of pollution and weather on insulators are considered, it can therefore be taken as a pre-deposit pollution (as described in IEC 507) layer with salt fog wetting.

If the rainfall trends are compared to that of the ESDD/NSDD it is seen that high rainfall coincides with low ESDD/NSDD levels and vice versa. The rainfall for the two year period is given in figure 4.

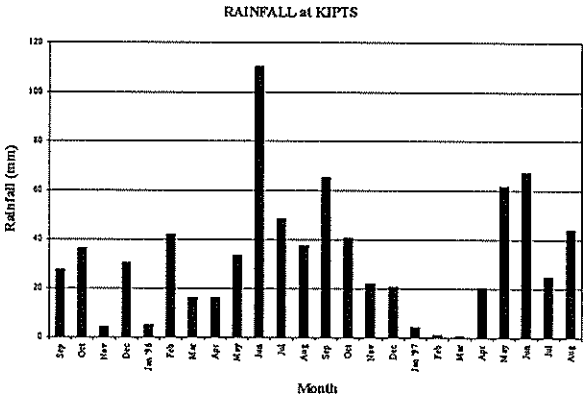

Figure 4 Rainfall measurements for a period of two years at KIPTS

It is expected that an environment has a specific maximum severity level, usually obtained during the drier season. The line insulation level, in terms of the minimum creepage distance, is determined from that maximum pollution severity level.

However, by comparing the results obtained for the F160/146 and the U120BS, it is found that the ESDD severity levels indicated, differ between the two profiles by an average factor of 1.5 for the same site. It is difficult to correctly and accurately define the severity behaviour of an area. However, the behaviour of the insulator *with respect to the area* can well be verified. Each insulator profile will interact differently with the environment due to the aerodynamic properties and thus indicate dissimilar severity levels. It is therefore of great importance to use the correct insulator profile if a site severity needs to be established [4].

The pollution deposit in the dust gauges, accumulated over one monthly periods, are given in figure 5.

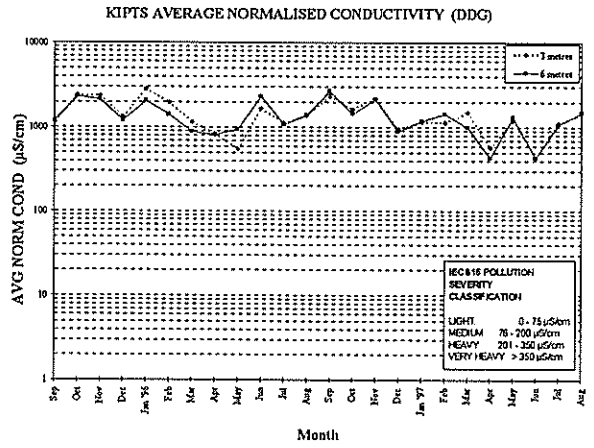

Figure 5 Results of monthly DDDG measurements for a period of two years at KIPTS

It is seen that the DDDG defines KIPTS as a site with a very heavy pollution severity throughout the two year test period, unlike that found with the ESDD and NSDD results. This is attributed to the accumulated pollution in the dust gauge, compared to an insulator surface exposed to natural cleaning. From figure 5, a 100% probability for the dust gauge level to indicate a very heavy pollution severity, can be seen. The southern and eastern gauges contain pollutant with the highest conductivity.

In figure 6 the wind parameters for the two year period are given. This indicates wind trends during the summer and winter seasons. The wind directions indicate whether high or low pollution influx has occurred from the various sources. Wind speeds influence the movement, deposition and removal of pollution particles. It has been found that southerly winds contribute predominantly to the high pollution levels and pollution build-up is usually greatest on the southern side of polymeric insulators.

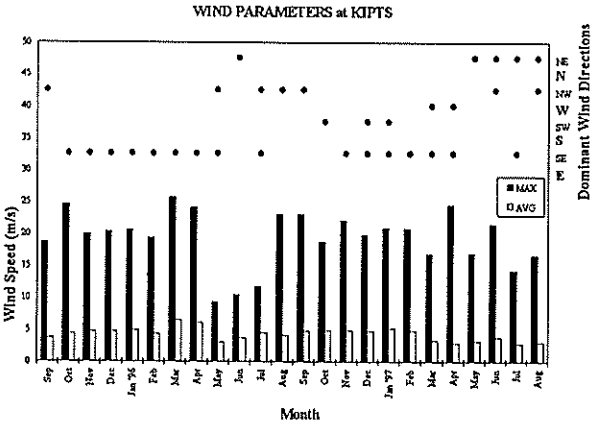

Figure 6 Results of wind speed and direction for a period of two years at KIPTS

6 CONCLUSIONS

The impact of weather patterns and pollution on a specific area is determined. It has been found that wind parameters and natural wetting play a significant role in the accumulation or removal of pollution from insulation surfaces.

KIPTS has been classified as a site with a medium to heavy pollution severity, using the ESDD and NSDD results. The dust gauge results (DDDG) indicate a very heavy polluted site. If the three monitors are used together to obtain the pollution index at KIPTS, the NSDD indicates the lower severity level, the DDDG the higher and the ESDD an average monthly site severity value.

The type of pollution at KIPTS can be described as a combination of heavy marine, industrial and agricultural pollutants. The insulators at KIPTS therefore contain a pre-deposited pollution layer and are exposed to natural salt fog wetting.

It was found that the F160/146 and U120BS insulator profiles had similar ESDD trends. However, all measurements of the U120BS were higher than the F160/146. This indicates that insulators respond and interact differently to the same environment. This is due to the difference in profile and its effect on the aerodynamic properties. Therefore, if the correct insulation level of a line needs to be found, care should be taken in selecting the correct insulator profile.

7 ACKNOWLEDGEMENTS

The authors acknowledge the key role of Eskom in supporting the research on which this paper is based and the assistance of colleagues within the Eskom Insulator Study Committee who have contributed to the work.

8 REFERENCES

[1] IEC Publication 815, "Guide for the selection of insulators in respect of polluted conditions", 1986.

[2] Cigré Task Force 33.04.03, "Round Robin Pollution Monitor Study Test Protocol", 1993.

[3] Riquel G., Spangenberg E., Mirabel P., Saison J.K., "Wetting processes of pollution layer on high voltage glass insulators", 9th Intern. Symp. on HV Engineering, Graz, Austria, 28 Aug. – 1 Sept. 1995.

[4] Van Wyk L., "Insulator pollution monitoring: evaluation of various methods of severity measurements at a coastal site", Masters thesis, University of Stellenbosch, December 1996.

A UNIFIED APPROACH TO AC INSULATOR FLASHOVER MODELS
Part I : DC Models adapted for AC

J P Holtzhausen, D A Swift*, F S van der Merwe

Department of Electrical and Electronic Engineering
University of Stellenbosch
Stellenbosch, South Africa
University of Natal

Abstract: In this paper, the first of two companion papers, the fundamental principles underlying insulator pollution flashover are discussed. Firstly, a model for DC energisation is discussed, including the fundamental phenomena, responsible for flashover. Thereafter the implications of AC energisation are discussed. It is shown that, provided reignition occurs every half cycle, the DC model can be used for AC with adjusted arc constants.

Keywords: Insulator pollution, modelling

INTRODUCTION

Air at ambient pressure and temperature is the primary insulation on outdoor power lines and substations. The dielectric strength of the insulators, used to position the high voltage conductors, is higher than that of air. With proper insulation coordination, systems can be designed to withstand the highest expected lightning and switching surge voltages. The surface of these insulators, when covered by a conducting pollution layer, therefore often turns out to be the weak point in the insulation system. The conducting layers derive from saline fog near the coast or from industrial pollutants, wetted by natural fog. Looms [1] refers to this phenomenon as "*the apparent paradox whereby catastrophic electrical discharges are produced, spanning up to several metres of air, by voltages that would normally not result in breakdown of air clearances of only a few centimetres*".
A power system that is well designed from a lightning- or switching surge- point of view for dry and clean insulation, may be unreliable in the presence of surface pollution. The pollution testing of insulators is time consuming and expensive and it has been a quest for many years to develop a theoretical model that would replace costly testing. The nature of the phenomenon, however, defies exact mathematical treatment, not only because of the stochastic nature of the pollution deposition and weather parameters, but also due to uncertainties relating to the actual flashover mechanism and the values to employ for the various parameters.

AIR FLASHOVER, CORONA AND ARCS

The evolution of discharges and arcs in the case of air flashover can be explained, referring to Fig. 1 If a direct voltage between two electrodes in a gas is raised gradually, the voltage/current characteristic shown in Fig. 1 is obtained. Initially, electron avalanches lead to Townsend discharges, until the sparking potential V_s is reached. At this point stable glow and abnormal glow corona sets in. Eventually the glow discharge changes into an arc. A characteristic of an arc is that more or less constant voltage drops occur near the cathode and anode, respectively. The longitudinal voltage gradient in the remainder of the arc between the electrodes (the positive column) is constant, determined by the gas, pressure and arc current. The high pressure positive column of the arc consists of a plasma with a temperature higher than 5000 K and is maintained by thermal ionization. Cobine [2, p. 292] states that the current density of the arc is practically independent of the arc current.

An important property of the arc is its negative resistance characteristic, i.e. the voltage decreases with increasing current. This instability feature that plays an important role in the flashover process can be explained by considering the heat exchange of the arc.

Heat exchange of a cylindrical arc:
Von Engel [3] modelled the arc as as a cylindrical column and analysed the heat exchange thereof. In the

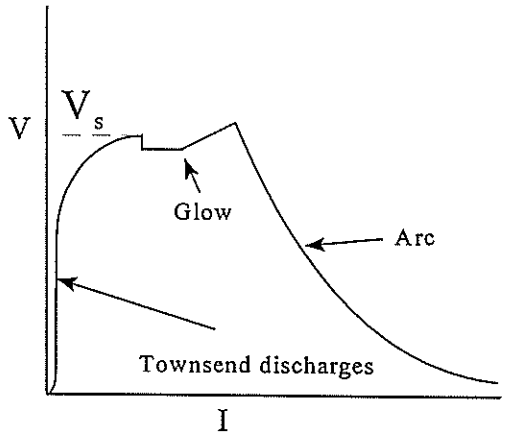

Fig. 1: V-I characteristic for DC discharges and arc in a gas discharge tube.

following equation the heat input per unit length into the arc is given by the left hand side. The two terms on the left hand side reresent the radiation and cooling losses, respectively.

$$I\ E = P_R(T) - 2\pi R_b \Lambda \left(\frac{dT}{dr}\right)_{R_b} \qquad (1)$$

where T: gas temperature in K
R_b: arc boundary radius in m
Λ: thermal conductivity of the gas in W/(K.m)
$P_R(T)$: radiation losses in W/m

Substitution of the the following radial temperature profile (T_r, T_0 at r and R_b , respectively)

$$\frac{T_r}{T_0} = \left(\left(\frac{r}{R_b}\right)^2 + 1\right)^{-1} \qquad (2)$$

the following result is obtained:

$$E = \frac{E_R(T) + \pi \Lambda T_0}{I} \qquad (3)$$

This equation is a special case, with a =1, of the Ayrton equation,

$$E_a = A\ I^{-a} \qquad (4)$$

wherein A and a are constants.

POLLUTION FLASHOVER

The flashover mechanism of polluted insulators differs markedly from that of air gaps and clean surface flashover. Pollution flashover is characterised by the following points when compared with normal air flashover:

- a much lower flashover voltage
- a much slower breakdown process
- a much higher current is involved during breakdown, making test equipment expensive
- the radiation of light (yellow for sodium chloride) with a colour different from the bluish light radiated during air flashover.

These differences are due to the presence of a conducting layer, consisting of electrolyte, over part or all of the distance between the electrodes. Possible sources of the electrolyte are: wind-driven salt spray or wetting of a previously deposited dry pollution layer. Leakage current flows over the surface of the insulator. Due to heating, the temperature of the layer increases and its resistance drops (an electrolyte has a negative resitance- temperature coefficient), causing an initial increase in leakage current. Once the electrolyte reaches boiling point, evaporation starts with the result that the layer thickness is reduced and the salt or acid concentration is increased. The nett effect is a relatively constant leakage current during this stage. When the electrolyte exceeds its saturation level, further heating results in the precipitation of the salts and the formation of dry bands. These dry bands often occur on the narrow sections of the insulators where the highest current density exists and also in shielded portions of the insulator where the pollution and/or the wetting is less. Such shielded areas are usually adjacent to end fittings and under the insulator sheds.

Since a large portion of the applied voltage appears across the dry band, glow and pulse corona discharges will occur across these dry bands, eventually leading to arc formation, as shown in fig. 2. Under certain circumstances these arcs grow to such an extent that they sweep across the pollution layer, causing flashover of the insulator.

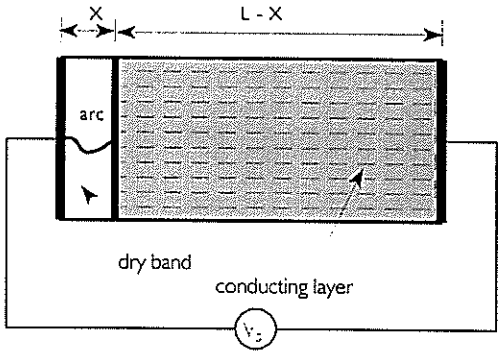

Fig. 2: Conductive layer with arc across dry band.

A DC MODEL, ADAPTED FOR AC

DC arc maintenance criteria

Obenaus [4] provided the first analysis of the pollution flashover phenomenon. He showed that the unexpectedly low flashover voltages of polluted insulators when compared to clean insulators arose due to the interaction of the negative (and nonlinear) arc resistance, and the linear resistance representing the pollution layer. This is shown schematically in the equivalent circuit of Fig. 3 where a voltage V_S is applied to the insulator. In accordance with eq. (3), the arc is represented by the following voltage-current characteristic:

$$V_a = A\ X\ I^{-a} \qquad (5)$$

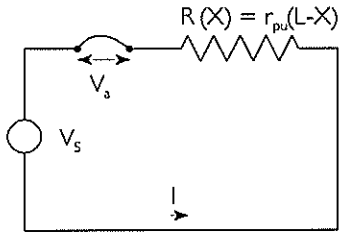

Fig. 3: Equivalent circuit of Fig. 2.

where V_a: arc voltage
A, a: arc constants
X: length of the arc and dry band

The voltage equation for the complete circuit, shown in Fig. 3, is therefore

$$V_s = V_a + R(X)\, I \qquad (6)$$

where R(X): the resistance of the conducting layer from the arc root to a metallic conductor of width W, spaced at distance L-X from the arc root, and
I: the leakage current (A).

In eq. (6) the anode and cathode voltage drops on the electrolyte and the metal electrode have been ignored. The sum of these voltages is estimated to be of the order of 400 V [Alston 1969] and can be assumed to be negligible if the applied voltage exceeds a few kilovolt.

The linear R-X relationship,

$$R(X) = r_{pu}\,(L\text{-}X) \qquad (7)$$

can be assumed when L - X is long relative to the region of current concentration near the arc root (with r_{pu} the resistance per mm).

By way of illustration of the stability problem that causes flashover, consider eqs. (5), (6) and (7) with the following typical parameter values: L = 100 mm, r_{pu} = 100 ohm/mm, A = 10 and a=0.5. The individual terms on the right hand side of eq. (6) are shown in Fig.4 for X=67 mm, using the above numerical values. The sum of the terms represents V_s, the supply voltage. The leakage current, I, corresponding to V_s, can be read from this curve. It will be noted that the V_s - I -curve has a minimum value, V_{min}. If the supply voltage drops below this value, no stable arc is possible. In Fig. 5, curves of the required supply voltage for different arc lengths are

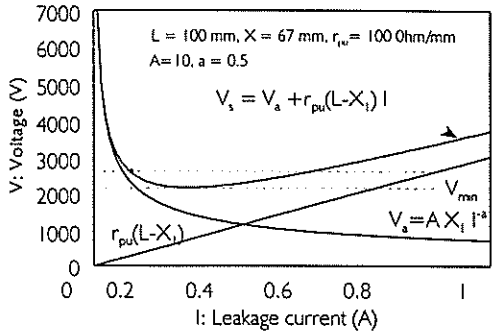

Fig. 4: Supply voltage required as a function of leakage current (X = 2L/3)

shown. Note that V_{min} is different for each value of X and that the highest value, the critical voltage, V_c, occurs for X = 2 L/3 = 67 mm. The significance of this fact is that, if $V_s > V_c$, stable arcs can exist for all values of X, and that the arc will bridge the whole length of the insulator, i.e. it will flashover. The corresponding critical current, I_c, is also shown in Fig. 5.

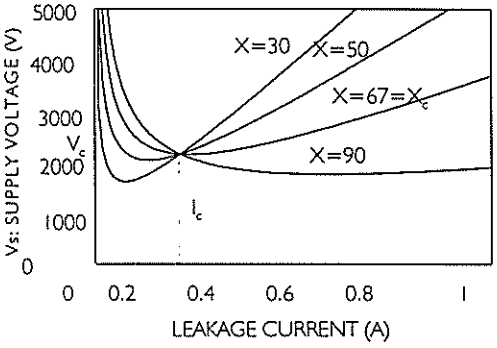

Fig. 5: Supply voltage as a function of leakage current for varying values of X.

Alston [5] formally analysed the above interrelationship of the variables X, V_S and I, that affect the arc stability. He arrived at the following relationship for the critical voltage stress, E_c, leading to flashover:

$$E_c = A^{\frac{1}{a+1}}\, r_{pu}^{\frac{a}{a+1}} \qquad (7)$$

where $E_c = V_c/L$ and V_c is the critical value of the supply voltage.

This occurs at an arc length, X_c, of

$$X_c = \frac{L}{a+1} \qquad (8)$$

The corresponding critical current, I_c, is

$$I_c = \left(\frac{A}{r_{pu}}\right)^{\frac{1}{a+1}} \qquad (9)$$

The arc constants A and a have been determined empirically by Alston as A = 6.3 and a=0.76. These values are called the *"basic DC values"* further on. When the basic values are used, E_c, the critical stress in V/mm is given by

$$E_c = 2.85\ r_{pu}^{0.43} \qquad (10)$$

with r_{pu}: the resistance in ohm / mm.
It follows from equations (7) and (9) that

$$E_c\ I_c^a = A \qquad (11)$$

In the case of AC energisation the polarity reverses twice per cycle and the arc may extinguish at or before the current zero crossings. Furthermore the arc may reignite during the next cycle. Nishimura [6] suggested that the flashover process consists of the following stages: *reignition, propagation and extinction.* These conditions are explained diagrammatically in Fig. 7.

Although the Obenaus formulation, given in eq. (6), strictly only applies for DC energisation, it is applied in this work to the AC case. With DC energisation a constant voltage stress is applied to the insulator, theoretically resulting in a constant leakage current. In the AC case, as shown in Fig.6, a "block " of voltage with width T_p and average height slightly less than the sinusoidal peak is applied every half-cycle, resulting in leakage current pulses of roughly the same duration.

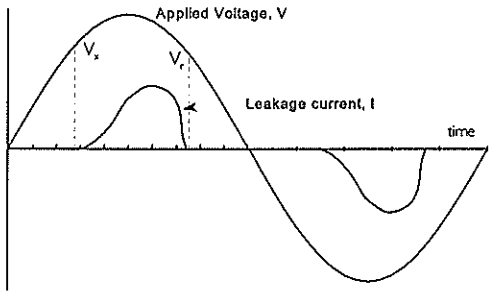

Fig.6 : Schematic presentation of leakage current pulses , showing the reignition (V_r) and extinction (V_x) voltage levels and propagation period, T_p

If the energy balance equation, given in eq. (1) is therefore applied to the AC energised case of Fig.6, the *rms-values of I and E* should clearly be used to represent the power source on the left hand side of the equation. For the current and voltage waveforms shown in Fig. 7, the heating effect of the column will evidently be appreciably less than that of constant DC energisation with current and voltage stress equal to the peak values. In the AC case, the thermal ionization will therefore be less, resulting in a higher arc resistance. Based on the above argument, it is to be expected that the current peak in the AC case will be lower than the values obtained by applying the DC theory of eqs. (6) and (7), when V is made equal to the peak value of the sinusoidal voltage. The theory could, however, still be applied for AC, using the peak voltage but then a higher value of A must be used to allow for the lower arc temperature (T_0 in eq. (3)).

CONCLUSION:

It appears that the DC model can be successfully applied in the case of AC pollution flashover, provided the arc constants are adjusted for the incomplete thermalisation of the arc. The case where a reignition constraint is considered is discussed in the companion paper. The DC and AC reignition models are also compared with each other.

The situation when reignition does not occur every half cycle is dealt with in the companion paper. A comparison is made between the two models.

REFERENCES:

1. Looms J. S. T., "Insulators for High Voltages", Peter Peregrinus, London, 1988.
2. Cobine, J. D., *Gaseous Conductors: Theory and Engineering Applications*, Dover Publications Inc., 1941.
3. Von Engel, A., *Ionized Gases*, Oxford at the Clarendon Press, 1965.
4. Obenaus, F., "Fremdschichtüberschlag und Kriechweglänge", *Deutsche Elektrotechnik*, Vol. 4, 1958.
5. Alston, L. L., "Growth of discharges on polluted insulation", *Proc. IEE*, Vol. 110, No. 7, pp. 1260-1266, 1963.
6. Nishimura, S., "Evaluation of Flashover Characteristics of Polluted Insulators", Fifth International Symposium on High Voltage Engineering, Braunschweig, 1987.

A UNIFIED APPROACH TO AC INSULATOR FLASHOVER MODELS
Part II: AC Reignition Models, compared to DC models.

J P Holtzhausen, D A Swift*, F S van der Merwe
Department of Electrical and Electronic Engnieering
University of Stellenbosch
Stellenbosch, South Africa
*University of Natal

Abstract: In this paper the principles introduced in the first of the two companion papers are further developed. It is shown that, under certain conditions the arc across the dry band fails to reignite. The reignition phenomenon is analysed and the flashover model is modified to include the reignition criterion. The equivalence of the two models is investigated. It is found that the simple DC model cannot accurately represent flashover and leakage current data.

Keywords: Insulator pollution, modelling

1. INTRODUCTION

In a companion paper the application of DC models to AC energised insulators is discussed, using the equivalent circuit, shown in Fig. 1. It was shown that the DC models can be applied in the case of AC, provided the phenomena of premature arc extinction and arc reignition, following a current zero, are allowed for. It is shown that this can be done by choosing a higher arc constant than would be chosen for DC

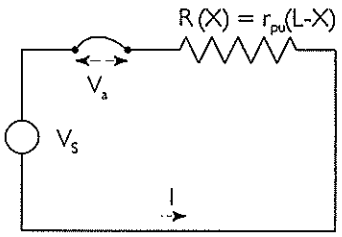

Fig. 1: Equivalent circuit for AC energised insulator

energisation, provided reignition takes place every half-cycle. It was also explained that, if the DC theory is applied to the case of AC energisation, V_s and I should refer to peak values . As before, the circuit equation for Fig. 1 can be written as:

$$V_s = V_a + r_{pu} (L-X) I \qquad (1)$$

In the above analysis, the supply voltage was varied while keeping r_{pu} (the pollution) constant. Fig. 2 shows an alternative representation where the supply voltage is kept constant while the pollution severity (r_{pu}) is allowed to vary. This condition is similar to that existing in the field.

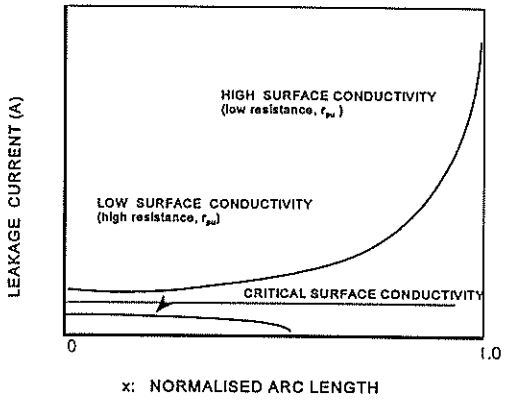

Fig. 2: Leakage current as a function of the normalised arc length, x = X/L with varying pollution severiry.

One limitation of the above model is that it does not allow for the case where the conditions in the arc are such that reignition does not occur at all in the next cycle. A typical case in point is shown in Fig. 3 where the arc eventually fails to reignite. This failure to reignite could be due to

- loss of heat and ionization, following

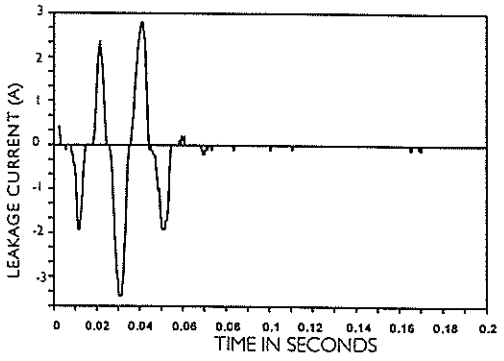

Fig. 3: Leakage current waveform, showing the failure to reignite.

extinction,
- excessive length of the arc,
- the current in the previous half-cycle being too low as a result of the drying out of the insulator surface.

The conditions that determine arc reignition, following extinction in the previous half-cycle, are discussed in this section.

Rizk [1] analysed the difference between AC and DC pollution flashover and investigated the reignition process. He pointed out the existence of two possible mechanisms of arc reignition: the *energy balance* and the *dielectric breakdown* mechanisms. In the energy balance mechanism the post zero current between the electrodes causes thermal breakdown near the current zero. In the dielectric breakdown model the gap is treated as a hot gas and reignition takes place considerably later in the half cycle. Rizk analysed both models and concluded that the dielectric breakdown model is more applicable to insulator pollution flashover. He derived an analytical relationship for the reignition voltage and showed that it is a function of the arc length and the current during the previous half cycle. The dielectric breakdown model can be used to explain the reignition phenomena.

Experimental evidence of the reignition process was also provided by other researchers. Jolly [2] measured reignition angles during wet contaminant tests on a circular disc. In one test the angle increased from half cycle to half cycle as drying of the layer progressed and eventually flashover occurred at an angle of 75 degrees. In another test, with a lower pollution severity, the reignition angle increased to 99 degrees when all activity ceased. Johnson[3] observed that, as the severity of leakage current activity increases during steam fog testing of insulators, the reignition angle decreased from 70 degrees to a value between 20 and 5 degrees at the point of no return, just before flashover.

The Dielectric Reignition Model Due to Rizk

In this model Rizk [4] assumes that the electrical conductance of the arc practically vanishes at the zero of the current wave. The residual gap is treated as a cylindrical hot gas column that cools down from an initial temperature of 3000 K, mainly by conduction. He solved the energy balance partial differential equation of the residual plasma in terms of radial distance from the arc axis and time, eventually arriving at the following equation for the dielectric strength, E_d :

$$E_d = E_{da}\left(1+\frac{51.9}{1+(0.00567/R_b^2)\,t}\right)^{-0.636} \qquad (2)$$

where E_{da} : dielectric strength of the gap at ambient temperature (300 K) in V/mm
t: time in seconds
R_b: arc boundary radius in m.

This equation is based on empirical gas constants, valid over the temperature range 300 to 3000 K and the assumption that the dielectric strength is inversely proportional to the absolute temperature.
The arc boundary radius, R_b , depends on the current in the arc (the power input) and on factors such as the ambient atmosphere, wind speed and the proximity of the insulating surfaces (the cooling effect). For known conditions, an expression can be determined relating R_b to the maximum current in the arc during the previous half-cycle in the arc, I_r. Rizk derived such an expression and after substitution in eq. (2), the following relationship resulted:

$$E_d = 0.113\ E_{da}\ I_r^{-0.53} \qquad (3)$$

It was found that this equation shows acceptable agreement with measured test data.
For a nonuniform gap, E_{da} was taken as 523 V(peak)/ mm, leading to

$$E_d = 59\ I_r^{-0.53} \qquad (4)$$

The significance of eq. (4) is that the arc will reignite, provided the voltage across the gap exceeds the reignition voltage, $V_r = X_a E_d$, i.e.

$$V_r = N\ X_a\ I_r^{-n} \qquad (5)$$

where I_r : the peak current in the previous half- cycle in A (peak),
N = 59 and n = 0.53: arc reignition constants
X_a: arc length in mm.

Based on a large number of tests, Claverie [5] also established, empirically, that the relationhip in eq. (5) with A = 80 and n = 0.5 fits the test data.

The supply voltage, V_s, to produce flashover is therefore not only determined by eq. (1), but also by the constraint,

$$V_s > V_r \qquad (6)$$

The solution of eq. (1) is obtained in the following form:

$$I = G_1(\sigma, X),$$

while eq. (5) can be written in the form:

$$I_r = G_2(E, x),$$

where G_1 and G_2 are function operators.
These two functions are shown in Fig. 4. If it is assumed that, after a restrike, the current will reach a peak value roughly equal to that attained in the previous half-cycle, it can be assumed that $I \approx I_r$. The coordinates of the

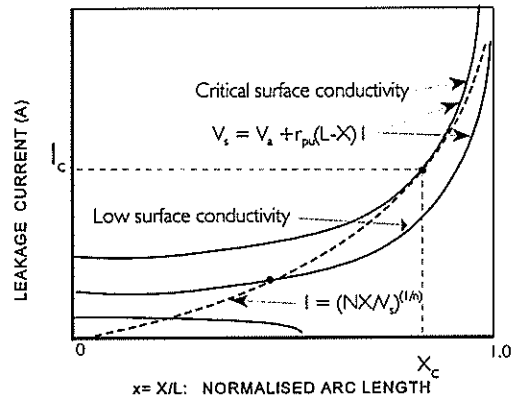

Fig. 4: "DC" flashover curve and reignition curve.

intersection of the two curves therefore represent the solution of the two equations and give the arc root position and the leakage current associated with the surface conductivity. It will be noted that, at the critical surface conductivity, the two curves intersect tangentially and that the exact point of intersection is somewhat indeterminate.

For the case without an arc root, the partial derivatives, $\partial I/\partial x$ and $\partial I_r/\partial x$, are evaluated for eqs. (1) and (5). By equating these two derivatives and also making $E = E_r$ and $I = I_r$ the critical normalised dry band (or arc length as $k_c=1$), x_c, is obtained.

$$x_c = \frac{1 - (a-n+1)\ A/N\ I^{-(a-n)}}{n+1 - (a+1)\ A/N\ I^{-(a-n)}} \qquad (7)$$

It will be noted that, if a = n, as often is the case, $x_c = 1/(n+1)$. For the values, used by Rizk [6] (A= 6, N = 59, a=0.83 and n= 0.53, for currents up to 3 A) , x_c is found to be approximately 0.65, i.e. $x_c \approx 1/(n+1)$, as is also confirmed by inspection of eq. (7). This is also shown in Fig. 5, where the maximum value indicates the flashover stress capable of maintaining the arc for all x. In a paper [4] , Rizk presents the same results, but makes the invalid conclusion from the graph, that $x_c = 1/(a+1) = 1/(1+0.83) = 0.575$. His proof of this statement, using dimensional analysis, is also not correct. The source of the inconsistency is unclear, but

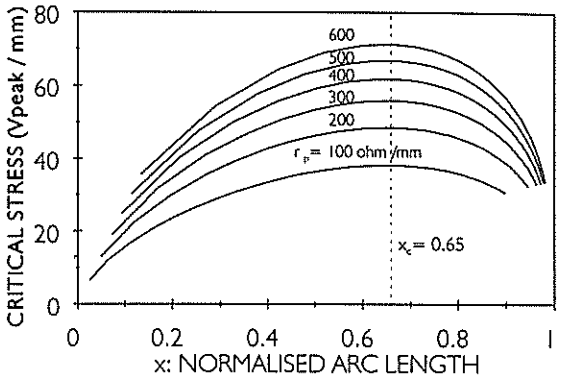

Fig. 5: Variation of the critical stress with average pollution resistance per unit length [Rizk 1971b].

is probably based on invalid assumptions, regarding the equivalent recovery time constant. Eq. (7) is however correct and confirms the importance of the reignition constants over the arc constants.

Based on the data in Fig.5, the formula given by Rizk, should be

$$E_c = 7.6\ r_{pu}^{0.35} \qquad (8)$$

instead of

$$E_c = 5.8\ r_{pu}^{0.4} \qquad (9)$$

Discussion of the reignition models of Rizk and Claverie

From the above it is clear that the mathematical treatment of the methods of Rizk and Claverie is similar, although the numerical values of the constants used are different. The main difference is that the reignition criterion of Rizk was derived from thermodynamics, while that of Claverie was obtained empirically. However, also in Rizk's method, some empirical constants and simplifying assumptions were necessary.
Rizk also used his dielectric recovery model to analyse the AC source-insulator interaction in HV pollution tests [7].

The equivalence of the AC and DC models:

In Table 1 the equations of the DC model and the AC reignition model are compared. It is clear from this table that, in the AC model, the consants N and n , to some extent, assume the roles of the constants A and a in the DC model. Based on equivalent flashover stresses the following relationship is required:

Table 1: Comparison of AC and DC Models:

DC Model	AC Model
$E_c = \frac{V_c}{L} = A^{\frac{1}{a+1}} r_{pu}^{\frac{a}{a+1}}$	$E_c = \frac{1}{n+1} N (N-A)^{-\frac{n}{n+1}} n^{\frac{n}{n+1}} r_{pu}^{\frac{n}{n+1}}$
$I_c = (\frac{A}{r_{pu}})^{\frac{1}{a+1}} = (\frac{A}{E_c})^{\frac{1}{a}}$	$I_c = (\frac{N}{(n+1)E_c})^{\frac{1}{n}}$
$X_c = \frac{L}{a+1}$	$X_c = \frac{L}{n+1}$

$$A = \frac{N}{n+1} \left[\frac{Nn}{(N - A_{ac})(n+1)}\right]^n \qquad (10)$$

Comparison of leakage currents, on the other hand, leads to:

$$A = \frac{N}{(n+1)} \qquad (11)$$

In these equations A refers to the DC model arc constant, A_{ac} to the AC model arc constant and N to the AC reignition constants. The equations are also based on the assumption that a = n.

The conflict between eqs. (10) and (11) is evident. Thus, a value of A can be found to match the AC flashover stress equation, but then the leakage current characteristics would be different. Where $N >> A_{ac}$, eqs. (10) and (11) however correspond approximately.

DISCUSSION

The DC theory is often used to analyse AC flashover phenomena. Where reignition occurs every half cycle, this can be allowed for by using a higher value of A. However, if the reignition criterion needs to be considered, the model becomes more complex and a simple equivalence does not exist between the models. The DC model cannot represent both the flashover voltage and critical leakage current accurately.

In this analysis the effect of the current concentration at the arc root was neglected. It can however be shown that its effect can be allowed for by adjusting the reignition constant [8].

REFERENCES:

1. Rizk, F. A. M., "Mathematical models for pollution flashover", *Electra*, Vol. 78, pp 71-103, 1978.

2. Jolly, D.C., "Contamination flashover, Part 2: Flat plate model tests", *IEEE Trans. on PAS*, Vol. 91, pp. 2443 - 2451, 1972.

3. Johnson, J. et al., "Field and laboratory tests of contaminated insulators for the design of the State Electricity Commission of Victoria's 500-kV system", *IEEE Trans. on PAS*, Vol. 87, pp. 1216 - 1239, 1968.

4. Rizk, F. A. M.," Analysis of dielectric recoverywith reference to dry-zone arcs on polluted insulators", *IEEE Conference paper No. CP 134-PWR, 1971.*

5. Claverie, P.,"Predetermination of the behaviour of polluted insulators", *IEEE Trans. on PAS*, Vol. 90, pp. 1902 - 1924, 1971

6. Rizk, F. A. M., "A criterion for AC flashover of polluted insulators", *IEEE Conference paper No. CP 135-PWR, 1971*

7. Rizk, F.A.M., Nguyen, D.H., "AC source-insulator interaction in HV pollution tests", *IEEE Conference paper No.83SM452-0,*1983.

8. Holtzhausen, J. P., *A critical evaluation of AC pollution models for HV insulators having hydrophilic surfaces*, Ph. D. thesis, University of Stellenbosch, 1997.

A PROCESS CONTROL SYSTEM FOR A TYRE CURING PRESS

A RETIEF[1] and T VAN NIEKERK
E-mail: theoian@ml.petech.ac.za
Department Digital Systems Engineering, Faculty of Electrical Engineering, Port Elizabeth Technikon, Port Elizabeth, Republic of South Africa

ABSTRACT

To succeed in a competitive global environment a manufacturer requires highly informed workers, advanced production equipment as well as a far-reaching organizational strategy involving factory automation systems [10]. Automation technologies and manufacturing strategies are available worldwide today, however, every business is unique in the way it converts raw material to finished products and this implies that there is no single "plug and play" magical solution offered by a single vendor. Supervisory Control and Data Acquisition (SCADA) software can play a pivotal role in the development of these unique solutions [11][12]. This paper outlines the design and implementation of a complete process control system for a tyre vulcanizing press involving Wonderware's[2] Intouch SCADA software package operating on a Mitac industrial computer linked to a Siemens S5-95U PLC and the company network.

Keywords: Dynamic Data Exchange (DDE), Graphical User Interface (GUI), Human Machine Interface (HMI), Proportional Integral Derivative (PID).

1. INTRODUCTION

The implementation of automation technology is vital component of any modern manufacturing environment [1]. Fierce internal and external competition and rising costs of materials and labour are forcing South African companies to re-examine every aspect of their operations [2]. As manufacturing contributes to a high proportion of production costs, systems need to be put in place to eliminate waste, continuously improve production processes, increase resource utilization and control downtime.

SCADA systems, if designed correctly play an important role in providing information from the shop floor operator level to the board room level of a company. Information from SCADA systems can be provided in real time allowing critical production decisions to be made instantly by senior management. No manufacturing concern can run effectively and efficiently if the production information received is not of the highest standard and up to date.

Gentyre Industries, is in the process of refurbishing and upgrading a number of machines in the factory both electrically and mechanically with new state of the art process control systems. Their intention is not only to increase machine utilization, tyre production and overall product quality, but also to keep in step with the rapidly advancing trends in factory automation and in particular focusing on the field of SCADA.

One specific type of machine under the spotlight for refurbishment and upgrading is the 42-inch tyre curing (vulcanizing) press. It has slow and outdated relay logic control systems that are: Very difficult to maintain, to make changes on and is operator unfriendly. The solution and research project is therefore to design a complete process control system which would optimize this process and not only cater for current needs but also for future needs within this specific area of the company. The research project included the electrical control system design, the PLC control software design and programming as well as the SCADA software design and programming of the operator interface or HMI for the tyre curing press.

The tyre curing press could simply be described as a giant jaffle machine that contains two heated segmented moulds that surround the tyres to vulcanize them for a specified time during a curing cycle. The segmented moulds, which contain the specific tyre's tread pattern, are heated and controlled to about 174 °C by means of super heated steam. As the two tyres are automatically loaded into the press for curing,

[1] Andre Retief is a Project Engineer at Gentyre Industries.
[2] Wonderware Intouch is a trademark of the Wonderware Corporation.

bladders are inflated by steam inside the tyres so that they maintain their shape as the moulds close around them. The bladders also serve the purpose of curing the tyre from the inside during the curing cycle. A curing cycle lasts approximately 11 minutes after which the steam is shut off, the bladders are drained, then vacuumed to remove any residual steam and the press's bridge opens for the tyres to be automatically removed by unloaders and placed onto offloaders behind the press where the tyres cool down for about nine minutes.

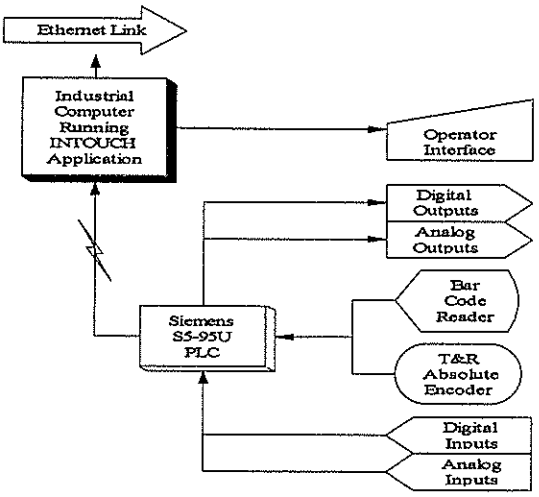

Figure 1

2. ELECTRICAL CONTROL SYSTEM

Figure 1 shows a block diagram of the complete process control system including:

- Siemens S5 95U PLC with dual serial ports, one of which is connected to a Mitac industrial computer running the SCADA application,
- Electrical inputs: absolute optical encoder, inductive proximity switches, photoelectric sensing devices, thermocouple and PT100 temperature probes, steam pressure sensors, limit switches and pushbuttons,
- Electrical output devices: steam control valves, semiconductor relays, solenoid control valves and motor contactors.
- A barcode reader connected to the PLC via a Siemens CP521 communications module. The function of the barcode reader is access control to the SCADA control system [7].

Due to heat considerations within this part of our factory, where the ambient temperature may be as high as 45°C in summer it is very critical to choose the correct digital and analog electrical devices which will be sending information to the PLC or receiving information from the PLC.

3. PLC SOFTWARE DESIGN AND PROGRAMMING

Once all the digital and analog electrical inputs and outputs have been determined they are assigned to addresses on the PLC I/O modules by the electrical schematic drawings. This I/O assignment is the first step in the design and programming of the PLC control software [8]. On establishment of the complete process cycle of the tyre curing press, the second step is to break up the complete process cycle into each independent sequence of operations that occur during the whole cycle and draw up a flowchart for each series or different operation of the machine. For instance, the loading of the uncured tyres into the press would have its own flow chart and the events which take place during the actual cure cycle from the time when the press is completely closed to when the tyre curing is complete would be another flow chart.

3.1 PLC Control Software

The Siemens PLC family uses their programming software called STEP 5 in which PLC programs are written in a format of structured programming using program blocks. The main controlling block being OB1 or organizational block one, from which all other program blocks may be called during a scan cycle of the PLC [6]. The PLC program is structured in a way that each different sequence of operations is programmed into its own program block, for example, PB 1 (program block 1) may be for control voltage manipulation, emergency stop condition control and machine startup condition control. PB2 may be programmed for automatic tyre loader control according to its flowchart, and so on. Each of these program blocks is then called from OB1.

Analog input and output signal manipulation and the PID control algorithms however are controlled by blocks reserved for special functions and mathematical calculations, which are, called function blocks or FB's.

The function blocks may be called from OB1 or from within a PB. To make the structure of the program consistent a program block was used for all the analog input and output signals, as well as one for each PID algorithm. Values would then be passed to and from these blocks for the PID control of temperatures and pressures.

Setpoint data received from the SCADA system for the temperature and pressure control is passed from the SCADA application into data blocks (DB's) within the PLC program. The data is then transferred from the data blocks to the correct program block for use.

3.2 PLC to PC Communication

To establish communication between the PLC and the industrial computer, PLC software to interface with the SCADA is written in a function block and uses send and receive blocks to transfer blocks of data either way across the serial link. On the industrial computer side, the communication software as well as the SCADA application run under Windows 3.11. The SCADA software is DDE (Dynamic Data Exchange) aware and communicates through the communication software called L1DIRECT to the PLC [5].

3.3 Barcode Scanner Interface

To interface the barcode scanner to the PLC, software is written for the CP521 serial communications module and stored in EPROM on the CP521. Software is also written in a PLC function block so that the PLC processing unit can communicate with the CP521 and retrieve the data that has been sent by the barcode scanner. Once the operator swipes his card through the scanner to access the SCADA control system, the scanned barcode and resulting string of numbers is sent on a serial link to the CP521 which transfers the information to a data block within the PLC [7]. This data is then retrieved by the industrial computer software via the PLC-PC serial link and transferred through the L1DIRECT communications software to the SCADA application [5]. The SCADA application then checks his barcode against a database of users and gives him limited control of the machine determined by his access level in the database.

All the control from the SCADA application, whether during automatic or manual operation is done via the PLC to the field devices. The PLC software still however controls all temperatures and pressures on the machine by means of the PID control loops as well as all cure cycle timing, but setpoints and cycle times are received from the SCADA application for the specific selected tyre type's recipe.

4. HUMAN-MACHINE INTERFACE DESIGN

Due to the harsh conditions and extreme temperatures within this area of our factory the computer hardware that was decided upon included: A Mitac 486 DX2-66 industrial computer with 16 megabytes of RAM, a 540 megabyte hard drive, a built-in SVGA monitor and with built-in alpha-numeric and function keypad on the front panel.

The SCADA application and its Human Machine Interface was designed using Wonderware's Intouch SCADA software operating within a Windows 3.11 environment. Intouch is an object-orientated, graphical HMI application generator for industrial automation, process control and supervisory monitoring. It is one of a range of products from the Wonderware Factory Suite on which Gentyre has standardized for SCADA and factory automation requirements. The HMI or GUI was developed to be user-friendly, as not all users would be computer literate, and includes:

- Access Control
- On-line Fault Diagnostics
- Alarm Summary and History [3]
- Recipe Management [4]
- Real-time and Historical Trending [3]
- Real-time Graphical Process Animation
- Automatic and Manual Control
- PID Control
- Menu Driven Function Key Operation

Careful note was taken to make full usage of the function keypad to make operation of the machine as easy as possible at the push of a single key [9].

Figure 2 (on the following page) is an example of a typical graphical display which the operator uses to view current information such as recipes selected, cure step number, cure countdown times and whether the press is in automatic or manual.

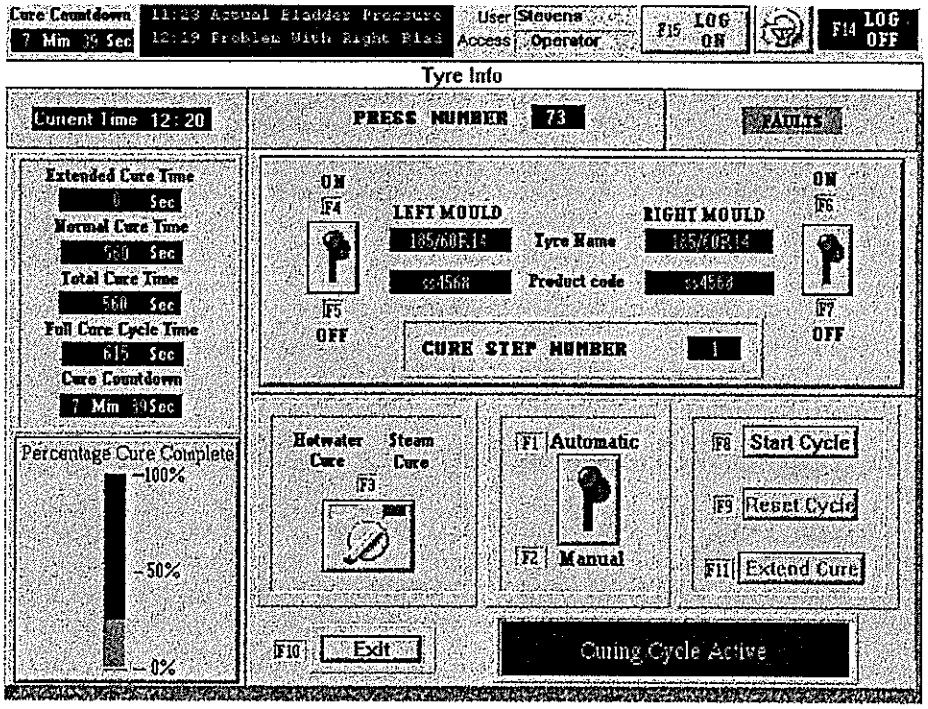

Figure 2 Typical HMI

The design and development of HMI is an essential part of the whole process control system and due to its user friendly designed interface and multitude of information from the machine that can be monitored and manipulated it made commissioning of the control system very easy. Operator involvement with the decisions on the design of the GUI meant that acceptance to a relatively unknown entity, the computer, became second nature and their required training was minimal. They now could see the complete process happening before their eyes and monitor each step of the automatic cycle in graphic form as well.

5. CONCLUSION

The upgrade of the tyre curing press and the implementation of the new process control system have been readily accepted by management, technical staff, maintenance personnel and operators. This is due to its user friendliness, flexibility, simplification of operation and precision in temperature and pressure control, which are two critical parameters in tyre vulcanization. The tyre curing press is not only used for normal production purposes, but also for special test runs on new tyre types that are introduced. To provide management with crucial production information the Tyre Curing Intouch SCADA application are currently linked to Wonderware Intrack system via the company Ethernet network.

6. REFERENCES

[1] Instrumentation and Control monthly. October 1995. Pg. 35.

[2] Instrumentation and Control monthly. November 1995. Pg. 44.

[3] Wonderware Corporation. (1994). Intouch Users Manual. Irvine USA : Microsoft.

[4] Wonderware Corporation. (1994). Intouch Recipe Manager. Irvine USA : Microsoft.

[5] Wonderware Corporation. (1994). Sinec L1 Direct DDE Server - User Manual. Irvine USA : Microsoft.

[6] Siemens AG. (1994). Siemens S5 95U Manual. Nürnberg Germany : Siemens Automation.

[7] SCADA Primer. Available from Internet URL http://www.iinet.net.au/~/ primer.html

[8] Automation News Group. Available from the Internet : automation@cthulhu.control.com -

[9] Intech [online]. [Cited November 1995]. Available from Internet URL http://www.isa.org.

[10] Gray, D. (1995, December). Can you still afford to install a SCADA system today? Instrumentation and Control, pp. 44-49.

[11] Dorfling, D. (1997, June). Manufacturing control in the new millenium. Instrumentation and Control, p.47.

[12] Graham, G. (1997, April). Control system design. Instrumentation and Control, pp. 47-48.

An Investigation Of Flicker Emission Prediction Techniques For Crushers In Power Systems

M.Y. Martin, H.S. Mostert
Eskom - Quality of Supply

G. Atkinson - Hope
School of Electrical Engineering, Cape Technikon

ABSTRACT

The use of flicker emission prediction techniques can provide utilities with the tools to predict flicker levels at any point on the network. This paper investigates flicker emission prediction techniques for a 250 kW "Nordberg" cone crusher and a 185 kW Barmac "ROTOPACTOR" crusher.

1. INTRODUCTION

The term "flicker" refers to the variation of light intensity as perceived by the human eye, due to voltage fluctuations on the electrical network. This variation in light intensity eventually leads to irritable and annoying visual discomfort. The human eye is highly sensitive to any variation in light intensity. The area of greatest sensitivity occurs where the frequency of voltage fluctuations is in the region of 8 to 10 Hz. [1,2]

The voltage fluctuations are caused by the variation in load current drawn by the variable loads, and the supply impedance of the power system, as illustrated in Figure 1. [1]

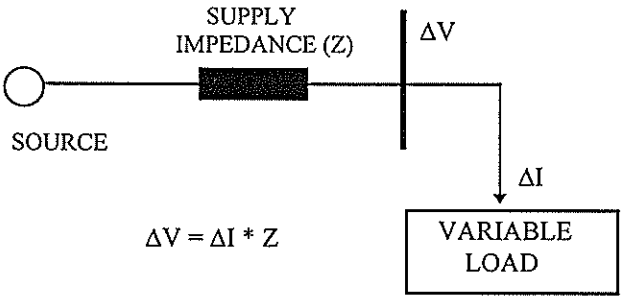

Figure 1: Variable Load Currents Creating Voltage Fluctuations

When the flicker emission of an individual load is investigated, the flicker emission level is evaluated in terms of Pst (short term flicker severity). The threshold at which flicker is perceptible to the human eye is at Pst =1.
Considering the fact that crushers are non - cyclic flicker emitting loads, the flicker emission cannot be predicted by way of deterministic methods using standard flicker curves as depicted in IEC 555 - 3 and IEC 1000-3-7.[3]

The only way of effectively predicting the flicker emission is by way of an empirical formula. [1]

Pst = Kst*load size (VA)/fault level (VA).....(1)

The Kst factor (characteristic coefficient) refers to the behaviour of an electrical motor subjected to a specific mechanical process. This process causes the motor to accelerate and decelerate, and hence a variation in load current drawn by the motor.

2. LOAD DESCRIPTIONS

2.1 Mechanical Description of the "Nordberg" Cone Crusher

Figure 2 shows a "Nordberg" cone crusher, model HP 400, commonly known as the "giro crusher". It crushes stone in the order of 50 mm to standard sizes of 6 mm, 13 mm, 19 mm, 25 mm, and 39 mm, and is driven by a 525 volt, 250 kW, 3Ø a.c. motor.

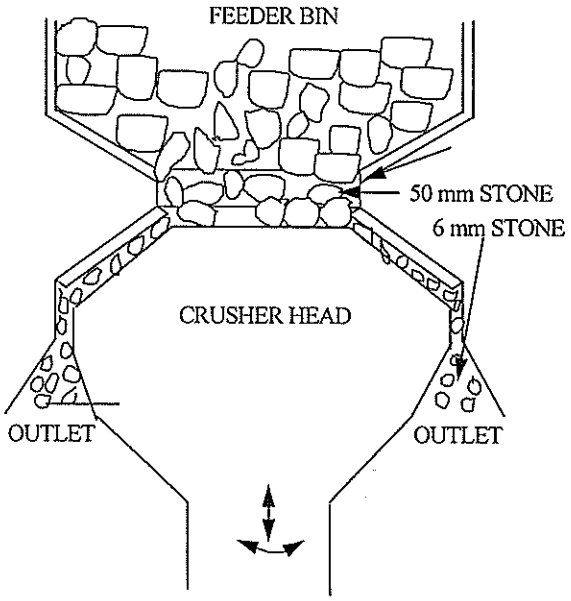

Figure 2 : Mechanical Illustration of the "Nordberg" Cone Crusher

The crusher head has a up-down-side-to-side twisting action. The stone gets crushed as the crusher head moves up to the right and then to the left respectively.

The current fluctuation is caused by the mechanical action of the crusher head, during the crushing

process. During normal operation of the crusher, the load current varies between 305A and 386A.

2.2 Measuring Flicker Emission of the "Nordberg" Cone Crusher

In order to predict the flicker emitted by a cone crusher, measurements were performed at a specific industrial site to determine the actual flicker emitted by this type of machine. The "GRAZ" flickermeter was used to measure flicker emission of the 250 kW cone crusher.

The flickermeter measures flicker emission of the load supplied by the transformer. The flickermeter (FM) was connected as shown in Figure 3.

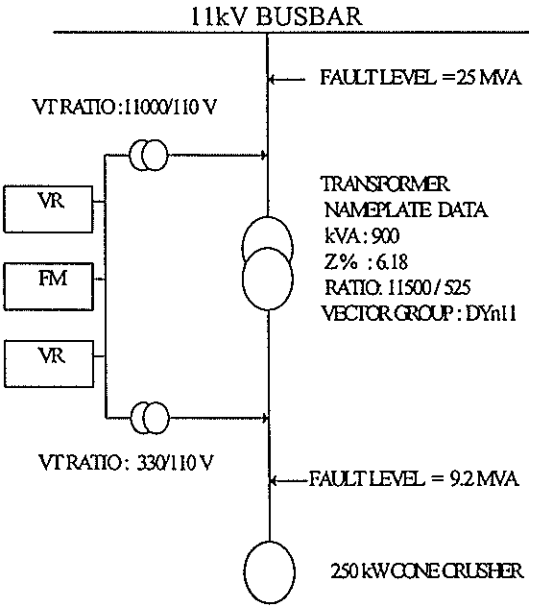

Figure 3 :Measuring Flicker Emission of the Cone Crusher

Voltage recorders (VR) were connected on the secondary sides of the VT's to monitor the voltage on the primary and secondary sides of the transformer. The voltage recorders were set to a voltage dip threshold of 3% of the nominal voltage. The data retrieved from the voltage recorders would confirm that the assessed flicker levels measured were not affected by voltage dips occurring on the rest of the power system.

2.3 Mechanical Description of the Barmac Crusher

The Barmac crusher , model "ROTOPACTOR", crushes stone in the order of 25 mm to standard sizes of 6 mm, 9 mm, and 13 mm, and is driven by a 525 V, 185 kW 3Ø a.c. motor. The stone fed to the crusher from the feeder is fed into an opening on the top of the rotating flywheel. A mechanical illustration of the Barmac crusher is presented in Figure 4.

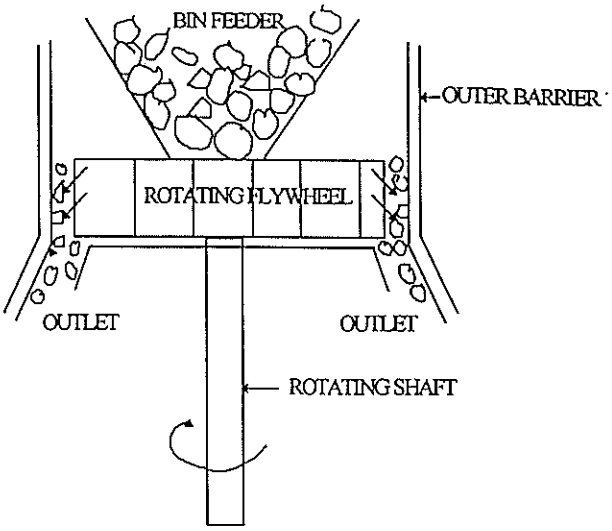

Figure 4: Mechanical Illustration of the Barmac Crusher

With the flywheel rotating, stone enters its top opening, and gets flung out via the blades against the outer barrier as shown in Figure 5.

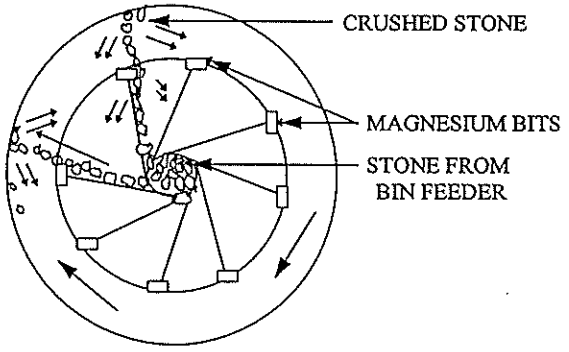

Figure 5: Mechanical Illustration of the Rotating Flywheel

The centrifugal force with which the stone is flung, and the collisions with other stones causes it to break, leading to the crushing effect.
The load current of the crusher varied between 188A to 200A during normal operation.

2.4 Measuring Flicker Emission of the Barmac Crusher

The measuring instruments and the power system for the Barmac crusher was exactly similar to that described for the "Nordberg" cone crusher in 2.2, except for the following :

1. The transformer rating was 1500 kVA and a 5.3% percentage impedance.
2. The kVA rating of motor driving the Barmac crusher was 185 kW.
3. The fault level on the secondary of the transformer was 12.15 MVA.

The fault level on the primary sides of the transformers feeding the Barmac crusher and the

"Nordberg" cone crusher were the same, as both the transformers were fed from the same busbar.

3. DATA ANALYSIS

3.1 "Nordberg" HP400 Cone Crusher

3.1.1 Analysing Flicker Measurements for the Cone Crusher

Figure 6 shows the flicker emission levels measured on the "Nordberg" cone crusher from 28 May to 3 June 1997.

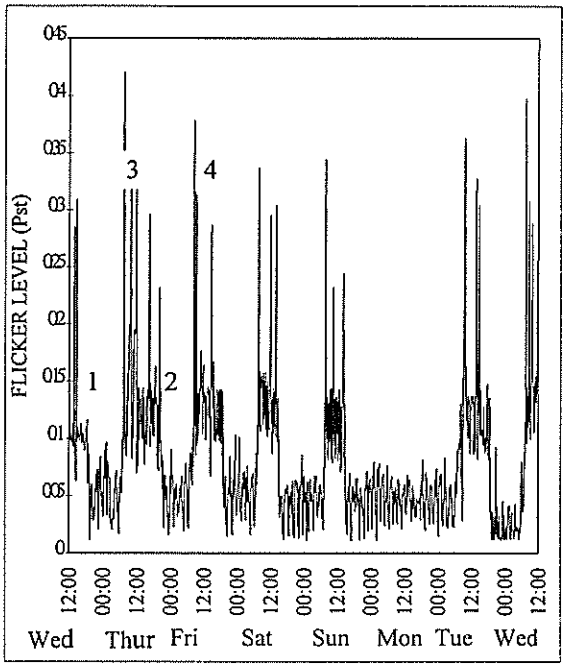

Figure 6: "Nordberg" Cone Crusher Flicker Emission

In the evenings (1,2) the plant was shut down, and the flicker emission levels were at a minimum. During the day (3,4) from approximately 07h00 to 19h00 the plant was fully operational. The flicker levels at these times rose quite significantly in comparison to the levels at night.

For greater clarity a detailed description of the crusher daily flicker emission on Thursday the 29/5/97 is shown in Figure 7. The flicker emission levels measured up to 08h00 when the crusher was inoperative, was assessed as Pst = 0.05.

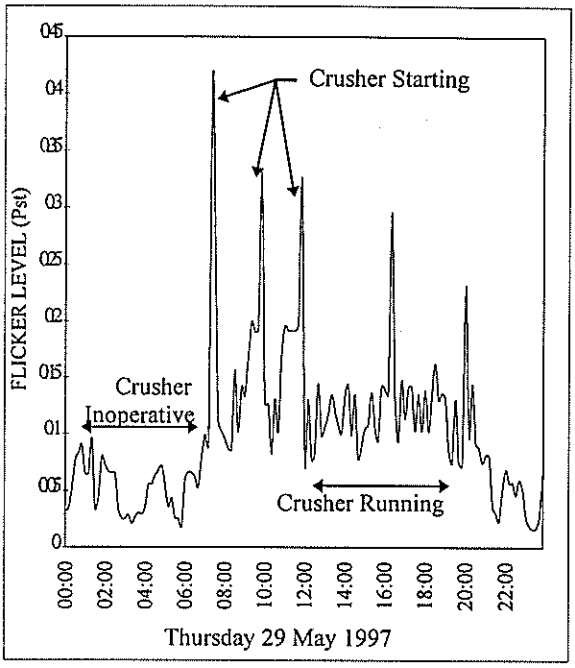

Figure 7: Daily Flicker Emission by "Nordberg" Cone Crusher

A summary of the measured flicker levels for the cone crusher is given in Table 1.

Table 1: Flicker Level Summary Table

Crusher Status	Inoperative	Starting	Running
Flicker Emission	0.05	0.4	0.12

3.1.2 Predicting Flicker Emission of the Cone Crusher

During **normal running** of the crusher the flicker emission was assessed as Pst = 0.12. The Kst factors can be calculated using the empirical formula (1):

Pst ≈ Kst * [VA (load) / VA (fault level)]

Load size ≈ 250 kW (Assuming unity pf)

H.V. Fault level = 25 MVA

Therefore the Kst value is:

[(0.12 * 25 MVA) / 250 kW] ≈ **12**

3.2 Barmac "ROTOPACTOR" Crusher

3.3 Analysing Flicker Measurements for the Barmac Crusher

Figure 9 presents the flicker emission levels measured of the Barmac crusher, for the period from the 14 to 18 June 1997.

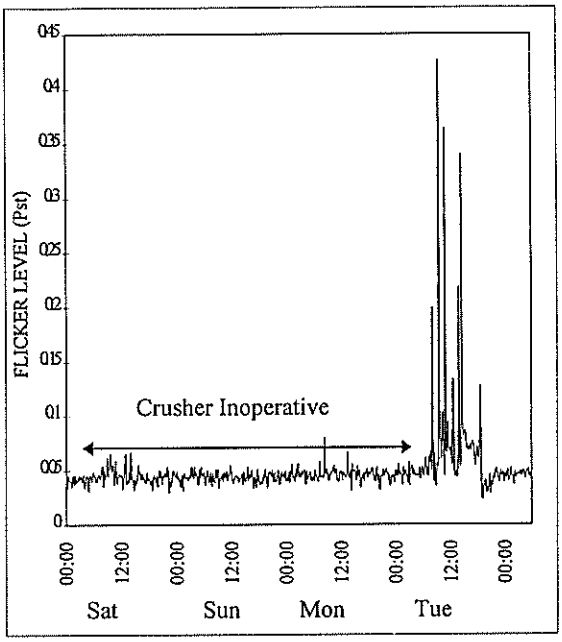

Figure 9: Barmac Crusher Flicker Emission

The weekly flicker emission levels measured indicates a Pst = 0.05 during the period when the crusher is inoperative. The flicker emission level was constant due to the fact that no other loads, with the exception of lighting circuits, were connected to the transformer.

The daily flicker emission levels measured for the 17/6/97 is shown in Figure 10.

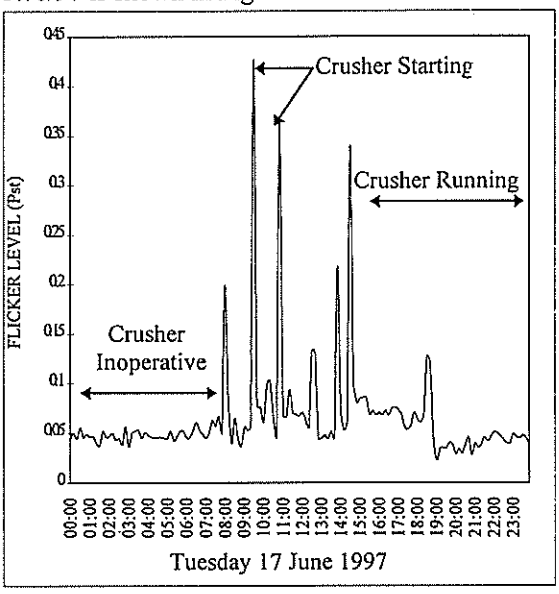

Figure 10: Daily Flicker Emission By Barmac Crusher

A summary of the flicker levels measured is given in Table 2.

Table 2: Flicker Level Summary Table

Crusher Status	Inoperative	Starting	Running
Flicker Emission	0.05	0.4	0.09

3.2.2 Predicting Flicker Emission of the Barmac Crusher

During **normal running** of the crusher the flicker emission was assessed as Pst = 0.09. The Kst factors can be calculated using the empirical formula (1):

Pst ≈ Kst * [VA (load) / VA (fault level)]

Load size = 185 kW (Assuming unity pf)

H.V. Fault Level = 25 MVA. Therefore the Kst value is:[(0.09 * 25 MVA) / 185 kW] ≈ **12**

4. CONCLUSION

A flicker emission of Pst = 0.12 and Pst = 0.09 by the "Nordberg" cone crusher and the Barmac crusher respectively, is assessed as being very small. From this the Kst factors calculated for the "Nordberg" cone crusher and the Barmac crusher is 12. These Kst factors are applicable only to these types of crushers, under these specific of operating conditions. The Kst factors together with the empirical formula (1), could provide utilities the tools to effectively predict the possible flicker level these crushers can emit on the power system.

5. REFERENCES

1. Koch, R.G., Rossouw, P.M., Boake, I.G., Peterson, H.: "Flicker Compatibility Planning and Design" ESKOM, Quality of Supply, Technology Group Research Report, pp.10-40, November 1995.
2. National Union for Electro-Heat, Disturbances Working Group: "Flicker Measurement and Evaluation", pp.3-70, 1986.
3. I.E.C.,: "Electromagnetic Compatibility, Limitation of Voltage Fluctuations and Flicker for Equipment Connected to Medium and High Voltage Power Systems" Committee Draft, pp.9-21, I.E.C.1000-3-7, July 1995.

6. AUTHOR ADDRESSES

M.Y. Martin and H.S. Mostert
Eskom
P.O. Box 222
Brackenfell 7560

G. Atkinson - Hope
School of Electrical Engineering
Cape Technikon
P.O. Box 652
Cape Town 8000

SOLAR PUMPED WATER STORAGE SYSTEM FOR ELECTRICTY GENERATION IN RURAL AREAS

O.D. Dintchev -Technikon Northern Gauteng

A.S. Meyer -University of Witwatersrand

Abstract. The sustainable development of electricity generation industry and especially the rural electrification require application of renewable energies. An alternative Solar Water Pumped Storage System for Electricity Generation is proposed. The system provides a solution for both water and electricity supply for rural communities, if certain conditions are present. It is based on low-price components such as induction motors, centrifugal pumps and variable speed motor drives which are produced for industry at large quantities.

Keywords: rural electrification, sustainable development, photovoltaic water pumping, water storage, induction motors, self-excited induction generators, centrifugal pumps / turbines, power conditioner, inverter, electronic voltage regulator.

1. Background

Recent scientific studies categorically relate the global climate changes to the emissions of industry and especially of the power plants.

ESKOM as world fourth largest electricity producer contributes to the pollution with "greenhouse" gases(GHG). South Africa as a whole is responsible for about 2% of the world's greenhouse gas emissions although it has only 1% of the world's population.[3]

ESKOM's electrification programme aims facilitating RDP goal: "electricity for all" which in numbers means electrifying an additional 2,5 million households by the year 2000, increasing the percentage of the houses electrified from 52% to 72%. Further RDP recommends that electrification should be done with grid and non-grid power sources. The latter being predominantly solar power systems. [2]

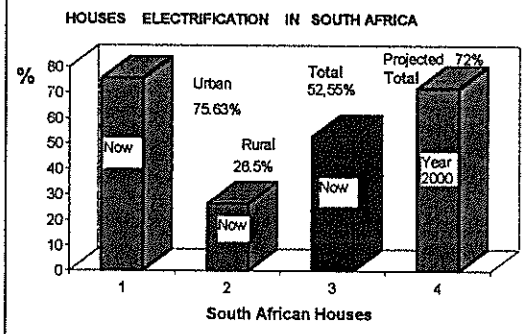

Fig.1. Houses Electrification

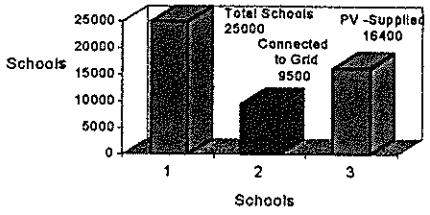

Fig. 2. School Electrification in South Africa

Regarding the school electrification ESKOM plans to electrify 9500 out of 25000 schools in South Africa, that are not electrified yet. The remaining 16400 mostly rural schools will be electrified by solar power.[2]

The requirements for a sustainable development, demand that fossil fuels should be replaced with renewable sources that produce less or even zero GHG. RDP is pursuing development policies geared to reduce poverty, access to energy and water, which will rise the basic services such as electric lighting, refrigeration etc. As part of its Rural Electrification Programme, ESKOM is planning to accomplish the task with application of renewable energies and with an accent of photovoltaics. Involvement of the communities would be crucial for the process, therefore contributing to their employment, training and creation of small businesses.

Although that the cost-effectiveness of the PVs is debatable, when considered for rural purposes one should bare in mind the ***kind of service*** that solar electricity can provide.

All rural communities are in need of water, as well as electricity. With effects of El Nino on South Africa's doorsteps the water supply is becoming an important task of the government and the people themselves. Saving of water and increasing the efficiency of utilisation of the water sources is necessary.

2. Solar Pumped Water Storage Electricity Generating System (SPWSEG).

The proposed system gives an answer to both water supply and electricity generation if certain conditions regarding availability of water resources are present.

As a rule, all photovoltaic electricity generating systems require storage medium to make the electricity available when needed.

The system may eliminate the usage of the batteries which are commonly used with PVs nowadays. The

idea of the SWPSEG is simple: during the day a photovoltac pump is pumping water uphill in a reservoir and during the night the pump is reversed as a turbine which rotates the motor, in turn, reversed as a generator. The SWPSEG has a purpose to serve rural communities and to be a basic energy supply for their social, agricultural and educational development.

Orientation Fundamentals.

When designing the system and choosing the materials and components the following factors should be taken into account:

- simplicity of the materials,
- very high reliability,
- long life and
- low cost.
- the total efficiency should be high, but it should be looked up after satisfying the criteria of simplicity, reliability and the utilisation of the system.

3. System Description. The base system arrangement is shown in Fig.3

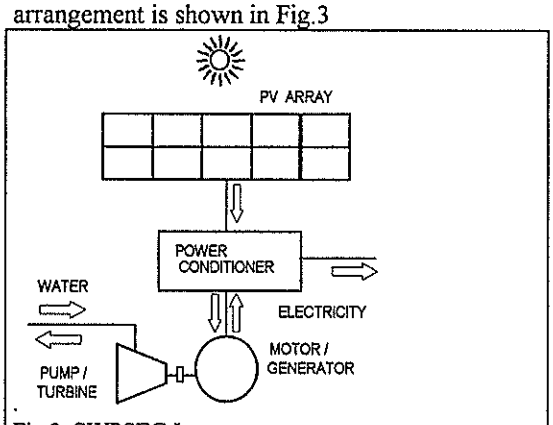

Fig.3. SWPSEG Layout

3.1.PV Array.

PV array is the power source of the system . It consists of a number of solar modules connected in series and parallel in order to supply the system in pumping mode with the desired electric power.

3.2.Power Conditioner (PCU).

The PCU in a PWEG is the most complicated and complex element as it is in the majority of PV systems. The PCU can be considered as an active and "intelligent" link between the PV array and the motor driving the pump. Among the other functions the PCU has the following particular ones:

- to invert the DC from the array into AC necessary for operation of the machine as a motor during the day when solar power is available,
- to provide the motor with low-voltage and low-frequency supply at the time of first starting in early morning when sun intensity is low and the array power may be not sufficient to start and run the motor and the pump,
- at accomplishing the starting to restore the frequency and the voltage supplied to the motor to their rated values of 50 Hz and 220 V respectively.
- various protections of the PV array and the load.

3.3. Motor / Generator

The electrical machine to be used in the SPWG system has to be chosen according the following criteria:

- reliability /robustness/,
- low maintenance and low need for human supervising,
- low cost.
- efficiency,

A squirrel cage induction motor satisfies the above requirements. Apart for the obvious advantages of induction motor there are some additional advantages of the induction machine when used as a self-excited generator(IG):

- simple construction,
- robust,
- low maintenance,
- allow to dispense the mechanical governor control of the turbines,
- low price,
- no need of rotating means of excitation and controlling equipment such as field rheostats etc.,
- the fault current of IG is limited since the excitation of the machine is reduced with the reduction of terminal voltage.

Disadvantages of Induction Generators.

- need a constant control of voltage and frequency at changing loads and speeds.
- efficiency is lower than that of alternators,
- need compensation for reactive loads.

3.4. Pump / Turbine

Centrifugal pumps reversed as turbine seem to satisfy best the requirements for low cost and simplicity of operation of SWPSEG.

Modifications Necessary to transform a Pump into a Turbine.

A portion is cut on the chamber of the pump, as shown in Fig.4. below.

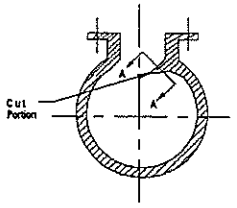

Fig.4. Modification of the pump chamber[1].

The maximum turbine efficiency $\eta_{T.max}$ is the same as that of the pump $\eta_{P.max}$ but takes place at different head and discharge as shown in Fig.5. [1]

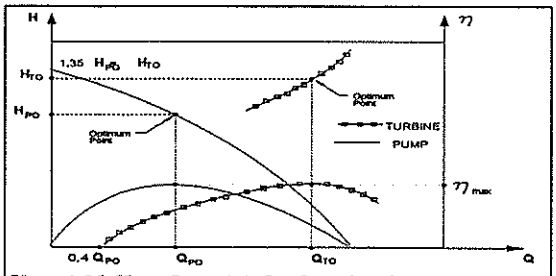

$H_{TO} = 1,35.H_{PO}$ $Q_{TO} = 1,4.Q$ $Q_T = 0,4.Q_{TO}$

Fig.5. Performance and efficiency curves of a Centrifugal Pump Operating as a Turbine.

3.5.Control of the System.

Since the generator operates as a stand alone supplying electrical loads by itself, to keep a constant frequency it is necessary at any moment of time to maintain the real power generated equal to the real power absorbed by the loads.

One of the methods used is to adjust the generated power to the demand without influencing the input hydraulic power. This method is known as ***electronic method*** or ***electronic load governor*** (ELG). Generally it works as follows: the output frequency is sensed and if tends to increase a number of resistors are connected to the alternator output and as a result its speed drops and so does the frequency.

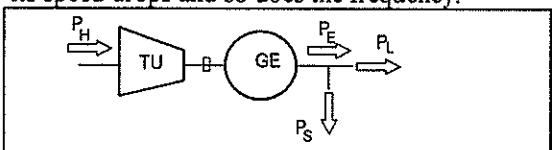

Fig.6.Electronic Control by the Absorption of the Electrical Energy Generated / Electronic Load Governor/.

Combined Control applying Hydraulic Turbine Control and ELG.

Obviously the waste of water for the purpose of control is not desirable.

The hydraulic control is applied for rough adjustment of the turbine power. Usually the load supplied by the system is well known and typical for the period of operation. A good load management study may be helpful to install a control of the water input to the turbine, governed by a time programmed device. In addition a ELG will adjust the power available to the load according to the demand at the particular time. An example for this type of control is shown in Fig.7 .

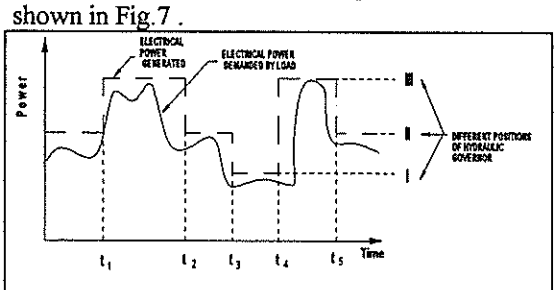

Fig. 7. Hydraulic Programmable Power Control .

Control of the Generated Output by means of Power Conditioner.

The variation of the output frequency may be avoided by passing the generator output to the AC input of the PCU. After a rectification it will be inverted in a form of 50 Hz AC available on the AC output terminals of PCU.

4.System Size and Specifications

The system is based on commercially available components: industrial three-phase induction motor, centrifugal pump and AC motor drive used as a Power Conditioner. These components are at considerably lower prices than the corresponding ones used for solar power applications.

There are several possible variants of PSWSEG arrangements which are based on the requirements of the load: if the power generated is to be used at the time of generation or to be stored in a battery bank.

System I

The solar power from PV array is inverted in form of 3-phase 220-V 50 Hz and supplies the induction motor which rotates the centrifugal pump and water is pumped when sun is available. Inverter provides variable V/f motor starting at low irradiance.

In generating mode the pump acts as a turbine, induction motor as induction generator. The reactive power necessary for excitation of the induction generator is provided by a capacitor bank. The generator output is at 220 V, 50 Hz, single-phase AC, which vary with load. Than it is rectified as a DC and via a Regulator charges the Battery Bank at suitable DC voltage. The DC loads are supplied and also AC ones via an inverter. As an alternative, the AC output of the generator is passed trough the PCU and an AC output is available on the PCU AC output terminals.

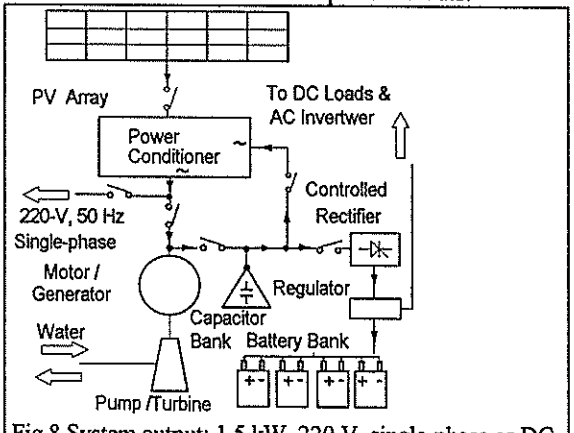

Fig.8.System output: 1,5 kW, 220 V ,single-phase or DC

System II

Here are no batteries and voltage control is done by electronic regulator. The system operates in a similar manner as the first one. The difference being that, the Electronic Voltage Regulator and Ballast Resistors keep the voltage and frequency constant with variations of the load.

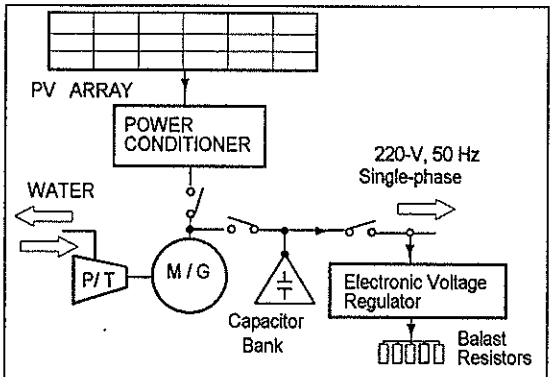

Fig.9. System output : 1,5 kW, 220 V ,single-phase

System III

System Description:

The difference from the previous one is that the battery bank and controlled rectifier are not used. The generator output is output is rectified by power conditioner and inverted in as 3-phase 220-V, 50 Hz.. Detailed view of SWPSEG is shown below in Fig. 10.

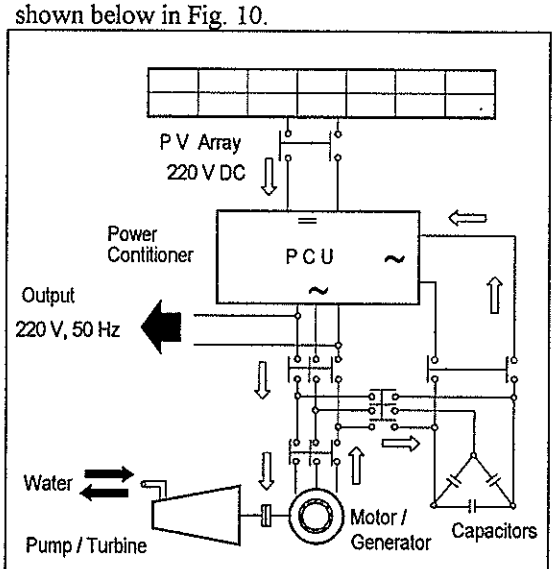

Fig.10.System output : 1,5 kW, 220 V ,single-phase

Generator Performance:

A 3-kW, 4-pole, 220-V, Δ-connected induction motor, working as induction generator is used.

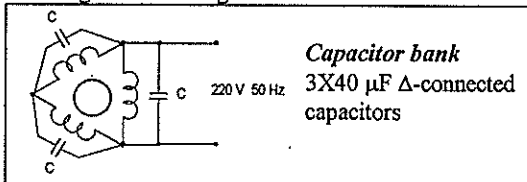

Fig.11. Connection of a Three-Phase Induction Motor as a Single-Phase, Self-Excited Induction Generator

A set of experimental characteristics $V_G = f(P_{LOAD})$ is shown in Fig.12. The graphs are plotted at rated speed and two sets of capacitors, connected in delta.

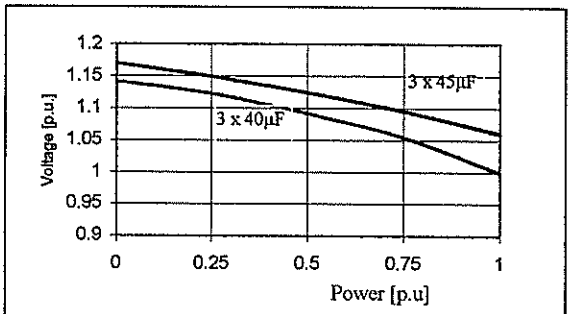

Fig. 12. Voltage / Power Characteristics

Power Conditioner

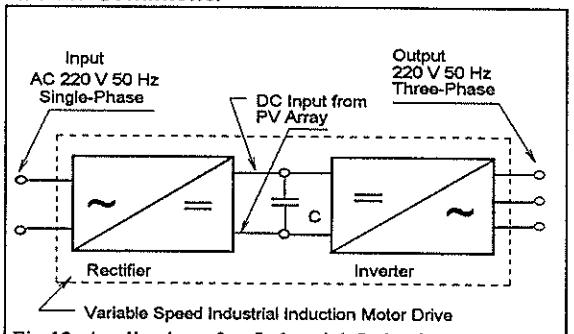

Fig.13. Application of an Industrial Induction Motor Drive as Power Conditioner

CONCLUSION:

The conventional power pumped storage plants which work in parallel with the grid, are designed in majority of the cases to meet certain peaks in the load of the system, and therefore are left to run at maximum power output ensuring maximal efficiency at maximum power output for the period of time corresponding to the amount of water stored. In contrast to that PSWSEG has its purpose in supplying certain load for an optimal period of time. Therefore a longer time for running is suggested with reduced power output namely to 1,5 kW. PSWSEG can be applied in situations where a source of water like a dam is available and there is a possibility for a second dam situated above the first to be build.. As a hydro-electric power generating plant the main cost will be for the extensive civil work. Therefore the use of special and proper equipment such as turbine and alternators could be advantageous worth.

The plant could be justified if the pumped water is used for irrigation and stock purposes but not for electricity generation only. In other words the system will be best of use if applied as **energy recovery part** of an existing Photovoltaic or Hybrid Electricity Generation System. Use of industrial type components such as: motor, pump and variable speed drive as PCU will reduce the price of the system considerably.

REFERENCES

1.Alain Bonade : Microcentrales Hydroelectriques, D3 II Génie Electrique /Machines/ . Techniques de l'Ingénieur 1990 Paris.

2. ESKOM Web Home Page http://www.eskom.co.za

3.South Africa -USA Summit on Sustainable Energy Development August 1995 Concept Papers

A MICROCONTROLLER-BASED DATA ACQUISITION AND MONITORING SYSTEM FOR FACTORY APPLICATIONS

F ADLAM, TI VAN NIEKERK and H VERMEULEN
E-mail: fadlam@ml.petech.ac.za theoian@ml.petech.ac.za 9449868@ml.petech.ac.za
Department Digital Systems Engineering, Faculty of Electrical Engineering, Port Elizabeth Technikon, Port Elizabeth, Republic of South Africa

ABSTRACT

In South Africa, and more specifically the Eastern Cape, some small to medium sized manufacturing enterprises (SMMEs) collect production related information either manually or with limited computer intervention before it is processed and analysed. Gathering and processing production related information on a real-time basis would increase the competitive nature of these companies.

This paper outlines the design, development and implementation of a cost effective data acquisition and monitoring system consisting of a centralised personal computer networked with microcontroller-based nodes.

Keywords: industrial network, serial communication network protocol, microcontroller, Windows NT.

1 INTRODUCTION

The Eastern Cape has an integrated discrete-part motor manufacturing industry, which include SMMEs.

A bearing manufacturing company, with a history of upgrading and refurbishing existing production equipment, approached our institution to develop a computer based system that will connect all bottle-neck machines to a centralised server and enable them to

- decrease batch set-up time,
- monitor bearing production,
- monitor machine down-time,
- communicate to supervisors/operators on shop floor and
- make better decisions regarding preventative maintenance.

Similar problems exist in other SMMEs so the emphasis was on the cost effectiveness and flexibility of the design.

The following sections describe and propose a computerised system as a solution.

2 A MICROCONTROLLER-BASED DOWN-TIME MONITORING AND INFORMATION SYSTEM

A block diagram of the down-time monitoring and information system is shown in Figure 1 and the following subsections describe design and implementation arguments thereof.

2.1 Centralised Computer:

A personal computer provides the interface between the company Ethernet network and the industrial shop floor network. All the shop floor production information logged from the microcontroller nodes are stored in a database for daily and long term reporting as well as real-time analysis capability. It also serves as a master in the industrial network and as an information server in the existing factory/company local and wide area network.

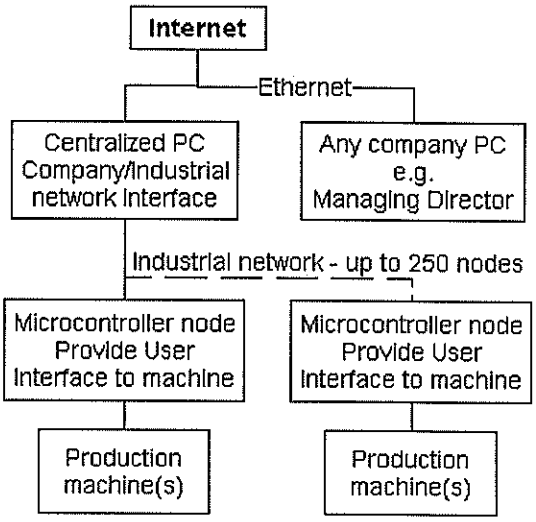

Figure 1 A microcontroller-based downtime system

A master / slave communications network protocol was selected to communicate to the microcontroller nodes as it is fairly simple to implement as well as economical.

Each node on the network must be polled and be allowed to transmit on the network so that the centralised computer (master) can receive production information.

The total time to poll all nodes are determined by:

- network baud rate,
- number of connected nodes,

- the time which the master will wait in the case of a non-responding node,
- the maximum time a node will be transmitting on the network,
- the maximum time it will take the master to poll a node,
- the maximum time it will take the master to process data and
- the number of open application programs that need to be serviced by the operating system.

To enable the centralised PC to integrate into the existing company's network, the Windows NT operating system was selected. Windows NT version 4 provides a Windows 95 like user interface and a build-in platform for supporting graphical, communication and information systems development. The potential of NT in industrial control and manufacturing is enormous as it has the ability to handle soft real-time systems [1]. In hard real-time systems it is imperative that a network response occurs within a specified time whereas in soft real-time the system will still function correctly even if deadlines are occasionally missed [2].

The centralised computer will enable management and line supervisors to monitor machine stoppage as well as the type of fault within two minutes from when the fault event occurred. Information is available three minutes after the real event has occurred. It is therefore safe to classify the application as a soft real-time system.

A program was written to view down-time events and the reason of failure is colour coded. Figure 2 shows the identity of each machine in the left column and the corresponding down-time intervals are shown on the x-axis in the time domain.

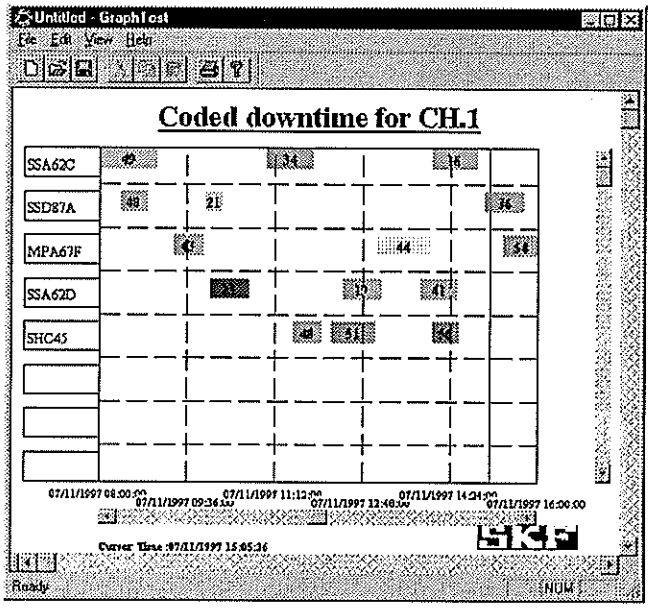

Figure 2 Trending software

A network testing program was written to test different aspects of the network. The data in the RAM space as well as the ports of each node can be viewed or changed. A network map can be built of all the nodes currently connected to the network and the connection to a specific node can be tested using a loopback-echo method. All network errors are logged and displayed in an events list. Figure 3 shows the user interface for accessing the internal RAM of any node.

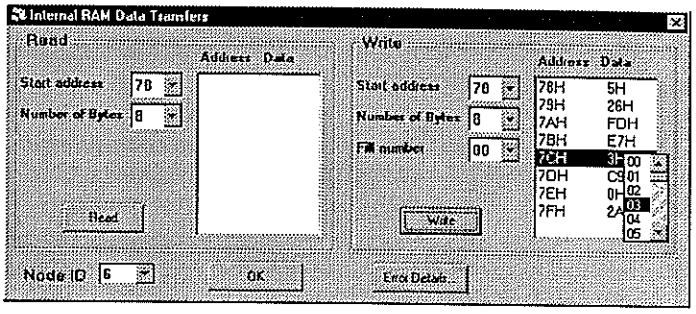

Figure 3 Internal RAM data transfers

The user selects the node address, internal RAM address and number of bytes to be transferred. Data can be transferred in single byte or block format.

2.2 Industrial network:

Connecting multiple microcontrollers or microprocessors on a network requires a method of arbitration to determine which microcontroller can transmit on the network. These methods are called media access control and the following protocols ranked in order of hardware and software cost effectiveness, were found to be suitable for embedded systems [3]: Polling, Time Division Multiple Access, Token Ring, Token Bus, Binary Countdown and Carrier Sense Multiple Access (CSMA).

Polling is the least expensive and CSMA the most expensive, when used for real-time embedded applications.

Because the application is cost sensitive it was decided to use polling as communications protocol. A proprietary communication protocol based on the 9-bit serial multi processor communications of the Intel Corporation microcontrollers has been selected for media access control on the network [4]. It saved time because we did not have to write a communication protocol but cost about R 2500 per network with a maximum of 256 nodes including the PC and repeaters.

The proprietary communication protocol allows read or writes to internal and external random access memory of the node in blocks of 250 bytes maximum. All node input and output ports can be accessed individually.

On power up, the master polls all the nodes with a TEST command to determine which nodes are connected to the network. The connected nodes will respond with TEST

(test code message). The master then attempts to make a connection with the slave by sending a CON (connect) command. Slaves which respond with UA (unnumbered acknowledgement) are considered functional and ready to communicate.

The program used by the master to poll the network can be used to add/delete nodes to the polling sequence. Furthermore the rate at which each node must be polled can be set for each individual node. When a node is polled and new data is available for transmission, only that data is transmitted over the network to the master, which in turn updates the database with this new data. A dialogue box of the program is shown in Figure 4.

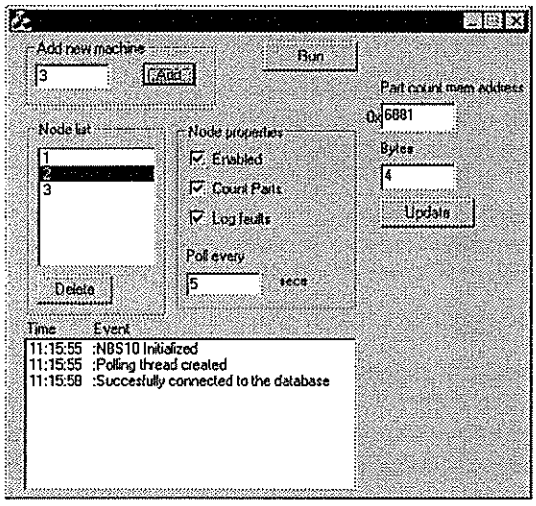

Figure 4 Polling program

Typical network media for industrial networks are copper coax or twisted pair cable, radio frequency link or fibre optic cable.

The RS-485 serial interface standard, operating in half duplex mode, was selected as the network media. Its use of balanced lines ensures good noise immunity and it handles the differences in ground potential between nodes well [5]. It is widely used, easy to maintain, has good noise immunity, is cheap, can use unshielded or shielded twisted pair cable and is proven technology.

The industrial network connects to the PC by means of a network interface card and the corresponding Windows NT software device driver from Cimetrics Corporation.

2.3 Microcontroller-based Node:

A microcontroller system was developed consisting of:

- 80C251 microcontroller
- 32/64k read only memory
- 32k random access memory
- 20 character by 4 line liquid crystal display module
- 32 digital inputs
- 32 digital outputs
- 16 optically isolated digital inputs
- 8 individual potential free relay outputs
- printed circuit board mounted dual in line switches to select the node address in hardware
- real time clock
- RS-485 half duplex serial interface.

The design is modular so that other peripheral hardware can be developed and easily interfaced to the existing system. The 80C251 microcontroller was selected due to past experience with the 8051 and current infrastructure in the faculty. Any other microcontroller can be used as a node as long as it can facilitate the 9 bit multi processor communications from Intel Corporation.

The real-time software developed for the node

- monitors the operation of a machine,
- communicates with the master using the 9 bit serial protocol,
- provides an interface to the operator,
- receive instructions from line management and
- keeps count of the number of discrete parts manufactured.

The program was written in ANSI C language, using the Keil C51 professional developer's kit, to ensure portability. The C-code to implement the low-level functions is hardware and compiler specific and is the only code that must be changed when a different microcontroller is selected.

3 CONCLUSION

A cost effective microcontroller-based system was designed, developed and implemented providing real-time shop floor production monitoring. The possibility of developing a generic software framework for factory shop floor data acquisition is currently under investigation.

4 REFERENCES

[1] Timmermans, M. & Monfret, J.C. (1997). Windows NT as Real-time OS? Real-time Magazine[online]. Available from Internet URL: http://www.realtime-info.be/encyc/magazine/articles/winnt/winnt.htm

[2] Son, S.H. (1995). Advances in real-time systems. New Jersey : Prentice-Hall.

[3] Upender, B.P. and Koopman, P.J. (November 1994). Communication Protocols for Embedded Systems. Embedded Systems Programming, pp. 46 - 58.

[4] Mackenzie, I.S. (August 1995). The 8051 Microcontroller. New Jersey : Prentice-Hall.

[5] Axelson, J. (1995). Networks for Monitoring and Control. Microcomputer Journal, pp.27 - 36.

SCHEDULING OF COGENERATION SYSTEMS IN RESPONSE TO REAL-TIME PRICING

HM Pretorius and GJ Delport
Centre for New Electricity Studies
University of Pretoria

ABSTRACT
Industries with the availability of cogeneration plants are in the advantageous position of managing their generation in accordance to the utility's supply and electricity tariff. Eskom has introduced a pilot project aimed at developing and introducing a Real-time Pricing (RTP) tariff to its customers [1]. The potential electricity cost savings that this tariff will have on the cogeneration industry will be modelled. The effects of this tariff on a cogeneration plant, specifically on the rescheduling, of not only the cogeneration of the industry, but also on the steam generation and usage are an important consideration for the plant engineers. The model is set up for two different cogeneration configurations. Together with the utility they make up the electricity supply to the industry.

Keywords
Scheduling, Cogeneration, Real-time Pricing, Steam usage, Modelling, Cost savings, Hourly marginal costs.

1 INTRODUCTION

Industrial power generation is competing with utility power generation, and the link between the two industries is becoming of economical importance [2]. Cogeneration industries in the USA do not only have to buy electrical power from the utility industry, but are also in the position to sell energy back in the form of either electrical or high-temperature energy [3]. This possibility is only in the beginning stages of development in South-Africa, and due to the fast growing development of the dynamic pricing structures from Eskom becoming a point of research.

In this study two different already established cogeneration configurations will be investigated and together with the utility will make up the three suppliers of electricity to the industry. The purpose of this study will be to find the optimum schedule of all three suppliers under the RTP structure. The cogeneration process under investigation is an example of a typical topping cycle cogeneration system [4], [5]. This self generated power is fed into a parallel network together with the electricity supply from Eskom. The cogeneration plant will have a maximum installed capacity, this will limit the supply of electricity to the process from cogeneration. The shortage of power must be supplied by the utility industry. The tariff structure of the utility will be the deciding factor in the scheduling of the power demand from the utility.

The cost of generating own power and the cost of electricity from the utility will be weighed against each other. In the peak periods when the prices of electricity is high, more self generated power will be used. In off-peak hours the price of electricity from the utility will be more economical than generating own power with cogeneration. The hourly marginal rates of the two cogeneration plants will be assumed constant. The hourly marginal rate from Eskom will be different for each hour of the day.

2 SIMPLIFIED SYSTEM CONFIGURATION

A simplified configuration diagram is given in Fig 2.1. Generation plant 1 is purchasing HP and LP steam from the boiler plant. The LP steam exhausted from the turbine is condensed in the condenser and A grade condensate is sold to the rest of the industry. The main output will be the electrical power sold to the chemical plant. Generation plant 2 does not have any condenser and will sell the LP steam exhausted back to the waterworks plant. The steam not sold back is exhausted into the atmosphere as wasted heat. Again the important output will be the electrical power sold to the chemical industry. The Eskom supply is also shown, the output of Eskom to our configuration will be the electrical power supplied and the RTP structure for the specific hours in question in our analysis. Figure 2.2 shows the schematic layout of the model. The model relies on the inputs to derive the outputs. It can be seen that the model consists of two subsections, the cost function and the energy block.

3 HOURLY MARGINAL RATES FOR THE COGENERATION PLANTS

Before any scheduling can be done, the two marginal rates of the cogeneration plants have to be calculated in order to weigh them against the marginal rates from Eskom. The marginal rates for the two on-site power stations will be constant for every hour over the billing period. *(ps1_hmr and ps2_hmr)*
The marginal rates of the two cogeneration plants are derived using steam measurements and costs of steam as variables. The result must be in the following form:

$$ps1\_hmr < ps2\_hmr \qquad (1)$$

4 ELECTRICAL ENERGY BLOCK

The Eskom hourly marginal rates for a day is given to the industry one day in advance, in order to calculate the

generation schedules of the cogeneration plants together with the required power from Eskom for the following day. A certain hourly marginal rate cut-off value, $HMR_{cut}1$, exits, which will provide the threshold price above which the power levels purchased from Eskom should be shut down to Esk_{min} [1]. An hourly marginal rate duration curve (HMRDC) can be used to graphically display this concept and to form the basis of the mathematical expressions [6]. Because the marginal rate of cogeneration plant 2 is higher than the marginal rate from power station 1, the following will apply:

$HMR_{cut}\ 1 = ps2\_hmr$ [c/kWh](2)
$HMR_{cut}\ 2 = ps1\_hmr$ [c/kWh](3)

For hour i the power level required by the chemical industry will be $P_{req}i$. In anticipation of this, the supply from Eskom will be Esk_{interm}. The remaining power needed will be supplied by the two on site power stations. The levels of these two respectively will be determined later. The total energy required by the industry will be ($\sum P_{req}i$).
Three different price intervals exist:

- $esk\_hmr\ i > ps2\_hmr$ (4)
- $ps2\_hmr\ i \geq esk\_hmr > ps1\_hmr$ (5)
- $esk\_hmr\ i \leq ps1\_hmr$ (6)

When the variable input parameter esk_hmr i is given, the first thing to do will be to use equations (4)-(6) and determine which one holds true. This will give the model an indication of which equations to use
for determining the generation schedules of the three supplies. If equation (4) is true, the equations in paragraph 4.1. is used. These equations will calculate generation schedule A. For equation (5), generation schedule B is calculated, using the equations in paragraph 4.2, and for equation (6), generation schedule C is calculated. Only one schedule is used for each hour respectively.

4.1 Generation schedule A

$PS1\ i = PS1_{max}$ [kW](7)
$Esk\ i = Esk_{min}$ [kW](8)
$PS2\ i = P_{req}i - PS1_{max} - Esk_{min}$ [kW](9)

If equation (10) holds true, equations (7)-(9) must be replaced with equations (11)-(13) respectively.

$PS2\ i > PS2_{max}$ (10)
$PS1\ i = PS1_{max}$ [kW](11)
$PS2\ i = PS2_{max}$ [kW](12)
$Esk\ i = Esk_{interm}i = Preqi - PS1_{max} - PS2_{max}$ [kW](13)

If equation (14) holds true, equations (7)-(9) must be replaced with equations (15)-(17) respectively.

$PS2\ i < PS2_{min}$ (14)
$PS2\ i = PS2_{min}$ [kW](15)
$Esk\ i = Esk_{min}$ [kW](16)
$PS1\ i = P_{req}i - PS2_{min} - Esk_{min}$ [kW](17)

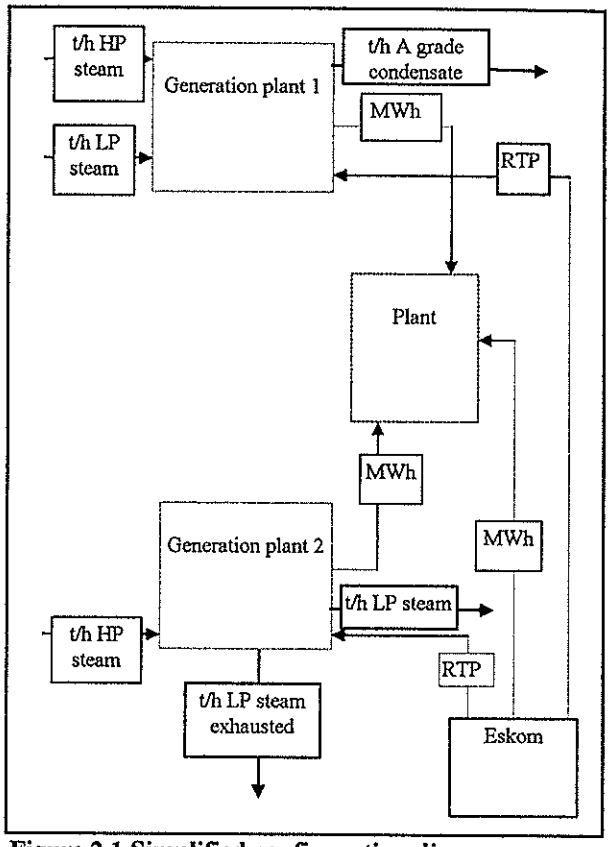

Figure 2.1 Simplified configuration diagram

4.2 Generation schedule B

$PS1\ i = PS1_{max}$ [kW](18)
$PS2\ i = PS2_{min}$ [kW](19)
$Esk\ i = Esk_{interm}i = P_{req}i - PS1_{max} - PS2_{mi}$ [kW](20)

If equation (21) holds true, equations (18)-(20) must be replaced with equations (22)-(24) respectively.

$Esk\ i > Esk_{max}$ (21)
$PS1\ i = PS1_{max}$ [kW](22)
$Esk\ i = Esk_{max}$ [kW](23)
$PS2\ i = P_{req}i - PS1_{max} - Esk_{max}$ [kW](24)

If equation (25) holds true, equations (18)-(20) must be replaced with equations (15)-(17) respectively.

$Esk\ i < Esk_{min}$ (25)

4.3 Generation schedule C

$PS2\ i = PS2_{min}$ [kW](26)
$Esk\ i = Esk_{max}$ [kW](27)
$PS1\ i = P_{req}i - PS2_{min} - Esk_{max}$ [kW](28)

If equation (29) holds true, equations (26)-(28) must be replaced with equations (22)-(24) respectively.

$PS1\ i > PS1_{max}$ (29)

If equation (30) holds true, equations (26)-(28) must be replaced with equations (31)-(33) respectively.

$PS1\ i < PS1_{min}$ (30)
$PS1\ i = PS1_{min}$ [kW](31)
$PS2\ i = PS2_{min}$ [kW](32)

$$Esk\,i \quad = Esk_{interm}i = P_{req}i - PS1_{min} - PS2_{mi} \ [kW](33)$$

5 COST FUNCTION BLOCK

The schedules from the previous three sections are for a specific hour i. The procedures must be followed for every hour until the generation schedules of the three supplies are known for the entire billing period, in this case one month. These schedules will now be used to calculate the cost savings in the billing period, when switching from the Nightsave tariff option to the RTP option. In the calculations following it is assumed that a one part RTP option is used.

In order to calculate the cost saving, the actual cost for electrical energy must be calculated for both electricity tariff structures. The costs connected to the cogeneration of power by the two on site power stations are also calculated, these values are also incorporated into the cost saving calculations.

6 CASE STUDY

The first case study will deal with a chemical industry currently incorporating the Nightsave tariff. The industry has two cogeneration plants with the configuration corresponding to figure 2.1. Cogeneration plant 1 has a full capacity of 86MW and cogeneration plant 2 a capacity of 39MW. The maximum levels of generation are chosen as 85% of full capacity and the minimum levels as 25% of full capacity. The supply schedule of Eskom according to the model is shown in figure 6.1 for one day together with the RTP prices for that day.

It can be seen that when the esk_hmr value is below ps1_hmr the supply from Eskom is a maximum. When esk_hmr is between ps1_hmr and ps2_hmr the Eskom supply is an intermediate value calculated by the model. When esk_hmr exceeds ps2_hmr, the supply from Eskom drops to a minimum.

The effect the maximum demand component has on the electricity costs can now clearly be seen. The savings according to these calculations will be **R1 690 463**. The maximum demand component does not exist in the RTP structure, this fact has an impact of 76.6% on the savings made. The remaining savings is due to the fact that less energy is supplied by the more expensive cogeneration plant 2. The power supplied by both Eskom and cogeneration plant 1 is substantially increased.

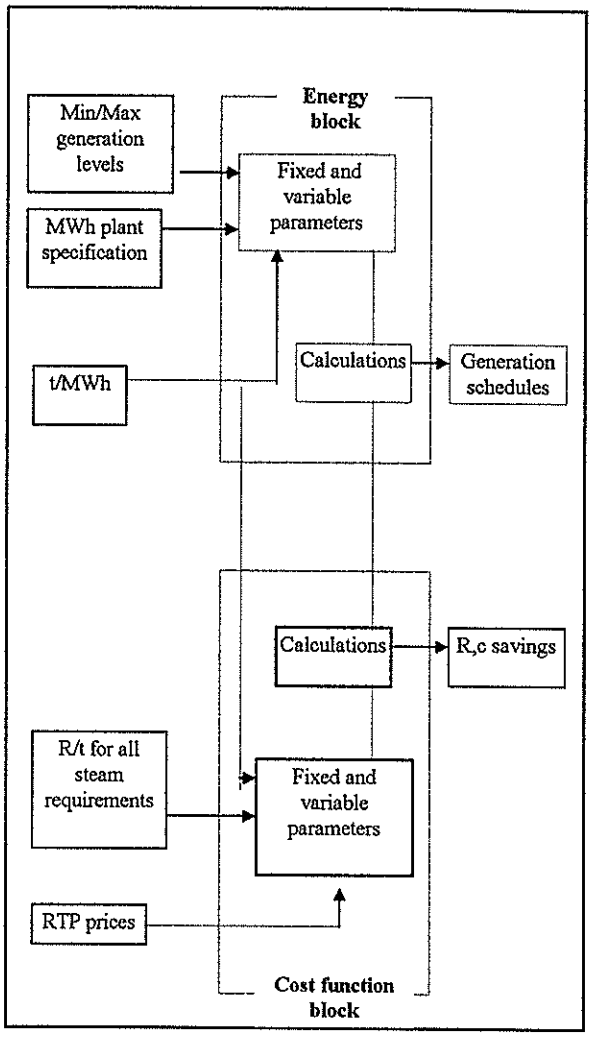

Figure 2.2 Schematic model layout

6.1 Verification and results for case study

In figure 6.2 it can clearly be seen that according to the previous schedules under the Nightsave tariff, cogeneration plant 1, PS1, is not being scheduled to generate at different levels. The average power level is 60 MW. The scheduling is done between PS2 and Eskom. The Eskom supply will dominate during the night and PS2 during the day.

Figure 6.3 is also showing generation schedules of the three supplies. This figure shows the schedules given by the model. The same data for three weeks is used as in figure 6.2. In this case it can be seen that PS1 is also being switched between different generation levels. It can be seen in figure 6.3 (RTP) that PS2 is generating much less power than in figure 6.2 (Nightsave). The only times PS2 is generating at a higher level than the minimum is when the Eskom marginal rate exceeds the cogeneration plant 2's marginal rate.

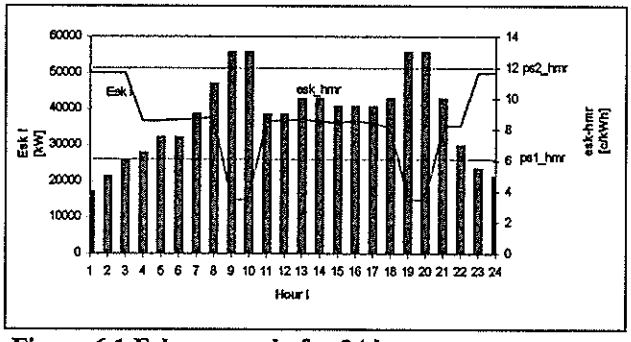

Figure 6.1 Eskom supply for 24 hours versus esk_hmr

Table 6.1 Costs of electrical energy for one month.

	Nightsave			RTP	
	Energy [MWh]	MD [kW]	Costs [R] Milj	Energy [MWh]	Costs[R milj
Eskom		38 702	1, 295		
	22 358		1, 444	27 543	2, 031
PS1	44 195		2, 704	50 225	3 ,073
PS2	19 102		2, 302	7 887	0,950
Total	85 656		7, 746	85 656	6, 056

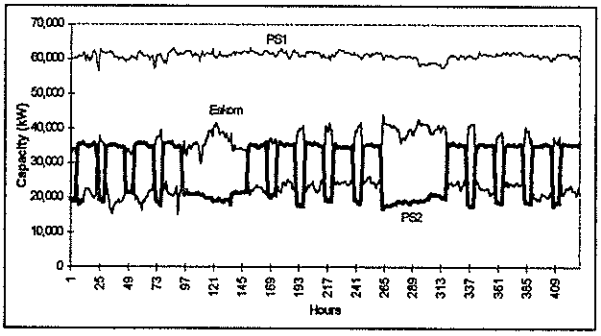

Figure 6.2 Previous schedules for the Nightsave tariff.

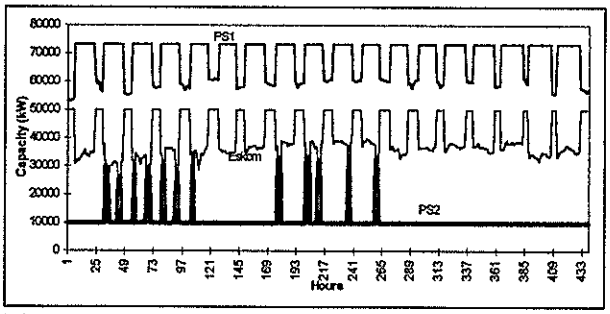

Figure 6.3 Model schedules for RTP tariff.

7 CONCLUSIONS

The previous results are for the specific configuration of the two cogeneration plants. The model can be used to analyze other cogeneration plants not corresponding to the ones showed above. As long as the marginal rate for the specific plant can be calculated, the model can be altered to calculate the schedule of generation of the plant, and the cost saving potential of the RTP tariff.

8 REFERENCES

[1] Roos JG and Kern C, "Real-time Pricing of electricity and its cost saving potential to industry through intelligent demand management", Key Customer Marketing ESKOM, January 1997.

[2] Tabors R.D., Schweppe F.C., Caramanis M.C., " Utility experiences with real time rates ", IEEE transactions on power systems, Vol. 4, No. 2, May 1989, pp 463 - 471.

[3] Puttgen H.B.," Optimum Scheduling Procedure for Small Power Producing Facilities ", IEEE transactions on power systems, Vol.4, No.3, Augustus 1989, pp 957.

[4] Walshaw A.C.," Applied thermodynamics. ", London and Glasgow, 1947, pp 131-168, 208-236, 242-251.

[5] Singer J.G.," Combustion Fossil Power Systems : a reference book on fuel burning and steam generation.", - 3rd edition, Combustion engineering, inc, 1981, chapter 1 and 5.

[6] Roos JG, "Incrementing Industrial Cost savings to Intelligent Demand Management". Ph.D Thesis, University of Pretoria, 1996.

9 NOMENCLATURE

Variable parameters:

$P_{req}i$= Power required by industry for hour(i) [kW]

esk_hmr i= Hourly marginal rate for power supplied by Eskom for hour(i) [c/kWh]

Fixed parameters:

ps1_hmr= Fixed hourly marginal rate for power generated in power station1 [c/kWh]

ps2_hmr= Fixed hourly marginal rate for power generated in power station2 [c/kWh]

Variable parameters:

PS1 i = Power generated by power station 1 for hour(i) [kW]

PS2 i = Power generated by power station 2 for hour(i) [kW]

ESK i= Power supplied by Eskom for hour(i) [kW]

THE FEASIBILITY OF VARIABLE SPEED DRIVES FOR AIR-COOLED HEAT EXCHANGERS WITH RESPECT TO ENERGY CONSUMPTION AND PERFORMANCE

F. Endrejat G.J. Delport H.R. van Niekerk
Centre for New Electricity Studies - Department of Electrical and Electronic Engineering - University of Pretoria

Abstract: This paper describes a model for an air-cooled heat exchanger (ACHE) with special attention to the fan drive equipment and the introduction of variable speed drives (VSDs). The goal of the modelling was to estimate the effect of variable air flow, obtained by different fan drive configurations (including VSD operation), on both the heat transfer and energy consumption of the system. Furthermore the paper discusses special merits of VSD operation on ACHEs.

Key Words: Variable air flow, variable speed drives, air-cooled heat exchangers, energy consumption

1 INTRODUCTION

ACHEs are heat exchangers which cool down a certain process fluid or product by means of air flow. There are several methods which can be used to control the output temperature of the process fluid. The temperature can be controlled by controlling the air flow, by controlling the process fluid flow rate, by introducing additional external cooling water or by a combination of these methods [1]. This paper investigates the option of controlling the air flow with VSDs because of energy, maintenance and controllability considerations.
A model was developed for determining the feasibility of VSDs on ACHEs in the chemical process industry. The model estimates the effect of VSDs or variable air-flow on the operation of ACHEs, specifically on the heat transfer performance and energy consumption of the system. The mathematics is capable of estimating the effect of different configurations of the system including different numbers of VSDs. The VSD effect was compared to the usual method of switching the fans on and off to control the output temperature of the system. The intention of the paper is not to give very accurate results, but to give an indication of the effect of VSDs on ACHEs. Very accurate results are in any case quite impossible because of the influence of factors like weather conditions, process fluctuations, fouling etc.

2 FAN DRIVES WITH VSDs

When air flow is controlled by means of damping, the fan efficiency varies, but the efficiency stays constant when changing the fan speed (as is the case in this project) [2]. Characteristic curves, for axial (this paper) and centrifugal fans as a function of speed variation, are similar [2]. According to the fan laws, fan power varies approximately with the cube of the air flow [6]. A similar relationship, with practical considerations, is given by equation 1. Equation 1 is a curve fit [1] to the generalised per unit power consumption values [3] which are scaled by the rated conditions. Induction motor, gearbox, fan and VSD efficiencies are considered.

$$P_{VSD_x}(Q_{\%_x}) = \frac{pQ_{100\%}dk_p}{1.2\eta_m\eta_g\eta_{VSD}\eta_f} \cdot 0.0868e^{0.0244Q_{\%_x}} \text{ [W]} \quad \ldots(1)$$

k_p is a compression factor and can be expressed as follows [3]:

$$k_p = \left[1 - \left(0.0035 \cdot p \cdot \frac{\eta_f}{p_a}\right)\right] \quad \ldots (2)$$

The on load power consumption measurement of the motors, without VSDs, should closely agree to the result of equation 1 at a flow rate of 100% (without including the efficiency η_{VSD}).

3 THE HEAT EXCHANGER

The fundamental relationships for the heat transfer from the air to the process fluid in heat exchangers are indicated in equations 3 to 6 [7].

$$q = U \cdot A_T \cdot F \cdot \Delta T_{lm} \text{ [W]} \quad \ldots (3)$$

where $$\Delta T_{lm} = \frac{(T_{HI} - T_{CO}) - (T_{HO} - T_{CI})}{\ln\left(\frac{T_{HI} - T_{CO}}{T_{HO} - T_{CI}}\right)} \text{ [°C]} \quad \ldots(4)$$

$$q = \frac{dm_w}{dt} \cdot Cp_w \cdot (T_{HI} - T_{HO}) \text{ [W]} \quad \ldots(5)$$

and $$q = \frac{dm_a}{dt} \cdot Cp_a \cdot (T_{CO} - T_{CI}) \text{ [W]} \quad \ldots(6)$$

Equation 3 can be used at rated conditions, but with variable air flow a more sophisticated approach is required. An estimation of the overall heat transfer-air flow curve can be obtained, based on overall transfer coefficient(U)-air flow curves [9], [4], correction factor (F) curves [8] and simultaneous solution of equation 3 to 6 for q (and T_{HO}, T_{CO}) for different air flow rates. The other required information for equations 3 to 6 are obtained from the heat exchanger specification sheet.
The results must be verified at the rated conditions with the specification sheet of the ACHE and the obtained curve should be verified by border conditions. The heat transfer coefficient curves will depend on the tube and fin configurations. The obtained curve in this project, is based on a forced draft exchanger with a given fluid inlet temperature, given air inlet temperature and rated process fluid rate. The curve includes the small effect of natural convection and radiation. An example of such a curve is shown in the case study in figure 2. Such a curve should be used in combination with the mathematics presented further in this section. The mathematics is based on heat exchangers of the cross-counterflow type with a return bend or exchangers with more than one pass. Furthermore separate chambers for each fan are assumed. The assumption is made that the heat transfer characteristics of the different bundle sections served by the separate fans, are identical functions of air flow. The theory is merely developed to give a quick and easy indication of the effect of variable air flow and different configurations. More accurate results can be obtained on a basis of division into small parts (ideally, finite element analysis).
The following equations are derived in [1] and include the heat transfer obtained by any combination of VSDs and fixed speed drives:

$$q = (N - N_{VSD}) \cdot \frac{q_{nt}}{N} + N_f q_f + \sum_{k=1}^{N_{VSD}} q_{VSD_k}(v_{k\%}) \text{ [W]} \ldots (7)$$

$$\text{where } q_f = \frac{q_{RATED}}{N} - \frac{q_{nt}}{N} \text{ [W]} \quad \ldots (8)$$

$$\text{and } q_{VSD_k}(v_{\%_k}) = q_{tf} \cdot q_{pu}(v_{\%_k}) \text{ [W]} \quad \ldots (9)$$

The total power consumption at a specific operating condition is the sum of the power of the fixed speed drives and that of the VSDs:

$$P = P_{FIXED} + P_{VSD} = N_f P_f + \sum_{k=1}^{N_{VSD}} P_{VSD_k}(Q_{\%_k}) \text{ [W]} \quad \ldots (10)$$

(The percentage values of air speed and volume flow rates would be the same because air speed and volume flow rate are proportional to one another because of a fixed cross sectional chamber area.)

By using equations 7 and 10, a relationship between the total heat transfer and the power consumption can be obtained for different fan drive configurations.

4 CASE STUDY

The system that was evaluated has 4 fans (each with a 525 V 45 kW induction motor) and functions as a circulation water cooler in the chemical industry. The rated specifications are: a heat transfer 10.58 MW, an effective mean temperature difference of 24.2 °C, air flow of 129.5 m^3/s per fan, fluid flow of 303000 kg/h, fluid temperatures of 80 °C (in), 50 °C (out) and air temperatures of 28 °C (in) and 51 °C (out). The complete specifications are given in [1]. The average air density is calculated to be 1.007 kg/m^3 [1]. The power consumption - air flow relationship for a *single fan unit* is obtained as discussed in section 1 and shown in figure 1. The calculated power consumption closely agrees with the measured power consumption at the rated air flow value of 129.5 m^3/s (the calculated power is 2.4% higher, because of the VSD). If a curve for 4 VSDs is required, the power-axis values must be multiplied by 4 (for each VSD at the same speed with respect to each other).
The heat transfer-air flow curve was obtained by means of the theory in section 3. The curve is given on a per unit basis in figure 2.
A total heat transfer - power consumption curve can now be obtained from figures 1 and 2 and the theory in section 3. The relationship is indicated in figure 3. Note that the top curve is the curve for 4 VSDs running at the same speed. The other curves are examples of configurations to give an indication of the effect of a lower number of VSDs (based on the assumptions in section 3). The motors not at variable speed are at full speed. The heat transfer obtained by switching of the motors are also indicated (based on the assumptions in section 3). The left most points of the 1, 2 and 3 VSD curves respectively represent 3 , 2 and 1 motors switched on. The right most point represents 4 motors switched on at the rated heat transfer rate. In [1] it was indicated that VSDs should, if possible be operated at the same speed, therefore the curves are presented with all VSDs at the same speed with respect to each other.
Figure 3 clearly indicates that the electrical energy efficiency of the system can be improved by VSDs with respect to on and off switching of fans, especially at the low heat transfer of the system. It is also clear that a more continuous heat transfer range can be obtained by VSDs and therefore better temperature control. In the case of on/off switching of fans, the water flow rate needs to be varied to assist in temperature control, because of the discontinuous heat transfer which is then obtained. Even with well planned fan switching and fluid flow control, energy can be wasted (the water flow rate might not be ideal for maximum heat transfer

and a fan may unnecessarily be switched on). VSDs will clearly reduce this problem (especially with ACHEs which have a low number of fans). It might still become necessary to switch motors with VSDs off, to obtain a more rapid and higher temperature control response (because of the low incline of the curve with 4 VSDs in the region of the rated heat transfer).

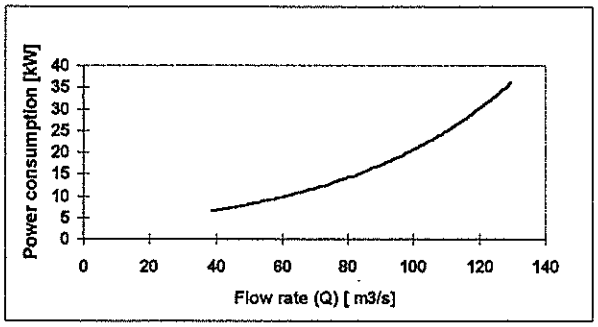

Figure 1 Power consumption - air flow relationship for a single fan unit

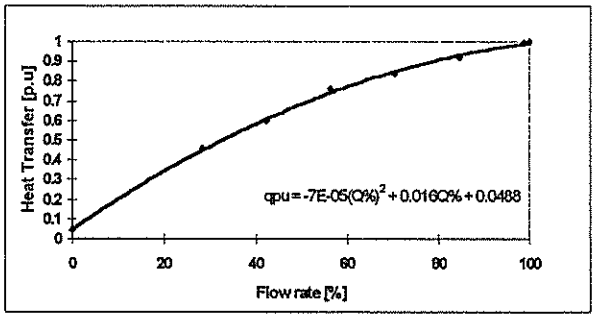

Figure 2 Heat transfer - air flow relationship

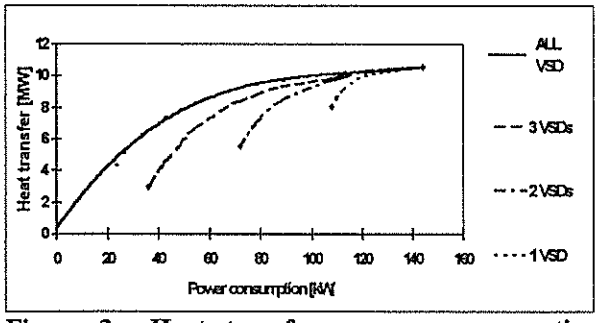

Figure 3 Heat transfer - power consumption relationship

5 OTHER VSD CONSIDERATIONS

Apart from air flow control (and therefore temperature control) and electrical energy efficiency advantages, there are several other merits and considerations that are being investigated.

Overrated motors (for example, because of standard factory motor ratings) are sometimes installed for ACHEs. The case study is an example. (The motors are rated at 45 kW whereas the requirement is a maximum of 37 kW.) It is therefore possible to increase the speed of the motor by means of the VSD, and perhaps even into the field weakening region of motor operation, that is of course, if the fan power curve allows it. The increase in speed is unfortunately drastically limited because of the nature of a fan load. Furthermore the heat transfer increase is limited by the low incline of the heat transfer - air flow curve in the region of the rated heat transfer. The speed increase might be of greater advantage to other types of loads like constant torque loads.

A further merit of VSDs and induction motors is that the torque can significantly be increased at intervals for short periods as is indicated in user's manuals. An effective increased air flow (because of both the additional available speed and the torque boosts) must then be calculated and used in conjunction with a heat transfer-air flow curve to evaluate the feasibility of the increased air flow. Such an increased air flow may be of advantage in demanding conditions (exceptional high ambient temperatures, increased process demand, etc.), especially when fouling of the heat exchanger become significant.

Care has to be taken in such a study, because of thermal and mechanical limits of the motor when operated with VSDs at higher speeds and torque boosts. The mechanical limits of the equipment driven by the motor must also be considered.

When VSDs of the frequency converter type are used, non sinusoidal waves are present (for example PWM waves), harmonics are present, the motors should be derated and a loss study is necessary to determine the amount of efficiency drop [5]. The motors that are used on ACHEs (especially old ones) are not necessarily the ideal motors for VSD operation. An energy efficient motor can mean additional energy savings and a special motor can be designed which is capable of higher mechanical and thermal limits.

Some ACHE systems have a high record of motor repairs. When VSDs are installed on all motors and they are driven at the same speed with respect to each other, each motor has a mean lower operating speed, especially with ACHEs with a low mean heat transfer requirement. This necessarily means lower currents because of the fan load and it can mean longer motor life.

The above effects are being researched with the objective of quantifying them and applying them to other applications as well.

6 CONCLUSIONS

Apart from temperature control, VSDs can increase the system energy efficiency (and most probably reliability), especially if the system works most of the time below rated conditions. Even if there is a need, in extreme cases, that performance above rated conditions is required, VSDs (for overrated motor configurations)

might here also assist in the goal of increased performance.

7 NOMENCLATURE

$\frac{dm_w}{dt}$	Total mass flow rate of the process fluid (water)	kg/s
$\frac{dm_a}{dt}$	Total mass flow rate of the cooling air	kg/s
ρ	Air density	kg/m^3
η_f	Fan efficiency at rated conditions	p.u.
η_{lg}	Gearbox efficiency at rated conditions	p.u.
η_{lm}	Motor efficiency at rated conditions	p.u.
ΔT_{lm}	Logarithmic Mean Temperature Difference	°C
η_{VSD}	VSD Efficiency	p.u.
ACHE	Air-cooled Heat exchanger	-
A_T	Total heat transfer surface	m^2
Cp_w, Cp_a	Specific heat of the warm and cold stream respectively	kJ/kg-K
F	Correction factor obtained from curves for the specific configuration	
N	Total number of fans	-
N_f	Number of fixed speed fans (without VSDs)	-
N_{VSD}	Number of fans with VSDs	-
p	Rated total pressure increase of fan	Pa
P	Total power consumption	Watt
p_a	Air pressure at suction inlet	Pa
P_F	Power consumption associated with one fixed speed drive	Watt
P_{FIXED}	Power consumption associated with the fixed speed drives	Watt
P_{VSD}	Power consumption associated with the variable speed drives	Watt
$P_{VSD_k}(Q_{\%_k})$	Power consumption of VSD k at a flow rate of Q in %	W
PWM	Pulse with modulation	-
q	Heat transfer	W
$q_{pu}(v_{\%_k})$	Heat transfer associated with a single fan k at an air speed of v in %	p.u.
$q_{VSD_k}(v_{k\%})$	Heat transfer associated with VSD k which produces an air speed of v in %	W
$Q_{\%_k}$	Air flow rate caused by VSD k	%
$Q_{100\%}$	Full volume (air) flow rate (fixed volume flow rate)	m^3/s
q_f	Heat transfer contribution of a full speed fan	W
q_{nt}	The total heat transfer because of natural convection and radiation alone	W
q_{RATED}	Rated heat transfer of complete heat exchanger	W
q_{tf}	Total heat transfer in a specific fan area (natural convection and radiation included)	W
T_{CI}	Inlet temperature of the cold stream (air)	°C
T_{CO}	Outlet temperature of the cold stream (air)	°C
T_{HI}	Inlet temperature of the hot stream (water)	°C
T_{HO}	Outlet temperature of the hot stream (water)	°C
U	Overall heat transfer coefficient	W/m^2°C
VSD	Variable speed drive	-

8 REFERENCES

[1] F. Endrejat, Load Modelling of a FFCS, *EKX 716 report*, Centre for New Electricity studies - University of Pretoria, 1997

[2] C. Tanner-Tremaine, Variable speed drives for large fans, *Vector Electrical Engineering*, June 1981, pp 10-14

[3] ABB, *Energy Savings Calculator for pump drives*, User's Manual, ABB Industry, Finland, 1994

[4] E.M. Cook, 'Rating Methods for Selection of Air-cooled Heat Exchangers', *Chemical Engineering*, August 3, 1964, pp 97-104

Journal referencing

[5] F.G.G. de Buck, Losses and Parasitic Torques in Electric Motors Subjected to PWM Wave forms, *IEEE Transactions on Industry Applications*, Vol. IA-15, No. 1 January/ February 1979, pp 47 -53

Book referencing

[6] W.C. Osborne , *Fans*, Pergamon Press, 1977

[7] S.P. Sukhatme, *A Textbook on Heat Transfer*, Third edition, Orient Longman 1990

[8] D.Q. Kern and A.D. Kraus, *Extended Surface Heat Transfer*, McGraw-Hill Inc., 1972, p 572

[9] P. Paikert '*Air-cooled Heat Exchangers-Thermal Rating*', Hemisphere Publishing Corporation, 1983, pp 3.8.5-1 to 3.8.5-3

AC and Negative Lightning Impulse Voltage Breakdown Characteristics of Gas Mixtures in a Coaxial Cylinder Gap

M Zhou and JP Reynders

Department of Electrical Engineering
University of the Witwatersrand

Abstract - *AC* and negative lightning impulse (*NLI*) breakdown voltages for pure gases and gas mixtures were studied using a coaxial cylinder geometry. The experimental pressure ranged from 1bar to 4bar. The mixtures comprised strongly electronegative gas SF_6 and electron retarding gases N_2 and CO_2. Synergism effects were found in the binary and ternary mixtures. The dielectric behaviour is different for pure gases/gas mixtures under AC compared with *NLI*. Studies demonstrated the important role of electron scattering processes in effecting the electron attaching abilities and in improving the dielectric strength of gas mixtures.

Keyword: dielectric, ionization, electron attachment, electron scattering, electron retarding, electronegativity, electron affinity, cross section, *NIR* state, synergism effect.

1 INTRODUCTION

It is well known that SF_6 has excellent dielectric characteristics and is the most commonly used insulating gas at present. However, its disadvantages such as green house effect [3], high sensitivity to conductor surface roughness [6] and high cost, limit its application. Using gas mixtures containing SF_6 can minimise the above problems. If an appropriate additive gases can be chosen, an improved dielectric/cost performance will be provided.

The theory of the behaviour of electrons in gases provides a much more general approach for such a purpose. It has been found that the dielectric properties of gases are controlled by very complex electron-molecule interactions at the molecular level, especially by those free electron producing and depleting processes in the low energy range (0-20*eV*) which is the energy range of principal significance to gaseous dielectrics. Knowledge of these processes allows a tailoring of the dielectric gas and a choice of the appropriate gas mixtures for particular applications.

The key processes influencing gas dielectric strength include ionization, electron attachment and electron scattering. Comparing these three processes, the effects of the large electron attaching and the large electron scattering processes are proposed to be the most significant ones. Normally, the strongly electron attaching and electron scattering gases have high breakdown strengths, weakly/non-attaching or non-scattering gases have low breakdown strengths.

Therefore it is suggested that to obtain a mixture with a high dielectric strength, not only must the component gas have an electron attachment cross section as large as possible, and the electron ionization cross section as small as possible, but also the reduction of the electron energies is of significance. The latter can be achieved by adding electron retarding gas components.

As is well known, SF_6 is a strongly electronegative gas. It has been found that N_2 and CO_2 are effective electron retarding gases. For this reason, mixtures of SF_6 with N_2 and CO_2 have been investigated in our experiments.

2 ELECTRONEGATIVE GAS

Electronegative gases are electron attaching gases in which long-lived negative ions can be formed. To form a stable long-lived negative ion, the electron affinity of the gas molecule must be positive (>0*eV*).

SF_6 is a strongly electronegative gas. Its molecules posses very attractive properties in attaching low energy electrons. Fig.1 shows that the attachment of very slow electrons to SF_6 molecules has a strong peak in the range 0-1*eV*.

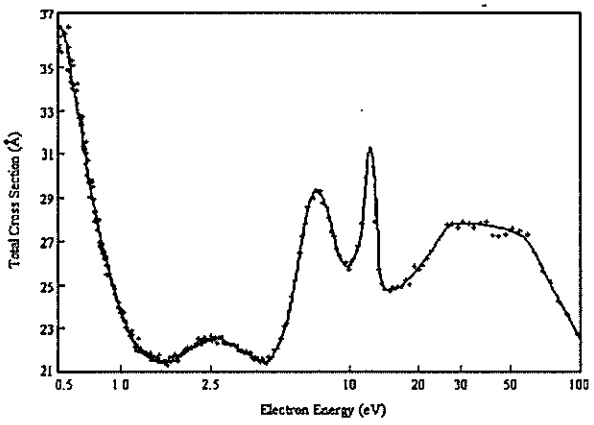

Figure 1: The total electron scattering cross section for SF6 from 0.5eV to 100eV (Cite from [2]).

From the electron energy distribution function, we know that there is only a small fraction of electrons whose energies are expected to be below 1*eV*,

especially below $0.5eV$. However, the exceptionally large electron attachment cross section in SF_6 can remove all free electrons with energies in this low energy range very quickly by forming stable negative ions. Since the number density of slow electrons is reduced, the electron energy distribution has to recover its functional form to keep its steady-state unchanged by feeding the depleted low-energy tail from the higher energies at a very short time. Those regenerated low energy electrons will be removed again by the strong attachment processes at low energies in SF_6 and the electron energy distribution has to recover its shape again. Free electrons can thus be removed by this repetitive depletion/feeding process from the dielectric via the low-energy tail of the electron energy distribution.

This unusual capability of SF_6 molecules to attach slow electrons ensures a very high breakdown strength. With other attractive properties such as high ionization threshold, large electron affinity, SF_6 is an excellent dielectric gas. However, its disadvantages such as green house effect, high sensitivity to conductor surface roughness and high cost, limit its application. Using gas mixtures can minimise the above problems

3 ELECTRON RETARDING GASES

Electron retarding gases are gases in which fast electrons can be slowed and the electron energy can then be reduced. The electron scattering processes in gases, especially the indirect electron scattering via the negative ion resonance (*NIR*) state is the most effective way to retard free electrons.

NIR state is formed when an incident electron is temporarily captured by the target molecule to form a temporary negative ion. The attachment of this electron occurs at a definite energy, leading to a peak in the attachment cross section therefore a longer lifetime of the negative ion than the time of the electron traversing the target molecule. Because the state of this negative ion lies above the ground state of the neutral molecule, this negative ion will ultimately decay by autodetachment. With these short-lived negative ions, however, fast electrons can be retarded significantly which leads to a significant enhancement of the scattering cross section of gas molecules. In the low-energy range, such indirect processes constitute an efficient retarding mechanism.

Molecular *NIR* states are abundant [1]. It has been found that *NIR* states also exist in gases such as H_2, N_2, O_2, CO, CO_2 CH_4, *etc.* However, we are only interested in those gasses in which strong *NIR* states lie in the low energy range.

N_2 is a typical electron retarding gas. Fig.2 shows the total scattering cross section of the e-N_2 collision. The large hump at $\sim 2.3eV$ in this figure represents a strong *NIR* state and hence a strong inelastic scattering process. The rate of collisional electron-energy loss is thus correspondingly enhanced significantly [7] to keep free electrons from initiating the gases to breakdown. The excellent electron retarding properties of N_2 molecule promise a good dielectric characteristics in N_2.

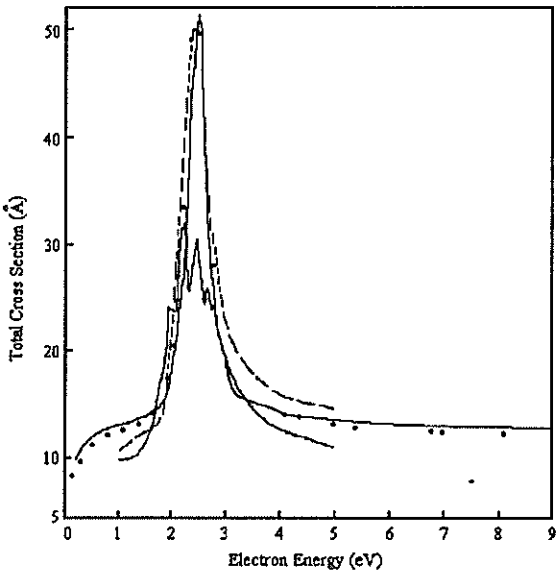

Figure 2: The electron scattering cross section for N2. (Cite from [4]).

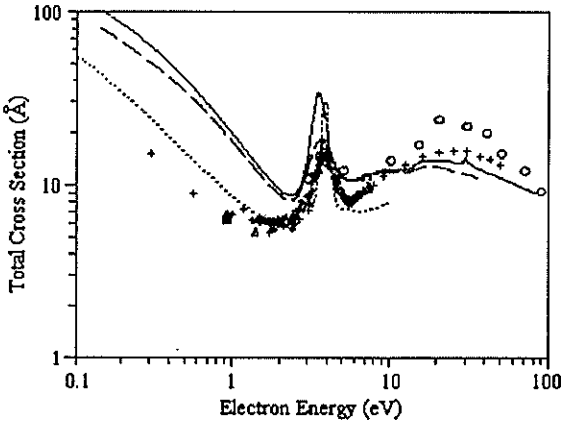

Figure 3: The electron scattering cross section for CO2 from 0eV to 100eV. (Cite from [5]).

In CO_2, there is also a strong *NIR* state lying at $\sim 3.85eV$ (Fig.3). Its electron retarding process is similar to that of N_2, but not as strong as that one.

4 EXPERIMENTAL SETUP AND PROCEDURE

The experimental setup is illustrated in (Fig.4). The test gap is a coaxial cylinder. The two electrodes are made of steel. The outer electrode is 63mm in

diameter. The inner electrode is 23.8mm in diameter and the surface roughness, measured on a Taylor roughness tester with an amplification of 20 in the axial and 1000 in the radial-direction, is shown in Fig.6. The gap length is then 19.6mm. The testing pressure range is 1bar-4bar (absolute). All investigations have been done under *AC* and *NLI*.

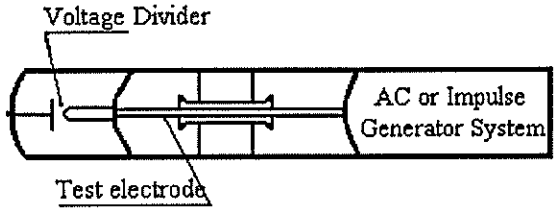

Figure 4: Experimental setup

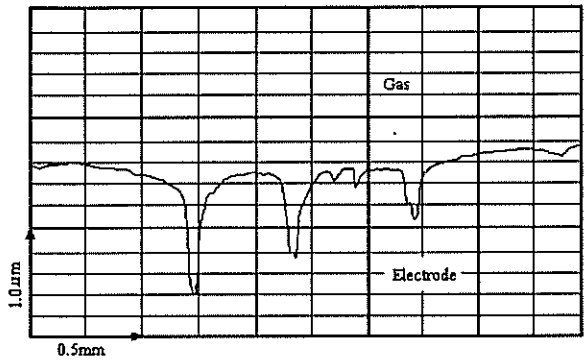

Figure 5: Electrode surface profile

After mounting the electrodes, the test vessel is evacuated and filled with the selected mixtures at the maximum pressure. The filled vessel is left for at least two hours before making the first measurements to guarantee a good mixture of gases. The pressure is successively reduced for each series of measurements. Mean peak breakdown voltages have been measured under *AC* and 15-25 observations were taken for each breakdown value. 50% breakdown voltages, which are determined by the up-and-down method, have been measured under *NLI* and 30-50 observations were taken for each breakdown value.

5 RESULTS AND DISCUSSION

The breakdown voltages for pure gases and gas mixtures under *AC* and *NLI* are shown in Fig.6 and Fig.7.

Pure SF_6 shows a much higher breakdown voltage than that of pure N_2 and CO_2 under both conditions. It is suggested to be contributed to its extremely strong electron attaching ability in the thermal energy range.

The dielectric behaviour for pure N_2 and pure CO_2 are quite different under both conditions.

Under *AC*, the breakdown voltage of N_2 is higher than that of CO_2. As shown in Fig.2 and Fig.3, the *NIR* state in N_2 (~2.3*eV*) not only lies below, but also stronger than the *NIR* state in CO_2 (~3.85*eV*), more efficient electron retarding processes can be built up in N_2 at low pressure to keep free electrons from initiating gas breakdown. Therefore a higher breakdown voltage can be observed in N_2. As the pressure increased, however, more and more electrons have been shifted to the high energy range, the electron retarding process in CO_2 becomes more efficient, the breakdown voltage of CO_2 thus increases more rapidly than that of N_2. At 4 bar, these two gases almost have the same breakdown voltage.

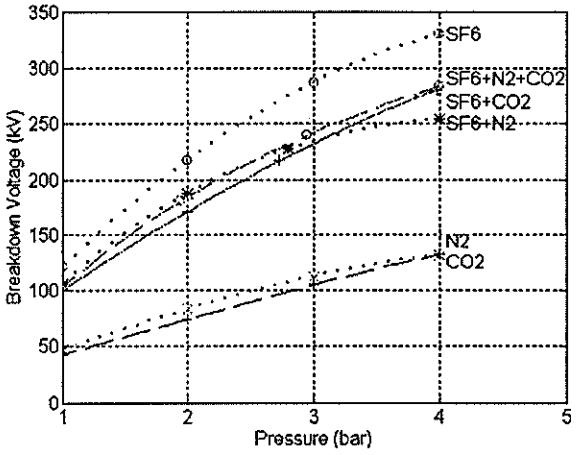

Figure 6: Mean breakdown voltage for SF6 and its mixtures under *AC*.

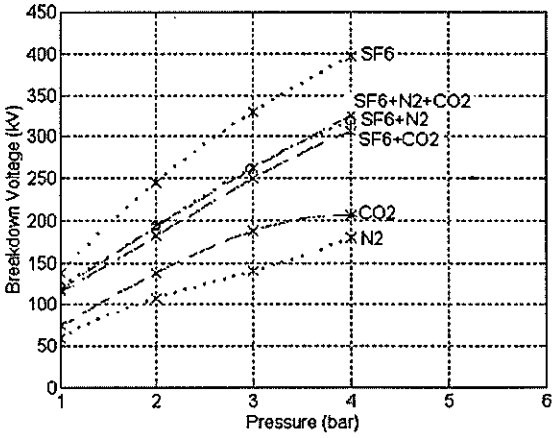

Figure 7: 50% breakdown voltage for SF6 and its mixtures under negative lightning impulse.

Under *NLI*, the breakdown voltage for CO_2 is higher than that of N_2 over the pressure range we investigated. Such a difference under both conditions is suggested to be caused by the time difference to reach the peak voltage under both conditions. Under *AC*, the voltage reach its peak value in ~10*ms* and under *NLI*, the voltage reach its peak voltage in a much short time ~1μs. As we mentioned before, when the low energy electrons are removed, the electron energy distribution function has to reshape and to shift high energy electrons to the low energy range. It takes time for such a procedure. Under *NLI*, there is no enough time for N_2 and CO_2 molecules to build up

an effective and stable electron retarding processes. However, CO_2 is slightly electronegative and its molecules can attach free electrons as well as retarding them. This property indicted a better dielectric performance in CO_2 under *NLI* than in N_2.

Synergism effects can be observed in SF_6 mixtures. With only 50%SF_6, the breakdown voltage of mixtures were found to be 77~85% of that of pure SF_6. The combination of gases provides a better dielectric characteristic than the sum of the individual gas components. This synergy can be explained by the fundamental electron-molecule interactions in mixtures. As shown in Fig. 1, the electron capturing ability of SF_6 is only strong for nearly zero-energy electrons. When N_2/CO_2 is added to pure SF_6, the narrow but strong low-lying *NIR* state in N_2/CO_2 can slow fast electrons into a low energy range very effectively. Therefore although the breakdown voltage of N_2/CO_2 is much lower than that of SF_6, the breakdown voltage of mixtures does not lie significantly below that of pure SF_6.

The dielectric behaviour of gas mixtures is also different under AC and *NLI*.

Under *AC*, considering the electron retarding process is more efficient in N_2 at the low pressure and in CO_2 at the high pressure (explained in the above), the breakdown voltage of SF_6/N_2 is higher at the low pressure and is lower at the high pressure than that of SF_6/CO_2.

Under *NLI*, however, the breakdown voltage of SF_6/N_2 is higher than that of SF_6/CO_2 over the pressure range investigated. In this case, a stable electron retarding process can't be established in such a short time in N_2 and CO_2. Considering the *NIR* state in N_2 is stronger and lie below than the *NIR* state in CO_2, the dielectric behaviour of SF_6/N_2 is therefore better than that of SF_6/CO_2 over the pressure range investigated.

The synergism effect in the ternary mixture is more significant under *AC*. The breakdown voltage of 50%SF_6/34%N_2/16%CO_2 is higher than that of binary mixtures over the pressure range investigated. The improved dielectric performance can be attributed to the more efficient electron retarding processes over a wide energy range via the two low-lying *NIR* states in the mixtures. However, such phenomena can't be observed under *NLI*. The breakdown voltage of the ternary mixture is almost the same as that of binary mixture of SF_6/N_2 under *NLI*. The time plays a very important role in this case.

The gas mixtures also provide other advantages. As is well known, SF_6 is a `greenhouse' gas. Its global warming potential is estimated to be ~25000 times greater than that of CO_2 [3]. Unlike the naturally occurring greenhouse gas CO_2, SF_6 is largely immune to chemical and photolytic degradation and therefore its contribution to global warming is expected to be cumulative and quasipermanent. The replacing of pure SF_6 with gas mixtures will reduce this disadvantage.

6 CONCLUSION

Our present work has discussed the breakdown strength of gas mixtures containing strongly electronegative gas and strongly electron retarding gases. Experimental results carried out with mixtures of SF_6, N_2 and CO_2 displayed the excellent synergism effects. Mixture with only 50%SF_6 can provide a breakdown voltage up to 77-85% of that of pure SF_6. Experimental results demonstrate the important role of electron scattering processes, especially the scattering via the *NIR* state in the low energy range, in enhancing the attaching ability of electronegative gases and in improving the gas dielectric properties. The dielectric characteristics for gases/gas mixtures are different under *AC* and *NLI*. Such differences are suggested to be caused by the time difference to reach the peak voltage under *AC* and *NLI*.

From the above discussions, we know that the optimum gas is not a single gas but rather a mixture in which the best combination of strongly electron attaching and electron retarding properties can be provided.

7 REFERENCES

[1] Bardsley JN, F Mandl, Resonant scattering of electrons by molecules, *Rep. Prog. Phys.*, Vol 31, 1968, pp472-531.

[2] Kennerly RE, RA Bonham, The total absolute electron scattering cross sections of SF_6 for incident electron energies between 0.5 and 100eV including resonance structure, *J. Chem. Phys.*, 1979, pp2039-2041.

[3] Ko MKW, ND Sze, *et al*, Atmospheric SF_6: sources, sinks and greenhouse warming, *J. Geophys. Res.*, Vol 98, 1993, pp10499-10507.

[4] Lane NF, The theory of electron-molecule collisions, *Rev. Mod. Phys.* 52, No 1, 1980, pp29-119.

[5] Maureen GL, Dan Dill, Elastic electron scattering by CO_2, OCS and CS_2 from 0 to 100eV, *J. Chem. Phys.* 71, 1979, pp4249-4254.

[6] Pedersen A, The effect of surface roughness on breakdown in SF_6, *IEEE Trans. Power App. Syst.*, Vol 94, No 5, 1975, pp1749-1753.

[7] Sun W, MA Morrison, *et al*, Detailed theoretical and experimental analysis of low electron-N_2 scattering, *Phys. Rev. A*, Vol 52, No 2, 1995, pp1229-1256.

CORONA NOISE AS A MEASURE OF CORONA POWER LOSS ON SINGLE CONDUCTORS

J. P. Reynders & M S Engelbrecht

Department of Electrical Engineering
University of the Witwatersrand
Private Bag 3, WITS, 2050, South Africa

Corona can be responsible for significant losses on a power line and these need to be considered when the capacity of the line is assessed. Unfortunately the difficulty of measuring this loss under service has severely limited our ability to determine the extent of the loss problem. Audible noise measurements provide a totally non-intrusive means of measuring a direct consequence of the noise. This paper describes a series of carefully constructed experiments which demonstrate a linear relationship between audible noise and corona power loss on single conductors with distributed noise sources.

Keywords: Corona, audible noise, power loss.

1 INTRODUCTION

Corona is responsible for power losses which may be significant. For example Bartnikas [1] cites the following: a 3 phase overhead transmission line with a 10m flat spacing and a conductor diameter of 42mm may lose up to 2,5kW per km of length at 350kV in dry weather. In wet weather the corona loss can be as high as 44kW per km. At 400kV, the same line loses 6kW per km in dry weather and 114kW per km when wet.

These values are high and they represent the peak corona power loss. The average corona loss measured experimentally in project UHV [4] for an EHV line had been found to be only a small proportion of the resistance loss. However, the peak losses have been viewed as having a significant influence on the demand requirements which the generation must provide. Therefore the probability of peak corona losses coinciding with peak load requirement needs to be carefully examined for any proposed line, otherwise the line designer has no basis for evaluating the effects of conductor or voltage changes on corona loss economics [4].

Work has been done on corona power loss and its prediction. The most significant of these being part of project UHV [5]. This project demonstrated a linear relationship between corona power loss and audible noise. However, no attempt was made to generalise this observation.

2 AUDIBLE NOISE

The audible noise generated by corona on power lines may be considered to be composed of 2 major components [5]. The first is a broadband component that has a significant high frequency content. The random phase relationship of the pressure waves combined with a significant high frequency content produces the crackling or hissing characteristics that is heard [5].

The second component is a pure low-frequency tone superimposed on the broadband noise. Corona discharges produce positive and negative ions that, under the influence of the alternating electric field around the conductors, are alternately attracted to and repelled from the conductors. The motion establishes sound pressure waves having a frequency twice that of the voltage wave, i.e. 100 Hz for a 50Hz system [5]. The high frequency components referred to above are present in bursts which occur synchronously with the power frequency voltage and are therefore represented in the twice-power frequency noise.

3 EXPERIMENT

3.1 Measurement of corona power loss

The average corona power loss, for experimental purposes, was calculated using the integral of the instantaneous voltage multiplied by the instantaneous corona current:

$$P = \frac{1}{T}\int_0^T v.i.dt = VI\cos\theta$$

where :

P = average power	T = measurement period
V = rms voltage	I = rms current
θ = power factor angle	v = inst. voltage
i = inst. corona current	

3.2 Measurement of Audible Noise

This was done using a free field microphone in conjunction with a sound level meter.

3.3 Experimental set-up

Two solid aluminium corona cages as illustrated in Figure 1 were used. The first cage had an outer diameter of 300mm and the second an outer diameter of 480mm. In the centre of each cage a 15,0mm diameter a copper conductor was supported. Small metallic cones 4,5mm in length with a base diameter of 3,3mm and a tip diameter 0,55mm were soldered to the surface of the conductor and used as sources of corona activity.

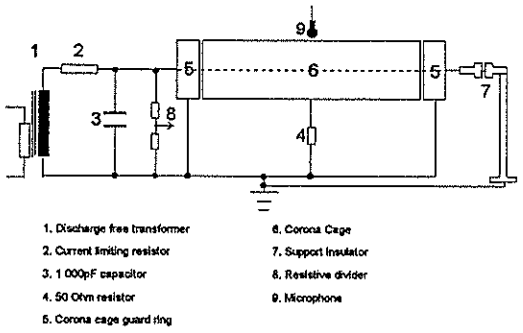

Figure 1. Corona cage layout.

The voltage waveform was measured using a 1000:1 resistive voltage divider. Corona current was measured by measuring the voltage across the 50Ω resistor connected between the outer electric cage and ground. The voltage the current and the output of a sound level meter were digitised at 250kHz and stored for periods of 3 cycles.

3.4 Experimental method

Measurements followed the same procedure for both cages. Starting with a single point on the surface of the conductor 10 readings of the corona loss were taken while increasing the voltage in 10 stages. The measurement of audible noise was made at the highest value of applied voltage. A Fast Fourier Transform (FFT) was performed on the waveforms to determine the frequency components of the measured signal and the 100 Hz power. The highest value of voltage applied to each conductor was selected to give identical electric fields at the tips of the corona points for each of the cages. Field simulations were done using 3D finite element package to establish these voltages. The notion was behind this is that corona activity is field related and identical fields at the corona source will produce identical corona currents. Voltages of 27,9kV (rms) and 35,7kV (rms) were selected for the 2 cages respectively.

4 OBSERVATIONS

The corona currents are illustrated in Figures 2, 3 & 4. Figures 2 & 3 illustrates the instantaneous current for each the cages while in Figure 4 the 50Hz currents for the maximum test voltage (identical fields at the cone tips) are superimposed for both cages. As anticipated these 2 currents are of the same magnitude.

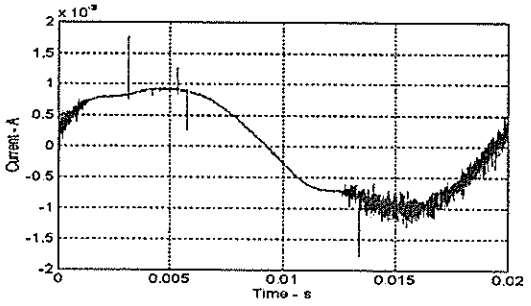

Figure 2. Current Measured Across 50Ω Resistor at 27.9kV(rms) in the 300mm Cage

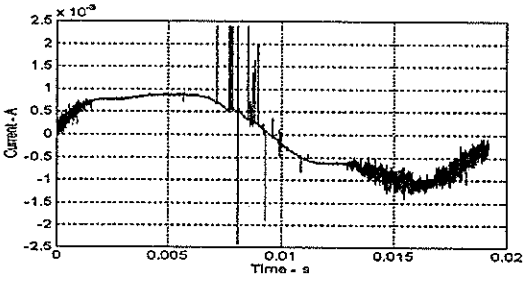

Figure 3. Current Measured Across 50Ω Resistor at 35,7kV (rms) in the 480mm Cage

The corona power increased linearly with the number of sites giving a different slope for each cage as illustrated in Figure 5. Similarly the 100Hz noise

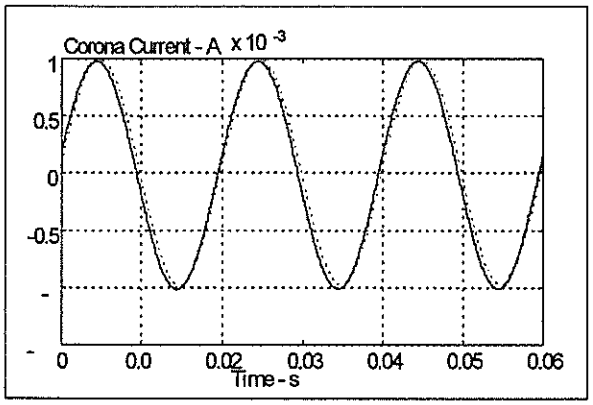

Figure 4. 50Hz Components of corona current as measured at the peak equivalent electric fields, in both corona cages

showed a linear relationship with corona power for each of the cages as illustrated in Figures 6 & 7. The noise measurements were normalised to the 300mm cage as follows:

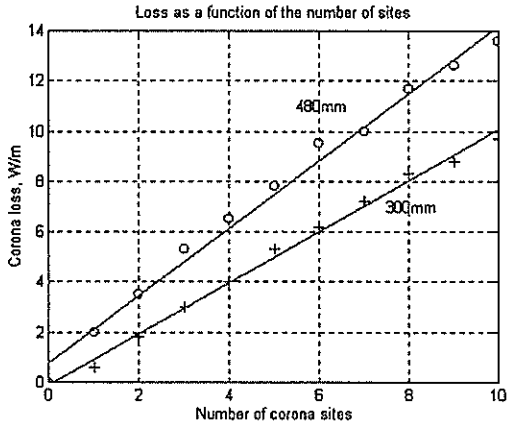

Figure 5. Corona power loss as a function of the number of sites for both cages.

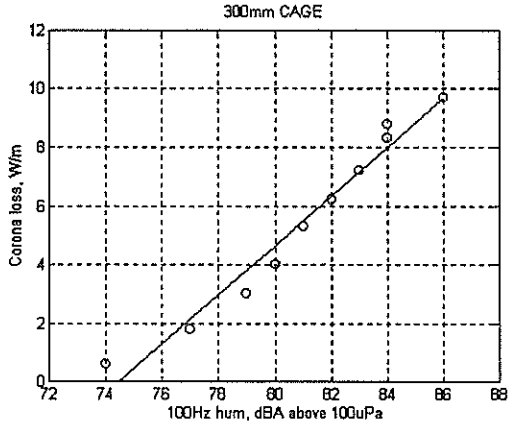

Figure 6. The relationship between corona power and noise for the 300mm cage

The ratio of the diameters is 1,6. Assuming that the attenuation of the sound is as the square root of distance, the difference in dBA between the noise in the 300mm and the 480mm cage is:

$$20\log_{10}\sqrt{1.6} = 2$$

Therefore 2 was subtracted from each of the dBA observations for the 480mm cage and the resulting noise was plotted on the same graph as the noise from the 300mm cage. The results are shown in Figure 8.

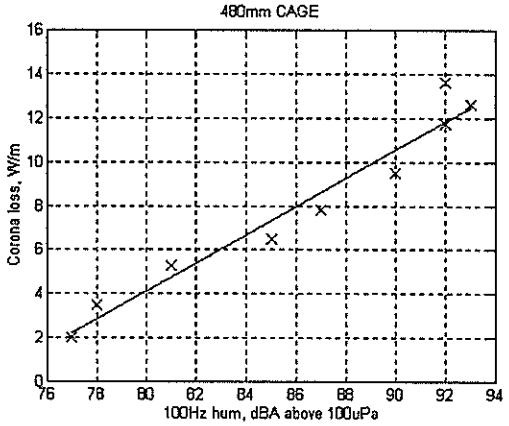

Figure 7. The relationship between corona power and noise for the 480mm cage

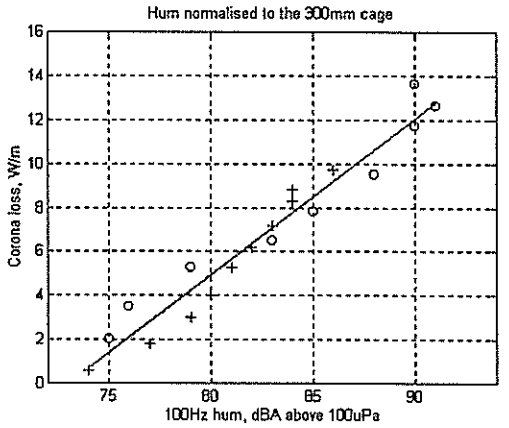

Figure 8. An empirical relationship for the relationship between corona power and noise for a single conductor.

5 CONCLUSIONS

a) For single conductors there is a linear relationship between corona power and audible noise.

b) As the distance from the conductor changes the dBA noise attenuates as $20\log_{10} x$, where x is the distance from the conductor.

6 REFERENCES

1. Bartnikas R, McMahon E, "Engineering Dielectrics Vol.1 - Corona Measurement and Interpretation", American Society for Testing and Materials, ASTM Special Technical Publication 699, STP 699, 1979.

2. Britten AC, Clarke EG, Konkel HE,. "Radio interference, corona losses, audible noise and power frequency electric fields as factors in the design of Eskom's 765kV lines", Paper 3, Cigre Open Conference on EHV Transmission Systems, Johannesburg, 1987, pp 3.1- 3.13.

3. Comber MG, Zaffanella , "The use of single-phase overhead test lines and test cages to evaluate the corona effects of EHV and UHV transmission lines", IEEE Trans. Paper T 73 376-1 presented at IEEE PES Summer Meeting, Vancouver, B.C., Canada, 1973.

4. Comber MG, Zaffanella LE, Deno DW. "Transmission line reference book - 345 kV and above. Chapter 4 - Corona phenomena on AC transmission lines", pp 169-204.

5. Comber MG, Zaffanella LE, Nigbor RJ. "Transmission line reference book - 345 kV and above. Chapter 6 - Audible Noise", pp 267-318.

6. Vinh T, Shih CH, King JV, Roy WR, "Audible Noise and Corona Loss Performance of 9-Conductor Bundle for UHV Transmission Lines", IEEE Trans. on Power Apparatus and Systems, Vol. PAS-104, No.10, pp 2764-2770, 1985.

Author

J P Reynders
Department of Electrical Engineering
University of the Witwatersrand
Private Bag 3
PO Wits
2050
South Africa

reynders@odie.ee.wits.ac.za

Neural network recognition of Partial Discharge signals

A. J. Hoffman and C. J. A. Tollig
Potchefstroom University for CHE

Abstract

This paper investigates the application of neural networks to the classification of PD signals. General aspects of the methodology for developing a classifier are discussed, including the definition and extraction of features and the construction of a PD database. The results obtained with a neural classifier are compared against the results of a rule-based approach. It is shown that neural classifiers tend to be more immune to noise than a rule-based approach. It is further demonstrated that complex signals, involving more than one simultaneous PD mechanism, can be successfully identified with a neural classifier, proving the advantage of neural pattern recognition over rule-based techniques for non-trivial classification problems.

1. Introduction

It has been recognised for a long period of time that partial discharge (PD) has deleterious effects on insulation[1]. With the advent of new measurement techniques, PD detection became an indispensable tool for the evaluation of insulation materials[2]. When PD occurs in insulating systems, it is usually important, both for the manufacturer of the equipment and for the end-user, to identify the responsible mechanism. The type of mechanism causing the PD will give an indication of the seriousness of possible damage, as well as of the expected remaining life for the insulating material.

During the early years of PD detection the recognition of patterns were performed by experts. Developments in the fields of digital computers and advanced pattern recognition techniques however opened up possibilities for automated PD recognition[3]. The current practice at power plants is to rely mostly on a rule-based approach, which is provides satisfactory results should the PD signal be clearly observable above noise levels, and should only one dominant PD mechanism be present[4]. Rule-based techniques however fail catastrophically when the statistical variations in the PD signals results in the failure of one of the decision rules, or if more than one PD mechanism is present at the same time. More advanced pattern recognition techniques have recently been shown to be very successful for the classification of PD signals. These include statistical techniques[5], hidden Markov models[6], neural networks[7,8,9], as well as a combination of knowledge-based and neural techniques[10].

This paper investigates the application of neural networks to the classification of PD signals. Section 2 gives an overview of the typical nature of PD signals, while section 3 discusses the extraction of suitable features for the classification of PD signals. In section 4 the requirements for constructing a PD database to support the development of a reliable automated recognition technique are discussed. Section 5 gives a short overview of neural classification techniques that can be applied to PD pattern recognition, and motivates the type of network used in this study. In section 6 the classification experiment that was conducted is described in some detail, while section 7 discusses the results obtained.

2. The nature of PD signals

PD signals are characterised mainly by the following three attributes:

- the phase position φ within the 50 Hz AC cycle (0° - 360°) where the discharges occur;
- the magnitude Q (in pC) of the detected discharges;
- the number of discharges N detected which falls inside a specific range of magnitude values.

PD signals are usually represented as either 2-D or 3-D patterns; a 2-D graph would normally be obtained by integrating over one of the dimensions φ, Q or N. The seriousness of PD activity is reflected by the peak magnitude of discharges, as well as by the summation over all observed discharges. To be able to compare the level of PD activity between different measurements, or to derive reliable trends, it is necessary to also measure several machine operating conditions affecting PD, including load and temperature.

Important features of PD signals which characterises a specific PD mechanism, includes the following:

- the number of positive discharges +PD versus the number of negative discharges -PD;
- the relationships between +/-PD and load, and between +/-PD and temperature;
- the shape of the graph of N against Q;
- the shape of the 3-D pattern in φ-Q-N space;
- the total number of charges detected NQN;
- the maximum charge magnitude detected Q_m.

Figures 1 and 2 displays typical 2-D graphs of the number of pulses against charge magnitude, for a winding with low levels of PD activity, and for a case of PD caused by significant thermal deterioration, respectively.

3. Extraction of features from PD data

The aim of feature extraction is to reduce the dimensionality of the original PD pattern, while retaining those aspects of the data which distinguishes one class of patterns from the next. Although it may in principle be possible to automatically classify patterns based on the raw data, better results will normally be obtained if features, capturing specific characteristics of the signals, are defined on the basis of past experience, theoretical insight and intelligent guesswork[11]. The lower the number of features, the faster and the more reliable the subsequent classification will be. It also has to be kept in mind that features must be extracted from the data in

real time. Based on these arguments, it will not be an optimal approach to use the raw data from the 2-D or 3-D representations of the PD signals described in the previous paragraph.

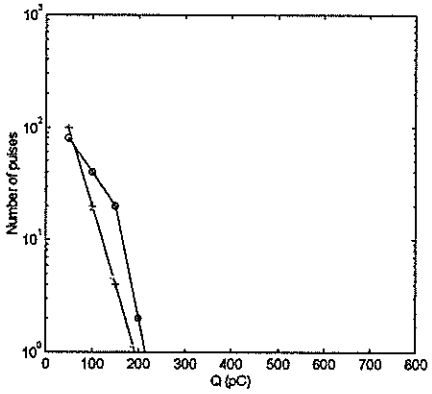

Figure 1 Typical PD signal for winding in good condition

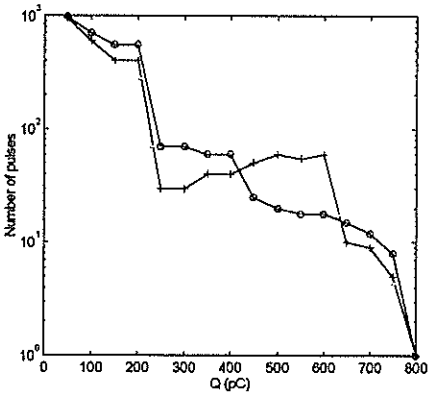

Figure 2 Typical PD signal for thermal deterioration

Several types of features have been successfully used for the recognition of PD patterns, including statistical parameters like skewness, kurtosis and asymmetry of the patterns[12], and more recently fractal features[13]. It has been shown that 29 statistical features or even two fractal features can distinguish between patterns just as well as 1120 raw data points from the 3-D φ-Q-N pattern can do. An alternative technique is to describe the PD pulse shape with time resolved techniques by its peak amplitude, pulse area, rise time, fall time and width[14]. Other possibilities for describing the pulse shape include the Fourier transform[15], the wavelet transform[16] or the Karhunen-Loève transform[17], which all provides a significant reduction in the dimensionality of the original PD signal.

In this paper we investigate the performance of a neural classifier compared against a rule-based technique to distinguish between the mechanisms responsible for PD signals. The rule-based technique is based on the standard interpretation of the data obtained from the PD analysers from Iris Power Engineering, Ontario, Canada[4]. The features that were extracted were derived from the defined rules, to make direct comparison between the two techniques possible. The features used were defined as follows:

- +PD as quantified by its NQN and Q_m;
- -PD as quantified by its NQN and Q_m;
- the temperature dependence of +PD and -PD;
- the load dependence of +PD and -PD;
- the distribution of +PD across the AC cycle;
- +PD at 225°;
- -PD at 45°.

These features can be used to distinguish between the following causes for high levels of PD activity:

- Loose windings;
- thermal cycling deterioration;
- overheating deterioration; and
- Semicon/grading coating deterioration.

4. Construction of a database for PD recognition

The purpose of a PD database is to allow patterns of unknown origin to be compared against previously collected patterns for which the origin have been established. A carefully designed database will provide a high level of similarity between a new fingerprint and the class to which it belongs, and low similarity with all other classes.

A typical structure for a PD database may be as follows:

- at the lowest level the "fingerprints" or features are stored;
- at the next level decision rules or decision surfaces are defined, which subdivides the feature space into separate domains for different classes;
- at a higher level data is sorted according to 'problems' (the type of mechanism which has been identified as the cause for the particular observation - this can be viewed as a class label);
- at the highest level data can be sorted according to the type of equipment from which the measurements were taken, since optimal classification of PD data from different origins may require different approaches.

Since the magnitude of PD discharges is influenced by various effects, the values of parameters like temperature, load and ageing time should be stored together with the features extracted from the PD signals. In order to derive long term trends from the database, it is essential to first compensate for the effects of such influencing factors.

The number of observations required in the database depends on both the number of features per observation, and on the difficulty of the classification problem. The so-called 'curse of dimensionality' requires the number of observations to have an exponential relationship to the number of features, to properly represent the entire feature space. Should a non-linear mapping technique (typically a neural network) be used to construct optimal discriminant functions for the different classes, the number of observations should be at least ten times the number of degrees of freedom in the non-linear model[11]. This is required to ensure good generalisation properties for the classifier. The required complexity of the neural classifier is determined by the ability of the selected features to separate classes in feature space.

5. Neural classification techniques

A pattern recognition system normally consists of the following processes:

- construction of a data base, from which both a training and test set could be generated;
- pre-processing of data, to get rid of unwanted phenomena, e.g. outliers, which may confuse the classifier, and to transform the raw data to a format which facilitates the extraction of features;
- the extraction of features pertinent to the classification problem at hand, to provide easier separation between classes in feature space than in the original raw data space;
- classification of the feature sets, either through a rule-based approach, through linear discriminants, or through a non-linear neural network classifier.

In the case of neural classifiers the non-linear modelling capabilities of the neural network are employed to construct a set of non-linear discriminant functions which optimally classify a labelled set of training data. Although neural networks in principle have the ability to model with arbitrary accuracy any non-linear relationship, there are many potential unwanted effects that should be avoided in order to arrive at a reliable classifier with good generalisation properties.

A common problem occurs when the network is fed with input variables of very high dimensionality (typically all the components in the 3-D PD signal pattern). In such a case it will in principle be possible to design a neural network of high complexity which will correctly classify almost all the observations from the training set. However, should the input data contain a significant amount of noise, or should a substantial portion of the components in the input data have no significant effect on class membership, a large percentage of the modelling capability of the network will be used to model noise or to model unimportant variations in the data. In both cases it would lead to bad generalisation properties, i.e. the classification capability of the network would normally not be good for data not taken from the training set.

Should one however reduce the raw data set to a smaller number of features, all of which can be shown to directly impact on class membership, the likelihood that the neural network will capture the general underlying relationships between input data and class membership will be much better. At the same time it is important to maintain a specific ratio between the number of observations in the training set and the number of degrees of freedom in the classifier, to prevent the classifier from modelling relationships that are present in one or a few observations only.

In classification problems the choice of an optimal feature set is often not a trivial task. In this respect one can normally distinguish between two types of scenarios:

- In some cases one has sufficient foreknowledge of the problem to accurately define a relatively small number of features with a high likelihood of capturing class differences. These features would typically represent the raw data in the vicinity of the class boundaries. In such a case it may be possible to use a relatively simple neural network, since the feature extraction already accomplishes the most difficult part of the task at hand.
- In other cases it may not be obvious how to define the features, and the best one can do is to reduce the dimensionality of the raw data set in an optimal way without discarding any important variations in the data set. Optimal features sets can then be constructed from this reduced set of possible features, either through trial and error, or by applying systematic techniques like the mutual information criterion. In this way the neural network is given an incentive to model the classes more accurately close to the class boundaries, rather than in the central region for each class.

6. Comparing neural classification of PD data against a rule-based approach

The objective of this exercise was to show that neural classifiers are superior to rule-base approaches in the following respects:

1. *Observations suffering from a low signal-to-noise ratio:* since the rule-based approach uses predetermined decision levels, and considers different features sequentially rather than in parallel, it tends not to perform well in the presence of noise. A neural classifier considers all features simultaneously, and is hence able to utilise alternative features, should one feature not allow a clear decision. In addition it can adjust its decision levels based on the data in the training set.
2. *Observations characterised by multiple mechanisms:* In practice more than one mechanism could contribute to observed PD activity at the same time. While it is possible in theory to expand a rule-based approach to handle multiple mechanisms, the number of rules required will increase exponentially with the number of possible mechanisms, rendering such an approach impractical. A neural classifier, on the other hand, could be trained to recognise multiple mechanisms simply by including such observations in the training set. While this may increase the size of the training set as well as network complexity and training time, it will not have a significant effect on processing time when the classifier is used for on-line decision making.

The features selected to compare a neural classification approach against a rule-based approach, were discussed in section 3. Since only a relatively small data set was available from practical measurements, it was decided to expand the set of observations based on the observed statistical variations between observations from the same class. The average feature set was determined for each class, and the standard deviation of each feature was used to generate additional observations, assuming a normal distribution for each feature. The expanded data set consisted of 120 observations from each of the following classes:

- normal windings (no apparent PD activity);
- loose windings;
- thermal cycling deterioration;
- overheating deterioration;

- Semicon/grading coating deterioration;
- the combined presence of loose windings and thermal cycling deterioration.

A feedforward neural network with backpropagation of errors was used to construct a classifier. The network structure consisted of 14 input nodes, 7 nodes in the single hidden layer using sigmoid activation functions, and 5 output nodes, one for each of the 5 classes. The available set of observations was divided into two equal sets of 360 observations each, the first used for training, and the second used as test set.

During training the network output corresponding to the class label of the input was forced to assume a value of 1, while all other outputs were forced to 0. In the case of multiple mechanism observations, both classes present in the observation were forced to 1. The training technique used random selection of observations. The criteria used to terminate training, was the maximisation of the generalisation ability of the network. In this case the generalisation ability was defined as the classification accuracy that was achieved within the test set.

After training the neural classifier, both the rule-based and the neural classifiers were applied to observations from the training and the test sets. When no temperature effects were present, the rule-based approach performed reasonably satisfactorily, with a classification accuracy of 78%. This however dropped to 62% as soon as temperature effects had to be taken into account, even for low noise levels.

The results obtained for observations contaminated with different levels of noise, and including load and temperature effects, are summarised in Table 1 below. The classification accuracies achieved are shown as percentages, for both the training and test sets at different signal-to-noise ratios, respectively.

The neural classification approach not only managed to compensate both for the presence of temperature and load effects, but also displayed better noise immunity than the rule-based approach. The majority of observations containing more than one mechanism were classified correctly by the neural classifier, while the standard rule-based approach could not handle any of these cases. Out of the 15% misclassifications from the test set with a S/N ratio of 200, the neural classifier still correctly identified one out of the two PD mechanisms present for a further 4% of observations.

Table 1 Classification results: comparison between rule-based and neural approaches

S/N Ratio	Rule-based Approach		Neural Approach	
	Train	Test	Train	Test
600	61%	62%	100%	99.7%
400	55%	54%	100%	98.9%
200	48%	44%	99.2%	85%

7. Conclusion

The recognition of partial discharge signals is an important aspect of the condition monitoring of critical power plant equipment, including turbo-driven generators. The accurate classification of PD signals, based on knowledge about past behaviour, forms the basis for such recognition. The definition of a feature set which represents class differences in a compact form, is of critical importance for the development of reliable classification techniques. In addition it is essential to build up a systematic database of PD signals which is representative of PD behaviour for different operating conditions. It was demonstrated in this paper that neural classifiers display significant advantages over a rule-based approach to PD signal classification. In particular the neural approach was more immune to noise, and had the ability to recognise the simultaneous presence of more than one PD mechanism.

References

[1] D. M. Robinson, *Dielectric phenomena in high voltages cables*, Chapman and Hall, 1936.

[2] IEC Publication 270, *Partial discharge measurements*, 1981.

[3] A. Krivda, *Automated recognition of partial discharges*, IEEE Transactions on Dielectrics and Electrical Insulation, Vol. 2, No. 5, October 1995, pp. 796 - 821.

[4] G. Stone, *Interpreting partial discharge test results*, Short course notes, Iris Power Engineering, 1996.

[5] E. Gulski and F. H. Kreuger, IEEE Transactions on Electrical Insulation, Vol. 27, No. 1, February 1992, pp. 83 - 92.

[6] L. Satish and B. I. Gururaj, *Use of Hidden Markov Models for partial discharge pattern classification*, IEEE Transactions on Electrical Insulation, Vol. 28, No. 2, April 1993, pp. 172 - 182.

[7] E. Gulski and A. Krivda, *Neural networks as a tool for recognition of partial discharges*, IEEE Transactions on Electrical Insulation, Vol. 28, No. 6, Dec. 1993, pp. 984 - 1001.

[8] A. A. Mazroua and M. M. A. Salama, IEEE Transactions on Electrical Insulation, Vol. 28, No. 6, Dec. 1993, pp. 1082 - 1089.

[9] L. Satish and W. S. Zaengl, *Artificial neural networks for recognition of 3-d partial discharge patterns*, IEEE Transactions on Dielectrics and Electrical Insulation, Vol. 1, No. 2, April 1994, pp. 265 - 275.

[10] C. Cachin and H. J. Wiesmann, *PD recognition with knowledge-based pre-processing and neural networks*, IEEE Transactions of Dielectrics and Electrical Insulation, Vol. 2, No. 4, Aug. 1995, pp. 578 - 589.

[11] C. Bishop, *Neural networks for pattern recognition*, Clarendon Press, Oxford, 1995.

[12] F. H. Kreuger, E. Gulski and A. Krivda, *Classification of partial discharges*, IEEE Transactions on Electrical Insulation, Vol. 28, pp. 917 - 931, 1993.

[13] L. Satish and W. S. Zaengl, IEEE Transactions on Dielectrics and Electrical Insulation, Vol. 2, pp 352 - 359, 1995.

[14] A. A. Mazroua, R. Bartnikas and M. M. A. Salama, IEEE Transactions on Power Delivery, Vol. 10, pp. 92 - 96, 1995.

[15] P. Morshuis, *Ultra wide-band PD detection and the assessment of dielectric degradation*, IEEE Transactions on Dielectrics and Electrical Insulation.

[16] X. Wu, H. Xie and S. Wu, *Application of wavelet analysis for detection of defects in insulation systems*, 5th International Conference on Conduction and Breakdown in Solid Dielectrics, Leicester, England, pp. 229 - 233, 1995.

[17] D.Wenzel, H.Borsi and E. Gockenbach, *A new method of partial discharge localization in transformers via the Karhunen-Loève transform*, 4th International Conference on Properties and Applications of Dielectric Materials, Brisbane, Australia, pp. 622 - 625, 1994.

Interpretation of PD data for rotating machines

P.P. Marx

Abstract - **Partial discharge (PD) monitoring is increasingly recognised as an important part of comprehensive predictive maintenance programs, especially in the power generation industry. In the South African context, the diagnosis of insulation using on-line partial discharge testing of large generators has only recently been implemented. It is the purpose of this paper to review both the expert and automated diagnosis of insulation, paying attention to some problematic issues in the field.**

Keywords - **partial discharges, predictive maintenance, pattern recognition, defect assessment**

I. INTRODUCTION

IT is known that ageing and failure of rotating machine stator insulation are initiated by thermal, electrical, environmental and mechanical stresses experienced during manufacturing and operation [1]. Partial discharges (discharges that only partially bridge the gap between electrodes [2]) can occur at local sites of overstressing under certain conditions, causing further degradation of the insulation. This is a phenomenon found on rotating machines having ratings of over 4000V [3]. The process of diagnosing the insulation integrity of rotating machine stators by monitoring the PD activity is shown in Figure 1.

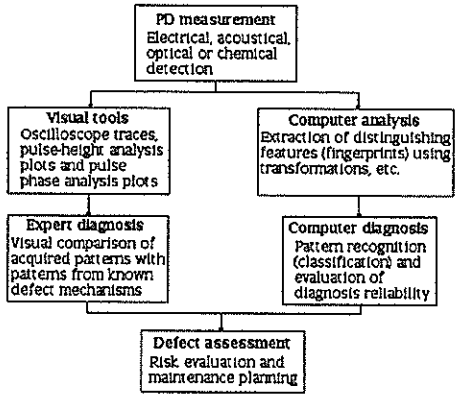

Figure 1: Expert versus automated computer diagnosis of insulation

The purpose of this paper is to review the process of on-line PD testing, paying attention to certain problematic aspects encountered when using this system as part of a comprehensive maintenance strategy.

II. PD MEASUREMENT

Electrical detection methods are often used for on-line PD testing on rotating electrical machines. Concerning the measurement of PD, some issues need to be discussed.

A. The calibration problem

Arising from the intricate geometry of stator windings is the absence of an acceptable calibration procedure for PD measurements on rotating machines [4]. Although calibration methods are prescribed in *Publication 270* of the IEC [2], there are much on-going debate concerning these procedures [4]. Our primary concern is not to discuss the details of the problem, but rather to take note of the way it affects on-line PD testing. Sedding pointed out that the lack of a calibration standard does not invalidate the data obtained by using any of the current PD detection schemes. This is true as long as the results are used for single machine trending purposes only. Quantitative comparisons between different machines are thus not possible [4].

B. Behaviour of PD in the time and frequency domain

Wilson and his co-workers [5] have shown that a PD pulse consists of two "components". The first of these is a fast travelling wave that arrives at times at the machine terminals that are independent of the defect location. The other slower travelling component arrives at the terminals at times that are directly proportional to the distance travelled. Frequency spectrum analyses (e.g. [5]) have revealed that the stator winding essentially acts as a low-pass filter. It modifies the frequency content (and thus the shape) of the pulse as it is propagated in the stator winding from the defect site to the detector terminals. This modification is dependent on - among others - the distance travelled from the defect site to the machine terminals [6]. Experiments revealed that a detection bandwidth of $<300kHz$ would be preferable when detecting PD signals at the machine terminals [5] (which are relatively "far" from discharge locations in the winding).

C. Noise considerations

During the on-line detection of PD signals there are interfering signals that make the task of identifying PD patterns reliably rather difficult. These signals are orders of magnitude larger than the PD signals [8]. Discrimination between noise and actual PD activity generally requires experienced personnel, a rare commodity in South Africa. Expert noise separation is only possible if the different characteristics of PD and noise are known. The attributes of PD and noise are discussed in a report of a CIGRE working group [9]. Apart from noise extraction by a human expert, a few alternative methods are being used/studied.

Frequency content (pulse shape) This becomes a possibility when the bandwidth of the detection system is $>500MHz$. The sensor must be in close proximity to the discharging source so that attenuation and distortion is minimised. Discrimination is done on a pulse-by-pulse basis (see discussion on UWB partial discharge detection later on).

Time-of-flight techniques This form of noise extraction has successfully been used by Ontario Hydro to eliminate noise from their hydrogenerator installations. Stone [3] and Campbell *et al.* [12] give clear descriptions of the principles of this technique.

PD pattern recognition Much attention is being paid to this particular method of noise extraction. Discrimination is facilitated by making use of the temporal, frequency or statistical characteristics of PD and noise. Techniques reported on include the use of adaptive filters (e.g. [10]) and neural networks (e.g. [11]).

D. PD on-line detection installations

The basic layout of a computerised PD detection system is shown in Figure 2.

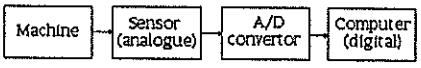

Figure 2: Typical layout of computer based PD detection system

1. PD sensing circuit

Various sensing circuits can be used for on-line PD monitoring. These circuits detect the PD signal at the generator neutral, at the line end of each phase, or inside the stator slots. Based on the measuring bandwidth of detection systems, the following distinction can be made between the various measuring schemes:

Narrow and Wide Band systems Not having bandwidths in excess of about $300kHz$, these systems are primarily concerned with detection of the slower component of PD pulses. Attenuation of signal amplitude is not a severe problem, but the pulse shape (fre-

quency content) is lost. A further disadvantage of these detection systems is that a superposition of two or PD pulses could easily be treated as one large discharge, leading to grave errors in data collection.

Ultra-wide band (UWB) systems It can easily be seen why the practical implementation of this technique proved to be very successful. When using conventional, narrow band detection systems the operator is faced with the arduous task of discriminating between noise and genuine partial discharges. Few people are experienced enough to facilitate PD analysis in noisy environments, leading to a reluctance to implement on-line insulation monitoring systems. A development by Ontario Hydro [14] is considered a major breakthrough in the field of on-line PD detection. The sensor they developed consists of a directional antenna with a bandwidth of $1GHz$. It is installed into the stator slot in direct contact with the winding. The *stator slot coupler* (SSC) results in several advantages [3], [13], [14]:

- It increases the sensitivity to PD signals by an order of magnitude, leading to an improvement in the signal-to-noise ratio.
- It facilitates noise elimination on a pulse-by-pulse basis by making use of the pulse width properties of noise and PD. Wide band detection experiments have revealed that PD pulses have pulse widths ranging from 1 to $5ns$, while noise have pulse widths in excess of $20ns$.
- This detection method allows one to observe the true shape of individual pulses. Thus, it can assist one in developing an automated PD classification system that uses features from the "true" pulse shape as input to an advanced pattern recognition system.
- Being a two-port directional antenna, it facilitates the separate measurement of slot PD and PD from the end winding.

2. A/D interface and digital computer

The portability of modern day computers is one of the main contributing factors why their application to PD recording is so successful. Being able to store measured PD data on a computer has tremendous advantages, including the fact that it facilitates the recording of data for trending purposes. As the sensing circuits used to detect PD signals are analogue devices, the data must first be converted to digital format before storage on the computer can take place. Once the on-site measurements have been transferred to hard drive, the data can be presented to the user in the form of visual plots. From Iris Power Engineering there is a recording device available that interfaces directly with the SSC. This unit is called a *turbine generator analyser* (TGA) and is discussed in various publications (e.g. [3], [12]).

III. Data Representation, Feature Extraction and Classification

The interpretation of PD data is not a trivial matter. One important requirement for expert diagnosis is that the person should have a thorough knowledge of the common defect mechanisms within the HV insulation [1]. For that reason, a summary of the common insulation problems found on motors, hydrogenerators and turbogenerators will be given.

A. Terminology

Equipment available to the author were manufactured by Iris Power Engineering, and included a TGA unit. Therefore, discussions will for be based on the functionality of said equipment. The following terms are important [13].

Pulse Polarity[1] Negative PD pulses are pulses that occur from 0 to 180° of the $50Hz$ ac cycle, while positive PD occur from 180 to 360°.

Pulse-Height Analysis (PHA) Plot It is a two-dimensional plot that shows the number of pulses per second occurring over 360° of the ac cycle at each PD magnitude (Figure 3).

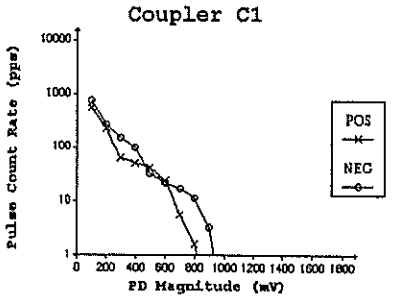

Figure 3: Typical pulse-height analysis plot

Pulse Phase Analysis (PPA) Plot It is a three-dimensional graph showing the ac phase position on one axis, the magnitude of PD pulses on the next and the number of pulses per second at any combination of pulse magnitude and phase position on the last axis (Figure 4).

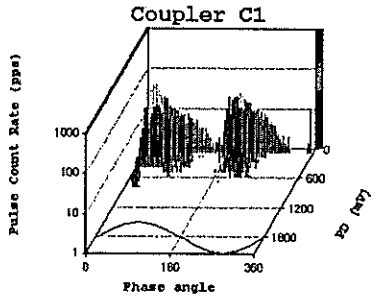

Figure 4: Typical pulse phase analysis plot

Normalised Quantity Number (NQN) A number proportional to the area under the lines on the pulse-height analysis plot (related to the total charge transfer due to partial discharges). A large NQN corresponds to widespread deterioration.

Maximum discharge magnitude (Q_m) The peak PD magnitude that corresponds to a pulse repetition rate of at least 10 pulses per second. Q_m corresponds to the severity of deterioration.

B. Common failure mechanisms in rotating machinery

Internal groundwall discharges Discharges within the groundwall insulation of rotating machines are caused by either inadequate quality control during manufacturing [15], or due to thermal cycling [16]. The main characteristics of this mechanism are that the positive and negative PD activity is about equal, while the phase distribution of the PD peaks at 45° and 225° [3], [16].

Discharges at the interface between copper conductors and the groundwall insulation Cavities appearing at the interface between the groundwall insulation and the copper stack indicate that the winding is experiencing thermal deterioration. This mechanism is characterised by a negative PD predominance, peaking at the expected phase values of 45° and 225° [4], [15].

Semi-conducting/gradient paint discharges In order to prevent corona and destructive slot discharges, a coat of semi-conducting/grading paint is applied to the winding insulation surface. This discharging mechanism is the result of the degradation of this coating (due to excessive movement or chemical attack [4]), leading to discharging between the surface of the stator bar groundwall and the stator core iron. Characteristic of the mechanism is a positive PD predominance, peaking at the usual phase positions of 45° and 225° [3], [4].

Slot discharges Excessive vibration (due to loose wedging and/or side packing of the stator bar) will eventually lead to discharging between the stator bar surface and core iron [4]. The slot discharge mechanism shows characteristics similar to grading paint degradation.

[1] The definition used by many North American workers is reversed from the one used by the Europeans (cf. [9]).

Discharges due to girth cracks This is a less common mechanism, but still of particular importance on hydraulic generators used for peak-time reserve. Numerous start/stop cycles may eventually lead to cracking of the insulation at the core exit area, leading to slot discharging during thermal cycling. It shows the same characteristic height and phase distributions than slot discharges, but there is no in-service method of discriminating between slot discharging and discharging due to girth cracks. Off-line visual inspection may reveal a characteristic white powder where the winding exits the core [16], an indication of girth crack PD.

End winding discharges End winding discharges can be due to several different mechanisms, including internal cavities, contamination of the winding surface, poorly designed inter-phase clearances or the junction between the semi-conducting coating (slot region) and stress grading paint (end winding). Erratic PHA plots (at high pulse magnitude) and a phase shift of ~30° from the expected phase values are the most important characteristics of end winding discharges. This is due to line-to-line discharging (line-to-ground discharging characterise the other mechanisms) [4].

C. *Expert diagnosis with visual tools*

Single measurements of PD activity within machine insulation should be treated with caution [3]. Some types of insulation will tolerate discharge magnitudes of over $1000mV$, while other (particularly the modern epoxy-mica insulation) must not have a maximum discharge in excess of $500mV$. Take note, however, that newly installed insulation tends to display a "settling in" behaviour: it takes about 5 to 10 months before PD testing equipment will give consistent readings [7].

On-line PD testing serves dual purposes [3]. The main purpose is to identify which machines need maintenance. This can be accomplished by trending of both NQN and Q_m. Consistently flat trends over time probably indicate that the winding is in relatively good condition. A doubling over a six-month period is indicative of an increased rate of deterioration of the HV insulation, and maintenance should be planned. If a trend has increased over time and then suddenly forms a plateau, the winding is probably close to failure, and urgent maintenance action should be taken [3]. The secondary purpose of on-line PD testing is to identify the root cause of any deterioration. For this purpose, the ratio of NQN+ to NQN- (NQN of positive and negative PD, respectively) or the ratio of Q_m+ to Q_m- are to be calculated (refer to Section III.B).

Even when using equipment that utilises built-in noise extraction, it still requires a fair amount of experience to successfully interpret PD data. For this reason, the drive towards automated recognition seems a worthy cause, as few people have the skill and experience required for the task at hand.

D. *Automated feature extraction and diagnosis*

While most of the work in this area is concentrated on laboratory test samples (cf. [17]), some attempts have been made to apply the different pattern recognition techniques to industrial equipment (cf. [18]). There are a few matters of concern that need to be addressed before systems would achieve the reliability necessary to be taken seriously by utilities.

Selection of Features At the core of any automated system there would be a pattern recognition algorithm or technique. These techniques usually take inputs in the form of a *feature set* or finger print. The aim of feature extraction is to reduce the dimensionality of the input data, calculating certain distinguishing properties from the given data set. Techniques used to automatically extract these feature sets include neural network pre-processing, the calculation of statistical parameters, Fourier analyses, wavelet transforms as well as the Karhunen-Loève transform [19], [20].

Statistical Properties of PD It should be recognised from the outset that, because the behaviour of PD are influenced by factors such as the severity of local electrical overstressing and the availability of starting electrons [1], statistical variations in the data be taken into account when extracting features.

Classification of the PD Data The general aim of classification is to assign a label to a PD pattern of unknown origin. There have been numerous attempts in classifying PD data, and techniques such as neural networks, hidden Markov models, fuzzy logic and conventional classification have been used, with varying amounts of success [19].

Memory Effects It has been demonstrated through experimental observation that pulsating partial discharges are controlled by a non-Markovian process. This essentially means that both the statistical probabilities for the growth and initiation of a PD pulse is determined by the amplitude and phase of previous discharges. Unconditional statistical analyses of PD data are thus susceptible to non-stationary behaviour [21].

Effects of Ageing Changes in the stochastic behaviour of pulsating PD have been observed which can be attributed to the local degradation (ageing) of the discharge sites [22]. This essentially means that the PHA and PPA plots will change over time as the insulation is deteriorating. The influence of non-stationary behaviour on the automated classification process has recently been investigated by Gulski and Krivda [23]. Their study should be considered as a prompt to more rigorous investigations in this regard.

Having established the need for maintenance and discussed the relevant defect mechanisms acting on a certain machine under question, an assessment of the severity can be made. Maintenance action can then be planned based on this assessment.

IV. Defect Assessment and Maintenance Action

The different defect mechanisms exhibit different levels of danger to rotating machine insulation. Some of these effects can be repaired with a minimal outage, while some may require more drastic maintenance action (Table I).

Table I: Common defect locations and suggested maintenance action

Location	Risk	Action
Internal ground-wall	Medium	Replace winding
Copper-groundwall interface	Medium	Replace winding
Grading paint	High	Repair coating
Slot section	High	Retighten wedging
Girth cracks	High	Replace winding
End winding	Slight	Clean winding

Prediction of the maximum time available until the next maintenance outage will be needed is no trivial matter, and can only be done by highly experience personnel. Some effort is going into methods of mathematically modelling the remaining life of insulation based on PD measurements alone. The fact of the matter still remains that remaining insulation life depend on both the state of a gradually deteriorating object and on the stresses that act on it later on during operation. Simplistic modelling of ageing is not possible, as the stresses acting on the machine may be constant, load dependent or even random. The process of hunting for a suitable "life" model would only be fruitful if, and only if:

- the calibration problem is suitably addressed, and
- a modelling technique is applied that can successfully model the highly non-linear relationships that exist between remaining life and parameters such as Q_m.

V. Conclusions

Concepts that are relevant to on-line detection of partial discharges have been reviewed. Some problematic issues, including the calibration problem on rotating electrical machines, have been highlighted. Some practical information has also been given for expert diagnosis of rotating machine insulation. Some recent advances in the field of pattern recognition that could help automate the diagnostic process have also been discussed. It was finally

pointed out why simplistic modelling of remaining insulation life can be considered impossible.

ACKNOWLEDGEMENTS

The author wishes to express his appreciation of the useful contributions and suggestions made by both Prof. A.J. Hoffman (PU for CHE) and Dr. S.A. Higgins (Eskom) during the period of his Master's Degree studies.

REFERENCES

[1] B.A. Fruth and D.W. Gross, "Partial discharge signal generation, transmission and acquisition", *IEE Proc. - Sci. Meas. Technol.*, vol. 142, no. 1, pp. 22-28, 1995.

[2] IEC, *Publication 270: Partial discharge measurement*, 2nd edition, 1981.

[3] G.C. Stone, "Techniques for on-line partial discharge testing of motors and generators", in *CEA/Ontario Hydro Conference on Partial Discharge Testing*, Toronto, Canada, April 1994.

[4] H.G. Sedding, "Basics of rotating machine partial discharge testing", Ontario Hydro, Toronto, Canada, 1993.

[5] A. Wilson, R.J. Jackson and N. Wang, "Discharge detection techniques for stator windings", *IEE Proc. B*, vol. 132, no. 5, pp. 234-244, 1985.

[6] J.W. Wood, H.G. Sedding, W.K. Hogg, I.J. Kemp and H. Zhu, "Partial discharges in HV machines: initial considerations for a PD specification", *IEE Proc. A*, vol. 140, no. 5, pp. 409-416, 1993.

[7] J.F. Lyles, "Test requirements to achieve consistent PDA results", in *CEA Fourth Motor and Generator Partial Discharge Testing Conference*, Houston, Texas, May 1996.

[8] W. Hutter, "Partial discharges - part XII: partial discharge detection in rotating electrical machines", *IEEE Electrical Insulation Magazine*, vol. 8, no. 3, pp. 21-32, 1992.

[9] CIGRE Working Group 21.03, "Recognition of Discharges", *Electra*, no. 11, pp. 61-98, 1969.

[10] U. Köpf and K. Feser, "Rejection of narrow-band noise and repetitive pulses in on-site PD measurements", *IEEE Transactions on Dielectrics and Electrical Insulation*, vol. 2, no. 6, pp. 1180-1191, 1995.

[11] H. Borsi, E. Gockenbach and D. Wenzel, "Separation of partial discharges from pulse-shaped noise signals with the help of neural networks", *IEE Proc. - Sci. Meas. Technol.*, vol. 142, no. 1, pp. 69-74, 1995.

[12] S.R. Campbell, G.C. Stone, H.G. Sedding, G.S. Klempner, W. McDermid and R.G. Bussey, "Practical on-line partial discharge tests for turbine generators and motors", *IEEE Transactions on Energy Conversion*, vol. 9, no. 2, pp281-287, 1994.

[13] *User Manual: TGA Model SB*, Iris Power Engineering, Ontario, Canada, January 1995.

[14] H.G. Sedding, S.R. Campbell, G.C. Stone and G.S. Klempner, "A new sensor for detecting partial discharges in operating turbine generators", *IEEE Transactions on Energy Conversion*, vol. 6, no. 4, pp. 700-706, 1991.

[15] J.F. Lyles, G.C. Stone and M. Kurtz, "Experience with PDA diagnostic testing on hydraulic generators", *IEEE Transactions on Energy Conversion*, vol. 3, no. 4, pp. 824-832, 1988.

[16] V. Warren, W. McDermid and G. Haines, "PDA/PPA testing of asphaltic-mica insulation systems on hydraulic generating units", in *CEA Fourth Motor and Generator Partial Discharge Conference*, Houston, Texas, May 1996.

[17] F.H. Kreuger, E. Gulski and A. Krivda, "Classification of partial discharges", *IEEE Transactions on Electrical Insulation*, vol. 28, no. 6, pp. 917-931, 1993.

[18] E. Gulski, "Discharge pattern recognition in high voltage equipment", *IEE Proc. - Sci. Meas. Technol.*, vol. 142, no. 1, pp. 51-61, 1995.

[19] A. Krivda, "Automated recognition of partial discharges", *IEEE Transactions on Dielectrics and Electrical Insulation*, vol. 2, no. 5, pp. 796-821, 1995.

[20] T. Hücker and H.-G. Kranz, "Requirements of automated PD diagnosis systems for fault identification in noisy conditions", *IEEE Transactions on Dielectrics and Electrical Insulation*, vol. 2, no. 5, pp. 544-556, 1995.

[21] R.J. van Brunt, E.W. Cernyar and P. von Glahn, "Importance of unravelling memory propagation effects in interpreting data on partial discharge statistics", *IEEE Transaction on Electrical Insulation*, vol. 28, no. 6, pp. 905-916, 1993.

[22] R.J. van Brunt, P.J. von Glahn and T. Las, "Nonstationary behaviour of partial discharge during discharge induced ageing of dielectrics", *IEE Proc. - Sci. Meas. Technol.*, vol. 142, no. 1, pp. 37—45, 1995.

[23] E. Gulski and A. Krivda, "Influence of ageing on classification of PD in HV components", *IEEE Transactions on Dielectrics and Electrical Insulation*, vol. 2, no. 4, pp. 676-684, 1995.

Fire-induced Corona on Power Lines

AC Britten, CR Evert
Technology Group [revert@tri.eskom.co.za]
Eskom

DA Swift
Electrical Department
University of Natal

This paper describes the results obtained in the analysis of high frequency conducted signals to detect the presence of large ground fires under 275 kV and 400 kV power transmission lines. The paper completes the series of papers first presented at SAUPEC in Durban in 1992[1] and in Cape Town in 1994[2].

Keywords: Transmission line, fires, electrical breakdown, prevention, early warning

1. INTRODUCTION

Over the last ten years Eskom has experienced a significant increase in load demand and a demand for quality power.

The quality of supply is jeopardised when a fire is present under the 275 kV and 400 kV transmission networks. Veld fires, fynbos fires and sugar cane fires have in the past all caused faults resulting in a voltage depression at the customer.

2. CORONA

The presence of particles and flames with the associated heat (and reduction in air density) induces ionisation. With the high electric fields at those operating voltages corona follows.

Given a sustained condition of flames or particles or both, breakdown between conductors or conductor to earth takes place.

3. EARLY WARNING

The generated corona has high frequency components which are radiated and conducted from the point of origin on the conductor.

The conducted portion of the signal is transmitted along the line towards both ends. By intelligently monitoring the signals at either or both ends, the fire can be recognised.

With recognition, a warning can be initiated to alarm the appropriate mechanisms to proactively manage the transmission network and avoid the voltage depressions.

4. PLANT LAYOUT

To maximise the benefits of this methodology, the existing plant was considered. Currently capacitive voltage transformers (CVT) are used to monitor voltages in the 275 kV and 400 kV networks. In addition, at least one of the three phases of a line is used for communication with power line carriers (PLC).

In conjunction with the CVT the PLC system uses line matching equipment (LME) to filter the high frequency signals from the overhead power line. The capacitive component of the CVT in series with the LME produces a filtered band of 450 kHz from 50 kHz to 500 kHz. In the laboratory work undertaken in Eskom's High Voltage Test Facility (HVTF)[3] the results showed that the amplitude was inversely proportional to the frequency monitored[4]. That is, the lower the frequency the higher the amplitude of the generated signal.

Although the plant identified may not be optimal, the implementation costs would be minimal as the LME output is available within the substation control rooms (known as "switching " and "carrier" rooms). Any further optimisation will still be possible - at a price.

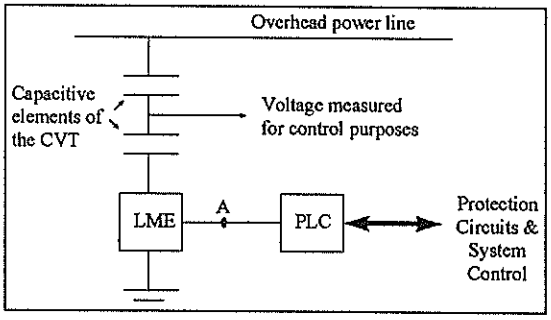

Figure 1 Connection to primary plant

The high frequency analysis is initiated from point A in figure 1 above.

5. CIRCUIT LAYOUT

Two measurements were taken from point A in figure 1.

Instantaneous data capturing the transient activity related directly to the corona present on the line and an RMS measurement capturing the level of interference due to the corona activity.

5.1 ANALOGUE AND DIGITAL ANALYSIS

5.1 ANALOGUE AND DIGITAL ANALYSIS

From point A in figure 1 the signal was filtered for a second time down to a bandwidth of 4 kHz at a center frequency of 53 kHz via the TRI-ADD monitoring unit developed by Eskom[5].

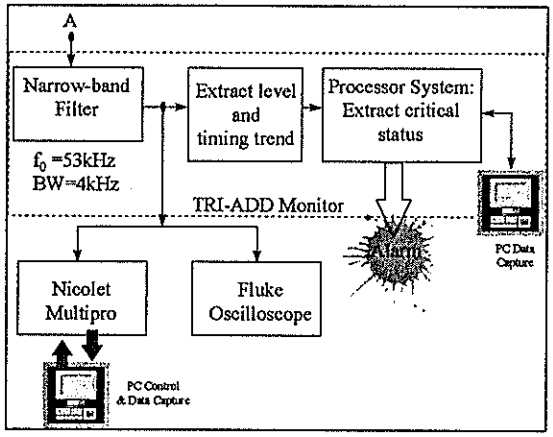

Figure 2 Real-time Activity Circuit Layout

The information through the narrow-band filter was analysed and processed in relation to the applied voltage and associated electric field on the respective phase.

5.1.1 Assessing the Real-Time Instantaneous Activity

A BNC output from the filters on the TRI-ADD was used to capture the real-time transient high frequency activity on the line in the presence of the fire.

A Nicolet Multipro digital storage oscilloscope and a Fluke combination oscilloscope were used to quantify the data.

5.1.2 TRI-ADD System monitor

Using quasi-digitising, the output of the narrow-band filter was stored in random access memory (RAM) in a wrap-around buffer via a microprocessor. The microprocessor in turn also activated an alarm when the anticipated signature was received. Battery backup protects the data.

The TRI-ADD system registered an alarm with two activities: (1) Record the date and time of the event and transmit an alarm signal, and (2) record the quasi-digitised data for a full ten minutes - five minutes pre-trigger and store to a PC. The TRI-ADD also functions as a stand alone unit providing output (1) above.

Figure 2 shows the TRI-ADD and oscilloscope connections.

5.2 RMS SIGNAL ANALYSIS

The signal at point A in figure 1 was also transferred via a matching impedance to an HP spectrum analyser.

Here the signal was filtered to 53 kHz with a bandwidth of 3 kHz using the spectrum analyser settings.

The DC logarithmic output from the spectrum analyser was passed to a strip chart recorder where the fire induced RMS signals for the full duration of each fire was captured. Figure 3 shows the circuit layout for this measurement.

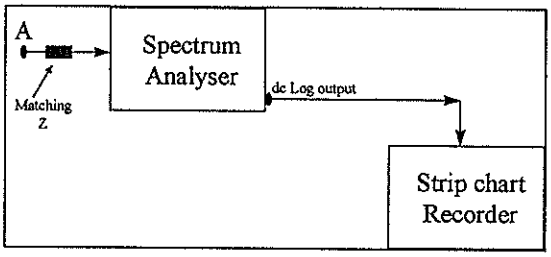

Figure 3 RMS Measurement Circuit Layout

6. THE APPLIED FIRES

To adequately test the theory, actual fires under energised transmission power lines were necessary.

A series of three fires were arranged with Eskom doing extensive network splitting to protect the customer from possible voltage depressions should a flashover occur.

Three fires were planned approximately 5km from the monitoring substation. The fires all reached the conductors with temperatures at the conductors momentarily reaching 455°C, 1088°C and 2053°C respectively.

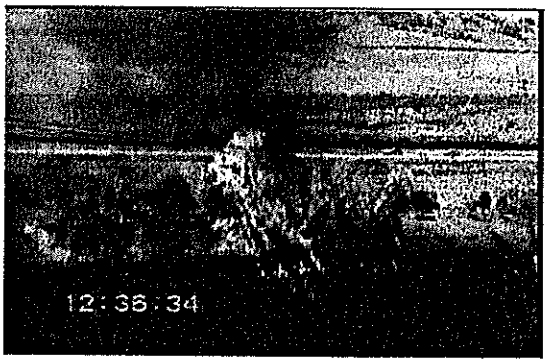

Figure 4 Cane fire during testing

Figure 4 shows one of the three successful controlled fires which were completed.

7. RESULTS

7.1 RMS SIGNAL ANALYSIS

The RMS signals produced significant evidence of high frequency signals generated during a large ground fire.

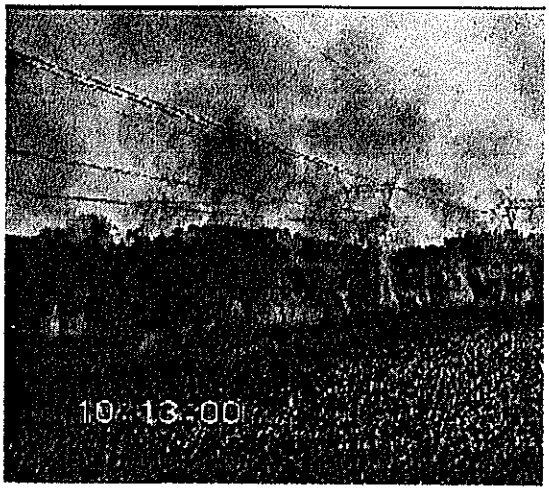

Figure 5 Source of Signals

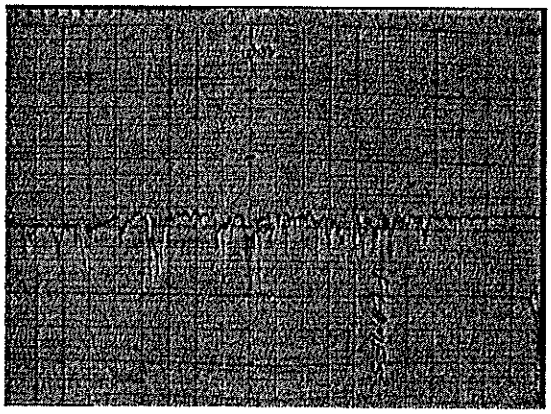

Figure 6 RMS logarithmic measurement

Figure 6 showed increased signal levels of up to 10 dB with the fire in figure 5 present at the overhead conductors.

In figures 7 through 9 the build up to a flashover during the second fire can be seen. The sequence showed that the RMS variation was visible 1 minute and 22 seconds prior to flashover.

In addition, directly prior to flashover an unexpected sequence of energy absorption and release is visible in figure 9. Figures 6, 7 and 8 showed the expected "random" variations in the signals due to the "random" nature of the fires. The final fire generated patterns similar to figure 6 with no flashover taking place.

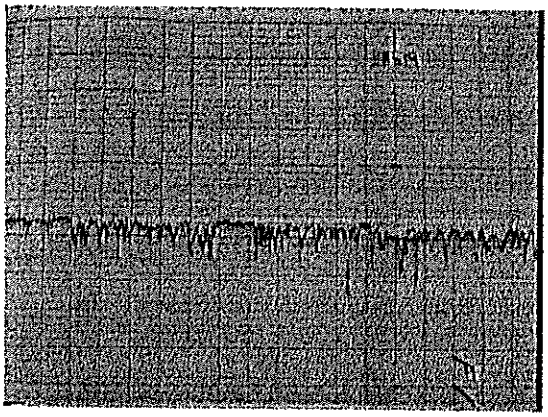

Figure 7 Sequence 1 of 3

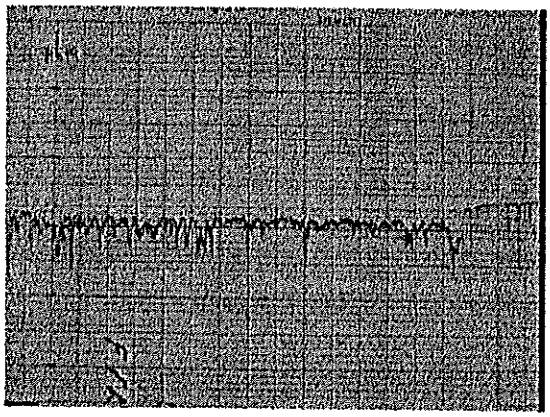

Figure 8 Sequence 2 of 3

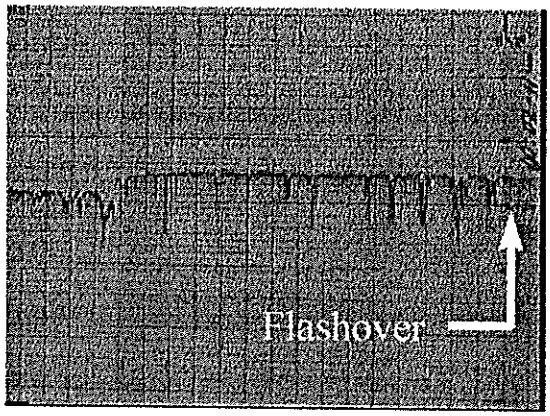

Figure 9 Sequence 3 of 3

7.2 ANALOGUE AND DIGITAL ANALYSIS

The TRI-ADD and oscilloscopes registered low signal levels above "background" noise levels. Whilst the signals were detected from the monitored fires, there appeared to be some discrepancy between the expected signal levels and the actual signal levels measured.
The amplitudes were small making it superfluous to attempt to interpret the signature of the fires. In November 1992 the captured signals from a large sugar cane fire under a delta configuration twin

"Bear" conductor bundle generated significant data[4] indicating some error in the results captured here.

After further analysis the narrow band filtering stage shown in figure 2 was found to be the culprit. The unit did not respond favourably to step response activity with a delay of 445 µs before the high frequency signals were registered. That is, a total delay of 23 cycles for a 53 kHz.

The signals captured did show characteristics of a source dependent on the 50 Hz applied voltage and the associated electric fields. Past research show that the signals could have been due to some form of plant deterioration in the form of electrical discharges in the power system[6],[7].

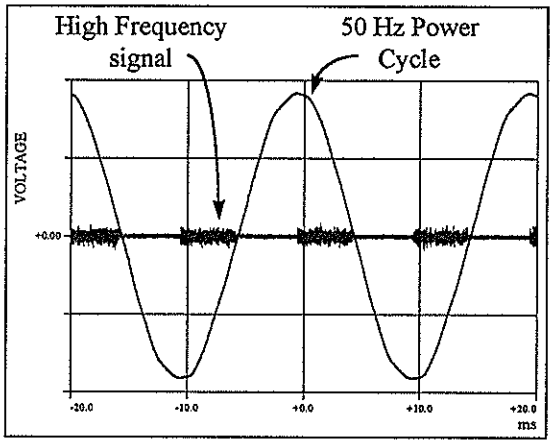

Figure 10 Actual signals present on the power network

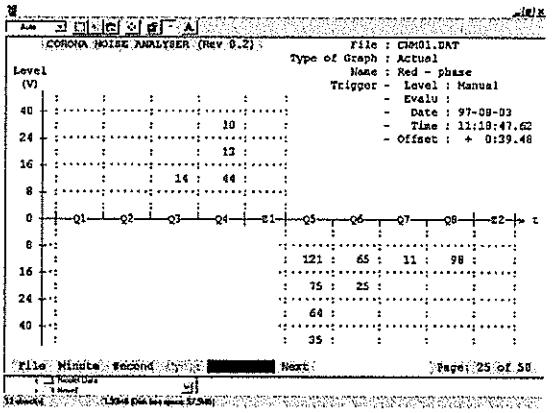

Figure 11 TRI-ADD data prior to flashover

8. CONCLUSION

Large ground fires produce sufficient corona to detect those fires from within the adjacent substation. The RMS results produced indicate that extensive corona activity is present at the overhead power line before breakdown takes place.

Two of three large ground fires with flames and particles in the air insulation gap did not cause a flashover. In all three instances the presence of the fires were visible via the high frequency signals generated from those fires.

Filtering alterations to the TRI-ADD system will be necessary to complete the detection structure.

9. REFERENCES

[1] Evert, CR; Britten, AC; van Coller, JM; Analysis of fire-induced corona on power lines; Southern African Universities Power Engineering Conference; 13-14 July 1992, University of Natal, Durban, South Africa.

[2] Evert, CR; Britten, AC; Holtzhausen, JP; Vosloo, WL; Discrimination between electromagnetic noise generated by sugar cane fires, conductor corona and polluted insulators on overhead lines; Southern African Universities Power Engineering Conference; 13-14 January 1994, Cape Town, South Africa.

[3] Evert, CR, Britten, AC; Analysis of fire-induced corona on power lines; 8th International Symposium on High Voltage Engineering, 23-27 August 1993, Paper 79.09, Yokohama, Japan.

[4] Evert, CR; The detection of fires under high voltage transmission lines; Eskom Internal Report, TRR/E/93/EL017; Technology Research and Investigations, July; 1993.

[5] Evert, CR; de Klerk, PJ; Fire-induced corona on high voltage power lines - an opportunity for detection and prevention of flashover; 2nd Southern African regional Conference Electric Power Systems in Sub-Equatorial Africa; 25-26 May 1994, Durban, South Africa.

[6] Evert, CR; de Klerk, PJ; Corona Noise as a Diagnostic tool; 4th International Conference on Properties and Applications of Dielectric Materials; Paper 6227, July 3-8, 1994, University of Queensland, Brisbane, Queensland, Australia.

[7] Evert, CR; Swift, DA, Britten, AC; Analysis of plant-deterioration related EM noise; 9th International Symposium on High Voltage Engineering, August 1995, Graz, Austria.

Partial Discharge Results From a Point in Air Obtained Under Impulse Voltage Conditions Using an Improved Experimental Set Up.

S.D. Nielsen and J.P. Reynders
Department of Electrical Engineering
University of the Witwatersrand
Johannesburg.

Abstract

This paper presents an alternative experimental set up for the detection of partial discharges under impulse voltage conditions. The principal of the set up is to reduce the capacitive coupling between the point and the plane. This is done by placing a grounded metal shield around the point. This results in the coupled impulse signal onto the discharge signal being so small, it can be ignored. Shielding of the point also reduces the amount of noise coupled onto the measurement from the firing of the impulse generator. A theoretical investigation of the experimental set up is presented as well as some experimental results in air at atmospheric pressure.

Keywords: partial discharge, impulse voltages

1. Introduction

The totally enclosed nature of Gas Insulated Substations (GIS) makes defect detection and location in the system more difficult than in its air insulated counterparts. It is well known that defects in GIS give rise to Partial Discharge (PD) activity within the system. Due to space charge development in the region of the defect under power frequency excitation voltage, the discharge activity associated with the particular defect will be reduced /1/. This reduction in discharge activity associated with the defect reduces the electrical discharge signals from that defect to a point where the signal can become buried in the noise of the detection system. This reduction in detection sensitivity can be avoided if the partial discharge detection is performed in association with a supply voltage waveform that does not allow the formation of space charge at the systems particular gas pressure. In general under voltage impulse conditions with rise times greater than about 10μs ion induced space charge effects become important /1/.

Preliminary work done on detecting partial discharges under impulse conditions using a conventional point to plane arrangement utilising filtering to reduce the capacitivly coupled impulse voltage signal, still resulted in the discharge signal being hidden in the noise of the system and the impulse voltage coupled into the measurement system /2/.

An improved measurement system has been proposed that relies on shielding of the point /3, 4/. The proposed experimental set up consists of placing a shielded point into a uniform background electric field, thus creating a field inhomogenity in the region of the tip of the point. This experimental set up reduces the total capacitive coupling between the plane (Rogowski profile electrode) and the point. This is done by placing a insulated point into a grounded metal shield. The only part of the point that will then be exposed to the electric field generated by the impulse voltage will be the tip of the point where the partial discharge activity takes place.

2. Theoretical investigation of experimental set up

Figure 1 shows the basic experimental set up. The shielded point arrangement protrudes through the grounded Rogowski profile electrode. The point consists of insulated copper wire ground to a hemisphere. The difference between the outer diameter of the shield and that of the point must be kept as small as possible.

2.1. Shape and magnitude of the supply voltage impulse present across the detection resistance

In order to determine the effectiveness of the proposed experimental set up in limiting the amplitude of the supply voltage impulse that will be coupled onto the measured partial discharge signal, a model of the set up was obtained. This is shown in Figure 1. The insulated point is placed in a uniform background electric field produced by two Rogowski profiles. The point is shielded along most of its length. The partial discharge signal is measured by a shunt resistance. The voltage impulse is applied to the top electrode.

Where:

C_R = Capacitance between the Rogowski profiles.

C_P = Capacitance between the Rogowski and the point.

C_S = Capacitance between the Rogowski and a shield.

C_{PS} = Capacitance between the point and the shield.

C_M = Capacitance of the measurement system.

R_M = Measurement resistance.

V_{HV} = Impulse supply voltage.

V_O = Output voltage.

Figure 2 shows a simplified model of Figure 1. The output voltage $V_O(t)$ is lead through 2,25 m of 50 Ω co-axial cable to a 500 MHz bandwidth oscilloscope, with an input impedance of 50 Ω. Therefore under lightning impulse excitation, the measurement capacitance C_M will be the capacitance of the cable ≈225 pF and the value of the measurement resistor R_M will become the physical measurement resistor in parallel with the 50 Ω input impedance of the oscilloscope

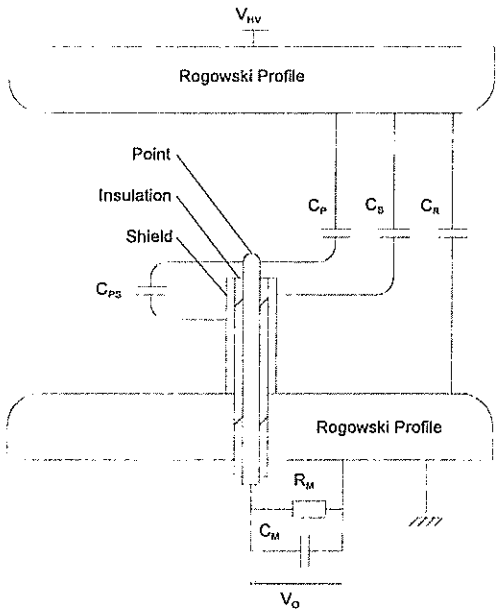

Figure 1 shows the basic experimental set up with the associated capacitive components used to predict the output voltage due to in impulse voltage.

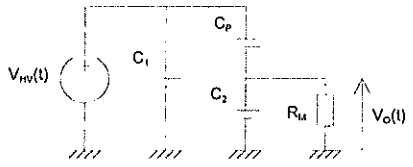

Figure 2. Simplified circuit of Figure 1.

Where:

$$C_1 = C_R + C_S$$

$$C_2 = C_{PS} + C_M$$

The formula relating the output voltage (V_O) across the detection resistance (R_M) to the supply voltage (V_{HV}), is described by Equation 1.

$$\frac{dV_{HV}(t)}{dt} = V_O(t)\frac{1}{C_P R_M} + \frac{dV_O(t)}{dt}\left[\frac{C_2 + C_P}{C_P}\right]$$

Equation 1

The impulse applied will take the form of a flat toped voltage pulse of infinite duration with a front rise time (0 - 90%) T_R. The impulse will have a 1 Volt amplitude i.e. 1 p.u. This voltage impulse can be described by Equation 2.

$$V_{HV}(t) = 1 - e^{-\alpha t}$$

Equation 2

Where:

$$\alpha = \frac{-\ln(0,1)}{T_R}$$

Solving for $V_O(t)$ using Laplace transforms gives Equation 3.

$$V_O(t) = \frac{A\alpha}{B\left(\frac{1}{B} - \alpha\right)}\left(e^{-\alpha t} - e^{-\frac{1}{B}t}\right)$$

Equation 3

Where:

$$A = C_P R_M$$

$$B = R_M[C_P + C_2]$$

2.2. The shape and magnitude of the partial discharge signal across the detection resistance

In order to determine the magnitude and the shape of the of the output voltage due to a partial discharge current, a model of the set up was obtained. This is shown in Figure 3.

Figure 4 shows the simplified model of Figure 3. The output voltage $V_O(t)$ is lead through 2,25 m of 50 Ω co-axial cable to a 500 MHz oscilloscope, with an input impedance of 50 Ω. Therefore under a partial discharge, the measurement capacitance C_M will be negligibly small and the value of the measurement resistor R_M will become the physical measurement resistor in parallel with the 50 Ω surge impedance of the co-axial cable.

The formula; using Figure 4; relating the output voltage (V_O) across the detection resistance (R_M) to the partial discharge current (I_D), is described by Equation 4.

$$I_{PD}(t) = V_O(t)\left(\frac{C_P + C_1}{C_1 R_M}\right) + \frac{dV_O(t)}{dt}\left(\frac{C_2 C_P}{C_1} + C_P + C_2\right)$$

Equation 4

Where:

All the other components are the same as those in Figure 1.

I_D = Current associated with a partial discharge.

The partial discharge current applied will take the form of a double exponential current with a approximate front rise time (0 - 90%) T_R and an approximate fall time (100 - 50%) T_F. This current impulse can be described by Equation 5.

$$I_{PD}(t) = e^{-\alpha} - e^{-\delta}$$

Equation 5

Where:

$$\delta = \frac{-\ln(0,1)}{T_R}$$

$$\varepsilon = \frac{-\ln(0,5)}{T_F}$$

Solving for $V_O(t)$ using Laplace transforms gives Equation 6.

$$V_O(t)=\left(\frac{\delta-\varepsilon}{D}\right)\left(k_1e^{-\alpha}+k_2e^{-\beta}+k_3e^{-\frac{C}{D}t}\right)-\left(\frac{\delta-\varepsilon}{D}\right)(k_1+k_2+k_3)$$

Equation 6

Where:

$$C=\left(\frac{C_P+C_1}{C_1R_M}\right)$$

$$D=\frac{C_2C_P}{C_1}+C_P+C_2$$

$$k_1=\frac{1}{(\delta-\varepsilon)\left(\frac{C}{D}-\varepsilon\right)}$$

$$k_2=\frac{1}{(\varepsilon-\delta)\left(\frac{C}{D}-\delta\right)}$$

$$k_3=\frac{1}{\left(\varepsilon-\frac{C}{D}\right)\left(\delta-\frac{C}{D}\right)}$$

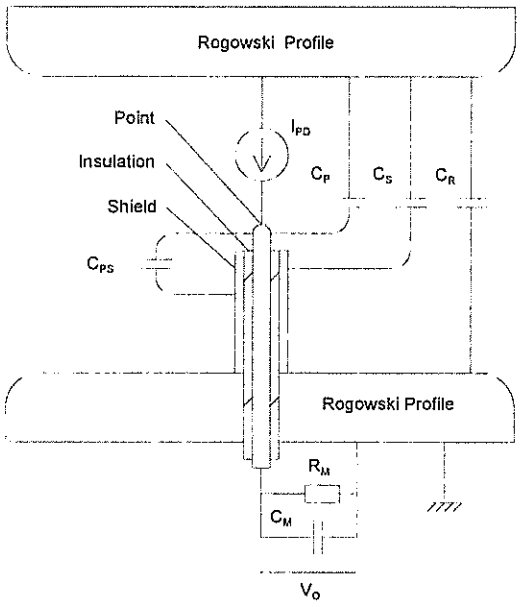

Figure 3. Shows the basic experimental set up with the associated capacitive components used to predict the output voltage due to a partial discharge.

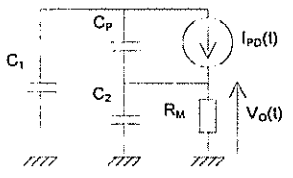

Figure 4. Simplified equivalent circuit of Figure 3.

Where:

$$C_1=C_R+C_S$$

$$C_2=C_{PS}+C_M$$

2.3. Results

Table 1 shows the predicted values for the components used in the models.

Figure 7 in Appendix A shows the rising edge of the lightning impulse voltage $V_{HV}(t)$ with T_R = 1,2 µs and the associated output $V_O(t)$. C_P = 0,6 mpF, C_{PS} = 49,9 pF, C_M = 225 pF and R_M = 25 Ω.

Figure 8 in Appendix A shows the output voltage $V_O(t)$ due to a partial discharge represented by a current $I_{PD}(t)$. C1 = 2 pF, C2 = 49,6 pF, CP = 0,6 mpF, CM = 0 and RM = 25Ω. The total charge in $I_{PD}(t)$ is Q_{TOTAL} = 13,5 nC.

From these two Figures it can be seen that the magnitude of the impulse coupled on to the output signal will be much smaller than in previous experimental set ups /2/. The shape of the output voltage associated with a partial discharge should represent the true shape of the current pulse relatively accurately.

Table 1. Predicted model parameters.

C_R	C_P	C_S	C_{PS}	C_M	R_M
≈30 pF to ≈2 pF	≈0,6 mpF to ≈0,06 mpF	≈30 mpF to ≈0.03 mpF	≈49,6 pF	Partial discharge : ≈0 Lightning impulse :≈225 pF	25 Ω

3. Experimental results

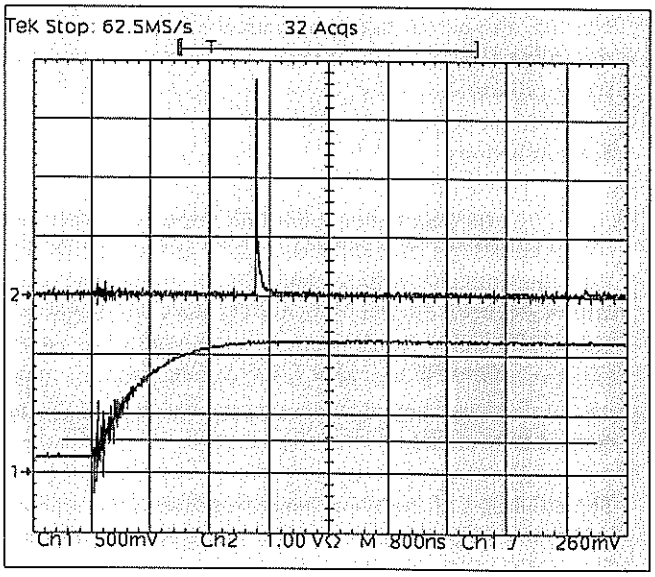

Figure 5. This figure shows a partial discharge in air at atmospheric pressure. Channel 1 rising edge of the impulse voltage, Vertical scale : 8,019 kV/div, Horizontal scale : 800 ns/div. Channel 2 measured partial discharge signal, Vertical scale : 1 V/div, Horizontal scale : 800 ns/div.

The experiments were carried out in atmospheric air for convenience. The Rogowski profile electrodes had a diameter of 196 mm and a separation between them of 21,24 mm. The point protruded 7,12 mm out of the ground Rogowski profile electrode. The point was hemispericaly capped and had a diameter of 0,91 mm. The shield had a outer diameter of 1,28 mm.

Figure 5 shows a partial discharge occurring on the peak of the applied impulse. As can be seen from this figure, the impulse signal coupled onto the partial discharge signal is negligibly small. The only noise present is due to the firing of the impulse generator.

Figure 6 shows the partial discharge signal in more detail. The rise time of the measured signal is approximately 1,5 ns, with little or no parasitic oscillation present

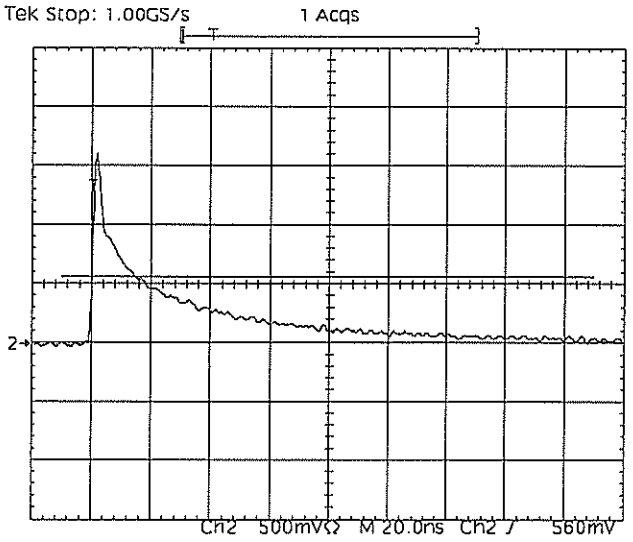

Figure 6. This figure shows the measured partial discharge current in more detail. Channel 2 measured partial discharge signal, Vertical scale : 500 mV/div, Horizontal scale : 20 ns/div.

4. Conclusions

It has been shown that the improved experimental set up consisting of a shielded point has reduced the signal from the impulse voltage that will be capacitivly coupled onto the partial discharge signal via the capacitance of the point. This has been shown theoretically as well as experimentally. It has also been shown that the detected partial discharge signal represents the true partial discharge current very closely.

The shielding of the point has also reduced the amount of noise that is coupled onto the measurement due to the firing of the impulse generator.

The above improvements have resulted in a clean output voltage having a good representation of the true partial discharge current.

References

/1/ Luxa G. et al, Resent Research Activity on the Dielectric Performance of SF_6, with Special Reference to Very Fast Transients, International conference on Large High Voltage Electric Systems, August/September, 1988, Paper 15-06.

/2/ Nielsen S.D. et al, Preliminary Work on the Detection of Partial Discharges in SF_6 Under Impulse Voltages, 10th International Symposium on High Voltage Engineering, Montréal, 1997.

/3/ Bhutt S. et al, Preliminary Investigation of Positive-Impulse Discharges in SF_6, 10th International Symposium on High Voltage Engineering, Montréal, 1997.

/4/ Niemeyer L. et al, Phase Resolved Partial Discharge Measurements in Particle Contaminated SF_6 Insulation, Gaseous Dielectrics VI, Proceedings of the Eighth International Symposium on Gaseous Dielectrics, Knoxville, 1991.

Address of Author

S.D. Nielsen
Department of Electrical Engineering
University of the Witwatersrand
PO Wits
Johannesburg
2050
South Africa
Nielsen@odie.ee.wits.ac.za

Appendix A

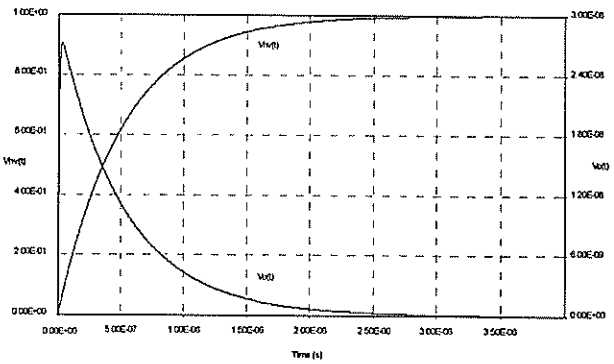

Figure 7. This figure shows the rising edge of the lightning impulse voltage $V_{HV}(t)$ with T_R = 1,2 µs and the associated output $V_O(t)$. C_P = 0,6 mpF, C_{PS} = 49,9 pF, C_M = 225 pF and R_M = 25 Ω.

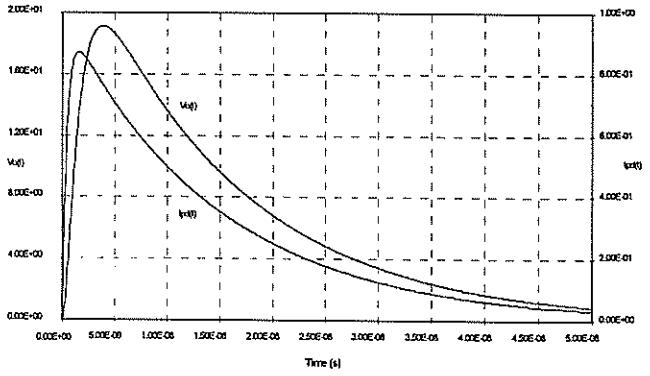

Figure 8. Shows the output voltage $V_O(t)$ due to a partial discharge represented by a current $I_{PD}(t)$. C1 = 2 pF, C2 = 49,6 pF, CP = 0,6 mpF, CM = 0 and RM = 25Ω. The total charge in $I_{PD}(t)$ is Q_{TOTAL} = 13,5 nC.

A CONTINUOUSLY ONLINE TRAINED ARTIFICIAL NEURAL NETWORK CONTROLLER FOR A MICRO-TURBOGENERATOR

GK Venayagamoorthy, RG Harley

University of Natal, Durban

ABSTRACT

This paper reports on the simulation studies carried out on a single turbogenerator connected to an infinite bus through a short transmission line, with a Continuously Online Trained (COT) Artificial Neural Network (ANN) controller to identify and another COT ANN to control the turbogenerator. This identifier/controller augments/replaces the automatic voltage regulator and the turbine governor. Results are presented to show that this COT ANN identifier/controller has the potential to allow turbogenerators to operate more closely to their steady state stability limits and nevertheless "ride through" severe transient disturbances such as three phase faults. This allows greater usage of existing power plant.

1. INTRODUCTION

Offline trained Artificial Neural Network (ANNs) have been investigated by others [1,2] to provide supplementary damping signals, (such as power system stabilisers) to turbogenerators. ANNs are basically nonlinear controllers and have the potential to allow turbogenerators to operate more closely to their steady state stability limits and nevertheless "ride through" severe transient disturbances such as three phase faults. This allows greater usage of existing power plant.

Ref. [3] improved on earlier work of others by proposing the use of two ***Continuously Online Trained*** (COT) Artificial Neural Networks (ANNs), one as an adaptive turbogenerator identifier, and the other as a controller to augment and perhaps even replace not only the automatic voltage regulator (as previous researchers have suggested), but also the ***turbine governor***. The conventional automatic voltage regulator (AVR) and turbine governor are usually designed to control the nonlinear turbogenerator in some optimal fashion, around a fixed operating point; therefore this performance is degraded at any other operating point, but the COT ANN identifier/controller designed in Ref.[3] overcomes this problem. The present paper is an extension of the work of Ref.[3].

2. SIMULATION MODEL DEVELOPMENT

2.1 Micro-Turbogenerator Modelling

A 3 kW Mawdsley micro-turbogenerator shown in Fig.1 is available in the "micro-machine" research laboratory at the University of Natal and is modelled by using the general state variable equation of a synchronous machine:

$$\dot{x} = Ax + Bu + F(x) \qquad (1)$$

where $F(x)$ represents the non-linear terms.

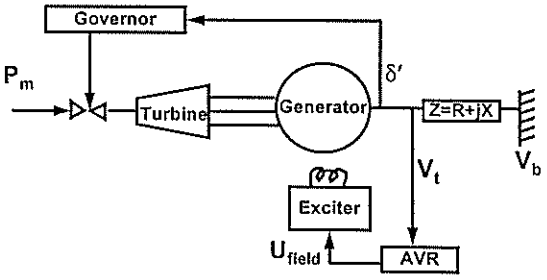

Fig.1 A single machine connected to an infinite bus through a short line.

This micro-turbogenerator is designed to have per-unit parameters which are typical of those normally expected of 30-1000 MW generators, except for the field winding resistance.

Table 1. Machine Constants

X_{md}=1.98 pu	X_{fld}=0.1 pu	X_{kq}=0.2557 pu
X_{mq}=1.87 pu	R_{fd}=0.00099 pu*	R_{kq}=0.027 pu
X_a=0.11 pu	X_{kd}=0.125 pu	X_q''=0.164 pu
R_a=0.006 pu	R_{kd}=0.0212 pu	

**Depends on the TCR setting*

A Time Constant Regulator (TCR) which stimulates negative resistance in the field winding circuit, is used to reduce the actual field winding resistance to the correct per-unit value. The machine parameters are given in Table 1 above.

The generator is described by the two axis dq-equations with the machine currents, speed and rotor angle taken to be the state variables, with one damper winding on each axis giving a seventh order model.

The AVR and the exciter combination are modelled in state space as a second order device with limits on its output voltage levels. The turbine (simulator) and governor combination are also modelled in state space as a fourth order device so that reheating between the high pressure and intermediate pressure stages may be included in the model. The output of the turbine simulator is limited between zero and 120%.

A relatively short transmission line connecting the generator to the infinite bus is modelled.

The mathematical implementations of these state space models were carried under the MATLAB/SIMULINK environment since these proved to be simple to implement nonlinear differential equations.

2.2 ANN CONTROLLER ARCHITECTURE

The following aspects make it difficult to apply ANNs to complex nonlinear devices such as turbogenerators:

(a) a turbogenerator is a nonlinear device and it is difficult to use a simple model as a reference for adaptive control as proposed by Ref.[4].

(b) an inverse model suggested by Ref.[5] would be difficult to implement reliably and consistently due to the high gain loops around turbogenerators.

(c) the ANN based model structure as suggested by Ref.[6] is for a single-input-single-output system and therefore not suitable because the turbogenerator is a multivariable device.

The method adapted in this paper as proposed in Ref.[3] is a two stage architecture shown in Fig.2. The ANN regulator consists of two separate ANNs, namely one for the identifier and one for the controller.

2.2.1 COT ANN Turbogenerator Identifier

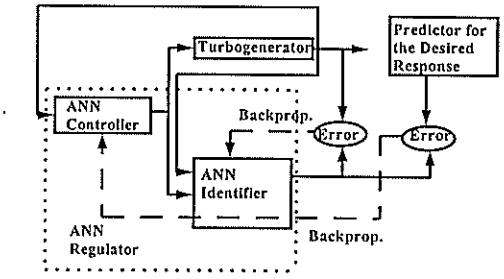

Fig.2 Neural Network Identifier and controller architecture

The Identifier ANN (IANN) in Fig.2 has three layers consisting of an input layer with twelve inputs, a single hidden layer with fourteen neurons and an output layer with two outputs. The inputs to the IANN are also the deviation in the input to the turbine simulator, the deviation in the input to the TCR-exciter, the output voltage deviation and speed deviation of the generator. These four ANN inputs are delayed by the sample period of 20 ms and together with eight previously delayed values form twelve inputs altogether to the IANN. The IANN outputs are the terminal voltage deviation and speed deviation of the generator.

The number of neurons in the hidden layer of the IANN were determined empirically. The IANN weights were set to small random values and the conventional backpropagation algorithm was used to update these weights of the IANN. The differences between the respective outputs of the turbogenerator model and the outputs of IANN generates the error signals for the updating of weights in the IANN. A reasonable learning rate was determined by running this neural network and setting the learning rate parameter so that a compromise between the training time and the accuracy of the network is achieved.

The training of the IANN was simulated using pseudorandom binary signals generated in MATLAB and fed into the exciter and the turbine. These random signals excite the full range of the dynamic response of the turbogenerator. The results obtained proved that a COT ANN can successfully model or identify a turbogenerator (Fig.3), thereby eliminating the need to have any detailed mathematical model and accurate machine parameters.

2.2.2 COT ANN Turbogenerator Controller

In addition, Ref.[5] proposed a controller ANN as a nonlinear controller to augment/replace the AVR and governor and this COT ANN is similar in structure to the identifier ANN above.

The COT Neural Network Controller (NNC) is a three layer network with six inputs, ten hidden neurons and two outputs. The inputs are the turbogenerator's speed and terminal voltage deviations. Each of these inputs was time delayed for one, two and three sample periods. The outputs of the NNC formed the inputs to the turbogenerator's TCR-exciter and the turbine simulator. The number of neurons and learning rate were determined empirically as for the IANN.

The NNC in Fig.2 operates with online learning, however, it is necessary to train the NNC initially before online control operation is undertaken. As with IANN the NNC was trained by using pseudorandom input signals to the TCR-exciter and turbine simulator. Training was carried out for 30 seconds to ensure that the NNC had learnt the turbogenerator sufficiently accurately for online control to be undertaken.

Once the controller has undertaken online operation the following basic steps are used thereafter:

(a) sample the output of the turbogenerator and the IANN (see Fig.2). Using the square differences between these two outputs and the backpropagation algorithm, update the weights in the IANN. Fix these weights.

(b) the same input signals as in step (a), again sample the output of the IANN and compare the output of the identifier with the desired response for the turbogenerator. Use the square of the difference of these two signals to form the error and backpropagate this error signal through the IANN to the output of the NNC.

(c) use the error signal at the output of the NNC obtained in step (b), and the backpropagation algorithm, update the weights in the NNC. Apply the output of the NNC (obtained with these weights) to the TCR-exciter and turbine simulator of the turbogenerator.

(d) Repeat steps (a) to (d).

An advantage of this controller architecture is that the signals used are deviations from the setpoints and therefore when the turbogenerator is operating at the desired operating point there will be zero inputs to the NNC and zero outputs. This means that online learning takes place only when deviations from setpoints occur, and therefore ensuring minimum controller drift.

3. SIMULATION RESULTS

The dynamic and transient operation of the ANN regulator was compared with operation of the conventional controller (AVR and turbine governor) under two different conditions: a three phase short circuit on the infinite bus, and ± 5% step changes in the terminal voltage setpoint. Each of these was investigated for the turbogenerator driven at different power factors and transmission line configurations.

A sample of results obtained is shown in Fig.4 to Fig. 6. Fig.4 shows the performance of the NNC for ± 5% step changes in the terminal voltage with turbogenerator operating at 1 pu power and 0.85 lagging power factor (in all the result graphs conventional controller is shown with solid lines while the neural network with dashed lines). Fig.5 shows a turbogenerator operating under the same conditions and experiencing a 50 ms three phase short circuit on the infinite bus. Fig.6 shows a turbogenerator experiencing a 50 ms three phase short circuit on the infinite bus with double the transmission line impedance used in Fig.5. In each of these tests it can be seen that the ANN regulator has a performance at least comparable to that of a conventional controller and in each the NNC has similar response times with better damping.

Tests at other operating points confirmed that the controller is self-learning and performance does not degrade as with the conventional controllers.

4. CONCLUSIONS

Early conclusions of this work indicate that the two COT ANNs can identify and control the turbogenerator almost as well as a traditional AVR and governor combination, when the network configuration and system operating point conforms to that for which the AVR and governor were tuned. However, when system conditions change, such as different power levels and transmission line configurations, the ANN identifier and controller track these changes and do not give a degraded performance as the AVR and governor do. The successful performance of the COT ANNs even when the system configuration changes, comes about because the ***online training never stops.***

5. REFERENCES

[1] Kobayashi T, Yokoyanna A, "Nonlinear adaptive control of synchronous generator using neural network based regulator", *ISAP'94, International Conference on*

Intelligent Systems Application to Power Systems, Vol 1, p55.

[2] Zhang Y, Chen GP, Malik OP, Hope GS, "An artificial neural network based power system stabiliser", *IEEE Transactions on Energy* Conversion, Vol 8, No 1, 1993, pp 71-77.

[3] Shepstone NM, Harley RG, Jennings G and Rodgerson J, "An investigation into the feasibility of using neural networks to control turbogenerators", *IEEE-Africon* '96, Vol 2, 24 - 27 Sept. 1996, Stellenbosch, pp 849 - 852.

[4] Narenda KS, Parthasarathy K, "Identification and control of dynamical systems using neural networks", *Artificial Neural Networks*, eds Sanchez-Sinencio and Lau, IEEE Press, 1992, ISBN 0-87942-289-0.

[5] Hunt KJ, Sbarbaro D, "Studies in neural network based control", *Neural Networks for Control and Systems*, Peter Peregrinus Ltd, 1992, pp 95 -122, ISBN 0-86341-279-3

[6] Chen S, Billing SA, Grant PM, "Nonlinear systems identification using neural networks", *International Journal of Control,* Vol 51, 1990, pp 1191- 1214.

Address of authors: GK Venayagamoorthy, RG Harley, Department of Electrical Engineering, University of Natal, Private Bag X10, Dalbridge 4014, South Africa. Tel: (031)260-2725, Fax: (031)260-1300. Email: venayaga@eng.und.ac.za
Email: harley@eng.und.ac.za

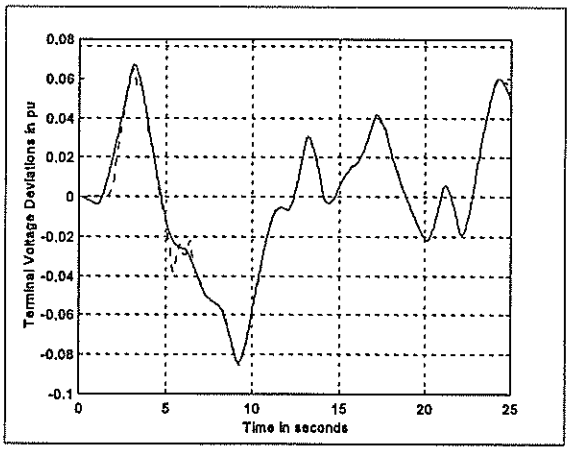

Fig.3 Neural Network modelling of the dynamic characteristics of the micro-turbogenerator

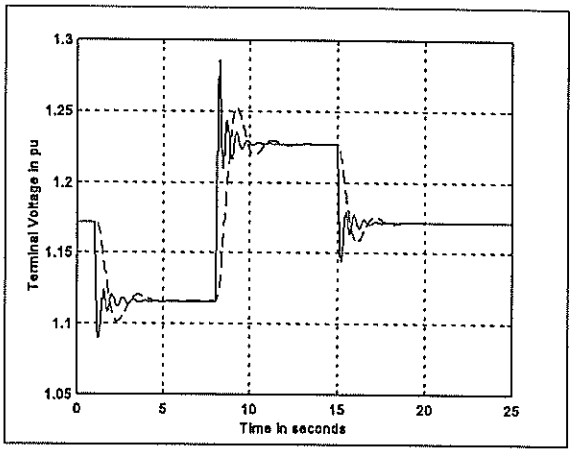

Fig.4 ± 5% step changes in the terminal voltage (P = 1.0 pu, pf = 0,85 lagging)

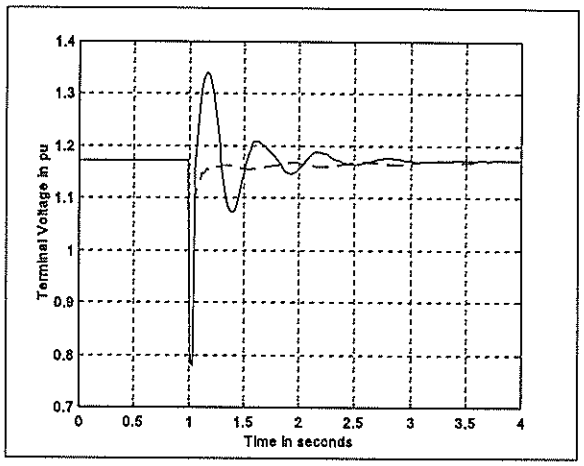

Fig.5 A 50 ms three phase short circuit at the infinite bus (P = 1 pu, pf =0.85 lagging)

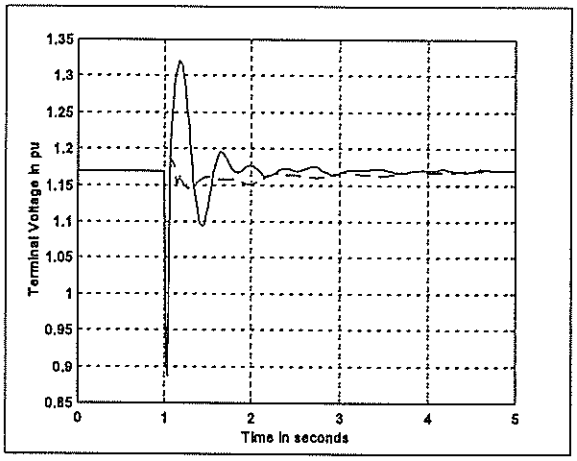

Fig.6 A 50 ms three phase short circuit at the infinite bus (P = 1 pu, pf = 0.85 lagging) with double the transmission line impedance used in Fig .5

A LOW COST, HIGH PERFORMANCE PC BASED INTEGRATED REAL-TIME MOTION CONTROL DEVELOPMENT SYSTEM

AW Stylo and G Diana

Department of Electrical Engineering, University of Natal, Dalbridge 4041, South Africa.
e-mail : styloa@eng.und.ac.za , gdiana@eng.und.ac.za
Web : http://www.ee.und.ac.za/electric/research.htm

ABSTRACT

This paper outlines the development of an integrated system for the design, simulation and real-time prototyping of motion control systems, based on the Simulink and Real Time Workshop (RTW) package from MathWorks and a PC32 DSP card from Innovative Integration. The entire process of design, simulation through to final prototyping takes place in a common integrated environment, without the need to write a single line of code. Once the prototype controller is working satisfactory, the final code generated can easily be ported to a standalone controller board.

1. INTRODUCTION

Real-time testing of a prototype controller provides the greatest insight into how well a design performs with real sensors, and under realistic test conditions.

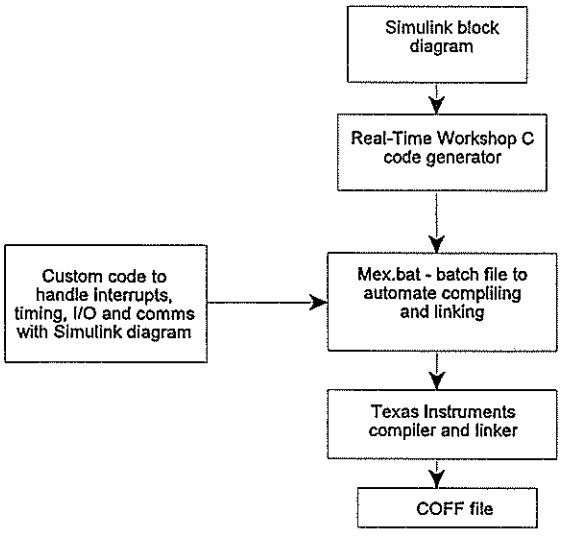

Fig. 1 Generating Executable code from an Simulink diagram

Rapid prototyping can be defined as a process for automatic implementing of a block diagram on real-time hardware. It offers exceptionally fast design iterations, including real-time testing, that allows designs to be finalized significantly faster than with traditional design approaches. The tools being developed in this project are not limited to the design of motion control, but can easily be applied to other real-time types of control as well as areas like signal processing etc. Also a variety of hardware platforms can be targeted.

In addition the integrated development environment allows parameters to be changed without recompiling. Being able to change parameters "on-the-fly" allows easy adjustment and tuning of control systems without interrupting real-time execution.

2. OBJECTIVE

The primary objective of this project is to develop an integrated environment to allow for rapid prototyping of motion control systems to enable new concepts to be implemented and evaluated in real-time on hardware quickly and easily. This can be particularly useful when exploring cost versus performance trade-offs. For example, the effects of quantization (number of bits in I/O device), sample rate, and performance of algorithms can be studied well before making commitments that can have an impact on final hardware selection. Interfacing the prototype control hardware to the physical system enables us to determine how well it performs with alternative sensors. Ultimately, the code generated from the set of block diagrams can be ported onto stand-alone hardware.

The key to rapid prototyping is automatic code generation. Because design iterations become repetitive during the implementation and testing phase, the process of coding, compiling, linking and downloading to target hardware should be automatic and transparent to the user. This automation allows design changes to be made directly to the block diagram, and with code generation

the entire process of creating the real-time executable is fast, effortless, and reliable.

3. SYSTEM OUTLINE

Matlab, Simulink, RTW and additional toolboxes form an extensive set of tools for modeling, control design, analysis and simulation. Using these tools the desired controller can easily be designed, configured and simulated on a PC. Because of its inherent power, the Simulink environment is widely used in industry and is becoming the defacto standard in terms of simulation.

After a system has been designed and simulated in Simulink, the resultant block diagram can be automatically compiled, linked with the necessary components and libraries and then downloaded onto the dedicated target hardware to be executed in real time. While the code is executing in real time various parameters can be changed in the Simulink block diagram and may be automatically updated in the code executing on the hardware without interrupting execution.

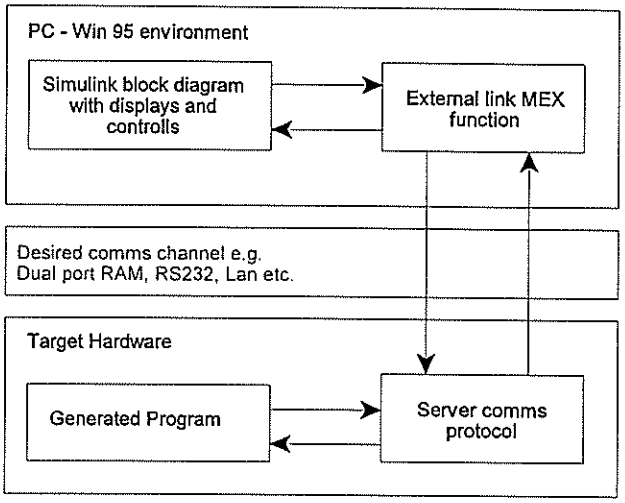

Fig. 2 Simulink external mode

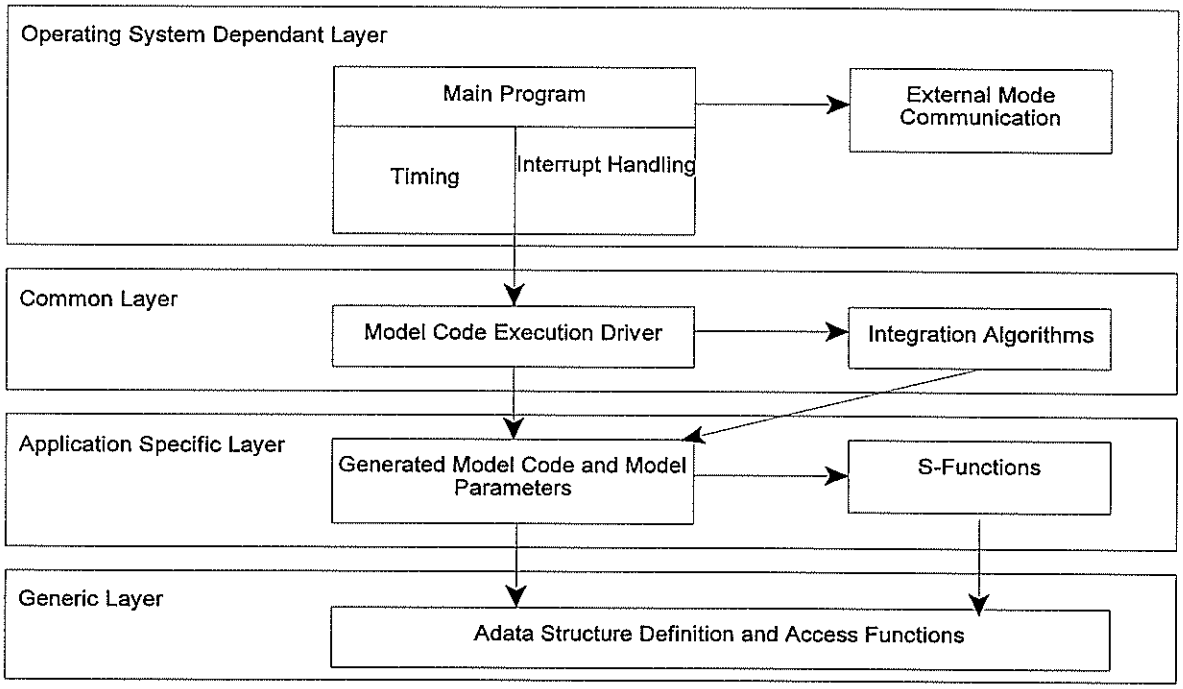

Fig. 3 Real-Time Program Architecture

The process of compiling a block diagram into the final COFF file is shown in Fig.1.The outline of the system running in external mode is shown in Fig.2. The communication between the PC and the target hardware is accomplished via the dual port RAM built into the PC32 card. In the case of a stand alone card communication channel could easily be implemented via the serial port.

4. Generated Program

4.1. Program Architecture

Generating code for a Simulink model results in two files - *model.c* and *model.h*, where *model* is the name of the Simulink model. This code implements the model's system equations, contains block parameters, and performs the necessary initialization steps.

In addition to this we need to provide source code

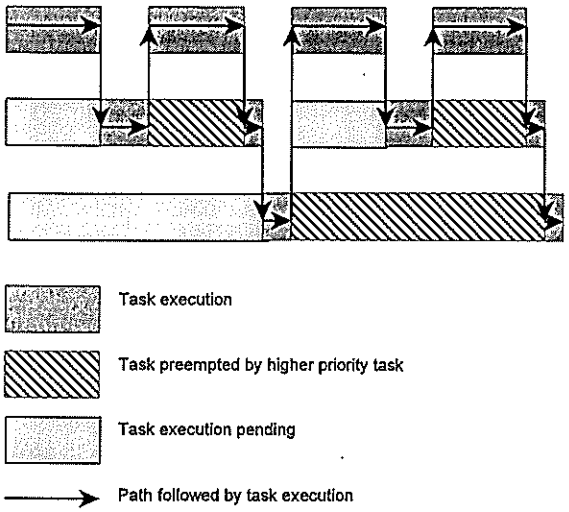

Fig. 4 Pseudomultitasking using overlapped interrupts

necessary to build the model code into a complete, stand-alone program. The program framework consists of application modules - source code files to implement required functions. A custom batch file program (mex.bat) ensures that all necessary components are compiled and linked into the final executable COFF file.

The structure of a real-time program consists of a number of layers. Each layer has a dependancy on a different part of the environment in which the program executes, in this case a DSP processor card. Fig.3 demonstrates this structure.

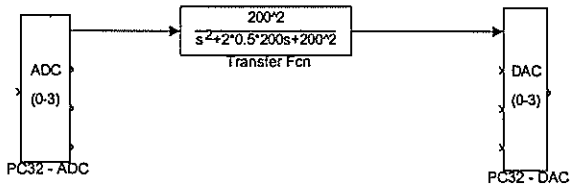

Fig. 5 Sample Simulink Diagram

By isolating the dependencies in each program layer it is easy to adapt this architecture to a variety of platforms.

Real-time programs require careful timing to ensure that all tasks in the model code execute to completion before next interrupt arrives. This includes the time to read and write to and from external hardware I/O.

In the single-tasking environment of the PC32 card we need to implement a scheme to emulate multitasking - pseudomultitasking. This is done using overlapping interrupts and manual context switching. An interrupt can occur while another interrupt is currently in progress. When this happens, the current interrupt is preempted, the context saved and the higher priority interrupt executes. This scheme is illustrated in Fig.4. The highest priority interrupt is the top one, and the bottom one has the lowest priority.

4.3. Common Layer

This layer is called common as it remains unchanged in all environments. Here the program steps through the model code and calls one of the integration algorithms if necessary. The model code execution driver calls the functions in the model code to compute the model outputs, update the discrete states, integrate the continuous states (if any) and update time. These functions then write their calculated data to the common data structure - SimStruct.

At each sample time interval, the main program passes control to the model execution function. This function then decides which blocks need to be executed. Continuous blocks get updated every time. Discrete blocks with sampling rates slower than the base sampling rate only get executed when necessary. Due to the pseudomultitasking setup, all sampling rates in system need to be multiples of the base sample time.

4.4. Application Specific Layer

This layer contains the code generated from the Simulink block diagram, including the code for any S-functions in the model. Apart from functions to execute the model, this code also includes functions to perform initialization, and facilitate access to the data structure.

4.5. Generic Layer

Here, the code that defines, creates, and destroys the Simulink data structure, SimStruct, is found. The model code and all extra S-functions define their own copy of SimStruct. This data structure contains all data relating to the model or S-function, including block parameters and outputs. When in external mode, the server communication function accesses those fields to update the model parameters without the need of recompiling the program.

5. Device Driver Blocks

In order for the code generated from a Simulink diagram to be able to access low level devices like A/D or D/A converters, additional blocks have to be defined. Those device driver blocks are implemented as S-functions and linked into the final code.

In addition to providing the basic I/O functionality, S-

functions can be used to provide access to custom external hardware. For example custom PWM boards.

6. Sample Block Diagram

To illustrate the performance of the system a sample Simulink block diagram is shown in Fig. 5. This diagram was used initially to verify that the system generated code correctly and that execution on PC32 hardware in real-time correlated to simulations.

The diagram in Fig.5 was compiled using the tools developed during the project. It was then downloaded to a PC32 card and executed in real-time. With a 62.5 Hz (16ms period) square wave as input it produced the second order response shown in Fig.6. The same second order transfer function was then simulated in Simulink

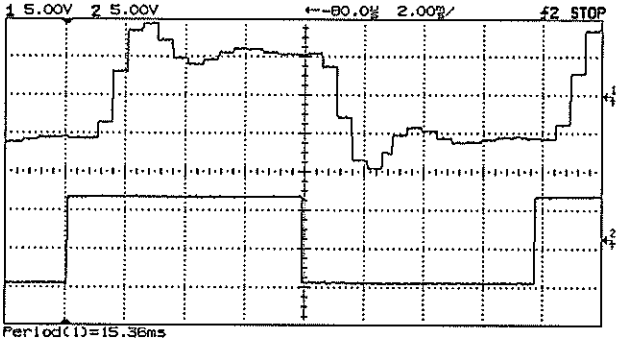

Fig. 6 Digital scope output

using a signal generator block to provide identical input conditions. This block diagram is shown in Fig. 7. The results of the simulation were captured to Matlab's workspace and plotted to obtain Fig.8.

As can be seen the code was generated correctly as the real-time execution corresponded to simulation.

7. Conclusion

Once the whole system is running smoothly it will provide a robust tool for any control engineer. It combines the proven and widely accepted mathematical

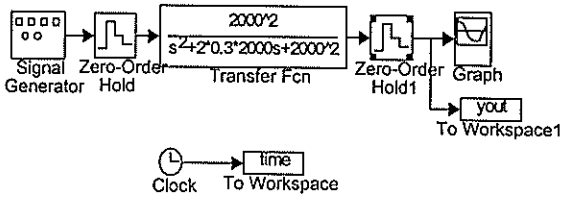

Fig. 7 Simulation Block Diagram

power of the Matlab environment with the ease of use and hassle free code generation of dedicated packages like Hypersignal.

The DSP hardware utilised in this project represents extremely good value for money. The entire system is specifically designed to provide a low cost, complete

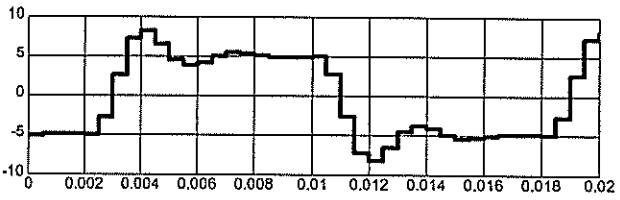

Fig. 8 Simulink simulation

solution for all motion control requirements. The Simulink environment is widely available in practically all laboratories, and at minimal cost it can now be upgraded into a full blown environment, which will allow the engineer to design, simulate and implement motion control systems without writing a single line of code.

8. References

[1] The Math Works Inc., "Real-Time Workshop, User's Guide"

Test Bed System to Evaluate the Efficiency of Variable Speed Drives Under Varying Load Conditions

M L Walker and G Diana

Department of Electrical Engineering, University of Natal, Dalbridge, 4041, Durban
e-mail: walkerm1@eng.und.ac.za, gdiana@eng.und.ac.za

Abstract

This paper describes the aims and requirements for a user friendly, easy to use test bed system to evaluate the efficiency of variable speed drives under variable load conditions.

1.0 Introduction

The control of air or liquid flow in industry is used frequently and vital to the production of many products. When using motors running at fixed speed the control of the air or liquid flow (oil, water, etc.) has been done mechanically by restricting the air or liquid flow and at low flow rates these systems become very inefficient. A test bed system is being built to measure the power savings that can be made in those applications where Variable Speed Drives (VSDs) can be used.

The test bed system, will allow the VSD to be loaded with any desired load characteristics. The efficiency of the VSD can then be evaluated at various speeds under the specified load condition.

2.0 Objectives

In most industrial applications the motor is stiffly coupled to either a pump or fan. The motor is then driven directly from the main (fixed Frequency) as shown in Fig.1. When low flow

Fig 1 Typical system using and induction motor

rates are required the flow has to be retarded causing the efficiency of the system to drops. Fig. 2 shows the power required from the induction motor for a specified speed of the pump (no head) or fan. Fig. 3 shows the flow rate of the air or liquid for a specific speed of the pump (no head) or fan. From the above figures it can be

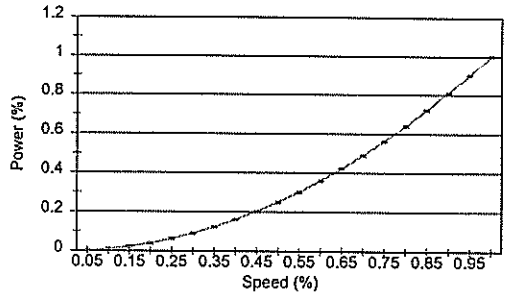

Fig. 2 Speed Versus power required by pump or fan

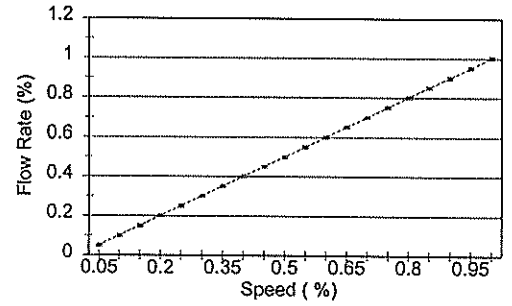

Fig. 3 Speed versus Flow rate for Pump or Fan

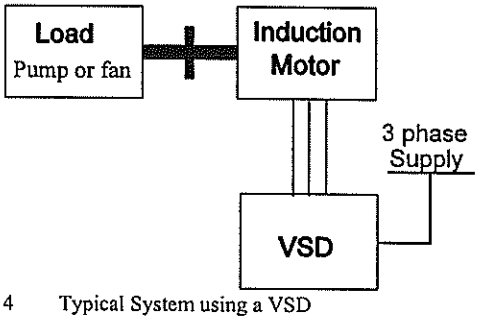

Fig. 4 Typical System using a VSD

concluded that if a low flow rate is required it would be beneficial to reduce the speed of the pump or fan, large savings would thus be observed where low and variable flow rates are required.

Fig. 4 shows a VSD supplying the induction motor with a variable frequency supply, this enables the speed of the motor to be varied according to the flow rate required.

The main objective of the test bed system is to evaluate the savings that can be made by using a VSD to control the flow rate of liquids or gasses as shown in Fig. 4 compared to that of Fig. 1.

3.0 System Description

A block diagram of the proposed test bed is shown in Fig 5.

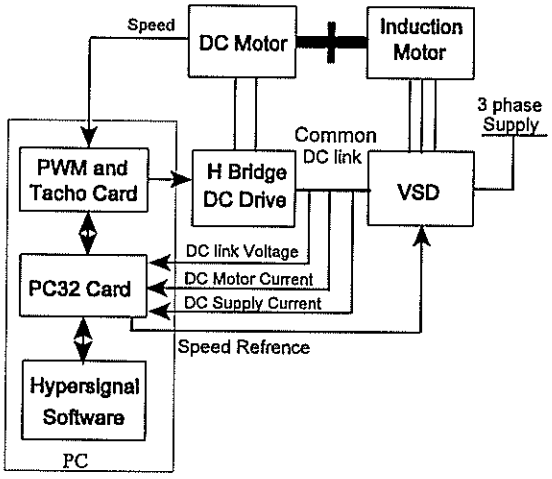

Fig. 5 System Block Diagram

The load (pump or fan) will be simulated by a DC machine which is stiffly coupled to an induction motor. The DC machine will be controlled such that it loads the induction motor with a torque speed curve of a pump or fan under various load conditions. The required load torque produced by DC machine is controlled in accordance with the induction motor speed and the desired torque for that speed (from the torque speed curve enter by the user).

The VSD remains unaltered, receiving only a speed signal from the PC. The VSD and the DC Drive are connected together via a common DC link, allow the DC machine to regenerate power back onto the DC link thus allowing power to be saved. Only the power lost inside the test bed system will be drawn from the mains supply thus keeping the efficiency of the test bed system high (lower running costs).

A 30kW test bed system is being built, which ensures that the power drawn is large, such that switching losses in the inverters are small and do not have any significant impact on the accuracy of the results gained.

3.1 DC Motor Control

The control of the DC machine is critical in the implementation of the test bed. The DC machine runs as a generator and thus a load it places on the induction motor is dependent on the armature current flowing. This armature current can be controlled in two ways.

I. By varying the field current thus changing the flux and the internal EMF of the DC machine.

II. By controlling the DC current that is allowed to flow back into the DC link. This can be achieved by changing the PWM pulses on the H bridge.

The second options was opted for as this will allow the DC machine to effectively cover a large speed range. The electrical torque developed by the DC machine is given by eq. 1.

$$T_f = K\phi I_a \qquad (1)$$

where

K is the machine constant	
ϕ is the machines flux	(wb)
I_a is the armature current	(A)
T_f is the machine torque	(N.m)

The value of $K\phi$ can be measured and saturation and other effects can be programmed into the control algorithm.

Due to the DC machine current being measured it is possible to estimate the electrical losses inside the machine as in eq. 2.

$$P_{dcl} = R_a I_a + V_b I_a \qquad (2)$$

where	P_l is the electrical losses	(W)
	R_a is the armature resistance	(Ω)
	V_b is the brush Voltage drop	(V)

The mechanical torque opposing the rotational motion due to the DC machines mechanical system is given in eq. 3.

$$T = J\frac{d\omega}{dt} + B\omega + K_f\omega^2 \qquad (3)$$

where J is the inertia for the DC machine
B is the coefficient of viscous friction
K_f is the fan and windage coefficient

Since the efficiency of the variable speed drive is only being measured at steady state eq. 3 can be simplified to eq. 4

$$T = B\omega + K_f\omega^2 \quad (4)$$

The above torque opposes that of the induction motor and can be measured from the DC machine while performing no load tests. Therefore the total torque that the DC machine applies to the induction motor is given by eq. 5.

$$T = (B\omega + K_f\omega^2) + K\phi I_a \quad (5)$$

Since the required load torque is known (from the speed torque curve defined by the user), the required armature current can then be calculated from eq. 6

$$I_a = \frac{T_l - (B\omega + K_f\omega^2)}{K\phi} \quad (6)$$

The value of the term ($B\omega + K_f\omega^2$) can be measured at different speeds while running the machine at no load and steady state. T_l is the required load torque which is derived from the desired torque speed curve entered by the user.

3.2 PC controller

The PC used to control the test bed system has three main components. Namely

(A) RIDE 4.0 software
(B) PC32 Card
(C) PWM and tacho card

(A) RIDE 4.0 software

The users interface to the system is via RIDE 4.0 which is a visual Simulation/Real-time software package developed by Hypersignal® [1]. It allows a user to implement block diagrams which are then complied, downloaded and run on a DSP card (PC32 card). The desired load characteristic (speed torque curve) can be loaded into RIDE 4.0 which will passes the information onto the PC32 card.

(B) PC32 Card

The PC32 card is a standard DSP card manufactured by Innovative Integration. The PC32 card contains its own DSP processor (TMS320C32), which communicates with the PC via dual port RAM [2]. The Card contains 4 D/A converters of which one is used to control the speed of the VSD, and 4 A/D converters which are used to measure the current and voltage values in the system. The current controller to control the torque of the DC machine and to load the induction motor will be implemented in the software running on the DSP processor.

(C) PWM and tacho Card

A PWM/Tacho card has been developed to allow the PC32 card and Hypersignal to be used to directly control power electronic drives. The PWM/Tacho card connects directly to the memory expansion header on the PC32 card. This allows one to easily and efficiently implement different control methods for AC and DC drives with little or no extra hardware.

The Card contains a three phase PWM control IC (PBM 1/87) [3] which accepts Ua, Ub and frequency as its inputs and outputs six sets of pulses that can be used to trigger the devices in each of the legs in a three phase inverter. By using the trigger pulses from one of the three phase legs and setting the three phase frequency to zero a DC drive can be implemented (using a H Bridge).

The card also has a tacho controller IC (TC 3005H) [4] which can return the speed (in a register) from an incremental tacho. Extra resolution is gained by using an absolute incremental tachometer, these signals are then fed to analog to digital converters which enable positions to be measured in between quadrants of the tachometers.

3.3 Common DC Link

For the efficiency of the Variable speed drive to be calculated the power flowing in the system has to be known Fig. 6 shows the various currents flowing into or out of the DC link, these currents can be physically measured.

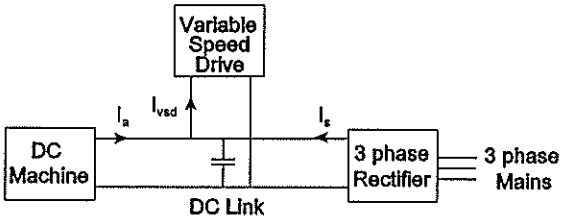

Fig. 6 DC link Representation

where I_a is the DC machine armature current
I_s is the supply current to the DC link
I_{vsd} is the current drawn by the VSD
V_{DC} is the DC link voltage

The current drawn by the VSD (I_{vsd}) can be calculated using eq. 7.

$$I_{vsd} = I_a + I_s \quad (7)$$

It can be seen that we only need to measure three parameters (I_a , I_s , V_{DC}) to calculate all the powers that flow or are lost in the system.

The total power lost in the system is given by eq. 8 and is equal to the power supplied to the system by the mains.

$$P_{tl} = I_s.V_{dc} \quad (8)$$

The power being drawn by the variable speed drive is given by eq.9

$$P_{vsd} = V_{DC} (I_s + I_a) \quad (9)$$

The power lost in the DC machine is known and is given by eq. 2. The power lost inside the induction motor and the variables speed drive can thus be calculated by using eq. 10

$$P_{vl} = P_{TL} - P_{dcL} \quad (10)$$

The efficiency of the variable speed drive can now be calculated using eq. 11.

$$efficiency = \frac{P_{vsd} - P_{vl}}{P_{vsd}} \quad (\%) \quad (11)$$

4.0 Conclusion

The system will prove useful in demonstrating the power savings that can be made if older methods of controlling air or liquid flow (restricting the flow) are replaced by varying the speed of the pump or fan which moves the air or liquid. The test bed system will be able to measure the energy saved under any load conditions imposed on Induction motors. The test bed system will enable the efficiency of loads that have a duty cycle to be evaluated. By disconnecting the DC machine from the DC link and by allowing the DC machine it is further possible to study the effects of Quality of Supply on either the DC or AC VSD. In this case either VSD can serve as the load whilst the other is subjected to Voltage Dips for example.

5.0 References

[1] Hypersignal® "Block Diagram/RIDE User's Manual" Hypersignal, 1996

[2] Innovative integration " PC32 Hardware Users Manual " Innovative Integration, 1995

[3] Hanning Electro-Werke " Pulse width Modulator PBM 1/87 . PBM 1/89 Data sheet " Revision 2.0, 1993

[4] Hanning Electro-Werke " Tacho-Controller TC 3005H Data sheet "Revision 1.1, 1994

A METHOD OF INCREASING ECCENTRICITY HARMONIC ACCURACY AS APPLIED TO SENSORLESS SPEED DETECTION OF AN INDUCTION MOTOR

PS Somaroo, B Burton, RG Harley

University of Natal, Durban

ABSTRACT

This paper reports on a method of increasing low frequency eccentricity harmonic accuracy by the use of a phase-locked-loop (PLL) based frequency multiplication to obtain greater resolution within a short time period. Results of a test machine are presented, which show that the technique is promising for the field of sensorless speed estimation of an induction motor.

1. INTRODUCTION

High accuracy and high precision in all fields of science and engineering will always be a topic of discussion. It has been so in times of the past and will be so in the future as well. This paper briefly describes a method of improving the accuracy of low frequency signals that may be used to determine the rotor speed of an induction motor, with the requirement that the improvement be done within a small amount of time as possible.

The technique chosen stems from studies into stator current harmonics by Hurst [1,2], who investigated the harmonics present in the current due to induction motor slots (for an open rotor slot induction motor) and airgap eccentricities.

This paper briefly introduces Hurst's work and proposes a technique using PLL based frequency multiplication scheme in order to improve on his method.

2. ROTOR SPEED ESTIMATION USING CURRENT HARMONICS

In the current harmonic speed measurement (CHSM) scheme, two types of harmonics get reflected onto the stator currents. One type is in the low frequency range of the spectrum, typically centered around supply frequency f_1 (50Hz) and is called rotor eccentricity harmonics or just eccentricity harmonics. The other type is in a higher frequency range, of the order R/P of f_1 spaced $2f_1$ apart and is called saliency harmonics, where R,P is the number of rotor slots and number of pole pairs respectively. For this paper R=36 slots, P=2 pole pairs and f_1=50 Hz.

Saliency harmonics are caused by the rotor slots generating harmonics through the airgap flux into the stator currents as the rotor moves past the stator. This paper will not discuss these harmonics any further.

Hurst's work investigates the use of saliency harmonics for speed estimation in detail, showing how these can be used to obtain an accurate speed estimation after every 8 cycles of mains frequency. The downfall of using saliency harmonics for speed estimation is that too many unknown harmonics are nearby the required saliency harmonics, an initial speed estimate is needed in order to obtain a window of investigation for the saliency harmonics, the saliency harmonics are motor dependent because the number of rotor slots are needed as well as the requirement that the rotor slots be opened, and these saliency harmonics are barely distinguishable above the noise band when the machine is unloaded. Thus a closer look at eccentricity harmonics was undertaken.

The eccentricity harmonics are caused by stator core ovality, bearing wear, shaft misalignment and rotor bar resistance variations. These imperfections result in airgap flux eccentricities which end up as harmonics that get reflected into the stator currents. This is an improvement over saliency harmonics because rotor slots are not required and neither the need for open rotor slots is necessary.

The eccentricity harmonics occur at the following frequencies

$$f_{eh} = f_1\left[n_d\left(\frac{1-s}{P}\right)+1\right] \qquad (1)$$

where

f_{eh} = eccentricity harmonic in Hz
f_1 = stator frequency in Hz
n_d = integer values, order of eccentricity and usually the first order is most prominent
s = slip in p.u.
P = number of pole pairs.

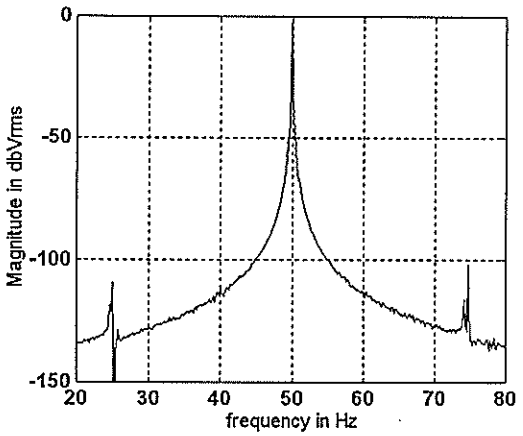

Figure 1: Graph showing Eccentricity Harmonics

Figure 1 shows an example of eccentricity harmonics of an induction motor at approximately 25 Hz and 75 Hz, with supply frequency at 50 Hz.

Usually one finds that the first order of harmonics is most prominent, and it corresponds to n_d=±1. This results in a simplified formula for f_{eh} with becomes

$$f_{eh} = f_1\left[1 \pm \left(\frac{1-s}{P}\right)\right]. \qquad (2)$$

In a 2 pole machine, for low slips (s near zero) one expects harmonics close to f_1± ½ f_1. While for slips near one these harmonics approach f_1.

Problems are evident if high accuracy estimates and short periods of estimation of the eccentricity harmonics are needed. The low frequencies of eccentricity harmonics present problems at low supply frequencies. Many periods of data have to be captured to obtain the desired accuracy or resolution and this may take many seconds before the desired number of periods is obtained.

3. FREQUENCY MULTIPLICATION TECHNIQUE TO IMPROVE RESOLUTION

To achieve better resolution in the frequency domain, a long sampling time is required. Unfortunately, when using frequency analysis to determine the speed of an induction motor, this long time period is unacceptable, especially if the frequencies are close to DC. This may result in sampling periods of the order of seconds.

However, by using frequency multiplication techniques the desired resolution may be achieved or improved within a short period of time. For example, if detection of 0.1Hz change in frequency is desired, or putting it another way, a resolution of 0.1Hz in frequency is desired, using normal sampling techniques and standard FFT analysis would require at least 10 seconds of sampling time. This means that the induction motor could have changed its speed significantly before the speed is obtained.
If the signal is now multiplied 10 times in frequency, the 0.1 Hz detection becomes a 1 Hz detection which results in one second of capture to obtain the 1 Hz resolution and effectively still be able to achieve an accuracy of 0.1 Hz without multiplication. For example, a 0.1 Hz change in a signal at 25 Hz means an error of 0.4%. If this signal is multiplied in frequency 10 times it would result in a 250 Hz signal and a 1 Hz change in 250 Hz would also mean and error of 0.4%.

Thus in order to reduce the sampling period, frequency multiplication techniques can be used. This may be summarised as follows : if a speed-up in the sampling period by a factor N is required, while keeping the same accuracy, then the signal under investigation must be multiplied in frequency by a factor of N and the sampling period will be reduced to 1/N times the original sampling period.

4. PLL BASED FREQUENCY MULTIPLICATION

The Phase-Locked-Loop (PLL) based frequency multiplication technique involves the use of a classic frequency synthesis algorithm to obtain the desired frequency multiplication discussed in the previous section. The detailed operation of a PLL is beyond the scope of this paper but a good tutorial on PLL design appears in references [3,4].

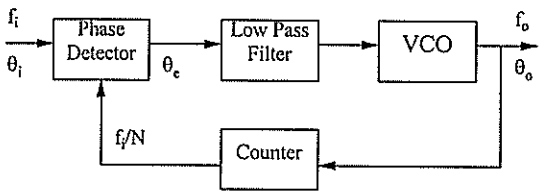

Figure 2: Phase Locked Loop block diagram

A block diagram showing the technique is given in Fig. 2, where the input frequency is f_i, output frequency is f_o, θ_e is the phase error, θ_i is the input phase and θ_o is the output phase.

If N is set in the programmable counter to 16, then the output frequency will be 16 times the input frequency. Clearly this scheme will work for frequency multiplication of the input signal.

5. FREQUENCY MULTIPLICATION OF ECCENTRICITY HARMONICS

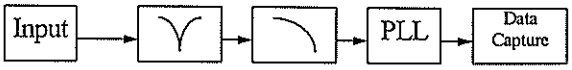

Figure 3: System block diagram

Looking at the eccentricity harmonics at about 25 and 75 Hz in Fig. 1, the 50Hz mains signal must be filtered off and can be done by the use of a notch filter. Thereafter a low pass filter is used to filter off the lower eccentricity harmonic at approximately 25Hz, because PLL's are able to track primarily only one frequency. The filtered signal then needs to be passed on to a PLL with a divide by N counter in the feedback to obtain N times the input frequency at its output. The resulting waveform then simply needs to be processed by the data capturing equipment and analysed using standard FFT techniques.

Depending on the divide by N counter and the chosen value of N, the sampling period will be reduced by 1/N according to the previous sections, but still have the desired resolution.

6. SOME RESULTS

Fig. 4 shows results of a 4 pole, 36 rotor slot machine running with no load and supply at 220V, 50 Hz . The multiplication factor used was N=16.

Fig. 4(a) is the input signal from the filtered stator current to the PLL. A 25.29 Hz signal can be seen with a significant amount of noise. Distortion of this signal is due to the 50 Hz mains still present.

The PLL output is shown and a signal of 404.6 Hz which about 16 times the input signal. The PLL was able to track the 25 Hz signal without problems of the 50 Hz supply.

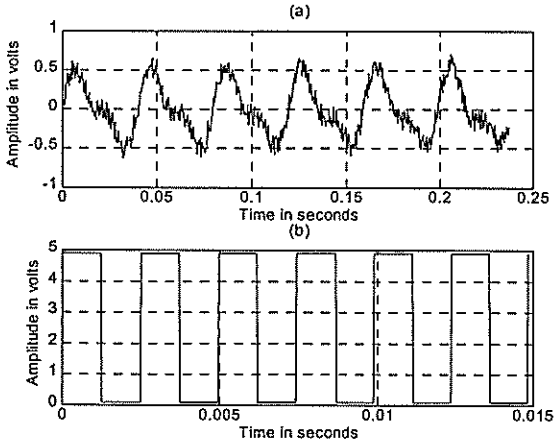

Figure 4: Sample results. (a) 25.29 Hz input signal (b) 404.64 Hz output of PLL

The actual slip measured using a tachometer placed on the rotor shaft measured a slip of 0.007 which corresponds to a lower eccentricity harmonic for this machine of 25.18 Hz. The PLL output produced a signal with frequency of 404.64 Hz. Now 404.64 Hz divided by 16 yields a frequency of 25.29 Hz, which is then the measured eccentricity harmonic. Using eq. (2), this corresponds to an actual slip of 0.0116, thus yielding an error of 0.4%.

7. CONCLUSION

A brief look at the eccentricity harmonics was presented to show their nature. These harmonics are used to determine the rotor speed but they have a very low bandwidth. A method was presented which uses a PLL frequency multiplication technique in order to improve the low frequency eccentricity harmonics bandwidth in a small sampling time and early results are promising.

8. REFERENCES

[1] Hurst KD, Habetler TG, Griva G, Profumo F, "Speed Sensorless Control of Induction Machines Using Current Harmonic Spectral Estimation", *Conference Record of the IEEE IAS Annual Meeting*, 1994, pp. 601-607.

[2] Hurst KD, Habetler TG, "Sensorless Speed Measurement Using Current Harmonic Spectral Estimation", *Proceedings of the Power Electronics Specialists Conference PESC '94*, 1994, pp. 10-15.

[3] Nash G, "Phase-Locked Loop Design Fundamentals", *Communications Device Data book, Rev 4.*, Motorola Application note AN535, 1996.

9. ADDRESS OF AUTHORS

Mr. PS Somaroo, Mr. B Burton, Prof. RG Harley, Department of Electrical Engineering, University of Natal, King George V Avenue, Durban 4001
Tel: (031) 260-2725, Fax: (031) 260-1300, E-mail:
somaroo@eng.und.ac.za
bburto@eng.und.ac.za
harley@eng.und.ac.za

PRACTICAL IMPLEMENTATION OF A PAPER REWINDER

B D Van Blerk and G Diana

Department of Electrical Engineering, University of Natal
P. Bag X10, Dalbridge, 4041, South Africa
GDIANA@ENG.UND.AC.ZA

ABSTRACT

This paper presents the practical results of a paper rewinder test-bed system developed to demonstrate and train people in the principles of tension control. The practical results are compared to simulation results generated from the system model [1].

1. INTRODUCTION

In the local steel and paper industries it is important to maintain correct tension in the material to ensure high and consistent product quality and output. Most tension control systems are imported and there is little understanding of the principles involved. The paper rewinder system was chosen as the test-bed demonstration system as it is relatively inexpensive to implement. The controller for the demonstration system was required to be easy to configure and had to provide for the visualisation of results.

To size the components of the practical system, a simulation model of the rewinder system was developed from first principles and the results used to size the components of the practical system [1]. The practical system was subsequently designed and constructed and the results from tests conducted are compared with results from the simulation model.

2. REWINDER SIMULATION MODEL

Fig. 1 shows the SIMULINK simulation system model developed for the rewinder system [1] which was used to generate the simulation results with which the practical results will be compared.

In Fig. 1 the rewinder system is divided into four models, namely the paper, winder reel, unwinder reel and master controller models. The winder and unwinder reel models are identical and only differ by the different inertia's depending on the amount of paper on the relevant reel. The paper is modelled as an undamped spring and yields the paper tension as a function of the difference in the angular velocities of the winder and unwinder reels.

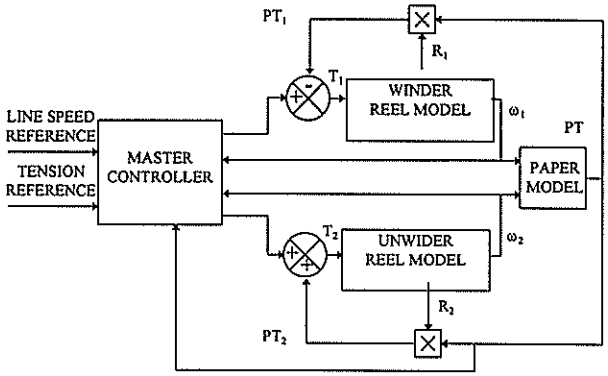

Fig. 1 Rewinder Simulation System Model

The master controller depicted in Fig. 2 comprises an inertially compensated speed PI controller for the winder and unwinder and a paper tension PI controller whose output is fed into the line speed references for the reel as what is termed a "line speed differential". This rewinder system model was used to generate the simulation results presented in this paper.

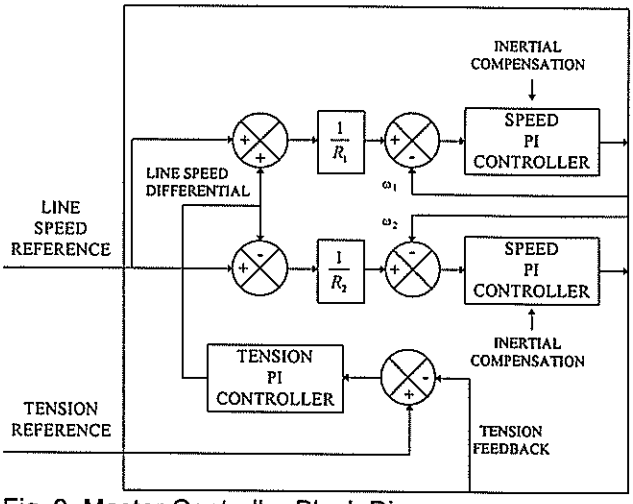

Fig. 2 Master Controller Block Diagram

3. WINDER MODEL TEST

In modelling the rewinder it was assumed that the three phase induction motors used to drive the paper reels operated under ideal FOC. Under this assumption a linear model of the controller, inverter and electrical dynamics of the Squirrel

Cage Induction Machine applied [2]. To justify this assumption the simulated and actual responses of the motor when connected to a reel containing no paper is presented.

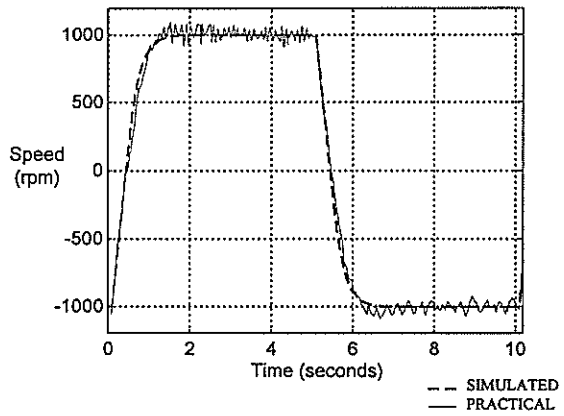

Fig. 3 Speed Response of Winder

Fig. 3 shows the practical and simulated responses to a square wave speed reference of ± 1000 rpm. The responses correspond very closely to one another, thereby justifying the use of the linear model.

4. Triangular Tension Test

To verify the tension controller operates correctly, a triangular tension reference is applied to the system with the line speed reference held at zero and the results appear in Fig. 4.

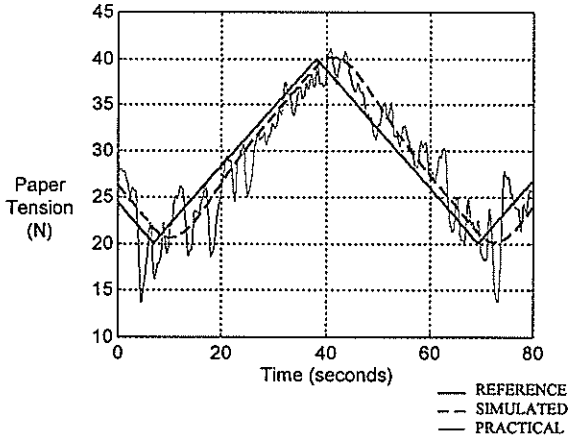

Fig. 4 Tension Response to Triangular Reference at Zero Speed

As Fig. 4 shows the tension response is as predicted by the simulations. The oscillations on the practical result are due to the poor dynamic response of the loadcells and loadcell amplifiers used. These loadcells and amplifiers are being replaced with loadcells with better dynamic performance.

5. Acceleration Ramp Test

With both the tension and speed controllers responding as predicted, a further test was performed to verify whether tension could be maintained under a typical wind/rewind run at the desired line speed. A final requirement of the rewinder was to accelerate the paper to 1000 m/mim in 30 seconds, however it was found that due to vibration it was not advisable to run the practical system above 333 m/min. As such the system was accelerated to 333 m/min in 20 seconds. The tension was ramped to the desired value of 30 N in 5 seconds before accelerating the paper reel. The practical and simulated tension responses are shown in Fig. 5 and the practical and simulated speed responses and the line speed reference are shown in Fig. 6.

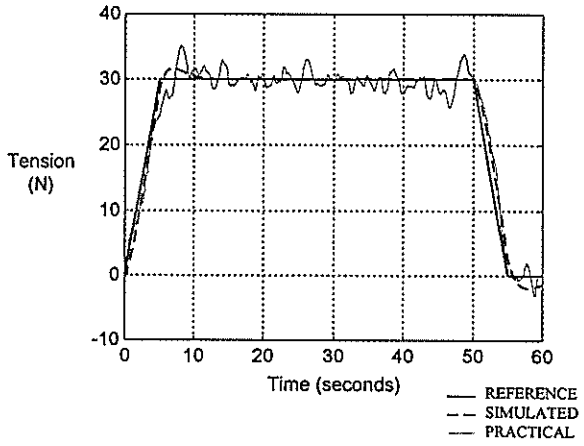

Fig. 5 Tension Response During Line Speed Acceleration and Deceleration

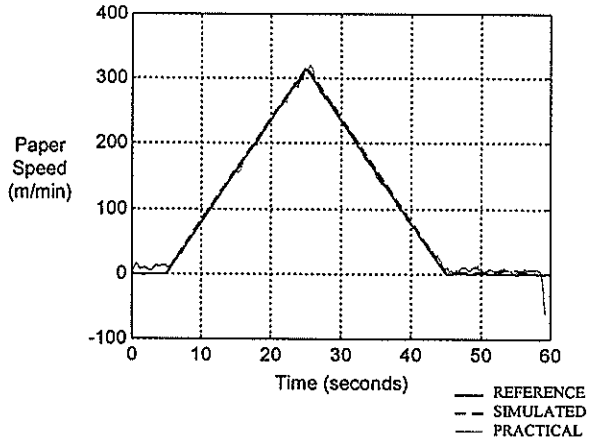

Fig. 6 Line Speed Tracking Under Line Speed Acceleration and Deceleration.

As seen from the two figures above, the practical and simulated results correspond very closely, thus validating the simulation model of the rewinder. In order to perform the inertial compensation on the speed PI controllers, it is

necessary to estimate the reel radius. The method used to estimate the reel radius in the practical controller is the same as that used to determine the reel radius in the simulations. As an accurate reel radius estimation is critical to perform the inertial compensation on the speed PI controllers the practical and simulated results are shown in Fig. 7.

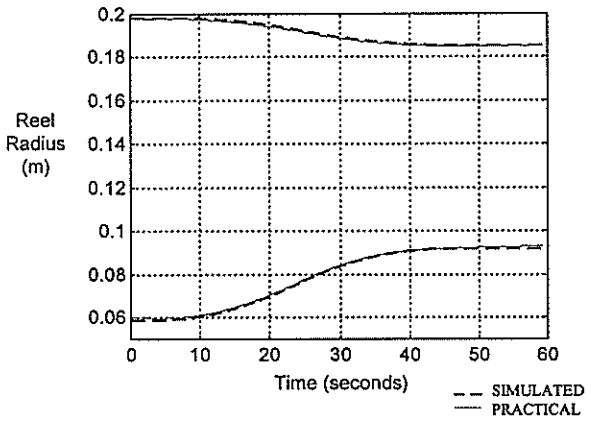

Fig. 7 Reel Radius Estimation Under Line Speed Acceleration and Deceleration

The measured reel radii at the end of the test differed from the estimated reel radii by one millimetre. This is however within the measurement tolerance of one millimetre of the reel radius measurement method employed. The reel radius estimation was thus found to be very accurate and thus the good correlation between simulation and practical results.

6. HYPERSIGNAL REAL TIME INTEGRATED DESIGN ENVIRONMENT

To create the training capacity for the rewinder system the ease of controller implementation and the graphical visualisation of results was required. This requirement was fulfilled by the Hypersignal Real Time Integrated Design Environment (RIDE) package. This package allowed the graphical configuration of the master controller on the PC screen and compiled and ran the master controller at the click of the PC mouse. Data capture from the controller platform is performed by this package and the results may be plotted to the screen or saved as the test is conducted.

7. CONCLUSION

Practical results were presented in this paper of a paper rewinder demonstration rig and compared with simulation results generated from the rewinder system simulation model. The practical and simulation results were found to correspond to one another thus verifying the simulation models of the components of the rewinder system. Finally a discussion of the package used to provide the ease of master controller configuration and the visualisation of results for training purposes is presented. Thanks is expressed to ESKOM and the FRD for their support of this project

8. REFERENCES

[1] Van Blerk BD, Diana G, "DEVELOPMENT OF A GENERIC TENSION CONTROL SYSTEM", Proceedings of the Sixth Southern African Power Engineering Conference SAUPEC, pp. 105-108, Johannesburg, South Africa, January 1996

[2] Diana G, Harley RG, "An aid for teaching Field Orientated Control applied to Induction Machines", IEEE Trans. On Power Systems, Vol. 4, No. 3, Aug., 1989, pp 1258-1262

AN IMPROVED CONTROLLER FOR AN IGBT INVERTER FORMING PART OF A VOLTAGE DIP TEST BED

AK Keus JM van Coller RG Koch*

University of the Witwatersrand,
Tel (011) 716-5440 Fax: (011) 403-1929
Private Bag 3, Wits 2050, South Africa

*ESKOM Technology Group,
Tel: (011) 629-5720 Fax: (011) 629-5540
Private Bag 40175, Cleveland 2022, South Africa

The voltage dip test bed was developed to evaluate the performance of industrial equipment under voltage dip conditions. Initially a simple controller, to control the waveform presented by the IGBT inverter to the load, was built to verify the functioning of the test bed and to perform some tests on equipment. This controller was used for some basic tests but the controller was found unsuitable for further tests as the output regulation and transient response were poor. This paper describes the development of an improved controller for the inverter which achieves good steady-state and transient regulation.

Keywords: DC-AC conversion, voltage dips, PWM inverters

1 INTRODUCTION

The layout of the voltage dip test bed has been described in [1] and [2] but a short overview will be presented here. The layout of the voltage dip test bed is shown in Figure 1. The PC is used to synthesise the voltage dip waveform. The programmable supply amplifies the control waveform from the PC to provide a 3-phase power supply to the equipment to be tested. The programmable supply will be discussed in more detail at a later stage.

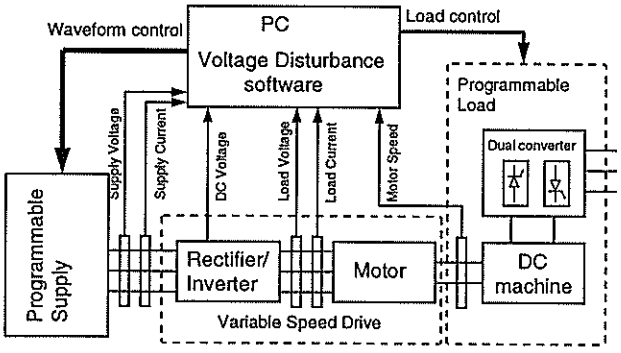

Figure 1: Block diagram of the voltage dip test bed when testing a VSD

During the applied voltage dip the PC is used to measure equipment parameters such as input and output voltage, input and output current, DC bus voltage and speed. If the equipment to be tested is a motor or variable speed drive, the programmable load emulates normal loading.

2 PROGRAMMABLE SUPPLY COMPONENTS

The programmable supply is basically a modified IGBT inverter that is supplied from a DC source such as a rectifier. The circuit diagram for one phase is shown in Figure 2. At present the DC source is a 3 phase, 380V variac connected to a 3-phase rectifier so that the DC voltage can be adjusted from 0 to approximately $540V_{DC}$. Connected to the DC bus are three separate IGBT H-bridges, one for each phase so that each phase can be independently controlled. The output of each IGBT H-bridge is passed through a low-pass L-C filter and the filter output is connected to one winding of the primary of a 3 phase, 5 limb output transformer. The transformer secondary is then used to supply the equipment under test. Ideally, the three-phase power waveform output by the programmable supply would be a scaled version of the input control waveform from the computer. Before the control of the programmable supply is discussed, the modelling of the programmable supply, types of programmable supply waveform and the programmable supply loading will be discussed.

2.1 MODELLING THE PROGRAMMABLE SUPPLY

From the circuit diagram in Figure 2, the model of the system can be developed as is shown in Figure 3. The output transformer is modelled as part of the load.

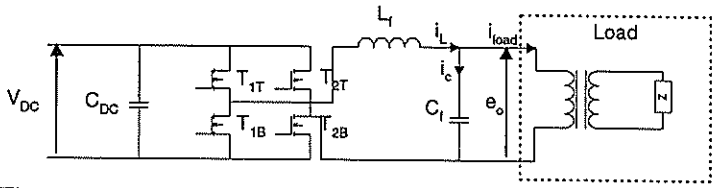

Figure 2: Circuit diagram of one phase of the programmable supply

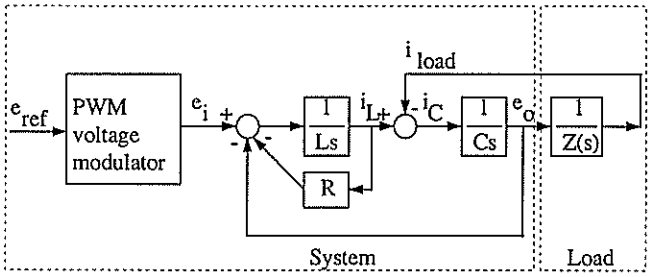

Figure 3: Model of the system with a voltage modulator

Programmable supply ratings

IGBT current rating	200A (maximum continuous)
IGBT voltage rating	1200V (maximum)
Output filter inductance, L	2.2 mH
Output filter capacitance, C	100 uF
Nominal DC bus voltage	540V
Transformer input phase voltage	$220V_{rms}$
Transformer output phase voltage	$220V_{rms}$
Transformer rated current	$380A_{rms}$

2.2 PROGRAMMABLE SUPPLY CONTROL WAVEFORMS

Under normal operating conditions the voltage dip control software generates a 3-phase, 220V, 50 Hz power waveform reference. During the voltage dip a change in amplitude and/or phase could occur. Depending on the type of voltage dip to be generated, the control signal could be regarded as a step change in voltage multiplied by the sinusoidal reference and/or a change in phase. The actual voltage dip waveform depends on the waveform the user has specified.

2.3 EQUIPMENT TO BE TESTED BY THE VOLTAGE DIP TEST BED

The voltage dip test bed was designed to test many diverse types of equipment and so the loading on the programmable supply will depend on the equipment to be tested. The currents drawn from the programmable supply will differ according to the load: for example a contactor will draw a lagging sinusoidal current whereas a diode bridge and capacitor load (such as the input stage of a VSD) will draw a highly non-linear current with large current peaks.

3 CONTROL OF THE PROGRAMMABLE SUPPLY

From the system model, it can be seen that with only a simple voltage loop the controller will exhibit poor control because the 180-degree phase lag caused by the output filter limits the controller. Ryan et al [3] discusses control strategies of single-phase inverters with inner current loops. If an inner current loop is used, this is advantageous since output currents may rapidly be controlled in response to load current before a significant change in output voltage occurs [4]. If the current loop is modelled as ideal, the closed loop model becomes a gain stage with zero phase shift incorporating the inductor. Two types of current loop can be implemented, a capacitor current loop and an inductor current loop:

3.1 CAPACITOR CURRENT LOOP

If a capacitor current loop is implemented, the load current disturbance is included inside the current loop. The outer voltage loop directly controls the capacitor current and the output voltage can be found from

$$i_c = C\frac{de_o}{dt} \quad \text{.....(3.1)}$$

$$\therefore \frac{de_o}{dt} = \frac{i_c}{C} \quad \text{.....(3.2)}$$

A drawback with this method is that there is no direct control over the IGBT currents. The IGBT currents must be monitored to ensure that device current ratings are not exceeded.

3.2 INDUCTOR CURRENT LOOP

An advantage of the inductor current loop is that the IGBT currents are controlled directly and thus current limiting can be implemented by limiting the reference signal to a suitable value. If an inductor current loop is implemented, however, the load current disturbance is moved outside the current loop, which means that the loading will need to be investigated.

3.3 INDUCTOR CURRENT LOOP WITH LOAD CURRENT DECOUPLING

If the load current is measured then the load current can be decoupled by summing it into the inductor current reference, see Figure 4. This allows the load current to be compensated for before a change in output voltage occurs. If the load current is completely decoupled then the capacitor current is controlled directly so that the output voltage again becomes

$$\frac{de_o}{dt} = \frac{i_c}{C} \quad \text{.....(3.2)}$$

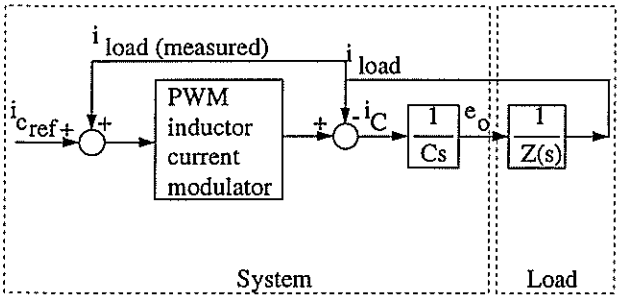

Figure 4: System with inductor current loop and load current decoupling

4 CURRENT CONTROL PWM IMPLEMENTATION

To implement a current control loop, different control strategies are possible, including triangle modulation, peak current control, hysteresis current control etc. Hysteresis current control allows the current reference to be accurately followed and offers unsurpassed transient response in comparison with other digital and analogue techniques exhibiting high accuracy, wide bandwidth and robustness [5]. A drawback with ordinary hysteresis control is that the switching frequency is not constant, although several papers [5-6] have been written describing methods to achieve constant frequency hysteresis control. Much of the literature concentrates on the problem of three phase inverters where altering the switches in one phase leg causes the current in the other two phases to vary. For this inverter, because a separate H-bridge is used for each phase this problem is not encountered and each phase of the inverter can be regarded as a separate single phase inverter.

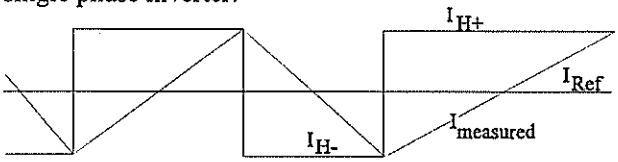

Figure 5: Diagram illustrating hysteresis current control

The controller implemented uses standard hysteresis control, with the IGBTs switching the output voltage from the bridge between -VDC and VDC. From Figure 5 it can be seen that the rate of change of current and the amount of hysteresis determine the switching frequency. We also know that

$$V = L\frac{dI}{dt} \text{ and } \therefore \frac{dI}{dt} = \frac{V}{L}$$

Thus the rate of change of current is dependent on the inductance and the voltage across the inductor which is dependent on the DC bus voltage, the output voltage, the voltage drop across the IGBTs and the IR volt drop across the inductor resistance. The rate of change of current will be different for the increasing and decreasing current intervals except for a specific interval. For this controller, the DC bus voltage was made much larger than the output peak voltage so that when the output voltage is a maximum, the current is still able to follow high bandwidth input current references. The present controller switching frequency varies from approximately 4 KHz at the output voltage zero crossing to 3 KHz at the output voltage peak. This was thought to be acceptable although constant frequency hysteresis will be investigated. At a later stage the DC bus voltage will be increased allowing a larger rate of change of current and the hysteresis level will be adjusted for a higher switching frequency.

5 VOLTAGE CONTROL LOOP

Once the current controller has been designed, the voltage loop is designed around the current loop and the output capacitor. For control design purposes the current loop is treated as a simple gain stage, which is valid if the bandwidth of the voltage controller is much less than that of the current controller. The voltage controller must be designed to achieve good 50Hz regulation (implying high open loop gain at 50Hz) but should have attenuation at the switching frequency so that switching frequency noise is not present in the output voltage waveform and so the system is stable. The phase margin of the voltage loop controller will determine the overshoot of the system to a step input such as when the controller is turned on or during a voltage dip. The present system with the implemented controller has approximately 40dB of gain at 50 Hz, -10 dB of gain at the switching frequency and a phase margin of approximately 60 degrees. Figure 6 shows the Bode plot of the complete open loop system with the implemented controller. When the bandwidth of the current loop is increased the present controller will be further improved.

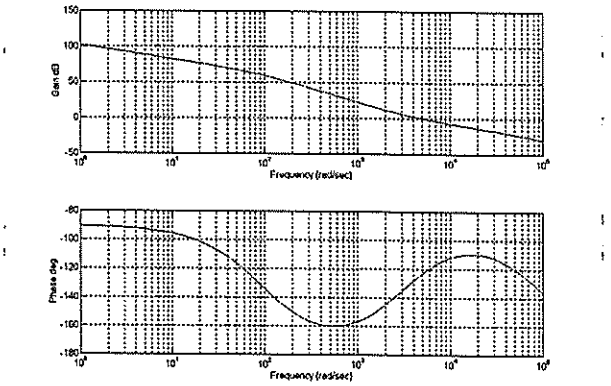

Figure 6: Bode plot of the controlled open loop system
(a) Magnitude
(b) Phase

6 PRACTICAL RESULTS

To illustrate the functioning of the programmable supply with the improved controller, three different tests were undertaken. In the first test a severe voltage dip control signal was applied—Figure 7 shows the input control signal and the output waveform of the programmable supply. Figure 8 shows the programmable supply output voltage and current waveform when a step change in resistive loading is applied. Figure 9 shows the programmable supply output voltage and current waveforms with a variable speed drive as the load. This is a three-phase variable speed drive which consists of a full wave rectifier driving a capacitor bank directly as the input stage, hence the current waveform.

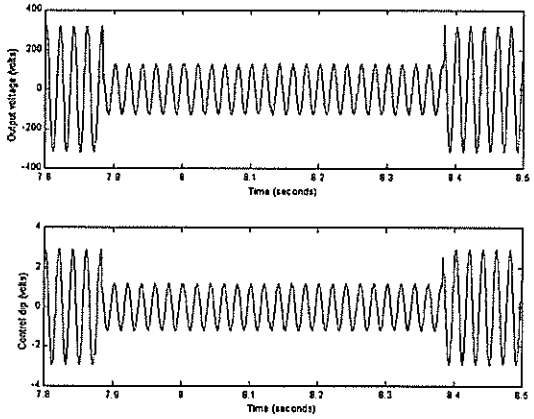

Figure 7: Measured dip waveform:
(a) Programmable supply output voltage waveform
(b) Programmable supply control voltage waveform

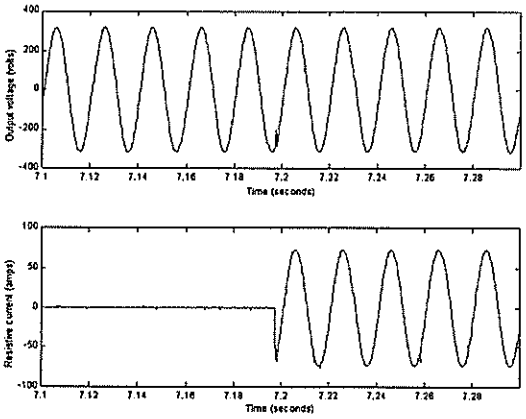

Figure 8: Measured step load response:
(a) Programmable supply output voltage waveform
(b) Resistive load current waveform

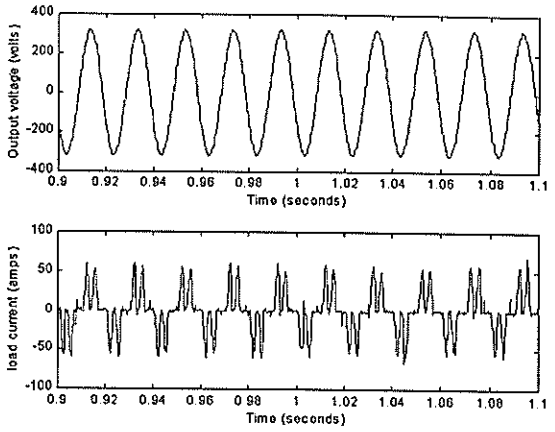

Figure 9: 3 phase VSD (diode bridge/ capacitor) load
(a) Programmable supply output voltage waveform
(b) VSD current waveform

7 CONCLUSIONS

For successful operation of the voltage dip test bed a controller able to control the programmable supply adequately for a wide variety of linear and non-linear loads was required. The controller developed exhibits good transient and steady state performance while maintaining a good quality output sinewave waveform.

8 REFERENCES

[1] R.G. Koch, J Van Coller and A Keus, "The quantification of equipment and plant sensitivity to voltage dips (sags)," Conference paper, PQA '97, Columbus Ohio, March 1997.

[2] A Keus, J Van Coller and R Koch, "Development of a test facility to generate complex voltage dips," Conference paper, FSAPQC, Durban 1997.

[3] M.J. Ryan, W.E. Brumsickle and R.D. Lorenz, "Control topology options for single-phase inverters," IEEE Trans. Ind. Applicat., vol. 33, pp. 493-501, March/April 1997.

[4] O Wasynczuk et al, " A voltage control strategy for current-regulated PWM inverters," IEEE Trans. Ind. Applicat., vol.11, pp.7-15, January 1996.

[5] L. Malesani, P. Mattavelli and P. Tomasin, "Improved constant frequency current control of VSI inverters with simple feedforward bandwidth predication," IEEE Trans. Ind. Applicat., vol. 33, pp. 1194-1202, September/October 1997.

[6] L. Malesani and P Tenti, "A novel hysteresis control method for current-controlled voltage source PWM inverters with constant modulation frequency," IEEE Trans. Ind. Applicat., vol.26, pp.88-92, January/February 1990.

An Active Turn-off Snubber for IGBT Converters

H du T Mouton and JHR Enslin

Department of Electrical and Electronic Engineering, University of Stellenbosch, Stellenbsoch, 7600

This paper presents a resonant active turn-off snubber for high power IGBT converters. The main feature of this snubber is that the peak current rating of the auxiliary switching devices is small compared to that of the main switches. Comparing the costs of the snubber elements, to the benefits of the snubber makes it an extremely attractive option for reducing switching losses and EMI in high power converters. The snubber components can be combined into a single module which can be fitted to an existing converter without any modifications to the control method or basic structure of the converter.

The basic operation of the snubber is described. An experimental version of the snubber is evaluated on an 80kVA phase-arm which resulted in a 40% reduction of the total switching losses.

Keywords: Resonant snubber, IGBT Converter, EMI, switching losses.

1 Introduction

Snubber circuits and soft switching techniques are applied to power electronic switches to reduce switching losses, limit EMI by reducing $\frac{di}{dt}$ and $\frac{dv}{dt}$, and to reduce the total power losses of converters. By reducing switching losses higher switching frequencies can be obtained which result in higher bandwidth and improved dynamics. A number of soft-switching topologies can be applied to IGBT based converters. However, most of these topologies introduce special control requirements or high peak voltage or current ratings on the switching components.

The auxiliary resonant commutated pole converter (ARCP) (see [1] - [5]) is particularly suited to high power converters. It acts as both a turn-on and turn-off snubber and effectively reduces switching losses as well as EMI (see [5]). Unlike the resonant DC link converter [6] it does not require any special control algorithms. One problem with the ARCP is the selection of the auxiliary switches at high power levels. Even though the RMS rating of these switches is relatively small, the peak current capability is between 1.2 and 1.8 times the maximum load current. Thyristors are an obvious choice for the auxiliary switches, but ultra-fast thyristors at high power ratings are not readily available. The reverse recovery of thyristors also cause practical problems in the implementation of the ARCP. IGBTs are another possibility. However, using IGBTs at currents above their peak rating may result in the device entering its linear region of operation which may result in thermal destruction of the device. As a result of this problem, using IGBTs as the auxiliary switches will require a power rating comparable to that of the main switches.

This paper introduces an active resonant turn-off snubber for which the peak power rating of the auxiliary switches is significantly smaller than that of the main switches. The peak current rating of the auxiliary switches is typically 10% to 20% that of the main switches, which leads to a compact and inexpensive design. Even though the snubber does not provide the full benefit of a combined turn-on and turn-off snubber the benefits of the snubber is significant compared to the cost of the snubber components.

2 Snubber operation

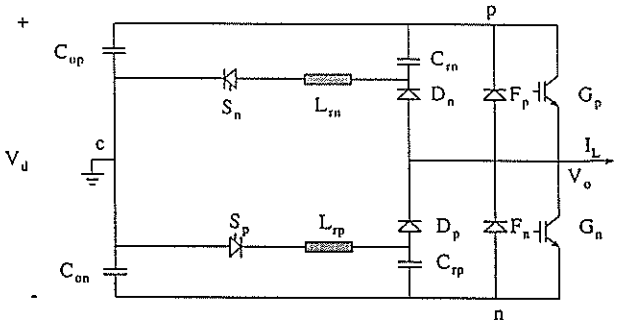

Figure 1: An IGBT phase arm with the resonant turn-off snubber.

The arrangement of a phase leg is shown in figure 1. The resonant turn-off snubber is formed by auxiliary switches S_n and S_p, together with diodes

D_n and D_p, capacitors C_{rn} and C_{rp} and inductors L_{rn} and L_{rp}. The values of C_{rn} and C_{rp} are equal and will be referred to as C_r. C_{op} and C_{on} are the regular DC-bus capacitors. Similarly L_{rp} and L_{rn} are equal and will be referred to as L_r. Point c is the center-tap of the DC-filter capacitor. In its simplest form the auxiliary switches may be thyristors, but IGBTs, MOSFETs and GTOs may also be used. The devices require a reverse blocking capability which can be achieved through the use of series diodes. The auxiliary devices are only required to carry current for a very short period of the total cycle.

To explain the operation of the snubber consider commutation of the load terminal from the negative rail to the positive rail under positive load current. For the moment ideal switching of all the switching elements is assumed. Diode F_n is conducting the load current when G_p is turned on. Simultaneously auxiliary switch S_p is switched on and capacitor C_{rp} is charged through resonance with L_{rp}. The voltage over $V_{C_{rp}}$ is given by

$$V_{C_{rp}} = \frac{V_d}{2}\cos(\omega_o t),$$

where $\omega_0 = \frac{1}{\sqrt{L_r C_r}}$. The current $I_{L_{rp}}$ through the resonant inductor L_{rp} is given by

$$I_{L_{rp}} = \frac{V_d}{2}\sqrt{\frac{C_r}{L_r}}\sin(\omega_0 t).$$

At time $t = \frac{\omega_0}{\pi}$ the voltage across capacitor C_{rp} is equal to V_d and I_{Lr} reaches zero. The resonant components must be chosen in such a way that this time is shorter than the minimum conduction period of G_p. It is important to note that auxiliary switch S_p turn on and off at zero current, thereby significantly reducing switching losses in the auxiliary switches.

When G_p is switched off diode D_p starts conducting and takes over the load current from G_p. The output voltage of the phase arm decreases in a linear manner and reaches the negative rail after a time period of

$$t_{\text{off}} = \frac{C_r V_d}{I_L}.$$

Due to the symmetric topology the operation of the snubber during periods of negative load current is similar to that described above. In this case auxiliary switch S_n is used.

The main advantage of this topology is that the peak current through the auxiliary switches is small compared to the peak current rating of the main switches. The peak current through auxiliary switch S_p is $\sqrt{\frac{C_r}{L_r}}\frac{V_d}{2}$. Typically the peak current rating of these switches is 10% to 20% of the

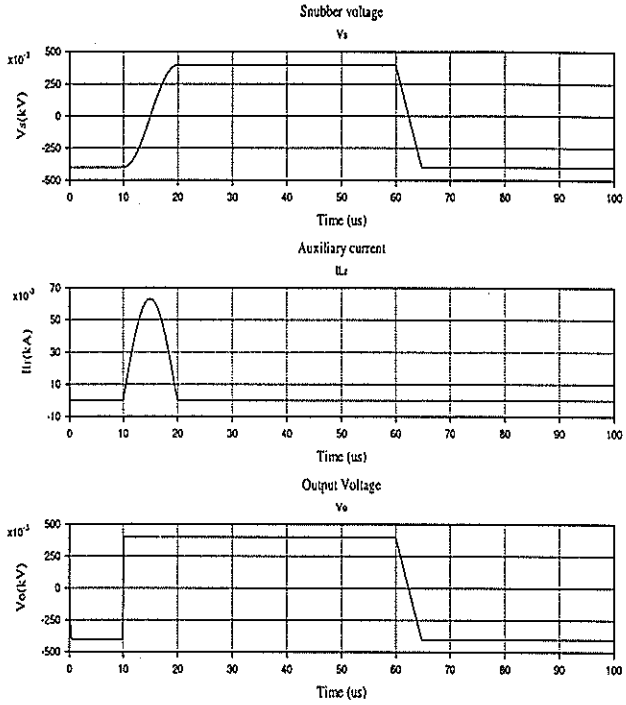

Figure 2: EMTDC simulations of the turn-off snubber circuit.

peak rating of the main switches. Even though the auxiliary diodes C_{rp} and C_{rn} have to carry the full load current, they function at a low duty cycle. The peak current rating of diodes are usually significantly higher that their RMS rating. The relatively small size of the snubber components makes it feasible to combine the snubber components into a single module. This module can be added to an existing hard-switched converter to reduce switching losses and EMI.

Under small load current capacitor C_{rp} discharges slower than under maximum load current. If G_n is switched on before C_{rp} is fully discharged additional switching losses in G_n will arise. This is a problem common to all turn-off snubbers. One way to solve this problem is not to activate the snubber when the size of the load current falls below a certain threshold.

Figure 2 is an EMTDC simulation of the circuit in figure 1. The bus voltage V_d is 800 V, $L_r = 20\mu$H, $C_r = 500$nF and the load current is 100A. The output voltage, snubber voltage and current through the resonant inductor are shown. The simulations show exact agreement with the theoretical predictions.

3 Experimental verification

An experimental version of the snubber was constructed at an 80kVA level using a main phase-arm IGBT module with ratings of 200A, 1200V. The

ratings of the auxiliary switches is 50A, 600V. Capacitors C_{rp} and C_{rn} is 500 nF and L_{rp} and L_{rn} is 4μH. The bus voltage Vd is 400V, the load consists of an inductor of 350μH. The output voltage is a square wave at 1.5kHz with a load current is 100A.

Figure 3 shows the output turn-off waveform of the IGBT module with the snubber. The total turn-off time is 2μs. Without the snubber the typical turn-off time of the module is about 300ns. The small dent in the voltage at -1.5μs is a result of the snubber capacitor taking over the current from the main module.

Figure 4 shows the voltage over C_{rp} during one switching cycle. Note the sinusoidal charging waveform and the linear discharge waveform. As a result of the voltage undershoot during-main module turn-off the snubber capacitor discharges to approximately -25V. This is beneficial during the charge cycle of the snubber capacitor as it in effect compensates for conduction losses in the snubber components. Because of this undershoot the snubber capacitors charges to rail voltages.

The reduction in switching losses was calculated by measuring the input and output power of the converter. As a result of the snubber the effective turn-off losses was reduced by 75% which results in a reduction of approximately 40% in the total switching losses.

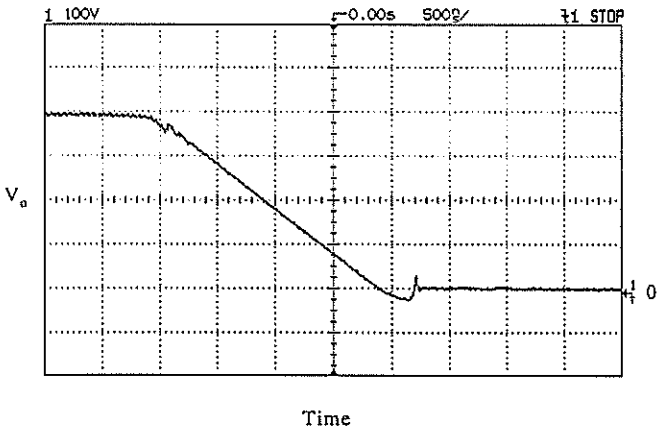

Figure 3: Turn off waveform of the IGBT module with the resonant snubber.

Future work includes an evaluation of the effect of the snubber on the EMI performance of the converter.

4 Conclusions

This paper describes a new resonant turn-off snubber with relatively small ratings for the auxiliary components and no special control requirements.

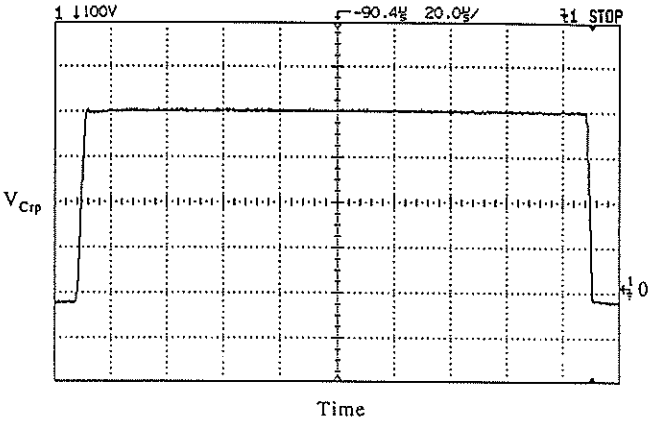

Figure 4: Voltage over resonant capacitor C_{rp}.

Compared to existing snubber topologies, the advantages of the snubber compared to the cost of the added active components makes it an attractive option to reduce turn-off losses and EMI in high power converters.

References

[1] G.A. Fisher, High power transistor inverters – potential for single device operation at 1000 A and 800 V, *16th Universities Power Eng. Conf. Rec.*, Sheffield, U.K. 1981.

[2] W. McMurray, Resonant snubbers with auxiliary switches,*IEEE-IAS Conf. Proc.*, 1989, pp. 829–834.

[3] R.W. De Doncker, J.P. Lyons, The auxiliary resonant commutated pole converter, *IEEE-IAS Conf. Rec.*, 1990, pp. 1228–1235.

[4] H.J. Beukes, J.H.R. Enslin, R. Spée, Experimental evaluation of AC/AC converter topologies in utility applications, *IEEE-PESC Conf. Rec.*, Vol. 1, 1995, pp. 517–522.

[5] H.J. Beukes, J.H.R. Enslin, R. Spée, Performance of the auxiliary resonant commutated pole converter in converter based utility devices, *IEEE-PESC Conf. Rec.*, Vol. 2, 1996, pp. 1033–1039.

[6] D.M. Divan. The resonant DC link converter - A new concept in Static Power conversion, *IEEE Transactions on Industry Applications.*, Vol. 25, 1989, pp. 317–325.

CONTROL OF A SIMULATED SINGLE-PHASE TO THREE-PHASE CONVERTER

E N Tshivhilinge M Malengret
Department of electrical Engineering, Power Electronics
University of Cape Town
mmaleng@eleceng.uct.ac.za

Keywords: Single-phase to three-phase, regulation, unity power factor

Abstract

Due to recent progress in power electronics, static single-phase to three-phase converters is gaining in acceptance [7]. Many single to three-phase converters for low cost ac motor drives have been proposed [1], however most of these converters employ many components, which add to their high cost and do not provide a regulated output with unity power factor [2]. In this paper an investigation into the performance of the regulated, power factor corrected and cost reduced single phase to three phases proposed converter is shown. The dc bus voltage of the converter is kept constant by making use of the dc bus voltage controller, the dc bus voltage is controlled by shifting the phase shift angle δ [10] between the supply and inverter, whilst maintaining the inverter as a balanced static VAR compensator. The performance of the converter with dc bus voltage controller is shown under two conditions, namely

1. Variation of the load over a specific range.

2. Variation of the input voltage with the load kept constant.

For each condition the simulated waveforms, which shows that constant dc bus voltage, near unity power factor and ac regulation is achieved.

1 INTRODUCTION

In this paper a single phase to three-phase converter is proposed, this is shown on figure 1. The converter makes use of only six switches and can deliver sinusoidal input current with close to unity input power factor under different loads. The inductor Li helps to get rid of harmonics and is needed for energy balancing and regulation. Pulse width modulation (PWM) waveforms, which were generated by simple comparison between the sinusoidal voltage (control voltage) and triangular voltage (Vtriangle) [10] controlled the switches of the proposed converter. The amplitude modulation ratio ma is given as the ratio of the sinusoidal voltage amplitude to the triangular voltage amplitude. The best method of control used was to keep m_a at unity and control the dc bus at a constant value, this ensured a regulated ac output with voltage supply variation.

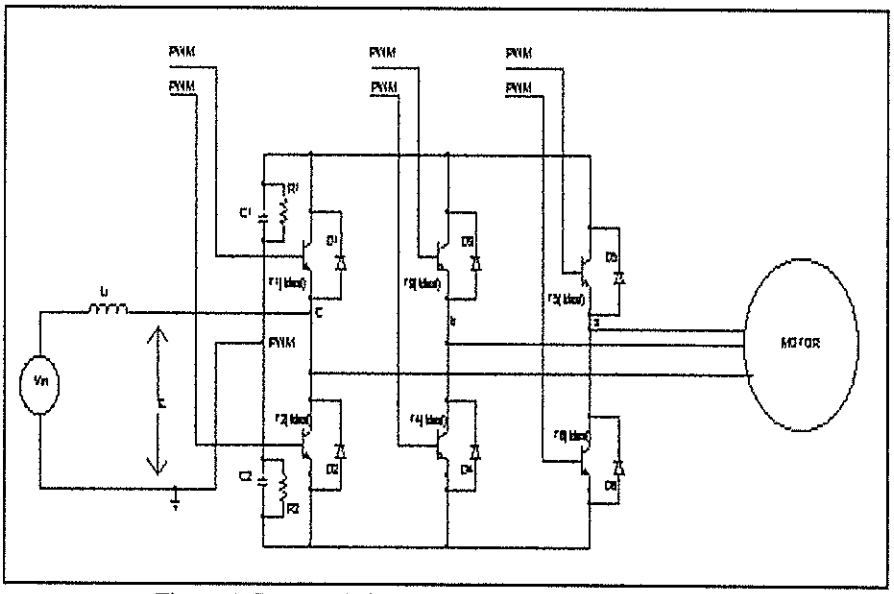

Figure 1: Proposed single phase to three-phase converter

2 OPERATION OF THE CONVERTER

For the operation of the proposed converter, front-end rectifier of the converter was considered. By controlling the phase shift angle δ, the input power can be varied as given by equation (3)[10]. The input current is given as below.

$$I_{in} = \frac{Vin\angle 0 - E\angle\delta}{jX} \qquad \text{.....(1)}$$

The average power flowing to the inverter from the source is given by the equation below.

$P_{in} = V_{in} I_{in} \cos(\theta)$ .....(2a)

Where $\cos(\theta)$ is the input power factor and θ is the angle between V_{in} and I_{in}, from triangle ΔBDC and ΔABD on figure 2

BD=IXcos(θ) = Esin(δ) .....(2b)

From equation (2a) and (2b) input power can be expressed as follows:

$$P_{in} = \frac{VE\sin(\delta)}{X} \quad \text{.....(3)}$$

Equation (3) shows the real average input power P_{in} flowing across the inductor Li from the ac mains into the converter. This equation indicates that the input power P_{in} can flow either from the source into the load or from the load into the source depending on the sign of the angle δ.

Equation (3) shows that the proposed converter can operate for example in the regenerative braking mode of an ac motor drive

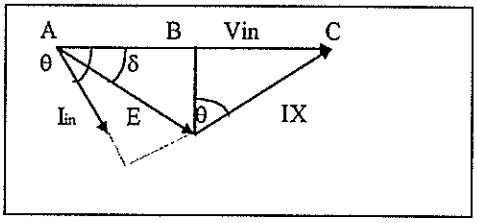

Figure 2: Phasor diagram of a front end rectifier

If the controller operates in such a way as the input average power from the supply is equal to the real average power of the load., the inverter will require no real power (except for some losses).Hence in order to balance the input power and the output load power, the following equation must be satisfied: $\frac{V_{in}E\sin(\delta)}{X} = E^2_{linetoline} G_m$ [9]. Gm is the conductance per phase of the three-phase load. From the topology of the single phase to three-phase converter proposed in this paper, a balanced system can be represented as follows:

$$\frac{E}{X} = \frac{\sqrt{3}Vin\sin(\delta)}{3X^2 Gm} \quad \text{...(4), where E is voltage between c and capacitor mid point n (see figure 1)}$$

Equation (4) is satisfied if the operating point of the inverter is on a circle c of diameter $D = \frac{\sqrt{3}Vin}{3X^2 Gm}$ and it can be constructed as shown on figure 3.

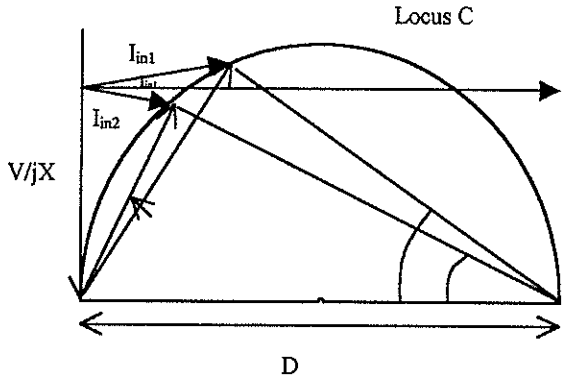

Figure 3 Locus of operating point for power balance system

Any operating point on the circle represent a power balance between input power and power delivered to the load . Hence a constant dc capacitor voltage is achieved. Varying the angle δ is a necessary and sufficient condition to ensure a constant dc bus voltage. Variation of supply voltage and load can be compensated under the required range with judicious choice of DC bus voltage and inductance Li. Hence having kept the amplitude modulation ratio constant , a constant DC bus naturally results into a constant three phase output voltage under input voltage and load variation.

3 CONTROL IMPLEMENTATION

The controller feedback regulates the dc bus voltage by varying the angle δ of the voltage control (Vcont). Figure 4 shows the block diagram of the dc bus voltage controller, which compares the dc bus voltage with the reference voltage. From the reference between Vdc and Vref, the controller will then shift the control voltage by angle δ required to keep the dc bus voltage constant at a specified value [10] and compare it with Vtri to create the

PWM. From figure 4 Vref is the voltage that the controller will force the dc bus voltage to and keep it constant at that value.

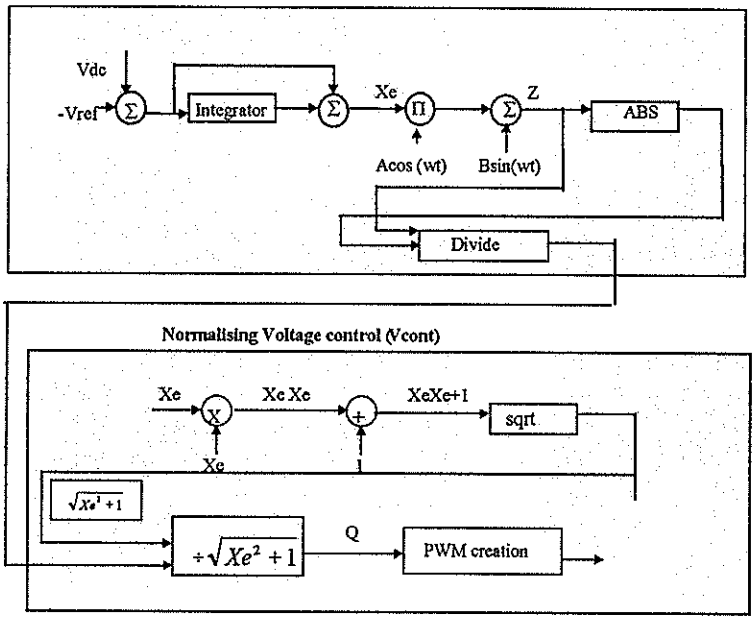

Figure 4: Block diagram for dc bus voltage feedback controller

The constant amplitude of the function Z was obtained, by dividing it by its magnitude. The sinusoidal function Z on figure 4 is mathematically expressed as follows:

$$Z = Xe\cos(wt) + Sin(wt)$$
$$= \cos(wt)\left[\frac{1}{2}(Xe+1)+\frac{1}{2}(Xe-1)\right]+$$
$$j\sin(wt)\left[\frac{1}{2}(Xe+1)-\frac{1}{2}(Xe-1)\right] \quad (5)$$

To normalise the function Z, the sinusoidal waveform must be divided by its magnitude. By either increasing or decreasing the magnitude of BC, one can therefore control the angle δ of the control voltage. The output function Q (see figure 4) is the sinusoidal function that is shifted by the required angle δ and has the amplitude of one, and is used to create the PWM signal.B=1 is the amplitude of component in phase with the supply Bsin(wt). A = 1, is the amplitude of Acos(wt) at 90 degree . X is the voltage difference between Vdc and Vref Y = A.Xecos(wt).
Z = A.Xecos(wt) + Bsin(wt). Q is the normalised value of Z and has the angle δ.

RESULTS

In order to test the performance of the proposed converter under various supply voltage and load conditions, Software simulation package Microsim V8.0 was used. The load resistance was varied between 6 ohms and 16 ohms. The desired dc bus was set at 460V. With voltage feedback controller the dc bus voltage was kept constant at approximately 460 V. Figure 5 and figure 6 shows dc bus voltage, input voltage and input current for Rload of 6 ohms and 16 ohms respectively. For power load between 10kW and 26kW, the single phase to three phase converter is able to supply power to the load at close to unity input power factor. Comparing the phase shift angle between the input voltage and the input current on the waveforms shown on figure 5 and figure 6 can see this.
Figure 7 and figure 8 shows the dc bus voltage can be constant when the input voltage varies by plus and minus 10 %.

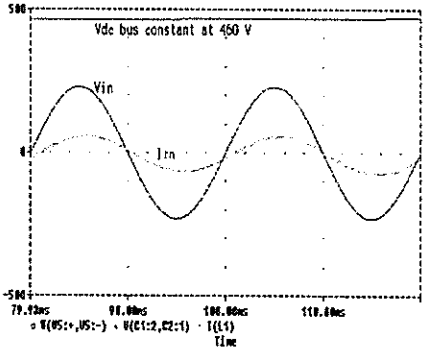

Figure 5: Constant DC bus voltage at 460 V, load of 6 ohms per phase and single phase input of 230V.

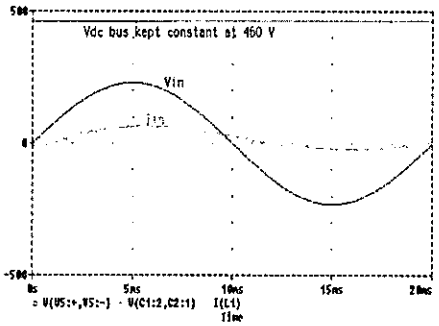

Figure 6: DC bus voltage constant at 460V,load per phase 16 ohms and single phase input voltage of 230V.

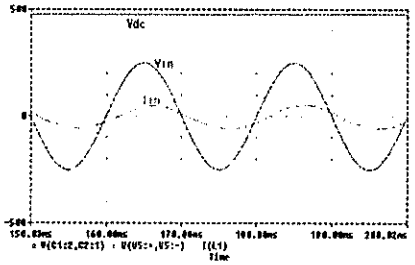

Figure 7: DC bus voltage constant at 460V,load per phase 6 ohms and single phase input voltage of 210V.

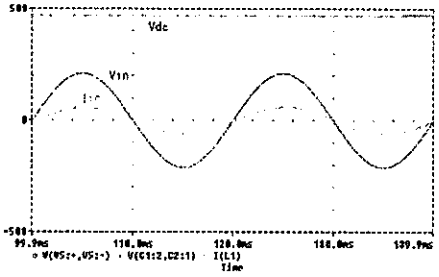

Figure 8 DC bus voltage constant 460V,load per phase 16 ohms and single phase

CONCLUSIONS

A new single phase to three-phase converter has been proposed. The proposed converter is capable of driving a three-phase load from a single-phase ac main while maintaining sinusoidal input current with input power factor at close to unity [10].

The dc bus voltage feedback controller was used to keep the dc bus voltage constant at a desired value under different loads. It was also used to keep the dc bus voltage constant for a particular load when there is variation in the input voltage[10]. A constant dc bus voltage implies constant ac voltage output with amplitude modulation ratio held constant.

REFERENCES

[1] N E Prasad and A Rahman, *A new single phase to three phase converter with active input current shaping for low cost ac motors*. IEE Trans. On industry Appl vol 29 no. 4 July/August 1993 pp806-813.

[2] S I Kahn and M H Rashid, *A novel single phase to three phase static converter*. IEEE Trans. on industry Appl vol 25 no 1 Jan/Feb 1989 pp143-151.

[3] N.E Mahao, *Economics of converters in rural electrification*. 1995 thesis University ofCapeTown, pp75-80

[4] L H Soderholm and C M Hertz, *Automatic balance of three phase motor currents for variable motor loading using a static phase converter*. IEEE Trans. on industry Appl. vol26 no4 July/Aug 1990 pp679-681

[5] M G Jayne, S R Bowes and B M Bird, *Developments in sinusoidal PWM inverters*. University of Bristol, England. Pp145-154

[6] *On the ordinary and modified sub-harmonics control*. Control in power electronics and electrical drives pp155-163

[7] G T Kim and T A Lipo, *VSI-PWM rectifier/inverter system with reduced switch count* pp1331-1338

[8] *An improved high power factor and low cost three phase rectifier*. IEEE Trans. on industry Appl vol 33 no 2 March/April 1997 pp485-492

[9] M. Malengret *Theory of operation of static VAR Generator (SVG)*. University of Cape Town.

[10] Tshivhilinge E N, *Simulation of single phase to three phase converter using Microsim V8.0 with dc bus voltage regulation using feedback controller*. BSc thesis in partial fulfilment of a degree in Electrical Engineering, University of Cape Town. October 1997.

Neural Network Controlled Boost Rectifier

C.A. Worthmann, G. Diana

Department of Electrical Engineering, University of Natal, Dalbridge, 4041, South Africa
worthmannc@eng.und.ac.za, gdiana@eng.und.ac.za

ABSTRACT

This paper describes the investigation of an continuous on-line trained (COT) Artificial Neural Network (ANN) controlled boost rectifier. Specific control of this type is used for Variable Speed drives (VSD's), to overcome voltage dips on the mains supply. A energy investigation will also be performed on the system, to determine its viability for practical uses in industry. The paper will analyse simulation results of an ANN controlled Variable Speed drive System.

1. Introduction

Most AC variable speed drives employ the cascaded Voltage Source Inverter (VSI) configuration, shown in figure 1.1.

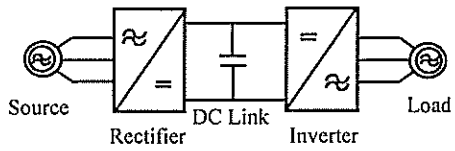

Fig. 1.1 Voltage Source Inverter

The rectifier shown in Fig. 1.1 is normally a six-pulse diode stack. Unfortunately this results in non-sinusoidal currents in the AC supply, which generates harmonic voltages in the supply impedance, thus resulting in harmonic distortion of the AC supply voltage.

AC Variable speed drives are also susceptible to voltage dips present in the mains supply. In addition VSD's in the larger power ranges employ a means to regenerate energy back into the mains for economical reasons, under braking. This is normally done by using a thyristor controlled inverter unit making the system even more susceptible to voltage dips. Voltage dips are generally caused by a varying input impedance, and due to a mains fault or mains disturbance. Thus the supply can no longer source input current, causing a drop in the DC link voltage, and a reduction in the control capabilities of the variable speed drive.

The proposed solution to voltage dips, is to use a neural network controlled boost rectifier. The standard boost rectifier system has its own problems, and the controller must be designed to account for the continually changing system impedance that it sees back into the mains supply. An investigation will be performed, to determine the feasibility of using a neural network controlled boost rectifier to compensate for impedance changes due to the self learning properties of the neural network. It is proposed to use a COT ANN, to perform the control, so that the controller can continuously update according to the ever changing mains supply. This should allow for better stability, and a more reliable system.

2. System Outline

To compensate voltage dips, it is viable to use a boost rectifier in place of the diode rectifier, to achieve a constant DC link voltage. To achieve this, the neural network has to monitor the supply voltages and currents, as well as the DC link voltage and current, as shown in Fig. 1.2.

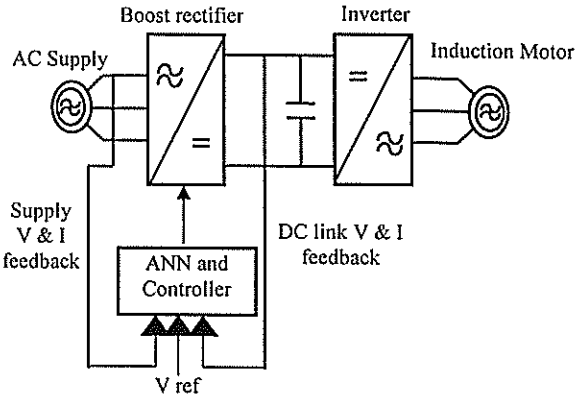

Fig. 2.1 Classified control loops

The advantages of using a COT ANN, is that if it may be applied to any Variable Speed Drive, and should be able to operate without any control changes. However to gain an idea of the nature and form of COT ANN as well as its operation under the non linear effects of an IGBT inverter as a boost rectifier, a comprehensive investigation of an existing COT ANN VSD system [BURTON] was first made.

3. Investigation of the Performance of a Cot ANN applied to a VSD

The observations when practically applying ANN's [BURTON] were that the neural network operation was dependent on a certain number of factors, namely:

1) Type of pre-training used,
2) ANN sampling rate,
3) Voltage constant Cv,
4) ANN learning rate
5) ANN momentum term, and
6) The number of hidden neurons .

The COT ANN considered for this investigation, utilises the back-propagation training method, to update the ANN's weights. Simulations were performed in CASED, to assess the viability of utilising an ANN to control the Boost rectifier under voltage dip conditions.

A model for the neural network was derived from previous work [BURTON], and for the Hanning PWM controller as well as for the induction motor and the mechanical load, and implemented in CASED, as shown in Fig. 3.1. These simulations were performed to become familiar with ANN's, and its operation under the non-linearities that would be experienced in practice.

Essentially the CASED simulations were performed to test what conditions were required by the neural network, so that it could operate and be stable with the inverter in place on a VSD, as previous work had not taken this into consideration [BURTON] .

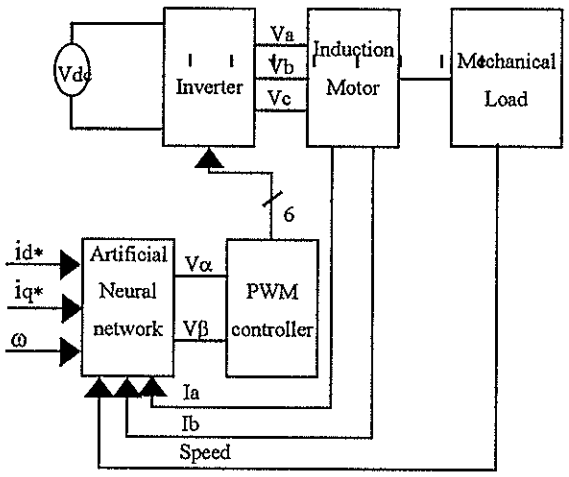

Fig. 3.1 CASED simulation Block

CASED simulations are provided for the case when the motor current is set at 1 pu, the supply frequency is 50 Hz and the motor initially at standstill.

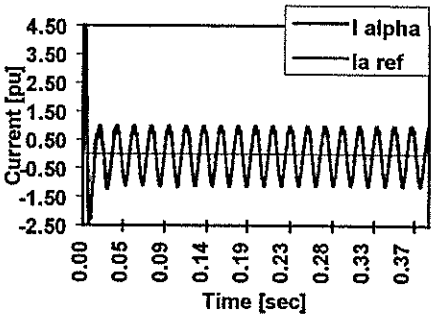

Fig. 3.2 Phase A supply current and ANN alpha current, with a ANN sampling frequency (fs) of 5 kHz, a learning rate (b) of 0.01, and a voltage constant (Cv) of 0.6

These results indicate that the neural network is able to operate in a stable state, to perform the required control. A plot was taken of the error generated by the ANN while tracking the supply current (shown in Fig. 3.3).

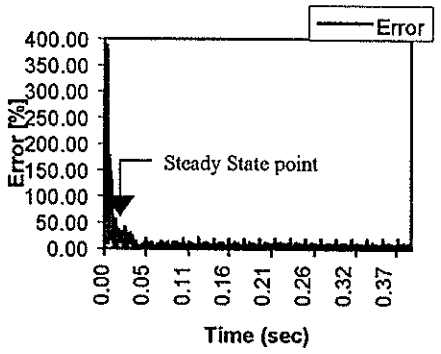

Fig. 3.3 Current tracking error

The following simulation result shows a case when the ANN becomes unstable, supply current remains at 1 pu, and the supply frequency at 50 Hz.

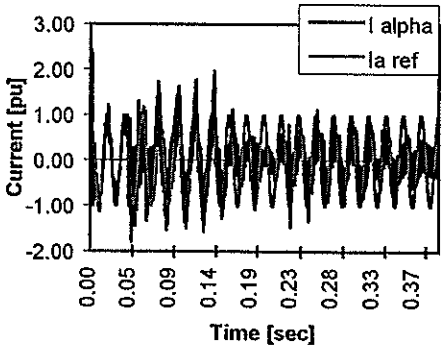

Fig. 3.4 Phase A supply and ANN alpha currents

It can clearly be seen that the ANN becomes unstable. The simulations show that the ANN can track the supply current up to supply frequencies of 50 Hz and higher, but there are a number of factors that affect the stable operation of the ANN controlled. It was found that the ANN's stability is dependent on a large number of its internal variables and constants. These dependencies were investigated, and plotted. The first plot shows the dependency from the time of start-up, in the first 20 milliseconds. All these simulations were taken while the ANN started with random weights. The second plot shows the dependencies of the ANN after steady state has been achieved.

4. ANN Stability considerations

Supply current dependency

As the current is increased, it can be seen that the ANN tracking error becomes smaller. Thus it can be seen that stability problems may be experienced at low supply currents.

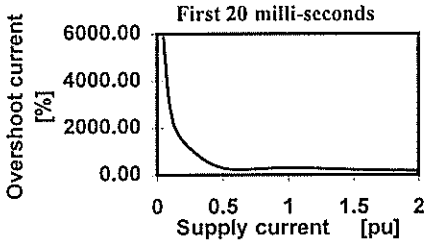

Fig. 4.1 Current dependence at start-up, fs = 10kHz, b = 0.01, Cv = 0.6, and Supply freq. (f) = 50 Hz

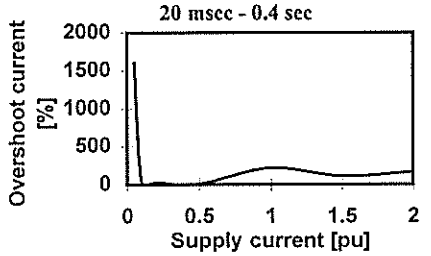

Fig. 4.2 Current dependence after steady state, fs = 10kHz, b = 0.01, Cv = 0.6, and Supply freq. (f) = 50 Hz

Supply frequency dependency

The ANN displays instability at large supply frequencies.

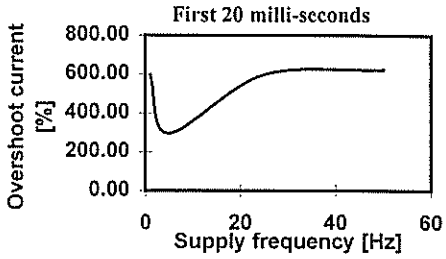

Fig. 4.3 Frequency dependence at start-up, fs = 10kHz, b = 0.01, Cv = 0.6, and Supply current (I) = 0.5pu

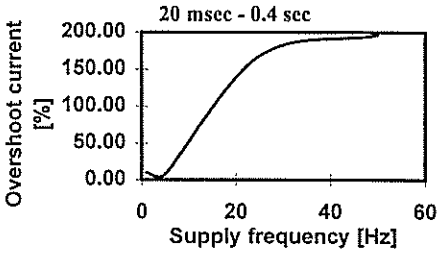

Fig. 4.4 Frequency dependence after steady state, fs= 10kHz, b = 0.01, Cv = 0.6, and I = 0.5pu

ANN learning rate dependency

To be able to operate the ANN at high frequencies, it is found that the learning rate must be low to achieve stability. This means that the ANN is allowed more time to learn the system, to ensure stability .

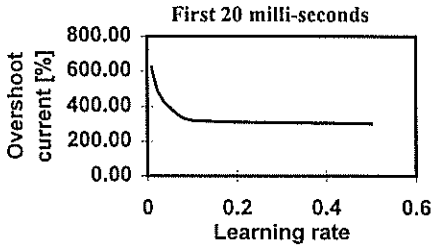

Fig. 4.5 ANN Learning rate dependence at start-up, fs = 10kHz, Cv = 0.6, f = 50Hz and I = 0.5pu

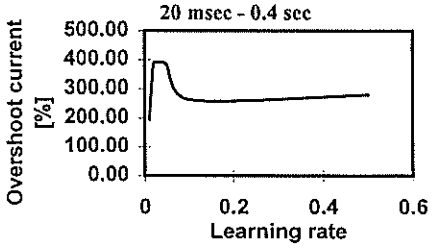

Fig. 4.6 ANN learning rate dependence after steady state, fs = 10kHz, Cv = 0.6, f = 50Hz and I = 0.5pu

ANN voltage constant (Cv) dependency

At start-up a large Cv is required, but once steady state is achieved, it becomes apparent that a smaller Cv is required for optimal ANN operation .

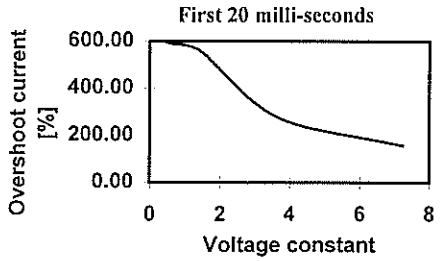

Fig. 4.7 ANN Voltage constant dependence at start-up, fs = 10kHz, b = 0.01, f = 50Hz and I = 0.5pu

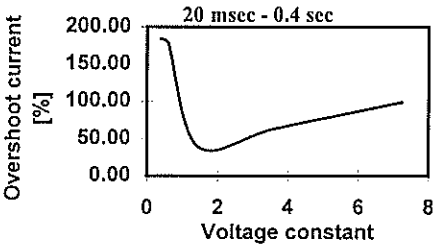

Fig. 4.8 ANN Voltage constant dependence after steady state, fs = 10kHz, b = 0.01, f = 50Hz and I = 0.5pu

ANN sampling rate dependency

A low start-up sampling rate is required, but during operation, a sampling rate of between 6 and 8 kHz is required for ANN stability.

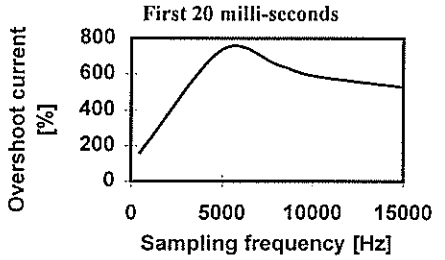

Fig. 4.9 ANN sampling rate dependence at start-up, Cv=0.6, b = 0.01, f =50Hz and I=0.5pu

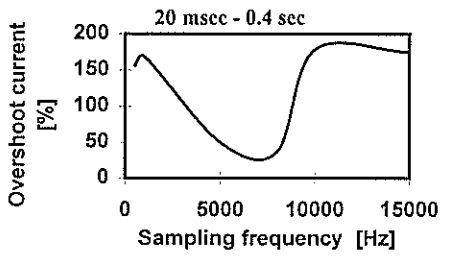

Fig. 4.10 ANN sampling rate dependence after steady state, Cv =0.6, b =0.01, f=50Hz and I=0.5pu

As can be seen from all the simulation results shown above, the ANN is dependent on a number of variables and constants, and all these dependencies need to be addressed when designing the ANN, to obtain a stable and well damped response with a fast speed of response.

The most important factor obtained from these simulations, is that an ANN can in fact be used to control a VSD system. In practice the ANN will be implemented on a PC32 DSP(digital signal processing) card, so that the high sampling speeds can be achieved.

7. Conclusion

A mathematical model of the system was developed, and simulated in CASED, in order to investigate the viability of using a ANN controlled Boost rectifier, to overcome voltage dips. The simulation results indicate that this method can be used for voltage dip protection, but the question still to be answered is, is it possible to obtain these results practically?

Pulse width modulation (PWM) switching sequences will be used for the boost rectifier. A card was designed incorporating the Hanning PBM 1/87 chip, to generate these PWM pulses. The card was designed to plug onto the expansion port of the PC32 DSP card, thus allowing the DSP card full control. The DSP is interfaced to the Computer via interface software called Hypersignal. User blocks will be written here, to drive the PWM card, and a block will be written to perform the operation of the ANN. This DSP based ANN will hopefully provide the high speed calculations and sampling rates that are required for the ANN to operate successfully. Further work will be to implement the ANN, and then to collaborate with the simulation results.

8. References

[1] Pinheiro H, Joos G, Khorasani K, "Neural Network-Based Controllers for Voltage Source PWM Front End Rectifiers", IEEE 21st International conference on inductrial electronics, control and instrumentation, Orlando, 1995, pp 488 - 493

[2] Lau C, "Neural Networks Theoretical Foundations and Analyses"

[3] Burton B, "Analyses and practical implementation of a continually online trained artificial neural network to identify and control VSI fed induction motor stator currents"

MODELLING OF THERMAL TRANSIENTS OF UNDERGROUND HIGH VOLTAGE CABLES

F Smith,

Sastech,
Secunda.

J P Holtzhausen

Department of Electrical and Electronic Engineering
University of Stellenbosch
Stellenbosch.

Underground cable systems are 10-20 more expensive to install than their overhead counterparts. It is therefore sensible to utilize them optimally for as long and as safe as possible. Previous papers [1,2,3] described the experimental set-up and the development of an equivalent electrical network for thermal simulations. The simulated and experimentally obtained transients were compared and a optimised model was developed. This paper summarises the work by applying the model to do a thermal analysis on three buried cables.

Keywords: thermal transients, electrical analogy, simulation, XLPE insulated cable

1. INTRODUCTION

Cross-linked polythene (XPLE) is a relatively new material (compared to paper and lead) when used as a dielectric in high voltage underground cables. Previously ordinary polyethylene was used, but cross-linking improves the thermal behaviour of the insulating material and increases its thermal limit to 90°C. Sustained operation above this level, will cause the insulation to soften and the copper conductor will sink into the insulation due to gravity. This will cause deformation of the electric field, a decrease in the stress handling capability of the cable and a derating with regards to its voltage capacity.

A convenient way of dealing with conduction heat flow problems, is to make use of electrical analogies. Heat flow through a thermal resistance can be calculated using the following equation:

$$P = \frac{\Delta T}{R_t} \qquad (1)$$

In this equation P is the heat generated in Watts, ΔT the temperature rise with respect to the ambient (in °C) and R_t is the thermal resistance given in K.m/W. Equation (1) is also known as Ohm's thermal law and the following analogies with respect to electrical quantities are identified:

ΔT (temp. difference)	$\leftrightarrow \Delta V$ (volts)
R_t (thermal resistance)	$\leftrightarrow R_e$ (electrical ohms)
P (heat in Watts)	$\leftrightarrow$ I (ampere)

Likewise, the thermal counterpart for capacitance is thermal capacitance. It is defined as the amount of heat (in Joule) absorbed per centigrade temperature rise. The product of the thermal resistance and the thermal capacitance is the thermal time constant of an object.

When considering heat dissipation from an underground cable, the thermal resistance and capacitance should be considered as distributed parameters radially away from the centre of the cable. The approach followed in this investigation is to divide the cable and the surrounding soil into cylindrical layers with a thermal resistance and capacitance calculated for each layer. The result is an equivalent lumped parameter network similar to the one shown in Figure 1.

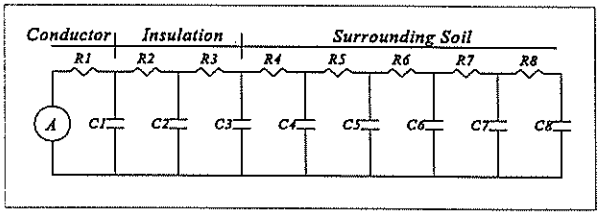

Figure 1: *Equivalent electrical ladder network*

Once the equivalent network has been developed, the transient heat flow problem can be solved with the electrical transient simulation packages such as EMTP.

2. PROBLEM STATEMENT

In the following sections the model that was developed from the background given in the previous paragraph, is applied to a practical example to illustrate how it can be used.

A typical application is shown in Figure 2, detailing three different possible cable configurations. In Configuration A, the cables are buried at a depth of 0.75

m in a flat formation with a horizontal spacing equal to the outer diameter of the cable, d. The soil characteristics are given in Table 1 and the boundary isotherm [3] is placed at a distance of 40 mm from the centre of the cable. The initial conditions for Configurations B and C are the same but the horizontal spacing between the cables is 1.5 times the cable diameter for B and 2 times the cable diameter for C, respectively.

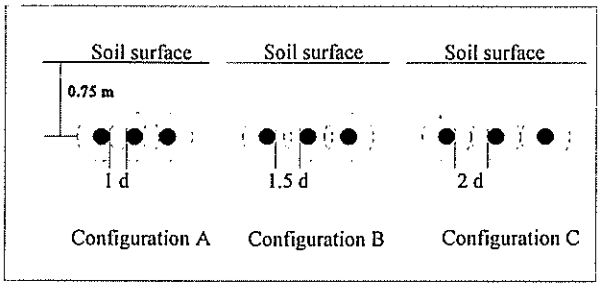

Figure 2: *Circuit configuration for example.*

3. THE PRINCIPLE OF SUPERPOSITION

The model was developed from measured data obtained for a single 150 mm² 6.35/11 kV buried cable [3]. There were no other heat sources in the vicinity of the cable and therefore proximity effects could be ignored. It is assumed that the thermal response of the above cable will be similar to that of bigger cables, as far as the shape and the location of the isothermal lines in the soil surrounding the buried cable is concerned. The procedure used in this example to determine the continuous current carrying capacity of the cables, can therefore also be used to determine the rating for bigger cables. It is only necessary to change the component values in the equivalent network model to account for the new dimensions and components of the bigger cable.

In this example there are three equally loaded cables that can be represented by three equal heat sources parallel to each other. The principle of superposition can be used to determine the influence of the neighbouring cables on the current carrying capacity of any one of the three cables as illustrated in Figure 3.

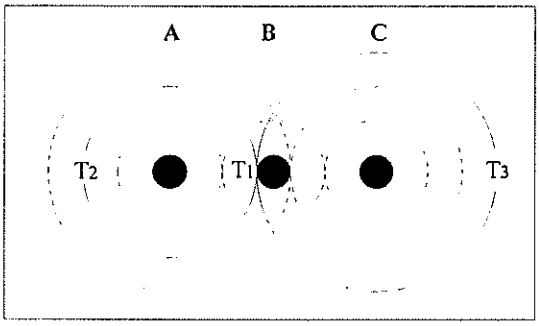

Figure 3: *Graphical illustration of superposition*

According to the superposition principle the temperature at any point is the sum of the temperature contributions of the three cables. The dotted lines represent the isothermal lines as they would appear for each of the three single buried cables. Figure 3 shows that the surface temperature on the left side of cable B, is the sum of its own heating T_1, the temperature as represented by the appropriate isotherm from cable A, T_2 and the temperature from the indicated isotherm from cable C, T_3.

By using the heat flow / electric current analogy, the new enhanced conductor temperature can be calculated using Equation 1 (Ohm's Law) and the illustration in Figure 4.

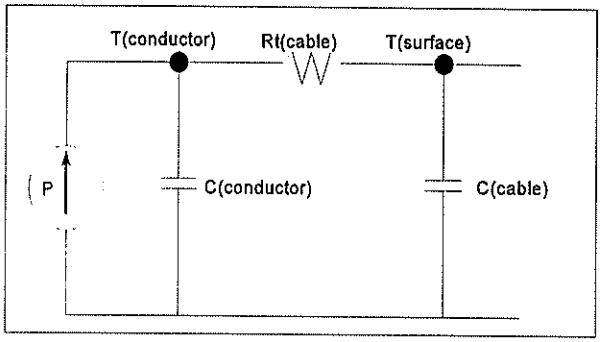

Figure 4: *Partial equivalent thermal circuit*

From

$$\frac{T_{conductor} - T_{surface\ (new)}}{R_{t\ (cable)}} = P$$

follows that

$$T_{conductor} = P \times R_{t\ (cable)} + T_{surface\ (new)} \qquad (2)$$

with

P = Heat flow from conductor (Watt)
$R_{t\ (cable)}$ = Total thermal resistance (K.m/W)
$T_{surface\ (new)}$ = New surface temperature

For this type of application, superposition is only valid if the soil is completely homogeneous, that is, without dried out zones in which the thermal resistivity is higher than that of the bulk material. Therefore it has to be assumed that the size of the dried out area (enclosed by the boundary isotherm) is sufficiently small compared to the ambient so that results of reasonable accuracy will still be obtained.

4. THE MODEL

The ladder network shown in Figure 1 was used. The components were calculated with Eqs. 3 and 4:

$$R_t = \frac{\rho_t}{2\pi} \ln \frac{r_2}{r_1} \quad (3)$$

where

R_t = Thermal resistance, K.m/W
ρ_t = Thermal resistivity, K.m/W
r_2 = Outer radius of cylinder, m
r_1 = Inner radius of cylinder, m

$$C_t = \kappa_t \pi (r_2^2 - r_1^2) \quad J/K.m \quad (4)$$

where

C_t = Thermal capacitance
κ_t = Heat capacity of the medium, $J/K.m^3$
r_2 = Outer radius of cylinder, m
r_1 = Inner radius of cylinder, m

The constants for the various materials are those shown in Table 1.

5. RESULTS OBTAINED WITH THE MODEL

Simulations were performed with currents varying from 400 Ampere (90% loading) to 630 Ampere (142% loading). The data was analysed on a spreadsheet and the results are as shown in Figure 5. The data shown in Figure 5 shows the temperature rise on the conductor with respect to time when ideal conditions pertain. These conditions are: moist soil, no heat memory and no other heat sources. It appears that, under these conditions with a 630 A loading, the cable temperature will stabilize at about 80°C after 18 days. The cable will therefore not be damaged.

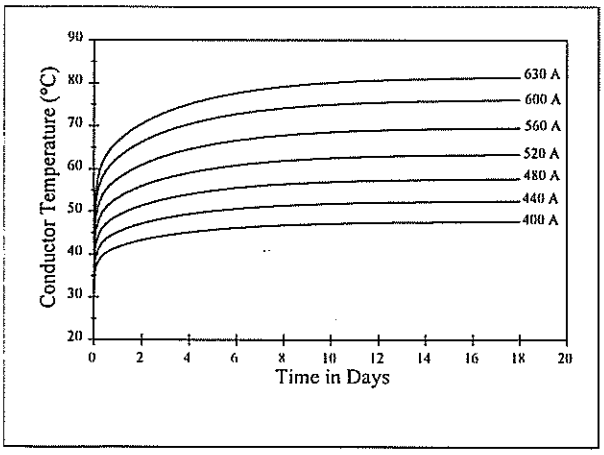

Figure 5: *Conductor temperatures without the heating effect of the surrounding cables.*

In Figure 6 the heating effect from neighbouring cables (typical flat formation) have been included. From this it is clear that a loading of 520 A will start to damage the cable after 5 days. For continuous loading the maximum sustainable current is 480 A. Figures 7 and 8 gives a different view of the simulation results. Figure 7 illustrates the effect of mutual heating on the maximum temperature (maximum was taken to be the point where the temperature stabilised after 18 days - Figures 5 and 6).

Figure 8 gives an indication of the safe permissible working area for the cable in a 3 phase flat formation. Due to the thermal time constant of the cable and its

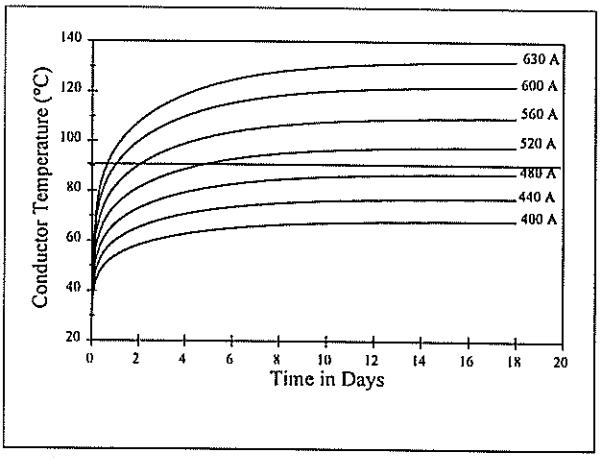

Figure 6: *Conductor temperatures as calculated with the superposition principle to include the effect of mutual heating (1 cable diameter spacing between cables).*

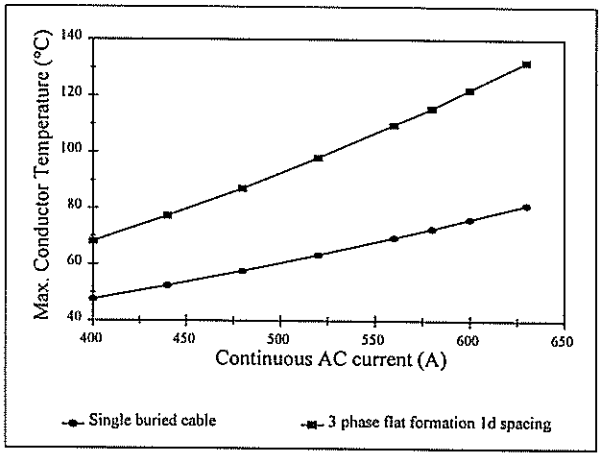

Figure 7: *Maximum conductor temperature against applied continuous AC current for the different laying configurations.*

surroundings, the cable can safely pass a load of 550 Ampere (124%) for at least 2 days. By then the temperature would have reached 90°C and therefore the load has to be dropped to 500 Ampere. This will allow at least another 7 days of operation. If continuous operation is required after this time, the load should be dropped to 480 Ampere.

As mentioned previously, this interpretation is idealistic. Another factor that has to be taken into account, is the heat memory of the cable and its surroundings. This has

Table 1: *Thermal characteristics and cable dimensions for example.*

	Thermal resistivity (K.m/W)	Thermal Capacity ($J/K.m^3$)	Inside radius (mm)	Outside radius (mm)	Diameter (mm)
Copper Conductor	negligible	3.45e6	0	7.4	14.8
XLPE Insulation	3.5	2.40e6	7.4	11.75	23.5
PVC Protection	5	1.70e6	11.75	12.75	25.5
Dried soil	2.2	1.82e6	12.75	40	80
Moist soil	1.5	1.97e6	40	750	1500

an effect on the thermal time constant during the heating and cooling cycles of the cable and has to be catered for during loading. From Figure 8 follows further that as expected, the maximum temperature decreases with increase in horizontal spacing between the cables / heat sources.

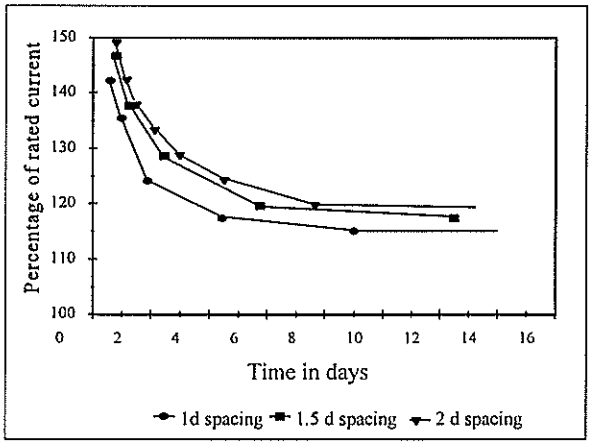

Figure 8: *Comparison between the maximum permissible continuous currents for different horizontal spacings.*

6. CONCLUSIONS

It has been previously shown that the developed network model is able to accurately simulate the transient response of the experimental set-up [4]. This paper illustrated an approach of solving thermal transients with electrical analogies known to electrical engineers (people most likely to design buried cable systems). It also gave an indication of the effect of nearby heat sources on the capacity of a buried cable, eg. spacing between cables in a flat formation or steam pipes crossing the cables.

It was also mentioned that although a fair amount of information can be obtained from the model and its simulation results, exact data on the environment is necessary.

The primary function of this model would then be to give the design engineer an indication of what kind of behaviour can be expected from his cable system. He can then decide to improve the model with more accurate data should a better simulation be required.

7. REFERENCES

[1] F. Smith and JP Holtzhausen, "The thermal modelling and analysis of underground cable systems", SAUPEC 94, University of Cape Town,

[2] F. Smith and JP Holtzhausen, "Experimental investigation and modelling of thermal transients of underground high voltage cables", UPEC 94, University of Galway, Ireland

[3] F. Smith and JP Holtzhausen, "Experimental investigation and modelling of thermal transients of underground high voltage cables", SAUPEC 95, University of Pretoria

[4] F. Smith, "Experimental investigation and modelling of thermal transients of underground high voltage cables", Masters Thesis presented in 1995, University of Stellenbosch.